Geographia Technica

Geographia Technica

Technical Geography

an International Journal for the Progress of Scientific Geography

2024 – No. 2

Cluj University Press

C o n t e n t s

Geographia Technica

GEOGRAPHY'S FUTURE IS TECHNICAL

- a letter from the editor -

Ionel HAIDU [1]

Abstract

Geography has evolved from a descriptive discipline, based on exploration and mapping, to a technical and analytical science, capable of offering solutions to the complex challenges of the modern world. The transition towards a technical Geography was facilitated by the introduction of advanced statistical methods and new technologies such as GIS, remote sensing, LIDAR, UAV, etc. Autocorrelation and frequency are core concepts of the new Geography but they are common also in research from technical fields such as Engineering or Physics, which clearly proves that Geography is based on technical foundations similar to those used in other applied sciences. However, in certain states, Geography did not sufficiently adopt these tools, which led to a decrease in its relevance. In order to regain its significance, Geography must become a prospective science, capable of anticipating and manage natural and social phenomena. Universities promoting technical Geography are ready to train future leaders, while those that remain anchored in classical approaches risk becoming irrelevant. Geography's future is therefore inextricably linked to the integration of advanced technologies and analytical methods

Key-words: *GIS, Remote Sensing, LIDAR, UAV, Autocorrelation, Frequency, Antefactum science, Geographia Technica, Technical Geography, Future of Geography, Technical integration*

1. INTRODUCTION

Geography as a discipline had a significant evolution from a descriptive science, focused on the exploration and mapping of the world, to a technical and analytical science, capable of offering solutions to the complex problems of the modern world. The book edited by Goodchild & Janelle, (2004), discuss the integration of spatial analysis and technical methods into social science geography, illustrating how geography's analytical tools can solve complex problems in areas such as urban planning, environmental management, and social policy. The Dictionary of Human Geography edited by Gregory *et al.*, (2009) details the historical and technical evolution of geography, describing how advancements in technology have reshaped the discipline into a science capable of addressing complex modern issues. It covers key concepts in human and physical geography that underscore this transition.

In recent years, more and more sources support the idea that Geography as a science, but also as an encyclopedia, is in a real transition from traditional mapping to a technical science through the adoption of advanced digital tools and techniques. For instance, the video segment of Penn State Public Broadcasting *Geospatial Revolution* (2024) explores the impact of these technologies on societal understanding and daily life, showcasing how tools like GIS and satellite data enable researchers to visualize spatial patterns and temporal changes globally. This digital evolution has also made geography a vital part of addressing contemporary global challenges, including climate change and resource management. The technical transformation of Geography has not only expanded its applicability into various fields, but it has also fundamentally changed the way we understand and manage the natural and social phenomena.

[1]*Université de Lorraine*, *Laboratoire LOTERR-EA7304, 57045 Metz Cedex 01, France,*
ionel.haidu@univ-lorraine.fr

In this essay, I will explore the arguments that support the claim that **Geography's future is, undoubtedly, technical,** highlighting both the discipline's stages of development and the impact of the technical methods on the research and applicability of Geography in society.

2. THE TRANSFORMATION OF GEOGRAPHY: FROM THE DESCRIPTIVE TO THE ANALYTICAL AND TECHNICAL SCIENCE

The history of Geography has started with the description and representation of the world known by maps and empirical observations. In its classic period, Geography was predominantly descriptive and it had a **postfactum role**, that is it explained phenomena that have already happened, offering retrospective perspectives on the environmental, climate and human activities changes. However, with the technological progress and development of quantitative methodologies, Geography has begun to change into an **analytical and technical science.**

At the beginning of the 20th century, Geography has started to integrate more and more quantitative models to understand the relationships between natural and human phenomena. The so-called *Quantitative Revolution* (Barnes, 2001) has set the basis of modern Geography, in which statistical methods and quantitative analyses were essential for describing and predicting spatial and temporal patterns. The book of Castree et al., (2013) provides an excellent overview of major concepts in human geography, including the historical development of geography as a discipline, the impact of the Quantitative Revolution, and the role of technologies like GIS and remote sensing.

The introduction of the *Geographic Information Systems (GIS)* and of the technologies such as *remote sensing* and *spatial modeling* represented a major technological leap, which consolidated Geography as an applied science, offering practical solutions for modern challenges.

3. THE MINIMIZATION OF THE ROLE OF GEOGRAPHY: AN EFFECT OF THE LACK OF TECHNICAL INTEGRATION

Over the last decades, in some countries and universities, Geography has suffered a *depreciation* of its role in education and society. This trend is partially the result of the perception that Geography is a discipline limited to the description of landscapes and the memorization of maps.
Lambert & Morgan (2010) explore issues in geography education across various countries, discussing how traditional teaching methods contribute to the discipline's decline in relevance. It advocates for incorporating technical skills like GIS to renew geography's appeal and importance.

In many educational systems, such as those in the United States or France, Geography has been reduced to a secondary component of social studies, losing ground to other disciplines that were more technical or oriented towards exact sciences. Bednarz *et al.,* (2013) addresses challenges in geographic education, specifically noting the lack of technical skills integration in many curricula and its impact on geography's perceived relevance in modern education. It highlights how GIS and other tools can enhance geography's role in science, technology, engineering, and mathematics.

This minimization may be directly correlated with the lack of integrating the technical methods into the teaching of Geography. In countries like Romania, Italy or Spain, Geography often remains a classical science focused on the description of the geographical phenomena without using enough technologies such as GIS or remote sensing. Without a promotion of the technical aspects, Geography risks to be perceived as irrelevant for the contemporary challenges, which leads to the decrease of interest in this discipline in schools and universities.

4. THE NEED TO TRANSFORM GEOGRAPHY IN A PROSPECTIVE SCIENCE

To regain the relevance and to respond to the needs of the society, Geography must evolve from a ***postfactum* science** to an ***antefactum* science**. A prospective approach that anticipates the geographical phenomena and provides proactive solutions, is essential in a constantly changing world.

Abler (2004) supports the idea of the need for a prospective shift in geography, emphasizing the role of technological advancements in fostering a predictive approach. Abler argues that geographers can use spatial models and data analytics to anticipate social and environmental changes. Goodchild (2010) provides insights into how GIS and geospatial technologies have expanded the role of geography into predictive and proactive realms. He discusses the potential for GIScience to anticipate and manage environmental risks and support sustainable development through real-time and predictive modeling.

The technical approaches allow Geography to become an **anticipatory science**. For example, the predictive models based on geospatial data collected via remote sensing and monitoring sensors enable the early identification of natural risks such as floods, earthquakes or climate changes and help with the efficient management of the natural resources and urban development. Technical Geography not only explains past phenomena, but it also plays an active role in shaping the future.

5. THE INCREASE OF THE TECHNICAL CHARACTER OF GEOGRAPHY. BEYOND PHYSICAL GEOGRAPHY

Physical Geography was the first branch of Geography that has benefited from the development of modern technologies. Techniques such as remote sensing and LIDAR are used to monitor the changes on the surface of the Earth, from soil erosion to extreme weather events. But this transition is not limited to physical Geography. **Land use planning** has become a profoundly technical discipline, using GIS for urban planning, infrastructure and resource management.

Jensen (2006) provides comprehensive insights into remote sensing and its applications in physical geography, including monitoring soil erosion, weather events, and other earth surface changes. It also highlights the role of LIDAR in studying landscape and environmental changes.

Human Geography and **Regional Geography** have also become increasingly technical. Batty (2013) explores the integration of GIS and spatial analysis in urban planning, discussing how geospatial technologies are essential for resource optimization, accessibility, and the creation of smart cities. This book covers technical advances in human and regional geography, particularly in urban planning. The quantitative models and spatial analyses are used to understand the dynamics of the population, the migrations, economic flows and distribution of public services. For example, in urban planning, GIS is used to optimize resource distribution, and accessibility to public services and public transport, contributing to the development of smart cities.

6. TECHNICAL FOUNDATIONS IN GEOGRAPHICAL RESEARCH: AUTOCORRELATION AND FREQUENCY

Another powerful argument for the technical direction of Geography is the integration of fundamental concepts of autocorrelation and frequency.

Many decades ago, Cliff & Ord (1981) developed a fundamental book which discusses spatial autocorrelation and its applications in geography, reactivating the ideas of Tobler (1970) and providing models and methodologies for analyzing spatial relationships. It covers spatial autocorrelation theory, essential for understanding distributions of phenomena like population and environmental patterns.

Spatial and temporal autocorrelation are essential concepts in the geographical analysis, enabling the study of how phenomena are distributed in space and time. These concepts are used in modern geographical research to understand the relationships between various spatial variables such as environmental factors, population distribution or seasonal migrations.

Fotheringham *et al*., (2000) provide an accessible introduction to quantitative methods in geography, including spatial and temporal autocorrelation. This book explains the significance of these concepts in modern spatial analysis and their application through autoregressive models and spatial frequency analysis.

More recently Haidu (2016) argues that in addition to autocorrelation, the distribution of geographic processes and phenomena is related to spatial and temporal frequency. Autocorrelation and frequency are core concepts of Technical Geography.

Moreover, the spatial and temporal frequency is crucial for the monitoring of recurring phenomena such as climate changes or land use patterns. These concepts are analyzed using advanced tools and techniques, such as Fourier models or autoregressive models, which are common in the researches in technical fields such as Engineering or Physics.

This clearly demonstrates that **Geography is based on technical foundations similar to those used in applied sciences**.

7. COUNTRIES AND UNIVERSITIES PROMOTING TECHNICAL GEOGRAPHY

There are countries and universities that fully acknowledge the need for Technical Geography and that have adapted their curriculum to reflect this transformation.

Some universities from USA such as the University of California, Santa Barbara (UCSB) and Stanford University are leaders in geospatial research, using GIS and remote sensing for climate studies, urban planning and analysis of natural resources. Goodchild (2006) provides an overview of the development of geospatial sciences within academia, particularly in U.S. institutions like UCSB. He discusses the impact of these universities on geospatial research, especially in areas like climate studies and urban planning.

In Canada, universities such as McGill University and University of British Columbia are known for their advanced GIS and remote sensing programs, integrating Technical Geography in its academic curriculum and in environmental and resource management research.

The paper of Schiewe & Ehlers (2006) covers the advancement of GIS and remote sensing in Germany. Universities such as the Technical University of Munich (TUM) and Humboldt University of Berlin are centers of excellence in using GIS and advanced technologies for spatial analysis and Technical Geography education.

8. COUNTRIES AND UNIVERSITIES PROMOTING CLASSICAL GEOGRAPHY

By contrast, there are countries and universities that remain oriented towards the classical Geography, less opened towards integrating modern technologies.

Claval (1998), a French geographer, provides an overview of regional and humanistic geography, particularly as it has been traditionally emphasized in France. This book explains how French institutions like Sorbonne Université have historically prioritized these approaches over technical methods.

Many French universities are known for promoting regional and humanistic Geography to the detriment of Physical Geography, with an insufficient emphasis on the use of GIS and other advanced spatial technologies and insufficient attention to the mathematical modeling of geographical processes or phenomena.

In Italy, universities such as Università di Bologna and La Sapienza (Hefferman, 2003) continue to focus on classical Physical Geography, without fully embracing the technical aspects of the modern Geography. This resistance to the integration of advanced technologies limits the relevance of Geography in addressing modern problems.

Donert (2007) examined in detail the State of Geography in European higher education and his results allow us to deduce which are the European countries where classical geography remains relevant in higher education. Donert's work should be updated to see if geographic education adapts to the recent achievements of technical geography and if the new achievements are integrated or not in the training of geographers.

9. GEOGRAPHY'S FUTURE: AN ESSENTIAL TECHNICAL DIRECTION FOR THE REVIVAL OF ITS ROLE

Adopting Technical Geography is essential for reviving its role in education and society. National Research Council (2006) drew up a report which highlights how spatial thinking and GIS are essential for modern geographic education, stressing that integrating geospatial technologies can prepare students to tackle societal and environmental challenges. It advocates for a more technical geography curriculum to enhance the field's relevance. Solem *et al.,* (2008) discusses the growing need for technical skills in geography to address global challenges. It emphasizes the importance of training students in geospatial technologies, which are crucial for careers focused on environmental management, urban planning, and migration studies.

With the increase of global challenges, such as climate changes, rapid urbanization, and migration, Geography has an immense potential of providing applied solutions to improve human life and protect the environment. Geospatial technologies are the key to achieving this objective, and the universities that integrate these technologies in their research are those that will train future leaders and experts in managing these challenges.

In 2006, I created the journal *Geographia Technica*, a journal unique in its vision to publish articles from **across entire discipline** which implements technical approaches in geographical research (please see Aims and Scope) and which found its place in the Wikipedia encyclopedia (please see Geographia Technica - Wikipedia). For several years this journal has been indexed in the Core Collection of WOS, in SCOPUS and in other databases of scientific journals.

As for Technical Geography, as a new branch or discipline of Geography, the page deserves to be opened and read Technical geography - Wikipedia.

10. CONCLUSION

Geography's future is, undoubtedly, **technical**. The evolution of this discipline from a descriptive to an analytical and applied science proves the importance of using advanced technologies in natural and social phenomena analysis. By adopting GIS, remote sensing, quantitative analysis, and spatial modeling, Geography becomes a central discipline in solving complex global problems. The countries and universities that embrace this transformation will play a crucial role in defining Geography's future, while those that remain attached to the classical approaches risk becoming irrelevant in addressing contemporary challenges.

REFERENCES

Barnes, T. J. (2001). Retheorizing Economic Geography: From the Quantitative Revolution to the 'Cultural Turn'. *Annals of the Association of American Geographers*, **91**(3), 546-565.

Batty, M. (2013). *The New Science of Cities*. MIT Press.

Bednarz, S. W., Heffron, S., & Huynh, N. T. (2013). *A Road Map for 21st Century Geography Education: Geography Education Research*. Association of American Geographers.

Castree, N., Kitchin, R., & Rogers, A. (2013). *A Dictionary of Human Geography*. Oxford University Press.

Claval, P. (1998). *An Introduction to Regional Geography*. Blackwell Publishers.

Cliff, A. D., & Ord, J. K. (1981). *Spatial Processes: Models & Applications*. Pion Ltd.

Donert, K., (2007). *Aspects of the State of Geography in European higher education.* Published by: HERODOT Network, Liverpool, UK.

Fotheringham, A. S., Brunsdon, C., & Charlton, M. (2000). *Quantitative Geography: Perspectives on Spatial Data Analysis*. Sage Publications.

Gregory, D., Johnston, R., Pratt, G., Watts, M., & Whatmore, S. (Eds.). (2009). The Dictionary of Human Geography. Wiley-Blackwell.

Goodchild, M. F., & Janelle, D. G. (Eds.). (2004). Spatially Integrated Social Science. Oxford University Press.

Goodchild, M. F. (2006). *GIScience, Geography, Form, and Process*. Annals of the Association of American Geographers, **96**(4), 709-717.

Haidu, I. (2016) What is Technical Geography. *Geographia Technica*, **11**(1), 1-5.
DOI: 10.21163/GT_2016.111.01.

Heffernan, M. (2003). Histories of Geography. In *Key Concepts in Geography*, edited by Sarah Holloway, Stephen Rice, and Gill Valentine, 3-22. Sage Publications.

Jensen, J. R. (2006). *Remote Sensing of the Environment: An Earth Resource Perspective*. Pearson Education.

Lambert, D., & Morgan, J. (2010). *Teaching Geography 11-18: A Conceptual Approach*. Open University Press.

National Research Council. (2006). *Learning to Think Spatially: GIS as a Support System in the K-12 Curriculum*. The National Academies Press.

Penn State Public Broadcasting, *Geospatial Revolution*, accessed 30 October 2024
< https://www.pbslearningmedia.org/resource/ate10.sci.ess.eiu.geospatial/geospatial-revolution/>.

Schiewe, J., & Ehlers, M. (2000). Remote Sensing and GIS: Developments in Germany. *ISPRS Journal of Photogrammetry and Remote Sensing*, **55**(1), 1-8.

Solem, M., Cheung, I., & Schlemper, M. B. (2008). Skills in Professional Geography: An Assessment of Workforce Needs and Expectations. *The Professional Geographer*, **60**(3), 356-373.

Tobler W. (1970). A computer movie simulating urban growth in the Detroit region. *Economic Geography*, **46**(2), 234-240.

*** Aims and Scope (accessed 30 October 2024)

*** Geographia Technica - Wikipedia (accessed 30 October 2024)

*** Technical geography - Wikipedia (accessed 30 October 2024)

ASSESSMENT OF GREEN HYDROGEN PRODUCTION POTENTIAL FROM SOLAR AND WIND ENERGY IN MAURITANIA

Elemine Adama SOW[1] [ID], Mohamed Mohamed VALL[2] [ID], Mohamed Mahmoud ABIDINE[3] [ID], Houda BABAH[4] [ID], Ahmed HAMOUD[5] [ID], Gayane FAYE[6] [ID], Bakari SEMEGA[1] [ID]*

ABSTRACT.
The aim of the present paper is to estimate the green Hydrogen potential from two sources of renewable energies that are solar and wind. This estimation has been done by using satellite data taken from the Global Solar Atlas (GSA) and Global Wind Atlas (GWA). Data were integrated into a Geographical Information System (GIS) to estimate, first the theoretical electricity from solar and wind by using different models. Then we used a third model to estimate the quantity of hydrogen that can be produced from the two different sources mentioned above. As far as we know this is the first attempt to estimate the green hydrogen potential in Mauritania. The results show that the total annual electricity from solar ranged between 275 and 329 GWh/km^2/year, with the north of the country having the highest potential, especially in the region of Tiris-Zemour and Adrar, in the other hand the south of the country and across the Senegal River line was the regions with the least potential of solar energy. Concerning wind, the values were between 28 and 108 GWh/km^2/year with the coastline regions localized in the Nouadhibou-Nouakchott axis having the highest potential. The total values of hydrogen production vary between 5428 to 6272 tons/km^2/year from solar versus 23 to 620 tons/km^2/year from the wind.

Key-words: Mauritania, Green hydrogen, GIS, Renewable electricity, Solar and Wind Energy.

1. INTRODUCTION

Meeting the global energy demand while striving for net-zero goals (Wang et al., 2023) presents a formidable challenge in today's world. Decarbonizing economic sectors and adopting non-pollutant energy sources are imperative steps toward achieving this objective (Acar & Dincer, 2022; Matute et al., 2022). Notably, a significant portion of CO2 emissions 86% emanates from power generation, transportation, and industrial activities (Ayodele et al., 2012; Jahangiri et al., 2020; Kojima et al., 2023). The promotion of renewable energy emerges as a crucial strategy to mitigate the adverse impacts of fossil fuels (Phap et al., 2022).

Green hydrogen, produced through renewable energy sources, emerges as a promising environmentally friendly solution (Dokhani et al., 2023; Mohammadshahi et al., 2022; S. Wang et al., 2021). However, despite its potential, green hydrogen constitutes only a small fraction (0.3%) of total hydrogen production, with the majority being derived from fossil fuels (Catumba et al., 2022; Kumar et al., 2023). To accelerate the energy transition, the European Union has set ambitious targets, including the installation of 40 GW of renewable-powered electrolysers by 2030 (Moradpoor et al., 2023).

[1]*Pollution and Environment Research Unit, Department of Chemistry, Faculty of Sciences and Techniques, University of Nouakchott, Mauritania, batal1989@gamil.com, semega@una.mr*

[2]*Ministry of Petroleum Mines and Energy of Mauritania, medmedvall87@gmail.com*

[3]*Unit of Biodiversity and Valorization of Vegetal Resources, Faculty of Sciences and Techniques, University of Nouakchott, Mauritania, corresponding author*: hmd108@yahoo.fr*

[4]*Materials Science and Environment, Faculty of Sciences and Techniques, University of Nouakchott, Mauritania, houdababah@gmail.com*

[5]*Department of Geology, Faculty of Sciences and Technics, University of Nouakchott, Mauritania, aohamoud@gmail.com*

[6]*Laboratory of Applied Remote Sensing, Institute of Earth Sciences of Cheikh Anta DIOP University, Senegal, gayane.faye@gmail.com*

Notably, regions rich in renewable energy resources, such as North Africa, hold the potential to become key energy suppliers, given the high demand and moderate renewable resource availability (Gallardo et al., 2021; Mukelabai et al., 2022). Mauritania, with its abundant solar and wind resources, has attracted considerable attention for green hydrogen investment. Companies like CWP Global, Chariot Limited, and British Petroleum have signed agreements with the Mauritanian government to develop green hydrogen projects (Aman et al., 2022; El Hacen Jed et al., 2020; Eren et al., 2022). Several studies have assessed the hydrogen potential using GIS and satellite data in various countries. For instance, research in Morocco by Touili et al. (2018) revealed substantial hydrogen production potential from wind and solar energy. Similar studies have been conducted in other countries, including Ecuador (Posso et al., 2016), Canada (Okunlola et al., 2022), and Algeria (Boudries & Dizene, 2008), highlighting the global interest in green hydrogen. Despite extensive research in many countries, studies evaluating green hydrogen production in Mauritania remain scarce. While efforts have been made to estimate solar and wind potential, there is a notable gap in assessing green hydrogen production (Bilal et al., 2021, 2023; El Hacen Jed et al., 2020; IRENA, 2021; Ould Bilal et al., 2008). This study aims to address this gap and provide valuable insights into green hydrogen production in Mauritania.

2. MAURITANIA COUNTRY PROFILE

Mauritania is an African country with a surface of 1.030.700 km^2, that has borders to the North with Morocco and Algeria to the East and South-East with Mali and to the South with Senegal. The western limit of the country is marked by the Atlantic Ocean for a distance of around 754 km (Hardy, 2017). Mauritania has a vast potential for solar energy. Masdar, an energy firm of Emirates, installed in the year of 2016 a total capacity of 16 MW solar plants. In 2017 Mauritania opened the Toujounine solar farm with a 50 MW capacity and the total installed solar capacity increased to 86 MW. The first Mauritanian wind farm capacity was installed in Nouakchott with a capacity of 30 MW followed by the Boulenouar wind farm with a capacity of 100 MW. According to the Ministry of Petroleum, Energy, and Mine, the demand for electricity in Mauritania will be around 1400 MW by 2025 (Group, 2019).

3. DATA AND METHODOLOGY

To estimate the potential of hydrogen production we need solar and wind data that are representative of the whole country. The data can be obtained by local measures or via satellite data. Satellite data and GIS were used in several studies (Jahangiri et al., 2020; Okunlola et al., 2022; Rahmouni et al., 2017; Touili et al., 2018) to estimate hydrogen potential. We first estimated the amount of energy that can be obtained from solar and wind then this energy was used as an input to an electrolyser model to estimate the quantity of hydrogen that can be produced. The satellite data used for this study was taken from the Global Solar Atlas and Global Wind Atlas.

3.1. Solar potential

Mauritania has a high potential for renewable energy resources. The solar photovoltaic (PV) potential is estimated to range between 2000-2300 kWh/m^2/year (IRENA, 2021). For estimating the solar potential, we used the data obtained from Global Solar Atlas an open-access online database application that allows access to solar resources and photovoltaic power potential for a site or a region. 228 grounds sites measurements have been used worldwide to validate the Global Solar Atlas data. The accuracy of annual Global Horizontal Irradiance (GHI) from the obtained data for the 228 site measurements ranged between ±4% to ±8% (Énergies et al., 2021). GIS data layers of the annual average of the Global horizontal irradiation with 250 m resolution were downloaded from the database and used as input to a GIS software using the models that we detailed below to deduce the Mauritania potential (Global Wind Atlas., 2023). For this study, we assumed a PV panel with 250 W rated power (Rahmouni et al., 2017), a module reference efficiency of 17%, and an efficiency of 85% for the power conditioning units (Touili et al., 2018). So, to estimate the energy

that can be produced from the PV array we used the following model (Rahmouni et al., 2017; Touili et al., 2018):

$$Epv = G \times npv \times npc \tag{1}$$

where:

   Epv, (kWh/km2): is the quantity of energy that can be produced by the PV solar system;

   G: is the horizontal irradiation;

   npv: is PV module reference efficiency;

   npc: is the power conditioning efficiency.

3.2. Wind potential

Recently in Mauritania, a wind resource assessment was made by Bilal et al., (2021), using more recent meteorological data measured every 10 min over one year collected from eight sites (with three different height levels) located mainly on the west coast of Mauritania, and the annual average of the wind characteristics was determined. The average wind speed was extremely high. The values were between 4.9 m/s (on site 2 at 10 m height) and 10.0 m/s (on site 7 at 80 m height). This was done for eight locations only and the data used were collected for one year. to estimate the wind potential, we should first know the wind average velocity and the characteristics of the wind in each region in Mauritania. And for this accurate data are required in the whole country. The best thing is to get data acquired in situ and for that meteorological stations are needed in the whole Mauritania region, but that is not the case. To overcome this issue, we used validated satellite data from open online sources (Gruber et al., 2019; Okunlola et al., 2022; Rahmouni et al., 2017; Touili et al., 2018). For the wind potential estimation, we used the data obtained from the Global Wind Atlas database. GWA is a free access online database application where we can find wind resource mapping at 10, 50, 100, 150, and 200 m above ground/sea level with 250 m resolution. The GWA starts with large-scale and ends with microscale wind climate data. In this study, we used the average mean wind speed at a height of 100 m (Global Wind Atlas., 2023). The characteristics of the wind turbine considered are Suzlon-82 with a Rated power of 1500 kW, and a swept area of 5281 m2. To estimate the electricity produced by the wind we used the formula below (Ayodele et al., 2012b; Ayodele & Munda, 2019; Rahmouni et al., 2017):

$$Ew = Eo \times hm \times hg \tag{2}$$

$$Eo = \frac{1}{2} \times \rho \times C \times A \times V^3 \times 8760 \tag{3}$$

where:

   Ew: is the electrical energy produced by the wind generator;

   Eo: power generated by the wind turbine;

   hm: gearbox efficiency 85%;

   hg: generator efficiency 95%;

   ρ: density of air (kg/m3);

   C: coefficient of performance of the turbine, and for the purpose of this study we used 45%;

   V: wind speed (m/s).

3.3. Electrolyser modeling

The reaction that split water into hydrogen and oxygen by electricity is called electrolysis. The tool used for this electrochemical reaction is an electrolyser. The hydrogen produced when the energy used to feed the electrolysers comes from a renewable source has a label of green hydrogen. DC power is used in the electrolysis process powered by renewable energy resources (Shiva Kumar & Lim, 2022). There are three main types of electrolysers in the market. The Solid Oxide (SO) Electrolyser, The Proton Exchange Membrane Electrolyser (PEM), and the Alkaline Electrolyser (AE). The SO electrolyser has a high efficiency, needs less electricity, and is able to split water into hydrogen and oxygen at high temperatures. PEM has a fast response, a small footprint, low operating temperature, and high efficiency at high density. Alkaline Electrolyser has a proven

maturity, and good durability and is the predominant electrolyser in the market (Yue et al., 2021). Alkaline electrolysers represent 61% of the installed capacity, 31% for the PEM, and the rest for SOEC and other electrolysers technologies (Nnabuife et al., 2022).

For this study, we used the PEM due to its high energy efficiency, purity of gases, and hydrogen production rate (Ueda et al., 2022). The PEM was used in several studies to estimate hydrogen production (Ayodele & Munda, 2019; Folgado et al., 2022; Okunlola et al., 2022; Posso et al., 2016; Rahmouni et al., 2017; Touili et al., 2018). To produce 1 kg of hydrogen the electrolyser is supposed to consume 53 kWh (Touili et al., 2018), with an efficiency of 75% (Okunlola et al., 2022; Posso et al., 2016; Rahmouni et al., 2017; Touili et al., 2018). The following equation was used to estimate hydrogen production from renewable sources:

$$MH2 = (nelec \times E/HHVH2) \tag{4}$$

where:

MH2:   *is the mass of hydrogen (ton/km2/year);*
Nelec: *electrolyser efficiency;*
HHVH2:   *Hydrogen higher heating value*

4. RESULTS

The calculations performed illustrate regional variances in solar and hydrogen production (**Fig. 1** and **Fig. 2**), with higher production rates observed in the Northeast regions compared to coastal regions and other parts of the country. This indicates that certain regions may be more favorable for solar and wind energy development. The annual average of the global horizontal solar irradiation ranged between 1900 and 2300 kWh/m^2/year (**Fig.3**) and the annual average of the wind speed was between 5-10 m/s (**Fig. 4**).
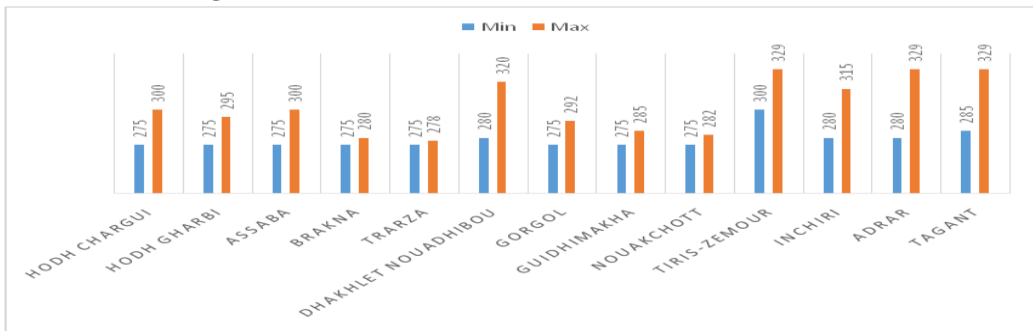
Fig.1. Solar Electricity yearly production in Mauritania (GWh/km²/year)
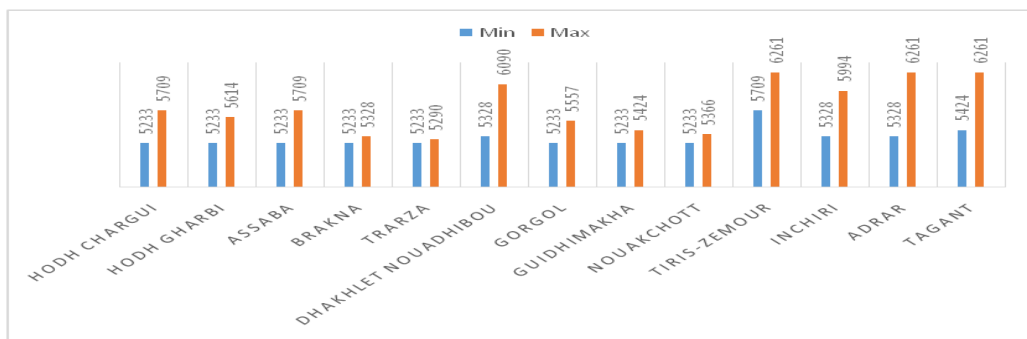
Fig.2. Hydrogen Production from Solar Energy in Mauritania (tons/km²/year).
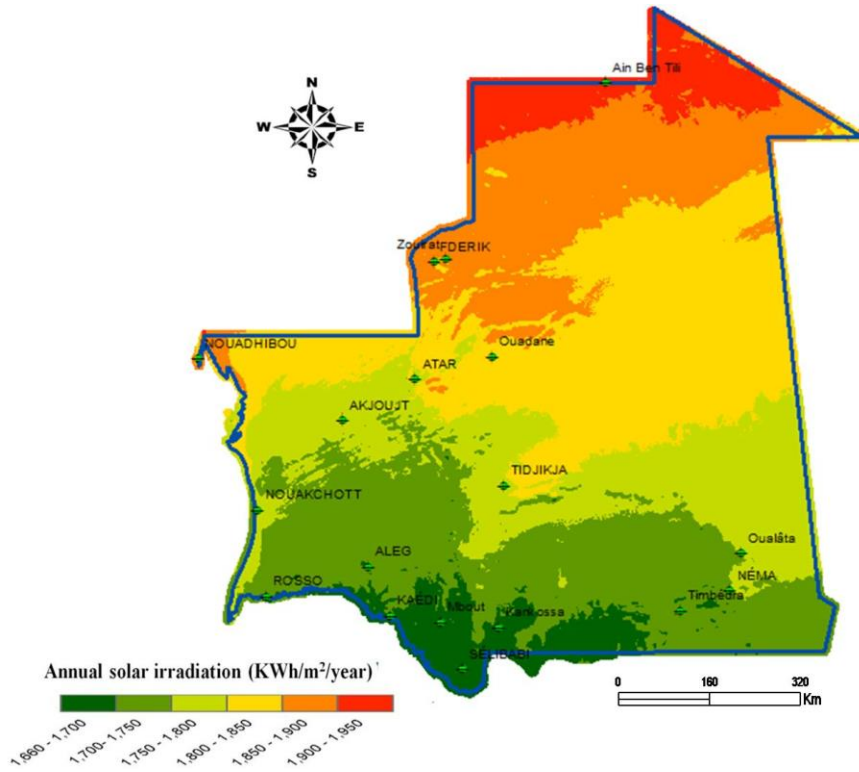
Fig. 3. Annual average of the global horizontal solar irradiation in Mauritania.
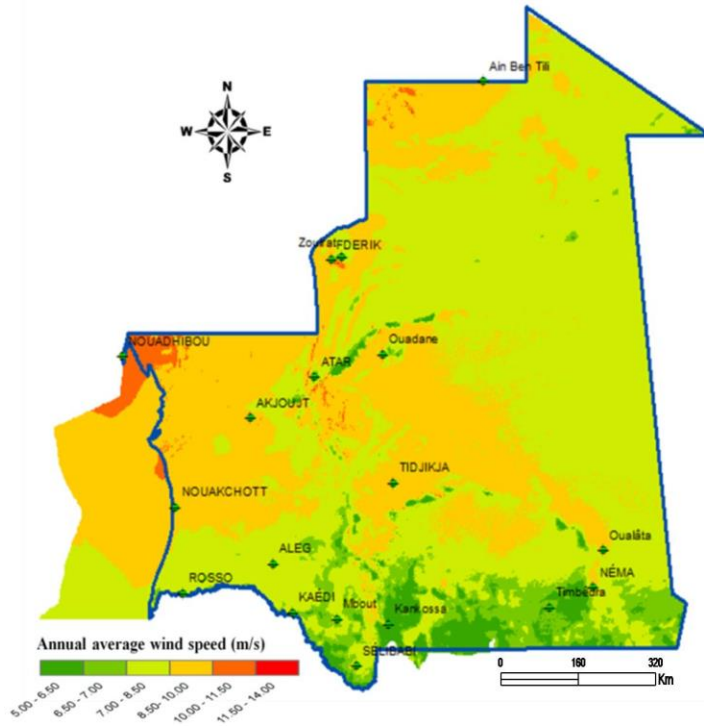
Fig. 4. Annual average of wind speed at 100 m above ground level in Mauritania.

Applying the models that we presented before regarding solar PV and wind turbines we found that the annual solar electricity production was between 275 and 329 GWh/km^2/year (**Fig. 5**) thus much higher than the wind 1-28 GWh/km^2/year (**Fig. 6**).
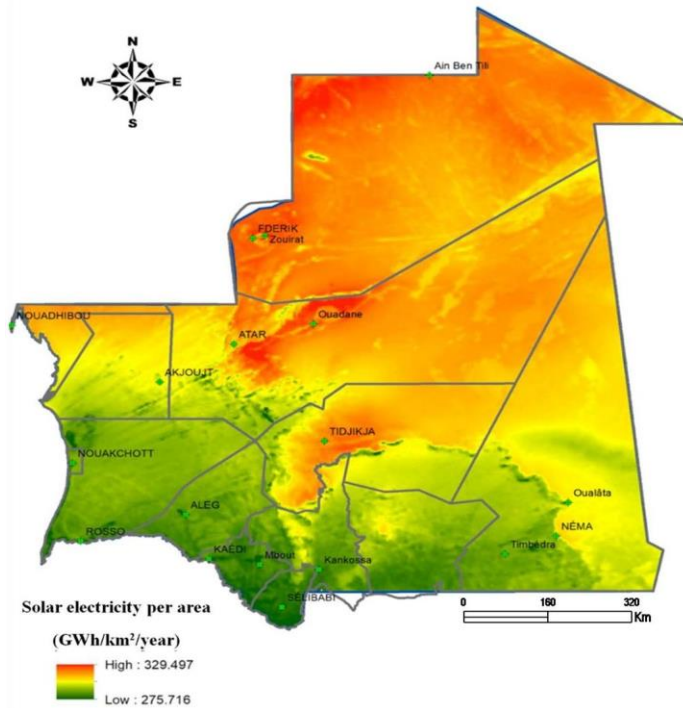
Fig. 5. Solar electricity production.
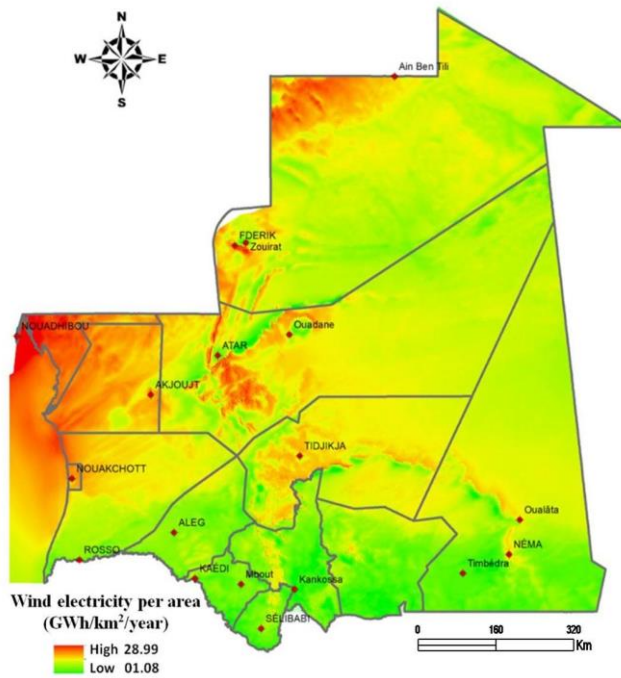
Fig. 6. Wind electricity production.

From **Fig.7** we can see that the estimated potential of solar hydrogen production in Mauritania with models that we used was high between 5248 and 6272 tons/km^2/year at least ten times greater than the estimated wind hydrogen 23-625 tons/km^2/year (**Fig.8**).
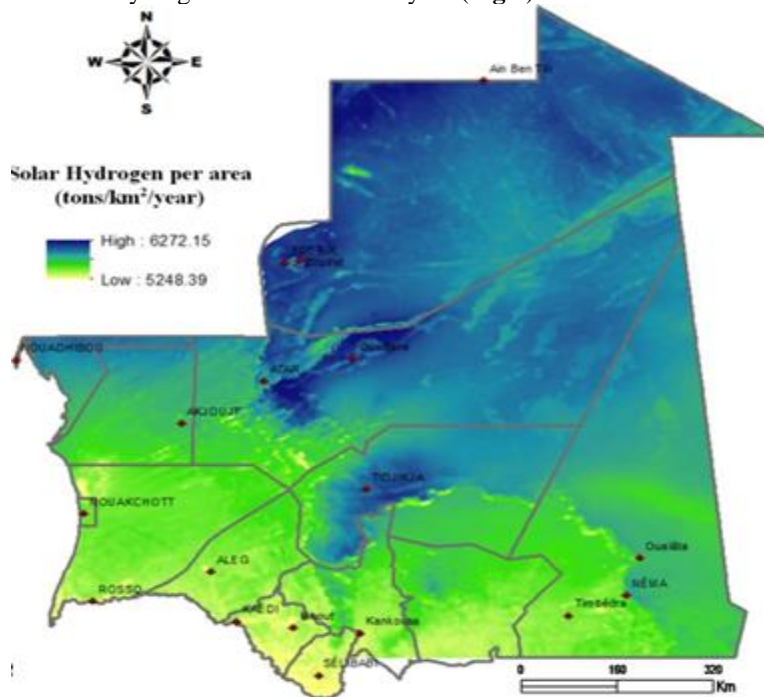
Fig. 7. Hydrogen potential from solar energy.
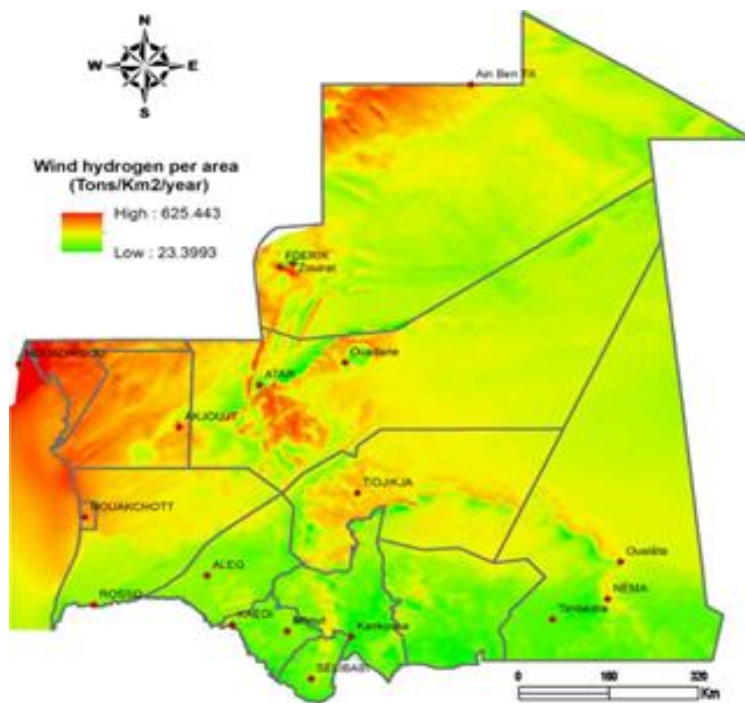
Fig. 8. Hydrogen potential from wind energy.

The bar chart displays the yearly production of solar electricity in Mauritania, broken down by region. The data is presented in GWh/km²/year, with the highest production in the Northeast regions at 329 GWh/km²/year, followed by Dakhlet-Nouadhibou and parts of Inchiri, Adrar, and Tiris-Zemour at 300 GWh/km²/year. The coastal regions and the rest of the country have a production of 290 GWh/km²/year and 275 GWh/km²/year, respectively.

The bar chart displays the hydrogen production from solar and wind energy in Mauritania, broken down by region. The data is presented in tons/km²/year, with the highest solar production in the Northeast regions at 5700-6200 tons/km²/year, followed by Dakhlet-Nouadhibou and parts of Inchiri, and Adrar at 5300-6000 tons/km²/year. The coastal regions and the rest of the country have a solar production of 5200-5500 tons/km²/year and 5300-5700 tons/km²/year, respectively.

5. DISCUSSION

The annual average of the global horizontal solar irradiation ranges from 1900 to 2300 kWh/m²/year, indicating substantial solar energy potential across Mauritania. The annual average of wind speed is between 5-10 m/s, suggesting moderate to high wind energy potential in the region.

Solar electricity production is significantly higher than wind electricity production. The annual solar electricity production ranges from 275 to 329 GWh/km²/year, while wind electricity production is only between 1 and 28 GWh/km²/year. This indicates that solar energy is a much more viable and productive source of electricity compared to wind energy in Mauritania.

Taking a close look at the solar irradiation map shows that solar irradiation decreases from the north to the south with an exception in the Nouadhibou region. In other words, the solar potential increase from the South to the North of Mauritania. Regions like Tiris-Zemour, Adrar, and Tidjikja have the highest potential for electricity production from solar panels. On the other hand, regions of Trarza, Brakna, Gorgol, and along the Senegal River with the least potential. And Dakhlet Nouadhibou, Inchiri, and the Northern part of the Hods fall in between in the matter of the potential of electricity that can be produced from solar panels.

Regarding the wind regions of Dakhlet Nouadhibou, Inchiri, the Northeast of Tiris-Zemour, the Middle of Adrar and Nouakchott has the most of potential and especially along the coastline from Nouadhibou to Nouakchott. Combining solar and wind hydrogen potential the coast of Nouadhibou region comes to be with the highest potential.

The estimated potential of solar hydrogen production is much higher compared to wind hydrogen production. Solar hydrogen production ranges from 5248 to 6272 tons/km²/year, while wind hydrogen production ranges from 23 to 625 tons/km²/year. Solar energy exhibits a potential at least ten times greater than that of wind energy for hydrogen production in Mauritania.

Given the substantial solar energy potential and higher electricity and hydrogen production rates compared to wind energy, policymakers and stakeholders in Mauritania should prioritize solar energy development for both electricity generation and hydrogen production. Investments in solar infrastructure, such as photovoltaic systems and solar thermal technologies, could significantly contribute to the country's energy independence and sustainability goals. However, wind energy should not be overlooked entirely, especially in coastal regions with favorable wind conditions. Hybrid renewable energy systems combining solar and wind resources could provide a more balanced and reliable energy supply.

Further research and investment are needed to optimize the integration of renewable energy sources into Mauritania's energy mix, considering factors such as grid stability, storage solutions, and socio-economic impacts.

We compared the results with those obtained by Touili et al., (2018) in Morocco and Rahmouni et al., (2017) in Algeria, as the methodologies used were quite similar and Mauritania has a border with the countries where those study has been made.

Touili et al., (2018)found the annual average of solar production was between 340 and 436 GWh/km^2/year which was little bit higher than the value that we obtained for Mauritania which was between 275 and 329 GWh/km^2/year. On the other hand, the results obtained by Rahmouni et al., (2017) for the annual solar production between 259-367, GWh/km^2/year was closer to our results. Thus, the annual hydrogen production per square km per year was quite similar.

It worth to mention that this paper does not discuss the effect of temperature in system efficiency, and the potential capture of excess heat. According several studies the PV efficiency decreases as the temperature increases (Ouédraogo et al., 2021; Sevela & Olesen, 2013; Wang et al., 2023), and due to excess heat the cells can experience long-term degradation when temperature is higher than certain limit(Royne et al., 2005). This decreases will impact the overall hydrogen production.(Skoplaki & Palyvos, 2009). Using PVT can be a solution to capture the excess heat and cool the solar panels; it was proved in India that PVT with wavy fin system increase the solar to hydrogen production efficiency from 1.4% to 3.4% according to the experiment conducted by Chandrasekar et al., (2022) at the site of Tiruchirappalli district, Tamilnadu state, for temperatures ranging between 25-34 °C. Using a cooling system assist in improving the efficiency of PV cells (Rajoria et al., 2013; Tripanagnostopoulos et al., 2002), this is explained by the reason that only a small portion of the solar irradiation is converted to electricity and the rest is dissipated as thermal energy(Rajoria et al., 2013), thus using a solar heating and cooling system offers the opportunity to generate energy and heat (Buonomano et al., 2013). The excess heat can be used for domestic or industrial application contributing in carbon footprint reduction especially in Mauritania where the country is located in the hot dessert climate where temperature can reach up to 45 °C in some region during the summer.

6. CONCLUSION

The study reveals a significant contrast between the potential of solar and wind energy resources in Mauritania. Solar power emerges as a dominant contender, exhibiting substantially higher electricity and hydrogen production capabilities compared to wind power.

Solar electricity production ranges impressively between 275 to 329 GWh/km²/year, showcasing the extensive energy-generating capacity of solar photovoltaic (PV) systems across the Mauritanian landscape. In contrast, wind electricity production lags behind, estimated at a modest 1-28 GWh/km²/year.

The advantage of solar energy extends further when considering hydrogen production potential. Solar hydrogen production figures range from 5248 to 6272 tons/km²/year, underlining the immense capability of solar energy to contribute to sustainable hydrogen generation. Conversely, wind hydrogen production, ranging from 23 to 625 tons/km²/year, falls significantly short in comparison.

However, in coastal areas, where solar potential might not be as dominant as in other regions, wind energy emerges as a compelling alternative. The study identifies coastal regions, such as Dakhlet Nouadhibou and Inchiri, as having high wind potential, especially along the coastline from Nouadhibou to Nouakchott. These areas present favorable conditions for wind turbine deployment, suggesting that a diversified energy approach incorporating both solar and wind resources could be advantageous.

It's essential to acknowledge the study's limitations, particularly the lack of discussion on temperature effects and excess heat management. Temperature fluctuations can impact PV efficiency, and implementing strategies such as photovoltaic-thermal (PVT) systems and cooling mechanisms could further optimize energy production.

REFERENCES

Acar, C., & Dincer, I. (2022). Selection criteria and ranking for sustainable hydrogen production options. *International Journal of Hydrogen Energy*, *47*(95), 40118‑40137. https://doi.org/10.1016/j.ijhydene.2022.07.137

Almutairi, K., Hosseini Dehshiri, S. S., Hosseini Dehshiri, S. J., Mostafaeipour, A., Jahangiri, M., & Techato, K. (2021). Technical, economic, carbon footprint assessment, and prioritizing stations for hydrogen production using wind energy : A case study. *Energy Strategy Reviews*, *36*, 100684. https://doi.org/10.1016/j.esr.2021.100684

Aman, T., Nouadhibou, D., Agreement, F., Summit, C., & Agreement, F. (2022). *Green Hydrogen Project (AMAN), Africa : Https://www.cwp.global/wp-content/uploads/2022/05/Mauritania-and-CWP-sign-a-framework-agreement-for-the-AMAN-project.pdf (Accessed on September 1, 2022)*. May.

Ayodele, T. R., Jimoh, A. A., Munda, J. L., & Agee, J. T. (2012a). Wind distribution and capacity factor estimation for wind turbines in the coastal region of South Africa. *Energy Conversion and Management*, *64*, 614‑625. https://doi.org/10.1016/j.enconman.2012.06.007

Ayodele, T. R., Jimoh, A. A., Munda, J. L., & Agee, J. T. (2012b). Wind distribution and capacity factor estimation for wind turbines in the coastal region of South Africa. *Energy Conversion and Management*, *64*, 614‑625. https://doi.org/10.1016/j.enconman.2012.06.007

Ayodele, T. R., & Munda, J. L. (2019). Potential and economic viability of green hydrogen production by water electrolysis using wind energy resources in South Africa. *International Journal of Hydrogen Energy*, *44*(33), 17669‑17687. https://doi.org/10.1016/j.ijhydene.2019.05.077

Bilal, B., Adjallah, K. H., Sava, A., Yetilmezsoy, K., & Ouassaid, M. (2023). Wind turbine output power prediction and optimization based on a novel adaptive neuro-fuzzy inference system with the moving window. *Energy*, *263*, 126159. https://doi.org/10.1016/J.ENERGY.2022.126159

Bilal, B., Adjallah, K. H., Yetilmezsoy, K., Bahramian, M., & Kıyan, E. (2021). Determination of wind potential characteristics and techno-economic feasibility analysis of wind turbines for Northwest Africa. *Energy*, *218*, 119558. https://doi.org/10.1016/j.energy.2020.119558

Boudries, R., & Dizene, R. (2008). Potentialities of hydrogen production in Algeria. *International Journal of Hydrogen Energy*, *33*(17), 4476‑4487. https://doi.org/10.1016/j.ijhydene.2008.06.050

Buonomano, A., Calise, F., & Palombo, A. (2013). Solar heating and cooling systems by CPVT and ET solar collectors : A novel transient simulation model. *Applied Energy*, *103*, 588‑606. https://doi.org/10.1016/J.APENERGY.2012.10.023

Catumba, B. D., Sales, M. B., Borges, P. T., Ribeiro Filho, M. N., Lopes, A. A. S., Sousa Rios, M. A. de, Desai, A. S., Bilal, M., & Santos, J. C. S. dos. (2022). Sustainability and challenges in hydrogen production : An advanced bibliometric analysis. *International Journal of Hydrogen Energy*. https://doi.org/10.1016/J.IJHYDENE.2022.11.215

Chandrasekar, M., Gopal, P., Ramesh Kumar, C., & Edwin Geo, V. (2022). Effect of solar photovoltaic and various photovoltaic air thermal systems on hydrogen generation by water electrolysis. *International Journal of Hydrogen Energy*, *47*(5), 3211‑3223. https://doi.org/10.1016/j.ijhydene.2021.04.205

Dabar, O. A., Awaleh, M. O., Waberi, M. M., & Adan, A.-B. I. (2022). Wind resource assessment and techno-economic analysis of wind energy and green hydrogen production in the Republic of Djibouti. *Energy Reports*, *8*, 8996‑9016. https://doi.org/10.1016/j.egyr.2022.07.013

Dokhani, S., Assadi, M., & Pollet, B. G. (2023). Techno-economic assessment of hydrogen production from seawater. *International Journal of Hydrogen Energy*, *48*(26), 9592‑9608. https://doi.org/10.1016/J.IJHYDENE.2022.11.200

El Hacen Jed, M., Ihaddadene, R., Ihaddadene, N., Elhadji Sidi, C. Elb., & EL Bah, M. (2020). Performance analysis of 954,809 kWp PV array of Sheikh Zayed solar power plant (Nouakchott, Mauritania). *Renewable Energy Focus*, *32*, 45‑54. https://doi.org/10.1016/J.REF.2019.11.002

Eren, T., Eren, T., Demol, F., & Vice-president, E. (2022). *CHARIOT PARTNERS WITH TOTAL EREN ON A GREEN HYDROGEN PROJECT IN MAURITANIA*. 1‑3.

Folgado, F. J., González, I., & Calderón, A. J. (2022). Simulation platform for the assessment of PEM electrolyzer models oriented to implement digital Replicas. *Energy Conversion and Management*, *267*, 115917. https://doi.org/10.1016/J.ENCONMAN.2022.115917

Gallardo, F. I., Monforti Ferrario, A., Lamagna, M., Bocci, E., Astiaso Garcia, D., & Baeza-Jeria, T. E. (2021). A Techno-Economic Analysis of solar hydrogen production by electrolysis in the north of Chile and the case of exportation from Atacama Desert to Japan. *International Journal of Hydrogen Energy*, *46*(26), 13709‑13728. https://doi.org/10.1016/J.IJHYDENE.2020.07.050

Global Hydrogen Review . (2022). *Global Hydrogen Review 2022*. https://doi.org/10.1787/a15b8442-en

Global Wind Atlas 3.0. *A free, web-based application developed, owned and operated by the Technical University of Denmark (DTU). The Global Wind Atlas 3.0 is released in partnership with the World Bank Group, utilizing data provided by Vortex, using fund*. (s. d.). Consulté 23 janvier 2023, à l'adresse https://globalsolaratlas.info/map?c=11.609193,8.4375,3

Group, W.B. (2019). *REGIONAL OFF-GRID ELECTRIFICATION PROJECT O ff -Grid Solar Market Assessment & Private Sector Support Facility Design MAURITANIA REPORT*. July.

Gruber, K., Klöckl, C., Regner, P., Baumgartner, J., & Schmidt, J. (2019). Assessing the Global Wind Atlas and local measurements for bias correction of wind power generation simulated from MERRA-2 in Brazil. *Energy*, *189*, 116212. https://doi.org/10.1016/j.energy.2019.116212

Hardy, M. (2017). *Le secteur du bâtiment Mauritanien enjeux, orientations et potentiel de réforme Architectures et matériaux durables formations adaptées et emplois décents*.

IRENA (2021). *Zones adéquates pour les énergies solaire et éolienne à échelle industrielle, Mauritanie*. Agence internationale pour les énergies renouvelables, Abou Dhabi. ISBN : 978-92-9260-248-2

Jahangiri, M., Shamsabadi, A. A., Mostafaeipour, A., Rezaei, M., Yousefi, Y., & Pomares, L. M. (2020a). Using fuzzy MCDM technique to find the best location in Qatar for exploiting wind and solar energy to generate hydrogen and electricity. *International Journal of Hydrogen Energy*, *45*(27), 13862‑13875. https://doi.org/10.1016/j.ijhydene.2020.03.101

Jahangiri, M., Shamsabadi, A. A., Mostafaeipour, A., Rezaei, M., Yousefi, Y., & Pomares, L. M. (2020b). Using fuzzy MCDM technique to find the best location in Qatar for exploiting wind and solar energy to generate hydrogen and electricity. *International Journal of Hydrogen Energy*, *45*(27), 13862‑13875. https://doi.org/10.1016/j.ijhydene.2020.03.101

Kojima, H., Nagasawa, K., Todoroki, N., Ito, Y., Matsui, T., & Nakajima, R. (2023). Influence of renewable energy power fluctuations on water electrolysis for green hydrogen production. *International Journal of Hydrogen Energy*, *48*(12), 4572‑4593. https://doi.org/10.1016/j.ijhydene.2022.11.018

Kumar, S., Baalisampang, T., Arzaghi, E., Garaniya, V., Abbassi, R., & Salehi, F. (2023). Synergy of green hydrogen sector with offshore industries : Opportunities and challenges for a safe and sustainable hydrogen economy. *Journal of Cleaner Production*, *384*, 135545. https://doi.org/10.1016/J.JCLEPRO.2022.135545

Matute, G., Yusta, J. M., & Naval, N. (2022). Techno-economic model and feasibility assessment of green hydrogen projects based on electrolysis supplied by photovoltaic PPAs. *International Journal of Hydrogen Energy*. https://doi.org/10.1016/J.IJHYDENE.2022.11.035

Mohammadshahi, S. S., Boulaire, F. A., Love, J., Gorji, S. A., & Mackinnon, I. D. R. (2022). A flexible analytical model for operational investigation of solar hydrogen plants. *International Journal of Hydrogen Energy*, *47*(2), 782‑808. https://doi.org/10.1016/J.IJHYDENE.2021.10.072

Moradpoor, I., Syri, S., & Santasalo-Aarnio, A. (2023). Green hydrogen production for oil refining – Finnish case. *Renewable and Sustainable Energy Reviews*, *175*, 113159. https://doi.org/10.1016/J.RSER.2023.113159

Mukelabai, M. D., Wijayantha, U. K. G., & Blanchard, R. E. (2022). Renewable hydrogen economy outlook in Africa. *Renewable and Sustainable Energy Reviews*, *167*(May), 112705. https://doi.org/10.1016/j.rser.2022.112705

Nnabuife, S. G., Ugbeh-Johnson, J., Okeke, N. E., & Ogbonnaya, C. (2022). Present and Projected Developments in Hydrogen Production : A Technological Review∗. *Carbon Capture Science & Technology*, *3*, 100042. https://doi.org/10.1016/J.CCST.2022.100042

Okunlola, A., Davis, M., & Kumar, A. (2022). The development of an assessment framework to determine the technical hydrogen production potential from wind and solar energy. *Renewable and Sustainable Energy Reviews*, *166*(May), 112610. https://doi.org/10.1016/j.rser.2022.112610

Ouédraogo, A., Zouma, B., Ouédraogo, E., Guissou, L., & Bathiébo, D. J. (2021). Individual efficiencies of a polycrystalline silicon PV cell versus temperature. *Results in Optics*, *4*, 100101. https://doi.org/10.1016/J.RIO.2021.100101

Ould Bilal, B., Kébé, C., Sambou, V., Ndongo, M., & Ndiaye, P. (2008). Etude et modélisation du potentiel éolien du site de Nouakchott. *Journal des Sciences Pour l'Ingénieur*, *9*(1). https://doi.org/10.4314/JSPI.V9I1.30056

Phap, V. M., Sang, L. Q., Ninh, N. Q., Binh, D. Van, Hung, B. B., Huyen, C. T. T., & Tung, N. T. (2022). Feasibility analysis of hydrogen production potential from rooftop solar power plant for industrial zones in Vietnam. *Energy Reports*, *8*, 14089‑14101. https://doi.org/10.1016/J.EGYR.2022.10.337

Posso, F., Sánchez, J., Espinoza, J. L., & Siguencia, J. (2016). Preliminary estimation of electrolytic hydrogen production potential from renewable energies in Ecuador. *International Journal of Hydrogen Energy*, *41*(4), 2326‑2344. https://doi.org/10.1016/j.ijhydene.2015.11.155

Rahmouni, S., Negrou, B., Settou, N., Dominguez, J., & Gouareh, A. (2017). Prospects of hydrogen production potential from renewable resources in Algeria. *International Journal of Hydrogen Energy*, *42*(2), 1383‑1395. https://doi.org/10.1016/j.ijhydene.2016.07.214

Rajoria, C. S., Agrawal, S., & Tiwari, G. N. (2013). Exergetic and enviroeconomic analysis of novel hybrid PVT array. *Solar Energy*, *88*, 110‑119. https://doi.org/10.1016/J.SOLENER.2012.11.018

Royne, A., Dey, C. J., & Mills, D. R. (2005). Cooling of photovoltaic cells under concentrated illumination : A critical review. *Solar Energy Materials and Solar Cells*, *86*(4), 451‑483. https://doi.org/10.1016/J.SOLMAT.2004.09.003

Sevela, P., & Olesen, B. W. (2013). Development and Benefits of Using PVT Compared to PV. *Conference Clima 2013*.

Shiva Kumar, S., & Lim, H. (2022). An overview of water electrolysis technologies for green hydrogen production. *Energy Reports*, *8*, 13793‑13813. https://doi.org/10.1016/J.EGYR.2022.10.127

Skoplaki, E., & Palyvos, J. A. (2009). On the temperature dependence of photovoltaic module electrical performance : A review of efficiency/power correlations. *Solar Energy*, *83*(5), 614‑624. https://doi.org/10.1016/J.SOLENER.2008.10.008

Touili, S., Alami Merrouni, A., Azouzoute, A., El Hassouani, Y., & Amrani, A. illah. (2018). A technical and economical assessment of hydrogen production potential from solar energy in Morocco. *International Journal of Hydrogen Energy*, *43*(51), 22777‑22796. https://doi.org/10.1016/j.ijhydene.2018.10.136

Tripanagnostopoulos, Y., Nousia, T., Souliotis, M., & Yianoulis, P. (2002). Hybrid photovoltaic/thermal solar systems. *Solar Energy*, *72*(3), 217‑234. https://doi.org/10.1016/S0038-092X(01)00096-2

Ueda, S., Hemeida, A. M., Krishna, N., Rangarajan, S., Collins, E. R., Mikhaylov, A., Takahashi, H., & Senjyu, T. (2022). Optimal Renewable Energy Configuration in Smart Cities Considering Shortened Annual Simulation. *SSRN Electronic Journal*. https://doi.org/10.2139/ssrn.4164019

Wang, D., Dhahad, H. A., Ali, M. A., Almojil, S. F., Almohana, A. I., Alali, A. F., Alyousuf, F. Q. A., & Almoalimi, K. T. (2023). Environmental/Economic assessment and multi-aspect optimization of a poly-generation system based on waste heat recovery of PEM fuel cells. *Applied Thermal Engineering*, *223*(November 2022), 119946. https://doi.org/10.1016/j.applthermaleng.2022.119946

Wang, G., Chao, Y., Jiang, T., Lin, J., Peng, H., Chen, H., & Chen, Z. (2023). Analyzing the effects of government policy and solar photovoltaic hydrogen production on promoting CO2 capture and utilization by using evolutionary game analysis. *Energy Strategy Reviews*, *45*, 101044. https://doi.org/10.1016/J.ESR.2022.101044

Wang, S., Lu, A., & Zhong, C. J. (2021). Hydrogen production from water electrolysis : Role of catalysts. *Nano Convergence*, *8*(1), 1‑23. https://doi.org/10.1186/S40580-021-00254-X/FIGURES/16

Yue, M., Lambert, H., Pahon, E., Roche, R., Jemei, S., & Hissel, D. (2021). Hydrogen energy systems : A critical review of technologies, applications, trends and challenges. *Renewable and Sustainable Energy Reviews*, *146*, 111180. https://doi.org/10.1016/J.RSER.2021.111180

GROUNDWATER POTENTIAL ASSESSMENT IN GIA LAI PROVINCE (VIETNAM) USING MACHINE LEARNING, REMOTE SENSING AND GIS

Huu Duy NGUYEN [1] 🆔 *, Van Trong GIANG [2]*, Quang-Hai TRUONG [2], Gheorghe ȘERBAN [3]* 🆔
Alexandru-Ionut PETRIȘOR [4,5,6,7] 🆔

ABSTRACT:
Population growth, urbanization and rapid industrial development increase the demand for water resources. Groundwater is an important resource in sustainable socio-economic development. The identification of regions with the probability of the existence of groundwater is necessary in helping decision makers to propose effective strategies for the management of this resource. The objective of this study is to construct maps of potential groundwater, based on machine learning algorithms, namely deep neural networks (DNNs), XGBoost (XGB), and CatBoost (CB), in the Gia Lai province of Vietnam. In this study, 12 conditioning factors, namely elevation, aspect, curvature, slope, soil type, river density, distance to road, land use/land cover (LULC), Normalized Difference Vegetation Index (NDVI), Normal Difference Built-up Index (NDBI), Normal Difference Water Index (NDWI), and rainfall were used, along with 181 groundwater inventory points, to construct the models. The proposed models were evaluated using the receiver operating characteristic (ROC) curve, the area under the curve (AUC), root-mean-square error (RMSE), mean absolute error (MAE). The results showed that the predictions of groundwater potential were most accurate using the XGB model; CB came second, and DNN was performed the least well. About 4,990 km^2 of the study area was found to be in the category of very low groundwater potential; 3,045 km^2 was in the low category; 2,426 km² was classified as moderate, 2,665 km^2 as high, and 2,007 km^2 as very high. The methodology used in the study was effective in creating groundwater potential maps. This approach, used in this study, can provide valuable information on the factors influencing groundwater potential and assist decision-makers or developers in managing groundwater resources sustainably. It also supports the sustainable development of the territory, including tourism. This methodology can be used in other geographic regions with a small change of input data.

Key-words: Groundwater potential, Deep neural network, XGBoost, CatBoost, Gia Lai, Vietnam.

1. INTRODUCTION

Groundwater is indispensable to humanity. Some 2.5 billion people depend on this resource every day (Prasad, Loveson et al. 2020, Gómez-Escalonilla, Martínez-Santos et al. 2022). The demand for groundwater is increasing rapidly, due to population growth and industrial development (Dey, Abir et al. 2023, Morgan, Madani et al. 2023). Today, 1.9 billion people (27% of the world's population) live in areas that can potentially be affected by severe water scarcity (Boretti and Rosa 2019). In 2050, it is estimated that this figure will increase to 2.7-3.2 billion, according to differing climate change scenarios (Boretti and Rosa 2019, Morgan, Madani et al. 2023).

_____

[1] *Faculty of Geography, National University of Vietnam, Hanoi, nguyenhuuduy@hus.edu.vn*

[2]* *Institute of Vietnamese Studies and Development Science, Vietnam National University, Hanoi,*
   Corresponding author: tronggv@vnu.edu.vn, truongquanghai.ivides@gmail.com

[3] *Faculty of Geography, Babes-Bolyai University, Cluj-Napoca, Romania; gheorghe.serban@ubbcluj.ro*

[4] *Doctoral School of Urban Planning, Ion Mincu University of Architecture and Urbanism, Bucharest,*
   Romania, alexandru_petrisor@yahoo.com

[5] *Department of Architecture, Faculty of Architecture and Urban Planning, Technical University of Moldova,*
   Chisinau, Moldova

[6] *National Institute for Research and Development in Constructions, Urbanism and Sustainable Spatial*
   Development URBAN-INCERC, Bucharest, Romania

[7] *National Institute for Research and Development in Tourism, Bucharest, Romania*

In Vietnam, survey data from the National Water Resources Planning and Investigation Centre show that the total national groundwater resource is around 91 billion cubic meters per year (250.7 million cubic meters per day), out of which the share of fresh water represents approximately 69 billion cubic meters per year (189.3 million cubic meters per day (Nguyen et al. 2024). Despite these figures, the country is currently facing severe pressure from decreasing water levels, and environmental pollution due to socio-economic growth and climate change. Thus, insufficient access to drinking water has become a major concern, and a key indicator of sustainable development according to international bodies (Kamali Maskooni, Naghibi et al. 2020, Prasad, Loveson et al. 2020). Therefore, the construction of groundwater potential maps plays an important role in optimizing water resources.

Several studies on the construction of such maps have been carried out using various approaches. The traditional method is largely based on drilling samples during field missions and hydrogeological testing in laboratories (Nguyen et al. 2024, Singh et al. 2024, Uddin et al. 2024). Although these methods can precisely identify regions with the probability of occurrence of potential groundwater, they are very expensive and time consuming and their application is limited to wide areas only. In recent years, with the development of remote sensing data and GIS technology, they have been effectively integrated into knowledge-based models such as AHP and weights-of-evidence used to delineate groundwater prospecting areas (Çelik et al. 2024, Diriba et al. 2024). However, these models depend on the opinion of experts, so such assessments are inherently subjective.

Currently, with increasing computing power and advancements in algorithms, data-driven models are widely used by researchers to construct groundwater potential maps. The statistical technique has been considered one of the most appropriate methods for constructing maps at scales of 1:20,000 or 1:50,000. Popular statistical models used include boosted regression tree (Naghibi et al., 2016, Sachdeva and Kumar 2021) and weights-of-evidence (Lee et al., 2012, Tahmassebipoor et al., 2016). However, these models do not consider nonlinear relationships, which can lead to errors in the identification of areas with probability of groundwater occurrence, particularly in the context of climate change. Machine learning models have been developed to solve these problems; these models include support vector machines (Lee et al, 2018, Anh et al., 2023), random forest (Naghibi et al., 2016, Rahmati et al., 2016), AdaBoost (Mosavi et al., 2021), and artificial neural networks (Nguyen et al., 2020, Tamiru and Wagari 2022). The goal of each study is to find the most effective model. Machine learning has the advantage of being able to mimic the complex, nonlinear relationships between groundwater points and environmental conditions, hydrology, climate and human activities without requiring an underlying understanding of physics. However, according to literature reviews, there are several machine learning models, and each model has advantages and disadvantages. Thus, selecting an appropriate model for specific data is a complex process. Additionally, extrapolation issues are considered a major challenge when using machine learning. This is because a machine learning model might not be able to make accurate predictions on data that differs significantly from the data used during training (Nguyen et al., 2024).

A number of studies have been carried out in recent years in Vietnam to assess groundwater potential. Bien et al. (2023) used five machine learning algorithms, namely partial decision trees (PART), Fuzzy Unordered Rule Induction Algorithm (FURIA), multilayer perceptron (MLP), Forest by Penalizing Attributes (FPA), and the DECORATE ensemble of learning techniques, to construct groundwater potential maps for the Central Highlands of Vietnam. The results showed that the DECORATE model performed better than the other ones. Nguyen et al. (2024) integrated deep neural networks (DNNs) with the optimization algorithms Adam, Flower Pollination Algorithm, Artificial Ecosystem-Based Optimization, Pathfinder Algorithm, African Vulture Optimization Algorithm (AVOA), and Whale Optimization Algorithm to predict groundwater potential in the Central region of Vietnam. The results indicated the DNN-AVOA model to be more effective than the others. Ha et al. (2021) applied machine learning ensemble models, namely Adaboost‑Quadratic Discriminant Analysis (ABQDA), Multiboost-Quadratic Discriminant Analysis, RealAdaboost-Quadratic Discriminant Analysis, to identify regions of probability of groundwater occurrence in Dak Nong province, Vietnam. The results showed that the ABQDA model was more accurate than the others.

Although there are several studies that have used machine learning to predict groundwater potential around the world and in Vietnam in particular, models have achieved differing levels of accuracy in different regions; there are no universally appropriate models. Therefore, it is necessary to find the appropriate algorithm(s) for each region to properly support decision makers and developers in the effective management of water resources, in order to better serve socio-economic development (Kumar et al., 2023; Masroor et al., 2023).

The objective of this study is to evaluate the potential of groundwater by applying machine learning algorithms, namely deep neural networks, CatBoost (CB), and XGBoost (XGB) in the province of Gia Lai in Vietnam. The novelty of this study is that for the first time these machine learning models are used to predict groundwater potential in this study area, where the problem of managing water resources is a great challenge, particularly in the context of climate change. This study also fills important knowledge gaps on groundwater potential investigations in Gia Lai Province, Vietnam. The results can support decision makers in proposing effective strategies in the management and optimization of water resources, not only in a specific region, but in other similar regions in the world (with minor changes in the input data).

2. STUDY AREA AND DATA USE

2.1. Study area

Gia Lai Province (12° 58' 40" -14° 37' 00" N, 107° 28' 04" -108° 54' 40" E) covers a natural area of 15,536.9 km2 in the north of Vietnam's Central Highlands. Gia Lai is located almost entirely west of the Truong Son range (**Fig. 1**).
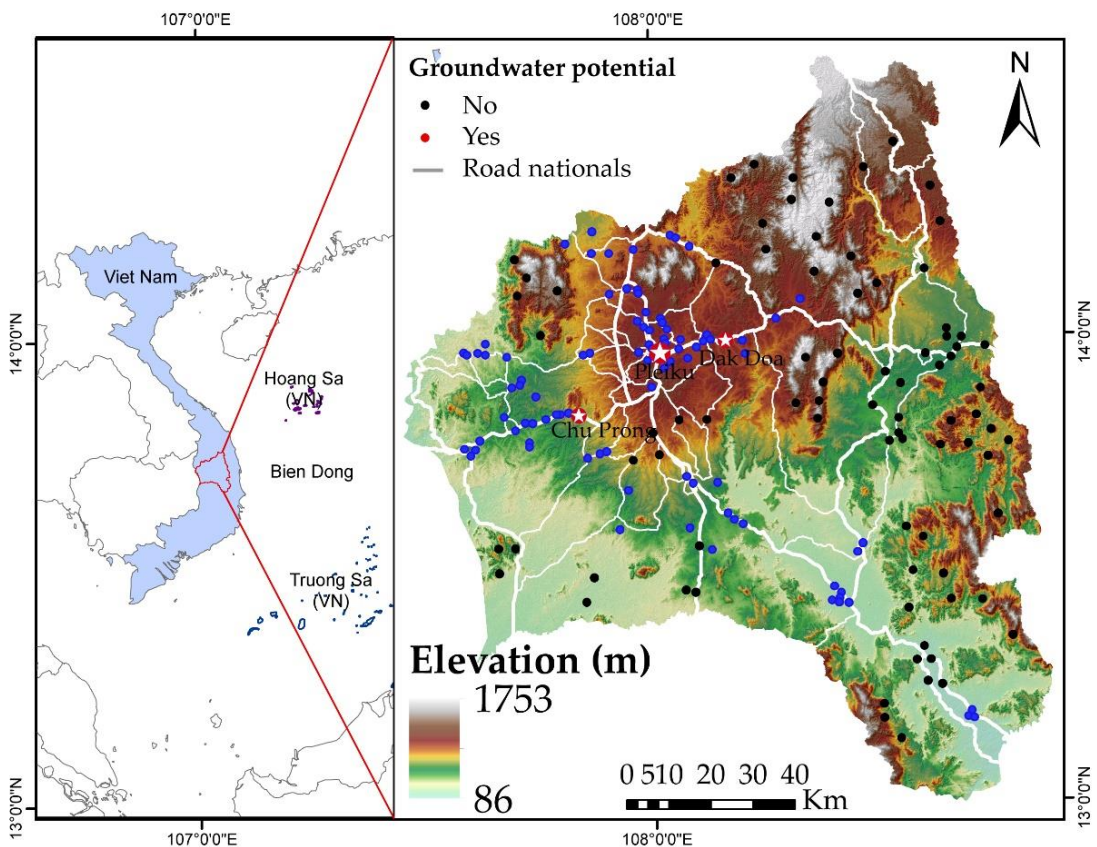
Fig. 1. Location of the study area.

The terrain gradually lowers from north to south and tilts from east to west, with quite complex alternating hills, plateaus and valleys. The average altitude is from 800 to 900 meters above sea level. The highest point is Kon Ka Kinh (1,748 m) in K'Bang district, while the lowest point is downstream of Ba River (100 m). The plateau is a popular and important terrain form of Gia Lai, with two plateaus made of basalt rock: Kon Ha Nung and Pleiku. Mountainous terrain accounts for 2/5 of the entire province's area, most of it located in the north, the mountain terrain is strongly separated, the surfaces of other terrain types of Gia Lai such as plateaus and valleys are also scattered with mountain. Relatively low-lying areas often form rivers when passing through sudden fault zones, typically An Khe valley in the East and Cheo Reo-Phu Tuc valley in the Southeast of the province.

Gia Lai has a provincial capital city, Pleiku, and two towns, An Khe, located in the West, and Ayunpa, located in the Southeast of the province. Pleiku City is located on Road 14, connecting with the provincial cities in the North and South, Kon Tum and Ban Me Thuat. Road 19 connects Pleiku City with the coastal city of Quy Nhon (Binh Dinh province) through An Khe town. Road 26 runs through Pleiku City, Ayunpa town to Tuy Hoa City (Phu Yen province). The province has an abundance of surface water, estimated at 23 billion m^3, distributed across the major river systems of the Ba and the Se San and tributaries of the Serepok. Groundwater potential is also considerable, and mainly concentrated in the basalt eruption water system, with total reserves of level A+B reaching 23,894 m3/day, level C1 61,065 m^3/day, and level C2 989,600 m^3/day. The surface water system also meets the community water needs of the province.

The climate is high-altitude tropical monsoon and is characterized by two distinct seasons: the rainy season lasts from May to October, and the dry season from November to April. The western Truong Son region enjoys average rainfall ranging between 2,200 and 2,500 mm, while in eastern Truong Son the figure is between 1,200- and 1,750-mm. Rainfall in the rainy season months accounts for about 75% of the total annual rainfall. Gia Lai province has 27 soil types, grouped into 7 main categories: red-brown and yellow-brown soils growing on basic and neutral igneous rocks (Rhodic Ferralsols), yellow-red soils on acidic magma soils (Ferralic Acrisols), red-yellow humus soils on mountains (Humic Acrisols), yellow-red soils changed by planting rice (Plinthic Acrisols), alluvial soils that are not deposited annually (Distric Fluvisols), eroded soils with bare stones (Lithic Leptosols).

Although Gia Lai province has abundant surface water sources, their distribution is uneven spatial and seasonal depending. In addition, the demand for domestic and irrigation water for industrial crops such as coffee, pepper, and cashew, as well as for fruit trees, is very high and increasing in recent years. En final, the Gia Lai province frequently experiences drought conditions. For example, in 2019, drought caused damage to thousands of acres of agricultural land and the damage to the economy was estimated at around 2 million dollars. Therefore, the construction of groundwater potential maps for the province is essential.

2.2. Data use

Well yields

Springs and wells are the points on land surfaces where groundwater is present. Spring and well data play a key role in the use of machine learning to predict groundwater potential. Thee is a complex relationships between groundwater points and natural and socioeconomic characteristics (Naghibi and Pourghasemi 2015, Prasad et al., 2020). Due to the high costs in the sampling process, spring and well data from previous studies were collected from the Department of Agriculture and Rural Development of Gia Lai Province and from a field mission, using GPS. 89 springs and well points were used as the final input data for the machine learning models.

This study used the binary model to identify areas with the probability of occurrence of groundwater potential. Therefore, the collection of non-spring and non-well samples was necessary to ensure the accuracy of the prediction model (Nguyen et al., 2024, Sharma et al., 2024, Singh et al., 2024). For the spatial model, several researchers have recommended that the number of spring and well points to be equal to the number of non-spring and non-well points.

Others have recommended that the number of non-spring and non-well points to be greater, if the study area is large (Arabameri et al., 2021). As Gia Lai is considered moderate in size, we collected an equal number of each of the two sets of points. 82 non-spring and non-well points were collected randomly throughout the study region with ArcGIS 10.6 software. A total of 181 data points were prepared to build the machine learning models. These points were identified as either 1 (for spring and well points) or 0 (for non-spring and non-well points).

Groundwater influencing factors

The selection of factors influencing the probability of groundwater occurrence is a difficult task, due to the complex and nonlinear nature of groundwater. There are no standard guidelines for their selection. The ambitious goal of this study was to integrate as many factors as possible. In the end, 12 influencing factors were selected, namely: elevation, curvature, aspect, slope (**Fig. 2a**); river density, distance to road, NDVI, NDBI (**Fig. 2b**); NDWI, rainfall, soil type and LULC (**Fig. 2c**).

Elevation, aspect, curvature, and slope were extracted from the ALOS PALSAR digital elevation model with a 12.5 m resolution. A topography map with a 1/50,000 scale was used to determine river density and distance to road with the ArcGis 10.6 Line Density and Euclidean Distance tool.

September 2023 Sentinel 2A imagery was used to extract NDVI, NDBI, and NDWI. 2023 LULC data was obtained from https://www.arcgis.com/apps/instant/media/index.html?appid=fc92d38533d440078f17678ebc20e8e2&fbclid=IwAR0V3ZEdUqhn79qN_JNPMtswxWfi2dE1_Gj-1ZD_XcN7oPyGMSn3-scE9KY

Annual rainfall from 2022 was accessed at https://chrsdata.eng.uci.edu/ . All these factors have been re-sampled at 12.5 m resolution using the ArcGIS 10.6 software.

Elevation and slope play an important role in the probability of the occurrence of groundwater resources, because altitude is directly linked to surface vegetation and recharge resources. In flat and low-lying regions, rainwater has more time to infiltrate and recharge groundwater. In the study region, the altitude ranges from 86 to 1753 m. The low-altitude regions are concentrated in the south and west (Ehsan et al., 2024, Oguntoyinbo et al., 2024). High altitude areas are distributed in the Kon Ka Kinh National Park area in the Northeast of the province.

Slope is another important topographical factor for a groundwater potential model because it is directly tied to the hydrological process and soil infiltration capacity. Regions with low slopes have the tendency to concentrate recharge resources (Raj et al., 2024). Areas with large slopes are concentrated in the eastern and northern mountains, and areas with small slopes are distributed in the Pleiku plateau area, located in the central and western areas of the province, and along the An Khe and Cheo valleys, Reo- Phu Tuc in the East and Southeast of the province.

Curvature was selected as a conditioning factor because it is directly related to the capacity of water accumulation and infiltration in the aquifer (Ray 2024). In Gia Lai, the curvature difference is not large by region, but tends to be small in river valleys, especially Ba River.

Aspect is linked to evaporation capacity and describes the flow direction, which strongly influences the recharge capacity of a region (Ehsan et al., 2024, Sharma et al., 2024). In the study area, the aspect is more complex in the northern mountainous areas and partly in the east.

LULC was chosen as it strongly influences hydrological processes, for example infiltration capacity, evaporation, and surface flow. The change of of land use has a significant influence on the recharge capacity of the groundwater resource. The increase in the surface area reduces the infiltration capacity of the soil, which leads to a reduction in the recharge capacity of the groundwater (Ray 2024, Tiwari et al., 2024). In Gia Lai, urban and construction lands are distributed in Pleiku city, An Khe and Ayunpa towns and along national and provincial highways; cultivated land is distributed mainly on the Pleiku and Kon Ha Nung plateaus, on river terraces; and natural and planted forests in mountain and hill areas. NDVI determines the density of vegetation in a region; therefore, it is considered an important factor in the probability of the occurrence of groundwater in a region.

NDBI measures the density of construction. Increasing the construction area reduces the infiltration capacity of the soil, which results in reducing the recharge capacity of groundwater (Huang et al., 2024, Rehman et al., 2024). High construction density is concentrated in Pleiku City, An Khe and Ayunpa towns.
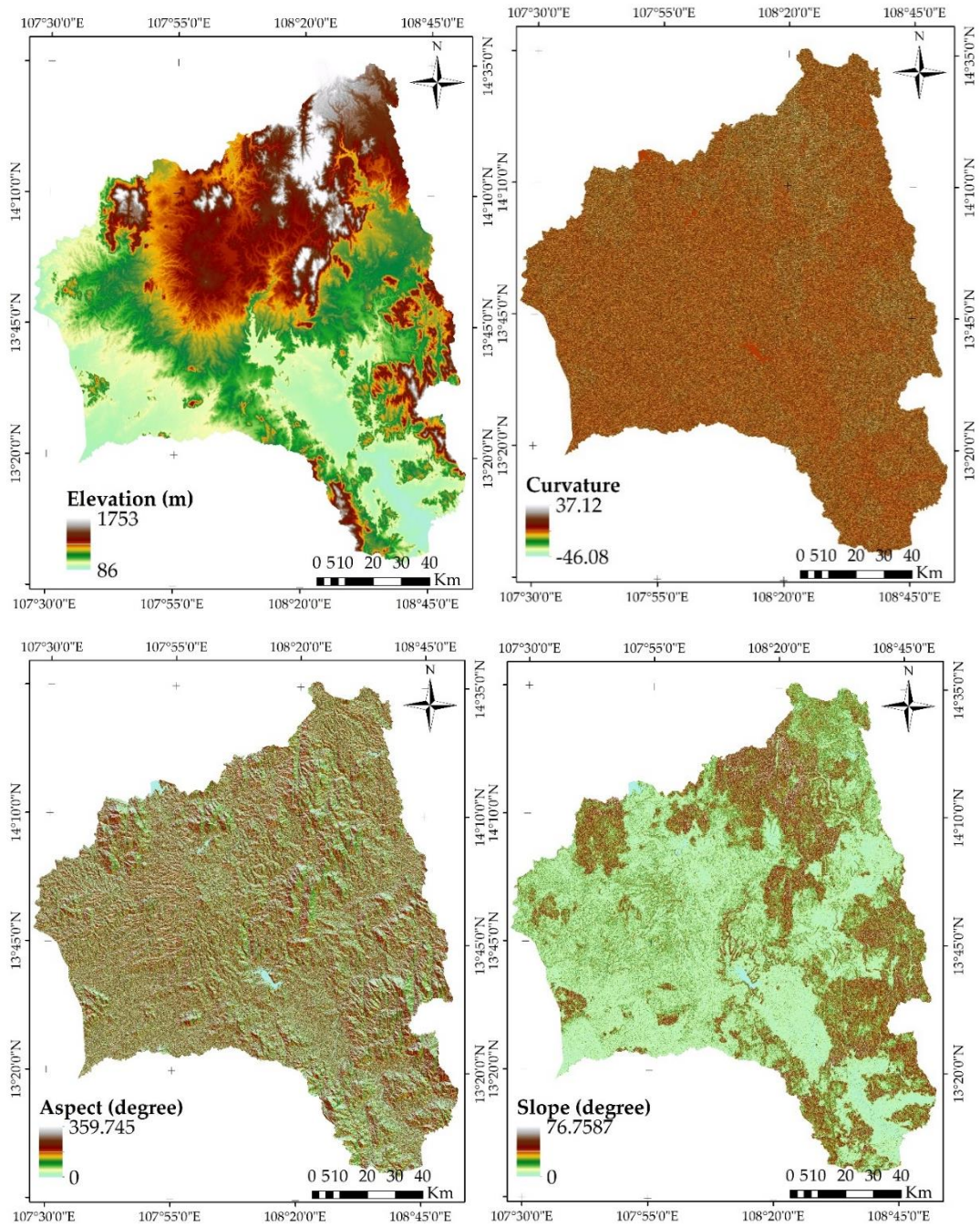
Fig. 2a. Conditioning factors used for the groundwater potential model: elevation, curvature, aspect, slope.

NDWI is considered an indispensable factor in identifying areas with the probability of groundwater occurrence because it is related to the groundwater recharge capacity in a region. The value of NDWI is proportional to the recharge capacity (Ghosh and Bera 2024). In Gia Lai, the NDWI index tends to be high in the Northeast, Southeast, Northwest and West; low in the center and south.
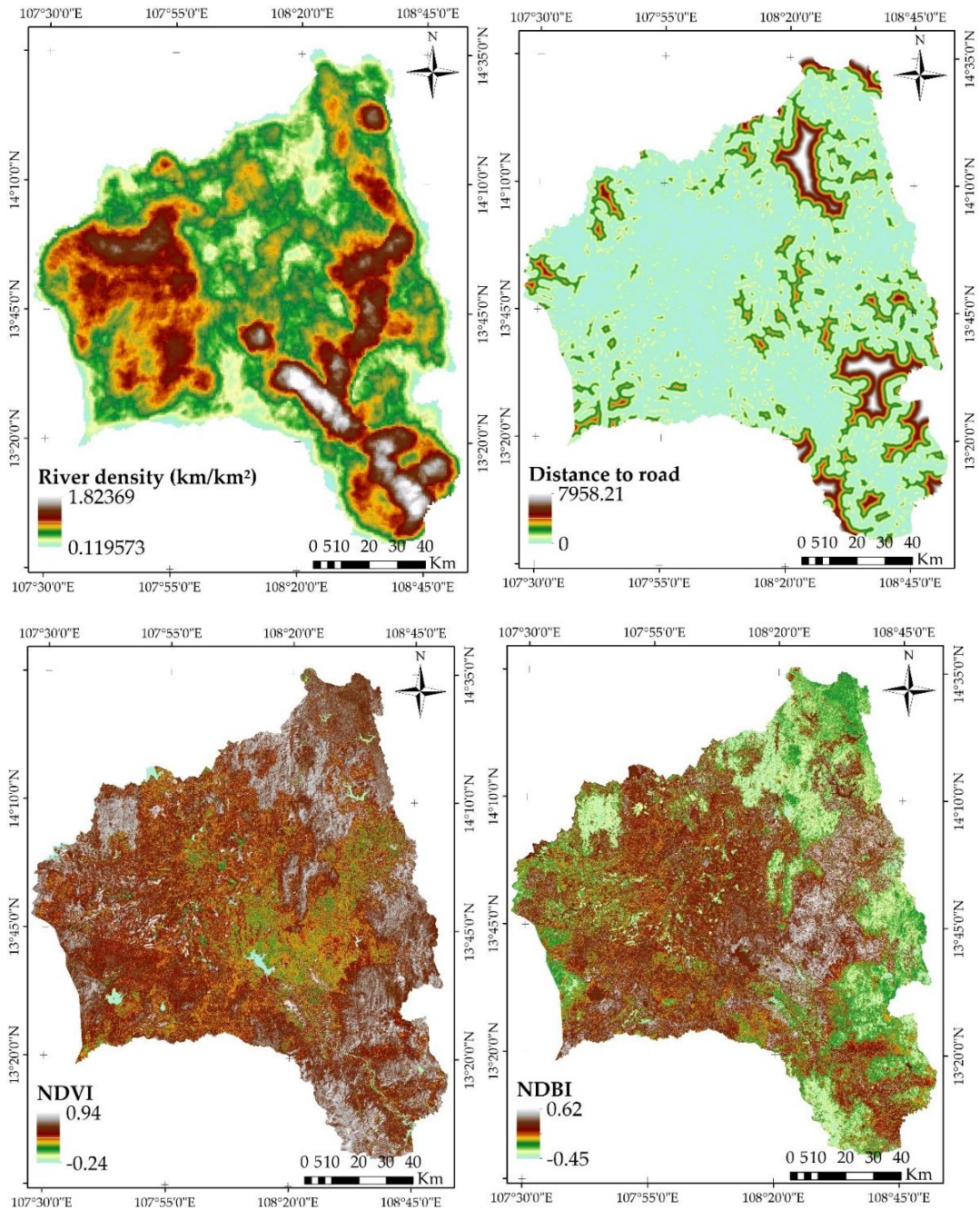
Fig. 2b. Conditioning factors used for the groundwater potential model: river density, distance to road, NDVI, NDBI.

Rainfall can increase groundwater recharge and so directly influences groundwater potential. Recharge depends on the amount of precipitation; precipitation value is proportional to groundwater recharge capacity (Raju et al. 2024). In the province, the rainfall is larger, about 1800 -2398 mm, concentrated in the northern region including mountains facing the wind; The Ba River valley area located in the Southeast has small rainfall, about 1432 mm -1600 mm.
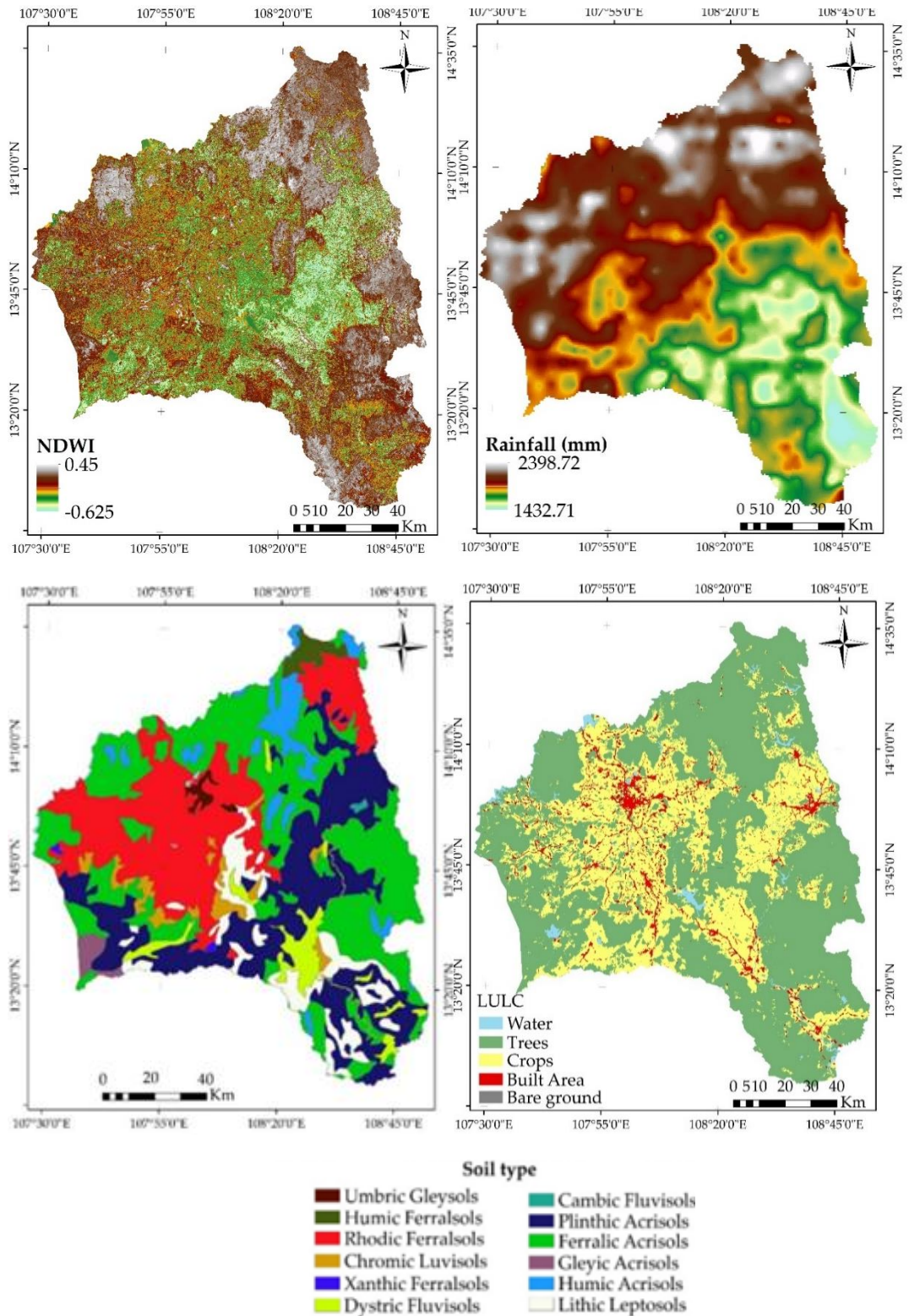
Fig. 2c. Conditioning factors used for the groundwater potential model: NDWI, rainfall, soil type, LULC.

Soil type plays an important role in predicting groundwater potential because it links to the permeability capacity of aquifer material and porosity of soil, which influence the groundwater recharge capacity (Dandapat et al., 2024, Nguyen et al., 2024). In Gia Lai, red-brown and yellow-brown soils develop on basic and neutral igneous rocks (Rhodic Ferralsols) distributed in the Pleiku Plateau and Kon Ha Nung Plateau. The soil absorbs water poorly but holds water well. Yellow-red soil on acid igneous soil (Ferralic Acrisols) has the ability to absorb water quickly, but poorer water retention ability. Humic Acrisols on the mountain have average water permeability and water holding capacity. Yellow-red soil changed due to rice cultivation (Plinthic Acrisols) has poor water absorption and retention capacity. Alluvial soils not deposited annually (Distric Fluvisols) have average water permeability and water holding capacity. Soil with eroded rocks (Lithic Leptosols) has very poor water absorption and water holding capacity. Alluvial soils not deposited annually (Distric Fluvisols) have average water permeability and water holding capacity. Soil with eroded rocks (Lithic Leptosols) has very poor water absorption and water holding capacity.

Rivers are, from a hydro-geological viewpoint, very important for controlling the movement and storage of potential groundwater. Areas with a high density of rivers and streams often have significant groundwater reserves (Ray 2024). In the study area, the river density is greatest along the Ba River valley in the east and the western edge of the Pleiku plateau.

Distance to road is considered another important factor because road construction can influence the infiltration capacity of the soil. Additionally, road construction can influence water drainage. All this can influence the water table recharge (Senapati and Das 2024).

3. METHODOLOGY

The construction of the groundwater potential map in Gia Lai province in Vietnam consisted of four main steps. The first was the preparation of input data, including the inventory map and conditioning factors; the second was the construction of groundwater potential models; the third was the validation of models, and the fourth was the analysis of groundwater potential map (**Fig. 3**).

i) Input data comprised the groundwater inventory map and 12 conditioning factors. The map was compiled using several sources: previous studies, data from the Department of Agriculture and Rural Development, and from a field mission. As conditioning factors were measured with different units, it was necessary to normalize the data with the assumption that the original values of all layers were retained, but the input database was standardized on similar ranges.

ii) Construction of groundwater potential model. The models DNN, CB, and XGB were used to predict groundwater potential. The DNN structure comprised three layers: the first was the input layer with 181 springs, well, non-spring, and non-well points, and 12 conditioning factors. These data was processed in the second layer, with 3 hidden layers and 11 neurons per layer. The weights in the hidden layers were optimized by Adam's optimization algorithm. In the end, the output layer consisted of two layers: groundwater and non-groundwater.

The performance of CB model depends on parameters such as iteration, depth, train direction, and loss function. In this study, the values of these parameters were 100, 3, logloss, and crossEntropy, respectively. The performance depended on $n\_$estimators, max_depth, learning rate, subsample and colsample by tree. These parameter values were 200, 4, 0.004, 0.4 and 0.4, respectively.

It should be noted that the machine learning models were developed on Python languages using the Tensorflow libraries.

iii) Evaluation of the performance of the proposed models. Statistical indices were used to evaluate the performance of the proposed models, namely AUC, RMSE, MAE and R^2.

iv) Analysis of the groundwater potential map. After evaluating the proposed models, they were used to construct groundwater potential maps for Gia Lai province. This process was carried out by assigning the values of the 12 conditioning factors to all pixels in the entire study area. The pixels in the study area are then identified as either groundwater or non-groundwater.
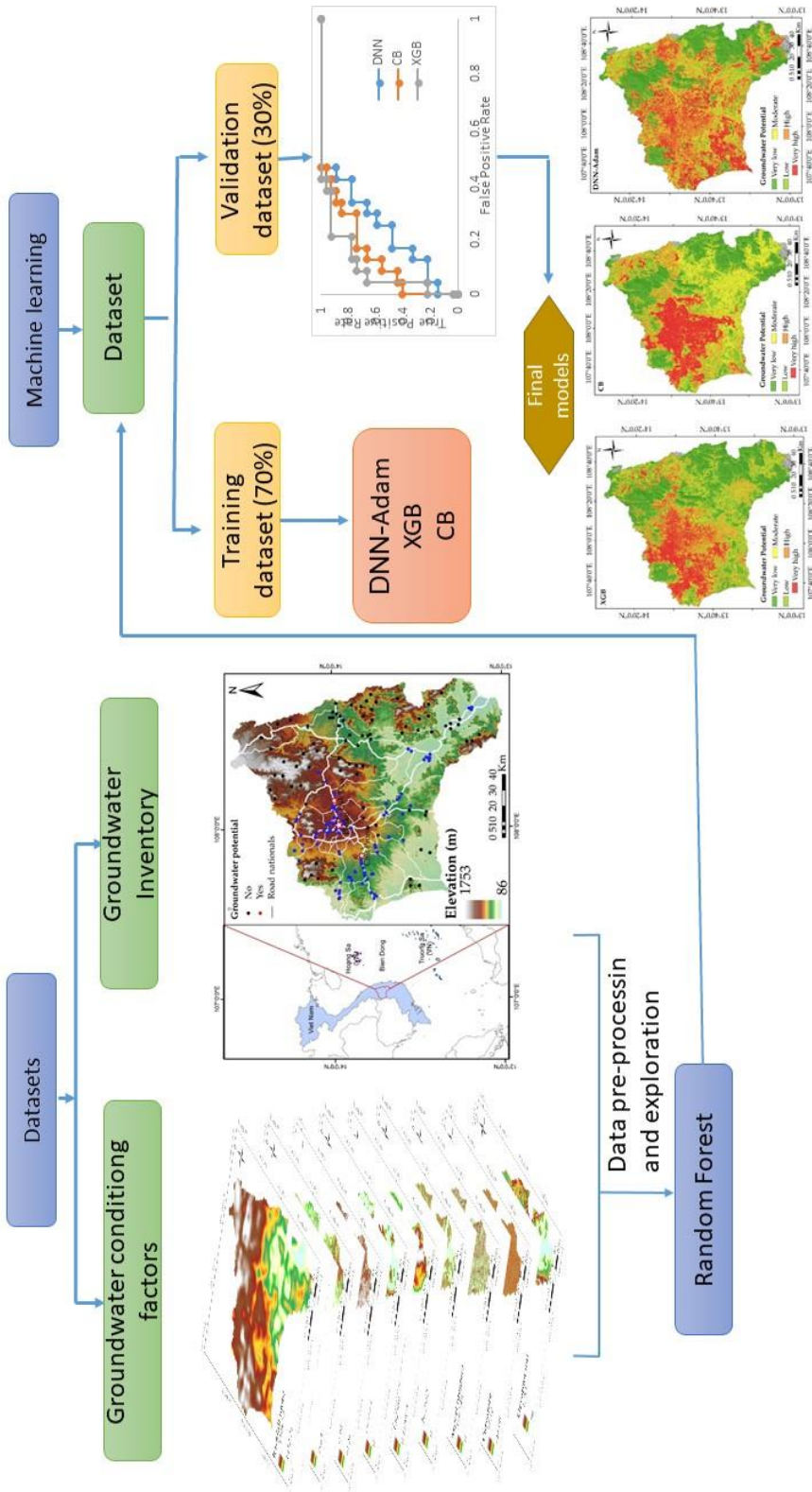
Fig. 3. Methodology used to create

3.1. Deep neural networks (DNN)

DNNs constitute a branch of machine learning that uses neural networks to solve complex, real-world, non-linear problems (Wang et al., 2022). DNNs have attracted the attention of researchers in recent years, particularly in Earth sciences, due to their ability to automatically learn complex data abstractions. The DNN model includes 3 layers: the input layer contains information related to groundwater prediction factors; this information is transmitted to and processed by the second layer, which includes one or more hidden layers; the output of the third layer is labeled groundwater and non-groundwater. With a large number of hidden layers, DNN models can solve many complex problems and are considered more powerful than simple neural networks (Bai et al., 2022, Hakim et al., 2022). The DNN model uses a backpropagation algorithm, which means that the output error is propagated to the hidden layers to update the weights. The DNN model computes the gradient of the loss function for each weight according to the chain rule and avoids redundant calculations from intermediate factors. During this operation, each neuron uses activation functions to process information in hidden layers. These activation functions are used for gradient training and are represented by rectified linear units (ReLU) (Hakim et al., 2022). There are many known optimization algorithms used to calculate weights of DNN models, such as SGD and AdaGrad. In this study, the weights of the DNN model were calculated using the adaptive moment (Adam). Adam is a stochastic optimization algorithm based on a first-order gradient. During the operation, Adam maintains the mean square of past slopes and also maintains the average of past slopes. Adam has the advantage of being simple to implement and requiring little memory. Previous studies have also shown Adam's optimization algorithm to be more accurate than other stochastic optimization models (Hakim et al., 2022).

3.2. CaTBoost (CB)

CB was first introduced by Yandex to solve both classification and regression problems using decision trees (Liang et al., 2023). CB is based on gradient boosting with the ideas of transforming weak learners into strong learners. It includes two main features: it works with categorical data ("Cat") and it uses gradient boosting ("Boost") (Tran et al., 2021). Gradient boosting is a process in which many decision trees are built iteratively (Koch et al., 2021). Each subsequent tree improves the result of previous tree, which optimizes the results. Each decision tree is then an evolution of an initial set of data. CB incorporates innovative techniques, such as target encoding and combining statistics from categorical variables, to leverage information present in categorical features and improve predictive performance (Abba et al., 2023, Yavuz Ozalp et al., 2023).

3.3. XgBoost (EXT)

XGB, or eXtreme Gradient Boosting, was first developed by Tianqi Chen in 2016 and can solve classification and regression problems (Chen and Guestrin 2016). The basic idea is to combine gradient descent with boosting methods in order to create a more powerful machine learning algorithm (Zounemat-Kermani et al., 2021). This involves assembling several algorithms with relatively low performance to create one that is much more efficient and satisfactory (Lim and Chi 2019, Tran et al., 2021). The result consists of the predictions of all the chained models. This method improves the model performance and stability while reducing its variance. Therefore, ensemble learning can achieve a much higher level of accuracy than using any of the individual models separately (Ghosh and Bera 2024).

3.4. Performance assessment

The models proposed in this study were evaluated using the statistical indices: AUC, RMSE, MAE. Details of information can be viewed in (Naghibi, Hashemi et al. 2020, Wang et al. 2023, Xiong, Guo et al. 2023):

$$AUC = \sum TP + \sum \frac{TN}{P} + N \tag{1}$$

$$RMSE = \sqrt{\frac{1}{n}\sum_{i=1}^{n}(Y_{predicted} - Y_{bserved})^2} \tag{2}$$

$$MAE = \frac{1}{n}\sum_{i=1}^{n}|Y_{predicted} - Y_{observed}| \tag{3}$$

$$R^2 = 1 - \frac{\sum_{i=1}^{n}(y_i - \ddot{y}_{\square})^2}{\sum_{i=1}^{n}(y_i - \ddot{y})^2} \tag{4}$$

4. RESULTS AND DISCUSSIONS

4.1. Pre-processing results

Careful selection of conditioning factors plays an important role in the performance of any prediction model. This study used data-driven models to analyze the relationships between spring and well points and the explanatory variables and, therefore, factor selection can help models concentrate important factors and eliminate non-useful factors. This study used the RF technique to select the factors and assign a weight to each one. **Figure 4** illustrates the importance of each conditioning factor. The results showed that distance to road, soil type, NDBI, and slope were the most influential in identifying areas of probable groundwater. These factors are directly linked to the capacity of water infiltration and accumulation, all of which influences the recharge capacity of water table. In Gia Lai province, construction area has been growing at an increasing rate in recent years, as a result of population growth and economic development. This increase has been mainly concentrated in the low slope region.
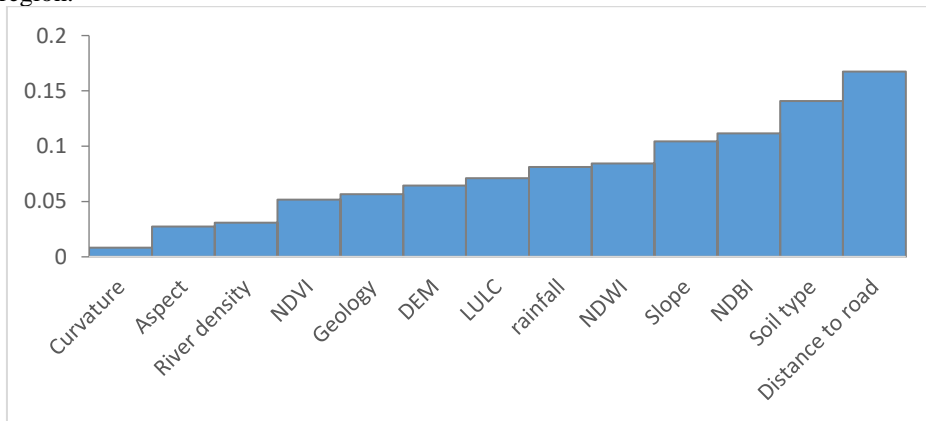
Fig. 4. The importance of groundwater conditioning factors, using RF.

NDWI, rainfall, LULC, and elevation were fifth to eighth most important, respectively. NDWI plays an important role in the occurrence of groundwater in a region because it is directly related to recharge capacity. In Gia Lai province, the region with a high NDWI value is concentrated in the eastern, southern and central regions of the province. Rainfall is important as it provides a source of water that can infiltrate the ground and recharge underground aquifers. Precipitation tends to accumulate in the region at low altitudes and, therefore, in these regions, conditions are conducive to strong recharge of underground aquifers. LULC reflects human activity in a region. The reduction of surface vegetation and increase of construction area led to the accumulation of water on the surface, which reduced the recharge capacity of underground aquifers.

Curvature, aspect, and river density appear to have less influence on the probability of occurrence of groundwater potential in Gia Lai province.

4.2. Modeling assessment results

This study used the AUC index to evaluate the performance of proposed models. Figure 5 shows the accuracy of proposed models when using training and validation data. The results show that the XGB model identified regions with a probability of occurrence of groundwater potential more accurately than the CB and DNN models. The DNN model was least effective.

For the validation data, the XGB model further identified regions with a higher probability of occurrence of groundwater potential than other models. The CB model ranked second. The DNN model performed worse than the XGB and CB models. The DNN model required a significant amount of data to provide more accurate results. Given the difficulties encountered in collecting data on spring and well points, only 82 points were available. Therefore, there may not have been enough data to properly train the DNN models (**Fig. 5**).
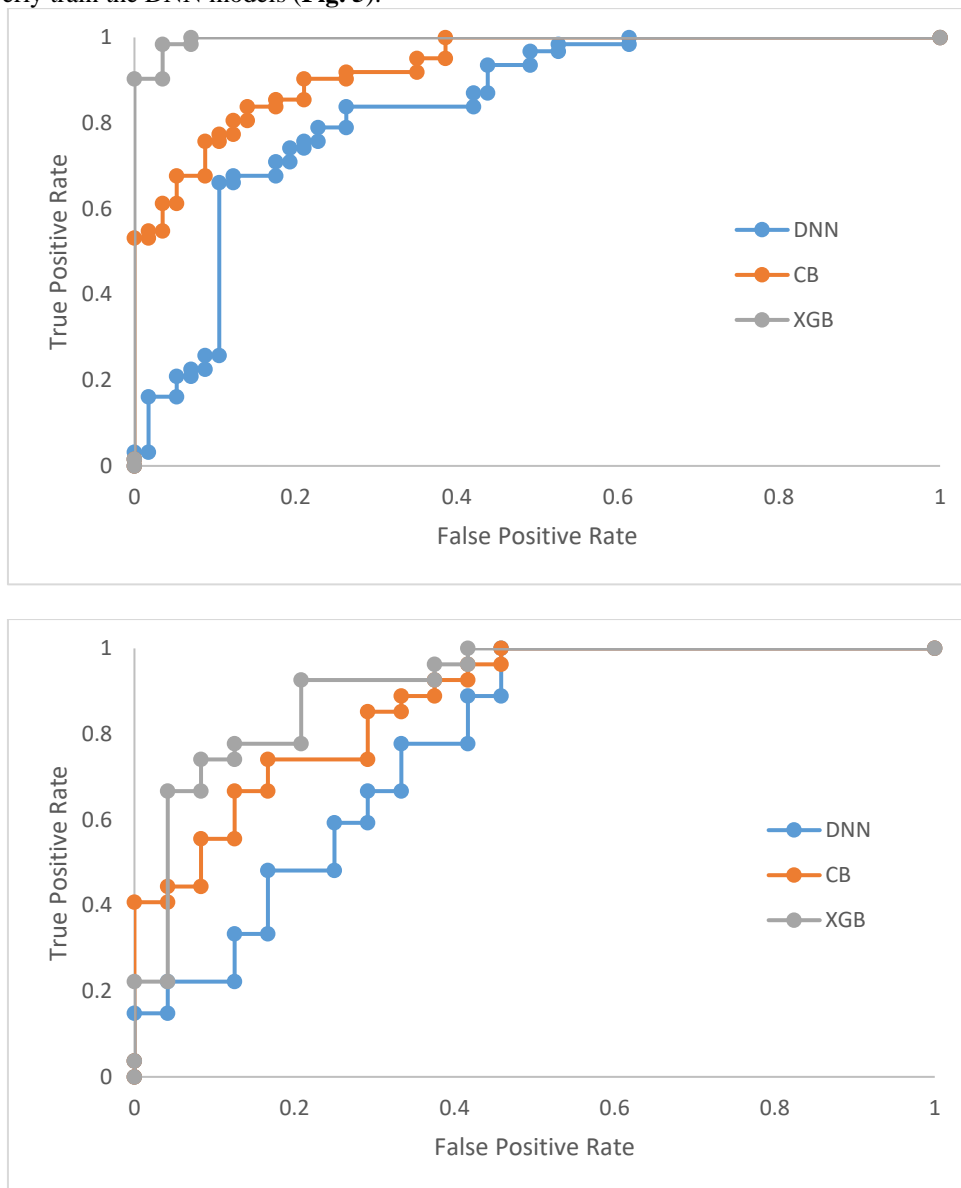
Fig. 5. AUC values for the training dataset (top) and validation dataset (bottom).

In addition to the AUC values, this study used the statistical indices RMSE, MAE, and R^2 to evaluate and compare the proposed models. The results show that the XGB model returned RMSE, MAE, and R^2 values higher than the other two models for the training data. For the validation data, XGB performed even better in terms of RMSE, MAE, and R^2. CB came second, and DNN performed least well.

In general, all proposed models were suitable for identifying regions with the probability of occurrence of groundwater potential in Gia Lai province. However, we recommend the use of XGB because several studies have pointed out that XGB has advantages in being able to solve problems with precision when data are not sufficient (**Table 1**).

Table 1.

Precision of DNN, XGB, and CB.

	Training dataset				Validation dataset			
	RMSE	**MAE**	**AUC**	**R^2**	**RMSE**	**MAE**	**AUC**	**R^2**
XGB	0.2	0.15	0.996	0.82	0.35	0.25	0.91	0.814
CB	0.4	0.36	0.929	0.80	0.41	0.373	0.87	0.796
DNN	0.41	0.373	0.835	0.78	0.42	0.383	0.77	0.779

4.3. Groundwater potential mapping

After the evaluation of the machine learning model, all the proposed models are performed to construct the groundwater potential map. The calculation of groundwater value in Gia Lai province is carried out by aggregating all pixels, which have 12 conditional factor values associated with them, in the machine learning model. The result of the model represents the groundwater value of the entire study area, on a scale from 0 to 1. The values were divided by five classes: very low, low, moderate, high and very high in using Break Natural methods. **Figure 6** shows the maps of groundwater potential produced by XGB, CB and DNN-Adam. The results reported that according to XGB, 4990 km2 of the province constituted the area of very low groundwater potential, with 3045 km2, 2426 km2, 2655 km2, and 2077 km2 were in the low, moderate, high and very high categories. For the CB model, the very low category covers 3325 km², low - 3573 km², moderate - 3489 km², high - 2308 km², and very high - 2489 km². According to the DNN-Adam model, approximately 3580 km² of the province is in the very low area of groundwater potential, 2198 km² - low, 2741 km² - moderate, 3377 km² - high, and 3298 km² - very high.

In general, although there are differences between the models, we found out that the regions of high and very high groundwater potential are located in the districts of Pleiku, Dak Doa, Ia Grai, and Chu Prong, as well as a small part of K'Bang. Although these areas are densely populated and have high construction density, the distance to the road is small, the rainfall quite large, slope is small, and the vegetation consists mainly of coffee and rubber, which helps to absorb and retain water well. Basalt soil is quite permeable and retains water well, providing a lot of water for the Pleistocene Basalt eruptive fissure aquifer.

The area with average groundwater potential is mainly distributed on the edge of the Pleiku plateau and Ba River valley in the south and southeast of the province. This area's terrain is less steep, there is not much rainfall, the road density is quite large, and the alluvial soil absorbs and retains water quite well, providing water for the aquifer, cracks and seams of Neogene sedimentary lagoon formations and modern alluvial porous aquifers.

Areas with low and very low groundwater potential are distributed mainly in the mountainous parts of Northeast, East and Northwest. Although there is heavy rainfall and forest cover, the construction density is small, but the altitude is high and slope steep, distance to the road long, and the weathered crust from metamorphic rocks has a weak ability to absorb and retain water, so the amount of surface water supplied to groundwater in the rainy season is very limited.
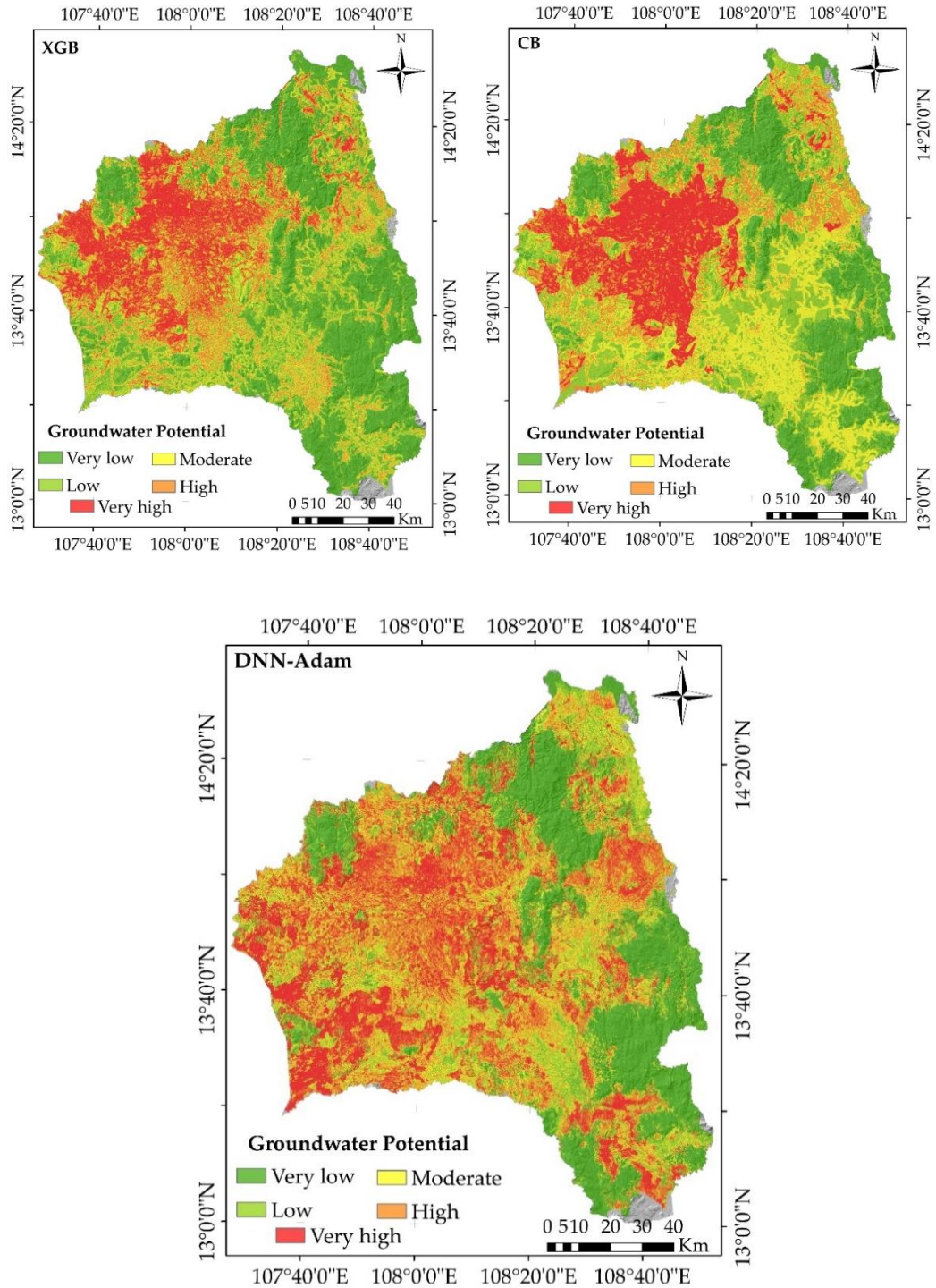
Fig. 6. Groundwater potential maping for the Gia Lai province.

5. DISCUSSION

Groundwater resources play an important role in the development of agriculture and industry all over the world (Pan et al., 2023, Huang et al., 2024). Construction of groundwater potential maps can be a successful method to support decision makers in effectively managing groundwater resources (Anh et al., 2023, Kumar et al., 2023, Vafadar et al., 2023, Wang et al., 2023). Many studies have used different methods to construct maps of groundwater potential.

Regional studies are still necessary to obtain appropriate information for water resource management in a specific locality. To this end, the objective of this study was to construct a groundwater potential map based on machine learning, namely DNN, XGB and CB, in Gia Lai province of Vietnam.

With the development of remote sensing and GIS, machine learning has received the attention of researchers in recent years, due to its application in spatial data modeling. One of is advantages is the ability to eliminate limitations linked to the lack of precise data. However, overfitting problems are considered a big challenge when using machine learning and each region has different characteristics, so selecting appropriate models is very important to build a groundwater potential map with accuracy (Anh et al., 2023, Wang et al., 2023, Nguyen et al., 2024).

Out of the three models used in this study, the XGB model was found to perform better than the other two. Several studies have also highlighted its ability to explain complex relationships between variables. Thus, it is considered an attractive choice for constructing a groundwater potential map. Additionally, XGB combines regularization techniques, which helps reduce overfitting issues. Additionally, it has the ability to handle missing data (Pan et al., 2023, Ngai et al., 2024). All these features allow the XGB model to yield more accurate predictions than other models.

The CB model came second. It can resolve missing data issues natively and is one of the most powerful algorithms in solving overfitting problems, by combining automatic regularization mechanisms (Gao et al., 2024, Raheja et al., 2024). The DNN model performed worst. In general, DNN models are suitable for big data studies. However, in this study, due to the difficulties encountered in data collection, only 181 data points were collected (Wang et al., 2024). The DNN model was not suitable for constructing groundwater potential maps.

The remaining question of this study is whether the proposed models can predict groundwater potential in the context of climate change, when precipitation and temperatures are not stable. This may not be an issue if the model can learn from climate change data. However, data collection is a big challenge, especially in developing countries like Vietnam, where data sharing policies are restrictive and financial resources limited (Nguyen et al., 2024, Nguyen et al., 2024, Nguyen et al., 2024).

The results of this study have also important implications for planners. The connection between water, particularly groundwater, and climate changes has been stressed out by previous studies (Dragoni and Sukhija, 2008, Earman and Dettinger, 2011, Amanambu et al., 2020). At the same time, other authors underlined the potential of planning to mitigate the impact of climate change (Wilson, 2006; Hurlimann and March, 2012, Petrişor et al., 2021). A good example of the relationship between water and planning comes from a World Bank study carried out in Romania, in order to develop specific guidelines for integrating the flood risk management in planning, with specific provisions related to groundwater (World Bank 2023). Therefore, accounting for the groundwater potential in planning may help increasing urban resilience to climate changes. In this regard, provided that other studies pointed out the presence of derogatory planning in Vietnam (Petrişor et al. 2020), i.e. making local exemptions from national planning provisions, our results plead for the need to enforce the planning provisions regarding underground water when planning for regions similar to the one investigated in our study. In addition, the important role in territorial or urban planning, the results of this study play an important role for tourism planning, because developing tourism, relies on tourist destinations that need to use water directly (food, accommodation, etc.) or indirectly. In these destinations water must be used in a way that balances tourist and resident populations, while ensuring water security. Therefore, developing new precise methods is very important to support decision-makers in tourism development too.

6. CONCLUSIONS

Groundwater resources play an important role in sustainable socio-economic development, particularly in the context of climate change and population growth. Therefore, the construction of precise groundwater potential maps is necessary to support those responsible for optimizing water resources. The objective of this study was to construct a potential groundwater map using the machine learning techniques DNN, XGB, and CB in the Gia Lai province of Vietnam. The conclusions of this study are stated below.

- The traditional machine learning model was more powerful than the deep learning model for the groundwater potential model, due to the collection of input data. The methodology in this study can be applied in other regions to construct groundwater potential maps.

- A comparison of the three proposed models showed XGB to have a better performance, with an AUC value of 0.91; second was CB (0.87), and third DNN (0.77). A successful implementation of these models can support decision makers in proposing effective strategies to optimize water resource management.

- The regions of high and very high probability of groundwater are concentrated in the west of the province, in the districts of Pleiku, Dak Doa, Ia Grai and Chu Prong, and a small part of K'Bang.

Although this study was successful in constructing groundwater potential maps, there were limitations relating to the selection of non-spring and non-well points. There are no universal guides for selecting these points. They were randomly selected from the study region. Inaccurate selection of areas without groundwater can lead to errors of the groundwater potential map. In addition, areas with groundwater potential are affected by surface temperature; regions with high surface temperatures are less likely to contain groundwater. Therefore, future research should try to integrate surface temperature into the groundwater potential model. Finally, the potential of groundwater is strongly influenced by climate change and human activities. Therefore, future studies should try to integrate these factors into a machine learning model to predict the future potential of groundwater.

The results of this study can support decision makers in identifying regions with high and very high probability of groundwater so they can implement appropriate infrastructure for developing agriculture and industry.

ACKNOWLEDGMENT

R E F E R E N C E S

Abba, S. I., M. A. Yassin, A. S. Mubarak, S. M. H. Shah, J. Usman, A. Y. Oudah, S. R. Naganna and I. H. Aljundi (2023). "Drinking Water Resources Suitability Assessment Based on Pollution Index of Groundwater Using Improved Explainable Artificial Intelligence." Sustainability 15(21): 15655.

Anh, D. T., M. Pandey, V. N. Mishra, K. K. Singh, K. Ahmadi, S. Janizadeh, T. T. Tran, N. T. T. Linh and N. M. Dang (2023). "Assessment of groundwater potential modeling using support vector machine optimization based on Bayesian multi-objective hyperparameter algorithm." Applied Soft Computing 132: 109848.

Arabameri, A., S. C. Pal, F. Rezaie, O. A. Nalivan, I. Chowdhuri, A. Saha, S. Lee and H. Moayedi (2021). "Modeling groundwater potential using novel GIS-based machine-learning ensemble techniques." Journal of Hydrology: Regional Studies 36: 100848.

Bai, Z., Q. Liu and Y. Liu (2022). "Groundwater potential mapping in hubei region of china using machine learning, ensemble learning, deep learning and automl methods." Natural Resources Research 31(5): 2549-2569.

Bien, T. X., A. Jaafari, T. Van Phong, P. T. Trinh and B. T. Pham (2023). "Groundwater potential mapping in the Central Highlands of Vietnam using spatially explicit machine learning." Earth Science Informatics 16(1): 131-146.

Boretti, A. and L. Rosa (2019). "Reassessing the projections of the world water development report." NPJ Clean Water 2(1): 15.

Çelik, M. Ö., L. Kuşak and M. Yakar (2024). "Assessment of Groundwater Potential Zones Utilizing Geographic Information System-Based Analytical Hierarchy Process, Vlse Kriterijumska Optimizacija Kompromisno Resenje, and Technique for Order Preference by Similarity to Ideal Solution Methods: A Case Study in Mersin, Türkiye." Sustainability 16(5): 2202.

Chen, T. and C. Guestrin (2016). Xgboost: A scalable tree boosting system. Proceedings of the 22nd acm sigkdd international conference on knowledge discovery and data mining.

Dandapat, K., U. Chatterjee, S. Das, A. Patra, H. Manna, A. Ghosh, S. C. Pal, A. R. M. Towfiqul Islam, R. Costache and E. Alam (2024). "Assessment of groundwater potential zones in data-scarce regions using GIS-based multicriteria decision making approach." Geocarto International 39(1): 2311202.

Dey, B., K. A. M. Abir, R. Ahmed, M. A. Salam, M. Redowan, M. D. Miah and M. A. Iqbal (2023). "Monitoring groundwater potential dynamics of north-eastern Bengal Basin in Bangladesh using AHP-Machine learning approaches." Ecological Indicators 154: 110886.

Diriba, D., S. Karuppannan, T. Takele and M. Husein (2024). "Delineation of groundwater potential zonation using geoinformatics and AHP techniques with remote sensing data." Heliyon.

Ehsan, M., H. Shabbir, A. M. F. Al-Quraishi, N. Al-Ansari, Z. Ahmad, K. Abdelrahman, M. T. Sohail, Z. Manzoor, A. Shafi and A. Elbeltagi (2024). "Groundwater delineation for sustainable improvement and development aided by GIS, AHP, and MIF techniques." Applied Water Science 14(2): 1-21.

Gao, W., M. Zang and G. Mei (2024). "Exploring influence of groundwater and lithology on data-driven stability prediction of soil slopes using explainable machine learning: a case study." Bulletin of Engineering Geology and the Environment 83(1): 2.

Ghosh, A. and B. Bera (2024). "Identification of potential dam sites for severe water crisis management in semi-arid fluoride contaminated region, India." Cleaner Water: 100011.

Ghosh, A. and B. Bera (2024). "Potentialities and development of groundwater resources applying machine learning models in the extended section of Manbhum-Singhbhum Plateau, India." HydroResearch 7: 1-14.

Gómez-Escalonilla, V., P. Martínez-Santos and M. Martín-Loeches (2022). "Preprocessing approaches in machine-learning-based groundwater potential mapping: an application to the Koulikoro and Bamako regions, Mali." Hydrology and Earth System Sciences 26(2): 221-243.

Ha, D. H., P. T. Nguyen, R. Costache, N. Al-Ansari, T. Van Phong, H. D. Nguyen, M. Amiri, R. Sharma, I. Prakash and H. Van Le (2021). "Quadratic discriminant analysis based ensemble machine learning models for groundwater potential modeling and mapping." Water Resources Management 35: 4415-4433.

Hakim, W. L., A. S. Nur, F. Rezaie, M. Panahi, C.-W. Lee and S. Lee (2022). "Convolutional neural network and long short-term memory algorithms for groundwater potential mapping in Anseong, South Korea." Journal of Hydrology: Regional Studies 39: 100990.

Huang, P., M. Hou, T. Sun, H. Xu, C. Ma and A. Zhou (2024). "Sustainable groundwater management in coastal cities: Insights from groundwater potential and vulnerability using ensemble learning and knowledge-driven models." Journal of Cleaner Production: 141152.

Kamali Maskooni, E., S. A. Naghibi, H. Hashemi and R. Berndtsson (2020). "Application of advanced machine learning algorithms to assess groundwater potential using remote sensing-derived data." Remote Sensing 12(17): 2742.

Koch, J., J. Gotfredsen, R. Schneider, L. Troldborg, S. Stisen and H. J. Henriksen (2021). "High resolution water table modeling of the shallow groundwater using a knowledge-guided gradient boosting decision tree model." Frontiers in Water 3: 701726.

Kumar, M., P. Singh and P. Singh (2023). "Machine learning and GIS-RS-based algorithms for mapping the groundwater potentiality in the Bundelkhand region, India." Ecological Informatics 74: 101980.

Lee, S., S.-M. Hong and H.-S. Jung (2018). "GIS-based groundwater potential mapping using artificial neural network and support vector machine models: the case of Boryeong city in Korea." Geocarto international 33(8): 847-861.

Lee, S., Y.-S. Kim and H.-J. Oh (2012). "Application of a weights-of-evidence method and GIS to regional groundwater productivity potential mapping." Journal of Environmental Management 96(1): 91-105.

Liang, Z., W. Peng, W. Liu, H. Huang, J. Huang, K. Lou, G. Liu and K. Jiang (2023). "Exploration and comparison of the effect of conventional and advanced modeling algorithms on landslide susceptibility prediction: A case study from Yadong Country, Tibet." Applied Sciences 13(12): 7276.

Lim, S. and S. Chi (2019). "Xgboost application on bridge management systems for proactive damage estimation." Advanced Engineering Informatics 41: 100922.Masroor M, Sajjad H, Kumar P, Saha TK, Rahaman MH, Choudhari P, Kulimushi LC, Pal S, Saito O (2023) Novel ensemble machine learning modeling approach for groundwater potential mapping in Parbhani District of Maharashtra, India. Water 15:419.

Morgan, H., A. Madani, H. M. Hussien and T. Nassar (2023). "Using an ensemble machine learning model to delineate groundwater potential zones in desert fringes of East Esna-Idfu area, Nile valley, Upper Egypt." Geoscience Letters 10(1): 9.

Mosavi, A., F. Sajedi Hosseini, B. Choubin, M. Goodarzi, A. A. Dineva and E. Rafiei Sardooi (2021). "Ensemble boosting and bagging based machine learning models for groundwater potential prediction." Water Resources Management 35: 23-37.

Naghibi, S. A., H. Hashemi, R. Berndtsson and S. Lee (2020). "Application of extreme gradient boosting and parallel random forest algorithms for assessing groundwater spring potential using DEM-derived factors." Journal of Hydrology 589: 125197.

Naghibi, S. A. and H. R. Pourghasemi (2015). "A comparative assessment between three machine learning models and their performance comparison by bivariate and multivariate statistical methods in groundwater potential mapping." Water resources management 29: 5217-5236.

Naghibi, S. A., H. R. Pourghasemi and B. Dixon (2016). "GIS-based groundwater potential mapping using boosted regression tree, classification and regression tree, and random forest machine learning models in Iran." Environmental monitoring and assessment 188: 1-27.

Ngai, C. H., A. J. Kilpatrick and A. Ćwiek (2024). "Sound symbolism in Japanese names: Machine learning approaches to gender classification." Plos one 19(3): e0297440.

Nguyen HD, Nguyen Q-H, Bui Q-T (2024) Solving the spatial extrapolation problem in flood susceptibility using hybrid machine learning, remote sensing, and GIS. Environmental Science and Pollution Research:1-22.

Nguyen, H. D., D. K. Dang, N. Y. Nguyen, C. Pham Van, T. T. Van Nguyen, Q.-H. Nguyen, X. L. Nguyen, L. T. Pham, V. T. Pham and Q.-T. Bui (2024). "Integration of machine learning and hydrodynamic modeling to solve the extrapolation problem in flood depth estimation." Journal of Water and Climate Change 15(1): 284-304.

Nguyen, H. D., Q.-H. Nguyen and Q.-T. Bui (2024). "Solving the spatial extrapolation problem in flood susceptibility using hybrid machine learning, remote sensing, and GIS." Environmental Science and Pollution Research: 1-22.

Nguyen, H. D., V. H. Nguyen, Q. V. V. Du, C. T. Nguyen, D. K. Dang, Q. H. Truong, N. B. T. Dang, Q. T. Tran, Q.-H. Nguyen and Q.-T. Bui (2024). "Application of hybrid model-based machine learning for groundwater potential prediction in the north central of Vietnam." Earth Science Informatics: 1-21.

Nguyen, P. T., D. H. Ha, A. Jaafari, H. D. Nguyen, T. Van Phong, N. Al-Ansari, I. Prakash, H. V. Le and B. T. Pham (2020). "Groundwater potential mapping combining artificial neural network and real AdaBoost ensemble technique: the DakNong province case-study, Vietnam." International journal of environmental research and public health 17(7): 2473.

Oguntoyinbo, P. O., O. M. Iyiola and A. A. Komolafe (2024). "Integrated GIS-based and geophysical techniques in groundwater potential zonation: a case study of Jos North local government area." Sustainable Water Resources Management 10(2): 58.

Pan, Z., W. Lu, H. Wang and Y. Bai (2023). "Groundwater contaminant source identification based on an ensemble learning search framework associated with an auto xgboost surrogate." Environmental Modelling & Software 159: 105588.

Prasad, P., V. J. Loveson, M. Kotha and R. Yadav (2020). "Application of machine learning techniques in groundwater potential mapping along the west coast of India." GIScience & Remote Sensing 57(6): 735-752.

Raheja, H., A. Goel and M. Pal (2024). "A novel approach for prediction of groundwater quality using gradient boosting-based algorithms." ISH Journal of Hydraulic Engineering: 1-12.

Rahmati, O., H. R. Pourghasemi and A. M. Melesse (2016). "Application of GIS-based data driven random forest and maximum entropy models for groundwater potential mapping: a case study at Mehran Region, Iran." Catena 137: 360-372.

Raj, S., K. S. Rawat, S. K. Singh and A. K. Mishra (2024). "Groundwater potential zones identification and validation in Peninsular India." Geology, Ecology, and Landscapes 8(1): 86-100.

Raju, A., R. P. Singh, P. K. Kannojiya, A. Patel, S. Singh and M. Sinha (2024). "Declining groundwater and its impacts along ganga riverfronts using combined Sentinel-1, GRACE, water levels, and rainfall data." Science of The Total Environment: 170932.

Ray, S. (2024). "Identifying the groundwater potential zones in Jamsholaghat sub-basin by considering GIS and multi-criteria decision analysis." International Journal of Environmental Science and Technology 21(1): 515-540.

Rehman, A., F. Islam, A. Tariq, I. Ul Islam, D. Brian J, T. Bibi, W. Ahmad, L. Ali Waseem, S. Karuppannan and S. Al-Ahmadi (2024). "Groundwater potential zone mapping using GIS and Remote Sensing based models for sustainable groundwater management." Geocarto International 39(1): 2306275.

Sachdeva, S. and B. Kumar (2021). "Comparison of gradient boosted decision trees and random forest for groundwater potential mapping in Dholpur (Rajasthan), India." Stochastic Environmental Research and Risk Assessment 35(2): 287-306.

Senapati, U. and T. K. Das (2024). "Delineation of potential alternative agriculture region using RS and AHP-based GIS techniques in the drought prone upper Dwarakeswer river basin, West Bengal, India." Ecological Modelling 490: 110650.

Sharma, Y., R. Ahmed, T. K. Saha, N. Bhuyan, G. Kumari, S. Pal and H. Sajjad (2024). "Assessment of groundwater potential and determination of influencing factors using remote sensing and machine learning algorithms: A study of Nainital district of Uttarakhand state, India." Groundwater for Sustainable Development 25: 101094.

Singh, G., J. Singh, O. A. Wani, J. C. Egbueri and J. C. Agbasi (2024). "Assessment of groundwater suitability for sustainable irrigation: A comprehensive study using indexical, statistical, and machine learning approaches." Groundwater for Sustainable Development 24: 101059.

Tahmassebipoor, N., O. Rahmati, F. Noormohamadi and S. Lee (2016). "Spatial analysis of groundwater potential using weights-of-evidence and evidential belief function models and remote sensing." Arabian Journal of Geosciences 9: 1-18.

Tamiru, H. and M. Wagari (2022). "Comparison of ANN model and GIS tools for delineation of groundwater potential zones, Fincha Catchment, Abay Basin, Ethiopia." Geocarto International 37(23): 6736-6754.

Tiwari, V., A. Kumar and M. Mukherjee (2024). "Spatiotemporal mapping of groundwater recharge potential zones for physical planning process−A case of Ajmer City, India." Ecohydrology & Hydrobiology.

Tran, D. A., M. Tsujimura, N. T. Ha, V. T. Nguyen, D. V. Binh, T. D. Dang, Q.-V. Doan, D. T. Bui, T. Anh Ngoc, L. V. Phu, P. T. B. Thuc and T. D. Pham (2021). "Evaluating the predictive power of different machine learning algorithms for groundwater salinity prediction of multi-layer coastal aquifers in the Mekong Delta, Vietnam." Ecological Indicators 127: 107790.

Uddin, M. G., M. H. Imran, A. M. Sajib, M. A. Hasan, M. T. M. Diganta, T. Dabrowski, A. I. Olbert and M. Moniruzzaman (2024). "Assessment of human health risk from potentially toxic elements and predicting groundwater contamination using machine learning approaches." Journal of Contaminant Hydrology 261: 104307.

Vafadar, S., M. Rahimzadegan and R. Asadi (2023). "Evaluating the performance of machine learning methods and Geographic Information System (GIS) in identifying groundwater potential zones in Tehran-Karaj plain, Iran." Journal of Hydrology 624: 129952.

Wang, X., Y. Zhang, B. He, J. Li, T. Yang, H. Sun, Q. Shao and C. Xu (2024). "Deep learning algorithms in predicting Cr (VI) removal performance of S-ZVI: Models building and optimal parameters prediction." Separation and Purification Technology 330: 125487.

Wang, Z., J. Wang and J. Han (2022). "Spatial prediction of groundwater potential and driving factor analysis based on deep learning and geographical detector in an arid endorheic basin." Ecological Indicators 142: 109256.

Wang, Z., J. Wang, D. Yu and K. Chen (2023). "Groundwater potential assessment using GIS-based ensemble learning models in Guanzhong Basin, China." Environmental Monitoring and Assessment 195(6): 690.

World Bank (2023). Proposed Guidance for Integrating Flood Risk Management into Urban and Spatial Planning Practices. World Bank, Washington, DC, USA.

Xiong, H., X. Guo, Y. Wang, R. Xiong, X. Gui, X. Hu, Y. Li, Y. Qiu, J. Tan and C. Ma (2023). "Spatial prediction of groundwater potential by various novel boosting-based ensemble learning models in mountainous areas." Geocarto International 38(1): 2274870.

Yavuz Ozalp, A., H. Akinci and M. Zeybek (2023). "Comparative analysis of tree-based ensemble learning algorithms for landslide susceptibility mapping: A case study in Rize, Turkey." Water 15(14): 2661.

Zounemat-Kermani, M., O. Batelaan, M. Fadaee and R. Hinkelmann (2021). "Ensemble machine learning paradigms in hydrology: A review." Journal of Hydrology 598: 126266.

REMOTE SENSING AND GIS-DRIVEN MODEL FOR FLOOD SUSCEPTIBILITY ASSESSMENT IN THE UPPER SOLO RIVER WATERSHED

Jumadi JUMADI[1,2] , *Dewi Novita SARI[1]* , *Umrotun UMROTUN[1], Muhammad MUSIYAM[3]* ,
Chintania NURMANTYO[1], Sadam Fadil MUHAMMAD[1], Mohd Hairy IBRAHIM[4]

ABSTRACT:
This study aims to develop an expedited flood susceptibility model with remote sensing data that can be effectively utilized for a large catchment area. We apply the model to the Upper Solo River Watershed in Indonesia. The model incorporates the hydrological attributes of the watershed obtained from remote sensing data, including elevation, slope, flow accumulation, proximity to rivers, rainfall, drainage density, topographic wetness index, land use land cover, normalized difference vegetation index, soil moisture, and land surface curvature. The flood susceptibility criteria are generated using remote sensing datasets such as The Shuttle Radar Topography Mission (SRTM), Sentinel 2 Multispectral Instrument, Global Precipitation Measurement (GPM) v6, and NASA-USDA Enhanced SMAP Global Soil Moisture Data. Through utilizing remote sensing data and GIS analytic tools, this study has discovered that it is possible to create a flood susceptibility model for large catchment regions cost-efficiently. Our study indicates that areas in the surrounding of Surakarta City, the most populated city in this watershed, are the most susceptible. Therefore, the government and community should increase their capacity to cope with this potential disaster.

Key-words: GIS, Remote sensing, Flood susceptibility, Watershed characteristics.

1. INTRODUCTION

Natural catastrophes are observed to escalate due to natural phenomena and human actions, resulting in substantial casualties, damage to property, and destruction of resources. Human actions such as deforestation, land clearance on mountain slopes, and cultivation in places with steep slopes might contribute to the occurrence of natural catastrophes. Indonesia is susceptible to natural disasters because it is situated in a region of active tectonics and volcanism resulting from the convergence of three tectonic plates: India-Australia, Pacific and Eurasia. Flooding is the most common natural disaster that we often suffer from in Indonesia (Susetyo, 2008). Moreover, compared to other Southeast Asian states, Indonesia had the largest number of flood disasters for the years 1980 to 2018 (Samphantharak, 2019).

The Upper Solo River Watershed is located in the Indonesian province of Jawa Tengah (South Central Java). This area has had long records of flood events for years. During flood events, the amount of water in this area forms due to the combination of different factors like much rain, high tides and failures to drain the water. The flooding damaged infrastructures and caused the loss of lives, including the collapse of bridges and roads. For example, the most colossal floods in over 50 years in 2007, were caused by extreme precipitation and insufficient drainage. The flood inundation is high, affecting more than 11,000 houses (Zein, 2010). There are thousands of people displaced from their houses, living in tents or temporary houses, which led to various health problems. Afterwards, the local municipal authorities strengthened the drainage system to mitigate the disaster. Although

[1]*Faculty of Geography, Universitas Muhammadiyah Surakarta, Indonesia, jumadi@ums.ac.id,*
  dns104@ums.ac.id, umrotun@ums.ac.id,

[2]*Center for Environmental Studies, Muhammadiyah Surakarta, Indonesia, jumadi@ums.ac.id.*

[3]*Department of Geography Education, Universitas Muhammadiyah Surakarta, Indonesia,*
  m.musiyam@ums.ac.id.

[4]*Department of Geography Education, Universiti Pendidikan Sultan Idris, Malaysia, hairy@fsk.upsi.edu.my.*

attempts have been made, the Upper Solo River Watershed is still highly prone to flooding, especially in the rainy season. Over the past few years, there has been a rise in the occurrence and intensity of extreme weather events, including heavy rainfall, leading to increasingly regular instances of flooding in the area. Therefore, it is necessary to continuously monitor and implement measures to decrease the adverse effects of flooding on the populations in the region.

A flood is defined as the occurrence of abnormally large volumes or elevations of water in rivers, lakes, ponds, reservoirs, and other bodies of water, which leads to land flooding beyond the normal boundaries of these water bodies (Marfai, 2003). Flooding is a frequent occurrence, as it is widespread across the entire earth. Flooding can arise from intense precipitation, glacial melting, tsunamis, hurricanes, and other oceanic occurrences. At the same time, flood hazard refers to the likelihood of a flood occurring of a specific size in a particular area during a specific period (Alkema and Middelkoop, 2005).

The floods may result from natural processes that affect the socio-economic system (Falguni and Singh, 2020; Komolafe et al., 2020). Several factors, such as climate, rainfall, land structure, vegetation, slope, human activities, and land use change, can also increase the intensity of flooding (Curebal et al., 2016; Chagas et al., 2022). In some areas, floods may have been a natural process in the past, but due to urbanization and land use change, they become disasters that lead to loss of lives, disturb livelihood, and devastate infrastructure (Rincón et al., 2018). In addition, forest and urban clearing decreases water absorption and increases the amount of runoff (Sugianto et al., 2022). As a sequent, this raises the level of floods and their intensity. Therefore, such geographical factors can be used to model flood susceptibility.

The utilization of the current dataset and technology will be the key to successfully building a cheaper and faster model. The integration of GIS and Remote Sensing technology will allow for the assessment of flood hazards on a large scale (Pradhan et al., 2009). Several studies have demonstrated different GIS and remote sensing technology approaches in mapping flood-prone areas across the globe (Elkhrachy, 2015; Islam and Sado, 2000). The investigations were carried out with different methods such as spatial multi-criteria analysis (Zhou et al., 2021), cell automata (Ghimire et al., 2013), and Analytic Hierarchical Processes (Negese et al., 2022; Sarmah et al., 2020); but application with widely accessible data that can be used to model large catchment with low-cost is limited. Furthermore, such studies in the Solo River Watershed are limited and need a more comprehensive approach. Farid et al. (2020) initiated their flood study in the region, more specifically, but not comprehensively covering the whole region. Therefore, this study aims to develop an expedited flood susceptibility model with remote sensing data that can be effectively utilized for a large catchment area, especially for the Upper Solo River Watershed.

The remainder of this paper is organized as follows. The second section provides a detailed description of the study area, highlighting its geographical characteristics. The third section outlines the data collection and methodology, detailing the types of remote sensing data used, the processing techniques, and the model development process. In the fourth section, the results of the model are presented. The fifth section discusses the implications of the findings, comparing them with existing models and highlighting the advantages of the proposed approach. The paper concludes with a summary of the key findings, potential applications, and suggestions for future research.

2. STUDY AREA

The Solo River water system is mainly drained by an extensive water system positioned between 6.48-8.07 S latitude and 110.26-112.41 E longitude (**Fig.1**). The area under consideration, which is designated as watershed, has a length of 12 districts from the province of Central Java to the province of East Java. It is also bounded by a range of mountains that clearly differentiate it from adjacent river basins. The regression is very surprising; it goes from zero meters above the seawater in the Madur Strait to 3,265 meters above sea level at Mount Lawu's peak. This watershed covers an area of 6,072 km^2 only. In this area, the diversity of the relief is striking. That goes from flatlands to mountains with gentle slopes to steep ones, which, in turn, cause lots of changes in the climates and rain patterns.

A thorough analysis is carried out, which deals with the urban area of the most developed city in Surakarta, which lies immediately upstream. The lithological characteristics of the erupted materials varied through time, as volcanic complexes like Merapi, Merbabu, and Lawu defined the region. Pumice, conglomerates, breccias, and tuff are among the volcanic materials abundant in the larger area, which are often mixed with andesitic ones. The creations of these volcanic formations are catalysts of the watershed's fertile soils, which support a diversity of land cover types. However, there has been a decrease in specific land cover categories like sub-aerial acidic clastic deposits in recent years. Hydrologically, the Solo River and its tributaries constitute an intricate network that plays an important role in the area's water resource management, with the river's flow originating from the eastern slopes of these prominent volcanic mountains. The watershed's unique topography and geological characteristics facilitate many ecosystems and present challenges and opportunities regarding water resource management, land use, and conservation efforts within this vital river basin area.
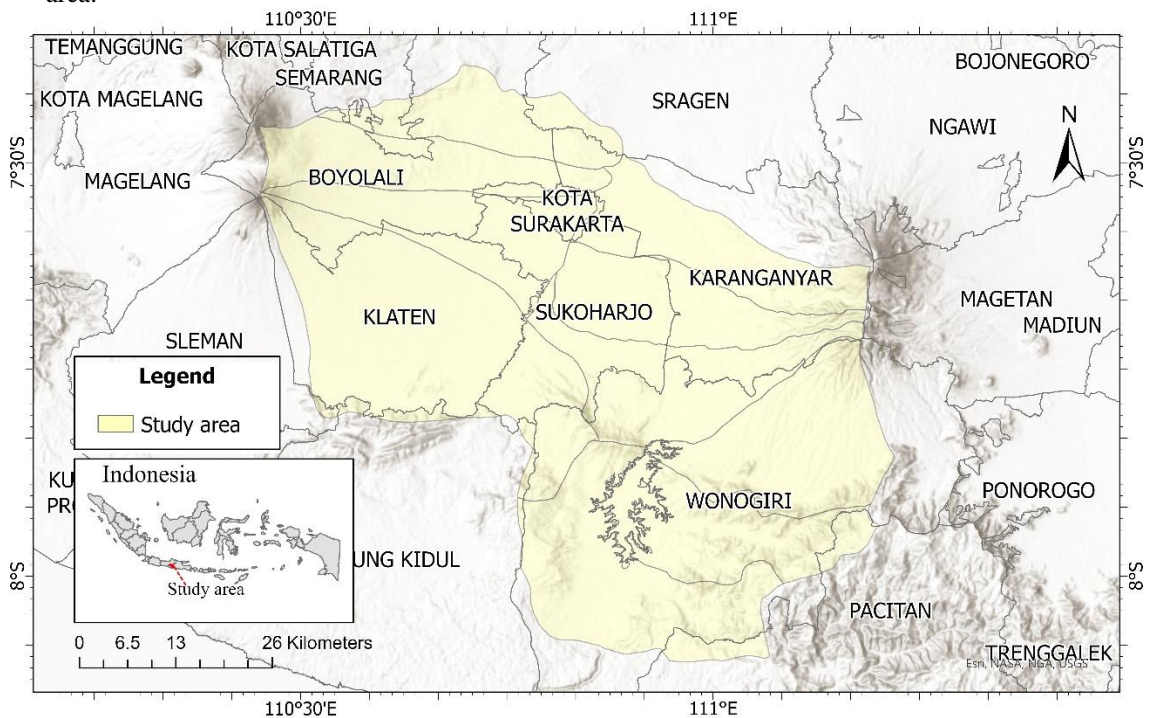
Fig. 1. Location of Upper Watershed of Solo River.

3. DATA AND METHODS

The model utilizes a range of physical characteristics derived from remote sensing datasets (**Table 1**), including elevation, slope, flow accumulation, distance to rivers, rainfall, drainage density, topographic wetness index, land cover, Normalized Difference Vegetation Index, soil moisture, and curvature. These parameters allow for a thorough assessment of flood susceptibility in the region. Floods have been broadly investigated, and many contributing factors have been tallied (Negese et al., 2022; Wanders et al., 2014). Local and wide-scale water flows are largely a function of topography, which causes more water concentration in low-lying areas and level lands due to the lack of movement (low velocity), which induces flooding. The flood risk linked to height and river distance is another factor. Lowlands are more susceptible to flooding mainly because of the higher high water and smaller river velocity. The occurrence of floods decisively depends on the velocity and the extent of the water stream and the capacity of drainage systems as well. When the amount of flowing water and the traffic volume of drainage channels are over the capacity, there will be more possibility of flooding. Land use/Land cover (LULC) affects the amount of runoff, therefore directly affecting the

flooding potential. Soil moisture expresses the ability to infiltrate water. Higher moisture represents that the soil has a lower ability to infiltrate water.

Additionally, areas with flat curvature are more prone to flooding than other topographic features. Finally, it is crucial to consider precipitation and topographic wetness index as significant factors, as heavy precipitation leads to more water build-up, while the topographic wetness index helps identify areas with possibly saturated land surfaces. Both of these factors contribute to an increased susceptibility to flooding.

Therefore, we derived eleven parameters from four datasets (**Table 1**). The parameters include elevation, slope, flow accumulation, distance to rivers, drainage density, topographic wetness index, curvature, land cover, Normalized Difference Vegetation Index, Rainfall, and soil moisture. DEM was derived into elevation, slope, flow accumulation, distance to rivers, drainage density, topographic wetness index, and curvature. On the other hand, land cover and Normalized Difference Vegetation Index were derived from Sentinel 2 MSI Image. Lastly, Global Precipitation Measurement (GPM) v6 and NASA-USDA Enhanced SMAP Global Soil Moisture Data produce rainfall and soil moisture data, respectively.

Table 1.

The source of datasets.

No	Data	Description	Source	Derived Data
1	DEM	The Shuttle Radar Topography Mission (SRTM).	USGS (Earth Resources Observation And Science (EROS) Center, 2017)	elevation, slope, flow accumulation, distance to rivers, drainage density, topographic wetness index, curvature
2	Images	Sentinel 2 Multispectral Instrument	ESA ("User Guides - Sentinel-2 MSI - Level-2 Processing - Sentinel Online," n.d.)	land cover, Normalized Difference Vegetation Index
3	Rainfall data	Global Precipitation Measurement (GPM) v6.	NASA ("GES DISC Dataset: GPM IMERG Final Precipitation L3 Half Hourly 0.1 degree x 0.1 degree V06 (GPM_3IMERGHH 06)," n.d.)	Rainfall
4	Soil Moisture Data	NASA-USDA Enhanced SMAP Global Soil Moisture Data.	NASA (Entekhabi et al., 2010)	soil moisture

The development of the flood susceptibility model consisted of two processes for the flood-controlling parameters (**Fig. 2**). The parameters were initially transformed into a raster format to facilitate analysis. The characteristics were subsequently standardized to a consistent geographic resolution through resampling. **Fig. 2** illustrates the division of the resampled parameters into five distinct measurement scales, ranging from 1 (indicating a minimal susceptibility to flooding) to 5 (indicating a significant susceptibility to flooding). Applying the weighted overlay technique achieved the integration of all the factors. This methodology enables the incorporation of numerous spatial datasets by allocating weights to each parameter. The weights allocated to the parameters were based on scoring and weighting by Negese et al. (2022).
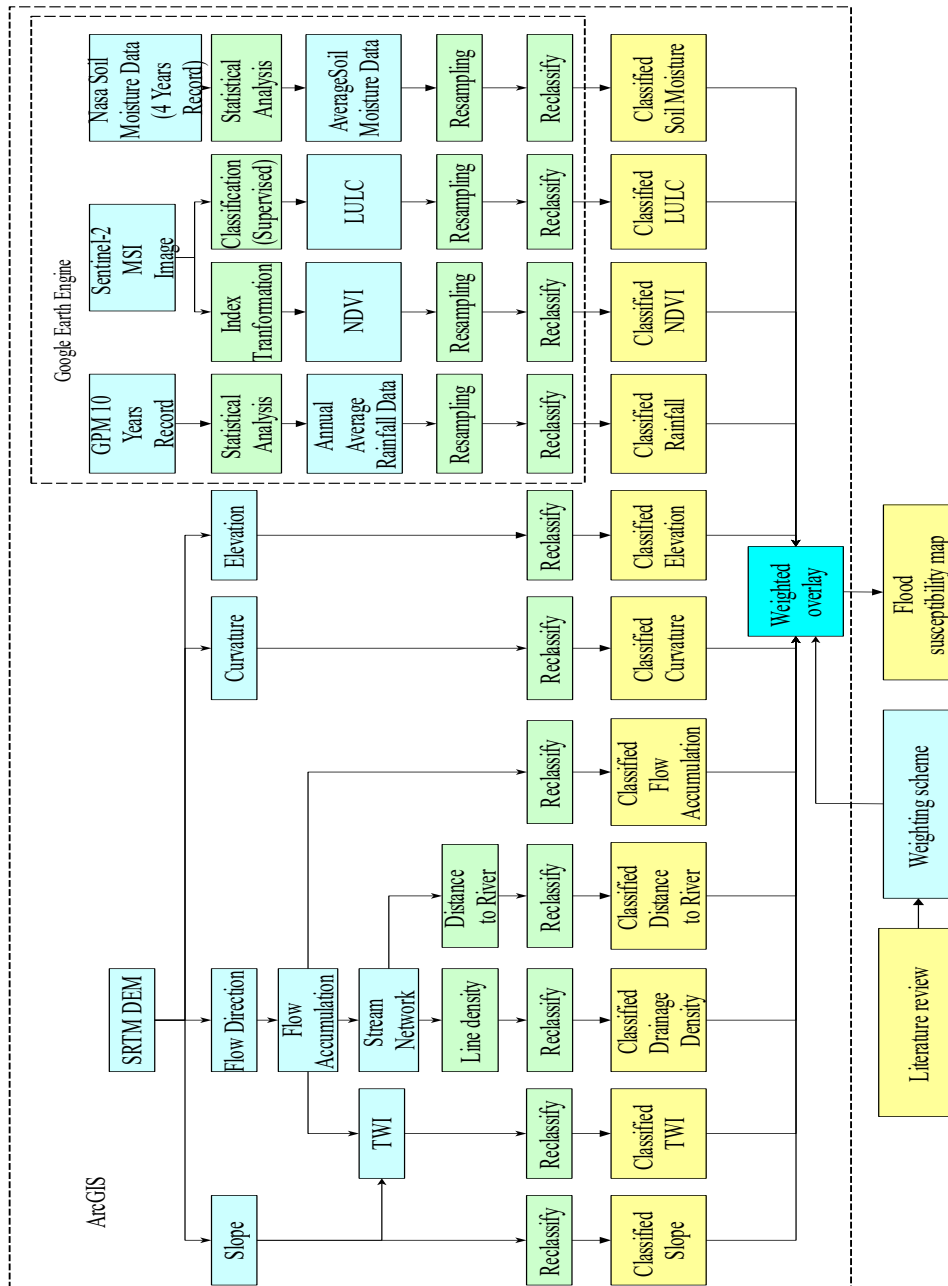
Fig. 2. The research framework.

4. RESULTS

The Flood susceptibility map for the Upper Solo River basin was generated using remote sensing data and GIS modelling. The flood susceptibility criteria were determined after a thorough analysis of the existing literature, which revealed information about the research area's topography, hydrology, meteorology, and anthropology. The flood susceptibility characteristics, as illustrated in **Fig. 3**, have simplified the ranking of flood susceptibility criteria based on their respective contributions to the susceptibility of flood occurrence.
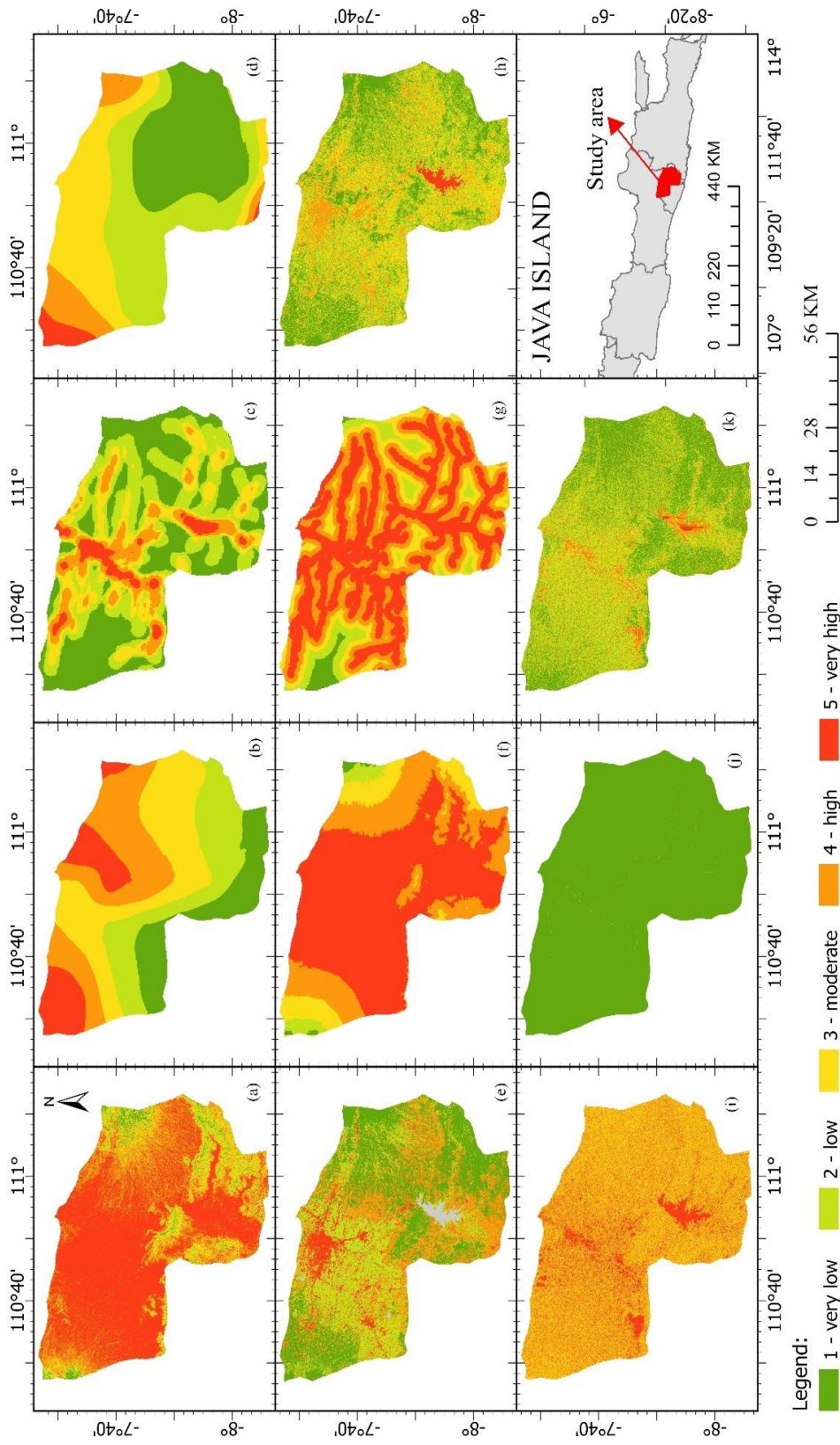
Fig. 3. Remote sensing datasets used to derive classified flood susceptibility parameters. Note: (a) Slope, (b) Relief, (c) Digital Elevation Model (DEM) Derived Drainage, (d) Soil Moisture, (e) Land Cover, (f) Elevation, (g) Digital Raster, (h) Normalized Difference Vegetation Index, (i) Curvature, (i) Flow Accumulation, (k) Topographic Wetness Index.

According to the data in **Fig. 3** and **Table 2**, the areas with a very low likelihood of floods (shown by the blue hue on the map) are Wonogiri, which covers 596.45 square kilometers (42.60% of the total area), Karanganyar, which covers 154.08 square kilometers (27.37% of the total area), and Boyolali, which covers 110.71 square kilometers (26.36% of the total area), (**Fig.4**). The places with the least susceptibility to flooding, represented by the dark green tint on the map, are Wonogiri (444.15 square kilometers, 31.72%), Klaten (268.63 square kilometers, 41.15%), and Karanganyar (146.26 square kilometers, 25.98%). The locations with significant flood vulnerability, indicated by the green-cyan color on the map, include Wonogiri (15.29%), Klaten (29.33%), and Sukoharjo (18.45%). Flood-prone areas, indicated by the light green color on the map, include Sukoharjo, which covers 281.29 square kilometers (57.46%), Boyolali, which covers 133.59 square kilometers (31.81%), and Karanganyar, which covers 29.18 square kilometers (19.98%). The locations with a high risk of flooding, shown by the yellow hue on the map, include Sukoharjo, which covers 50.08 square kilometers (10.20%), Surakarta, which covers 18.46 square kilometers (39.89%), and Karanganyar, which covers 19.98 square kilometers (3.5%). The existence of high and very high conditions may be a cause for concern, particularly when the wet season falls between October and March, when rainfall exceeds 200 mm.

The findings indicate that the Upper Solo River Watershed faces a substantial danger of flooding (**Fig. 4**), particularly in the center and northern sections (in the surrounding of Surakarta City). Water buildup in these areas is impacted by variables such as proximity to the Bengawan Solo River, the river's V-shaped cross-section, and the presence of steep terrain. Wonogiri, Karanganyar, and Boyolali are relatively less susceptible to floods than the other locations studied, but Sukoharjo, Surakarta, and specific sections of Karanganyar are more susceptible. These findings highlight the significance of caution, especially during the rainy season, because all enterprises within the extended watershed are vulnerable to the harmful consequences of flooding.
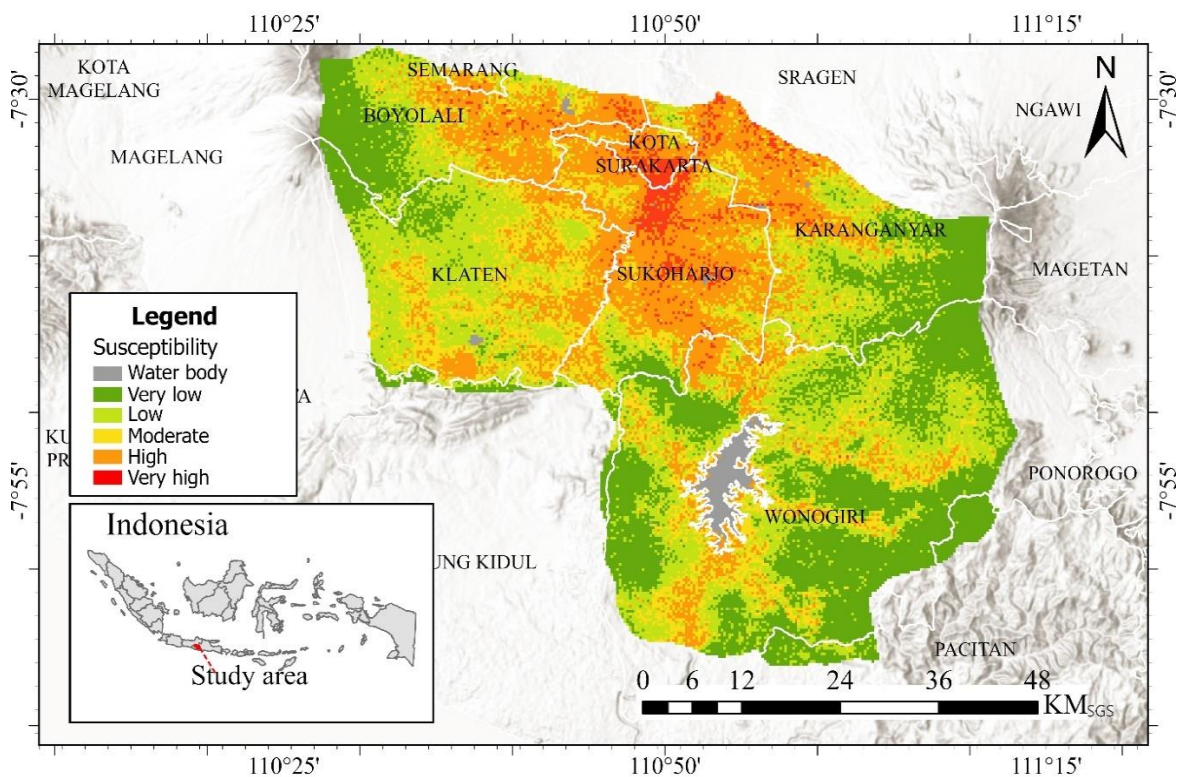
Fig. 4. The flood susceptibility map derived from the model.

5. DISCUSSION

The current investigation uncovers a wide range of flood susceptibility across the Upper Solo River Watershed, highlighting areas of notable susceptibility and the need for tailored flood prevention policies informed by data analysis. The analysis reveals a complex and varied flood-susceptibility environment, with significant differences in flood susceptibility among different cities/regencies within the watershed (Anna et al., 2021). Model of flood susceptibility also shows that Surakarta has the largest part of the whole area in 'High' level of potential threat. Historical records from spilled-over flood events each year backs this finding up. Surakarta City and its surrounding areas are the most densely populated areas in this watershed and have the highest potential for flood disasters. This condition requires the government and the community to be active in order to strengthen their ability to deal with and prevent the negative effects of such disasters. The objectives of disaster preparedness and response, the infrastructure which is resilient to disasters, and the community which is awareness of the community are the core points in the construction of disaster preparedness and response. The increased resilience to flood can to minimize flood impact to lives, properties and socio-economic stability.These findings give key insights for the state-and-impact analysis concerning flood mitigation and resilience measures. For a strategic allocation of resources and application of adapted flood measures across the regions of the watershed, decision-makers should know the distinct ground of flood susceptibility for diverse regions (Smith et al,2010; Xiang et al,2020). The use of GIS and RS in acquiring the related data precisely identifies the flood-subjected sections of a given location. This method will make it possible to identify Scanning more critical cities that lie in vulnerable locations, including Surakarta (Dinge et al.,2020; Hussain et al.,2021).

The studies emphasized the importance of taking precautions during the wet season to reduce the adverse effects of floods on activities within the watershed, especially due to climate changes (Damayanti, 2011; Musiyam et al., 2020; Mustikaningrum et al., 2023; Nada et al., 2023; Nurkhaida and Rejekiningrum, 2021; Purwanto et al., 2023; Saputra et al., 2022; Zein, 2010). Based on the climate forecast, it is estimated that the upper section of the Solo River Water Basin will see negative influences from the ongoing climate changes as well as impacts of future changes in earth's climate on the incidence of floods (Anna et al., 2016; Sipayung et al., 2018). Solo Upper River Watershed has recorded the growth of flood-affected rainfall that resulted from climate change, urbanization, and redevelopment of land uses. Given the course of events, flood management strategies should be flexible to tackle insightful situations (Janicka and Kanclerz, 2023; Kemp and Kemp, 2023).

Furthermore, the expected deviation from the current climate condition, characterized by a massive prevalence of heavy rains as well as the hike in temperatures brought by climate change, is undoubtedly an element that will contribute greatly to the intensification of flooding in the area. Apart from being high in volume and area, flood events, which are exacerbated by climate change and changes in moisture content and hydrological mechanisms, fail to yield the desired flood mitigation results (Modi et al., 2021). Besides that, the rise of the river flow may cause flood frequency (Tahmasebi Nasab et al., 2022; Yamamoto et al., 2021). Compared to recent studies by Mansour et al. (2024), Shakoor et al. (2024), Damayanti et al. (2024), Sari et al. (2024), Sahid (2024) and Shah & Ai (2024), this study offers a more cost-effective approach to flood analysis, primarily because it utilizes widely accessible data that can be applied across various regions. While the other studies may rely on specialized, localized, or expensive data sources and methodologies, this study's reliance on universally available data ensures broader applicability and reduces the financial barriers to conducting flood studies, making it a more practical option for researchers and policymakers in diverse geographic and economic contexts. Future studies need to identify the variable side of flood risk by focusing on environmental factors such as climate change, and urbanization and their potential to transform the frequency and severity of flood events. It is imperative to equip predictive models with meteorological scenarios and land-use patterns. With these models, we can understand the dynamics of the flood risk across seasons and space over time and develop comprehensive flood mitigation strategies that could adapt to various future scenarios. Striving at community interaction in the analysis of flood risk and contrivances of mitigation plans leads to social justice and cultural suitability as well as political solutions for poor and composed people issues along the flood-line.

Table 2. Susceptibility classification of the watershed.

Regency/city	%	VH	%	H	%	M	%	L	%	VL	%	WB	Total
						Area of Classes							
Boyolali	2.39	10	31.8	133.6	15.6	65.33	23.4	98.34	26.4	110.7	0.5	1.9	419.92
Gunung kidul	0		0.84	0.33	4.64	1.81	36.8	14.37	57.7	22.5	0		39.01
Karanganyar	3.55	20	29.2	164.3	13.7	77.08	26	146.3	27.4	154.1	0.2	1.3	563
Klaten	0.21	1.38	19.3	125.8	29.3	191.4	41.2	268.6	9.75	63.63	0.3	1.9	652.79
Surakarta	39.9	18.5	49	22.68	6.96	3.22	3.66	1.69	0		0.5	0.2	46.27
Magetan	0		0		0		0		100	0	0		0
Pacitan	0		0		0.86	0.6	13.6	9.47	85.5	59.38	0		69.44
Semarang	2.63	0.44	51.2	8.52	26.8	4.47	19.1	3.17	0.23	0.04	0		16.64
Sleman	0		0		0		18.8	0.86	81.2	3.73	0		4.59
Sragen	0		100	0.01	0		0		0		0		0.01
Sukoharjo	10.2	50.1	57.5	281.3	18.5	90.33	9.66	47.28	3.85	18.85	0.4	1.7	489.53
Wonogiri	0.14	2.01	9.95	139.3	15.3	214	31.7	444.2	42.6	596.5	0.3	4.2	1400.1

Note: WB represents the area of a water body in square kilometers. VL stands for very low susceptibility, L for low susceptibility, M for moderate susceptibility, H for high susceptibility, and VH for very high susceptibility, all measured in square kilometers.

6. CONCLUSIONS

The combination of remote sensing data with GIS modelling developed the Flood Susceptibility Map of the Upstream Solo River Basin. The driving factors for this model stemmed from the integral analysis of topography, hydrology, meteorology, and anthropology. The inundation concerns pertaining to the central and the northern sections of Surakarta City, particularly for areas adjacent to the Bengawan Solo River and the ones having high-sloped terrains, are critically mentioned. Inversely, Wonogiri, Karanganyar, and Boyolali seem to reveal very little vulnerability. The lowest areas with more flood susceptibility, like Sukoharjo and Surakarta, respectively, need additional attention, especially during the wet periods, when the whole catchment is vulnerable to flood hazards' contribution to downstream flooding.

Flood mapping of areas identified through Geographic Information System (GIS) and remote sensing can be used as the basis for developing plans in flood-prone cities, such as Surakarta. Future studies should serve to discover the dynamic nature of flood risk by setting up environmental factors such as climate change and urbanization, which will ultimately result in the alteration of the frequency and intensity of floods.

Using predictive models, including meteorological scenarios and land-use patterns, reduces uncertainties, thereby helping to develop holistic flood mitigation solutions. Engaging the community in flood risk analysis and mitigation planning ensures social justice, cultural suitability, and political solutions for affected populations in flood-prone areas. Moreover, the government and society should strengthen their ability to deal with this possible disaster.

R E F E R E N C E S

Alatas, H., Pawitan, H., Syafiuddin, A., 2022. Morphometric analysis of Ciliwung river and identification of suitable locations to build artificial dams for flood mitigation. Environmental Quality Mgmt 32, 45‑52. https://doi.org/10.1002/tqem.21822

Alkema, D., Middelkoop, H., 2005. The influence of floodplain compartmentalization on flood risk within the Rhine‑Meuse Delta. Natural Hazards 36, 125‑145.

Anna, A.N., Priyana, Y., Fikriyah, V.N., Ibrahim, M.H., Ismail, K., Pamekar, M.S., Asshodiq, A.D.T., 2021. Spatial Modelling of Local Flooding for Hazard Mitigation in Surakarta, Indonesia. International Journal of GEOMATE 21, 145‑152.

Anna, A. N., Priyono, K. D., Suharjo, S., & Priyana, Y. 2016. Using water balance to analyze water availability for communities (a case study in some areas of Bengawan Solo Watershed). In Forum Geografi Vol. 30 (2), pp. 166-175.

Arnell, N.W., Gosling, S.N., 2016. The impacts of climate change on river flood risk at the global scale. Climatic Change 134, 387‑401. https://doi.org/10.1007/s10584-014-1084-5

Chagas, V.B., Chaffe, P.L., Blöschl, G., 2022. Climate and land management accelerate the Brazilian water cycle. Nature Communications 13, 5136.

Chakraborty, L., Thistlethwaite, J., Scott, D., Henstra, D., Minano, A., Rus, H., 2023. Assessing social vulnerability and identifying spatial hotspots of flood risk to inform socially just flood management policy. Risk Analysis 43, 1058‑1078. https://doi.org/10.1111/risa.13978

Curebal, I., Efe, R., Ozdemir, H., Soykan, A., Sönmez, S., 2016. GIS-based approach for flood analysis: case study of Keçidere flash flood event (Turkey). Geocarto International 31, 355‑366.

Damayanti, S., 2011. Resilience for the 2007 flood event, using community knowledge: A Case in Part of Sukoharjo Regency, Indonesia (Master's Thesis). University of Twente.

Damayanti, H. N., Wikan, P. A., & Annurhutami, F. 2024. GIS-Based flood susceptibility mapping in Wawar Watershed, Purworejo Regency. In IOP Conference Series: Earth and Environmental Science, Vol. 1314, No. 1, p. 012051. IOP Publishing.

Dingle, E.H., Creed, M.J., Sinclair, H.D., Gautam, D., Gourmelen, N., Borthwick, A.G.L., Attal, M., 2020. Dynamic flood topographies in the Terai region of Nepal. Earth Surf Processes Landf 45, 3092‑3102. https://doi.org/10.1002/esp.4953

Earth Resources Observation And Science (EROS) Center, 2017. Shuttle Radar Topography Mission (SRTM) Non-Void Filled. https://doi.org/10.5066/F7K072R7

Elkhrachy, I., 2015. Flash flood hazard mapping using satellite images and GIS tools: a case study of Najran City, Kingdom of Saudi Arabia (KSA). The Egyptian Journal of Remote Sensing and Space Science 18, 261‑278.

Entekhabi, D., Njoku, E.G., O'Neill, P.E., Kellogg, K.H., Crow, W.T., Edelstein, W.N., Entin, J.K., Goodman, S.D., Jackson, T.J., Johnson, J., Kimball, J., Piepmeier, J.R., Koster, R.D., Martin, N., McDonald, K.C., Moghaddam, M., Moran, S., Reichle, R., Shi, J.C., Spencer, M.W., Thurman, S.W., Tsang, L., Van Zyl, J., 2010. The Soil Moisture Active Passive (SMAP) Mission. Proceedings of the IEEE 98, 704‑716. https://doi.org/10.1109/JPROC.2010.2043918

Falguni, M., Singh, D., 2020. Detecting flood prone areas in Harris County: A GIS based analysis. GeoJournal 85, 647‑663.

Farid, M., Gunawan, B., Kusuma, M.S.B., Habibi, S.A., Yahya, A., 2020. Assessment of flood risk reduction in Bengawan Solo River: A case study of Sragen Regency. GEOMATE Journal 18, 229‑234.

GES DISC Dataset: GPM IMERG Final Precipitation L3 Half Hourly 0.1 degree x 0.1 degree V06 (GPM_3IMERGHH 06), n.d. https://doi.org/10.5067/GPM/IMERG/3B-HH/06

Ghimire, B., Chen, A.S., Guidolin, M., Keedwell, E.C., Djordjević, S., Savić, D.A., 2013. Formulation of a fast 2D urban pluvial flood model using a cellular automata approach. Journal of Hydroinformatics 15, 676‑686.

Greene, R.G., Cruise, J.F., 1995. Urban watershed modeling using geographic information system. Journal of water resources planning and management 121, 318‑325.

Hussain, M., Tayyab, M., Zhang, J., Shah, A.A., Ullah, K., Mehmood, U., Al-Shaibah, B., 2021. GIS-based multi-criteria approach for flood vulnerability assessment and mapping in district Shangla: Khyber Pakhtunkhwa, Pakistan. Sustainability 13, 3126.

Islam, M.M., Sado, K., 2000. Development of flood hazard maps of Bangladesh using NOAA-AVHRR images with GIS. Hydrological Sciences Journal 45, 337‑355.

Janicka, E., Kanclerz, J., 2023. Assessing the Effects of Urbanization on Water Flow and Flood Events Using the HEC-HMS Model in the Wirynka River Catchment, Poland. Water 15, 86. https://doi.org/10.3390/w15010086

Kemp, S.J., Kemp, M.J., 2023. A flooded future for River Chub? Future impacts of climate change and urbanization on reproduction of a keystone native fish species. Transactions of the American Fisheries Society 152, 594‑609. https://doi.org/10.1002/tafs.10420

Komolafe, A.A., Awe, B.S., Olorunfemi, I.E., Oguntunde, P.G., 2020. Modelling flood-prone area and vulnerability using integration of multi-criteria analysis and HAND model in the Ogun River Basin, Nigeria. Hydrological Sciences Journal 65, 1766‑1783.

Liu, D., Li, Y., 2016. Social vulnerability of rural households to flood hazards in western mountainous regions of Henan province, China. Natural Hazards and Earth System Sciences 16, 1123‑1134.

Mahdizadeh Gharakhanlou, N., Perez, L., 2022. Spatial Prediction of Current and Future Flood Susceptibility: Examining the Implications of Changing Climates on Flood Susceptibility Using Machine Learning Models. Entropy 24, 1630. https://doi.org/10.3390/e24111630

Mandal, A., Stephenson, T., Campbell, J., Taylor, M., Watson, S., Clarke, L., Smith, D., Darsan, J., Wilson, M., 2022. An assessment of the impact of 1.5 versus 2 and 2.5° C global temperature increase on flooding in Jamaica: a case study from the Hope watershed. Philosophical Transactions of the Royal Society A: Mathematical, Physical and Engineering Sciences 380, 20210141. https://doi.org/10.1098/rsta.2021.0141

Mansour, A., Mrad, D., & Djebbar, Y. 2024. Advanced modeling for flash flood susceptibility mapping using remote sensing and GIS techniques: a case study in Northeast Algeria. Environmental Earth Sciences, 83(2), 60.

Marfai, M.A., 2003. GIS Modelling of river and tidal flood hazards in a waterfront city. Case Study: Semarang City, Central Java, Indonesia.

Modi, P.A., Fuka, D.R., Easton, Z.M., 2021. Impacts of climate change on terrestrial hydrological components and crop water use in the Chesapeake Bay watershed. Journal of Hydrology: Regional Studies 35, 100830.

Muryani, C., Koesuma, S., Yusup, Y., n.d. People Perception And Participation In Disaster Risk Reduction At Surakarta City, Central Java, Indonesia. GeoEco 7, 96‑105.

Musiyam, M., Jumadi, J., Wibowo, Y.A., Widiyatmoko, W., Hafida, S.H.N., 2020. Analysis of Flood-Affected Areas Due to Extreme Weather In Pacitan, Indonesia. International Journal of Geomate 19, 27‑34.

Mustikaningrum, M., Widhatama, A.F., Widantara, K.W., Ibrohim, M., Hibatullah, M.F., Larasati, R.A.P., Utami, S., Hadmoko, D.S., 2023. Multi-Hazard Analysis in Gunungkidul Regency Using Spatial Multi-Criteria Evaluation. Forum Geografi 37. https://doi.org/10.23917/forgeo.v37i1.19041

Nada, F.M.H., Nugroho, N.P., Sofwa, N.B.M., 2023. Lake and Stream Buffer Zone Widths' Effects on Nutrient Export to Lake Rawapening, Central Java, Indonesia: A Simple Simulation Study. Forum Geografi 37. https://doi.org/10.23917/forgeo.v37i1.21537

Negese, A., Worku, D., Shitaye, A., Getnet, H., 2022. Potential flood-prone area identification and mapping using GIS-based multi-criteria decision-making and analytical hierarchy process in Dega Damot district, northwestern Ethiopia. Appl Water Sci 12, 255. https://doi.org/10.1007/s13201-022-01772-7

Nurkhaida, R., Rejekiningrum, P., 2021. Trend analysis of agricultural water supply and demand for water conservation and climate change anticipation, in: IOP Conference Series: Earth and Environmental Science. IOP Publishing, p. 012102.

Ozkan, S.P., Tarhan, C., 2016. Detection of flood hazard in urban areas using GIS: Izmir case. Procedia Technology 22, 373‑381.

Paudyal, G.N., 1996. An integrated GIS-numerical modelling system for advanced flood management, in: Proceeding of the International Conference on Water Resources and Environment Research: Towards the 21st Century, Kyoto University, Japan. pp. 555‑562.

Pradhan, B., Shafiee, M., Pirasteh, S., 2009. Maximum flood prone area mapping using RADARSAT images and GIS: Kelantan river basin. International Journal of Geoinformatics 5.

Purwanto, A., Andrasmoro, D., Eviliyanto, E., Rustam, R., Ibrahim, M.H., Rohman, A., 2023. Validating the GIS-based Flood Susceptibility Model Using Synthetic Aperture Radar (SAR) Data in Sengah Temila Watershed, Landak Regency, Indonesia. Forum Geografi 36, 185‑201. https://doi.org/10.23917/forgeo.v36i2.16368

Rincón, D., Khan, U.T., Armenakis, C., 2018. Flood risk mapping using GIS and multi-criteria analysis: A greater Toronto area case study. Geosciences 8, 275.

Sahid, S. 2024. Enhancing Digital Elevation Model Accuracy for Flood Modelling‑A Case Study of the Ciberes River in Cirebon Indonesia. Forum Geografi, Vol. 38 (1). https://doi.org/10.23917/forgeo.v38i1.1839

Samphantharak, K., 2019. Natural Disaster and Economic Development in Southeast Asia. https://doi.org/10.2139/ssrn.3388396

Saputra, A., Sigit, A.A., Priyana, Y., Abror, A.M., Lia Sari, A.N., Nursetiyani, O., 2022. A Low-Cost Drone Mapping And Simple Participatory Gis To Support The Urban Flood Modelling. Geographia Technica 17.

Sari, D. N., Anna, A. N., Taryono, T., Maulana, M. F., & Khumaeroh, D. N. F. 2024. Detection of Flood Hazard Potential Zones by Using Analytical Hierarchy Process in Tuntang Watershed Area, Indonesia. Geographia Technica, 19 (1).

Sarmah, T., Das, S., Narendr, A., Aithal, B.H., 2020. Assessing human vulnerability to urban flood hazard using the analytic hierarchy process and geographic information system. International Journal of Disaster Risk Reduction 50, 101659.

Shah, S. A., & Ai, S. (2024). Flood Susceptibility Mapping Contributes to Disaster Risk Reduction: A Case Study in Sindh, Pakistan. International Journal of Disaster Risk Reduction, 104503.

Shafapour Tehrany, M., Shabani, F., Neamah Jebur, M., Hong, H., Chen, W., Xie, X., 2017. GIS-based spatial prediction of flood prone areas using standalone frequency ratio, logistic regression, weight of evidence and their ensemble techniques. Geomatics, Natural Hazards and Risk 8, 1538‑1561.

Shakoor, A., Ghumman, A. R., Arif, M., Pasha, G. A., & Masood, A. 2024. GIS-Based Assessment of Flash Flood Susceptibility around Thuwal-Rabigh Region, Saudi Arabia. Available at: https://www.researchsquare.com/article/rs-4134684/latest.pdf

Sharma, S., Gomez, M., Keller, K., Nicholas, R.E., Mejia, A., 2021. Regional Flood Risk Projections under Climate Change. Journal of Hydrometeorology 22, 2259‑2274. https://doi.org/10.1175/JHM-D-20-0238.1

Sipayung, S. B., Nurlatifah, A., & Siswanto, B. 2018. Simulation and prediction the impact of climate change into water resources in Bengawan Solo watershed based on CCAM (Conformal Cubic Atmospheric Model) data. In Journal of Physics: Conference Series, Vol. 1022 (1), p. 012042). IOP Publishing.

Smith, J.A., Baeck, M.L., Villarini, G., Krajewski, W.F., 2010. The Hydrology and Hydrometeorology of Flooding in the Delaware River Basin. Journal of Hydrometeorology 11, 841‑859. https://doi.org/10.1175/2010JHM1236.1

Sugianto, S., Deli, A., Miswar, E., Rusdi, M., Irham, M., 2022. The effect of land use and land cover changes on flood occurrence in Teunom Watershed, Aceh Jaya. Land 11, 1271.

Susetyo, C., 2008. Urban flood management in Surabaya City: anticipating changes in the Brantas River system. ITC.

Tahmasebi Nasab, M., Berg, S.S., Comba, L., Sellner, B., Epperson, C., 2022. Impacts of seasonally frozen ground on streamflow recession in the Red River of the North Basin. River Research and Applications 38, 1277‑1284. https://doi.org/10.1002/rra.4025

Tellman, B., Schank, C., Schwarz, B., Howe, P.D., de Sherbinin, A., 2020. Using Disaster Outcomes to Validate Components of Social Vulnerability to Floods: Flood Deaths and Property Damage across the USA. Sustainability 12, 6006. https://doi.org/10.3390/su12156006

User Guides - Sentinel-2 MSI - Level-2 Processing - Sentinel Online, n.d.

Wanders, N., Karssenberg, D., de Roo, A., de Jong, S.M., Bierkens, M.F.P., 2014. The suitability of remotely sensed soil moisture for improving operational flood forecasting. Hydrology and Earth System Sciences 18, 2343‑2357. https://doi.org/10.5194/hess-18-2343-2014

Xiang, Z., Yan, J., Demir, I., 2020. A Rainfall-Runoff Model With LSTM-Based Sequence-to-Sequence Learning. Water Resources Research 56, e2019WR025326. https://doi.org/10.1029/2019WR025326

Yamamoto, K., Sayama, T., Apip, 2021. Impact of climate change on flood inundation in a tropical river basin in Indonesia. Progress in Earth and Planetary Science 8, 5. https://doi.org/10.1186/s40645-020-00386-4

Zein, M., 2010. A community-based approach to flood hazard and vulnerability assessment in flood prone areas; A case study in Kelurahan Sewu, Surakarta City-Indonesia (Master's Thesis). University of Twente.

Zhou, Q., Su, J., Arnbjerg-Nielsen, K., Ren, Y., Luo, J., Ye, Z., Feng, J., 2021. A GIS-Based Hydrological Modeling Approach for Rapid Urban Flood Hazard Assessment. Water 13, 1483.

ASSESSING AGRICULTURAL BURNED AREAS USING dNBR INDEX FROM SENTINEL-2 SATELLITE DATA IN CHIANG MAI, THAILAND, FROM 2019 TO 2023

Ratchaphon SAMPHUTTHANONT [1,2] ⓘ

ABSTRACT

This study conducted an assessment of agricultural burned areas using the dNBR index from Sentinel-2 satellite data, HARMONIZED collection, in Mae Rim District, Chiang Mai Province, over 5 years from 2019 to 2023. A total of 118 satellite datasets, before and after burning, were used to analyze the severity levels. It is considered severe once the Moderate Low Severity level is above 0.27. Error correction employed scene classification data, derived from the European Space Agency's area classification algorithms, and the NDWI index was used to exclude water-covered areas. Accuracy verification through an Error Matrix was conducted at 73 survey points with a 95% confidence level, adhering to the principles of statistical probability. The overall accuracy of the burned area classification was 82.19%. Agricultural burned areas in the study area were predominantly found mostly on flat terrain. in the eastern direction. In general, there was a significant increasing trend in burning, especially in the latest year 2023. Changes in the distribution burning month distribution were observed; in 2019-2022 burning was more prevalent in May, while in 2023, it shifted to April. This study successfully detected rice field burning; a small-scale, low fuel load, and low temperature burning, which the satellite hotspot data could not detect such burning. The results provide valuable information to promote the creative reduction of burning in communities by utilizing post-harvest agricultural residue, demonstrating the timely and appropriate application of tools and data for societal benefits.

Keywords: Agricultural Burned Area, Remote Sensing, Difference Normalized Burn Ratio (dNBR), Sentinel-2

1. INTRODUCTION

Chiang Mai province, located in the northern region of Thailand, faces air pollution issues, particularly due to high levels of fine particulate matter (PM2.5), which exceed standards for many months especially during the dry season from the end of a year to the middle of another year (Buakhao, 2023). Open biomass burning (OBB), which typically involves in-field agricultural residues, is a significant source of air pollution. It releases various pollutants and particulate matter, including Total Particulate Matter (TPM), in significant quantities (Rongmuang, 2015).

Currently, remote sensing data are being utilized for monitoring, tracking, and assessing open burning areas. Various satellite data sources such as MODIS and Landsat are used for this purpose, whereas the popularity of Sentinel-2 satellite data has grown due to its superior spatial resolution capabilities, providing higher definition than other satellites (Linta et al., 2021). The Normalized Burn Ratio (NBR) is commonly used to classify and assess the severity of burned areas (García, 1991; Alcaras, 2022), proving high efficiency in identifying vegetation affected by fire (Boulghobra, 2021; Kovacs, 2019; Mohammad, 2023). It is the ratio between Near Infrared (NIR) and Short-Wave Infrared (SWIR)

---

[1] *Department of Geography and Geoinformatics, Faculty of Humanities and Social Sciences, Chiang Mai Rajabhat University, Thailand, ratchaphon_sam@cmru.ac.th*

[2] *Asian Air Quality Operations Center by Space Technology, Geoinformatics & Environmental Engineering (AiroTEC), Chiang Mai Rajabhat University, Thailand*

bands used by Alcaras (2022). However, assessing such burned areas using this method may introduce errors when overlapping with water bodies, built-up areas, and other land covers, which are considered as the least likelihood of burning (Khamrueangwong, 2021).

This study focused on classifying agricultural burned areas using Sentinel-2 satellite data in the Mae Rim District, Chiang Mai Province, from 2019 to 2023. The main emphasis was on post-harvest rice field areas, which are frequently subjected to burning, to analyze spatial and temporal changes in burned areas. The analysis involved filtering out non-vegetation-covered areas using Sentinel-2 Scene Classification data and classifying burned areas using the Difference Normalized Burn Ratio (dNBR) method. To enhance the accuracy of burned area classification., water-covered areas were excluded from the results. Additionally, field surveys were conducted to verify accuracy and facilitate activities in order to provide alternative solutions for farmers to utilize post-harvest agricultural residues, thereby reducing burning. The study area, located in the Mae Rim district of Chiang Mai province, comprises a significant portion of rice fields. To promote reduction of agricultural burning, farmers and various agencies are coordinated to integrate knowledge for public benefits.

2. STUDY AREA

The study area is the Mae Rim District, Chiang Mai province (**Fig. 1**). Data on land use within the Mae Rim district in 2021 were classified by the Department of Land Development using visual interpretation in combination with aerial photography and satellite imagery. It revealed a total agricultural area of 76,131.53 rai, accounting for 26.56% of the study area.

Fig. 1. Study Area and Land Use, Mae Rim District, Chiang Mai Province.

The predominant land use was rice cultivation where rice straw and stubble burning is a common practice among farmers. This burning significantly contributes to air pollution, causing health problems and soil fertility degradation.

3. DATA AND METHODS

3.1. Data Preparation from Satellite

Data preparation was carried out using Sentinel-2 satellite data from the HARMONIZED collection under the Harmonized Landsat and Sentinel-2 program by NASA. The objective was to generate a dataset that reflects surface reflectance jointly captured by the Operational Land Imager (OLI) on Landsat-8/9 satellites and the Multi-Spectral Instrument (MSI) on Sentinel-2A/B satellites (NASA, 2023). Due to ESA's adjustment of the processing baseline on January 26, 2022, digital number (DN) limitations were introduced in the original data, allowing negative values which were not possible previously. Therefore, to analyze these changes as smoothly as possible, the Sentinel-2 HARMONIZED collection dataset (Sentinelhub, 2021) was used to analyze burned areas within agricultural land post-harvest. Analysis involved assessing the difference in Normalized Burn Ratio (NBR) values between pre- and post-burning periods from January to May and November to December, excluding periods with heavy cloud cover during the rainy season where soil cover data could not be accurately recorded. Thus, satellite data before and after burning within a 5-year period from 2019 to 2023 were selected for analysis, totalling 118 datasets as shown in **Table 1**.

3.2. Normalized Burn Ratio (NBR) Analysis

Analysis to assess burned areas using the Normalized Burn Ratio (NBR) index is designed to differentiate areas affected by large wildfires. Evergreen areas reflect strongly in the Near Infrared (NIR) wavelength range and has low reflectance in the Short-Wave Infrared (SWIR) range, which is opposite to what is observed in the burning areas. Therefore, burned areas can be distinguished by the difference in NBR values between pre- and post-burning periods (Keeley, 2009), as illustrated in Equation 1 (García, 1991; Alcaras, 2022).

$$NBR = (NIR - SWIR)/(NIR + SWIR) \tag{1}$$

For Sentinel-2 satellite data, Equation 2 (Al-hasn et al., 2022)

$$NBR_{Sentinel-2} = \frac{(Band\ 8 - Band\ 12)}{(Band\ 8 + Band\ 12)} \tag{2}$$

3.3. Analysis of Differences in NBR between Pre- and Post-Burning Periods

To analyze the burned areas, the differences in the Normalized Burn Ratio (NBR) index must be assessed. This is achieved by calculating the difference in the Different Normalized Burn Ratio (dNBR) between the pre-burning and post-burning periods (Kovacs, 2019), as shown in Equation 3.

$$d\ NBR = (NBR_{Pre-fire} - NBR_{Post-fire}) \tag{3}$$

Table 1.

Satellite Data for Pre- and Post-Burning Analysis for the Years 2019 – 2023.

	2019			2020			2021			2022			2023	
no.	Pre-fire	Post-fire	no.	Pre-fire	Post-fire	no.	Pre-fire	Post-fire	no.	Pre-fire	Post-fire	no.	Pre-fire	Post-fire
1	18 Dec 2018	15 Jan	28	31 Dec 2019	10 Jan	47	25 Dec 2020	4 Jan	73	25 Dec 2021	9 Jan	94	20 Dec 2022	9 Jan
2	15 Jan	20 Jan	29	10 Jan	15 Jan	48	4 Jan	14 Jan	74	9 Jan	24 Jan	95	9 Jan	14 Jan
3	20 Jan	30 Jan	30	15 Jan	25 Jan	49	14 Jan	19 Jan	75	24 Jan	3 Feb	96	14 Jan	24 Jan
4	30 Jan	4 Feb	31	25 Jan	30 Jan	50	19 Jan	24 Jan	76	3 Feb	8 Feb	97	24 Jan	3 Feb
5	4 Feb	9 Feb	32	30 Jan	4 Feb	51	24 Jan	3 Feb	77	8 Feb	13 Feb	98	3 Feb	8 Feb
6	9 Feb	14 Feb	33	4 Feb	14 Feb	52	3 Feb	13 Feb	78	13 Feb	5 Mar	99	8 Feb	13 Feb
7	14 Feb	19 Feb	34	14 Feb	5 Mar	53	13 Feb	28 Feb	79	5 Mar	10 Mar	100	13 Feb	18 Feb
8	19 Feb	24 Feb	35	5 Mar	30 Mar	54	28 Feb	5 Mar	80	10 Mar	15 Mar	101	18 Feb	23 Feb
9	24 Feb	1 Mar	36	30 Mar	19 Apr	55	5 Mar	15 Mar	81	15 Mar	20 Mar	102	23 Feb	28 Feb
10	1 Mar	6 Mar	37	19 Apr	4 May	56	15 Mar	20 Mar	82	20 Mar	25 Mar	103	28 Feb	15 Mar
11	6 Mar	11 Mar	38	4 May	14 May	57	20 Mar	25 Mar	83	25 Mar	29 Apr	104	15 Mar	20 Mar
12	11 Mar	21 Mar	39	10 Nov	15 Nov	58	25 Mar	14 Apr	84	29 Apr	4 May	105	20 Mar	4 Apr
13	21 Mar	26 Mar	40	15 Nov	20 Nov	59	14 Apr	19 Apr	85	10 Oct	5 Nov	106	4 Apr	24 Apr
14	26 Mar	4 Apr	41	20 Nov	25 Nov	60	19 Apr	24 Apr	86	5 Nov	10 Nov	107	24 Apr	29 Apr
15	4 Apr	15 Apr	42	25 Nov	30 Nov	61	24 Apr	4 May	87	10 Nov	15 Nov	108	29 Apr	4 May
16	15 Apr	20 Apr	43	30 Nov	5 Dec	62	4 May	9 May	88	15 Nov	20 Nov	109	4 May	19 May
17	20 Apr	25 Apr	44	5 Dec	10 Dec	63	9 May	14 May	89	20 Nov	30 Nov	110	19May	24 May
18	25 Apr	30 Apr	45	10 Dec	15 Dec	64	14 May	29 May	90	30 Nov	5 Dec	111	10Nov	20 Nov
19	30 Apr	15 May	46	15 Dec	25 Dec	65	5 Nov	15 Nov	91	5 Dec	10 Dec	112	20Nov	25 Nov
20	15 May	20 May				66	15 Nov	20 Nov	92	10 Dec	15 Dec	113	25Nov	5 Dec
21	16 Nov	26 Nov				67	20 Nov	30 Nov	93	15 Dec	20 Dec	114	5 Dec	10 Dec
22	26 Nov	1 Dec				68	30 Nov	5 Dec				115	10 Dec	15 Dec
23	1 Dec	11 Dec				69	5 Dec	10 Dec				116	15 Dec	20 Dec
24	11 Dec	16 Dec				70	10 Dec	15 Dec				117	20 Dec	25 Dec
25	16 Dec	21 Dec				71	15 Dec	20 Dec				118	25 Dec	30 Dec
26	21 Dec	26 Dec				72	20 Dec	25 Dec						
27	26 Dec	31 Dec												

3.4. Classification of Burn Severity Levels

In this study, burned areas were classified based on the wildfire severity levels, which are into 7 levels by The United States Geological Survey (USGS). Among these, three levels indicate areas affected by fire are Moderate-low Severity, Moderate-high Severity, and High Severity. Specifically, the Moderate low Severity level is defined as having values higher than 0.27, indicating areas burned by wildfires.

3.5. Analysis of Post-Harvest Bare Areas

Areas covered by clouds, cloud shadows, and water bodies can introduce errors in the classification of burned areas. In this study, the results of the burned area classification overlapping with areas covered by vegetation, clouds, cloud shadows, and water bodies were removed. This was achieved using scene classification data, derived from the European Space Agency's (ESA) algorithm for land cover classification. The classification includes 12 different categories: No Data, Saturated or defective pixel, Topographic casted shadows, Cloud shadows, Vegetation, Not-vegetated, Water, Unclassified, Cloud medium probability, Cloud high probability, Thin cirrus, Snow or ice. Therefore, in this step, only post-harvest bare areas (Not-vegetated: Value = 5) were selected for analysis.

3.6. Analysis of Water-covered Areas

During the initial stages of rice cultivation, there is noticeable water coverage. To reduce errors in the classification of burned areas, Normalized Difference Water Index (NDWI) is used to monitor changes related to water quantity in water bodies. Since water bodies absorb light significantly in the electromagnetic spectrum, the visible spectrum (green) and the near-infrared spectrum are observed. Equation 4 illustrates this process. For Sentinel-2 data, Equation 5 is applied.

$$\text{NDWI} = (\text{green} - \text{near infrared}) / (\text{green} + \text{near infrared}) \tag{4}$$

$$NDWI_{Sentinel-2} = \frac{(Band\ 3 - Band\ 8)}{(Band\ 3 + Band\ 8)} \tag{5}$$

Then, water-covered areas are created by selecting only the NDWI areas with values greater than or equal to 0.25, which is determined by considering coverage of the initial stages of rice cultivation.

3.7. Verification of the accuracy of the burnt area classification.

Accuracy of the burnt area classification in this study was verified through random sampling points, with the sample size determined using the principle of binomial probability (Chucheep, 2018) as shown in Equation 6.

$$n = \frac{Z^2(p)(q)}{e^2} \tag{6}$$

where:
  n = minimum sample size (number of sampling points)
  p = probability of correctness (ranges from 0 to 1)
  q = probability of error (ranges from 1 - p)
  Z = value from the standard normal distribution table
  e = margin of error from sampling

It was, then, distributed in the form of an Error Matrix or Contingency Table, which can be used to analyze the Producer's Accuracy, indicating the method's efficiency, the User's Accuracy, and the Overall Accuracy. (Chucheep, 2018) as shown in equations 7 - 9. The entire sequence of work steps is illustrated in **Fig. 2**.

$$\text{Producer's Accuracy} = \frac{n_{ii}}{n_{+j}} \tag{7}$$

$$\text{User's Accuracy} = \frac{n_{ii}}{n_{i+}} \tag{8}$$

$$\text{Overall Accuracy} = \frac{\sum_{i=1}^{k} n_{ii}}{n} \tag{9}$$
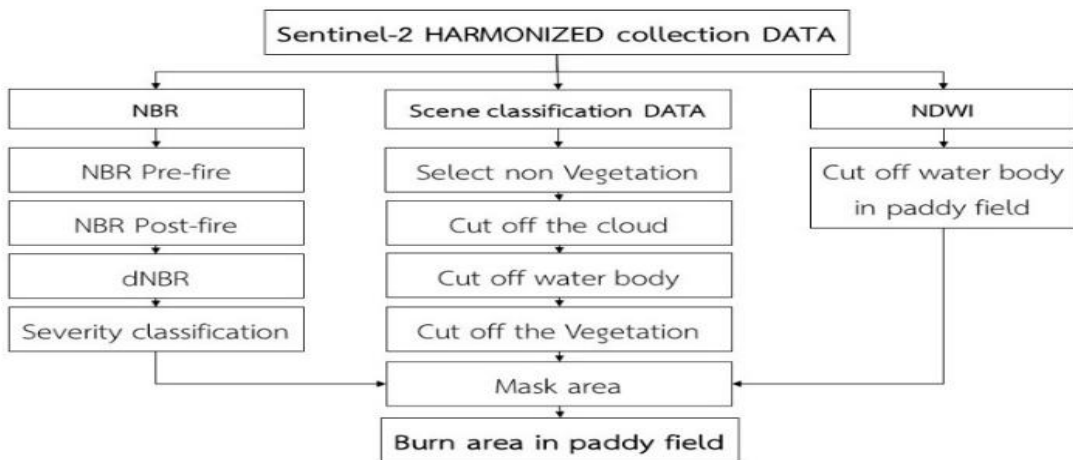
Fig. 2. The conceptual framework for analyzing burned areas in paddy fields using the dNBR index from Sentinel-2 satellite data.

4. RESULTS AND DISSUSSION

4.1. Fire Incidents and Trends in Agricultural Areas from 2019 to 2023

The changes in burned areas in rice fields in terms of both area and time revealed a higher incidence of burning during the months of April to May and November to December, corresponding to the post-harvest period (**Tab. 2**). Interestingly, during April to May 2023, there was a distinct shift in burning patterns, with more burning observed in April compared to May, which differs from the burning pattern during April to May of the years 2019-2022.

Table 2.

Displays the burned area in open fields (in hectares) categorized by month for the years 2019 to 2023.

Year/ Month	JAN	FEB	MAR	APR	MAY	NOV	DEC	sum
2019	2.18	3.19	6.61	45.63	239.81*	186.98	188.14	672.55
2020	1.21	0.7	4.48	30.78	167.14*	120.55	11.71	336.56
2021	6	2.06	12.14	28.92	127.67*	124.79	65.96	367.54
2022	2.54	33.01	28.52	11.74	558.29*	113.69	25.16	772.97
2023	40.15	34.21	39.08	715.03*	174.41	52.06	71.93	1126.87

* The month with the highest burning of the year.
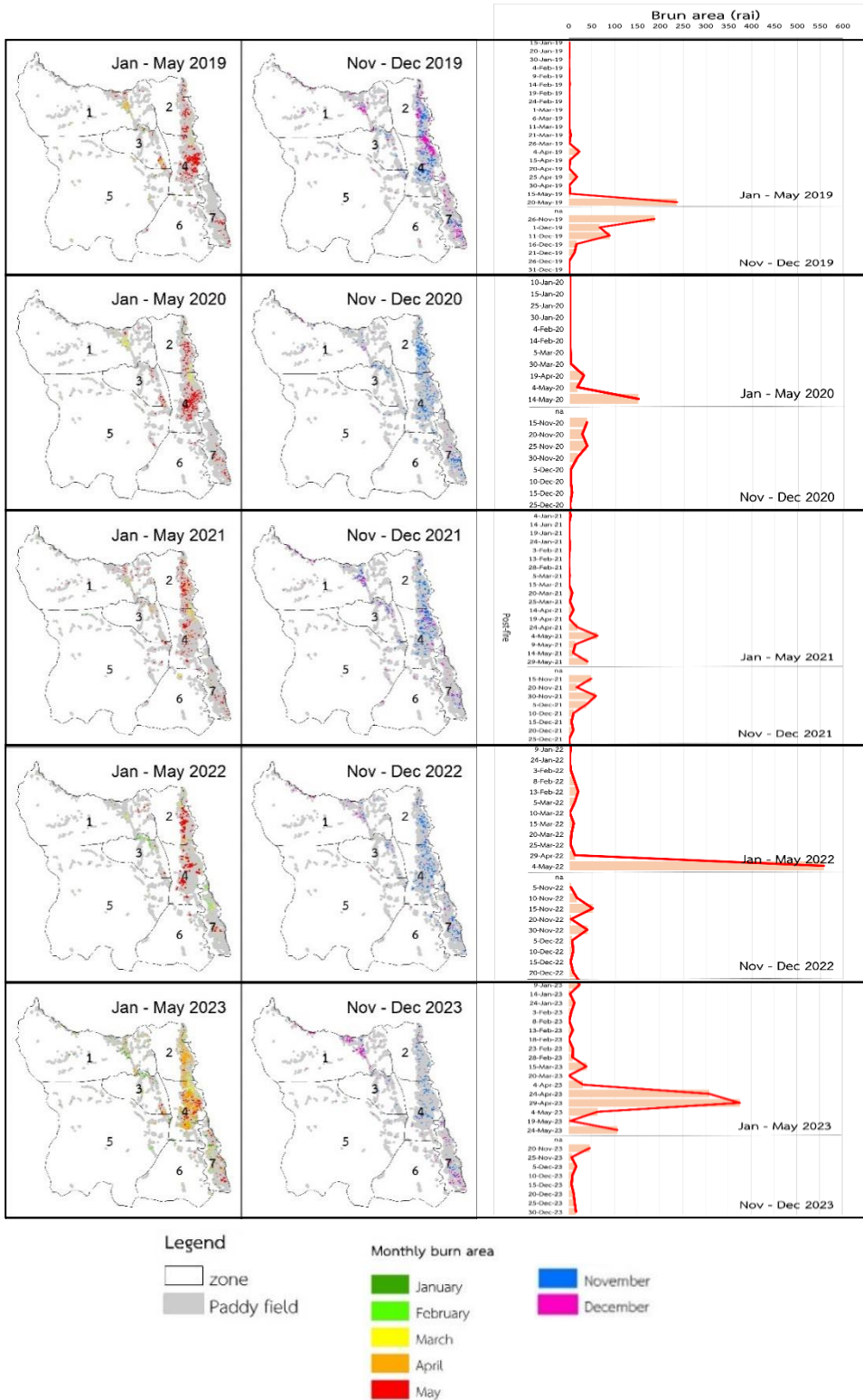
Fig. 3. Map of burned areas categorized by month from 2019 to 2023 (left), and line graph showing burned areas categorized by time intervals from 2019 to 2023 (right).

Due to the early onset of rain in April 2023 compared to previous years, farmers began burning stubble before planting as early as April. In contrast, from 2019 to 2022, the rainy season typically started in May, and the burning of stubble began accordingly. Meanwhile, it was observed that the burned areas tended to decrease from November to December during the years 2019-2023. Furthermore, each area exhibited somewhat consistent burning behavior, such as the upper part of Zone 4 burning faster than the lower part, as depicted in **Fig. 3.** In this study, the NDWI index was applied to extract burned areas in conjunction with other indices, enhancing efficiency, consistent with the study by Khamrueangwong (2021). For the date of the large fire event occurring on April 29, 2023, **Fig. 4** presents sample results of burn area, NBR, dNBR, NDWI, and scene classification.

Regarding the study on air pollution emissions resulting from burning in rice fields in Thailand, it was found that in 2018, burning covered 2.9% of the total rice cultivation area for that year (Junpen et al., 2018). This closely aligns with the burned areas observed in rice fields in Mae Rim District from 2019 to 2023, which accounted for 2.91%, 1.46%, 1.59%, 3.35%, and 4.88% respectively. However, a report in 2021 indicated that the northern region of Thailand had the highest incidence of burning in rice fields, accounting for 41.85% of the total rice cultivation area (Kanjanarueng, 2023).
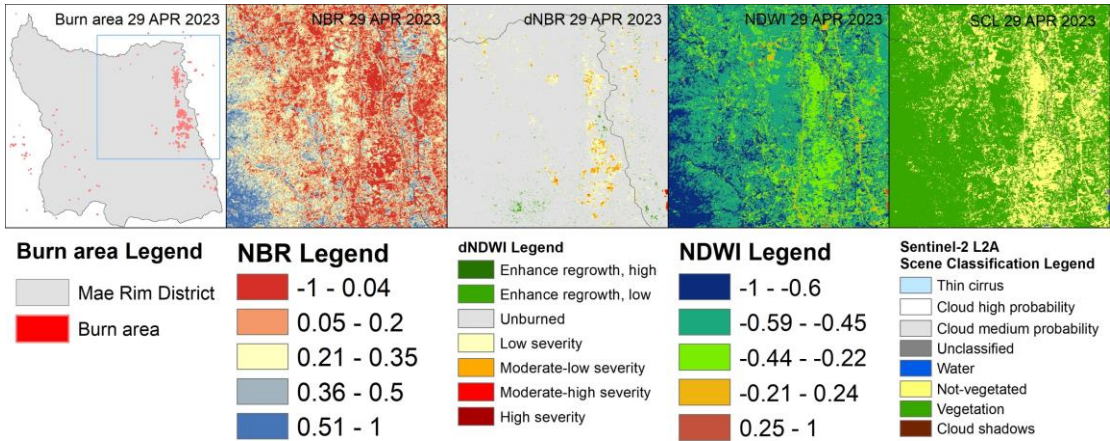
Fig. 4: Illustrates sample results of Burn area, NBR, dNBR, NDWI and Scene classification.

4.2. Verification of Burned Area Classification Accuracy

To verify accuracy of the burned area classification in this study, 73 sampling points were designated according to the criterion of binomial probability with a confidence level of 95%. These points were divided into 37 burned areas and 36 unburned areas. The results revealed that the classification of burned areas showed a producer's accuracy of 90% and a user's accuracy of 72.97%. Regarding the classification of unburned areas, the producer's accuracy was 76.74%, and the user's accuracy was 91.67%. The overall accuracy was found to be 82.19%, as shown in **Table 3** and **Fig. 5**.

Table 3.

Error Matrix of Fire Area Classification.

		Reference data from field		SUM	User's Accuracy (%)
		burn	non-burn		
Classified image	**burn**	**27**	10	37	72.97
	non-burn	3	**33**	36	91.67
	SUM	30	43	**73**	
	Producer's Accuracy (%)	90	76.74		

Overall Accuracy (%) = 82.19
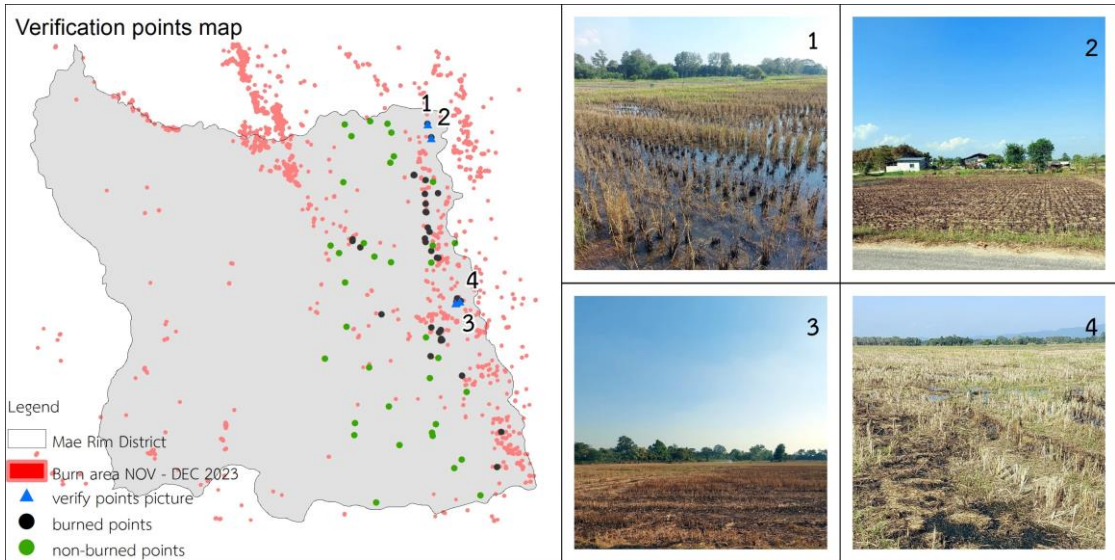
Fig. 5. Field Survey of Sample Areas.

In summary, the classification of burned areas in this study demonstrated a method efficiency of 90% and a reliability of 72.97%, while for unburned areas, it showed a method efficiency of 76.74% and a reliability of 91.67%. Overall, the classification accuracy in this study was 82.19% at a 95% confidence level. This validation method is commonly used for analyzing burned areas from satellite data. (Ruthamnong, 2019; Katagis, 2022).

4.3. Comparing Fire Detection between Hotspot Data and Satellite Imagery

Hotspot data refers to the Land Surface Temperature, especially abnormally high temperatures on the Earth's surface. The data can signify intense fire activity and even pinpoint the location of fire origins. At present, the Department of Forestry of Thailand utilizes the Visible Infrared Imaging Radiometer Suite (VIIRS) data onboard the Suomi National Polar-orbiting Partnership (Suomi-NPP) satellite which can capture global images every 12 hours, twice a day. The fire hotspot locations within a 375 x 375-meter area are accounted as a single data point. This data is considered before identifying areas with forest fire incidents and to monitor regions prone to frequent fire occurrences (Praesriwarothai, 2021).

When examining a composite image of Shortwave Infrared (SWIR) and True Color from Sentinel-2 satellite imagery, it becomes evident that areas of active burning and smoke plumes are clearly delineated.

Fig. 6. A composite of Shortwave Infrared (SWIR) and True Color imagery from Sentinel-2 satellite data during the occurrence of burning within rice field areas where hotspots could not be detected.

However, during the same timeframe, no hotspot data is available. This indicates that fire occurrences in rice fields, particularly smaller, low-intensity burns with lower burning temperatures, are better detected through dNBR index of satellite imagery compared to hotspot data, which may not be captured (GISGeography, 2024). This aligns with the findings of Mohammad (2023), which discovered that dNBR from Sentinel-2 outperforms in spectral discrimination between burned and unburned surfaces. This is illustrated in **Fig. 6.**

5. CONCLUSIONS

The area burned delineation in this study focused on categorizing burned areas within rice field areas after harvesting over a period of 5 years (2019 - 2023) using Sentinel-2 HARMONIZED satellite data, analyzed from the Normalized Burn Ratio (NBR) difference values before and after burning, with a threshold of Moderate Low Severity (0.27) and above indicating burned areas. Areas covered by dense vegetation, water bodies, and clouds/shadows were excluded using Sentinel-2 L2A Scene Classification and NDWI data. Accuracy of the classification was evaluated using an Error Matrix with 73 survey points at a 95% confidence level, following the principles of probabilistic sampling. The results showed that the burned area in rice fields was 672.55, 336.56, 367.54, 772.97, and 1,126.87 rai per year, respectively. It was observed that the burned area was higher during April to May and November to December, which corresponded to the post-harvest period within the study area. In April 2023, there was a significant increase of burned areas compared to other years. On the contary, it was found that during November to December of each year, the burned area tended to decrease. Furthermore, distinct patterns of burning before and after harvesting were observed in each area. Overall accuracy of the classification in this study was 82.19%. Regarding the burned area classification, there was a 72.97%.

R E F E R E N C E S

Alcaras, E., Costantino, D., Guastaferro, F., Parente, C., & Pepe, M. (2022). Normalized Burn Ratio Plus (NBR+): A New Index for Sentinel-2 Imagery. Remote Sensing, 14(7), 1727. https://doi.org/10.3390/rs14071727

Al-hasn R., & Almuhammad R. (2022). Burned area determination using Sentinel-2 satellite images and the impact of fire on the availability of soil nutrients in Syria. Journal of Forestry Science, 68(3), 96–106.

Boulghobra, N. (2021). Sentinel 2 Imagery and Burn Ratios for Assessing the July 5, 2021 Wildfires Severity in the Region of Khenchela (Northeast Algeria). Geographia Technica, 16 (2), 95-104. DOI: 10.21163/GT_2021.162.08

Buakhao, L. (2023). Model for Estimating PM2.5Concentration Using Aerosol Optical Depth Data in the Muang District of Chiang Mai Province. YRU Journal of Science and Technology, 8(1), 50-58.

Chucheep, K. (2018). Accuracy Assessment. Remote Sensing Technical. Note No. 3 (2018). Faculty of Forestry, Kasetsart University.

García, M.J.L., & Caselles, V. (1991). Mapping burns and natural reforestation using thematic mapper data. Geocarto International, 6(1), 31–37.

GIS Geography. (2024). Sentinel 2 Bands and Combinations. Retrieved from https://gisgeography.com/sentinel-2-bands-combinations/

Junpen A, Pansuk J, Kamnoet O, Cheewaphongphan P, Garivait S. (2018). Emission of Air Pollutants from Rice Residue Open Burning in Thailand. Atmosphere, 9(11) :449. https://doi.org/10.3390/atmos9110449

Keeley, J. E. (2009). Fire intensity, fire severity and burn severity: A brief review and suggested usage. International Journal of Wildland Fire, 18(1), 116–126.

Katagis, T., Gitas, I. Z. (2022). Assessing the Accuracy of MODIS MCD64A1 C6 and FireCCI51 Burned Area Products in Mediterranean Ecosystems. Remote Sensing. 14 (3).

Khamrueangwong, T., Kamthonkiat, D. (2021). Burn indices from Landsat 8 : Restrictions on Its Application. BURAPHA SCIENCE JOURNAL, 26(2), 1308-1325.

Kovacs, K.D. (2019). Evaluation of Burned Areas With Sentinel-2 Using Snap: The Case of Kineta and Mati, Greece, July 2018. Geographia Technica, 14 (2), 20-38. DOI: 10.21163/GT_2019.142.03

Linta, N., Mahavik, N., Chatsudarat, S., Seejata, K., & Yodying, A. (2021). Analysis of Burning Area from Forest Fire using Sentinel-2 image: A Case Study of Pai, Mae Hong Son Province. Journal of Applied Informatics and Technology, 3(2), 101–121. https://doi.org/10.14456/jait.2021.9

Mohammad, L., Bandyopadhyay, J., Sk, R., Mondal, I., Nguyen, T., Lama G., Anh D. (2023). Estimation of agricultural burned affected area using NDVI and dNBR satellite-based empirical models. Journal of Environmental Management. 343, 118226. https://doi.org/10.1016/j.jenvman.2023.118226

NASA. (2023). Harmonized Landsat and Sentinel-2. Retrieved from https://hls.gsfc.nasa.gov/

Praesriwarothai, U. (2021). Study of Active Fire Evolution in Northern Thailand Using Density Based Spatial Clustering of Applications with Noise (DBSCAN) and Kernel Density Estimation (KDE). Chulalongkorn University Theses and Dissertations (Chula ETD). https://digital.car.chula.ac.th/chulaetd/5520

Rongmuang, K. (2015). Assessment of pollutant emission from open field burning of agricultural. Degree of Master of Engineering in Agricultural and Food. Suranaree University of Technology.

Ruthamnong, S. (2019). Burned area extraction using multitemporal difference of spectral indices from Landsat 8 data: A case study of Khlong Wang Chao, Klong Lan and Mae Wong National Park. The Golden Teak : Humanity and Social Science Journal (GTHJ.) 25(2), 49-65.

Sentinel online. (n.d.). Level-2A Algorithm Overview. Retrieved from https://sentinels.copernicus.eu/web/sentinel/technical-guides/sentinel-2-msi/level-2a/algorithm-overview

Sentinelhub. (2021). Sentinel-2 processing baseline changes and harmonizeValues. Retrieved from https://forum.sentinel-hub.com/t/sentinel-2-processing-baseline-changes-and-harmonizevalues/4635

Sentinelhub2. (n.d.). NDWI Normalized Difference Water Index. Retrieved from https://custom-scripts.sentinel-hub.com/custom-scripts/sentinel-2/ndwi/

Kanjanarueng, Y, Miangbua, O and Ratanakaew, T. (2023). Cost-Benefit Analysis of Agricultural Waste Management Methods (Research Report). National Research Council of Thailand.

ENVIRONMENTAL MONITORING ON THE SURFACE OF THE ANDAMAN SEA OVER THE SOUTHWESTERN COAST OF THAILAND: A CASE STUDY OF SPATIAL AND TEMPORAL VARIABILITY OF CHLOROPHYLL-A

Jumpol ITSARAWISUT[1,3] , *Apiruk PUCKDEEVONGS[2]* , *Teerawong LAOSUWAN[1,3*]*

ABSTRACT
Chlorophyll-a is a pigment or substance used in photosynthesis that is found within the cell of phytoplankton, small unicellular algae that floats in water and is blown by waves, wind, and tide. Phytoplankton is essential for the aquatic ecosystem. This research studies the spatial and temporal variability of chlorophyll-a using data from the Aqua satellite in the MODIS system from 2018 to 2022, then analyzes the data with the SeaWiFS Data Analysis System (SeaDAS) program. The results show that chlorophyll-a on the surface of the Andaman Sea varies during the year according to monsoon activity. It has a high value during the northeast monsoon (November to March), and its maximum value is in January. On average, chlorophyll-a in June 2021 had a minimum value of 0.1994 mg/m^3, and chlorophyll-a in January 2022 had a maximum value of 0.8591 mg/m^3. The relationship between chlorophyll-a and sea surface temperature during the northeast monsoon, including wind stream at different times, shows the increase and decrease of chlorophyll-a, which may be consistent with upwelling and downwelling at the eastern coast of the Andaman Sea.

***Key-words**: Remote Sensing, Chlorophyll-a, Andaman Sea, Digital Image Processing, MODIS-Aqua*

1. INTRODUCTION

Open sea is divided vertically, light being an essential factor that separates it into the photic zone and aphotic zone. The photic zone has full sunlight and is located in the same zone as the continental shelf; photosynthesis can occur within this zone at a depth of approximately 200 m. The aphotic zone is deeper than the photic zone and cannot receive sunlight, so there is no photosynthesis and there are fewer organisms (Difference Between, 2023). It may be further divided according to marine organisms into five zones: 1) the epipelagic zone, which begins at the surface and reaches a depth of 200 m, and which can be compared to the photic zone as it obtains enough sunlight for photosynthesis; 2) the mesopelagic zone, with a depth of 200 to 1,000 m; 3) the bathypelagic zone, with a depth of 1,000 to 4,000 m; 4) the abyssalpelagic zone, with a depth of 4,000 to 6,000 m; and 5) the hadalpelagic zone, which is deeper than 6,000 m and always found at oceanic trenches (NOAA, 2023).

[1]*Department of Physics, Faculty of Science, Mahasarakham University, Thailand, jumpol.s@msu.ac.th, teerawong@msu.ac.th*

[2]*Department of Computer Engineering, College of Engineering, Rangsit University, Pathum Thani, Thailand, apiruk.pu@rsu.ac.th*

[3]*Space Technology and Geo-Informatics Research Unit, Faculty of Science, Mahasarakham University, Thailand*

*Corresponding author

The Andaman Sea is part of the continental shelf of the Indian Ocean. It is a submerged coast with a marginal sea surrounded by land, an island, and a peninsula. It also has an open part connected to the open sea at the surface and may have oceanic ridges. It is a semi-closed basin located to the east of the Bay of Bengal. There are different depths of seabed in the Andaman Sea (Marine Knowledge Hub, 2023); they can be divided into two zones according to sea contouring, which causes there to be diverse types and quantities of coral reefs. The seabed at the coastline of Ranong, western Phang Nga, and western Phuket has a high slope and an average depth of approximately 1,000 m. The Andaman Basin, the deepest part of the Thai Sea, reaches approximately 3,000 m, while the seabed at the coastline of southern Phang Nga, eastern Phuket, Krabi, and Trang have a slight slope, and the continental shelf has a depth of less than 300 m (Biodiversity CHM Thailand, 2023).

Phytoplankton is a small organism that floats in water and within its cell has pigment such as chlorophyll-a, a substance used for photosynthesis. Therefore, it is essential for the aquatic ecosystem. Phytoplankton is categorized by type of chlorophyll; chlorophyll-a is categorized as Cyanophyta (Laosuwan et al., 2022). Chlorophyll-a is a primary photosynthetic pigment that can capture sunlight by itself, while other chlorophyll are secondary photosynthetic pigments (accessory pigments) that capture the light's energy and pass it to chlorophyll-a (Zhao et al., 2023).

Remote sensing technology using satellites is considered an effective method for monitoring phenomenal changes in the atmosphere, land, and ocean (Gomasathit et al., 2015; Rotjanakusol & Laosuwan, 2018; Itsarawisut & Laosuwan, 2022; Itsarawisut et al., 2022; Ounrit et al., 2022). This technology uses electromagnetic waves to acquire information without making physical contact with objects (Uttaruk & Laosuwan, 2019; Rotjanakusol & Laosuwan, 2020; Uttaruk et al., 2022; Laosuwan et al., 2023). It can record data in a wide range and repeat it in the same area in each orbit of the satellite, so environmental changes can be monitored in different periods (Laosuwan & Uttaruk, 2017; Rotjanakusol & Laosuwan, 2019a; Rotjanakusol & Laosuwan, 2019b; Auntarin et al., 2021; Jomsrekrayom et al., 2021; Celik et al., 2022; Kanjanasiranont et al., 2022; Turton et al., 2022; Chen et al., 2023; Phoophiwfa et al., 2023). For this reason, this technology has been used for studying chlorophyll-a at the surface of the sea, such as in the studies by Lins et al. (2017), Silveira et al. (2020), Aranha et al. (2022), and Wang et al. (2022).

Phytoplankton is a significant manufacturer of food chains in water supply and has been used as a sea fertility index. Open sea has few plankton as it lacks nutrients, which causes low fertility, while the coastline or upwelling area has rich nutrients and plenty of phytoplankton, indicating the fertility and amount of aquatic animal resources in that area (Buranapratheprat & Meesook, 2013). The goal of this research is to study the spatial and temporal variability of chlorophyll-a by using data from the Aqua satellite in the MODIS system from 2018 to 2022.

2. MATERIALS AND METHODS

2.1. Study Area

The Andaman Sea (**Fig. 1**) is located to the east of the Bay of Bengal, a part of the Indian Ocean.

The north is close to the Irrawaddy Estuary, while the east is bounded by the coastlines of Myanmar, Thailand, and Malaysia. On the west side lie the Andaman Islands and Nicobar Islands. The southern end is at Sumatra Island and the Strait of Malacca. The territory's latitude extends from 6° to 14°N, and its longitude from 93° to 99°E. The length of the Andaman Sea from north to south is approximately 1,200 km, and the width is 650 km.

The sea has an approximate area of 797,700 km^2 and an average depth of 870 m, the deepest point being 3,777 m. It is influenced by the northeast monsoon from November to December and the southwest monsoon from May to September.
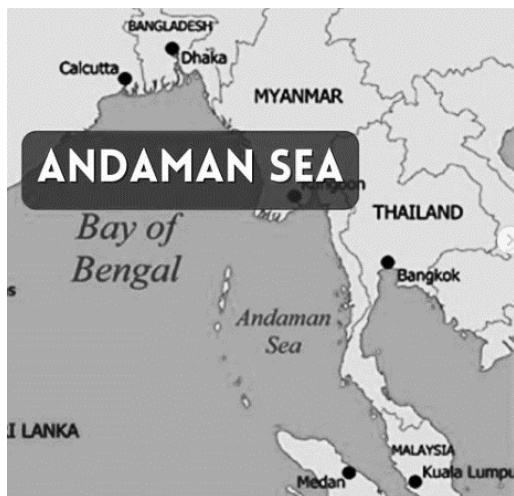
Fig. 1. The study area.

2.2. Operation

This study analyzes three sets of data:

1) Wind stream data (**Fig. 2**) from Remote Sensing Systems, which can be downloaded from www.remss.com/measurements/wind.

2) Level-2 product measured by a MODIS sensor installed on the Aqua satellite. It can be downloaded from Ocean Color (http://oceancolor.gsfc.nasa.gov) (**Fig. 3**). Level-2 MODIS Aqua data has a pixel size equal to 1,000 m. Data processing was conducted with SeaDAS.

Fig. 2. Wind stream data.

Fig. 3. MODIS Aqua Level-2 product.

3) Sea surface temperature data (**Fig. 4**) from EARTHDATA, which can be downloaded from https://giovanni.gsfc.nasa.gov/giovanni/.

Level-2 MODIS Aqua data was gathered from daily and monthly data each year, then calculated for the average annual data. Wind stream and sea surface temperature were analyzed with the average amount of chlorophyll-a at the sea surface to determine the spatial and temporal variability of chlorophyll-a.
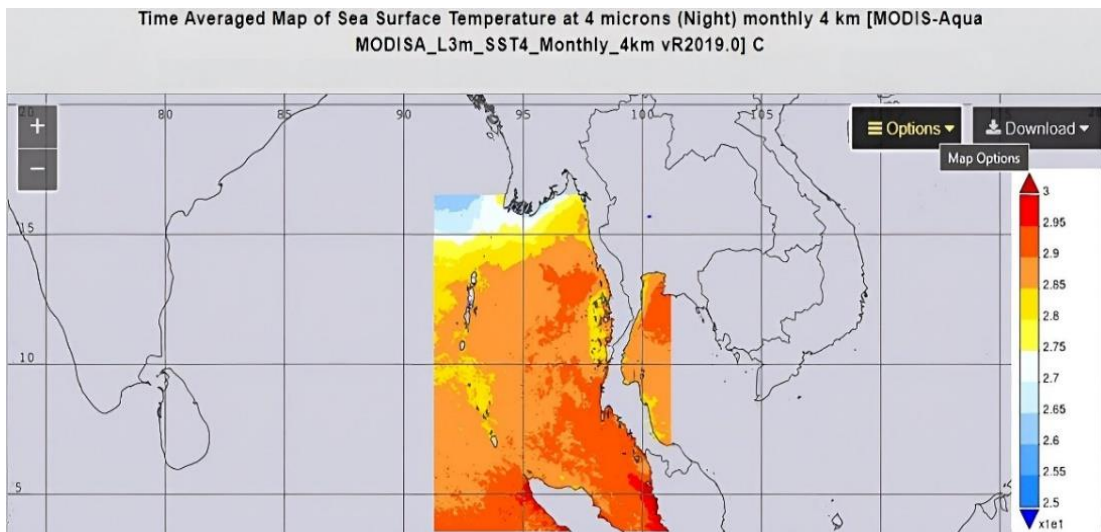
Fig. 4. Sea surface temperature.

3. RESULTS AND DISCUSSION

3.1. Analysis results of chlorophyll-a

The analysis results of the expansion of chlorophyll-a by monthly average at the surface of the Andaman Sea from 2018 to 2022 is shown in **Table 1**.

As recorded in **Table 1**, the average amount of chlorophyll-a at the surface of the Andaman Sea in 2018 had a maximum value in October of 0.6948 mg/m^3, a minimum value in April equal to 0.2802 mg/m^3, and an annual average value of 0.4055 mg/m^3. In 2019, the average amount of chlorophyll-a at the surface of the Andaman Sea had a maximum value in December of 0.6214 mg/m^3, a minimum value in May of 0.2709 mg/m^3, and an annual average value of 0.4174 mg/m^3.

In 2020, the average amount of chlorophyll-a at the surface of the Andaman Sea had a maximum value in November of 0.6483 mg/m^3, a minimum value in May of 0.2847 mg/m^3, and an annual average value of 0.4274 mg/m^3. In 2021, the average amount of chlorophyll-a at the surface of the Andaman Sea had a maximum value in November of 0.6380 mg/m^3, a minimum value in June of 0.1994 mg/m^3, and an annual average value of 0.4208 mg/m^3. In 2022, the average amount of chlorophyll-a at the surface of the Andaman Sea had a maximum value in January of 0.8591 mg/m^3, a minimum value in June of 0.2419 mg/m^3, and an annual average value of 0.4932 mg/m^3. The result of chlorophyll-a expansion by monthly average at the surface of the Andaman Sea was calculated for the annual average in each month, as shown in **Fig. 5** and **Fig. 6**.

Analysis results of the expansion of chlorophyll-a by monthly average.

2018		2019	
Month	Average amount of chlorophyll-a (mg/m^3)	Month	Average amount of chlorophyll-a (mg/m^3)
Jan	0.5319	Jan	0.5432
Feb	0.5936	Feb	0.5610
Mar	0.4180	Mar	0.4418
Apr	0.2802	Apr	0.3100
May	0.3353	May	0.2709
Jun	0.3828	Jun	0.3412
Jul	0.2833	Jul	0.3162
Aug	0.2818	Aug	0.3997
Sep	0.3950	Sep	0.3533
Oct	0.6948	Oct	0.4105
Nov	0.3281	Nov	0.4394
Dec	0.3411	Dec	0.6214
2020		2021	
Month	Average amount of chlorophyll-a (mg/m^3)	Month	Average amount of chlorophyll-a (mg/m^3)
Jan	0.5469	Jan	0.5427
Feb	0.5070	Feb	0.5391
Mar	0.3838	Mar	0.5094
Apr	0.3535	Apr	0.3646
May	0.2847	May	0.4090
Jun	0.3908	Jun	0.1994
Jul	0.3367	Jul	0.3059
Aug	0.3716	Aug	0.2565
Sep	0.3855	Sep	0.4398
Oct	0.3601	Oct	0.4428
Nov	0.6483	Nov	0.6380
Dec	0.5593	Dec	0.4026
2022			
Month	Average amount of chlorophyll-a (mg/m^3)		
Jan	0.8591		
Feb	0.7684		
Mar	0.5246		
Apr	0.5518		
May	0.4409		
Jun	0.2419		
Jul	0.3529		
Aug	0.3506		
Sep	0.3536		
Oct	0.5183		
Nov	0.4186		
Dec	0.5374		
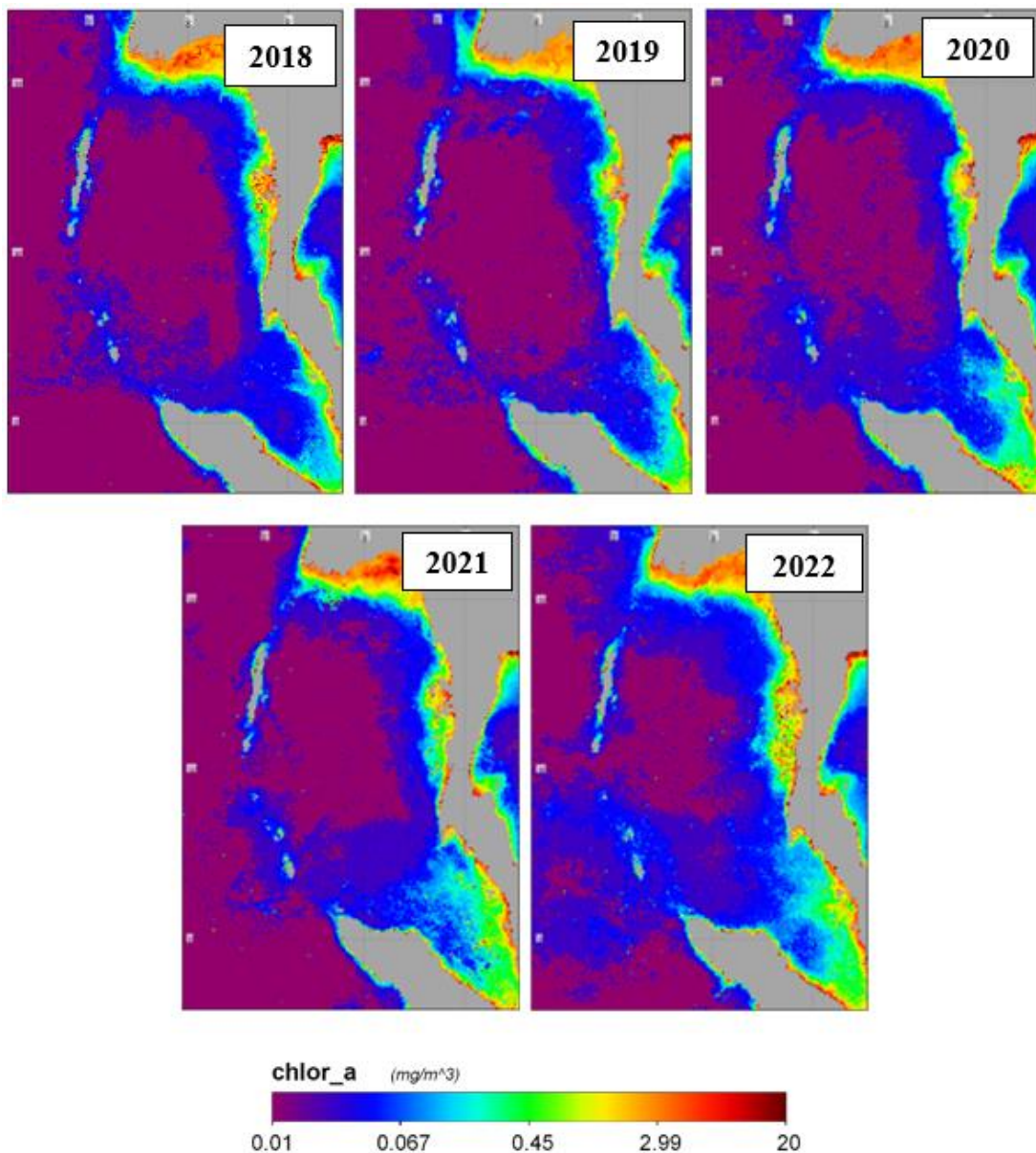
Fig. 5. The annual average distribution of chlorophyll-a in the Andaman Sea.

Fig. 5 and **Fig. 6** show that the average amount of chlorophyll-a at the surface of the Andaman Sea from 2018 to 2022 had a maximum value in January of 0.6845 mg/m³. The value decreased in March, and the minimum value in August was 0.3566 mg/m³. It started to rise again in October, the average steadily increasing. During those five years, chlorophyll-a at the surface of the Andaman Sea had a high value from December to March, which was influenced by the northeast monsoon, and a low value from April to September, which was influenced by the southwest monsoon. Chlorophyll-a will increase or decrease depending on season, weather condition, density, and the expansion of phytoplankton in each area.
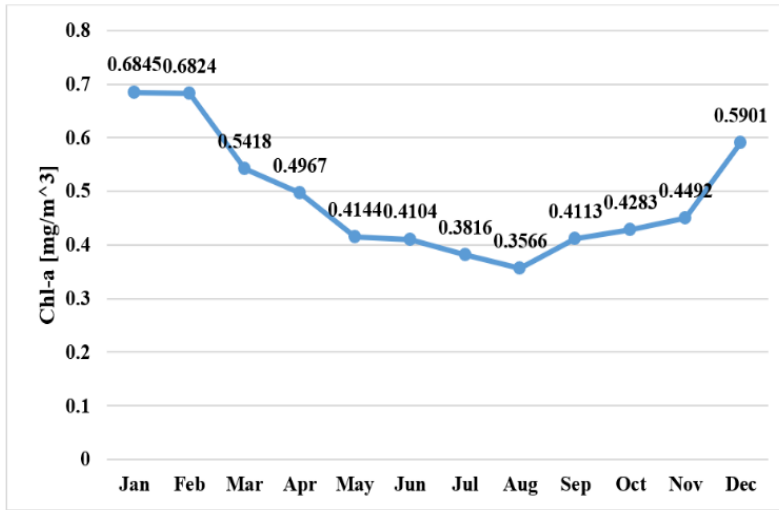
Fig. 6. Average amount of chlorophyll-a at the surface of the Andaman Sea from 2018 to 2022.

3.2. Analysis of the quantity and expansion of chlorophyll-a at the surface of the Andaman Sea with wind stream and surface temperature

Wind streams flow through the surface of the Andaman Sea in a different manner each month, but it is possible to track their directions. In this study, the directions of wind streams were downloaded from Remote Sensing Systems. For the analysis of the quantity and expansion of chlorophyll-a at the surface of the Andaman Sea with wind stream and surface temperature, an example wind stream chart from 2022 is shown in **Fig. 7**.

This study found that the quantity of chlorophyll-a at the sea surface varies according to season and monsoon activity. From November to March (the northeast monsoon), chlorophyll-a at the sea surface was higher than from May to September (the southwest monsoon), with a maximum value in January of 0.6845 mg/m^3 and a minimum value in August of 0.3566 mg/m^3. The increase and decrease of chlorophyll-a according to season were similar in each year. From the data of Level-2 product measured by a MODIS sensor installed on the Aqua satellite, chlorophyll-a at the surface of the Andaman Sea changed in line with wind stream. In addition, it had a high value during the northeast monsoon and a low value during the southwest monsoon. It was seen on the eastern coast of the Andaman Sea, consistent with Buranapratheprat and Meesook's study (2013).

The study "Temporal Variations of Sea Surface Chlorophyll-a in the Andaman Sea Based on Aqua MODIS Image Processing" found that chlorophyll-a at the surface of the Andaman Sea varies during the year according to monsoon activity; it has a high value during the northeast monsoon, its maximum value occurring in January, and a low value during the southwest monsoon. It is consistent with the study by Tan et al. (2006) that is referenced by Buranapratheprat and Meesook (2013). The study "Seasonal Variability of SeaWiFS Chlorophyll-a in the Malacca Straits in Relation to Asian monsoon" also found that chlorophyll-a at the surface of the Andaman Sea varies during the year according to monsoon activity. Chlorophyll-a at the surface of the northern part of the Malacca Strait starts to increase in November and has a maximum value in January (during the northeast monsoon), and it decreases in March and has a minimum value in August (during the southwest monsoon); it starts to increase again from November onward. In this study, chlorophyll-a from Level-2 product measured by a MODIS sensor installed on the Aqua satellite falls within the range that has been measured at the Andaman Sea (Buranapratheprat & Meesook, 2013).
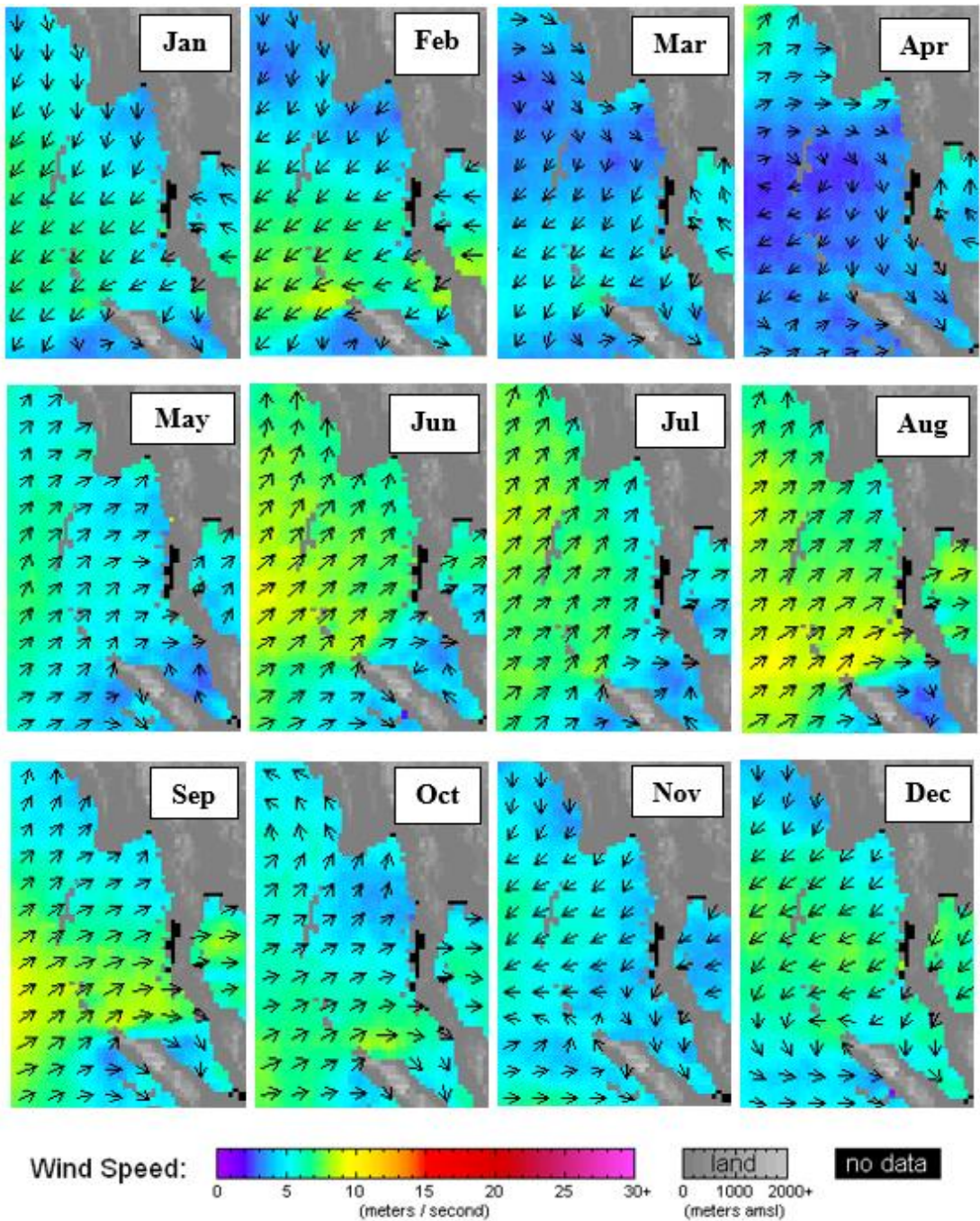
Fig. 7. Average amount of chlorophyll-a at the surface of the Andaman Sea in 2022.

The consistency of the result demonstrates the reliability of the chlorophyll-a data from this study. The increase of chlorophyll-a at the sea surface during the northeast monsoon may occur from upwelling at the eastern coast of the Andaman Sea—that is, the surface of the water has moved from the coastline according to the direction of the wind at a certain time (**Fig. 4**), then the lower layer of

the water, which has a low temperature, flows upward to replace the upper layer of water and bring all nutrients to the sea surface. Then plankton can use these nutrients to grow and increase, causing chlorophyll-a at the surface of the coastline to have a high value (Knauss, 1997; Buranapratheprat & Meesook, 2013). The sample of chlorophyll-a increased at the eastern coast of the Andaman Sea in January 2022, which is consistent with the temperature of the sea surface, and it had less value in the same area (**Fig. 8**).
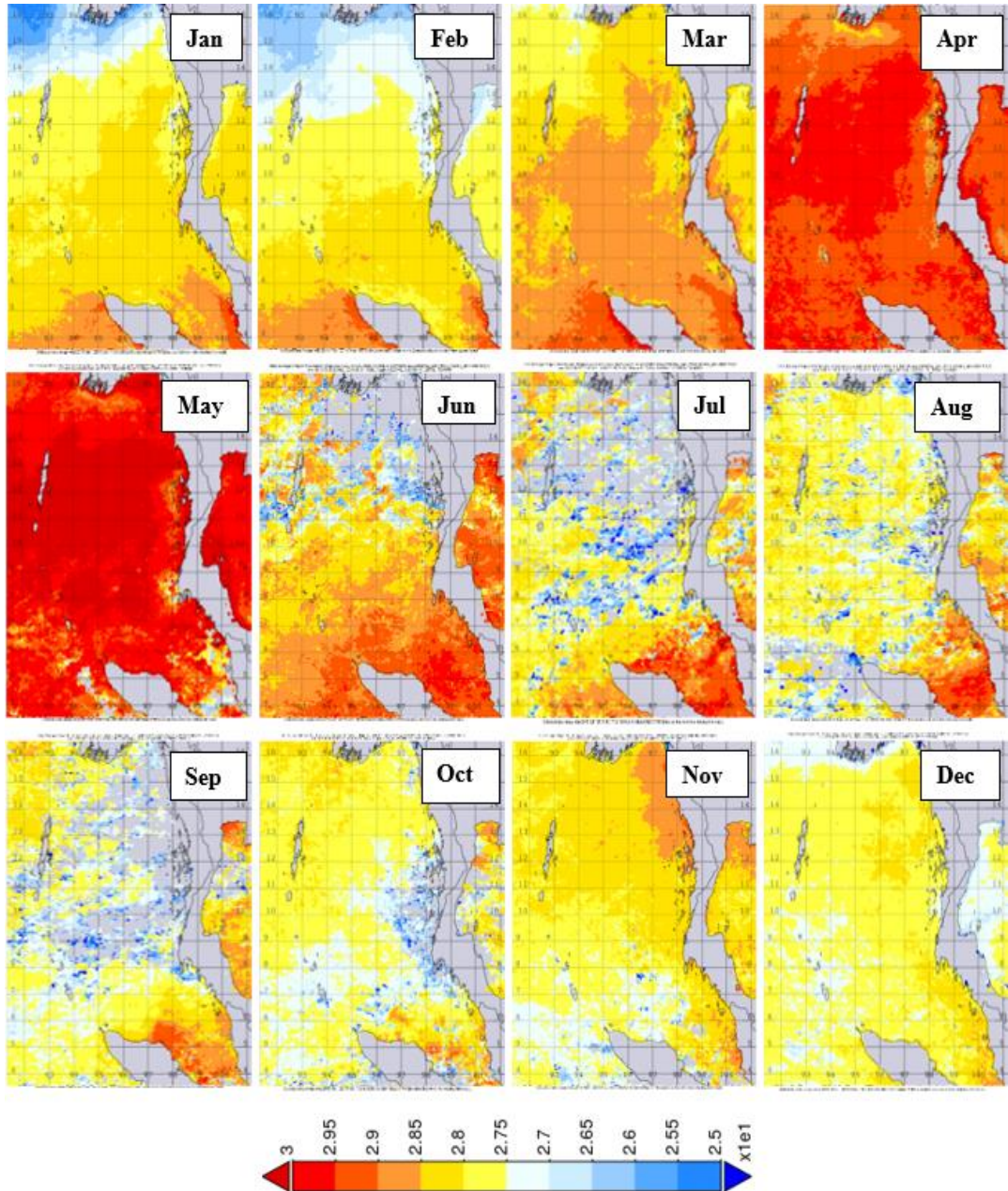
Fig. 8. Temperature of the sea surface in 2022.

This is a sign that upwelling occurred at this time. The decrease of chlorophyll-a during the southwest monsoon (**Fig. 5**) may relate to downwelling from the southwest wind stream that blows into the eastern coast (**Fig.7**). It is consistent with the research of Robinson et al. (2007) and Buranapratheprat and Meesook (2013), which study the relationship between chlorophyll-a, sea temperature, and the weather variation that causes oceanographic processes at Bali, Indonesia. They found that the increase and decrease of chlorophyll-a relate to upwelling, downwelling, monsoon activity, and sea water temperature.

4. CONCLUSION

This study conducted environmental monitoring on the surface of the Andaman Sea over the southwestern coast of Thailand. It examined the spatial and temporal variability of chlorophyll-a by using data from Level-2 product measured by a MODIS sensor installed on the Aqua satellite, finding that chlorophyll-a at the surface of the Andaman Sea in each period of the year tends to vary according to monsoon activity. The period from November to March (the northeast monsoon) had a high value of chlorophyll-a, while the period from May to September (the southwest monsoon) had a low value of chlorophyll-a. The relationship between chlorophyll-a, sea surface temperature during the northeast monsoon, and wind stream in different periods shows that the increase and decrease of chlorophyll-a may be consistent with upwelling and downwelling at the eastern coast of the Andaman Sea.

ACKNOWLEDGMENTS

REFERENCES

Aranha, T. R. B. T., Martinez, J.-M., Souza, E. P., Barros, M. U. G., & Martins, E. S. P. R. (2022). Remote Analysis of the Chlorophyll-a Concentration Using Sentinel-2 MSI Images in a Semiarid Environment in Northeastern Brazil. Water, 14(3), 451. https://doi.org/10.3390/w14030451

Auntarin, C., Chunpang., P., Chokkuea, W., & Laosuwan, T. (2021). Using a Split-window Algorithm for the Retrieval of the Land Surface Temperature via Landsat-8 OLI/TIRS. Geographia Technica, 16(Special Issue), 70-81. https://doi.org/10.21163/GT_2021.163.03

Biodiversity CHM Thailand. (2023). Open Sea. Available online: https://chm-thai.onep.go.th/?page_id=2615 (Accessed on 22 March 2023)

Buranapratheprat, A., Meesook, A. (2013). Temporal Variations of Sea Surface Chlorophyll-a in the Andaman Sea Based on Aqua MODIS Image Processing. Burapha Sciecne Journal, 18(1), 194-201.

Celik, M. F., Isik, M. S., Yuzugullu, O., Fajraoui, N., & Erten, E. (2022). Soil Moisture Prediction from Remote Sensing Images Coupled with Climate, Soil Texture and Topography via Deep Learning. Remote Sensing, 14(21), 5584. https://doi.org/10.3390/rs14215584

Chen, G., Wang, Y., Wen, Q., Zuo, L., & Zhao, J. (2023). An Erosion-Based Approach Using Multi-Source Remote Sensing Imagery for Grassland Restoration Patterns in a Plateau Mountainous Region, SW China. Remote Sensing, 15(8), 2047. https://doi.org/10.3390/rs15082047

Difference Between. (2023). Difference between Photic and Aphotic Zone. Available online: https://www.differencebetween.com/difference-between-photic-and-aphotic-zone/ (Accessed on 05 March 2023)

Gomasathit, T., Laosuwan, T., Sangpradit, S., & Rotjanakusol, T. (2015). Assessment of Drought Risk Area in Thung Kula Rong Hai using Geographic Information Systems and Analytical Hierarchy Process. International Journal of Geoinformatics, 11(2), 21-27.

Itsarawisut, J., Laosuwan, T. (2022). Estimation of Particulate Matter Less Than 10 Microns Volume through Various Formats of Spatial Interpolation Methods. Geographia Technica, 17(2), 26-34. https://doi.org/10.21163/GT_2022.172.03

Itsarawisut, J., Thammasaeng, P., Laosuwan, T. (2022). Relationship between the Rainfall from TRMM Satellites and Rainfall from Ground Rainfall Stations. International Journal on Technical and Physical Problems of Engineering. 14(2), 248-253.

Jomsrekrayom, N., Meena, P., & Laosuwan, T. (2021). Spatiotemporal Analysis of Vegetation Drought Variability in the Middle of the Northeast Region of Thailand using Terra/Modis Satellite Data. Geographia Technica. 16(Special Issue), 70-81.

Kanjanasiranont, N., Butburee, T., & Peerakiatkhajohn, P. (2022). Characteristics of PM10 Levels Monitored in Bangkok and Its Vicinity Areas, Thailand. Atmosphere, 13(2), 239. https://doi.org/10.3390/atmos13020239

Knauss, J. A. (1997). Introduction to Physical Oceanography. 1 st ed. Prentice- Hall, New Jersey.

Laosuwan, T., Uttaruk, Y., Rotjanakusol, T. (2022). Analysis of Content and Distribution of Chlorophyll-a on the Sea Surface through Data from Aqua/MODIS Satellite. Polish Journal of Environmental Studies, 31(5), 4711-4719. https://doi.org/10.15244/pjoes/150731

Laosuwan, T., Uttaruk, Y., Rotjanakusol, T. (2023). Atmospheric Environment Monitoring in Thailand via Satellite Remote Sensing: A Case Study of Carbon Dioxide. Polish Journal of Environmental Studies, 32(4), 3645-3651. https://doi.org/10.15244/pjoes/166170

Laosuwan, T., Uttaruk, Y. (2017). Carbon Sequestration Assessment of the Orchards using Satellite Data. Journal of Ecological Engineering, 18(1), 11-17. https://doi.org/10.12911/22998993/66257

Lins, R., Martinez, J.-M., Motta Marques, D., Cirilo, J., & Fragoso, C. (2017). Assessment of Chlorophyll-a Remote Sensing Algorithms in a Productive Tropical Estuarine-Lagoon System. Remote Sensing, 9(6), 516. https://doi.org/10.3390/rs9060516

Marine Knowledge Hub. (2023). Thai Sea. Available online: https://www.noaa.gov/jetstream/ocean/layers-of-ocean (Accessed on 20 March 2023)

NOAA. (2023). Layers of the Ocean. Available online: https://www.noaa.gov/jetstream/ocean/layers-of-ocean (Accessed on 10 March 2023)

Ounrit, I., Sinnung, S., Meena, P., Laosuwan, T. (2022). Flash Flood Mapping based on Data from Landsat-8 Satellite and Water Indices. International Journal on Technical and Physical Problems of Engineering. 12(1), 1-6.

Phoophiwfa, T., Laosuwan, T., Volodin, A., Papukdee, N., Suraphee, S., & Busababodhin, P. (2023). Adaptive Parameter Estimation of the Generalized Extreme Value Distribution Using Artificial Neural Network Approach. Atmosphere, 14(8), 1197. https://doi.org/10.3390/atmos14081197

Plybour, C., & Laosuwan, T. (2023a). Estimation of Chlorophyll-a Contents on the Sea Surface by Remote Sensing Technology. ARPN Journal of Engineering and Applied Sciences, 18(8), 900–905.

Plybour, C., & Laosuwan, T. (2023b). The Application of Remote Sensing Technology to Investigation of Areas Burned by Forest Fires. ARPN Journal of Engineering and Applied Sciences, 18(9), 1039–1045.

Plybour, C., & Laosuwan, T. (2023c). Assessment for the Severity of Forest Areas Burnt by Fire in the Phu Kradueng National Park by Retrieving Data from the Landsat 8 OLI satellite. ARPN Journal of Engineering and Applied Sciences, 18(11), 1282–1287.

Robinson, R.A.J, Bird, M.I., Oo, N.W., Hoey, T. B., Aye, M.M., Higgitt, D.L., Lu, X. X., Swe, A., Tun, T. & Win, S.L. (2007). The Irrawaddy River Sediment Flux to the Indian Ocean: The Original Nineteenth-Century Data Revisited. The Journal of Geology, 115, 629-640.

Rotjanakusol, T., & Laosuwan, T. (2018). Inundation area investigation approach using remote sensing technology on 2017 flooding in Sakon Nakhon province Thailand. Studia Universitatis Vasile Goldis Arad, Seria Stiintele Vietii. 28(4), 159-166.

Rotjanakusol, T., & Laosuwan, T. (2019a). Drought Evaluation with NDVI-based Standardized Vegetation Index in Lower Northeastern Region of Thailand. Geographia Technica, 14(1), 118-130. https://doi.org/10.21163/GT_2019. 141.09

Rotjanakusol, T., & Laosuwan, T. (2019b). An Investigation of Drought Around Chi Watershed during Ten-year Period using Terra/MODIS Data. Geographia Technica, 14(2), 74-83. https://doi.org/10.21163/GT_2019.142.07

Rotjanakusol, T., Laosuwan, T. (2020). Model of Relationships between Land Surface Temperature and Urban Built-Up Areas in Mueang Buriram District, Thailand. Polish Journal of Environmental Studies, 29(5), 3783-3790. https://doi.org/10.15244/pjoes/116384

Silveira Kupssinskü, L., Thomassim Guimarães, T., Menezes de Souza, E., C. Zanotta, D., Roberto Veronez, M., Gonzaga, L., & Mauad, F. F. (2020). A Method for Chlorophyll-a and Suspended Solids Prediction through Remote Sensing and Machine Learning. Sensors, 20(7), 2125.

Tan, C.K., Ishizaka, J., Matsumura, S., Yusoff, F.M. & Mohamed, M.I.H. (2006). Seasonal variability of SeaWiFS chlorophyll a in the Malacca Straits in relation to Asian monsoon. Continental Shelf Research, 26, 168-178.

Turton, A. E., Augustin, N. H., & Mitchard, E. T. A. (2022). Improving Estimates and Change Detection of Forest Above-Ground Biomass Using Statistical Methods. Remote Sensing, 14(19), 4911. https://doi.org/10.3390/rs14194911

Uttaruk, Y., Laosuwan, T. (2019). Drought Analysis Using Satellite-Based Data and Spectral Index in Upper Northeastern Thailand. Polish Journal of Environmental Studies, 28(6), 4447-4454. https://doi.org/10.15244/pjoes/94998

Uttaruk, Y., Rotjanakusol, T., Laosuwan, T. (2022). Burned Area Evaluation Method for Wildfires in Wildlife Sanctuaries Based on Data from Sentinel-2 Satellite. Polish Journal of Environmental Studies, 31(6), 5875-5885. https://doi.org/10.15244/pjoes/152835

Wang, D., Tang, B.-H., Fu, Z., Huang, L., Li, M., Chen, G., & Pan, X. (2022). Estimation of Chlorophyll-A Concentration with Remotely Sensed Data for the Nine Plateau Lakes in Yunnan Province. Remote Sensing, 14(19), 4950. https://doi.org/10.3390/rs14194950

Zhao, J., Chen, N., Zhu, T., Zhao, X., Yuan, M., Wang, Z., Wang, G., Li, Z., & Du, H. (2023). Simultaneous Quantification and Visualization of Photosynthetic Pigments in Lycopersicon esculentum Mill. under Different Levels of Nitrogen Application with Visible-Near Infrared Hyperspectral Imaging Technology. Plants, 12(16), 2956. https://doi.org/10.3390/plants12162956

IMPACT OF COVID-19 CONFINEMENT ON NO2 EMISSIONS IN MEXICO: TEMPORAL ANALYSIS AND OUTLOOK FOR AIR QUALITY

Baltazar SÁNCHEZ-DÍAZ[1] ⓘ

ABSTRACT

The decreases and increases in nitrogen dioxide (NO2) concentrations in Mexico during the periods are mainly due to changes in human activities and not only due to factors such as traffic and weather conditions. The confinement imposed by the pandemic has produced positive effects, such as the reduction of polluting emissions, including nitrogen dioxide (NO2). The pandemic offered a glimpse into how human activities impact air quality. To investigate the changes in the spatial concentration of NO2 in Mexico during the COVID-19 confinement and the subsequent period, comparing the months of April 2019 and 2020, as well as April 2023. The Sentinel-5P TROPOMI sensor was used to obtain images of NO2. They were processed with SNAP software for Geometric Re-projections and ArcGIS 10.2 for change detection. During the confinement in Mexico in April 2020, NO2 concentrations decreased by 21.45% compared to April 2019. However, in April 2023, concentrations increased by 14.48% compared to 2020. The findings support that the Confinement measures temporarily reduced NO2 levels in Mexico. Similar patterns were observed globally. However, once normal activities resumed, NO2 emissions increased. Lockdown restrictions produced a temporary decrease in NO2 pollution in Mexico, but when the measures were lifted, emissions increased again. More rigorous policies are needed to maintain air quality. Continuous use of Sentinel-5P can help monitor and control air pollution in the country. In addition, the implementation of sustainable practices is suggested to reduce polluting emissions and promote a more resilient and sustainable society.

Key-words: *Air pollution, Nitrogen dioxide (NO2), COVID-19 pandemic, Sentinel-5P TROPOMI, Climate change*

1. INTRODUCTION

In a future marked by a constantly changing climate, it is expected that natural communities will undergo modifications and many species will become extinct. Ecosystems, which are home to many species globally, have proven to be vulnerable due to factors such as population growth, habitat loss and fragmentation, and climate change, which has caused significant alterations in the state of the planet in recent last 50 years. Additionally, natural hazards, such as wildfires and wind-blown trees during severe storms, also pose a significant risk. All these events, exacerbated by climate change, threaten the integrity of ecosystems, as climate change is expected to increase surface temperatures and alter precipitation patterns (Navas, 2024; Muluneh, 2021).

The loss of biodiversity and the degradation of ecosystem health are closely related to anthropogenic activities that promote the emergence of zoonotic diseases. As wild species move closer to human populations, the risk of outbreaks and transmission of zoonotic diseases increases. Reducing emissions of air pollutants could slow climate change and, in turn, reduce the impact of diseases that can affect human health, as observed during the COVID-19 pandemic (Debone et al., 2020; Lawler et al., 2021).

---

[1] *Tecnologico Nacional de Mexico, 86650 Comalcalco, Tabasco, México,*
  baltazar.sanchez@comalcalco.tecnm.mx

The confinements implemented due to the COVID-19 pandemic have shown a notable decrease in atmospheric pollutants. This phenomenon is attributed to the reduction of anthropogenic activities, such as the decrease in transportation, the reduction of industrial activities and the stoppage of construction, which are the main sources of air pollution. Air quality in many urban areas saw considerable improvement during the lockdown period. Likewise, it has been observed that the transmission and mortality rate of COVID-19 decreased in correlation with the reduction in pollution levels in many cities. In addition, research has shown that the decrease in air pollution because of confinement measures has contributed to reducing mortality associated with respiratory diseases (Priya et al., 2023; Saha et al., 2022; Kovacs and Haidu, 2021).

Nitrogen dioxide (NO_2) is an indicator of air quality due to its association with combustion emissions and is classified as one of the six common air pollutants by the World Health Organization (WHO). It is recognized as highly harmful to human health, and can cause respiratory diseases, asthma, cellular inflammation, cardiovascular disorders, high blood pressure and lung cancer. Furthermore, the presence of NO_2 leads to the formation of nitric acid (HNO_3) and acid rain, which is harmful to the environment (Oo et al., 2021; Represa et al., 2021).

The Sentinel-5P TROPOMI sensor has great potential for the estimation of atmospheric pollutants, particularly NO_2 concentrations on a broad scale. Several studies have used Sentinel 5P data to investigate the relationship between air pollutants and confinement measures due to COVID-19 (Represa et al., 2021; Debone et al., 2020; Bassani et al., 2021; Kumar et al., 2020; Siddiqui et al., 2022; Naeger and Murphy, 2020; Dutta et al., 2021, Sunarta and Saifulloh, 2022). NASA and ESA have been using this data to track and report the concentration of NO_2 in the atmosphere for air quality monitoring purposes. Recent research based on satellite observations has revealed a marked decrease in NO_2 concentrations during the global lockdown period (Shami et al., 2022; Oo et al., 2021; Cárcel-Carrasco et al., 2021; Liu et al., 2021; Priya et al., 2023; Ialongo et al., 2023).

The objective of this study was to investigate the changes in the spatial concentration of NO_2 in Mexico during the COVID-19 confinement, comparing the months of April 2019 and 2020, as well as the post-COVID-19 period in 2023.

2. STUDY AREA

Mexico, a country located in North America, known for its geographical, cultural, and social diversity. With a considerable land area, Mexico is home to a wide range of ecosystems ranging from arid deserts to lush tropical jungles, as well as mountains, plains, and coasts in both the Pacific Ocean and the Gulf of Mexico and the Caribbean Sea.

3. DATA AND METHODS

In Mexico, the confinement due to COVID-19 began on March 16, 2020, and ended on June 1, 2020 (Abarca et al., 2020; Valdez-Santiago et al., 2021). Since June, with the reopening of additional sectors such as mining, construction, automotive and aerospace, it is very likely that economic production has begun to recover (Esquivel, 2020). Therefore, Sentinel-5 Precursor images were used to investigate the changes in the spatial concentration of NO_2 in Mexico during the COVID-19 confinement, comparing the months of April 2019 and 2020, as well as the post-COVID-19 period in 2023.

3.1. Obtaining satellite images

Sentinel-5P TROPOMI is a broom imaging spectrometer that covers wavelength bands between ultraviolet and shortwave infrared. It was launched in October 2017 as part of the Sentinel-5 Precursor satellite mission, carried out by the European Union (EU) and the European Space Agency (ESA). This instrument provides NO_2 measurements with a spatial resolution of 5.5 km $\times$ 3.5 km. The width of the scanning swath covers approximately 2600 km in the direction of the satellite track, allowing daily global coverage (Liu et al., 2021). Three satellite images were used to observe NO_2 changes during and post-pandemic (**Table 1**).

Satellite images used.

No.	Satelite	Sensor	Acquisition date	Source
1	Sentinel-5P	TROPOMI	17-04-2019	https://browser.dataspace.copernicus.eu/
2	Sentinel-5P	TROPOMI	30-04-2020	https://browser.dataspace.copernicus.eu/
3	Sentinel-5P	TROPOMI	17-04-2023	https://browser.dataspace.copernicus.eu/

3.2. Software used for data processing

The SNAP software (European Space Agency) was used to make the geometric reprojections of the images, and for the detection of changes, the ArcGIS 10.2 software (ESRI, RedLands, USA) was used to detect changes in the NO2 level between three different intervals.

4. RESULTS

The NO2 concentrations were carried out for Mexico on April 17, 2019, where a minimum concentration of 36.56 ppm and a maximum of 283.02 ppm are observed (**Fig. 1**; **Table 2**).
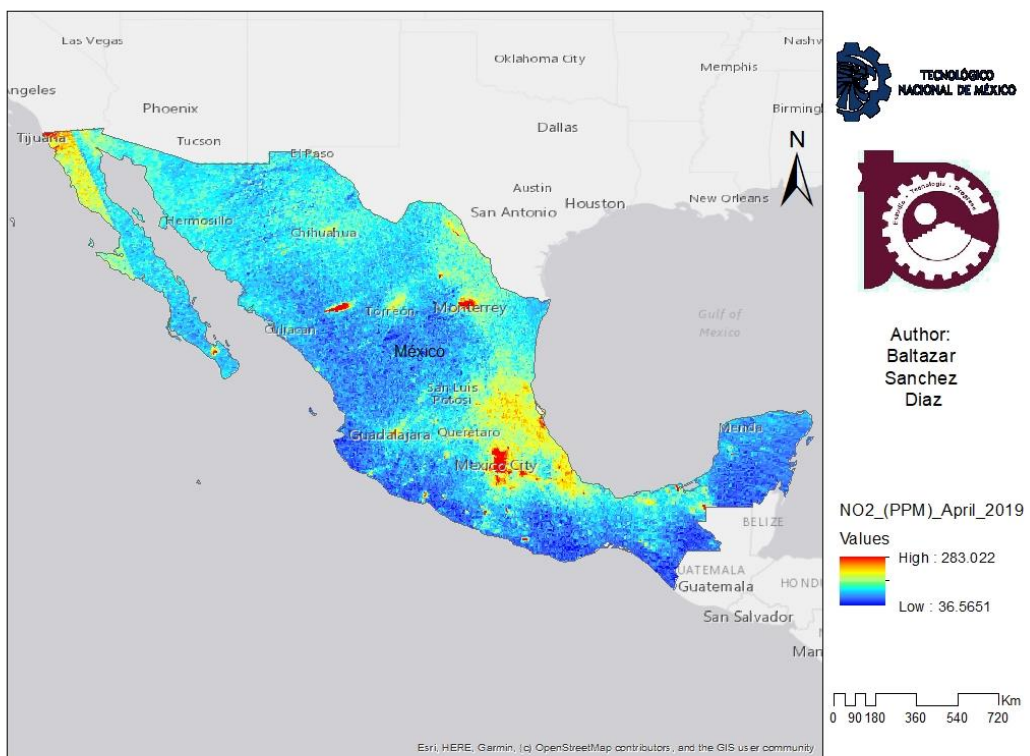
Fig. 1. Map of NO2 concentrations for Mexico in April 2019.

The NO2 concentrations were carried out for Mexico on April 30, 2020, where a minimum concentration of 23.87 ppm and a maximum of 222.32 ppm are observed (**Fig. 2**; **Table 3**).

Table 2.
Statistical data of NO2 concentrations in April 2019.

MIN:	36.565093994140625
MAX:	283.0219421386719
RANGE:	246.45684814453125
SUM:	5283191.383289337
MEAN:	66.98097498972231
STD_DEV:	10.810573086224124
SUM_OF_SQUARES:	9218002.184448304
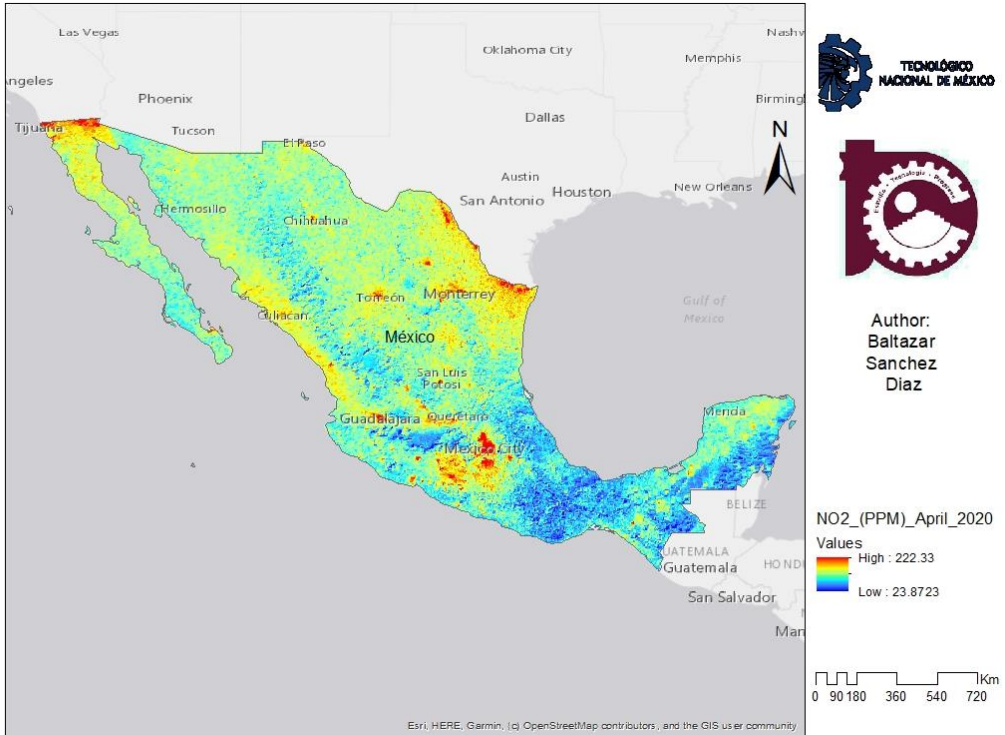
Fig. 2. Map of NO2 concentrations for Mexico in April 2020.

Table 3.
Statistical data of NO2 concentrations in April 2020.

MIN:	23.872339248657227
MAX:	222.3298797607422
RANGE:	198.45754051208496
SUM:	4548913.749929428
MEAN:	60.8249261225805
STD_DEV:	8.659350292238257
SUM_OF_SQUARES:	5607779.410914999

The NO2 concentrations were carried out for Mexico on April 17, 2023, where a minimum concentration of 19.72 ppm and a maximum of 259.95 ppm are observed (**Fig. 3**; **Table 4**).
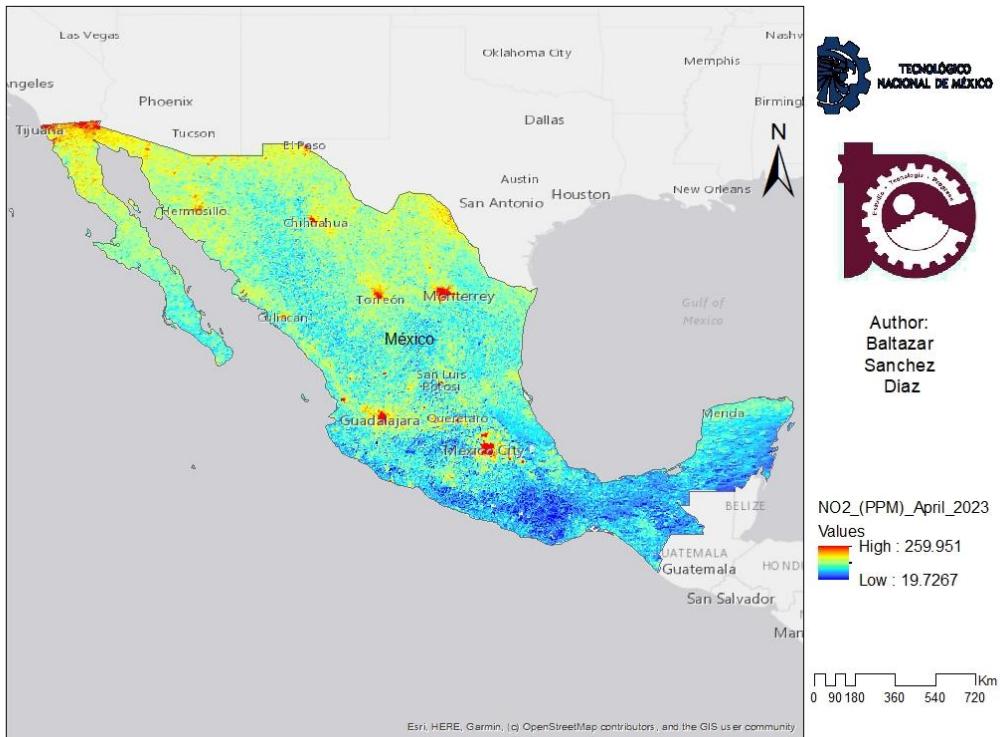
Fig. 3. Map of NO2 concentrations for Mexico in April 2023.

Table 4.
Statistical data of NO2 concentrations in April 2023.

MIN:	19.726686477661133
MAX:	259.950927734375
RANGE:	240.22424125671387
SUM: 4854318.655977249	
MEAN:	60.084150113591065

5. DISCUSSION

In Mexico, from April 2019 to April 2020, NO2 emissions decreased by 21.45%, although from April 2020 to April 2023 emissions increased by 14.48%, which our findings support that these measures temporarily reduced NO2 levels. Once all sectors resume normally, the amount of NO2 emissions appears to be picking up.

Similar behaviors were observed worldwide, the decreases during confinement were:

➢ 39.1 % for Buenos Aires in Argentina (Represa et al., 2021)

➢ 58 % for Sao Paulo in Brasil (Debone et al., 2020)

➢ 30% approximately in European countries such as Italy (Bassani et al., 2021), France (Kumar et al., 2020) and Spain (Cárcel-Carrasco et al., 2021)

➢ Decreases < -50% were mainly recorded in the greater Paris metropolitan area, in Alsace, and other locations of France (Kovacs, 2022)

➢ 30% in populated cities in China (Liu et al., 2021)

➢ 42% in India (Liu et al., 2021) but in cities like Delhi by 52.68% (Siddiqui et al., 2022)

➢ 34.9% on average in in western regions of the United States such as California, 31% in Los Angeles (Naeger and Murphy, 2020) and in southwestern United States (Dutta et al., 2021)

➢ the average NO_2 concentrations in Tabriz, Isfahan, and Mashhad in 2020 decreased by 19%, 13% and 17%, respectively, compared to those in 2019 (Shami et al., 2022)

➢ 9.5% throughout Thailand after the curfew was imposed, while in the Bangkok metropolitan area it decreased by 20.1% (Oo et al., 2021)

➢ in the capital of Ukraine, the monthly average of the tropospheric NO_2 column in April 2022 was almost 60% lower than in 2019 and 2021, and about 40% lower than in 2020 (Ialongo et al., 2023).

6. CONCLUSIONS

The confinement period represented a unique opportunity to examine the environmental environment and analyze the impacts derived from the reduction of various sources of emissions, as well as to evaluate the implementation of more rigorous air quality regulations and regulatory policies. This process demands global collaboration to develop more demanding regulatory standards and climate policies to achieve substantial improvements in air quality.

When the government relaxed confinement measures and the population resumed their daily activities, an increase in NO_2 concentration was observed, exceeding the levels recorded during the strict confinement period. In general, it has been found that the restrictions imposed during 2020 resulted in a decrease in NO_2 pollution. However, continuous data collection represents a considerable challenge for developing countries like Mexico, as it involves high costs and significant efforts. The Sentinel-5P mission provides a variety of continuous data that may be useful for monitoring air quality and pollution in Mexico. In the future, the use of Sentinel-5P and remote sensing analysis could be effectively deployed to monitor and control air pollution in the country.

Permanent or partial adoption of distance work and education, boosting e-commerce and promoting practices that increase energy efficiency and foster a low-carbon economy, along with investments in cleaner transportation alternatives, are suggestions to implement sustainable practices that reduce polluting emissions in urban areas. These measures can facilitate the transition towards urban resilience and sustainability.

The pandemic provided a valuable opportunity to discuss the effects of human activities on air quality and its impact on public health, highlighting the need for a socioeconomic transformation that promotes environmentally friendly transportation policies and a low-carbon economy. This would contribute to the construction of a sustainable and resilient society.

REFERENCES

Abarca, M. T., Hernández, A. M. A., & Barriguete, P. J. D. D. (2020). Estado emocional durante el aislamiento por COVID-19. *Milenaria, Ciencia y arte*, (16), 5-8. https://doi.org/10.35830/mcya.vi16.119

Bassani, C., Vichi, F., Esposito, G., Montagnoli, M., Giusto, M., & Ianniello, A. (2021). Nitrogen dioxide reductions from satellite and surface observations during COVID-19 mitigation in Rome (Italy). *Environmental Science and Pollution Research*, 28, 22981-23004. https://doi.org/10.1007/s11356-020-12141-9

Cárcel-Carrasco, J., Pascual-Guillamón, M., & Langa-Sanchis, J. (2021). Analysis of the effect of COVID-19 on air pollution: perspective of the Spanish case. *Environmental Science and Pollution Research*, 28(27), 36880-36893. https://doi.org/10.1007/s11356-021-13301-1

Dutta, V., Kumar, S., & Dubey, D. (2021). Recent advances in satellite mapping of global air quality: evidences during COVID-19 pandemic. *Environmental Sustainability*, 4(3), 469-487. https://doi.org/10.1007/s42398-021-00166-w

Debone, D., Da Costa, M. V., & Miraglia, S. G. (2020). 90 days of COVID-19 social distancing and its impacts on air quality and health in Sao Paulo, Brazil. *Sustainability*, 12(18), 7440. https://doi.org/10.3390/su12187440

Esquivel, G. (2020). Los impactos económicos de la pandemia en México. *Economía UNAM*, 17(51), 28-44. https://doi.org/10.22201/fe.24488143e.2020.51.543

Ialongo, I., Bun, R., Hakkarainen, J., Virta, H., & Oda, T. (2023). Satellites capture socioeconomic disruptions during the 2022 full-scale war in Ukraine. *Scientific Reports*, 13(1), 14954. https://doi.org/10.1038/s41598-023-42118-w

Kovacs, K. D. & Haidu, I. (2021). Effect of anti-COVID-19 measures on atmospheric pollutants correlated with the economies of medium-sized cities in 10 urban areas of Grand Est region, France. *Sustainable Cities and Society*, 74, 103173. https://doi.org/10.1016/j.scs.2021.103173

Kovacs, K. D. (2022). Nighttime light emissions explain the decline in NO₂ during a COVID-19 induced total lockdown in France. *Geographia Technica,* 17(1), 104-115. DOI: 10.21163/GT_2022.171.08

Kumar, A., Malla, M. A., & Dubey, A. (2020). With corona outbreak: Nature started hitting the reset button globally. Frontiers in public health, 8, 569353. https://doi.org/10.3389/fpubh.2020.569353

Lawler, O. K., Allan, H. L., Baxter, P. W., Castagnino, R., Tor, M. C., Dann, L. E., & Kark, S. (2021). The COVID-19 pandemic is intricately linked to biodiversity loss and ecosystem health. *The Lancet Planetary Health*, 5(11), e840-e850. https://doi.org/10.1016/S2542-5196(21)00258-8

Liu, S., Valks, P., Beirle, S., & Loyola, D. G. (2021). Nitrogen dioxide decline and rebound observed by GOME-2 and TROPOMI during COVID-19 pandemic. *Air Quality, Atmosphere & Health*, 14(11), 1737-1755. https://doi.org/10.1007/s11869-021-01046-2

Navas, A. G. (2024). Assessing Threats and Protections for the Elusive Marbled Murrelet on Land and Sea. https://repository.usfca.edu/capstone/1704/

Naeger, A. R., & Murphy, K. (2020). Impact of COVID-19 containment measures on air pollution in California. *Aerosol and Air Quality Research*, 20(10), 2025-2034. https://doi.org/10.4209/aaqr.2020.05.0227

Muluneh, M. G. (2021). Impact of climate change on biodiversity and food security: a global perspective—a review article. *Agriculture & Food Security*, 10(1), 1-25. https://doi.org/10.1186/s40066-021-00318-5

Oo, T. K., Arunrat, N., Kongsurakan, P., Sereenonchai, S., & Wang, C. (2021). Nitrogen dioxide (NO2) level changes during the control of COVID-19 pandemic in Thailand. *Aerosol and Air Quality Research*, 21(6), 200440. https://doi.org/10.4209/aaqr.200440

Priya, S., & Iqbal, J. (2023). Assessment of NO2 concentrations over industrial state Jharkhand, at the time frame of pre, concurrent, and post-COVID-19 lockdown along with the meteorological behaviour: an overview from satellite and ground approaches. *Environmental Science and Pollution Research*, 30(26), 68591-68608. https://doi.org/10.1007/s11356-023-27236-2

Represa, N. S., Della Ceca, L. S., Abril, G., Ferreyra, M. F. G., & Scavuzzo, C. M. (2021). Atmospheric pollutants assessment during the COVID-19 lockdown using remote sensing and ground-based measurements in Buenos Aires, Argentina. *Aerosol and Air Quality Research*, 21(3), 200486. https://doi.org/10.4209/aaqr.2020.07.0486

Siddiqui, A., Chauhan, P., Halder, S., Devadas, V., & Kumar, P. (2022). Effect of COVID-19-induced lockdown on NO2 pollution using TROPOMI and ground-based CPCB observations in Delhi NCR, India. *Environmental Monitoring and Assessment*, 194(10), 714. https://doi.org/10.1007/s10661-022-10362-8

Saha, L., Kumar, A., Kumar, S., Korstad, J., Srivastava, S., & Bauddh, K. (2022). The impact of the COVID-19 lockdown on global air quality: A review. *Environmental Sustainability*, 5(1), 5-23. https://doi.org/10.1007/s42398-021-00213-6

Shami, S., Ranjgar, B., Bian, J., Khoshlahjeh Azar, M., Moghimi, A., Amani, M., & Naboureh, A. (2022). Trends of CO and NO2 Pollutants in Iran during COVID-19 pandemic using Timeseries Sentinel-5 images in Google Earth Engine. *Pollutants*, 2(2), 156-171. https://doi.org/10.3390/pollutants2020012

Sunarta, I.N. and Saifulloh, M. (2022). Spatial variation of NO2 levels during the COVID -19 pandemic in the Bali tourism area. Geographia Technica, 17(1), 144-149. DOI: 10.21163/GT_2022.171.11

Valdez-Santiago, R., Villalobos-Hernández, A., Arenas-Monreal, L., Flores, K., & Ramos-Lira, L. (2021). Violencia en el hogar contra mujeres adultas durante el confinamiento por la pandemia de Covid-19 en México. salud pública de méxico, 63(6), 782-788. https://doi.org/10.21149/13244

UAV PHOTOGRAMMETRY AS A MULTIDISCIPLINARY APPROACH IN ENGINEERING DESIGN AND SUSTAINABLE LAND MANAGEMENT

Vincenzo Saverio ALFIO [1]

ABSTRACT:
The aim of the paper is to describe an integrated methodological approach of photogrammetric survey from UAVs (Unmanned Aerial Vehicles) that can be used in the field of engineering planning and design. In particular, a process is described in which the outputs from photogrammetric processing are implemented in different analysis or 3D modelling platforms to support all design activities in the field of engineering and in particular in the field of civil and environmental design. This approach was applied to an area of considerable landscape-environmental interest characterised by the presence of an estuary and a masonry bridge. The outputs of the photogrammetric processing have therefore constituted a valid support at cartographic level and for the production of two-dimensional CAD (Computer-Aided Design) drawings, as well as in the design of a cycle path, in the assessment of hydraulic risk or in the BIM (Building Information Modeling) design of the road infrastructure. The adopted methodology made it possible to obtain a high-performance and geometrically accurate dataset, characterised by high resolution, quickly and with low investment costs. In addition, by using UAV platforms, it was possible to reach inaccessible areas, limiting the risk of the operators specialised in surveying and optimising the time of operations, while still guaranteeing a complete product without loss of information necessary for BIM, GIS (Geographical Information System) and CAD procedures.

Key-words: *UAV, Dense Cloud, Photogrammetry, Engineering, 3D Model, DTM, BIM.*

1. INTRODUCTION

In recent years, aerophotogrammetric surveying using UAV has assumed a fundamental role in the planning, design and management of the territory and the structural and infrastructural works that insist on it. (Remondino et al., 2011). The result of this surveying activity generally consists of maps, 2D and 3D models of objects, as well as a series of outputs such as digital terrain or surface models, orthophotos, contour and other three-dimensional geodata; these outputs facilitate the design process in the field of engineering and architecture by reducing the workload of specialists in the field (Goncalves & Henriques, 2015). Another advantage of using UAVs is that it is possible to carry out good quality topographical surveys, taking less time to do the work than traditional measurement methods. The ability to acquire the dataset at lower altitudes than manned aircraft or satellite systems allows for high-performance and high-resolution datasets (Agueera-Vega et al., 2018; Mancini et al., 2013).

Furthermore, in classic topographic surveys, it is not possible to reach dangerous or unsafe areas or terrain unsuitable for traditional instrumentation, and in some cases, it is necessary to temporarily interrupt activities or roads, connection networks, etc.; with UAV topographic surveying, these difficulties are overcome as it is possible to carry out acquisitions in any area and at any time, without having to interrupt the operation of infrastructures and services. UAV photogrammetry, therefore, is now widely used in almost all areas of civil, environmental, and industrial engineering, and returns work that is much better than the results belonging to traditional surveys. (Jeelani & Gheisari, 2021).

Surveying from UAVs has in recent years assumed an increasingly fundamental role in the collection, interpretation and harmonisation of data (Tmušić et al., 2020). In fact, this surveying technique is applicable in different environmental contexts, such as in multi-platform and multi-scale environmental monitoring of a lake for the creation of Digital Surface Models (DSM) and orthophotos (Medvedev et al., 2020) or, in the identification of a suitable methodology for calculating the optimal

[1]*Polytechnic University of Bari - Department of Civil, Environmental, Land, Building Engineering and Chemistry (DICATECh), 70125, Bari, Italy, vincenzosaverio.alfio@poliba.it*

volume of waste by integrating Terrestrial Laser Scanning (TLS) and Unmanned Aerial Vehicle (UAV) technologies (Son et al., 2020). In the field of vulnerability assessment of coastal areas, this surveying technique has also assumed a key role in climate change assessment (Adade et al., 2021) thanks also to the equipping of drones with the latest sensor technologies that guarantee high spatial and temporal resolution. Furthermore, in the field of environmental monitoring, the support of UAVs is of considerable importance, for example in the field of forestry (Sferlazza et al., 2022), in photogrammetric techniques for the processing of very high resolution orthophotos and coastline extrapolation (Costantino et al, 2020), in the multi-temporal survey for assessing morphological changes due to different (natural and anthropogenic) factors in coastal areas (Zanutta et al., 2020), and also for bathymetric monitoring of shallow water bodies (Lewicka et al., 2022). The possibility of generating highly accurate Digital Elevation Models (DEM) as an alternative to satellite data also makes this survey technique interesting in the field of hydraulic modelling (Mazzoleni et al., 2020) or for the validation of two-dimensional hydraulic model simulations (Masafu et al., 2022).

In the field of civil engineering and infrastructure (Greenwood et al., 2019) and particularly in the field of inspection and monitoring, UAVs can represent a non-invasive approach in rapid mapping applications (Gaspari et al., 2022) flexible and low-cost (Lattanzi & Miller, 2017) through the use of optical and LiDAR sensors, for disaster assessment after calamitous events or for transport infrastructure damage reduction strategies (Mandirola et al., 2022). The possibility of creating 3D models from UAV surveys (Pepe et al., 2022) through the algorithms of Structure from Motion (SfM) and Multi View Stereo (MVS), has also become commonplace in the monitoring of construction progress on building sites (Teizer, 2015) with a comprehensive and efficient collection of images and the possibility of generating multi-temporal BIM models (Lin et al., 2015). In fact, from a modelling perspective, the use of UAVs for three-dimensional surveying enables the definition of high-performance 3D models from point cloud datasets (Klapa, 2023) both for the realisation of BIM models of structures and infrastructures of particular geometric complexity (Shults & Annenkov, 2023) as well as in the construction of Heritage BIM models (HBIM) when dealing with cultural heritage structures (Robador González et al., 2023).

Finally, wide use and application of such devices is also to be found in the availability of increasingly efficient navigation systems that integrate inertial systems and the integration of optical or LiDAR sensors for security control operations in certain areas (Baiocchi et al., 2023) and in transport systems, road safety and road infrastructure management with a view to the development of smart cities (Outay et al., 2020).

The aim of this article is to provide a multidisciplinary approach in the field of photogrammetric survey from UAVs and to show how some of the outputs produced can easily represent a useful and indispensable support tool for all levels of design in the field of civil and environmental engineering, from the design of sustainable works to the management of infrastructures in a BIM environment. The aim of this paper is to show the reader some possible uses of a point cloud dataset, obtained by means of a UAV photogrammetric survey, and the relative use of the processing outputs in the various disciplines of civil and environmental engineering.

2. STUDY AREA

The area under study represents an ancient river that flows through the rock and is called "Lama San Giorgio". This area has been identified by the Apulia Region as a protected natural area, due to its naturalistic, landscape, archaeological and cultural interest. In particular, the structure investigated for the application of this methodology, is an arched bridge located on the outskirts of the city of Bari (Italy) and located within the same swamp that slopes down towards the sea (**Fig.1**).

3. MATERIALS AND METHODS

In general, the main phases of a UAV photogrammetric survey can be distinguished into a first step involving the planning of the survey. In this phase, the different parameters such as overlap, sidelap, GSD (Ground Sample Distance), flight altitude, etc. are defined and set according to the area

to be surveyed. Furthermore, of particular importance is the preliminary study of the area to be surveyed in order to determine the presence of any obstacles that may affect the flight mission. The next phase is the survey phase in which all the topographic measurement operations are conducted, and, at the same time, the flight mission is carried out to acquire the photogrammetric dataset. The data acquired are then processed using appropriate photogrammetric processing software in order to produce point clouds, 3D models and a series of outputs that are useful in the spatial planning and design phases. The following pipeline (**Fig. 2**) shows the main stages of the methodological approach described in this manuscript.
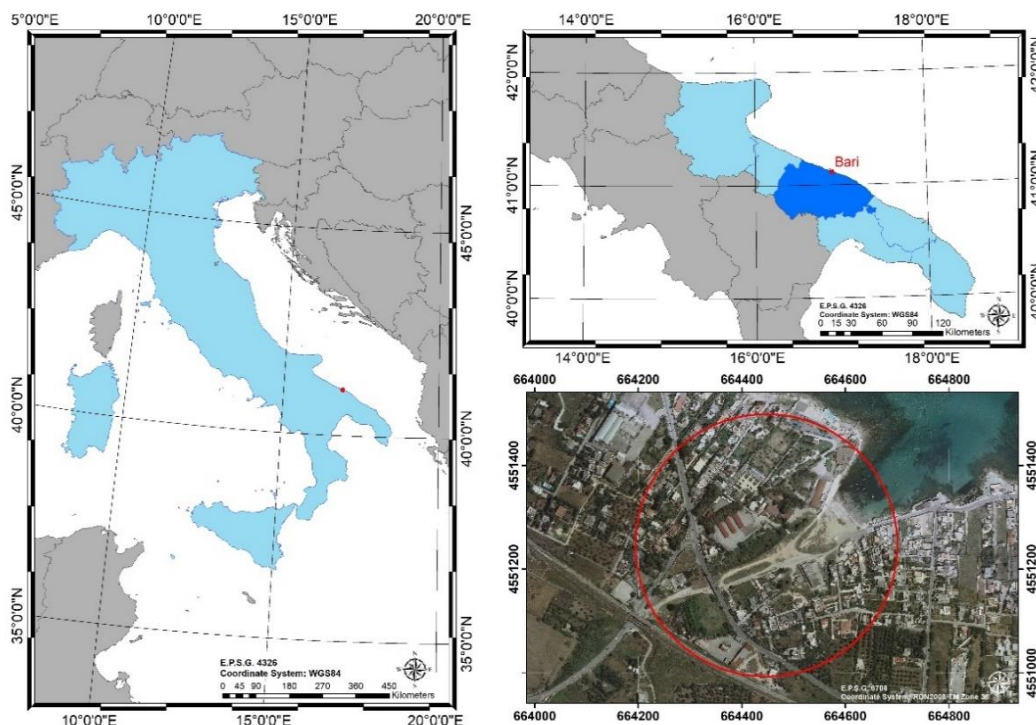
Fig.1. Cartographic overview of the study area.
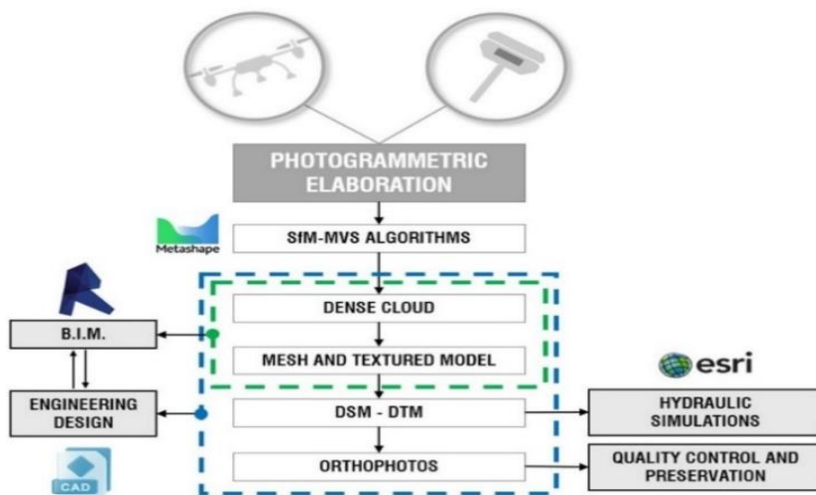
Fig. 2. Schematisation of the main stages of the methodological approach described.

3.1. UAV planning and photogrammetric survey

The methodological approach described in the following manuscript concerns the experience of an aerophotogrammetric survey from a UAV platform, for the realisation of various outputs to support engineering design in various fields of application. The survey was conducted through the use of a quadricopter for the acquisition of the photogrammetric dataset. In order to scale and georeference the final model, a GNSS (Global Navigation Satellite System) survey of GCPs (Ground Control Points) and CPs (Check Points) was also conducted, which were previously materialised homogeneously over the entire area to be surveyed.

GCPs and CPs are reference points, materialised on the area to be surveyed, which must be easily recognisable on the images; they can be natural points of the scene or they can be made on panels of impermeable and high-contrast material (e.g. black and white or yellow and black); their size varies according to the Ground Sample Distance (G.S.D.) value and consequently according to the flight altitude of the UAV(Alfio et al., 2023). In addition, each UAV device may have its own integrated camera so that, depending on the sensor, the GSD value must be established at the survey planning stage, which will then adjust the maximum attainable flight height (Pepe et al., 2018). Considering F_s the scale of the frame and L the width of single image footprint on the ground:

$$\frac{1}{F_s} = \frac{d}{L} \tag{1}$$

the following relationship can be defined:

$$GSD = \frac{Z}{c} \cdot d \tag{2}$$

where:
Z represents the flight altitude above the ground;
c represents the focal length of the sensor;
d size of the side of a photo sensor pixel.

Furthermore, relating Eq. (1) to Eq. (2) gives:

$$GSD = F_s \cdot d \rightarrow F_s = \frac{GSD}{d} \tag{3}$$

with which it is possible to relate the frame scale to the characteristics of the sensor used, the distance and the photographic lens.

3.2. SfM and MVS algorithms for point cloud generation

After the frame acquisition phase, through the SfM and MVS algorithms, it is possible to conduct the photogrammetric processing of the acquired dataset and obtain the dense cloud. In the first phase, after a calibration of the photographic sensor to establish the internal orientation parameters, the external orientation parameters defining the position and orientation of the camera during the shooting phase are also calculated; they consist of 3 translation components and 3 rotation angles. The next stage of dense cloud generation is based on depth maps calculated with dense stereo matching. The depth maps are calculated for the overlapping image pairs, considering the relative external and internal orientation parameters estimated with the Bundle Adjustment (BA).

In general, although BA is not strictly part of the SfM approach, it is a very common step used to refine and refine the initial SfM model. Given a set of camera parameters and a set of traces, BA minimises the following non-linear least-squares error (Furukawa & Hernández, 2015):

$$E(P, M) = \sum_{j} \sum_{i \in V(J)} \left| P_i(M^j) - m_i^j \right|^2 \tag{4}$$

where:

P_i camera parameters

M^j 3D co-ordinates of a track

m_i^j 2D co-ordinates of the projection of its image

$V_{(J)}$ list of camera indices where the point is visible M^j

$P_i(M^j)$ co-ordinate of the projected 2D image of the 3D point M^j in the camera i using the camera parameters P_i.

After the generation of the dense cloud, it is possible to assess the metric quality of the generated 3D model by taking GCPs and CPs into account and calculating the relative Root Mean Square Error (RMSE) using the formula:

$$RMSE = \sqrt{\sum_{i=1}^{n} \frac{(x_{i,est} - x_i)^2 + (y_{i,est} - y_i)^2 + (z_{i,est} - z_i)^2}{n}} \tag{5}$$

where:

x_i, y_i, z_i are the input values of the coordinates respectively x, y, z.

$x_{i,est}, y_{i,est}, z_{i,est}$ correspond to their estimated positions.

After processing the dense cloud, a triangular surface mesh can be generated; this surface can be textured to obtain a photorealistic digital representation of the object/scene. The irregular mesh, or Triangulated Irregular Network (TIN), is a surface in which the known points in the three coordinates, however they are distributed in space, are joined by lines that form flat, adjacent triangles and allow the surface of the object to be represented with continuity, respecting Delaunay's triangulation criterion.

3.3. Digital model and orthophoto processing

Through the photogrammetric processing pipeline, it is possible to generate Digital Surface Models (DSM) and Digital Terrain Models (DTM), in which the elevation information is recorded within a regular grid that can be represented with a numerical matrix. Usually, the grid has a square mesh, more rarely triangular or rectangular, whose lateral dimension provides the cell size (cell size or pixel size), which corresponds, once the projection is fixed, to the spatial resolution of the digital model. The steps involved in constructing and analysing a digital height model lead to a number of errors related to the measurement and/or data processing processes, generating model uncertainties. The quantification of error in such models can be performed by calculating the Root Mean Square Error (RMSE) of the digital model according to the following formula:

$$RMSE = sqrt\left(\frac{\sum(z_{i,est} - z_i)}{n}\right) \tag{6}$$

where:

z_i represents the quote of DEM.

z_j represents the reference measurement.

n the number of samples considered.

Within photogrammetric software, DEMs can be rasterised from a dense point cloud, a sparse cloud, a mesh or generated directly from depth maps. Using point cloud classification algorithms,

such as ATIN - Adaptive Triangulated Irregular Network, PTIN - Progressive Triangulated Irregular Network or MCC - Multi Curvature Classification, it is possible to classify the point cloud (Łącka, 2021) into other semantic classes and process the DTM, which represents the topographical terrain surface, without taking into account anthropic elements (trees, vegetation, etc.), i.e. artificial objects or elements (buildings, cars, etc.).

Starting from the processing of the dataset, it is possible to obtain the orthophoto, i.e. a composition of geometrically corrected photograms by means of an orthorectification process; furthermore, the orthophoto, considering the information obtained from the processing of the GNSS survey data, can be georeferenced so that the scale of representation becomes uniform throughout the territory. To construct this output, it is necessary to use a DEM to define the orthoimage matrix, where each pixel corresponds to an element of the ground plane. In order to improve the final result and eliminate projection differences and preserve the correct positions of objects and terrain features (Lamsters et al., 2020), it is possible to process a "True Digital Orthoimage" using a DSM instead of a DEM and ensuring the geometric accuracy of features and visibility of features (Shoab et al., 2022).

3.4. From photogrammetric processing to sustainable spatial planning

All outputs obtained from photogrammetric processing can be imported into various design and analysis software, (e.g. General Authoring software in the BIM field or parametric modelling, GIS, CAD, etc.) and help to strengthen design activities, guaranteeing high product quality standards and greater accuracy. In fact, for example in the BIM field, photogrammetric techniques provide an accurate basis for modelling objects. Also with a view to environmental design, the acquisition of datasets from UAV platforms for the generation of DEMs and DTMs as well as up-to-date orthophotos with high geometric resolution plays a fundamental role in the field of hydrological/hydraulic modelling, to support the realisation of new interventions and in the performance evaluation of existing ones. In this context, all photogrammetric products, which are fully interoperable with the various software available today, are able to create a valid multi-scale and multi-level support in the knowledge of the territory, representing an important basis for planning, as well as an indispensable metric support for conducting all the necessary design operations.

4. RESULTS

4.1. SfM-MVS approach and output processing

To acquire the photogrammetric dataset of the entire study area, a survey with UAV DJI Mavic 2 PRO developed by DJI Company, Shenzhen, was conducted. This device is a quadricopter equipped with a high-resolution colour camera Hasselblad L1D-20c with a 1" sensor and 20MP resolution. In particular, two different types of mission were carried out with this device: an automatic mission to cover the entire area with nadiral captures (flight planning app and Pix4Dcapture acquisition) and a manual mission (app for real-time image transmission and DJI GO 4 camera settings) for the 3D reconstruction of the masonry bridge; for this last dataset it was necessary to acquire a series of images with a camera tilted at 30° and 45° from different flight altitudes. The entire dataset consists of 175 images and covers an area of approximately 10,000 square metres.

In order to scale and georeference the point cloud, a survey with GNSS receiver Leica Viva GNSS 12 was performed. Nine GCPs were surveyed in kinematic Stop and Go mode. The GNSS survey data were processed using appropriate software and using the nearest HxGN SmartNet permanent station as the Master station. The coordinates of the acquired points were referred to the RDN2008-UTM zone 33N (E.P.S.G. code 6708), i.e. to the national implementation of ETRS89 (European Terrestrial Reference System), which is an ECEF (Earth-Centred, Earth-Fixed) geodetic Cartesian reference system. Using the Agisoft Metashape photogrammetric processing software, it was possible to obtain a dense cloud consisting of more than 20,000,000 points. According to Equation (5), the RMSE value was calculated, which in geometric terms was 0.037 m and in terms of pixel reprojection was 1.086. After the point cloud generation phase, the polygonal mesh model was then processed and textured with a photographic resolution of 6 mm. The DEM and a series of

orthophotos projected onto different reference planes were also processed and generated. In addition, in order to obtain a suitable DTM, an automatic classification of the point cloud was carried out to identify the class "Ground Points"; starting from this classification and through a triangulation process, the digital terrain model was then defined. **Table 1** below summarises the main characteristics of the outputs produced as part of this processing.

<div align="right">

Table 1.

</div>

<div align="center">

Pipeline of the described methodological approach

</div>

Output	Features	Memory
Dense Cloud	Points: 20,511,813 points	275 MB
TIN	Faces: 1,402,948 faces - Vertices: 707,546 vertices	74.81 MB
3D textured model	Resolution: 6 mm/pix	311.26 MB
DEM	Size: 5,954x4,983 pix - Resolution: 2.42 cm/pix	76.10 MB
Orthomosaic	Size: 23,816x19,932 pix - Resolution: 6.04 mm/pix	3.62 GB

4.2. DEM, DTM and orthophotos for the design of a cycle path

After an accurate hydrological-hydraulic analysis of the study area, using the information contained in the DTM, a series of contour lines were generated, and a cycle-pedestrian route was identified with a view to environmental sustainability and functionality. The route was identified by superimposing the information on the road layout on the generated orthophotos and thus identifying a suitable route connecting the provincial road to the cove, passing under the bridge at the second external arch. On the basis of the extracted profiles, in defining the hypothetical route, the topographical course of the terrain was evaluated so that a design profile could be drawn up that was as linear and adherent as possible to the terrain itself. By means of 3D modelling and the processing of orthomosaics on different projection planes, a series of design drawings and 2D graphic tables in a CAD environment were then produced to support the entire design cycle of new interventions and the maintenance of existing ones (**Appendix 1**).

4.3 DTM for hydrological land assessment

In the case study presented, through a photogrammetric approach, the accurate processing of a georeferenced DTM, with a high geometric resolution, allowed the elaboration of a hydrological analysis of the surface on an ArcGIS platform. The processing of the DTM in the GIS environment allowed the extraction of various information to support the estimates regarding the hydrology of the area and the basin considered, such as the perimeter and area of the basin, contour lines, slope map, drainage grids, etc.

In fact, the combined use of these 2.5D models and GIS tools makes it possible to identify sinks, flow directions, delineate watersheds and create flow networks. In particular, the use of an elevation raster or a digital elevation model as input makes it possible to automatically reconstruct a drainage system and quantify the characteristics of the system in order to identify the areas of the basin that are subject to flooding or all the areas that allow water to drain away.

In this context, it is obvious how the precision and accuracy of appropriately processed DTM (obtained from a UAV photogrammetric survey), as well as its spatial resolution offer greater homogeneity and uniformity of the data over larger areas, making the analyses and subsequent determinations of all factors and parameters involved in hydrological-hydraulic modelling more accurate, as well as in the more detailed construction of river profiles (**Appendix 2**).

4.4 BIM modelling of the bridge

A further application use in engineering of the point cloud obtained with the survey is the realisation of a BIM information model. Modelling according to the BIM approach, in fact, makes it possible to create a digital copy of the object to which useful information can be associated for constructing, managing, and monitoring the work during its useful life.

In particular, in the case under study, the dense cloud processed by the photogrammetric software was first filtered and cleaned by means of appropriate tools and algorithms; with this data treatment phase, any edge effects and outliers of the model were also removed. After this treatment phase, the cloud was imported into the Revit software, which allows three-dimensional modelling of objects, using both fundamental operations such as extrusions, unions, revolutions, sweeps, and classic Boolean operations for the manipulation and creation of new objects, as well as creating parameterised families. These operations are applied to 3D objects to obtain new complex shapes from the combination of simpler shapes.
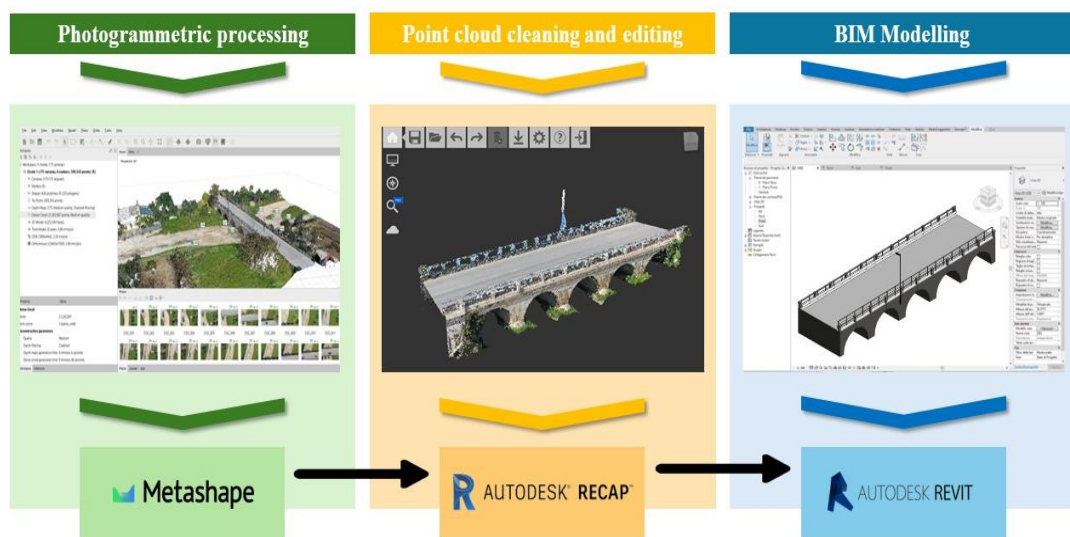
Fig. 3. Bridge BIM modelling in Revit software.

By importing the point cloud, it was possible to model the different components of the bridge and reconstruct the geometries of all the objects of which it is composed. In particular, by associating a series of semantic information for each element, the structure of the piers and arches, the road pavement, the safety barriers and the road lighting elements were modelled (**Fig. 3**). In this way, it is possible to keep track of the operations that have been carried out over time, from the installation of the components to maintenance operations, managing the work and reporting criticalities detected during inspections for the planning of future interventions.

4.5. High-resolution orthophotos for maintenance status assessment

The possibility of photogrammetrically generating an orthophoto with high geometric resolution also makes it possible to verify the state of maintenance, as in the case study, of the road pavement. In this way, it is possible to characterise the condition of wear and tear and optimally plan restoration work. In the case under examination, an orthophoto characterised by a pixel size of less than a centimetre made it possible to identify the most damaged areas in GIS environment; furthermore, the georeferencing of the model in the appropriate reference system makes it possible to identify the areas subject to the phenomenon under investigation, locating them more easily and enabling the priorities and types of intervention to be defined in the maintenance phase (**Appendix 3**).

UAV surveying in this context is most advantageous as it allows the acquisition of very high-resolution digital images even in areas that are difficult to access, possibly characterised by high traffic density, while still guaranteeing the safety of operators and workers.

5. DISCUSSION AND CONCLUSIONS

This manuscript shows an integrated approach to utilising the different outputs of photogrammetric image processing acquired from a UAV platform to support all design activities in the field of civil and environmental engineering. The proposed method shows how, in less time than traditional survey methods, it is possible to obtain a three-dimensional, accurate and geometrically correct dataset useful in all engineering design phases.

With UAV platforms, the possibility of reaching areas that are not easily accessible makes it possible to obtain a complete dataset that serves as a support in the drafting of all the design drawings required by the client (plans, elevations, typological sections, etc.), attributing a high degree of detail and with relatively low time and investment costs. Last but not least, by using a pipeline such as the one shown in this manuscript, it is possible to carry out all the desired measurements directly on the 3D model, completely eliminating the need to interrupt the operation of the infrastructure and design service for the acquisition of new information.

Analysing from a statistical point of view the scientific literature concerning the use of UAVs, it is possible to note that, to date, there are over 70,000 articles.

In particular, by setting up a series of search filters using keywords such as UAV, Unmanned Aeria Vehicle, UAS, etc., the publications in the Scopus database were classified and categorised with respect to a series of fields of application. **Fig. 4** below shows the results of this analysis and the relative percentages with respect to the different fields of application.
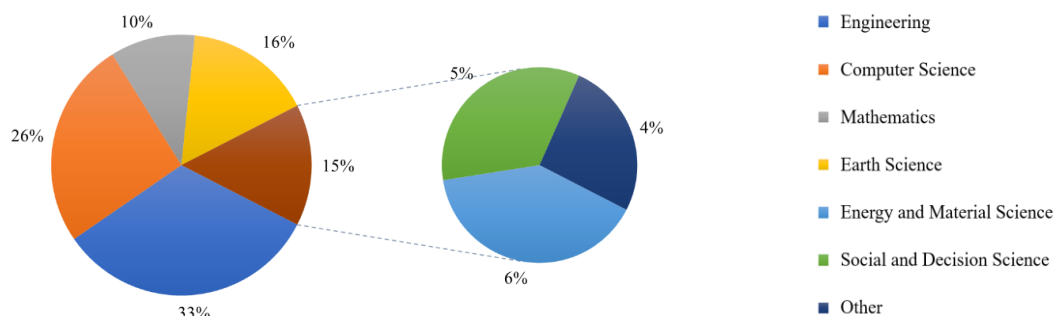
Fig. 4. Analysis of the different fields of application of UAVs.

In addition, the processing of the point cloud and the transition to a 3D model lend themselves well to interoperability, for example in BIM design, where it is possible to model with high accuracy objects characterised by complex geometries, which are difficult to achieve with classic 3D modelling operations. Certainly, greater detail in the three-dimensional representation of the topographical surface and the objects and infrastructures present in the observed scene, improves the quality of analysis and the level of final design.

Finally, thanks to the development of advanced algorithms, tools for the automatic extraction of features, filters for the classification of data and Artificial Intelligence (AI), it will be possible to map and monitor even in real time the phenomenon under investigation and send the relevant information and datasets acquired directly to a cloud system for subsequent processing.

APPENDIX 1
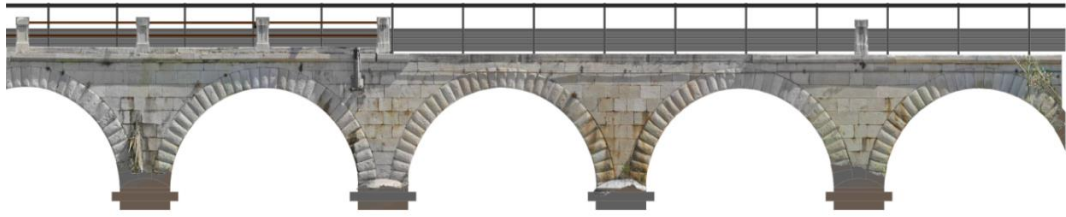
(a)
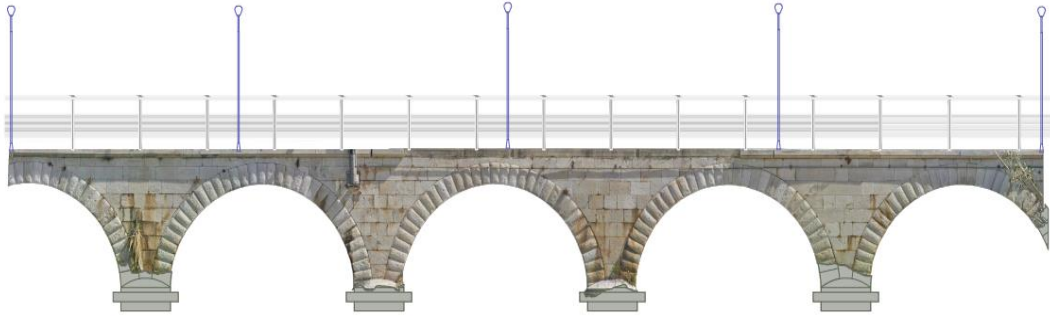
(b)
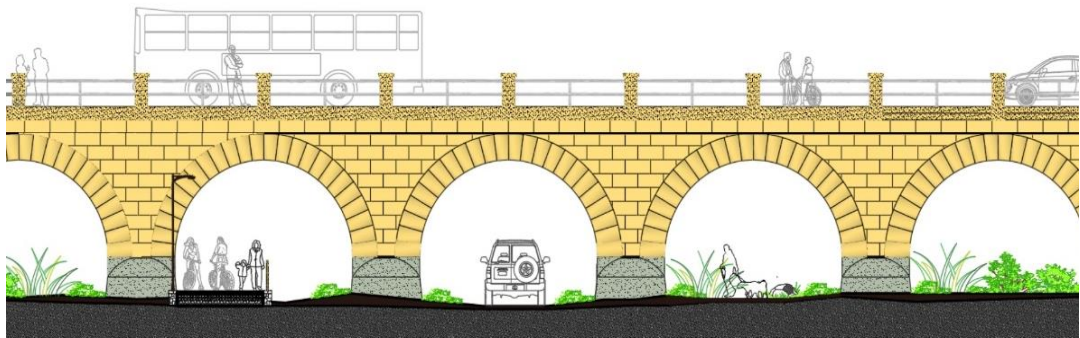
(c)

(d)

(e)

Appendix 1. Design of the cycle path: orthophotos of the bridge elevations (a,b), 2D CAD reconstruction of the bridge façade (c), road axis of the cycle path based on orthophotos (d) and final photo insertion (e).

A P P E N D I X   2
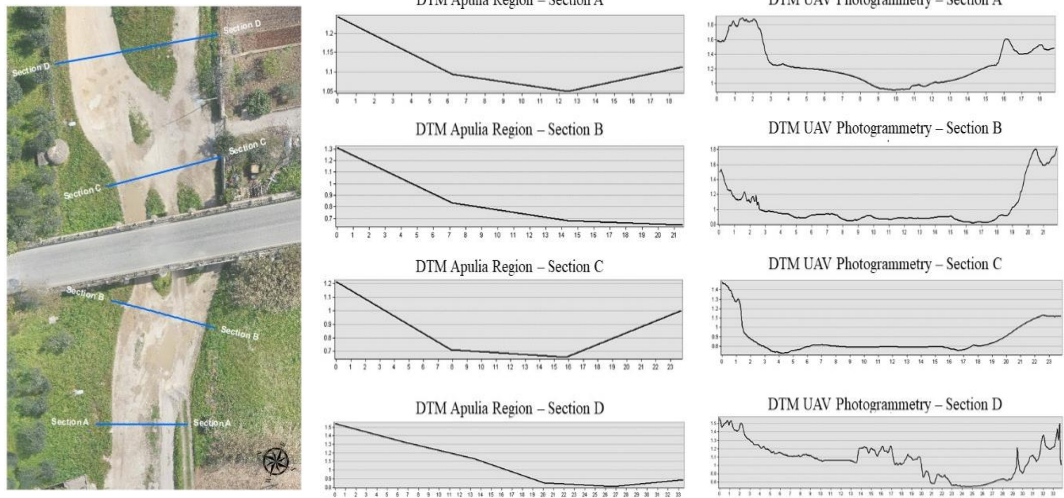
Appendix 2. Difference in the reconstruction of the riverbed profile using a DTM from the Apulia Region and a DTM obtained from a UAV photogrammetric processing. In particular, sections A and B are located upstream of the bridge while sections C and D are located downstream.

A P P E N D I X   3

(a)   (b)

Appendix 3. Identification of the state of cracking of the road pavement: difference between the orthophoto of the Apulia Region (a) and the orthophoto produced by photogrammetric processing (b).

REFERENCES

Adade, R., Aibinu, A. M., Ekumah, B., & Asaana, J. (2021). Unmanned Aerial Vehicle (UAV) applications in coastal zone management—A review. *Environmental Monitoring and Assessment*, *193*(3), 154. https://doi.org/10.1007/s10661-021-08949-8. https://doi.org/10.1007/s10661-021-08949-8.

Agueera-Vega, F., Carvajal-Ramirez, F., Martínez-Carricondo, P., López, J. S.-H., Mesas-Carrascosa, F. J., García-Ferrer, A., & Pérez-Porras, F. J. (2018). Reconstruction of extreme topography from UAV structure from motion photogrammetry. *Measurement*, *121*, 127–138. https://doi.org/10.1016/j.measurement.2018.02.062.

Alfio, V. S., Costantino, D., Pepe, M., Rossi, G., & Leserri, M. (2023). Production of high geometric resolution orthophotos by photogrammetric approach for the Royal Racconigi Castel park documentation. *Geographia Technica*, *18*(2). http://doi.org/10.21163/GT_2023.182.03.

Baiocchi, V., Fortunato, S., Giannone, F., Marzaioli, V., Monti, F., Onori, R., Ruzzi, L., & Vatore, F. (2023). LiDAR RTK Unmanned Aerial Vehicles for security purposes. *Geographia Technica*, 34–42. https://doi.org/10.21163/GT_2024.191.03.

Costantino, D., Pepe, M., Dardanelli, G., & Baiocchi, V. (2020). Using optical Satellite and aerial imagery for automatic coastline mapping. Geographia Technica, 15(2), 171-190. http://dx.doi.org/10.21163/GT_2020.152.17

Furukawa, Y., & Hernández, C. (2015). Multi-view stereo: A tutorial. *Foundations and Trends® in Computer Graphics and Vision*, *9*(1–2), 1–148. http://dx.doi.org/10.1561/0600000052.

Gaspari, F., Ioli, F., Barbieri, F., Belcore, E., & Pinto, L. (2022). Integration of UAV-LiDAR and UAV-photogrammetry for infrastructure monitoring and bridge assessment. *The International Archives of the Photogrammetry, Remote Sensing and Spatial Information Sciences*, *XLIII-B2-2022*, 995–1002. https://doi.org/10.5194/isprs-archives-XLIII-B2-2022-995-2022.

Goncalves, J. A., & Henriques, R. (2015). UAV photogrammetry for topographic monitoring of coastal areas. *ISPRS Journal of Photogrammetry and Remote Sensing*, *104*, 101–111. http://dx.doi.org/10.1016/j.isprsjprs.2015.02.009.

Greenwood, W. W., Lynch, J. P., & Zekkos, D. (2019). Applications of UAVs in Civil Infrastructure. *Journal of Infrastructure Systems*, *25*(2), 04019002. https://doi.org/10.1061/(ASCE)IS.1943-555X.0000464.

Jeelani, I., & Gheisari, M. (2021). Safety challenges of UAV integration in construction: Conceptual analysis and future research roadmap. *Safety Science*, *144*, 105473.

Klapa, P. (2023). Integration of terrestrial laser scanning and UAV-based photogrammetry for heritage Building Information Modeling. *Geomatics, Landmanagement and Landscape*, *no. 1*. https://doi.org/10.15576/GLL/2023.1.23.

Łącka, M. (2021). Analysis of algorithms for automatic classification of photogrammetric point clouds to build a digital terrain model in a shoreline area. *Zeszyty Naukowe Akademii Morskiej w Szczecinie*. https://yadda.icm.edu.pl/baztech/element/bwmeta1.element.baztech-26147478-b6f4-4e47-9686-fc9a357e39fb.

Lewicka, O., Specht, M., Stateczny, A., Specht, C., Dardanelli, G., Brčić, D., Szostak, B., Halicki, A., Stateczny, M., Widźgowski, S. (2022). Integration data model of the bathymetric monitoring system for shallow waterbodies using UAV and USV platforms. *Remote Sensing*, 14(16), 4075. https://doi.org/10.3390/rs14164075

Lamsters, K., Karušs, J., Krievāns, M., & Ješkins, J. (2020). High-resolution orthophoto map and digital surface models of the largest Argentine Islands (the Antarctic) from unmanned aerial vehicle photogrammetry. *Journal of Maps*, *16*(2), 335–347. https://doi.org/10.1080/17445647.2020.1748130.

Lattanzi, D., & Miller, G. (2017). Review of Robotic Infrastructure Inspection Systems. *Journal of Infrastructure Systems*, *23*(3), 04017004. https://doi.org/10.1061/(ASCE)IS.1943-555X.0000353.

Lin, J. J., Han, K. K., & Golparvar-Fard, M. (2015). A Framework for Model-Driven Acquisition and Analytics of Visual Data Using UAVs for Automated Construction Progress Monitoring. *Computing in Civil Engineering 2015*, 156–164. https://doi.org/10.1061/9780784479247.020.

Mancini, F., Dubbini, M., Gattelli, M., Stecchi, F., Fabbri, S., & Gabbianelli, G. (2013). Using unmanned aerial vehicles (UAV) for high-resolution reconstruction of topography: The structure from motion approach on coastal environments. *Remote Sensing*, *5*(12), 6880–6898. https://doi.org/10.3390/rs5126880.

Mandirola, M., Casarotti, C., Peloso, S., Lanese, I., Brunesi, E., & Senaldi, I. (2022). Use of UAS for damage inspection and assessment of bridge infrastructures. *International Journal of Disaster Risk Reduction*, *72*, 102824. https://doi.org/10.1016/j.ijdrr.2022.102824.

Masafu, C., Williams, R., Shi, X., Yuan, Q., & Trigg, M. (2022). Unpiloted Aerial Vehicle (UAV) image velocimetry for validation of two-dimensional hydraulic model simulations. *Journal of Hydrology*, *612*, 128217. https://doi.org/10.1016/j.jhydrol.2022.128217.

Mazzoleni, M., Paron, P., Reali, A., Juizo, D., Manane, J., & Brandimarte, L. (2020). Testing UAV-derived topography for hydraulic modelling in a tropical environment. *Natural Hazards*, *103*(1), 139–163. https://doi.org/10.1007/s11069-020-03963-4.

Medvedev, A., Telnova, N., Alekseenko, N., Koshkarev, A., Kuznetchenko, P., Asmaryan, S., & Narykov, A. (2020). UAV-Derived Data Application for Environmental Monitoring of the Coastal Area of Lake Sevan, Armenia with a Changing Water Level. *Remote Sensing*, *12*(22), Article 22. https://doi.org/10.3390/rs12223821.

Outay, F., Mengash, H. A., & Adnan, M. (2020). Applications of unmanned aerial vehicle (UAV) in road safety, traffic and highway infrastructure management: Recent advances and challenges. *Transportation Research Part A: Policy and Practice*, *141*, 116–129. https://doi.org/10.1016/j.tra.2020.09.018.

Pepe, M., Alfio, V. S., & Costantino, D. (2022). UAV platforms and the SfM-MVS approach in the 3D surveys and modelling: A review in the cultural heritage field. *Applied Sciences*, *12*(24), 12886. https://doi.org/10.3390/app122412886.

Pepe, M., Fregonese, L., & Scaioni, M. (2018). Planning airborne photogrammetry and remote-sensing missions with modern platforms and sensors. *European Journal of Remote Sensing*, *51*(1), 412–436. https://doi.org/10.1080/22797254.2018.1444945.

Remondino, F., Barazzetti, L., Nex, F. C., Scaioni, M., & Sarazzi, D. (2011). UAV photogrammetry for mapping and 3D modeling: Current status and future perspectives. *Proceedings of the International Conference on Unmanned Aerial Vehicle in Geomatics (UAV-g): 14-16 September 2011, Zurich, Switzerland*, 25–31. https://research.utwente.nl/en/publications/uav-photogrammetry-for-mapping-and-3d-modeling-current-status-and.

Robador González, M. D., Nieto-Julián, J. E., Millán-Millán, P. M., Galera-Rodríguez, A., Bruno, S., Debenedictis, D., & Moyano, J. (2023). Management properties and procedures in the information model of the historic building HBIM on building facades. *The International Archives of the Photogrammetry, Remote Sensing and Spatial Information Sciences*, *XLVIII-M-2–2023*, 1323–1330. https://doi.org/10.5194/isprs-archives-XLVIII-M-2-2023-1323-2023.

Sferlazza, S., Maltese, A., Dardanelli, G., & La Mela Veca, D. S. (2022). Optimizing the sampling area across an old-growth forest via UAV-borne laser scanning, GNSS, and radial surveying. *ISPRS International Journal of Geo-Information*, 11(3), 168. https://doi.org/10.3390/ijgi11030168

Shoab, M., Singh, V. K., & Ravibabu, M. V. (2022). High-precise true digital orthoimage generation and accuracy assessment based on UAV images. *Journal of the Indian Society of Remote Sensing*, *50*(4), 613–622. https://doi.org/10.1007/s12524-021-01364-z.

Shults, R., & Annenkov, A. (2023). BIM and UAV photogrammetry for spatial structures sustainability inventory. *The International Archives of the Photogrammetry, Remote Sensing and Spatial Information Sciences*, *XLVIII-5-W2-2023*, 99–104. https://doi.org/10.5194/isprs-archives-XLVIII-5-W2-2023-99-2023.

Son, S. W., Kim, D. W., Sung, W. G., & Yu, J. J. (2020). Integrating UAV and TLS Approaches for Environmental Management: A Case Study of a Waste Stockpile Area. *Remote Sensing*, *12*(10), Article 10. https://doi.org/10.3390/rs12101615.

Teizer, J. (2015). Status quo and open challenges in vision-based sensing and tracking of temporary resources on infrastructure construction sites. *Advanced Engineering Informatics*, *29*(2), 225–238. http://dx.doi.org/10.1016/j.aei.2015.03.006.

Tmušić, G., Manfreda, S., Aasen, H., James, M. R., Gonçalves, G., Ben-Dor, E., Brook, A., Polinova, M., Arranz, J. J., & Mészáros, J. (2020). Current practices in UAS-based environmental monitoring. *Remote Sensing*, *12*(6), 1001. http://dx.doi.org/10.3390/rs12061001.

Zanutta, A., Lambertini, A., & Vittuari, L. (2020). UAV photogrammetry and ground surveys as a mapping tool for quickly monitoring shoreline and beach changes. *Journal of Marine Science and Engineering*, 8(1), 52. https://doi.org/10.3390/jmse8010052

ASSESSMENT OF WATER EROSION DYNAMICS IN THE MOROCCAN'S CENTRAL PLATEAU FOR CURRENT AND FUTURE SITUATIONS USING RUSLE MODEL AND GEE PLATFORM: CASE STUDY OF KHAROUBA WATERSHED

Hasna TAHIRI [1] , Ahmed EL ABOUDI [2] , Youssef BOUSSALIM [1] and Youssef DALLAHI [1*]

ABSTRACT
The Kharouba watershed, located upstream of the Ouljet Soltane dam, has a crucial importance by preserving water and soil resources in the area. Belonging to the Beht watershed, this part of the Morocco's Central Plateau is subject to a relatively high level of soil degradation. In this context, the present study was conducted to assess the spatio-temporal dynamics of Soil Loss (SL) in the Kharouba watershed during the period 2001-2023, and to predict SL rate for the future period 2041-2060 (2050s). The methodological approach integrates the RUSLE model through the dynamic nature of the erosivity (R) and the vegetation cover (C) factors, and the Google Earth Engine (GEE) platform as a tool for the computational tasks. The results indicate that 52 to 82% of the Kharouba watershed surface is subject to intense to severe erosion. Annual Soil Loss varied from 54.29 t/ha in 2011 to 27.38 t/ha in 2023. The spatial distribution of SL values is mainly controlled by the variability of the topographical factor (LS) showing a good correlation with SL (R^2=0.58). While the temporal variability of SL annual average is jointly explained by fluctuations in R and C factors, demonstrating R^2 of 0.35 and 0.23 respectively with SL. Future projections in 2050s show that the average annual Soil Loss is expected to increase by 14 and 13% in the SSP2-4.5 and SSP5-5.8 scenarios respectively compared to the current situation. In addition, this study makes it possible to calculate the quantities of lost soil that will cause silting of the Ouljet Soultane dam located at the downstream end of our watershed, and consequently to determine the lifespan of the dam.

Key-words: *Water erosion dynamics, RUSLE model, GEE platform, Morocco's Central Plateau, SSP2-4.5, SSP5-5.8.*

1. INTRODUCTION

Morocco is located in the north-western part of Africa and the south-western side of the Mediterranean basin, and has an arid to semi-arid climate over most of its territory with very low rainfall and limited surface water resources (Aahd et al., 2009; Mekki, 2017). These hydric resources are conditioned by rainfall, which is highly irregular in time and space, resulting in highly variable flood flows and a significant water erosion (Dinar, 2024). Indeed, water erosion is caused and amplified by a number of factors, both natural and anthropogenic, including climatic erosivity, intensive agriculture, deforestation, over land-exploitation, rough topography and climate change (Sadiki et al., 2004 ; Dallahi et al., 2020; Kassou et al., 2023), resulting in a deterioration of soil quality, a loss of soil fertility, a drop in agricultural productivity and a reduction in the storage capacity of dams (Dionnet et al., 2006).

_____

[1] *Laboratory of Plant Biotechnology and Physiology (BioPV), Research Center on Plant and Microbial Biotechnology, Biodiversity and Environment, Faculty of Sciences, Mohammed V University in Rabat, 10000, Rabat, Morocco. hasna_tahiri4@um5.ac.ma, * Corresponding author: youssef.dallahi@fsr.um5.ac.ma, youssef.boussalim@um5r.ac.ma*
[2] *Laboratory of Botanic and Valorisation of Plant and Fungal Resources (BOVAREF), Faculty of Sciences, Mohammed V University in Rabat, 10000 Rabat, Morocco. a.elaboudi@um5r.ac.ma*

Moreover, water erosion is a major constraint for the sustainable development in watersheds (Mesrar et al., 2015). This process is very frequent and changes dynamically according to the evolution and spatial variation of the lithological nature of the rocks, the geomorphology of the landscapes, the geometry of the area and the bioclimatic situation (Zouaoui et al., 2019). This erosion is the main cause of soil degradation in Morocco. It affects almost all regions of Morocco, with different intensities. 60% of the cumulative annual SL due to water erosion is deposited in reservoirs and dams (Debbarh and Badraoui, 2003).

Several studies on water erosion have been carried out in Morocco such as El Garouani et al. (2008), Sadiki et al. (2009), Driss and Akdim (2018), Ait Yacine et al. (2019), Dallahi et al. (2020), Lakhili (2021) and Kassou et al. (2023). These studies have focused on both the quantitative and qualitative aspects of soil loss (SL) assessment, based mainly on the Revised Universal Soil Loss Equation; RUSLE (Renard et al., 1997) and the PAP-CAR (PAP/CAR., 2000; PAP/CAR., 1998) methods. However, there is a lack of research about the dynamic evolution of SL and their future projections. In this context, this study is carried out to assess the spatio-temporal dynamics of Soil Loss and to project their future evolution in the Kharouba watershed as a case study in the Moroccan's Central Plateau. This watershed plays an essential role in water and soil conservation in the area. It is characterised by primary geological formations with a relatively high specific degradation (Dallahi, 2017). Indeed, the objectives of this study are: (i) assessing the evolution of SL in the Kharouba watershed in order to analyse the current situation and identify the main factors controlling Soil Loss dynamics, and (ii) projecting the future situation based on the dynamic nature of R and C factors by using future data from global climate models (GCMs) under two scenarios of climate change (SSP2-4.5 and SSP5-8.5).

2. STUDY AREA

The Kharouba watershed is located in the province of Khémisset of Central Plateau (**Fig. 1**).
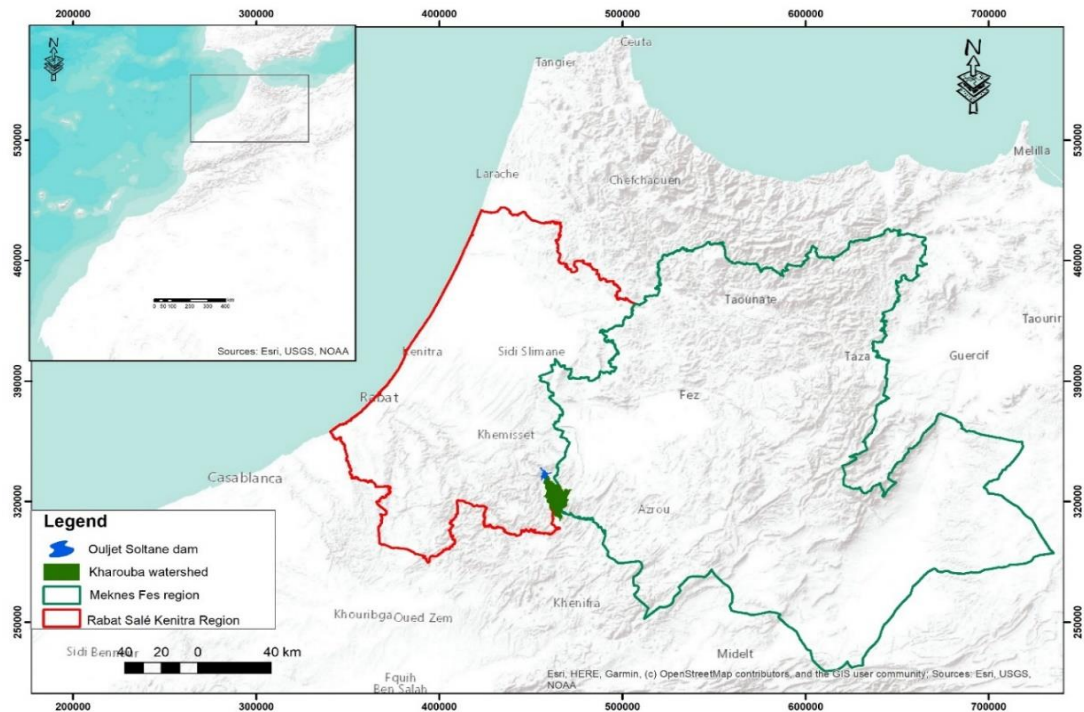
Fig. 1. Location of the Kharouba watershed.

It covers an area of 19,888.5 hectares (ha) and is located in the central part of Beht watershed. The area is dominated by Palaeozoic geological formations of shale and sandstone, which were heavily folded and tectonized during the Hercynian orogeny. In terms of vegetation, this watershed is dominated by forest formations organised by *Tetraclinis articulata* and *Quercus rotundifolia* (Dallahi et al., 2016, Dallahi et al., 2017) , which cover more than 87% of its total surface area (Fennane et al., 1987). Regarding the climate, the area is characterised by an arid to semi-arid climate with high spatial and temporal variability in rainfall.

3. METHODOLOGICAL APPROACH

3.1. Assessment of current SL dynamics

In order to assess the spatial-temporal dynamics of SL in the Kharouba watershed between 2001 and 2023, the Revised Universal Soil Loss Equation (RUSLE) (Wischmeier and Smith, 1978 ; Renard et al., 1997) was used:

$$A = R \times K \times LS \times C \times P \qquad \text{(imperial: tons/acre/yr)}$$

where:

R = is the rainfall and runoff factor depending by geographic location
K = is the soil erodibility factor
LS = is the slope length-gradient factor
C = is the vegetation cover used to represent the relative effectiveness of soil and crop management systems in controlling soil loss
P = is the support for anti-erosive practices, as the ratio of soil loss by a support practice like cross-slope cultivation, contour farming and strip cropping.

To calculate the R factor, the following formula was used (Singh et al., 1981):

$$R = 79 + 0 .363 \times P$$

where: P is the annual precipitation in mm.

To compute the LS factor, the following formula was used (McKague and Eng, 2023; Boussalim et al., 2022 ; Stone and Hilborn, 2012) :

$$LS = (0.065 + 0.0456 \times S + 0.006541 \times S^2) ((FlowAcc \times 30) \div 22.1^{0,5}))$$

where: S is the slope gradient in %;
FlowAcc is the flow accumulation having
30 as spatial resolution of the DTM;
0.5 as constant value used when the dominant slopes in the basin exceed 5%.

To compute the C factor, the following formula was used (Kouli et al., 2009) :

$$C = \exp [- \alpha \times NDVI / (\beta – NDVI)]$$

where: $\alpha = 2$ and $\beta = 1$ are constants.
NDVI (Normalized Difference Vegetation Index) was calculated by:
$$NDVI = (NIR – R) / (NIR + R)$$
NIR: infrared band
R: red band

We have calculated the K factor by using the correspondence table between soil texture and K, from Stone and Hilborn (2000). The values obtained were multiplied by 0.1317 (Chadli, 2016) to convert the values into the international system of units.

The P factor was estimated as a function of slope following Shin (1999) and taking into account land use types extracted from MODIS data.

The computational operations were performed on the Google Earth Engine (GEE) platform. CHIRPS data (Funk et al., 2015) were used for the generation of the R-factor using total annual precipitation. Landsat 7 (from 2001 to 2017) and Landsat 8 (from 2018 to 2023) data were used to give rise to the vegetation cover C factor. USDA data were used to determine surface soil texture (Hengl, 2018) to spatialise the K factor. Also, a 30 m resolution digital elevation model (DEM) was used to calculate the LS factor. The P factor was estimated from MODIS land cover data (Friedl et al., 2002) and the slope steepness from DEM. SL values resulting from the spatial modelling in tonnes/hectares/year (t/ha/yr) were classified into five categories (**Table 1**).

Table 1.

Soil Loss classification applied in the study.

Categories	Slight	Moderate	High	Very High	Severe
SL (t/ha/yr)	<10	10<SL<20	20<SL<30	30<SL<40	SL>40

A linear regression between the annual averages of Soil Loss and the averages of the two dynamic factors (R and C) was used to explain the temporal fluctuations of SL. Similarly, the spatial variability of SL was assessed using a pixel-to-pixel linear regression between SL and the various explanatory factors (LS, R, C, K and P). The Spearman correlation test was used to evaluate the significance of the correlation. The significance level (α) was set at 0.05. Also, the strength of the correlation is assessed by the coefficient of determination (R^2).

3.2. Prediction of SL in 2041-2060 (2050s)

To predict average Soil Loss in 2050, projected data were used to estimate the future climatic erosivity (R factor). These data were downloaded from the WorldClim database with 1 km of resolution. Precipitations values was bias-corrected and downscaled with the WorldClim version 2.1 data (1970-2000) (Fick and Hijmans, 2017). The average of 3 GCMs was used (ACCESS-CM2, EC-Earth3-Veg and MIROC6), for two SSP scenarios: SSP2-4.5 (medium scenario) and SSP5-8.5 (pessimistic scenario).

To project the future C factor, we have predicted the NDVI (Normalized Difference Vegetation Index) for 2050s using MOLUSCE extension (Modules for Land Use Change Evaluation) in QGIS Desktop 2.16.3 software. Two NDVI rasters were used between two different dates (2013 and 2023) to detect spatial changes. Indeed, the prediction was made by a logistic regression model based on changes between the two cited dates. The model showed a "Pseudo R-squared: PR^2" of 0.802, therefore, it was used to anticipate the NDVI state in 2050s. The assessment of changes between the two dates, the training of the prediction model and the simulation of the future state were carried out by NDVI classes since the MOLUSCE extension take into account categorized data. Therefore, six classes were adopted:

Class 1 : NDVI<0
Class 2 : 0<NDVI<0,1
Class 3 : 0,1<NDVI<0,2
Class 4 : 0,2<NDVI<0,3
Class 5 : 0,3<NDVI<0,4
Class 6 : NDVI>0,4

The rainfall erosivity (R) and vegetation cover (C) factors calculated for 2050s were integrated with the static factors (LS, K and P) to project SL in 2050s. Then, the current and future situations were compared via SL averages and the proportion of each SL category. For the current situation, the average of Soil Loss over the period 2001-2023 was considered for the comparison.

4. RESULTS

4.1. Assessment of the current SL dynamics (2001-2023)

The RUSLE model was used to map the spatial variability of Soil Loss (**Fig. 2**). Depending on the interannual fluctuations of rainfall and vegetation dynamics, the Kharouba watershed shows severe water erosion on 23 to 45% of its surface area. Very intense erosion varies between 15 and 24% and intense erosion between 12 and 19%. Moderate water erosion varies between 7 and 15%, while low erosion between 10 and 31% (**Fig. 3**). These results indicate that 52 to 82% of the watershed surface is subject to intense to severe erosion. This spatial variability is accompanied by a large spatial-temporal variability in SL, which ranges from 27.38 t/ha in 2023 to 54.29 t/ha in 2011 (**Fig. 4**).
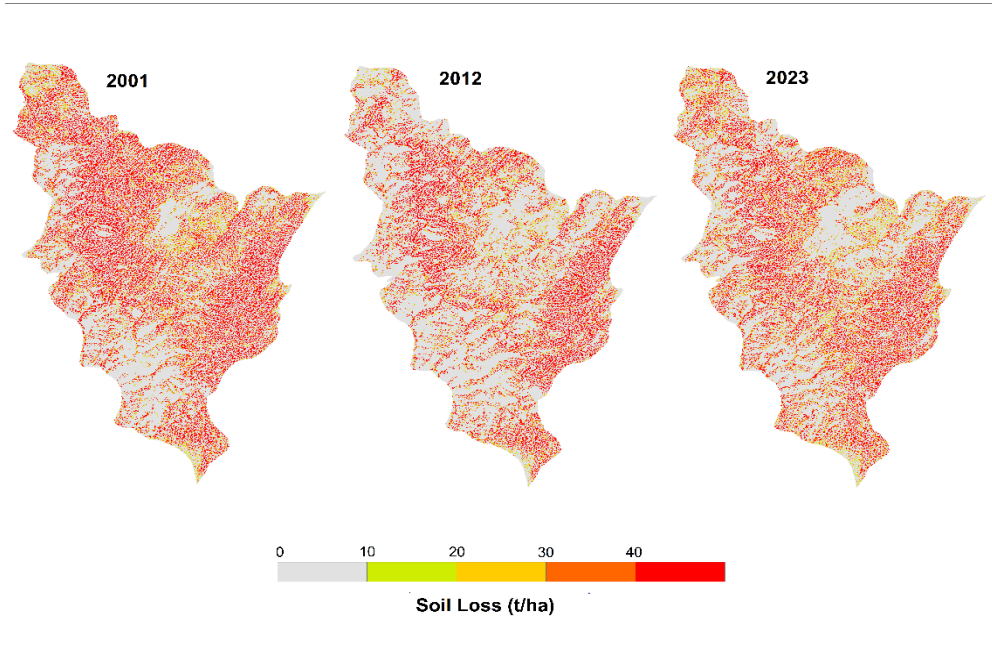
Fig. 2. Spatial distribution of SL categories in Kharouba watershed in 2001, 2012 and 2023.
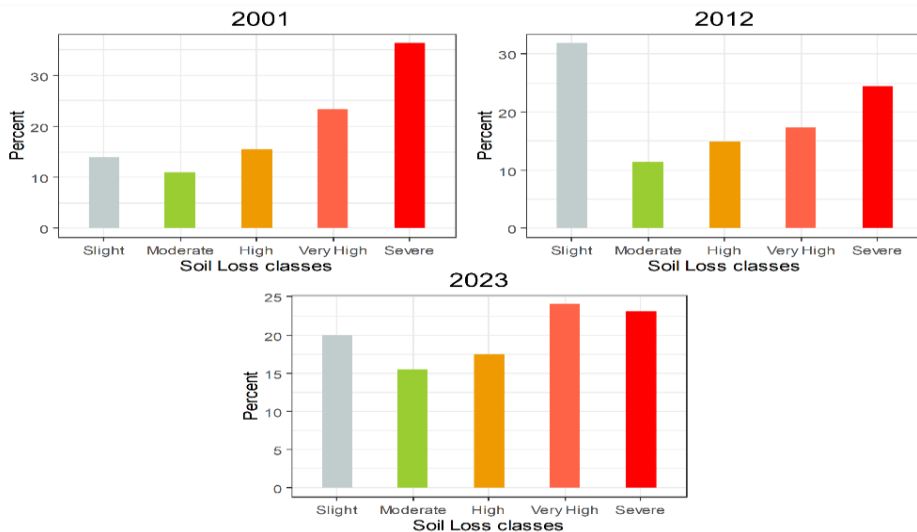
Fig. 3. Distribution of SL categories in Kharouba watershed in 2001, 2012 and 2023.
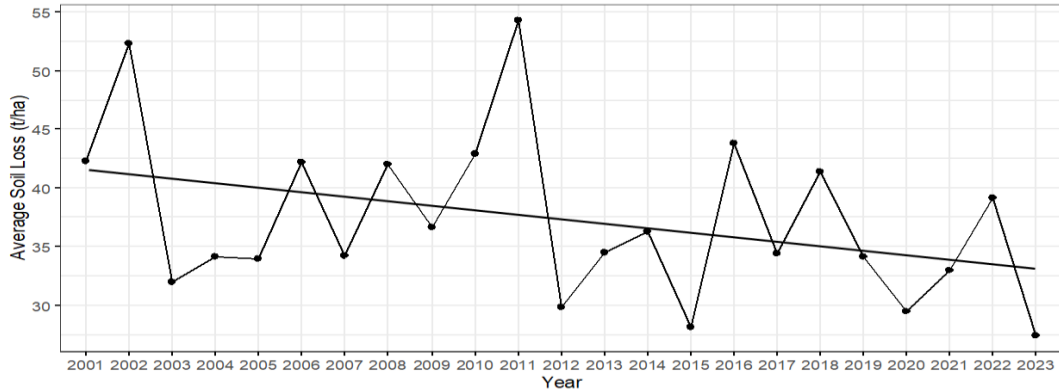
Fig. 4. Evolution of the SL averages between 2001 and 2023 in Kharouba watershed.

The pixel-by-pixel correlation between Soil Loss and the various explanatory variables shows that the LS factor is the most determinant variable influencing the spatial distribution of SL, with a coefficient of determination (R^2) of 0.58 (**Fig. 5, a**). The second and third most important variables are respectively the vegetation cover C factor, with an R^2 of 0.18 (**Fig. 5, c**) and the R factor, with an R^2 of 0.005 (**Fig. 5, b**). These three variables show a significant correlation with Soil Loss at α=0.05. The K and P variables, on the other hand, showed non-significant correlations to the same α level.

The correlation between annual Soil Loss average and the rainfall erosivity (R) and vegetation cover (C) factors shows that the temporal variation in SL is jointly controlled by the interannual variations of R and C, which demonstrated respective R^2 values of 0.35 and 0.23 (**Fig. 6**).
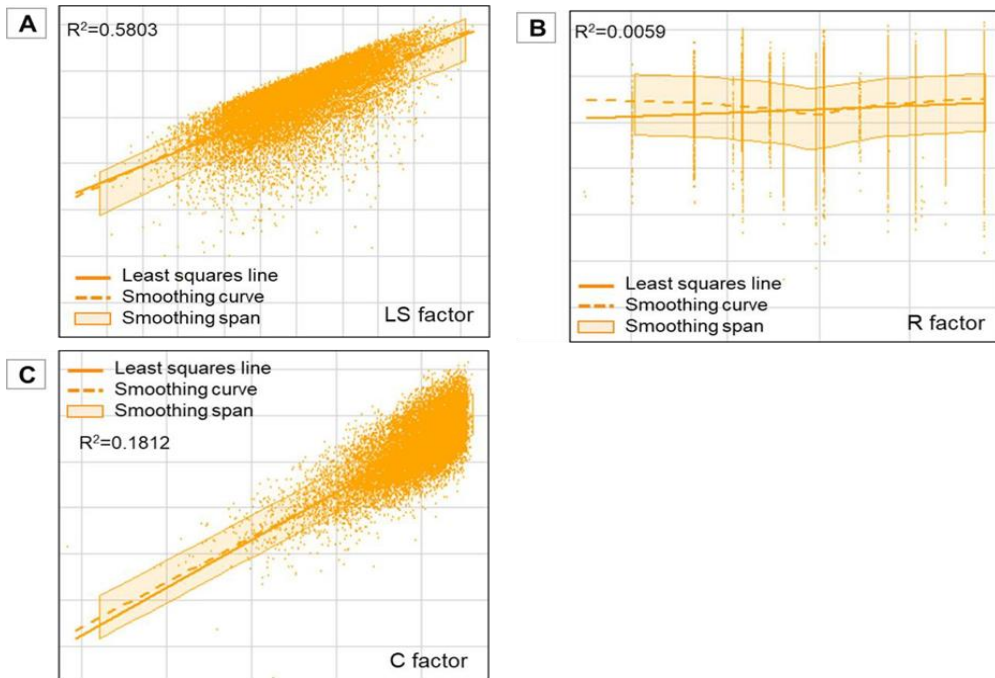
Fig. 5. Variables with significant correlation at α=0.05; pixel-to-pixel linear regression between SL and RUSLE factors.
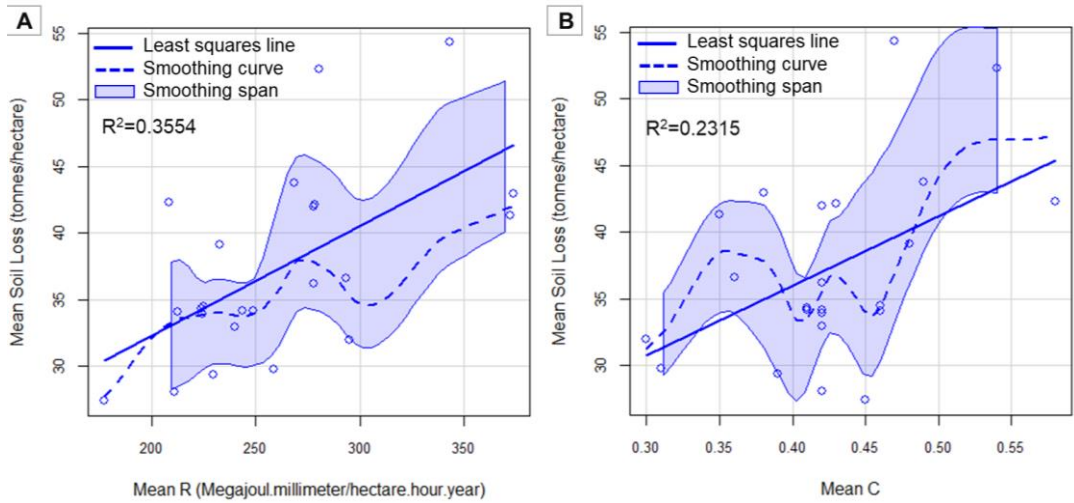
Fig. 6. Linear regression between the annual SL averages and dynamic factors of RUSLE: R (a) and C (b).

4.2. SL projections in 2050s

The NDVI compared between 2013, 2023 and projected for 2050s shows a regressive vegetation dynamic over time, with a decrease in areas with high NDVI values and an increase in those with low NDVI values (**Fig. 7**). Comparison of NDVI classes between 2013 and 2023 showed that 33% of areas with NDVI>0.3 were converted to areas with NDVI<0.3. Furthermore, the future NDVI projection in 2050s shows that 15% of areas with NDVI>0.2 should be converted to areas with NDVI<0.2 compared to 2023 (**Table 2**).
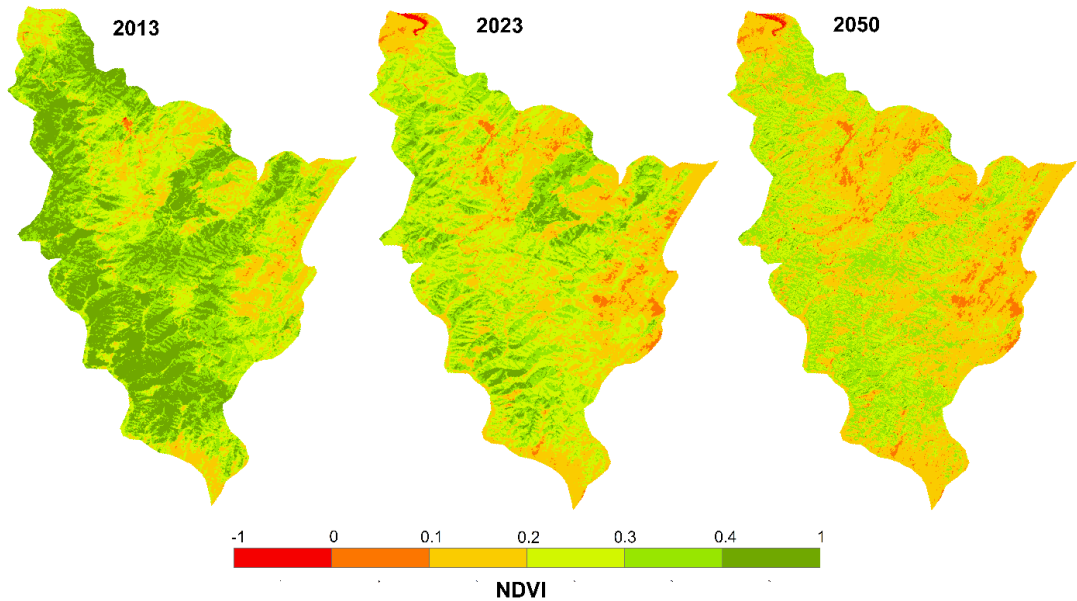
Fig. 7. Spatial changes in NDVI between 2013 and 2023, and prediction result for 2050s.

Comparison between classes of NDVI between 2013, 2023 and the predicted situation 2050s.

Area and change	2013 (ha)	2023 (ha)	From 2013 to 2023 (%)	2050 (ha)	From 2023 to 2050 (%)
NDVI<0	1,53	38,25	+0,16	50,04	+0,05
0<NDVI<0,1	65,79	553,41	+2,20	892,71	+1,53
0,1<NDVI<0,2	2954,16	7005,96	+ 18,31	10084,14	+ 13,91
0,2<NDVI<0,3	5760,63	8586,81	+ 12,77	6540,57	-9,24
0,3<NDVI<0,4	6449,58	4699,53	-7,90	4363,47	-1,51
0,4<NDVI<1	6893,55	1241,28	-25,54	194,31	-4,73

Future rainfall and NDVI projections were used to map the rainfall erosivity R and vegetation cover C factors for 2050s in order to anticipate Soil Loss status (**Fig. 8**). Comparison of the average SL obtained for the period 2001-2023 with the average projected for 2050s shows an increase in SL rate by 14% for SSP2-4.5 and 13% for SSP5-5.8 (**Table 3**).

Rainfall erosivity is expected to be less important in 2050s with an average decrease of 1.5% in the SSP2-4.5 scenario. This reduction is around 2.2% in the SSP5-8.5 scenario. Thus, the C Factor is intended to increase by +16% by 2050s (**Table 3**). The assumed increase in the rate of water erosion in 2050s is the result of an increase in areas with severe erosion to the detriment of areas with low erosion (**Fig. 9**). The distribution of the other categories of Soil Loss is projected to be relatively constant in space.
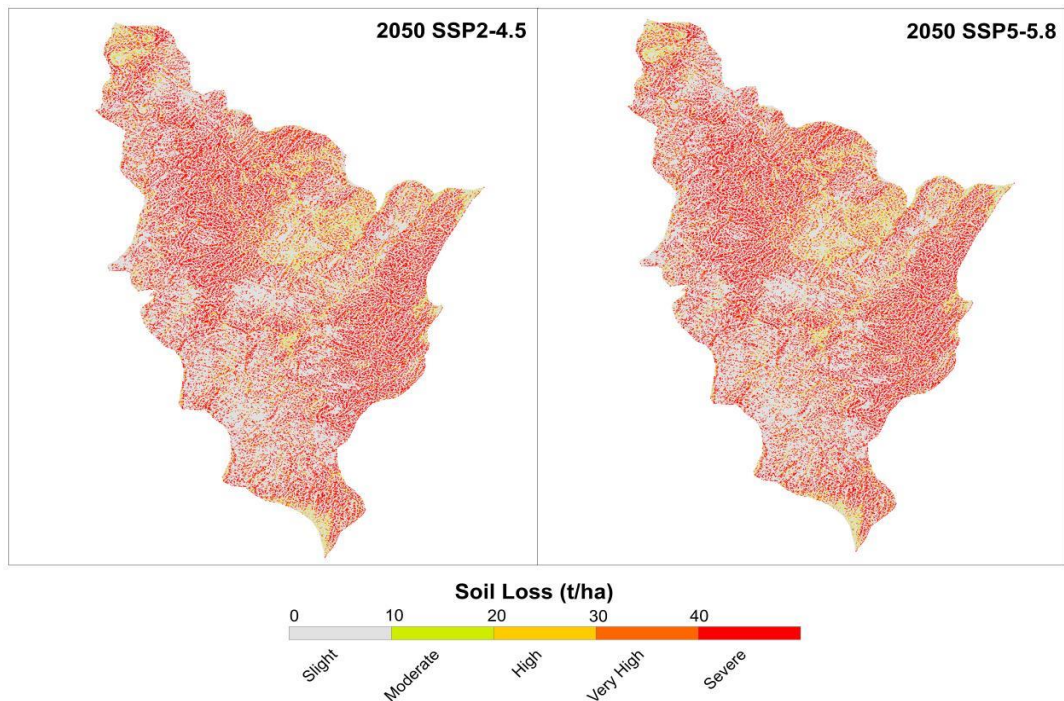
Fig. 8. Projected SL for 2050s: SSP2-4.5 and SSP5-8.5 Scenarios**.**

Table 3.
Means of R, C and soil loss calculated for the reference period 2001-2023 compared to projected means for 2050.

Period	2001-2023	2050s under SSP2-4.5	2050s under SSP5-8.5
R value (Mgj.mm/ha.h.yr)	260,79	256,65	255
C value	0,42	0,49	0,49
Mean of Soil Loss (t/ha)	37,29	42,54	42,27
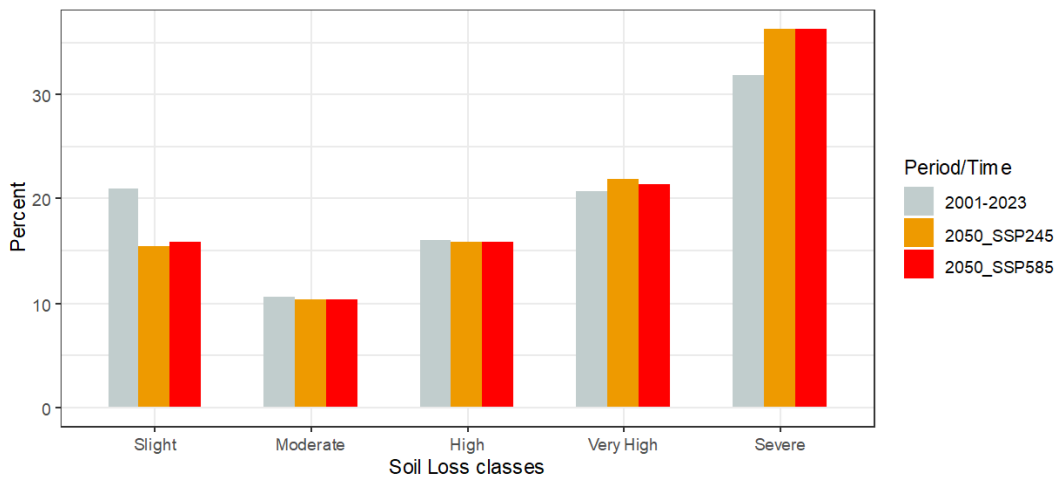
Fig. 9. Comparison of the averages soil loss by categories between 2001-2023 and the predicted situation in 2050.

5. DISCUSSION

The significance of the spatial-temporal dynamics of Soil Loss in the Kharouba watershed was evaluated by this study. The variability of the topographical factor, which demonstrated a determination coefficient of 0.58 with Soil Loss, primarily controls the spatial dynamics of SL. The slope influences water erosion mainly through its inclination and length; both parameters considered in the RUSLE model. The slope affects erosion in two ways: by transferring the ejected particles downstream, after the raindrops have hit the ground; and by imparting energy to runoff water along the slope, when large quantities of water are on the ground, run-off occurs more quickly, preventing the water from infiltrating the soil. Thus contributing to the uprooting and transport of soil particles (Sadiki, 2005).

In the western Meseta, including the area of the central plateau where the studied watershed is located, the topographical factor is the most determinant variable influencing water erosion, with a relatively greater effect than the other factors in the RUSLE model (Lamane et al., 2022). In the same geographical area, the correlation between SL and the various explanatory factors in the Oued Cherrat watershed also shows the dominance of the topographical factor over the other RUSLE variables, demonstrating a correlation coefficient of 0.67 (R^2=0.45) with Soil Loss (Boussalim et al., 2022).

On the other hand, our results show that Soil Loss at basin level are characterised by significant inter-annual temporal variability over the study period, with a minimum in 2023 and a maximum in 2011. This spatial variability is controlled by the dynamic factors in the equation.

The erosivity of rainfall has a greater impact on this variability than fluctuations in vegetation cover (R^2=0.35). This is essentially explained by the high inter-annual and intra-annual rainfall variability characterizing Morocco (Sebbar, 2013). These fluctuations in rainfall input are the main cause of the temporal variability of SL in Kharouba watershed. Indeed, fluctuations in NDVI, reflecting vegetation dynamics, contribute also significantly to the interannual variability of SL (R^2=0.23). The quality of the vegetation cover can considerably reduce or accentuate the effects of climatic erosivity. A dense vegetation can slow run-off, facilitate infiltration and decrease the intensity of erosion.

Our results show also that rainfall erosivity (R) and vegetation cover (C) factors have a weak but significant impact on the spatial variability of SL. This is explained by the fact that these two factors do not show great variability in their spatial distribution. Rainfall distribution is homogeneous throughout the watershed with low spatial fluctuations. Similarly for land use, which 87% of the watershed's area is occupied by *Tetraclinis articulata* and holm oak forests (Dallahi, 2017). The results also indicate that the two factors, soil erodibility (K) and anti-erosion practices (P) have no significant effect on the spatial distribution of Soil Loss. For the K factor, this result can be explained by the homogeneity of the edaphic substratum : more than 90% of crude mineral soils on schist substratum (Dallahi, 2017). Thus, P factor was mainly estimated on the basis of land use, which is more or less homogeneous as already explained (see above).

In the same watershed and using the PAP/CAR method, (Dallahi et al., 2020) showed that water erosion was intensified between 1986 and 2008 and that surfaces that are vulnerable to water erosion were increased by 6% between these two reference dates. The main cause was the regression of vegetation (Dallahi et al., 2023). According to HCEFLCD (2007), analysis of erosion maps demonstrated that erosion is active and apparent over more than 75% of the total surface area of the watershed. This result is similar to our findings, which showed that 52% to 82% of the watershed is subject to intense to severe erosion. Our results are therefore close to those obtained for the large Oued Beht watershed, which Kharouba is part of. The authors of the study concluded that potential erosion has been greatly accelerated in the Oued Beht watershed due to the low vegetation cover observed over 70% of its territory (HCEFLCD, 2007). Also, the study carried out by Lakhili (2021) in the Beht watershed showed that 76% of the area is exposed to moderate to severe erosion.

The results obtained show that the C factor will increase in 2050s because of the decrease in NDVI according to the projections made. Thus, climatic erosivity will decrease in 2050s, which directly translates into a reduction in annual precipitation in this period, since the equation for calculating the R factor only takes into account total annual rainfall in an equation where the two factors (climatic erosivity and annual precipitation) are positively correlated (see methodology section). As a result, the projected decrease in NDVI in 2050s can be attributed to this reduction in rainfall; the only future variable element in the soil loss quantification model used. However, the NDVI modelling process was not carried out in a multifactorial manner. As a result, other factors were not taken into account, such as temperature and stochastic forces (fires, etc.). Few of the existing models for the future projection of factor C take these into account, due to the nature and complexity of modelling these phenomena.

Our results show also that water erosion rate will rise in the watershed in 2050s with an increase in average Soil Loss by 14% and 13% in the SSP2-4.5 and SSP5-5.8 scenarios respectively. In Morocco, few studies have focused on SL future projections. Our study appears to be the first for the central Moroccan plateau. The finding of other studies are consistent with our result regarding the Moroccan context. A study conducted by (Jazouli et al., 2019) in the upper basin of the Oum Er Rbia river demonstrated that the average annual SL will go up in 2030 compared to year 2003. In the Haouz plain, for instance, (Bammou, et al., 2024) was projected SL in the future situations using SSP scenarios. The findings also show that water erosion will grow in this region in 2040s compared to the current situation.

6. CONCLUSIONS

The RUSLE dynamic approach was used to quantify Soil Loss in the Kharouba watershed and to make projections in the future situation. Our results highlight that the erosion is intense to severe in the Kharouba watershed and the regression of vegetation will be responsible in the future in an increase of Soil Loss rates in the Moroccan's Central Plateau. This will certainly lead to the silting up of the Ouljet Soultane dam located downstream of the watershed affecting also the limited water resources of the area. Anti-erosion practices are needed, particularly in the context of a rapid global warming to ensure soil protection and conservation and to preserve the ecosystems, avoiding therefore the Ouljat Soltane dam siltation.

Soil erosion and the effects of global warming are a vast and multidisciplinary area of research. To develop and improve soil management practices, we can develop a more advanced climate model to predict the effects of climate change on soil erosion rates in different regions, and develop sensors and networks to continuously monitor soil parameters. These research orientations can help to better understand the underlying mechanisms of soil erosion and to develop innovative and effective solutions to preserve soils and ecosystems in the face of the challenges posed by climate change.

R E F E R E N C E S

Aahd, A., Simonneaux, V., Sadik, E., Brahim, B. & Fathallah, S., (2009) Estimation des volumes d'eau pompés dans la nappe pour l'irrigation (plaine du Haouz, Marrakech, Maroc). Comparaison d'une méthode statistique et d'une méthode basée sur l'utilisation de la télédétection. *Réseau,* 22, 1–13. https://doi.org/10.7202/019820ar

Abdelali, S. (2013) Etude de la variabilité et de l'évolution de la pluviométrie au Maroc (1935-2005): Réactualisation de la carte des précipitations. https://doi.org/10.13140/2.1.1206.6084

Ait Yacine, E., Oudija, F., Nassiri, L. & Essahlaoui, A. (2019) Modélisation et Cartographie des Risques d'érosion Hydrique du Sol par l'application des SIG, Télédétection et Directives PAP/CAR. Cas du Bassin Versant de Beht, Maroc. *European Scientific Journal*, ESJ 15, 259–259. https://doi.org/10.19044/esj.2019.v15n12p259

Bammou, Y., Benzougagh, B., Bensaid, A., Igmoullan, B. & Al-Quraishi, A.M.F. (2024) Mapping of current and future soil erosion risk in a semi-arid context (haouz plain - Marrakech) based on CMIP6 climate models, the analytical hierarchy process (AHP) and RUSLE. Model. *Earth Syst. Environ.*, 10, 1501-1514.

Boussalim, Y., Rahine, N., Badri, W., Hassan, F. & Bouchra, R. (2022) Modeling of soil water erosion in Oued Cherrat wattershed (Morroco) by applying the Universel Soil Loss Equation (USLE). https://doi.org/10.38173/RST.2022.24.2.15:203-222

Chadli, K. (2016) Estimation of soil loss using RUSLE model for Sebou watershed (Morocco). Model. *Earth Syst. Environ.*, 2, 51. https://doi.org/10.1007/s40808-016-0105-y

Dallahi, Y. (2017). Apport de la télédétection spatiale pour l'étude écologique, phytosociologique et cartographique de la tétraclinaie du Site d'intérêt Biologique et Écologique (SIBE) de Kharouba en vue de son aménagement (Plateau central, Maroc). Faculté des Sciences, Université Mohammed V de Rabat.

Dallahi, Y., El aboudi, A. & Aafi, A. (2016) A contribution to the knowledge of the Moroccan Central Plateau plant communities. *Plant Sociology*, 53 (2), 41-46. DOI:10.7338/pls2016532/03

Dallahi, Y., Chahhou, D., El Aboudi & A., Aafi, A. (2017) Distribution Mapping and chemical composition of Tetraclinis articulata (Vahl.) Masters in the Site of Biological and Ecological Interest of Kharouba (Central Plateau, Morocco). *Journal of Materials and Environmental Science*, 8 (7), 2474-2479.

Dallahi, Y., Ouhammou, A., Sbai, M., El Aboudi, A. & Boujraf, A. (2020) Assessment of the vegetation cover change impacts on water erosion, using pap/rac method in upstream of "ouljet soltane" dam, central plateau-Morocco. *Geographia Technica*, Vol 15, Issue no.1/2020, pp. 153-161. DOI: 10.21163/GT_2020.151.14

Dallahi, Y., Boujraf, A., Meliho, M. et Orlando, C.A. (2023) Assessment of forest dieback on the Moroccan Central Plateau using spectral vegetation indices. *J. For. Res*. 34, 793‑808. https://doi.org/10.1007/s11676-022-01525-x

Debbarh, A. & Badraoui, M. (2003) Irrigation et environnement au Maroc : situation actuelle et perpectives [WWW Document]. Vers une maîtrise des impacts environnementaux de l'irrigation : actes de l'atelier du PCSI, 28 - 29 mai 2002, Montpellier, France. URL https://agritrop.cirad.fr/515405/ (accessed 2.15.24).

Dinar, A. (2024) Challenges to Water Resource Management: The Role of Economic and Modeling Approaches. *Water,* 16, 610. https://doi.org/10.3390/w16040610

Dionnet, M., Kuper, M., Garin, P., Hammani, A., Eliamani, A. & Saaf, M. (2006) Accompagner les acteurs dans le changement de leur système. https://agritrop.cirad.fr/558996/1/document_558996.pdf

Driss, E. & Akdim, B. (2018) Quantification del'érosion hydrique en utilisant le Modèle Rusle et déposition intégrée dans un Sig. Cas du Bassin Versant de l'oued Isly (Maroc Oriental). DOI: 10.19044/esj.2018.v14n5p373

El Garouani, A., Chen, H., Lewis, L., Tribak, A. & Abharour, M. (2008) Cartographie de l'utilisation du sol et de l'érision nette à partir d'images sateletaires du SIG IDRISI au Nord-Est du Maroc. *Teledetection,* 8, 193–201.

Fennane, H., Tattou, M.I., Najim, L., Benabid, A., Bellakhdar, J. & d'Ardancourt, J.L.W. (1987) La grande encyclopédie du Maroc. Flore et végétation. Grande Encyclopédie du Maroc (MAR). GEM, Rabat.

Fick, S. & Hijmans, R. (2017). WorldClim 2: New 1-km spatial resolution climate surfaces for global land areas. *International Journal of Climatology*, 37. https://doi.org/10.1002/joc.5086

Friedl, M.A., McIver, D.K., Hodges, J.C.F., Zhang, X.Y., Muchoney, D., Strahler, A.H., Woodcock, C.E., Gopal, S., Schneider, A., Cooper, A., Baccini, A., Gao, F. & Schaaf, C. (2002) Global land cover mapping from MODIS: algorithms and early results. Remote Sensing of Environment, The Moderate Resolution Imaging Spectroradiometer (MODIS): *a new generation of Land Surface Monitoring,* 83, 287–302. https://doi.org/10.1016/S0034-4257 (02) 00078-0

Funk, C., Peterson, P., Landsfeld, M., Pedreros, D., Verdin, J., Shukla, S., Husak, G., Rowland, J., Harrison, L., Hoell, A. & Michaelsen, J. (2015) The climate hazards infrared precipitation with stations—a new environmental record for monitoring extremes. *Sci Data*, 2, 150066. https://doi.org/10.1038/sdata.2015.66

HCEFLCD (2007) Plan d'action du (HCEFLCD) : Mise en Œuvre du Programme du Gouvernement [WWW Document]. URL https://faolex.fao.org/docs/pdf/mor164708.pdf (accessed 1.19.24).

Hengl, T. (2018) Soil texture classes (USDA system) for 6 soil depths (0, 10, 30, 60, 100 and 200 cm) at 250 m. https://doi.org/10.5281/zenodo.1475452

Jazouli, A.E., Barakat, A., Khellouk, R., Rais, J. & Baghdadi, M.E. (2019) Remote sensing and GIS techniques for prediction of land use land cover change effects on soil erosion in the high basin of the Oum Er Rbia River (Morocco). Remote Sensing Applications: *Society and Environment,* 13. https://doi.org/10.1016/j.rsase.2018.12.004

Kassou, A., Essahlaoui, N., Azzi, Y. & Essahlaoui, A. (2023) Quantification de l'Érosion Hydrique au Niveau du Bassin Versant à l'Amont du Barrage Hassan II, Haute Moulouya, Maroc, par l'Équation Universelle de Perte en Sol. *European Scientific Journal*, ESJ 19, 284–284. https://doi.org/10.19044/esj.2023.v19n9p284

Kouli, M., Soupios, P. & Vallianatos, F. (2009) Soil erosion prediction using the Revised Universal Soil Loss Equation (RUSLE) in a GIS framework, Chania, Northwestern Crete, Greece. *Environmental Geology*, 57, 483–497. https://doi.org/10.1007/s00254-008-1318-9

Lakhili, F. (2021) Estimation de l'érosion des sols basée sur le SIG à l'aide de la méthode EPM dans le bassin versant de Beht. *Environmental and Water Sciences, public Health and Territorial Intelligence Journal,* 5, 588–596. https://doi.org/10.48421/IMIST.PRSM/ewash-ti-v5i2.25897

Lamane, H., Moussadek, R., Baghdad, B., Mouhir, L., Briak, H., Laghlimi, M. & Zouahri, A. (2022) Soil water erosion assessment in Morocco through modeling and fingerprinting applications: A review. *Heliyon* 8(8). https://doi.org/10.1016/j.heliyon.2022.e10209

McKague, K. & Eng, P. (2023) Universal Soil Loss Equation [WWW Document]. URL http://www.ontario.ca/page/universal-soil-loss-equation (accessed 6.8.24).

Mekki, O.A.E. (2017). Spatialisation du potentiel de recharge diffuse d'un aquifère libre sous climat semi-aride par techniques géospatiales et hydrochimiques : cas de l'aquifère du Haouz (MARRAKECH, MAROC) [WWW Document]. URL http://www.abhatoo.net.ma/maalama-textuelle/developpement-durable/societe-durable/information-ecologique/systeme-d-information/systemes-d-information-geographiques-sig/spatialisation-du-potentiel-de-recharge-diffuse-d-un-aquifere-libre-sous-climat-semi-aride-par-

techniques-geospatiales-et-hydrochimiques-cas-de-l-aquifere-du-haouz-marrakech-maroc (accessed 6.8.24).

Mesrar, H., Sadiki, A., Navas, A., Faleh, A., Quijano, L. & Chaaouan, J. (2015) Modélisation de l'érosion hydrique et des facteurs causaux, Cas de l'oued Sahla, Rif Central, Maroc. *zfg* 59, 495–514. https://doi.org/10.1127/zfg/2015/0169

PAP/CAR. (2000) National reports on problems and practices of erosion control management in the mediterranean region [rapport]. - [s.l.] : PAP/RAC, split,.

PAP/CAR. (1998) Directives pour la cartographie et la mesure des processus d'érosion hydrique dans les zones cotieres mediterraneennes. [Section du livre]. [s.l.] : PAP8/PP/GL.1. 1998. Split, Centre d'activites regionales pour le Programme d'actions prioritaires (PAM/PNUE), en collaboration avec FAO.

Rapport (2023) Étude de révision de l'aménagement de la forêt d'Ait Hatem. Agence Nationale des Eaux et Forêts, Maroc.

Renard, K., Foster, G.R., Weesies, G., Mccool, D. & Yoder, D. (1997) Predicting soil erosion by water: a guide to conservation planning with the Revised Universal Soil Loss Equation (RUSLE). https://www.ars.usda.gov/arsuserfiles/64080530/rusle/ah_703.pdf

Sadiki, A. (2005) Estimation de l'état de dégradation des sols dans le bassin versant de l'oued Boussouab, Maroc nord oriental : Application du modèle empirique (USLE), de la technique du radio-isotope Césium 137 et de la susceptibilité magnétique. https://doi.org/10.13140/RG.2.1.3420.6246

Sadiki, A., Ali, F. & Zêzere, J., H., M. (2009) Quantification de l'érosion en nappes dans le bassin versant de l'oued Sahla, Rif central Maroc. *Cahiers Géographiques* N° 6.

Shin, G.J., (1999). The Analysis of Soil Erosion Analysis in Watershed Using GIS (Ph.D). Department of Civil Engineering, Gang-Won National University, Chuncheon.

Singh, G., Babu, R. & Chandra, S. (1981) Soil erosion prediction research in INDIA. *Tech. Bull* T-12/D-9. Central Soil and Water Conservation Research and Training Institute, Dehradun, India. pp70.

Stone, R.P. & Hilborn, D. (2012) Universal Soil Loss Equation (USLE), Factsheet. Ministry of Agriculture, Food and Rural Affairs, Ontario.

Stone, R.P. & Hilborn, D. (2000) Universal Soil Loss Equation (USLE), Factsheet. Ontario Ministry of Agriculture and Food, Agriculture and Rural Division; Factsheet,

Wischmeier, W.H. & Smith, D. (1978) Predicting rainfall erosion losses: a guide to conservation planning. The USDA Agricultural Handbook No. 537, Maryland.

Zouaoui, N., Mansour, R. & Ghali, A.E. (2019) Utilisation du modèle PAP/CAR et du SIG pour un zonage du risque d'érosion hydrique. Exemple du bassin versant de Tessa (Tunisie). *Rev. Int. Geomat.*, 29, 361–380. https://doi.org/10.3166/rig.2020.00096

THE FAVORABILITY FOR AEROIONOTHERAPY ON TWO TOURISTIC RESORTS FROM THE EASTERN FLANK OF ROMANIAN CARPATHIAN MOUNTAINS

Constantin ROŞU[1]* 📷, *Dumitru MIHĂILĂ[1]* 📷, *Petruţ-Ionel BISTRICEAN[1]* 📷, *Alin PRISACARIU[1]* 📷, *Emilian-Viorel MIHĂILĂ[2]* 📷, *Andrei MIHALACHE[1]* 📷, *Carmen BOICIUC[1]* 📷

ABSTRACT

Knowing the spatiality and temporality of the air ionization levels in different Romanian tourist resorts is necessary for the real appreciation of their climatotherapeutic potential.This study captures sequences of the air ionization process in two tourist resorts in the Subcarpathians of Moloava, in correlation with the values of meteorological elements (temperature, humidity, cloudiness and wind). Measurements were carried out during three consecutive days for each resort in January, April, July and October 2022, in the time interval 7.00h - 21.00h. The concentration of negative and positive air ions was recorded hourly, at a characteristic point for each resort. The annual air ionization regime showed a maximum in July, a minimum in January and higher values in October than in April. The average air ionization values ranged from 787 air ions cm^{-3} at Bălţăteşti to 821 air ions cm^{-3} at Târgu Neamţ, and the unipolarity coefficient (k), from a minimum of 0.78 at Tg. Neamţ to 0.90 at Bălţăteşti. Air ionization variability was positively correlated with air temperature, relative humidity and wind speed. The average values of air ionization in April - July, when k ranged between 0.6 and 1.2, demonstrate that the atmosphere of Bălţăteşti and Târgu Neamţ resorts can be therapeutically exploited by aeroionotherapy, in the summer season.

Key-words: *air ionization, aeroionotherapy, unipolarity coefficient, balneoclimatic tourism*

1. INTRODUCTION

Air ionization is a dynamic, continuous and variable process naturally generated by cosmic radiation, atmospheric electrical discharges, meteorological processes (Tang et al., 2011), water falls, spontaneous vegetation, etc. and strongly influenced by human activities (Mihăilă, 2014). The air we breathe contains atmospheric ions, which can influence both our mood and health (Enache, 2017). In 1751, Franklin made the first observations of atmospheric electricity, while Lemonier (1752) demonstrated that an electric charge could appear in the atmosphere, even under clear skies. Lemonier was also the first to discuss the possible effects of atmospheric electricity on humans and plants (cf. Licht, 1964).

The positive role of air ionization on humans has been researched since 1910 by Steffens (cf. Licht, 1964). In the 1930s, Ladenburg and Pantheinier continued these studies, which were deepened by Bricard in the 1950s. Subsequent studies (Winsor and Beckett, 1958; Krueger and Reed, 1976) confirmed the benefits of negative air ions in reducing the spread of viruses and bacteria, as well as in the complementary treatment of some medical conditions.

Subsequent research (Minth, 1963; Tromp, 1974; Kruger, 1976 şi 1985; Gates, 1980; Breton, 1994; Daniels, 2002; Hairong, 2005; Ji, 2007; Li, 2011; Mao, 2014; Hui, 2020; Mihăilă, 2023) has validated the connection between the phenomenon of air ionization and its multiple biological effects on organisms.

[1]*Department of Geography, „Stefan cel Mare" University of Suceava, Romania; dumitrum@atlas.usv.ro, petricabistricean@gmail.com, alinprisacariu@gmail.com, andreimihalache590@yahoo.com, carmen.boiciuc85@gmail.com*

[2]*Faculty of Computer Science, "Alexandru Ioan Cuza" University; Iaşi, Romania, emilian955@gmail.com*
*Corresponding author: rosuconstantin2007@gmail.com

Lately, research has begun to explore air ionization in connection with tourist activity (Jianwu și Jiayuan, 2002; Wang, 2003; Yao, 2005; Wu, 2006; Song, 2008; Tan, 2010; Deng, 2019), with a particular focus on air ionization in spa resorts, which have become focal points for aerometric analysis and bioclimatic assessments. These researches have highlighted the connection between the presence of air ions and the level of pollution, as well as the negative impact of the lack of negative air ions on health (Enache, 2017; Deng, 2019). Today, air ions are recognized as essential components of good air quality, and are a significant therapeutic natural resource with importance in health tourism and ecological assessments (Ling, 2019). However, research on the regime and spatiality of air ions is punctual, brief, both at the international level and in Romania.

Air ionization research in different cities or places of attraction for tourists started in our country relatively late (Deleanu and Elges, 1967) and then continued sporadically (Deleanu and Mozes-Lörincz, 1975; Teodoreanu et al., 1984) until the revolution in December 1989, which allowed Romanian research in the field to open up to new perspectives. After 1990 studies on air ionization in different tourist resorts or cities were few and were carried out by Enache 1990, 1999, 2005, 2017, Prisacariu et al., 2023; Mihăilă et al., 2023. For the territory of Romania, many aeroionometric studies are needed to be able to cover the existing gaps in the current research in this field. However, there are limitations in research related to the equipment, the available human resources and the fact that this kind of research is time-consuming, budget-consuming and often does not provide the expected spectacular results.

Starting from the foundation of previous research on atmospheric air ionization, this study brings the first results in the history of observations regarding the temporal coordinates of air ionization in the resorts of Bălțătești and Târgu Neamț. It is a study that, for the first time, places the air ionization from the two stations on the air ionization map in Romania which is still under construction. The main aim of the study is to identify the most favorable conditions during a day and a year for the practice of aeroionotherapy in the two resorts.

The research objectives of this study are 3: *i)* to evaluate the meteorological conditions on the days when aeroionometric measurements were carried out, in order to determine the role played by meteorological elements on air ionization, *ii)* to determine the minimum, average, maximum levels of negative and positive air ions in the most representative months of the year (January, April, July and October), and the average levels of k, in order to determine if, and when, during one year, aeroionotherapy can be practiced in the researched resorts and *iii)* to highlight the diurnal regime (hourly interval 07:00h– 9:00h) of air ionization and k, in order to identify the hourly intervals with the most favorable conditions to benefit from the aeroionotherapy properties of the atmosphere, by tourists who come for relaxation, cure and treatment in Bălțătești and Târgu Neamț resorts.

2. MATERIALS AND METHODS

2.1. Study area

Bălțătești and Târgu Neamț are two balneoclimatic resorts located in the northeast of Romania, in the subcarpathian region. The specific landscape is wooded hills and mountains. The resorts are located in the Neamț Depression and belong to the Bison Land, a tourist region known for its natural and cultural heritage: parks and nature reserves, salt springs, monasteries, memorial houses, museums (**Fig. 1**).

Bălțătești resort is located at an altitude of 457 m on the contact between the Stânișoara Mountains (700 - 800 m), well wooded, to the west and the Moldavian Subcarpathians (400-500 m), covered with deciduous forests and orchards, to the east. The resort has mineral waters (chlorinated, sulfated, iodized, brominated with a high concentration of salts) with curative and therapeutic qualities in the treatment of locomotor disorders, neurological disorders, related disorders, gynecological diseases. The average annual temperature is 8.2°C, the atmospheric circulation is moderate and marked by the presence of foehn processes, the bioclimate is optimal, and the medicinal salt of Bălțătești is appreciated in the treatment of many rheumatic and gynecological diseases.

The resort has a treatment base, the balneophysiotherapy and medical recovery sanatorium "Dr. Dimitrie Cantemir" which is equipped with modern installations for electrotherapy, showers, massages, aerosols, gynecological treatment, medical physical culture and recuperation, hydrokinetotherapy pool. The resort has an accommodation capacity of 354 beds and was visited by 5.630 tourists in 2022 (http://statistici.insse.ro/, accessed 2023).

The Târgu Neamţ resort is located in the northern part of the Neamţ Depression, in the Ozana valley, at an altitude of 365 m. The resort town is guarded by hilly heights with altitudes of 400 - 500 m. In Culmea Pleşului the altitude reaches 623 m. The hilly peaks are covered with deciduous and coniferous forests. Târgu Neamţ is a destination with important tourist attractions: Neamţ Citadel, Ion Creangă Memorial House, Agapia, Filioara and Neamţ monasteries. The tourist resort has 36 accommodation structures, which provide an accommodation capacity of 700 beds. In 2022, 21.446 arrivals and 21.521 overnight stays were recorded in the resort town of Târgu Neamţ.
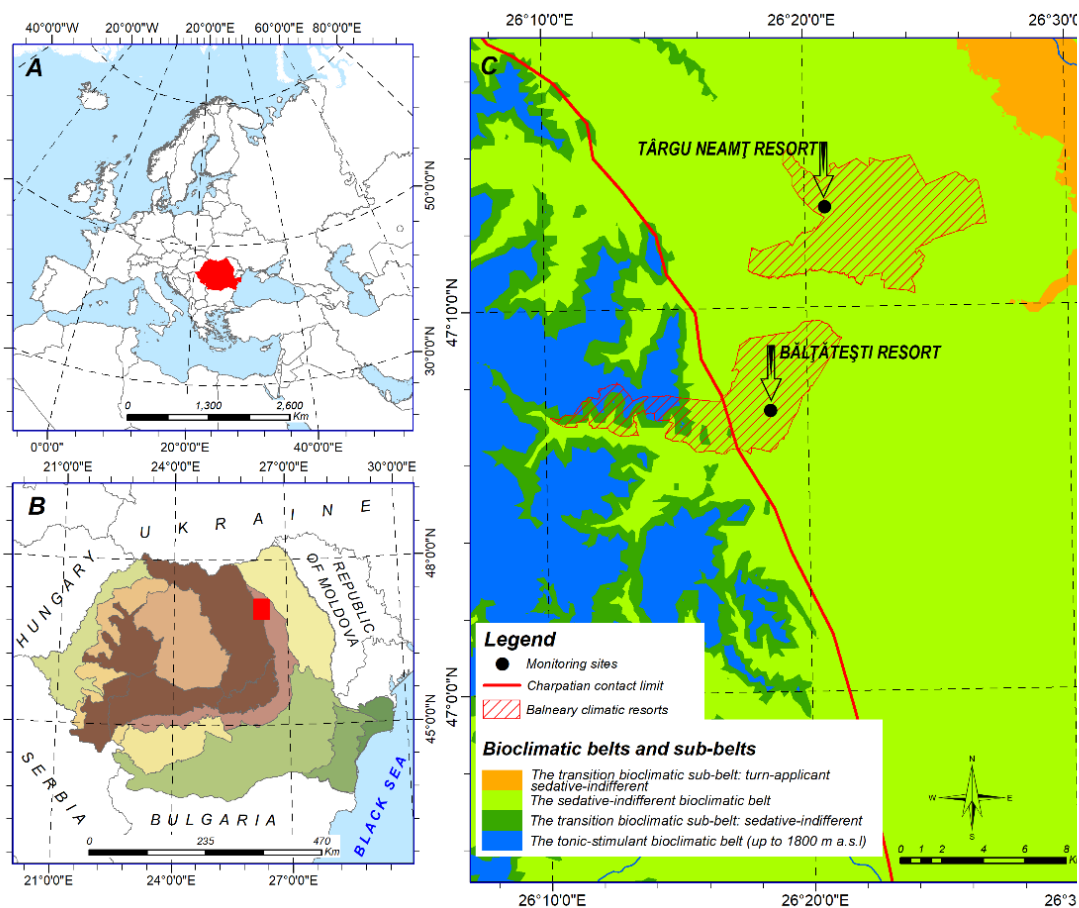
Fig. 1. Geographical localization of the places where aeroionometric measurements were made, in the tourist resorts of Bălţateşti and Târgu Neamţ

The locations where we carried out aeroionometric measurements in the two resorts were chosen according to the principle of their representativeness, from the point of view of our monitoring: absolute altitude (421 m in Bălţăteşti, respectively 376 m in Târgu Neamţ), absence of water courses, and tourist and recreational relevance (both points were located in parks near tourist attractions: the Sanatorium "D. Cantemir" in Bălţăteşti and the Neamţ Fortress in Târgu Neamţ), thus ensuring a comprehensive and representative approach for these measurements.

2.2. Methods and means

Aeroionometric measurements were carried out with the PC Connectable Highly Accurate Air Ion Counter Tester COM-3200 PRO II, which is equipped to record air temperature (with an accuracy of +/-1 %,) and relative humidity, with an accuracy of +/- 5 %, in addition to air ion levels. The data obtained were then downloaded, processed and analyzed using Microsoft Excel software. The device used has a certificate attesting to the metrological verification by its manufacturer.

Measuring and analyzing air ionization is difficult because the atmosphere is not an electrically uniform environment, but is constantly changing. Moreover, air ionization is susceptible to rapid value changes, due to variations in local weather conditions as a consequence of atmospheric circulation (Enache, 2017).

For precision measurements of air temperature and relative humidity at the 1.5 m level, we used the CEM DT-171 data logger sensor and the Windmaster 2 anemometer for wind speed determination. The cloudiness was visually assessed and expressed in oktas.

The analysis of Pearson correlation coefficient values between data series of aeroion levels (negative / positive) and determined meteorological elements, highlighted the role of some of them in the air ionization process.

In order to further investigate the interaction between meteorological elements and air ionization levels, we used the principal component analysis (PCA).

2.3. Data obtained

At each observation site in the two resorts, we obtained 45 hourly values of air ionization for January, April, July and October. Average values were calculated and minimum/maximum values of air ionization (negative n- and positive n+ ions) were extracted, as well as air temperature, relative humidity, cloudiness and average wind speed.

2.4 Research methodology

In order to determine the aeroelectric properties of Bălțătești and Târgu Neamț, we carried out measurements in each season, taking January, April, July and October as reference months. Observations were carried out for three days in each resort, hourly from 7:00h to 21:00h. Hourly determinations were carried out as follows: up to the 15th minute of each hour, we measured n-, and up to the 30th minute of each hour, we measured n+. Practically, on each time interval, in each resort, for each category of ions (n- / n+), 225 minutes of determinations were carried out, and cumulatively (in the 12 days of the 4 months considered), for each resort and category of air ions, each 2700 minutes of determinations. Due to the existence of only one air ion monitor, the measurements at the two resorts were asynchronous. By choosing in the determinations only days with stable weather, anticyclonic, without precipitation, with moderate cloudiness and with reduced atmospheric dynamics, we obtained, even in the conditions of asynchronous determinations, levels of ionization that can be analyzed comparatively for the two resorts.

3. RESULTS

3.1. Meteorological and micrometeorological conditions under which observations were made. Influence of weather on air ionization

3.1.1. Correlation between air ion levels and meteorological elements for the entire observation period based on their correlation analysis

During 2022, while the observations were being carried out, the weather was changeable in the two resorts.

a

b

c
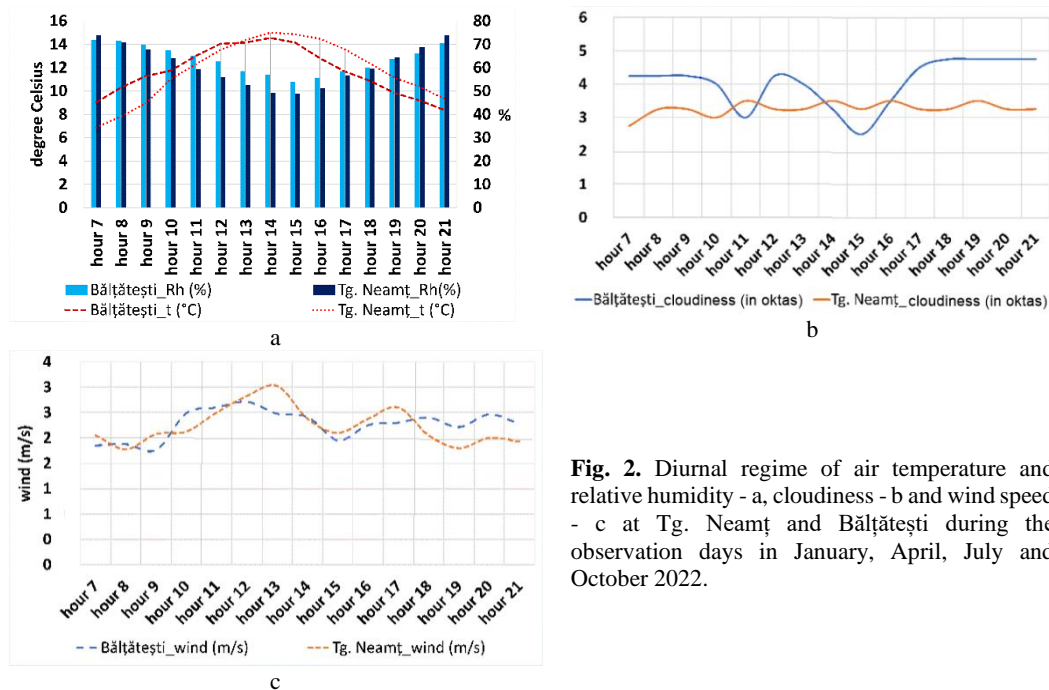
Fig. 2. Diurnal regime of air temperature and relative humidity - a, cloudiness - b and wind speed - c at Tg. Neamţ and Bălţăteşti during the observation days in January, April, July and October 2022.

The air temperature showed a high variability during the whole period analyzed (between -1.0°C and 22.8°C). Although the variability of this element was high, the average temperature differences between the two resorts were small (the average temperature value was 11.4°C in Târgu Neamţ and 11.6°C in Bălţăteşti). Relative humidity was higher in both resorts in January and October (over 70%), and significantly lower in July (50%). It is worth mentioning that the average relative humidity value during the whole period was higher in Bălţăteşti (63.4%) than in Târgu Neamţ (54.1%). The average hourly cloudiness fluctuated during the 12 days of observations made between 2.5 and 4.2 oktas in Bălţăteşti and between 2.5 and 3.5 oktas in Târgu Neamţ. The wind had close average values between the two resorts, its speed varying between 2.5 and 3.5 m s^{-1} (**Fig. 2**). These meteorological differentiations are due to the geographical setting at the microscale, which is different for the two monitoring points, and which had the ability to introduce these differentiations. They can be produced in the case of visual observations for cloudiness by a certain degree of subjectivity induced by the observer's attention, by his experience, or in the case of observations with sensors or other devices, by the asynchrony of the observations.

The geographical location of the two resorts in the same Subcarpathian depression, influenced both the local topoclimate and the level of air ionization. The analysis of Pearson correlation coefficient values, between the data series of (negative/positive) air ion levels and air temperature, revealed the importance of temperature in the air ionization process. Thus, in the two resorts, negative air ionization levels showed significant positive correlations with air temperature, the Pearson correlation coefficients between negative air ionization and air temperature being 0.55. Positive air ionization levels also correlated positively with air temperature, the Pearson correlation coefficients between positive air ionization levels and air temperature being 0.5.

3.1.2. Correlation between air ion levels and meteorological elements for the whole observation period, based on Principal Component Analysis (PCA)

In Bălţăteşti resort, the analysis of the main meteorological elements reveals that they contribute 66.3% to the total variation of air ionization (**Fig. 3a**).
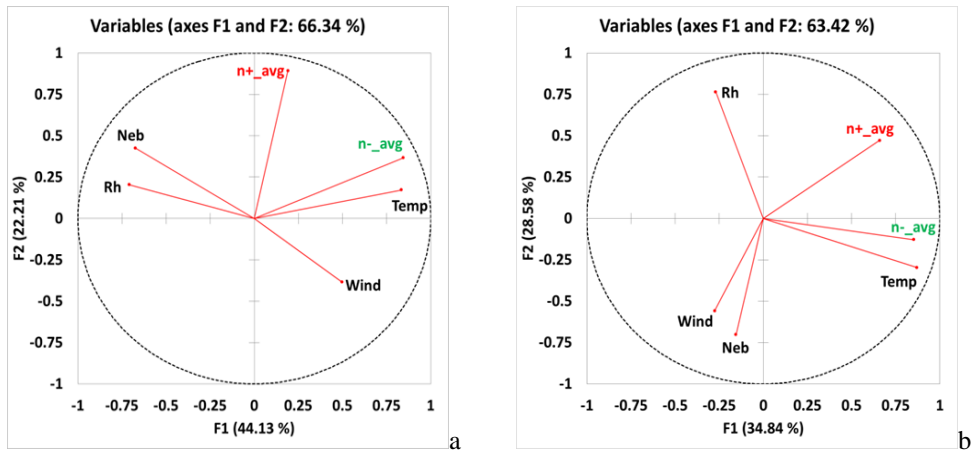
Fig. 3. Principal Components Analysis (PCA) between the levels of air ionization and meteorological elements in the tourist resorts of Bălțătești (a) and Târgu Neamț (b)

A positive association is observed between air ionization and air temperature, but also between air ionization and wind speed. Air temperature is more strongly correlated with negative air ionization, while the relationship with positive air ionization is less pronounced. A fluctuating but positive correlation in strength between air ionization and wind, is evident. Cloudiness and humidity show correlations of varying strength, but of negative sign with negative and positive air ionization.

In Târgu Neamț the influence of meteorological elements on air ionization is 63.4% (**Fig. 3b**). Also, in this resort temperature has a direct, stronger correlation with negative air ionization (weaker with positive air ionization), and wind and cloudiness were inversely correlated in value with negative and positive air ion levels. Between humidity and the air ionization process, as in Bălțătești, we note negative correlations for both air ion categories.

3.2. Air ion concentration in the air of the investigated resorts

3.2.1. Annual average values of negative and positive air ion levels, total air ionization and unipolarity coefficient

The data obtained from the two resorts show similarities in air ionization values, indicating a relatively similar natural environment. However, the slight differences observed between these two sites can be attributed to specific local factors, such as altitude and relative location to the forest (at Târgu Neamț, approx. 100 m), which, although subtle, may influence differently the air ionization processes and thus, the measurement results. The average values of total air ionization (n-+n+), during the 4 months of measurements, were 821.3 air ions cm^{-3} at Târgu Neamț and 786.6 air ions cm^{-3} at Bălțătești (**Fig. 4**). Total air ionization (n- + n+) was higher in Târgu Neamț than in Bălțătești, on average by 34.7 air ions cm^{-3}.
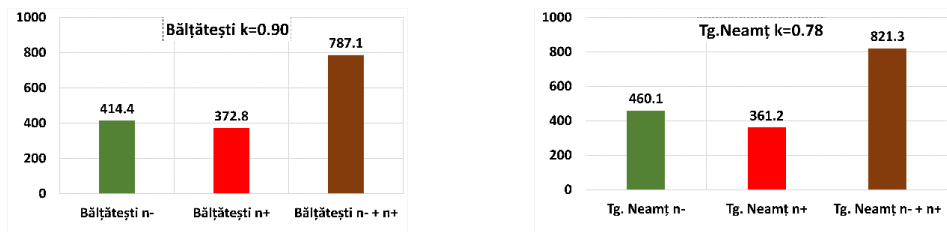
Fig. 4. Negative, positive and total air inization levels for the whole observation period from 2022 at Bălțătești and Târgu Neamț.

Negative (n-) air ionization was higher at Târgu Neamț than at Bălțătești (by 46.3 air ions cm^{-3}), and positive (n+) air ionization was higher at Bălțătești than at Târgu Neamț (by 11.6 air ions cm^{-3}).

These data indicate that the atmosphere in Târgu Neamț resort had a higher average negative air ionization, while Bălțătești resort had a higher average positive air ionization. However, the total air ionization is higher in Târgu Neamț.
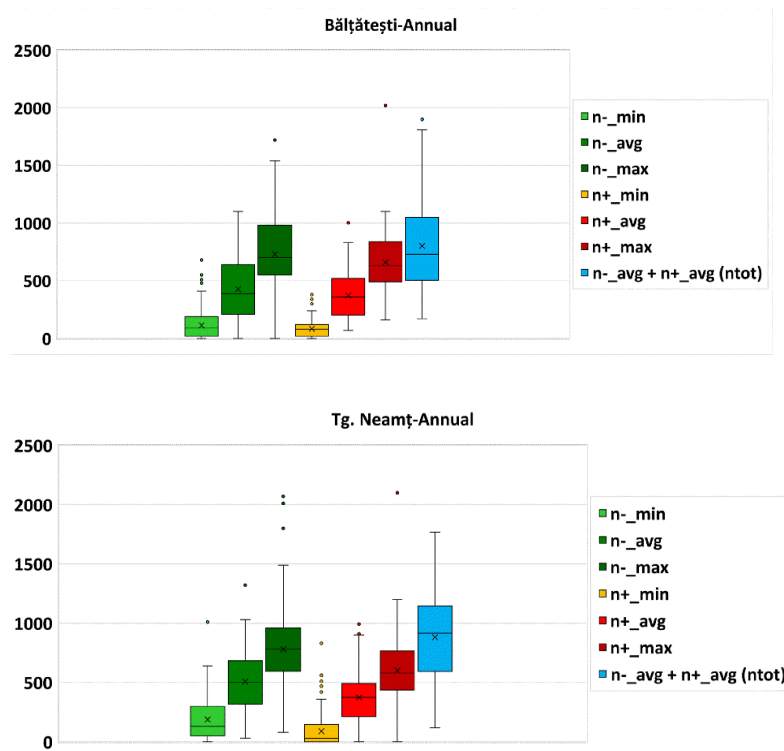
Fig. 5. Analysis of the variability of the number of negative, positive and their total number in Bălțătești and Târgu Neamț resorts during 2022

From the boxplots represented in **Figure 5**, it can be observed the whole range of air ionization values in the investigated resorts and also that the distributions of air ionization levels in Bălțătești and Târgu Neamț are almost identical. This approximate similarity of the air ionization levels is explained by the fact that the genetic and geographic determinants of air ionization are similar in the two resorts. The consequence in terms of air ionization is that local factors have a relatively similar impact on air ionization in the two studied resorts. Some differences related to the positions of 0 percentiles, lower quartiles, median quartiles, upper quartiles, 100 percentiles, outliers of positive and negative air ionization levels in the two resorts exist. The similarities, however, prevail and the differences are of nuance, rather than consistency and relevance.

3.2.2. The air ion levels in the median months of the four seasons indicate a minimum of 532 air ions cm^{-3} at Bălțătești and 418.8 air ions cm^{-3} at Târgu Neamț in January, and a maximum of 1205.8 air ions cm^{-3} at Bălțătești and 1121.2 air ions cm^{-3} at Târgu Neamț in July. Air ionization was higher in October (757.5 air ions cm^{-3} at Bălțătești, and 1054.8 air ions cm^{-3} at Târgu Neamț), than in April at both resorts (651.1 air ions cm^{-3} at Bălțătești and 690.3 air ions cm^{-3} at Târgu Neamț) (**Fig. 6**). In October, in the Subcarpathians of Moldova, there are still many warm summer days, with more active air ionization processes in the atmosphere than in April.
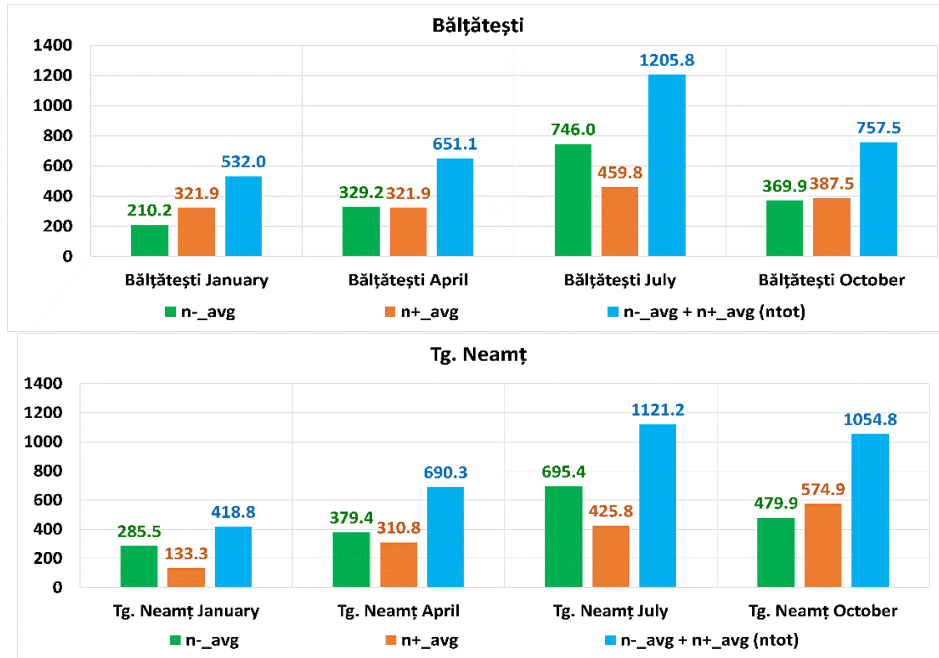
Fig. 6. Air ion levels (cm^{-3}) in the median months of the 4 seasons at Bălțăteşti and Târgu Neamț

The monthly values of the unipolarity coefficient k, ranged from 0.6 to 3.1 in Bălțăteşti, and from 0.5 to 1.5 in Târgu Neamț. The subunit values were recorded in July in Bălțăteşti, and in January and October in Târgu Neamț (**Fig. 7**).
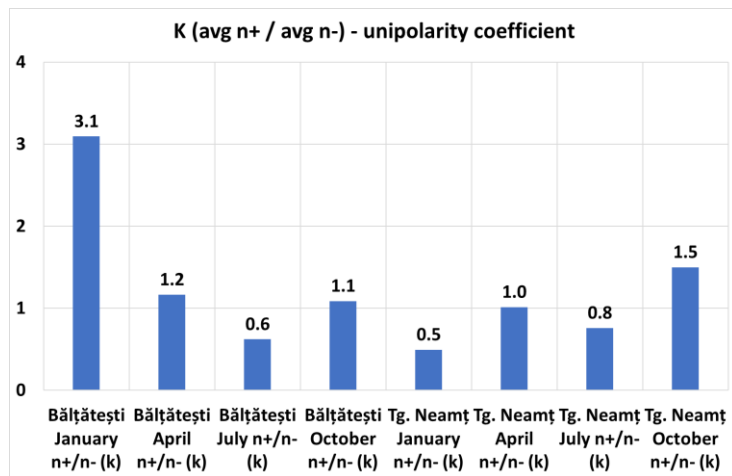
Fig. 7. Monthly values of the unipolarity coefficient k at Bălțăteşti and Tg. Neamț by months, in the two investigated resorts, in 2022.

A more detailed view of the distribution of air ion levels and k coefficient in the two resorts, during 2022, for the median months of each season in this year, can be followed with the boxplots (**Fig. 8** and **9**).
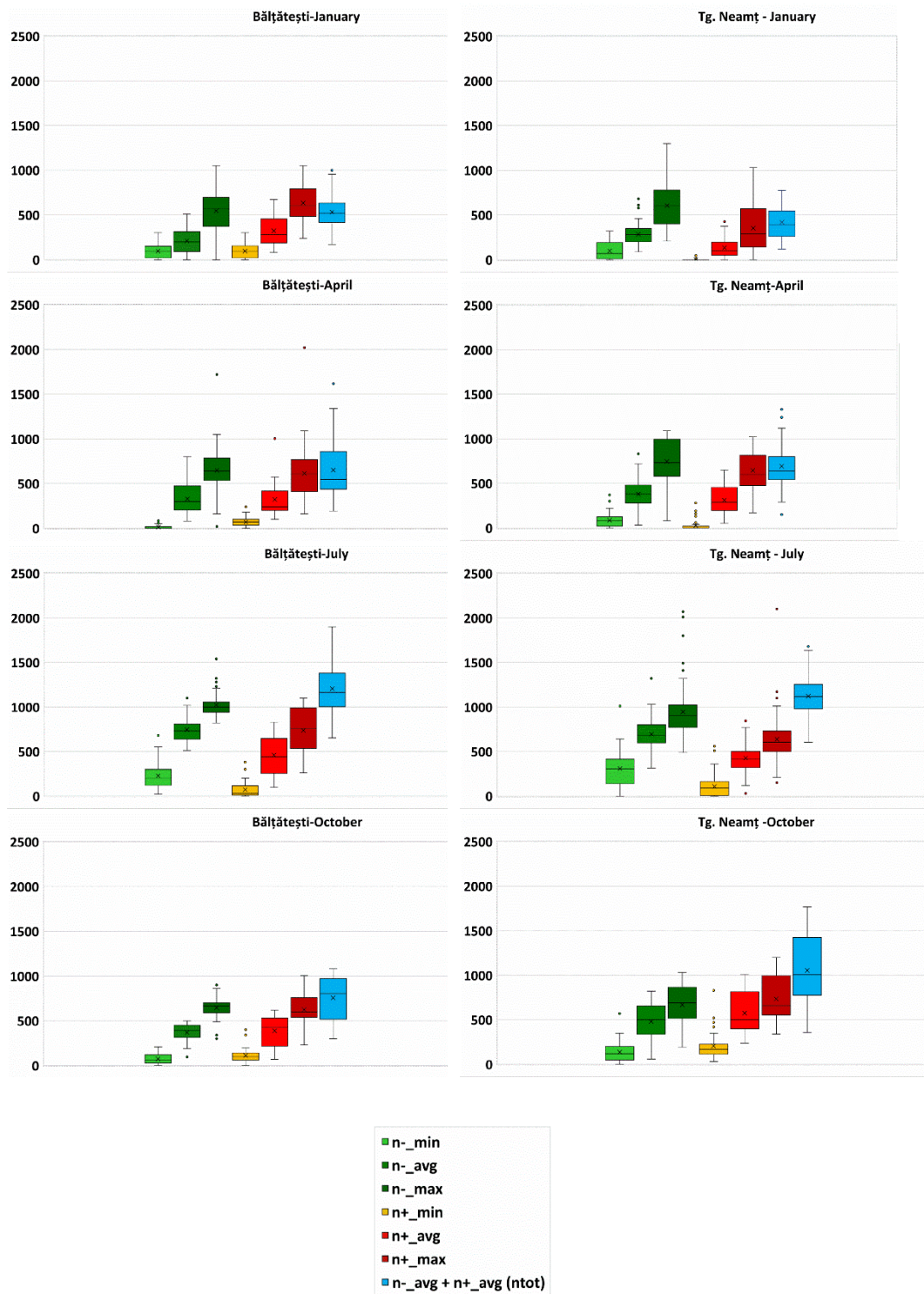
Fig. 8. Analysis of the variability of air ion levels (cm^{-3}) in Târgu Neamț and Bălțătești resorts, during the year 2022, in January, April, July, October.
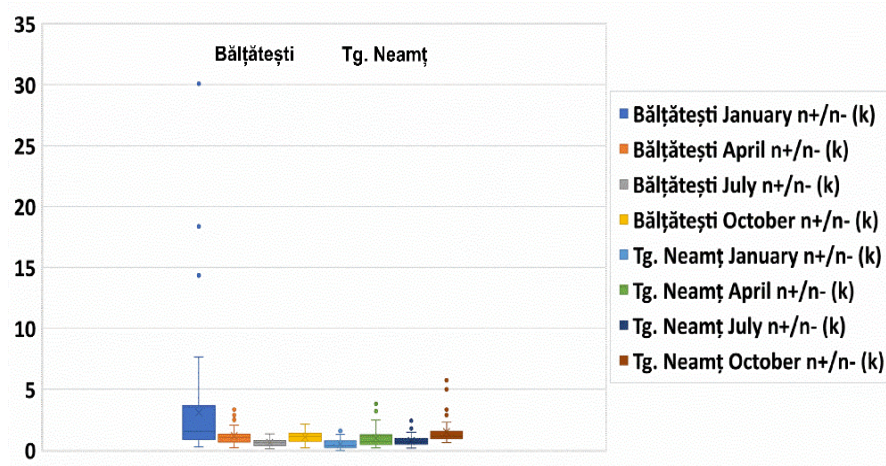
Fig. 9. Boxplot charts showing the full value spectrum of the unipolarity coefficient k, by month in the two resorts studied in 2022

The carefully analyzed **Figures 8** show the annual air ionization regime, peaking during the summer months. Negative air ionization was more intense and more variable as a process, in the atmosphere of Târgu Neamț resort, and positive in the atmosphere of Bălțătești resort. The total air ionization was very similar in the two resorts during the days of January, April and July, but, during the days of October in Târgu Neamț, it was more intense, compared to Bălțătești. From **Figure 9**, we can notice that the values of the unipolarity coefficients indicate a dominance of negative air ions during the summer months, making it favorable to practice aeroionotherapy in the two resorts. During the days of the cold season, the values of the unipolarity coefficients varied more, as can be seen from the boxplot for Bălțătești resort for January, or the one for Târgu Neamț resort for October (**Fig. 9**).

3.2.3. Daytime regime of negative, positive air ion levels, total number and unipolarity coefficient k at Bălţăteşti and Tg. Neamţ during the whole monitoring period in 2022

The daytime fluctuations of the averaged air ion levels and the k-coefficient for all days analyzed, can be seen in **figure 10**. We observe that air ion levels tend to reach higher values in the morning and towards midday (9:00 AM - 10:00 AM at Bălțătești, respectively 11:00h-12:00h at Târgu Neamț), when the statistics shown in the graph indicate a more pronounced maximum value. Then follows a slight decrease in the rate of the air ionization process around 14.00h, a slight increase in the rate of the process at 15:00h - 16:00h, after which the air ionization process decreases slightly, gradually towards the evening hours (20.00h – 21:00h). Also, we notice a more uniform distribution of the k coefficient during the day in Târgu Neamț, against a background of subunit hourly values (with a minimum around 17:00h– 18:00 h), while in Bălțătești for the first hours of the morning (7:00h-10.00h) and for 16:00h, superunit values of the k coefficient were determined.

The diurnal regime of air ionization is carried out on similar value coordinates imposed by the quasi-similarities between the factors participating in the generation of air ions in the atmosphere of the two resorts, and the differences are most likely given by the level of shading, shielding in relation to the solar rays of the horizon, at the monitoring points, the differences in the factors generating the local topoclimatic framework, the dynamics of the weather on the days of observations, which was not synchronous, but asynchronous, because several air ion counters were not available during the monitoring.

For a more detailed analysis of the *diurnal regime* of the air ionization process, we selected July as a case study, because it allows us to focus the observation results on the period of the year with the most intense tourist movement, and with the most important effects on the air ionization treatments they can benefit from.
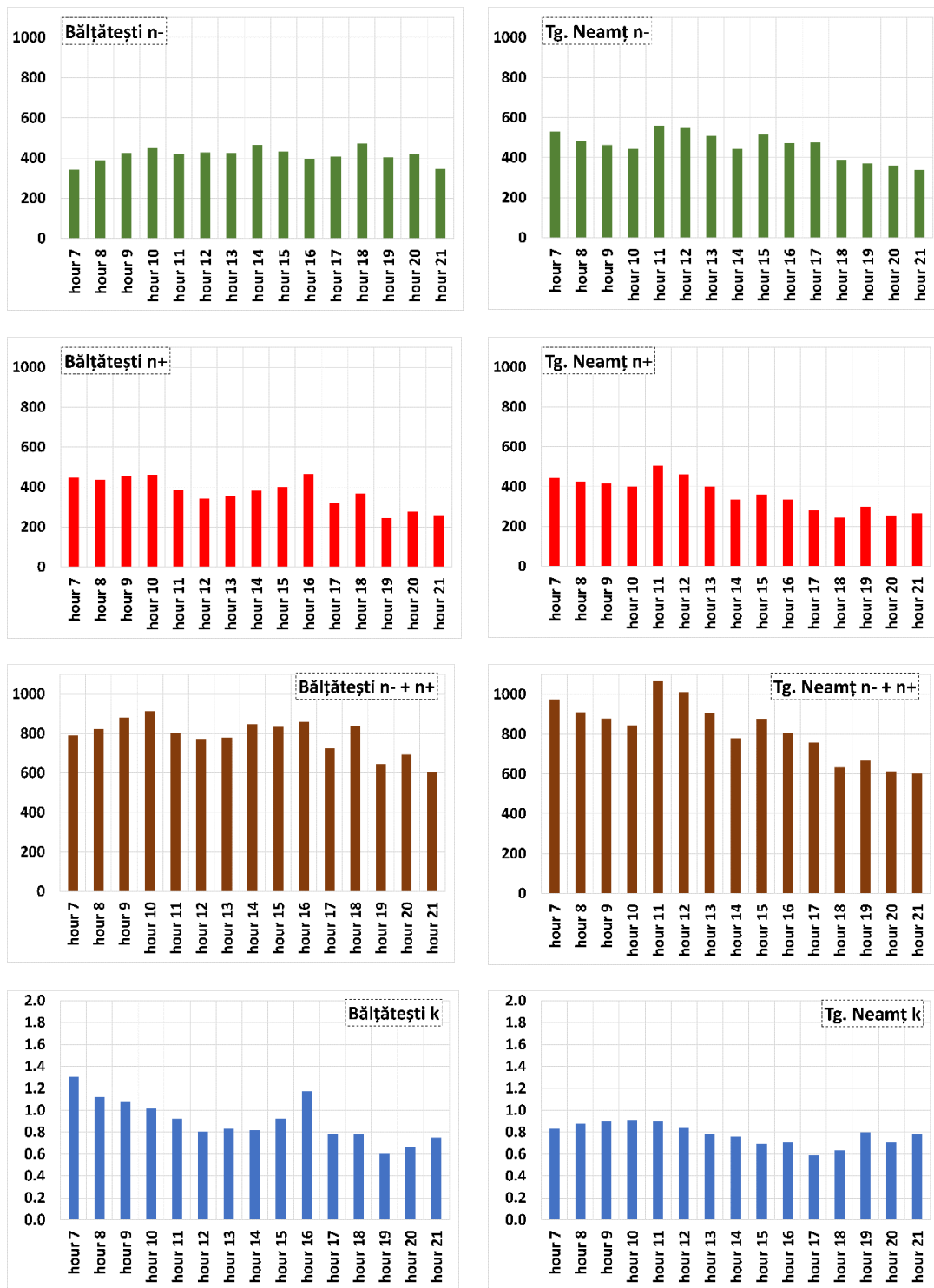
Fig. 10. Diurnal regime of negative, positive air ion concentration, total air ion number and unipolarity coefficient k at Bălţăteşti and Tg. Neamţ over the whole monitoring period from 2022.

The month of July corresponds to the highest average values of air ionization: 1400 air ions cm^{-3} at Bălțătești and 1200 air ions cm^{-3} at Târgu Neamț (**Fig. 11**). The maximum values of total air ionization were reached in the evening (18.00h) at Bălțătești and in the afternoon (15.00h) at Târgu Neamț.
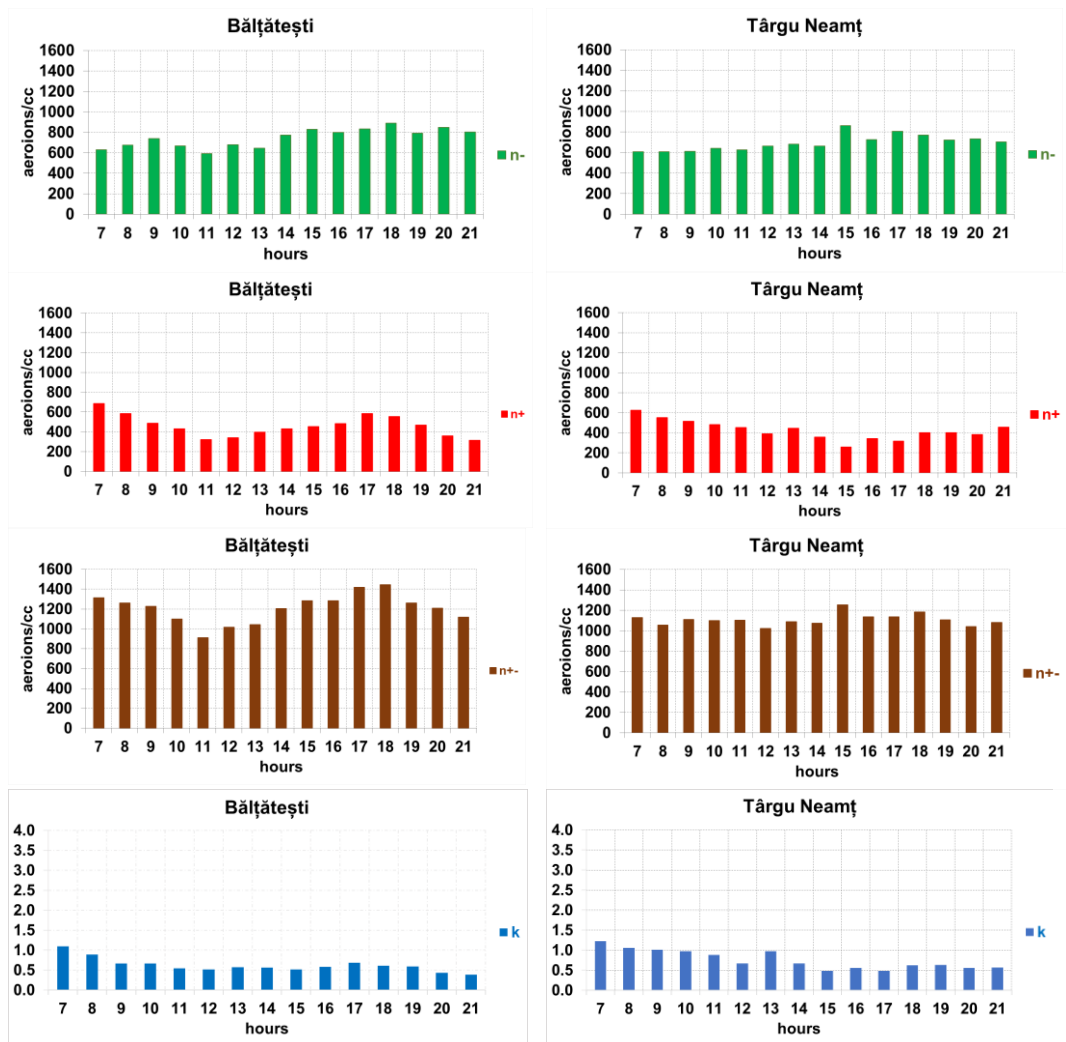
Fig. 11. The diurnal regime of the concentration of negative and positive air ions, the total number of air ions and the unipolarity coefficient k at Bălțătești and Tg. Ocna in the days of July 2022 when the monitoring was carried out.

Negative air ionization was maintained in the two resorts at values between 600 and 800 / 900 air ions cm^{-3}, throughout the observation hours. Positive air ionization ranged from 300 to 600 / 700 air ions cm^{-3}. We noted higher variability of air ionization at Bălțătești this month: average air ionization values ranged from 900 to over 1400 air ions cm^{-3}, compared to Târgu Neamț: 900-1200 air ions cm^{-3}. At Bălțătești, the total air ionization regime during the day, in July, was very clear (a minimum during 11.00h and a maximum during 18.00h), but at Târgu Neamț we did not notice a clear diurnal air ionization regime for this month.

The unipolarity coefficient, k, was subunit in the two resorts, in most of the observation hours, indicating a clean, sanogenous, aeroionized, predominantly negative air, suitable for balneotherapy but also for a wide range of outdoor tourist activities (**Fig. 11**).

3.2.4. Extreme values of air ion levels. Their analysis with reference to average levels

The extreme values of air ionization reached high values in both resorts (in April in Bălțătești, and in July in Târgu Neamț - **Tables 1** and **2**).

At Bălțătești negative air ionization reached a maximum of 1720 air ions cm⁻³ in April, and at Târgu Neamț 1800 air ions cm⁻³ in July. At Bălțătești, this value was reached against the background of an intensification of the wind speed (5 m/s) from the western sector, which favoured the advection of air rich in air ions from the surrounding wooded areas. In Târgu Neamț, the maximum level of negative air ionization can be attributed to the high temperature (26°C) and low humidity (55%), conditions favourable for the production and dispersion of air ions.

Table 1.

Parameters of air aeroionization in the tourist resort of Bălțătești, determined from observations made in January, April, July and October 2022.

Bălțătești	January		April		July		October	
	n-	n+	n-	n+	n-	n+	n-	n+
Minimum with the lowest value	0	0	0	0	20	0	0	0
Averages of minimums	60	115	136,7	134	589,8	315	96	70
Average	210	323	260	335	746	459,8	351,2	398,4
Median	228	253	296	244	773,3	454	388	421
Average maxima	434	536	550	562	889	685	480	619
Maximum with the highest value	1050	1050	**1720**	*2020*	1540	1100	860	1002

Table 2.

Air ionization parameters in the tourist resort of Târgu Neamț, determined from observations made in January, April, July and October 2022.

Târgu Neamț	January		April		July		October	
	n-	n+	n-	n+	n-	n+	n-	n+
Minimum with the lowest value	0	0	0	0	0	0	0	0
Averages of minimums	70,1	95,5	123,7	140,4	283,5	115,6	138	203
Average	290	169	360	416	678	470	483	557
Median	281	217	349,2	343,2	683	403	548,3	518
Average maxima	433,1	559,4	744	695,8	912,5	644,1	616,9	716
Maximum with the highest value	1300	1030	1090	1360	**1800**	*2100*	1200	1200

Positive air ionization reached a maximum of 2020 air ions cm⁻³ at Bălțătești, and 2100 air ions cm⁻³ at Târgu Neamț. At Bălțătești, the maximum value was recorded on the same day and at the same time as the maximum negative air ionisation. For Târgu Neamț, the peak of positive air ionization occurred on the same day as the peak of negative air ionization, but a few hours later, in the evening, in a context characterized by high temperatures (23°C) and wind speed exceeding 4 m/s. The minimum values were below 0 air ion (n- and n+) in both stations in almost all the months we monitored.

The Bălțătești resort is located 92 m higher than Tg. Neamț and it would have been expected that the air ionization levels would be higher in Bălțătești. However, it appears that in the higher levels of air ionization from Tg. Neamț the presence of the hydrographic axis of the Ozana river which favors an easy and constant gravitational drainage of air volumes coming from the west, from the Stânișoarei peaks to the east-southeast, along the axis of the valley, somewhat less cloudiness, combined with a longer duration of the Sun's brilliance, make the process of air ion production to be somewhat more intense at Tg, Neamț. This occurs despite the fact that the socio-economic activities (consumers of especially negative air ions, through the generated atmospheric pollutants) from Tg. Neamț are more intense than in Bălțătești.

4. DISCUSSION

4.1. Influences of meteorological factors on air ionisation

Regarding the relationship between air ionisation and air temperature, our study showed that an increase in air temperature usually leads to an intensification of the air ionisation process. Thus, the highest air ionisation values were recorded in the warmest month (July). These correlations are also highlighted in other researches (Crețeanu and Frimescu, 1961, 1963), which indicate an intensification of the number of small ions with increasing temperature. Also, Wang et al. (2004) find a positive correlation of air ionization with air temperature in the range 5-40°C at 35% humidity, but did not observe a significant influence of humidity. Wang finds that with increasing temperature, the kinetic energy of molecules or atoms increases, and the ability of oxygen to be ionized increases. Hui et al. (2020) observes different correlations between seasons: positive in spring and negative in summer and autumn. On divergent positions are Tingting et al. (2014) and Pengfei et al. (2015), who identify an inverse correlation between air ionization and air temperature.

We found that relative humidity with high values induces a decrease in the air ionization process. Humid air does not favour the dispersion of air ions in the atmosphere, leading to a lower concentration of negative or positive ions. The negative correlation between air ionisation and humidity has been shown by earlier studies (Geekel, Simpson cited by Schweidler and Kohlrausch, 1923), which observed a decrease in air ion concentrations with increasing air humidity. Deleanu (1986) also identifies an inverse dependence of ionization on humidity, but a moderate one, and Enache (2017) concludes that under high humidity conditions, the number of negative air ions decreases, but the number of positive air ions increases.

We note that cloudiness can affect the distribution and dispersion of ions in the atmosphere. In general, a clear sky day allows for better air ionisation, as high solar radiation helps to boost the air ionisation process. In contrast, on days with dense clouds or haze, air ionisation was lower. Similar results have been obtained in other studies (Wu et al., 2006; Ji, 2007; Tang et al., 2011; Li et al., 2011; Mao et al., 2014).

Wind can influence the distribution of ions in air. Strong wind can disperse ions and promote pulsating air ionization, depending on its structure. Lack of wind or weak wind can lead to the accumulation and concentration of ions in a confined space. In our study, at Bălțătești, the maximum values of air ion concentrations coincided with the highest wind speeds (5 ms^{-1}). The positive correlation between air ionization and wind has been confirmed by other research (Wang et. al., 1991; Ye et al., 2000; Qi et al., 2011; Si et al., 2014). Wind origin is also important in the process of air ionization: wind blowing from forest or natural environments (meadows, waters) generates increasing air ionization (Wu, 1996; Enache, 2017).

4.2. Practicability of aeroionetherapy in the researched resorts

The significantly high values of total air ionization in July in Bălțătești and Târgu Neamț resorts (over 1000 air ions cm^{-3}), correlated with subunit values of the unipolarity coefficient k, favour the practicability of aeroionotherapy in these resorts, in association with other climatotherapeutic procedures (air cure, ground cure, air bath, heliotherapy, hydrothermotherapy etc.) (Laza, 2000; Amiranashvili et. al., 2013).

According to other studies (Lazzerini, 2018, cited by Shu-Ye et al., 2018), the concentration exceeding 1000 negative air ions cm^{-3} was considered as threshold value for stimulating the human immune system. The effects of aeroionetherapy, demonstrated by extensive studies, have highlighted its role on the cardiovascular and respiratory system (Iwama et. al., 2002; Ryushi et. al., 1998; Ju et al., 1997; Wiszniewski, 2014). This reconfirms the climatotherapeutic potential of the local atmosphere, providing a valuable opportunity for those who wish to benefit from the positive role of air ionization in the process of prophylaxis, restoration of physical and intellectual capacity or healing of some diseases (Deng, 2019).

4.3. Diurnal regime of air ionisation

The maximum air ionisation values are recorded in the first part of the day, between sunrise and midday. This may be due to several factors, such as the increasing solar radiation during this period and the photosynthesis process of plants, which contributes to the release of negative ions into the atmosphere. The lowest values of air ionisation are observed in the midday (January and April) and evening (July and October). The U-shaped pattern with high air ionization values in the early morning and evening hours, has also been observed in other studies (Wu, 2001; Wang, 2003; Xu, 2004; Zhao, 2007; Hui et al., 2020).

4.4. Comparisons with other studies

Data from the most recent study on air ionization in the region at the Carpathian - Suceava Plateau contact carried out for the resorts of Solca, Cacica and Gura Humorului in July 2022 (Mihăilă, 2023) show a number of differences, but also similarities with the average values of air ionization in the resorts of Bălţăteşti and Târgu Neamţ.

The average values of total air ionization are higher at Bălţăteşti and Târgu Neamţ (1121.2 air ions cm^{-3} and 1205.8 air ions cm^{-3}, respectively), than at Solca and Gura Humorului (1052 air ions cm^{-3} and 1068.2 air ions cm^{-3}, respectively), but lower than at Cacica (1467.4 air ions cm^{-3}).

Negative air ionization is similar in Bălţăteşti and Cacica (746 air ions cm^{-3}, respectively 771 air ions cm^{-3}), with lower values in Târgu Neamţ (695.4 air ions cm^{-3}), Solca and Gura Humorului (612 air ions cm^{-3}, respectively 540.2 air ions cm^{-3}).

Positive air ionization has comparable values at Târgu Neamţ, Bălţăteşti, Solca and Gura Humorului (values between 425 and 528 air ions cm^{-3}) and higher values at Cacica (696 air ions cm^{-3}). Enache (2016) mentions average air ionization values of 1050 air ions cm^{-3} and a unipolarity coefficient of 0.88 at Bălţăteşti, and at Soveja, another subcarpathian resort, 1200 air ions cm^{-3}, respectively a k of 0.9. total air ionization.

Other studies carried out in the relatively recent past in balneoclimatic resorts in Romania have shown quantitative and qualitative differences between balneoclimatic floors: at Sinaia total values of 800 air ions cm^{-3} were recorded (Frimescu, 1964), at Sovata they exceeded 1100 air ions cm^{-3}, at Vatra Dornei the concentration of air ions varied between 951 and 1615 (Pascu and Ştefănescu, 1969), at Băile Herculane the total ionization exceeded 1000-2000 air ions cm^{-3} (Brînză, 1974), and on the Black Sea coast, the values of air ionization varied between 980 ions cm-3 at Sf. Gheorghe, and 1180 ions cm^{-3} at Sulina (Enache, 1978). Typically, in regions located at average altitudes of about 1000 m, a uniformity of data is observed, with values between 900 and 1300 air ions cm^{-3} (Enache, 2017).

4.5. Limitations and future research directions

This study is based on asynchronous measurements carried out at Bălţăteşti and Târgu Neamţ over a limited period of time, consisting of three consecutive days in January, April, July and October 2022. The study was not synchronous in the two resorts, due to the limitation induced by the existence of only one air ion counter used in the monitoring. In our analysis, we analyzed the local air ionization process in correlation and under the influence of four meteorological elements: temperature, relative humidity, cloudiness and wind.

In order to get a more comprehensive view and to show the annual and diurnal course of air ionization, it is necessary in the future to extend the measurement period, including the addition of additional days and months of the year (i.e. hours of the day) to analyze this process. The impact of air pollution on air ion concentrations, and the influence of air ionisation, its prophylactic and therapeutic effects, in the surveyed resorts, on tourists could also be investigated through questionnaires / surveys focused on this issue.

There are studies and reports in this regard showing that smoke and dust caused by human activity increase the likelihood that positive and negative ions annihilate each other, which reduces the

concentration of negative ions (Deng, 2019), that the level of negative air ions depends on the degree of air pollution (Amiranashvili, 2013), and that negative air ions can reduce the number of respirable and inhalable dust particles (Tanaka, 1996; Lazzerini, 2018). The high efficiency of negative air ions in removing PM_{10} and $PM_{2.5}$ has been confirmed in others research (Daniels, 2002; Lee et al., 2004; Grinshpun et al., 2005).

By combining air ionization and air quality data, we will obtain a more detailed picture of the valence of the local air environment, whose peculiarities result from the interactions between determining factors (Shu-Ye, 2018). This approach would provide a solid basis for identifying air quality protection and improvement measures to optimize the therapeutic benefits of air ion therapy (Lazzerini, 2018; Hui, 2020).

5. CONCLUSIONS

Measurements carried out in Bălțătești and Târgu Neamț resorts during January, April, July and October 2022, focused on environmental and weather conditions as factors determining the air ionization process. Measurements of air ion levels in the 4 months aimed to determine the major features of the annual regime of air ionization, and the hourly measurements aimed to outline the features of the daytime regime of this process.

Weather conditions during the observation period had an impact on the air ionisation process. Thus, the influence of the meteorological factors taken into account (temperature, humidity, cloudiness and wind speed), on air ionization was 66.3% at Bălțătești and 63.4% at Târgu Neamț. Air temperature was the element with the most pronounced impact on air ionisation. The highest values of air ionization were reached in the context of high thermal values, the Pearson coefficient indicating a positive correlation (0.5) between the process of air ionization and temperature. Wind speed was another meteorological element with a direct, positive influence on air ionisation. The maximum air ionisation values recorded overlapped with periods of wind intensification (wind speeds above 4-5 ms^{-1}), while humidity and cloudiness were negatively correlated with air ionisation with little impact on air ionisation.

Over a year, summer is the season with the highest degree of air ionisation. Average air ion levels in the atmosphere rose in July to 1100 - 1200 air ions cm^{-3} at Târgu Neamț and Bălțătești. These values highlight the most favourable time of the year for air ionisation therapy. In extenso, in the warm season of the year, the maximum values of air ionization generated negative air ion levels reaching 1720 air ions cm^{-3} at Bălțătești, 1800 air ions cm^{-3} at Târgu Neamț, and positive air ion levels reaching 1720 air ions cm^{-3} at Bălțătești and 1800 air ions cm^{-3} at Târgu Neamț. Annually, k values are lowest, even subunit, on days in the warm season months (especially summer), increasing on cold season days (especially winter).

The daytime air ionization regime averaged over the 4 months of observations, shows that the periods with the lowest total air ionization values at Bălțătești and Tg. Neamț correspond to the afternoon, to evening hours. In the morning, the air ionization values are also lower. The diurnal maxima of air ionization are positioned during the day, but precise temporal positioning with relevant statistical assurance would require longer periods of observations on the order of months and even years, not days. In this way, some random, disturbing meteorological events would be removed from the influence on the diurnal regime of some minor, local, long-term influencing factors, but which, in the short term, can impose abrupt increases or significant decreases, thus a certain air ionisation regime, difficult to sustain with plausible, stable explanations. When observations at two or more stations are asynchronous, the analysis becomes more complicated and the results are even more difficult to reconcile. During the daytime, k values were lowest (with some exceptions) in the midday and afternoon hours, and highest in the morning and evening. The 4-month averaged daytime regime of k at Bălțătești and Tg. Neamț revealed hours with predominantly subunit k. The daytime regime in July revealed an even longer range with sub-unit values (8.00-21.00h in Bălțătești and 9.00-21.00h in Târgu Neamț) of the k-index.

The geographic location in the Neamț Depression of the Moldavian Subcarpathians, in an optimal bioclimate, with mixed vegetation and active air ionization processes make the tourist resorts of Bălțătești and Târgu Neamț, attractive climatic-touristic destinations with high potential for practicing aeroionetherapy. These resorts can meet the requirements of tourists all year round. The warm season is favourable for all tourist activities. In summer there are no restrictions for tourism. The most favourable month for aeroionetherapy is July when air ionisation values exceed 1000 air ions cm^{-3} in both resorts. In Târgu Neamț, also October records high air ion levels (1040 air ions cm^{-3}). The recommended times of the day for aeroionetherapy are morning and afternoon in both resorts. The results obtained in this study encourage the effective use of aeroionetherapy for prophylactic and therapeutic purposes in Bălțătești and Târgu Neamț resorts.

FUNDING

R E F E R E N C E S

Bistricean, I. P. (2018). *Potențialul balneoclimatic al stațiunilor turistice din Moldova*. Editura Universității „Ștefan cel Mare" din Suceava, 117.

Brînză, V. (1974). Asupra ionizării naturale a aerului în zona stațiunii balneoclimatice Băile Herculane. *Hidrotehnica*, vol. 19, nr. 6, iunie, București, 297-300.

Crețeanu, V., Frimescu, M. (1961). Influența elementelor meteorologice asupra gradientului de potențial, conductivității electrice și concentrației ionilor la sol în perioada Anului Geofizic Internațional (1957-1959) la București. *Culegere de lucrări ale Institutului Meteorologic pe anul 1963*, 217.

Crețeanu, V., Frimescu, M. (1963). Ionizarea aerului la Mangalia și Govora, comparativ cu valorile obținute la Observatorul de Fizica Atmosferei. *Culegere de lucrări ale Institutului Meteorologic pe anul 1961*.

Daniels, S. L. (2002). On the ionization of air for removal of noxious effluvia (Air ionization of indoor environments for control of volatile and particulate contaminants with nonthermal plasmas generated by dielectric-barier discharge. *IEEE T. Plasma Sci*, 30 :1471‑1481). doi: 10.1109/TPS.2002.804211.

Deleanu, M., Elges, E. (1967). Observații privind ionizarea aerului la Cluj pe o perioadă de 11 ani (1955-1965). *Culegere de lucrări ale Institutului Meteorologic*, București, 517-530.

Deleanu, M., Mozes-Lörincz. (1975). Effect of negative ion exposure on adaptation to physical effort in young sportmen. *Biometeorology*. 6,1, under red. H. E. Landsberg și S. W. Tromp, Maryland, S.U.A., 131.

Deleanu, M. (1986). Elemente de fizica aeroionizării în troposfera joasă. *Al II-lea Simpozion național de aeroionizare, Comunicări științifice*, 11-13 sept., Botoșani, 41-64.

Deleanu, M., Aionesei, M., Alexa, M. E., Andrișan, C. (1988). *Aeroionizarea negativă*. Editura Tehnică.

Enache, L. M., Voiculescu, C. (1978). Aspecte ale ionizării aerului în stațiuni balneoclimatice de pe litoralul românesc al Mării Negre. *Lucrări științifice, serie E, XX-XXI, Îmbunătățiri funciare*, I.A.N.B., București, 3-18.

Enache, L. M., Andrișan, C. (1990). Determinări privind influența aeroionizării asupra poluării aerului. I.A.N.B. *Lucrări științifice, seria E, XXXIII, Îmbunătățiri funciare*, București, pp 35.

Enache, L. M. (1999). Ionizarea aerului și efectele sale biologice. *Sănătatea plantelor*, nr. 16 (9), pp 34.

Enache, L. M., Filipescu, C., Simionca, Iu. (Ghe) et al. (2005). Ionizarea naturală și artificială a aerului din spații subterane – factor de mediu cu potențial terapeutic. *Revista de Recuperare, Medicină Fizică și Balneoclimatologie. Societatea Română de medicină fizică și Recuperare*, București, Nr. 3-4, 136-141.

Enache, L. M. (2016). *Biometeorologie și bioclimatologie, climatul și bioclimatul stațiunilor balneare din România*. Editura Sitech. Craiova.

Enache, L. M. (2017). *Aspecte biomedicale ale ionizării aerului*. Editura Sitech. Craiova*,* 15, 53.

Enache, L. M., Bunescu, I. (2019). Air ionization - an environmental factor with therapeutic potential. *Geeoreview,* Vol. 29 / 2019, 31-39.

Frimescu, M., Crețeanu, V. (1964). Studiul ionizării naturale a aerului la Mangalia și Sinaia. *Culegere de lucrări ale Institutului Meteorologic pe anul 1964*, pp 173.

Grinshpun, S. A., Mainelis, G., Trunov, M., Adhikari, A., Reponen, T., Willeke, K. (2005). Evaluation of ionic air purifiers for reducing aerosol expose in confined indoor spaces. *Aer interior*, 15:235‑245. doi: 10.1111/j.1600-0668.2005.00364.x.

Hairong, S., Qingtang, H., Haiping, Y. (2005). Spatio-temporal changes of negative air ion concentrations in Beijing. *J. Beijing For. Univ*., 27 (30), 35-39.

Hui, W., Bing, W., Xiang, N., Qingfeng, S., Mingwen, L., Yuanyuan, L., Lidong, L., Pengfei, D., Wei, P. (2020). Study on the change of negative air ion concentration and its influencing factors at different spatio-temporal scales. *Global Ecology and Conservation*, 23 e01008. https://doi.org/10.1016/j.gecco.2020.e01008.

Iwama, H., Ohmizo, H., Furuta, S., Ohmori, S., Watanabe, K., Kaneko, T., Tsutsumi, K. (2002). Inspired superoxide anions attenuate blood lactate concentrations in postoperative patients. *Crit. Care Med*., 30, 1246‑1249.

Ji, Y. (2007). Study on the distributing and changing low of aeroation in Qipan Moutain scenic spot. Shenyang: *Shenyang Agricultural University*, pp. 1-46. (in Chinese).

Jianwu, H., Jiayuan, T. (2002). On the development of air anion resources and eco-tourism. J. Cent. China Normal Univ. (*Nat. Sci.*) 257-260, 02.

Ju, K., Kubo, T. (1997). Power spectral analysis of autonomic nervous activity in spontaneously hypertensive rats. *Biomed. Sci. Instrum*., 33, 338‑343.

Laza, V. (2000). The environment and gaseous ions. *CEJOEM*. Minireview, 6(1):3-10.

Lazzerini, F. T., Orlando, M.T., De Prá, W.(2018). Progress of negative air ions in health tourism environments applications. *Bol. Soc. Esp. Hidrol. Méd*. 2018, 33, 27‑46. doi: 10.23853/bsehm.2018.0450.

Lee, B. U., Yermakov, M., Grinshpun, S. A. (2004). Removal of fine and ultrafine particles from indoor air environments by the unipolar ion emission. *Atmos Environ*. 2004, 38 :4815‑4823. doi: 10.1016/j.atmosenv.2004.06.010

Li, P., Dai, H., Yang, H. (2011). Variation of negative air ion and Its relationship with environmental factors in Jigongshan. *Journal of Xinyang Normal University Natural Science Edition*, Vol. 24, No. 1, pp. 79-84.

Licht, S. (1964). *Medical climatology*. Elisabeth Licht Publisher.Waverly Press. New Haven. Maryland MD

Krueger, A. P., Reed, E. J. (1976). Biological impact of small air ions. *Science* 25 (193), 1209-1213. doi: 10.1126/science.959834

Maiorescu, G., Timotin, V., Simionca, Iu., Grudnicki, N., Zup, C. (2014). Existing and perspective arrangements to Salina Cacica in the context of tourism development in salt mines. *Balneo Research Journal*, 1061 vol. 5. http://dx.doi.org/10.12680/balneo.2014.1061

Mao, C., Yu, N., Du, J. (2014). Characteristic comparison of negative oxygen ions between typical urban and forest areas. *Meteorological Science and Technologyt*, Vol. 42, No. 6, pp. 1083-1089. (in Chinese).

Mihaila, D. (2014). *Atmosfera terestră. Elemente de favorabilitate si nefavorabilitate pentru organismul uman si activitatile turistice.* Editura Sedcomlibris Iasi, 47.

Mihăilă, D., Briciu, A. E., Costan (Briciu), L. A. (2019). Preliminary research on the thermo-hygrometric peculiarities of the Cacica salt mine microclimate. *Georeview,* Vol 29, No 1 (2019), pp 60 – 69.

Mihăilă, D., Roșu, C., Bistricean, P. I., Prisacariu, A., Mihăilă, E. V., Boiciuc, C. (2023). Research on air ionization in the tourist resorts of Solca, Cacica, Gura Humorului and in Cacica salt mine - north-eastern Romania. *Present Environment and Sustainable Development*. Volume 17, number 2, 2023. https://doi.org/10.47743/pesd2023172008

Pascu, Șt., Ștefănescu, S. (1969). Cercetări asupra electricității atmosferice în stațiunile Eforie, Sovata și Vatra Dornei. *Lucrări ale I.B.F*., București.

Pengfei, F., Xinwen, Y., Xu, Z. (2015). Variations in negative air ion concentrations associated with different vegetation types and influencing factors in Beijing. *Ecol. Environ*., 24 (5), pp. 818-824.

Pino, O., Ragione, F. L. (2013). There's something in the air: empirical evidence for the effects of negative air ions (NAI) on psychosiological state and performance. *Sci.Educ.*, 14 (4), 48-53. doi:10.12691/rpbs-1-4-1.

Prisacariu, A., Mihăilă, D., Bistricean, P. I., Roșu, C. (2023). The air ionisation in Suceava Metropolitan Area. *Present Environment and Sustainable Development*, Volume 17, Issue no.1, 351-370. https://doi.org/10.47743/pesd2023171024.

Ryushi, T., Kita, I., Sakurai, T., Yasumatsu, M., Isokawa, M., Aihara, Y., Hama, K. (1998). The effect of exposure to negative air ions on the recovery of physiological responses after moderate endurance exercise. *Int. J. Biometeorol*, 41, 132‑136.

Qi, B., Du, R., Shao, B. (2011). Charcterstics of a ion variation in Hangzhou. *Meteor Disaster Reduction Res*, Vol. 34, No. 4, pp. 68-71.

Qing, W., Weihua, H. (2005). Research on application of forest ecology in community virescence. *Hous. Sci.*, 2, 27-29.

Munteanu, R., Dumitroaia, G. (2010). Sursele de sare dintre Valea Sucevei si Valea Buzăului (PDF). cimec.ro. [Accesat în 04.02.2023].

Si, T., Luo, Y., Zhao, Z., et al. (2014). Relationship between negative air Ion concentration and meteorological elements in Diaoluoshan tropical rainforest. *Resources Science*, Vol. 36, No. 4, 2014, pp. 0788-0792. (in Chinese).

Schweidler, E., Kohlrausch, K. W. F. (1923). *Atmospharische Electrizitat, Handbuch der Electrizitat und des Magnetismus*, vol. III, sub red. L. Gretz, J. A. Barth, Leipzig, 193-276.

Shu-Ye, J., Ali, M., Srinivasan, R. (2018). Negative Air Ions and Their Effects on Human Health and Air Quality Improvement. *Int. J. Mol. Sci.*, 19(10), 2966. https://doi.org/10.3390/ijms19102966

Song, Z., Xian, B., Zhong, L. (2008). Different ecological conditions on the concentration aero anion research. *Modern Agricultural Science*, Vol. 28, No. 3, pp. 211-215. (in Chinese).

Tan, D., Zhang, X., Yang, J. (2010). A primary exploration on distribution and the variation ofnegative oxygen ion concentration in ChaShanZhuHai. *Environment and Ecology in the Three Gorges.* Vol. 186, No. 3, pp. 26-28. (in Chinese).

Tang, C., Cai, Z., Xiao, A. (2011). Concentration characteristics of air negative Ion and Its relations with meteorological conditions in Jinggang Mountain. *Journal of Anhui Agri. Sci*, Vol. 39, No. 1, 2011, pp. 495-496. (in Chinese).

Teodoreanu, E., Ardeleanu, C., Dacos-Swoboda, M. (1984). *Bioclima staţiunilor balneare din România.* Edit. Sport – Turism. Bucureşti.

Tingting, S., L, Yanju., Zhizhong, Z. (2014). Relationship between negative air ion concentration and meteorological elements in Diaoluoshan Tropical Rainforest Resour. *Sci.*, 36 (4) (2014), pp. 788-792

Wang, J., Li, X., Cai, J. (1991). The effect of sea waves on the concentration of negative ions in coastal air. *Chinese physiotherapy journal*, No. 4, pp. 157-158.

Wang, C. (2003). *Study on the cause of negative ion tourism resources distribution and development in Mount Huangshan scenic area*. Hefei: Anhui Agricultural University, pp. 1-57.(in Chinese).

Wang, J., Ji, Z., Sui ,T. (2004). Influence of temperature and humidity on negative ion concentration. *Research of Environmental Science*, vol. 17, No. 2: 68-70.

Winsor, T. J., Beckett, C. (1958). Biologic effects of ionized air in man. *Am. J. Phys. Med.*, 13 (37), 83-88.

Wiszniewski, A., Suchanowski, A., Wielgomas, B. (2014). Effects of Air-Ions on human circulatory indicators. *Pol. J. Environ. Stud.*, 23, 521‑531.

Wu, C., Zheng, Q., Zhong, L. (2001). A Study of the Aero-Anion concentration in forest recreation area. *Forestry Science.*, Vol. 37, No. 5, 2001, pp. 75-81. (in Chinese).

Wu, F. C., Yao, C., Guo, J. (2006). Distribution of negative air ions and its relation to air quality of the Yuelu Mountain. *Acta Scientiae Circumstantiae*, Vol. 26, No. 10, 2006, pp. 1737-1744. (in Chinese).

Xu, Z. (2004). *The anion resources research in tourism area of Anhui province*. Hefei: Anhui Agricultural University, pp. 1-58.

Yan, X. J. (2010). Spatial distribution of forest and wetland in Qingdao. *Sci. Sylvae Sin.*, 46 (6), 301-312.

Yao, C. (2005). *Study on the distribution and utilization of air negative ions in Yuelu Mountain.* Changsha: Changsha Teacher-training University, pp. 1-45. (in Chinese).

Ye, C., Wang, X., Guo, W. (2000). A preliminary study on the relationship between the concentration of negative ions in air and meteorological conditions. *Meteorological Science and Technology*, No. 4, 2000, pp. 51-52.

Zhao, X., Li, C., Ge, J., et al. (2007). Progress of aero anion in forest environment. *Journal of Northwest Forestry University*, Vol. 22, No. 2, pp. 57-61. (in Chinese).

Corine Land Cover 2018 dataset: https://land.copernicus.eu/ [accessed on 14/02/2023]

Geography of Romania, Volume IV (1992). The Peri-Carpathian Regions: The Hills and Plains of Banat and Crișana, Mehedinți Plateau, Subcarpathians, Getic Piedmont, Moldavian Plateau, Academy Publishing House (in Romanian).

INS 2021, Population and Housing Census, 2021 round - provisional data at territorial level https://insse.ro/cms/ro/content/recensământul-populației-și-locuințelor-runda-2021-date-provizorii-%C3%AEn-profil-teritorial [accessed February 28, 2023] (in Romanian)

*** Bălțătești - Balneoclimatic Cure, Indications and Contraindications, Collective Author under the auspices of the Ministry of Health, Medical Publishing House, Bucharest, 1986 (in Romanian)

*** *Bălțătești Resort - Archived on January 27, 2013, at Wayback Machine., Neamț Online portal – neamt.ro, [accessed March 20, 2023] (*in Romanian*)

*** Bălțătești Resort – Neamț County, viziteazaneamt.ro, portal of Neamț County Council, [accessed March 20, 2023] (in Romanian).

ASSESSING THE IMPACT OF METHODOLOGICAL DIFFERENCES ON GEOID MODEL PERFORMANCE

Kosasih PRIJATNA[1]* , Rahayu LESTARI[1], Brian BRAMANTO[1] ,
Arisauna Maulidyan PAHLEVI[2] , Dudy D. WIJAYA[1]

ABSTRACT
The geoid serves as a critical reference surface for precise mapping applications, particularly in the context of satellite-based positioning systems like the Global Navigation Satellite System (GNSS). While GNSS offers efficient positioning solutions, it relies on an ellipsoidal surface that lacks physical meaning for vertical reference, highlighting the need for accurate geoid height models. A precise geoid model is essential for converting geodetic heights into orthometric heights, which are crucial for practical applications. This study investigates potential discrepancies among geoid models derived from different methods, focusing on the Stokes-Helmert (SH), remove-compute-restore (RCR), and *Kungl Tekniska Högskolan* (KTH) methods. The primary differences among these methods lie in their approaches to modifying the Stokes formula and their reduction schemes. Conducted in the central part of Java Island, Indonesia, this study uses terrestrial gravity observations to model the geoid and GNSS/leveling data for validating the geoid models. The RCR method demonstrated the highest accuracy, with an RMS error of 8.4 cm, outperforming the KTH method (9.2 cm) and the SH method (10.7 cm). Discrepancies between SH and RCR models were less pronounced, with differences around 30 cm, compared to over 1 meter between KTH and the other methods. The comparison with the global EGM2008 model showed that the gravimetric geoid models were more accurate, with RMS differences reaching up to 10 cm, primarily due to systematic differences with the EGM2008 model. Statistical analysis using t-tests with 95% confidence intervals indicated that the differences among SH, RCR, and KTH methodologies were not statistically significant. Despite the RCR method's apparent superior performance, these differences did not achieve statistical significance. The study notes the limitations of using a relatively limited terrestrial gravity dataset and emphasizes the need for incorporating additional gravity data, such as recent airborne gravity datasets, to improve geoid model performance. Future research should also aim for denser GNSS/leveling observations with stricter measurement requirements to provide a more robust absolute assessment of gravimetric geoid models.

Key-words: geoid, Stokes-Helmert, remove-compute-restore, KTH.

1. INTRODUCTION

Geoid is an equipotential surface, that best approximates the mean sea level in the ocean under an ideal condition and mainly serves as a vertical reference system (Sideris, 2021). The availability of a precise geoid height (undulation) model, defining the deviation between the geoid and ellipsoidal surfaces is important in precise mapping applications, particularly in the era of satellite-based positioning systems, i.e. using Global Navigation Satellite System (GNSS). The accuracy of instantaneous position estimates from GNSS observations reaches several centimeters (Gumilar et al., 2023; Krzyżek & Kudrys, 2022). Therefore, GNSS helps users to improve the productivity of large-scale maps compared when using conventional terrestrial methods, such as mapping using a total station as it provides positioning estimates in real-time and requires less labor (Kizil & Tisor, 2011).

_____
[1]*Geodetic Science, Engineering, and Innovation Research Group, Faculty of Earth Sciences and Technology, Institut Teknologi Bandung, 40132 Bandung, Indonesia; prijatna@itb.ac.id, rlestari2001@gmail.com, brian.bramanto@itb.ac.id, dudy.wijaya@itb.ac.id*
[2]*Directorate for Geospatial Reference System, Geospatial Information Agency of Indonesia (BIG), 16911 Cibinong, Indonesia; arisauna.maulidyan@big.go.id*
*Corresponding author: prijatna@itb.ac.id

Although GNSS offers efficient yet accurate positioning solutions, it also comes with a major drawback. The height estimate from GNSS position solutions is defined at the geodetic height system, i.e., using ellipsoidal surface as the vertical reference surface. Ellipsoidal surface is a simplified mathematical approximation of the geoid (Hofmann-Wellenhof et al., 2008). Consequently, the positioning estimates from GNSS observations do not have any physical meaning, i.e., cannot be used for determining the flow water direction. Therefore, to obtain physical height estimates (orthometric height) on the Earth surface using GNSS observations, the information related to the geoid height must be available accurately. Specifically for future large-scale mapping applications, it is essential to have a geoid model with high accuracy.

Having geodetic height estimates from GNSS observations and precise geoid height model, one can easily convert the geodetic height into orthometric height using the following equation:

$$H = h - N \qquad (1)$$

where H is the orthometric height or the height difference between the geoid surface and the point on the Earth's surface, h is the geodetic height, defining the height on the Earth's surface referring to the ellipsoidal surface, and N is the geoid height undulating between the geoid and ellipsoid surfaces. It should be noted that geoid height can be positive or negative. It is positive when geoid surface lies above the ellipsoidal surface and vice versa. In simple, the relationship between Earth's topography, ellipsoidal and geoid surfaces is shown in **Fig. 1**.
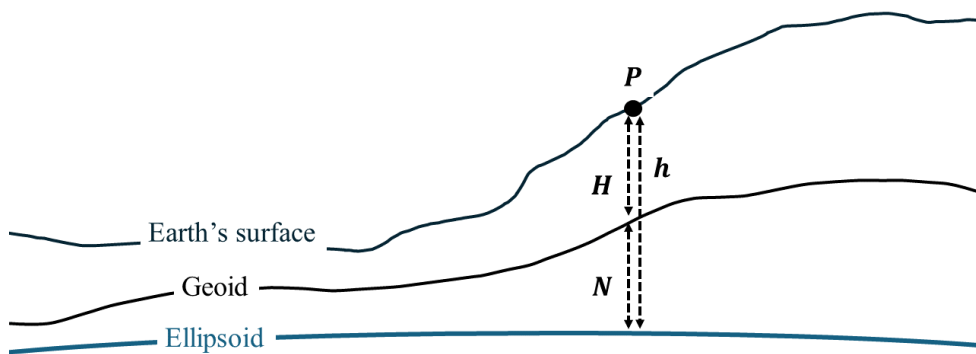
Fig. 1. A simplified diagram showing the relationship among the ellipsoid, geoid, and surface of the Earth.

The geoid height can be modeled based on geometric and gravimetric approaches. The geoid height modeled using the geometric approach relies on the combination of GNSS and leveling observations, providing heights that refer to ellipsoid and geoid surfaces. In principle, the geoid height can be then derived by calculating the difference between geodetic height from GNSS observation and orthometric height from leveling observation. While it seems that the computation of geometric geoid height is simple, the measurement is much more challenging and time-consuming (Erol & Erol, 2021). Therefore, the gravimetric approach is preferable as the technical aspects, e.g., measurement, are much more undemanding but a comprehensive understanding of gravimetric geoid height modeling is needed.

To model the geoid, there are many methods available such as the Stokes-Helmert (SH; Abbak et al., 2024; Ellmann & Vaníček, 2007; Lestari et al., 2023; Vaníček et al., 2013), Remove-Compute-Restore (RCR; Schwarz et al., 1990; Wu et al., 2020; Yildiz et al., 2012a), and *Kungl Tekniska Högskolan* (KTH; Sjöberg, 2003, 2020) methods. Each method has its own computational methodology, including procedures for handling terrain effects, mathematical models to continue gravity data and terrain effects, etc. Consequently, the geoid height estimates might vary depending on the selection of the methodology used regardless of the same gravity data used.

Consequently, ongoing research is crucial to develop a geoid model that achieves superior accuracy tailored to the specific conditions of our region, Indonesia, which includes varying topography with archipelagic situations. The three methods employed for comparison SH, RCR, and KTH represent the best practices currently available. Continued evaluation and refinement of these methods will be necessary to address the unique challenges posed by our geographic conditions and ensure the highest quality geoid modeling. Therefore, this paper aims to assess the geoid height estimates from different methods, i.e., the SH, RCR, and KTH methods, and investigates whether a significant discrepancy exists among the derived geoid models. For this purpose, we selected the central part of Java Island, Indonesia, as our test case as the relatively dense terrestrial gravity observations are available. In addition, GNSS/leveling observations that can be used to validate the resulting geoid height model are also available.

The remainder of this paper is described as follows: Section 2 describes the methodologies and data used to compute the geoid height model, Section 3 presents the results and discusses the findings, and finally, Section 4 presents the conclusion of the study and provides the direction for future research.

2. METHODS AND DATA

2.1. Stokes - Helmert Method

The Stokes-Helmert method is a method for geoid modeling that utilizes Stokes's Integral to convert gravity anomaly into geoid height, while Helmert's 2nd condensation serves as the reduction scheme. The calculation of geoid height using the Stokes method requires integration over the entire Earth with continuous gravity anomalies. The disturbing potential must obey to the Laplace equation above the geoid, ensuring that there is no mass above the surface where the gravity anomaly is situated (Hoffman-Wellenhof & Moritz, 2006; Jekeli et al., 2013). However, since gravity measurements using gravimeters are typically limited to the study area, the computations need to be supplemented with a lower-degree gravity field, such as the global geopotential model (GGM; Hoffman-Wellenhof & Moritz, 2006). The formula for calculating residual geoid height can be expressed as follows (Abbak et al., 2012):

$$N_{\Delta g} = \frac{R}{4\pi\gamma} \iint_{\sigma} \Delta g_{red} S(\psi) d\sigma \tag{2}$$

where N is the geoid height, Δg_{red} is the reduced Faye gravity anomaly that is defined as $\Delta g_{red} = \Delta g_{FA} - \Delta g_{GGM} - \Delta g_H$, with Δg_{FA} is the free-air gravity anomaly, Δg_{GGM} is the long-wavelength component from GGM, and Δg_H is the topographic gravity effect, γ is normal gravity, R is the mean of Earth's radius, and $S(\psi)$ is the Stokes' kernel can be written as:

$$S(\psi) = \sum_{n=2}^{\infty} \frac{2n+1}{n-1} P_n(\cos\psi) \tag{3}$$

where ψ is spherical distances between data points and computation points, $P_n(\cos\psi)$ is Legendre function, and n is degree.

The Helmert's 2nd condensation reduction scheme serves as a method to satisfy the requirements of Stokes's formula, which mandates the absence of masses above the geoid, and that the gravity anomaly must be referenced to the geoid (Heck, 2003a). This reduction involves several steps, initially, it involves calculating the direct topographical effect on gravity to replace the impact of surface masses on gravity with the effect of the mass layer on the geoid (Heiskanen & Moritz, 1967; Sideris & Forsberg, 1991; Vanicek & Kleusberg, 1987). Then, a downward continuation is applied to determine the gravity anomaly at the geoid by estimating the actual gravity anomaly at the geoid from

observation at the Earth's surface. Stokes' formula is then applied to the gravity anomalies at co-geoid. Finally, the computation of the indirect topographical effect is performed to complete the final geoid model, yields (Martinec et al., 1993):

$$N = N_{GGM} + N_{\Delta g_{red}} + N_{ind} \tag{4}$$

where N_{GGM} is the long-wavelength geoid contribution from GGM and N_{ind} is the indirect effect on the geoid height for Helmert's 2nd condensation.

2.2. RCR Method

The Remove-Compute-Restore (RCR) method, like the Stokes-Helmert method, uses Stokes' Integral but with a different reduction scheme. In this method, the computation involves the use of a quasigeoid for the approximation surface, which is done by using the RTM reduction scheme. The RCR method is commonly used in regional gravimetric geoid modeling, which aims to separate the long-, medium-, and short-wavelength geoid/gravity components (Schwarz et al., 1987, 1990; Sideris, 2013). Geoid modeling, when using the RCR technique, focuses on residual gravity anomaly data to streamline the calculation process (Hoffman-Wellenhof & Moritz, 2006). During the removal stage, the long-wavelength components (as derived from the global model) and short-wavelengths (as computed from the topographic model) are removed from the gravity data. Subsequently, in the computation stage, the band-pass filtered gravity anomalies are converted into either quasigeoid height or height anomaly using Stokes' formula. Once the computational stage is completed, the long-wavelengths and short-wavelengths are restored to obtain the complete quasigeoid height (Yildiz et al., 2012b). **Fig. 2** illustrates the contribution of each component: long-wavelengths (from the global model), medium-wavelengths (from gravity data), and short-wavelengths (from the topographic model).

In the RTM scheme, the reduction performed is not an isostatic topography reduction but produces anomalies similar to an isostatic topography anomaly. This scheme is often used for terrain reduction in quasigeoid modeling (Forsberg, 1984). This scheme involves the use of a reference surface (an average elevation surface) determined by introducing the low pass filter to the precise topographical model, obtaining a smoother elevation surface. This reduction technique requires the removal of the topographic mass above the reference surface and filling the mass below it (refer to **Fig. 3**; Bajracharya & Sideris, 2005; Yang et al., 2022).
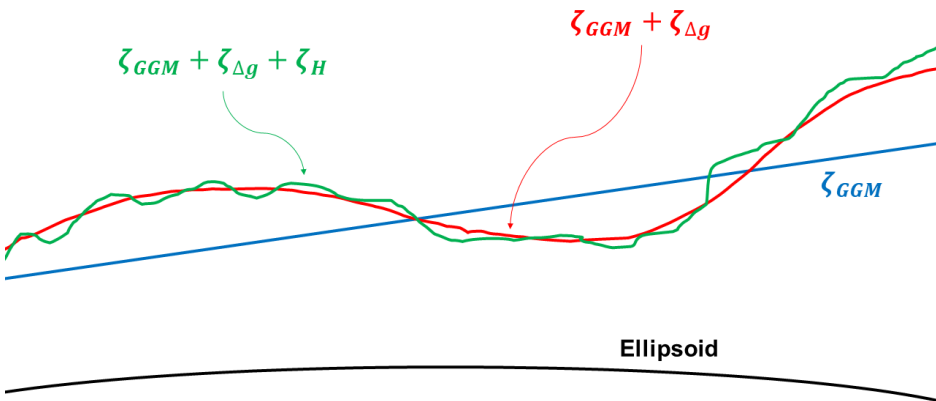
Fig. 2. Illustration of the contribution from various wavelength components to the quasigeoid height. ζ_{GGM} is the height anomaly of the long wavelength component, $\zeta_{\Delta g}$ is the height anomaly of the residual component, and ζ_H is the height anomaly of the short wavelength component.
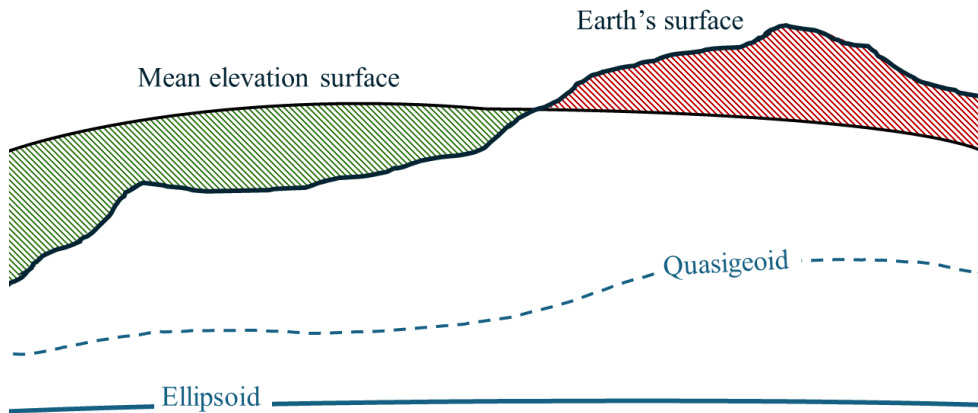
Fig. 3. An illustration showing the RTM configuration. The red-shaded area shows the region where more masses occur above the mean elevation surface, while the green-shaded area shows the region with a lack of masses below the mean elevation surface.

The method of utilizing geoid heights to depict the Earth's physical shape has a limitation: it necessitates knowledge of the mass density above the reference surface or requires certain assumptions to address this issue. To circumvent this limitation, an alternative approach is adopted, allowing for the formulation of the height anomaly as follows (Vu et al., 2019):

$$\zeta = \zeta_{GGM} + \frac{R}{4\pi\gamma} \iint_{\sigma} \Delta g_{res} S(\psi) d\sigma + \zeta_{RTM} \tag{5}$$

where Δg_{res} is the residual gravity anomaly defined as $\Delta g_{res} = \Delta g_{FA} - \Delta g_{GGM} - \Delta g_{RTM}$, with Δg_{RTM} is the corresponding RTM gravity effect, ζ_{GGM} is the height anomaly from GGM, and ζ_{GGM} is the RTM height anomaly. The height anomaly values are subsequently transformed into geoid height values using a formula that we call quasigeoid to geoid separation (QGS), expressed as follows (Heiskanen & Moritz, 1967):

$$QGS = \zeta - N \approx -\frac{\Delta g_{BA}}{\gamma} H \tag{6}$$

where Δg_B is the Bouguer gravity anomaly, γ is normal gravity, and H is the orthometric height. The Bouguer gravity anomaly, using a Bouguer plate approximation, can be mathematically defined as:

$$\Delta g_{BA} = \Delta g_{FA} - 0.1119H. \tag{7}$$

2.3. KTH Method

The KTH method, developed by *Kungl Tekniska Hogskolan* or KTH Royal Institute of Technology, utilizes the Modification Stokes by Sjoberg's technique to calculate the approximation of geoid height. By taking advantage of the orthogonality of spherical harmonics over the sphere, this method's equation can be represented as, with two sets of modification parameters s_n and b_n (Sjoberg, 1984; Sjöberg, 1991, 2003):

$$\tilde{N} = \frac{R}{4\pi\gamma} \iint_{\sigma_0} S^L(\psi) \Delta g_{FA} \, d\sigma + \frac{R}{2\gamma} \sum_{n=2}^{M} b_n \Delta g_{GGM} \tag{8}$$

where $S^L(\psi)$ is the modified Stokes' function, L is the selected maximum degree of the arbitrary parameters s_n of the modification, and M is the upper limit of the GGM used. The modified Stokes' function can be formulated as:

$$S^L(\psi) = \sum_{n=2}^{\infty} \frac{2n+1}{n-1} P_n(\cos\psi) - \sum_{n=2}^{L} \frac{2n+1}{2} S_n P_n(\cos\psi) \tag{9}$$

Then, modification parameter s_n can be expressed by:

$$h_k = \sum_{n=2}^{L} a_{kn} s_n, \quad k = 2,3,\ldots,L \tag{10}$$

where h_k is the element of the observable vector and a_{kn} is the element of design matrix.

Furthermore, the KTH method incorporates several additive corrections: the combined topographic correction (δN_{comb}^{top}) represents the combined direct and indirect topographical effects on the geoid, the combined atmospheric correction (δN_{comb}^{atm}) accounts for the combined direct and indirect atmospheric effects, and the ellipsoidal correction (δN_{ell}) adjusts for the spherical approximation of the geoid in Stokes' formula to the ellipsoidal reference surface. Thus, the geoid height can be expressed as (Sjöberg, 2003):

$$N = \tilde{N} + \delta N_{comb}^{top} + \delta N_{comb}^{atm} + \delta N_{ell} \tag{11}$$

2.4. Validation

The resulting gravimetric geoid models will be further validated against the geometric geoid model derived from GNSS/leveling observations (see Eq. 1). This validation process is referred to as absolute validation, where the discrepancy between gravimetric and geometric geoids is being assessed. This discrepancy reads:

$$\Delta N = N^{gra} - N^{geo} \tag{12}$$

where N^{gra} is the gravimetric geoid and N^{geo} is the geometric geoid.

To thoroughly evaluate the effectiveness of a geoid model using GNSS/leveling data, a relative validation method is further employed. This involves calculating the differences between the differential geoid heights of both the gravimetric and geometric models across various baselines derived from GNSS/levelling benchmarks. These discrepancies are then expressed in relative terms, measured in m/km, reads (Abbak & Ustun, 2015):

$$\Delta N_{ij} = \frac{\left|\left(N_i^{gra} - N_j^{gra}\right) - \left(N_i^{geo} - N_j^{geo}\right)\right|}{d_{ij}} \tag{13}$$

where ΔN_{ij} is relative value and d_{ij} is spherical distance from i to j.

2.5. Summary of Methodology for Each Method

The summary of the methodology of the Stokes-Helmert, RCR, and KTH methods is shown in **Fig. 4**. The variation between these three methods is mainly due to differences in their reduction schemes and how they handle the Stokes integration when transforming gravity values into geoid heights. The SH method employs co-geoid as an approximate surface for the geoid.
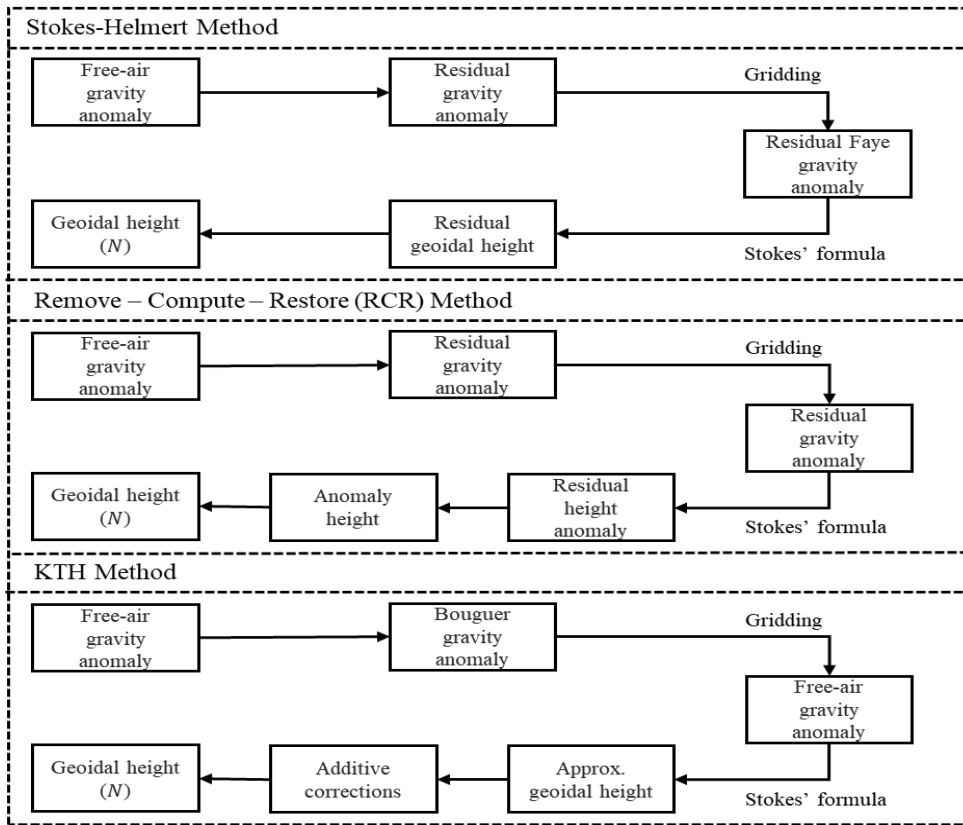
Fig. 4. Summary of the methodologies used in this study.

The reduction process utilizes 2nd Helmert's Condensation involves redistributing mass back to the geoid itself. Topographic mass is reallocated based on the local condensation procedure, which involves compressing the topographic column onto the condensation surface (Heck, 2003b). Then, the RCR method calculates residual gravity anomalies by incorporating short-wavelengths topographical gravity effects from RTM scheme. Consequently, the estimates read as height anomalies instead of geoid height. Therefore, further calculations are required to convert the height anomaly values into geoid heights, as previously mentioned (Omang & Forsberg, 2000). Finally, the KTH method does not use any reduction scheme, the calculation is carried out directly on the topographic surface. Instead, an additive correction (see eq. 11) is applied after the geoid approximation value is obtained.

A key difference among the methods compared, particularly noticeable in the KTH method, lies in the modification of the Stokes kernel used for geoid calculations (see eq. 8 and eq. 9). For the case of SH and RCR methods, a slightly different Stokes' modification is further introduced. Specifically, we applied the Wong-Gore modification to the Stokes function. The modified Stokes function for SH and RCR methods is defined as follows (Forsberg & Tscherning, 2008; Wong & Gore, 1969):

$$S_{mod}(\psi) = S(\psi) - \sum_{n=2}^{M} \alpha(n) \frac{2n+1}{n-1} P_n(\psi) \tag{14}$$

$$\alpha(n) = \begin{cases} 1 & for \quad 2 \leq n \leq M_1 \\ \dfrac{M_2 - n}{M_2 - M_1} & for \quad M_1 \leq n \leq M_2, \quad n = 2, \dots, M \\ 0 & for \quad M_1 \geq n \leq M_2 \end{cases} \tag{15}$$

where M_1 and M_2 represent the lower and upper degree of spheroidal modification for the kernel integration. To obtain the appropriate spherical caps, M_1, and M_2, a trial-and-error evaluation is conducted to achieve the best results.

2.6. DATA

2.6.1. GNSS/Leveling

The GNSS/leveling data utilized in this study were surveyed and processed by the Geospatial Information Agency (Badan Informasi Geospasial, BIG) at 186 points, spanning from north to south between Semarang and Yogyakarta (refer to **Fig. 5c**). The GNSS observations were conducted using the relative differential method, tied to the nearby CORS (Continuously Operating Reference System) within the research area. Additionally, leveling was performed with respect to the tidal benchmark (BM) in the research area. The geoid heights derived from the GNSS/leveling measurements serve as validation values against the geoid model generated using the gravimetric method as described in Section 2.4.

2.6.2 Terrestrial Gravity Data

The terrestrial gravity data was gathered by BIG in 2019. A total of 264 data points were collected, covering the central area of Java Island that were mostly clustered in Semarang and Yogyakarta. These measurements were conducted at 5-kilometer intervals using the Scintrex CG-5 relative gravimeters (refer to **Fig. 5a**).

2.6.3. Digital Elevation Model

The Digital Elevation Model (DEM) serves as the short-wavelength component and is essential for computing terrain correction, indirect effect, and generating the residual terrain model (RTM). We utilized SRTM 1" (SRTM, 2015) data for land areas and SRTM 15"+ (Tozer et al., 2019) for oceanic regions (refer to **Fig. 5d**). These data were further combined and resampled to 1", obtaining a consistent grid resolution. To derive parameters from the RTM, we employed the TGF software (Yang et al., 2020). Otherwise, an in-house program package is used to calculate the remaining parameters.

2.6.4. Global Geopotential Model

To address the scarcity of terrestrial gravity data, we incorporated a global geopotential model (GGM) to fill the gaps and enhance the quality of the gravimetric geoid. Additionally, GGM includes a long-wavelength component as it requires integration across the entire Earth due to the use of Stokes' integral. Specifically, we utilized the Earth Gravitational Model 2008 (EGM2008) with degrees and orders of 2190, which is known to have a resolution of approximately 5 arc minutes or roughly 9.13 kilometers (Pavlis et al., 2012).

2.6.5. Fill-in Gravity Data

The process of calculating a local gravimetric geoid model involves integrating terrestrial gravity data within a specific area. To ensure accuracy and precision, it's essential to address any gaps in gravity information by incorporating data from alternative sources (Matsuo & Kuroishi, 2020). In this study, we added the gravity data by combining EGM2008 with a degree and order of 2190 and RTM obtained from SRTM 1" for land areas, and SRTM 15"+ for oceanic regions (refer to **Fig. 5b**).
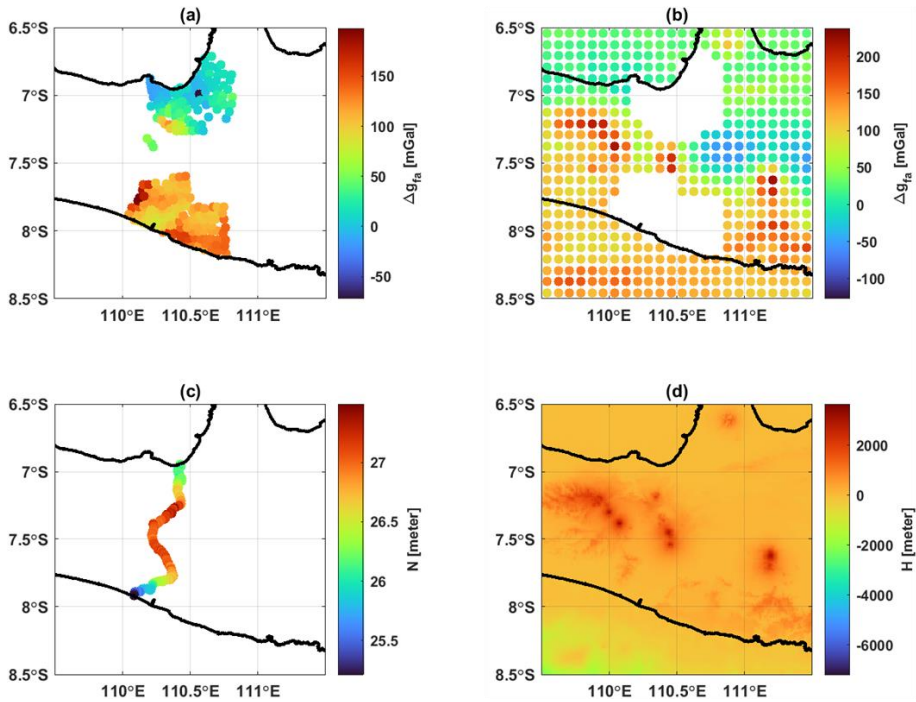
Fig. 5. Free-air gravity anomalies from terrestrial gravity data (a) and fill-in gravity data (b). Panel (c) and (d) show the distribution of geoidal height from GNSS/leveling and topography from the combination between SRTM1" and SRTM15"+ models, respectively.

3. RESULT AND DISCUSSION

The investigation involved the computation of three local gravimeters model using different methodologies: Stokes-Helmert (SH), Remove-Compute-Restore (RCR), and *Kungl Tekniska Högskolan* (KTH). The primary differences among these methods lie in their reduction schemes and how they handle the computational aspects of the Stokes formula. The SH method uses a reduction scheme based on the co-geoid surface, while RCR operates on the quasigeoid. The KTH method directly utilizes the geoid surface. In terms of the Stokes formula, the SH and RCR methods adjust the gravity anomaly, whereas KTH modifies the Stokes kernel. Computationally, both SH and RCR employ the multiband spherical Fast Fourier Transform (FFT), while KTH uses ordinary numerical integration. Geoid modeling performed using the SH and RCR methods was based on in-house programs package, while the KTH method utilized the LSMSSOFT software (Abbak & Ustun, 2015).

Despite these differences, all three approaches share common procedures during computation, including utilizing spherical caps of 1.28° and the application of bias correction on the resulting geoid models. Bias correction was obtained by calculating the average difference between the gravimetric geoid model and validation data. The variations observed among the three geoid models (refer to **Fig. 6**) are relatively minor. However, regions with elevated topography exhibit more distinct color contrasts in the KTH model compared to the SH and RCR models. According to the statistical data (refer to **Table 1**), the average geoid height within the study area (110°-111° E and 6.5°-8° S) for the SH, RCR, and KTH methods are 26.620 m, 26.593 m, and 26.605 m, respectively, representing a difference of approximately 3 cm. When considering the highest and lowest geoid height values within the study area, both SH and RCR methods demonstrate similar ranges, spanning from 24.347 m to 28.836 m for SH and 24.323 m to 28.766 m for RCR. In contrast, the KTH method exhibits a notable disparity in the minimum geoid height value within the study area, differing by 40 cm compared to the other methods. The range of geoid model values utilizing the KTH method extends from 23.938 m to 28.816 m.
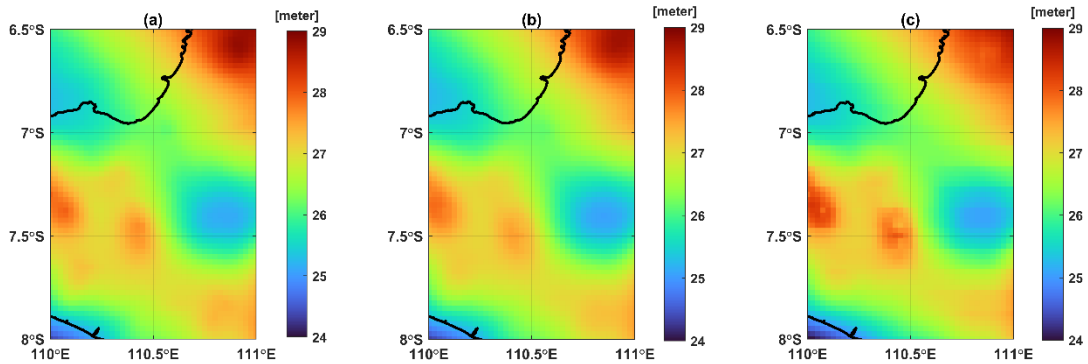
Fig. 6. Geoid models obtained when implementing SH (a), RCR (b), and KTH (c) methodologies.

Table 1.
Statistics of the geoid models when using different methodologies.

Geoid	Min [m]	Max[m]	Mean[m]
SH	24.347	28.836	26.620
RCR	24.323	28.766	26.593
KTH	23.938	28.816	26.605

Fig. 7 illustrates the discrepancies among each model, presenting the differences between the SH method and the RCR method (see **Fig. 7a**), between the SH method and the KTH method (**Fig. 7b**), and between the RCR model and the KTH model (**Fig. 7c**). The disparity between the SH and RCR models is relatively insignificant compared to the disparity between the KTH model and both the SH and RCR models. Particularly noticeable differences are observed between the KTH model and the other two models, notably in the northern and central mountainous regions, as well as in the southern areas. These variations are further elucidated by the statistical data presented in **Table 2**. The differences between the SH and RCR models range from -9.8 cm to 28.4 cm, while the disparity between the SH and KTH models spans from -4.5 cm to 70.8 cm. Similarly, the difference between the RCR and KTH models ranges from -47.2 cm to -62.9 cm. As previously outlined, the variation between the SH and RCR methods is relatively minor, with mean, root mean square (RMS), and standard deviation (STD) values of 2.7 cm, 4.4 cm, and 3.5 cm, respectively. In contrast, the disparity between the SH and KTH models yields mean, RMS, and STD values of 1.5 cm, 12.7 cm, and 12.7 cm, respectively. Meanwhile, the difference between the RCR and KTH models results in mean, RMS, and STD values of -1.2 cm, 11.7 cm, and 11.6 cm, respectively.
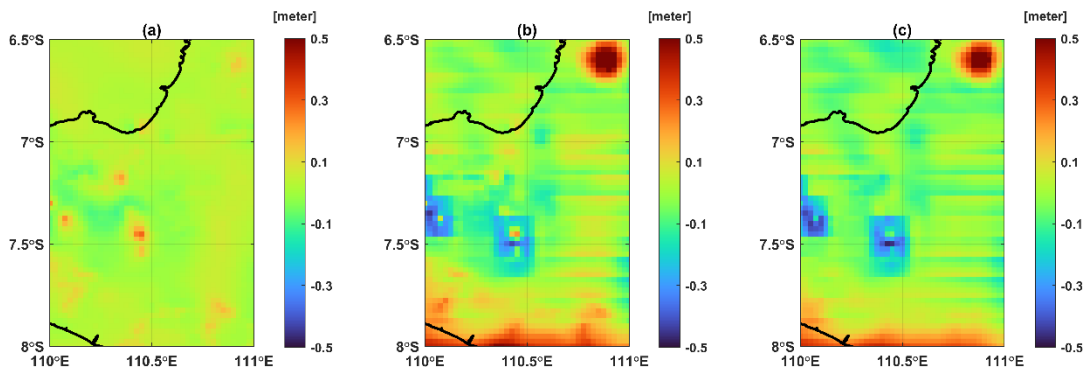
Fig. 7. Geoid differences between SH and RCR methods (a); SH and KTH methods (b); RCR and KTH methods (c).

Statistics of the differences between the geoid models across different methodologies.

Geoid	Min [m]	Max [m]	Mean [m]	RMS [m]	STD [m]
SH – RCR	-0.098	0.284	0.027	0.044	0.035
SH – KTH	-0.451	0.708	0.015	0.127	0.127
RCR – KTH	-0.472	0.629	-0.012	0.117	0.116

Following the reduction of the geoid model by its bias value relative to the gravimetric geoid model produced by GNSS/leveling, validation procedures are undertaken. Notably, the shape of the geoid surface in the validation area exhibits minimal discrepancies (refer to **Fig. 8**). We also incorporated EGM2008 into the validation process to assess the extent to which the global model (EGM2008) deviates from our gravimetric model. Based on the values from the figure, it appears that the difference between the EGM2008 geoid model and our gravimetric model, when compared to the validation geoid, is primarily due to a significant shift of about 15 cm.

The three models demonstrate standard deviation and RMS differences of only approximately 1-2 cm (refer to **Table 3**), with the RCR method yielding the most favorable outcomes compared to the others. Specifically, the standard deviation and RMS values for the SH, RCR, KTH, and EGM2008 models are 10.7, 8.4 cm, 9.2 cm, and 10.2 cm, respectively. This table shows that each model exhibits disparities with the validation data (GNSS/leveling), ranging from -50.2 cm to 25.3 cm for the SH method, -46.9 cm to 19 cm for the RCR method, -41.5 cm to 22.6 cm for the KTH method, and -66.5 cm to 3.7 cm for the EGM2008. In addition, the relative assessment demonstrates good overall precision of about 0.006 m/km or corresponds to an error of 6 mm for every one kilometer, making it suitable for most practical applications.
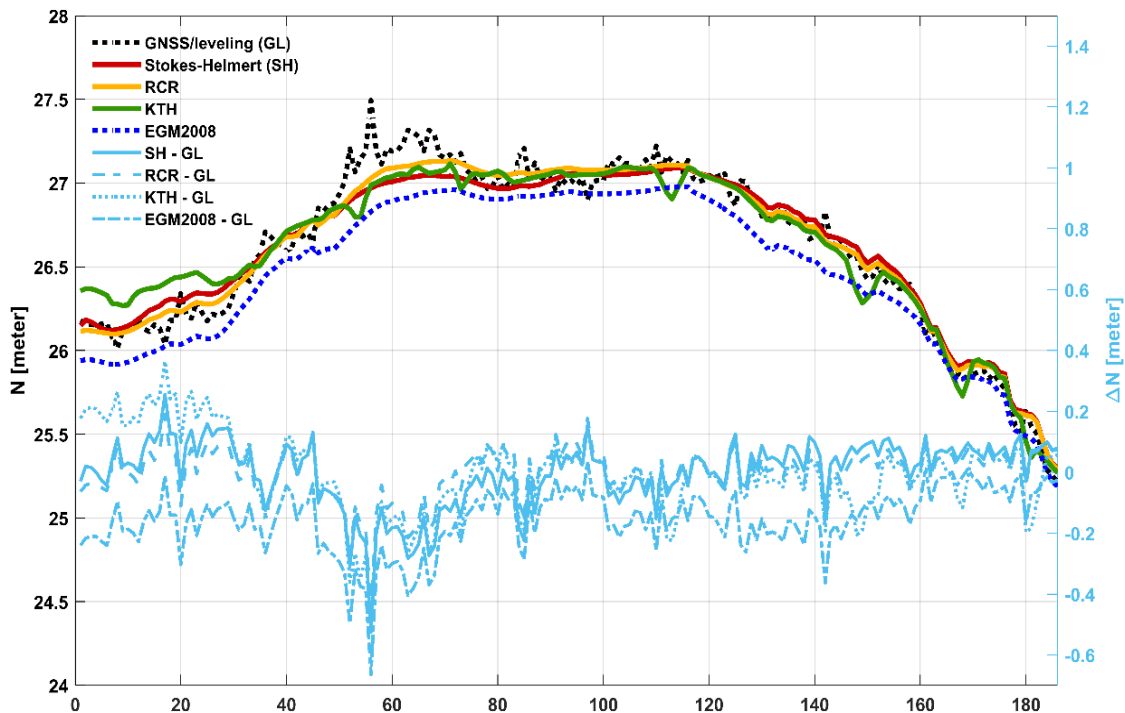
Fig. 8. The comparison between geometric and gravimetric geoid models. Light blue lines display the differences between geometric and gravimetric geoid models. Note the difference in scale.

Statistics from the validation of the SH, RCR, and KTH method geoid models.

Geoid	Absolute assessment					Relative assessment		
	Min [m]	Max [m]	Mean [m]	RMS [m]	STD [m]	Min [m/km]	Max [m/km]	Mean [m/km]
SH	-0.521	0.253	0.000	0.107	0.107	0.000	1.390	0.006
RCR	-0.469	0.190	0.000	0.084	0.084	0.000	1.389	0.005
KTH	-0.415	0.226	0.000	0.092	0.092	0.000	1.409	0.007
EGM2008	-0.665	0.037	-0.156	0.186	0.102	0.000	1.399	0.006

Looking closer at **Fig. 8** and **Table 3**, the discrepancy between geometric and gravimetric geoid models seems to be prominent at several points of validation. This affects the corresponding maximum and minimum discrepancy in absolute and relative assessments. Particularly for the absolute assessment, the absolute minimum discrepancy is larger than twice the standard deviation value (corresponds to 95% confidence intervals). At the same time, the maximum values for the relative assessment are significantly different compared to the mean values. This highlights possible outliers that are likely due to the errors in GNSS/leveling measurements. Lestari et al. (2023) stated that the leveling measurements underwent relatively strict measurement requirements, including the difference of height difference between forward and backward leveling was less than $8\sqrt{K}$ mm, with K being the distance of the leveling section in kilometer units. Hence, another possible error is likely caused by the GNSS measurements. The GNSS observations were set up using tripods, making it prone to error in measuring the height of the antenna.

In this study, modeling the geoid using RCR methodology seems to be better than those other methodologies, including the SH and KTH methods. Hence, we further conducted a statistical analysis to investigate whether the accuracy performance across methodologies is statistically significant or not, using a t-test analysis with 95% confidence intervals based on the results of the absolute assessment. The t-values across the geoid models computed in this study fell below the critical t-value, suggesting that the differences in geoid models generated by the SH, RCR, and KTH methodologies are not statistically significant despite the apparent superiority of the RCR method. This finding is consistent with previous research conducted by, e.g., Wang et al. (2021), which also observed minimal differences in the results of geoid models derived from various methodologies made by different agencies using a similar dataset. This further supports the robustness of different geoid modeling techniques.

4. CONCLUSIONS

Geoid modeling was conducted for the central part of Java Island using terrestrial gravity data and three different methodologies: Stokes-Helmert (SH), Remove-Compute-Restore (RCR), and KTH. The primary differences among these methods are in their approaches to the Stokes formula and reduction scheme. Among the methods, the RCR method emerged as the most effective in terms of geoid model accuracy, with an RMS of 8.4 cm, outperforming the KTH method at 9.2 cm and the SH method at 10.7 cm. At the same time. the discrepancies in the geoid surface between the SH and RCR methods were less pronounced compared to those observed with the KTH method. This is evident from the range of difference values generated, where the disparity between the surfaces of the SH and RCR method models spans around 30 cm, while the difference between the KTH method and both the SH and RCR methods exceeds 1 meter. Further comparison with the global model of EGM2008 indicates that the resulting gravimetric geoid models are better with the different in RMS reaches up to 10 cm. This discrepancy is primarily due to a systematic difference between the EGM2008 geoid model and our gravimetric geoid models.

Given the observed differences in geoid models, we conducted a t-test analysis with 95% confidence intervals to determine if these differences were statistically significant. The results revealed that the t-values were below the critical threshold, implying that the variations between the

SH, RCR, and KTH methodologies are not statistically significant. Despite the RCR method demonstrating apparent superior performance, these differences do not reach statistical significance.

We stress that this study is made with a relatively limited gravity dataset, where only terrestrial gravity dataset is used. Future studies should be incorporating more gravity datasets, e.g., recent airborne gravity dataset (Bramanto et al., 2021), covering the gaps in in-situ gravity observations. This effort could potentially improve the performance of geoid models as suggested by Bjelotomić Oršulić et al., (2020). In addition, we acknowledge that only one profile line of GNSS/leveling observations is available, making it challenging to make a robust external absolute assessment of the resulting gravimetric geoid models. Denser GNSS/leveling observations with stricter measurement requirements are essential for future work.

ACKNOWLEDGEMENT

R E F E R E N C E S

Abbak, R. A., Erol, B., & Ustun, A. (2012). Comparison of the KTH and remove-compute-restore techniques to geoid modelling in a mountainous area. *Computers and Geosciences*, *48*, 31–40. https://doi.org/10.1016/j.cageo.2012.05.019

Abbak, R. A., Goyal, R., & Ustun, A. (2024). A user-friendly software package for modelling gravimetric geoid by the classical Stokes-Helmert method. *Earth Sci. Inform.* https://doi.org/10.1007/s12145-024-01328-0

Abbak, R. A., & Ustun, A. (2015). A software package for computing a regional gravimetric geoid model by the KTH method. *Earth Science Informatics*, *8*(1), 255–265. https://doi.org/10.1007/s12145-014-0149-3

Bajracharya, S., & Sideris, M. G. (2005). *Terrain-aliasing effects on gravimetric geoid determination*. *54*(I), 3–16.

Bjelotomić Oršulić, O., Markovinović, D., Varga, M., & Bašić, T. (2020). The impact of terrestrial gravity data density on geoid accuracy: case study Bilogora in Croatia. *Survey Review*, *52*(373), 299–308. https://doi.org/10.1080/00396265.2018.1562747

Borghi, A., Barzaghi, R., Al-Bayari, O., & Al Madani, S. (2020). Centimeter precision geoid model for Jeddah region (Saudi Arabia). *Remote Sensing*, *12*(12). https://doi.org/10.3390/RS12122066

Bramanto, B., Prijatna, K., Pahlevi, A. M., Sarsito, D. A., Dahrin, D., Variandy, E. D., & Munthaha, R. I. S. (2021). Determination of gravity anomalies in Java, Indonesia, from airborne gravity survey. *Terr. Atmospheric Ocean. Sci.*, *32*(5.2). https://doi.org/10.3319/TAO.2021.06.04.01

Ellmann, A., & Vaníček, P. (2007). UNB application of Stokes-Helmert's approach to geoid computation. *Journal of Geodynamics*, *43*(2), 200–213. https://doi.org/10.1016/j.jog.2006.09.019

Erol, S., & Erol, B. (2021). A comparative assessment of different interpolation algorithms for prediction of GNSS/levelling geoid surface using scattered control data. *Measurement*, *173*, 108623. https://doi.org/10.1016/j.measurement.2020.108623

Forsberg, R. (1984). A study of terrain reductions, density anomalies and geophysical inversion methods in gravity field modelling (No. OSU/DGSS-355). Ohio State Univ Columbus Dept of Geodetic Science and Surveying. In *Ohio State Univ Columbus Dept of Geodetic Science and Surveying*.

Forsberg, R., & Tscherning, C. C. (2008). *An overview manual for the GRAVSOFT: Geodetic Gravity Field Modelling Programs* (Issue August).

Gumilar, I., Fauzan, S. A., Bramanto, B., Abidin, H. Z., Sugito, N. T., Hernandi, A., & Handayani, A. P. (2023). The benefits of multi-constellation GNSS for cadastral positioning applications in harsh environments. *Appl. Geomat.*, *15*(4), 975–989. https://doi.org/10.1007/s12518-023-00525-8

Heck, B. (2003a). On Helmert's methods of condensation. *Journal of Geodesy*, *77*(3), 155–170. https://doi.org/10.1007/s00190-003-0318-5

Heck, B. (2003b). On Helmert's methods of condensation. *Journal of Geodesy*, *77*(3), 155–170. https://doi.org/10.1007/s00190-003-0318-5

Heiskanen, W. A., & Moritz, H. (1967). *Physical Geodesy*. Freeman.

Hoffman-Wellenhof, B., & Moritz, H. (2006). *Physical Geodesy (Second, corrected edition)*. SpringerWienNewYork. https://doi.org/10.1007/978-3-211-33545-1

Hofmann-Wellenhof, B., Lichtenegger, H., & Wasle, E. (2008). *GNSS – Global Navigation Satellite Systems: GPS, GLONASS, Galileo, and more*. Springer-Verlag.

Jekeli, C., Yang, H. J., & Kwon, J. H. (2013). Geoid determination in South Korea from a combination of terrestrial and airborne gravity anomaly data. *Journal of the Korean Society of Surveying Geodesy Photogrammetry and Cartography*, *31*(6 PART 2), 567–576. https://doi.org/10.7848/ksgpc.2013.31.6-2.567

Kizil, U., & Tisor, L. (2011). Evaluation of RTK-GPS and Total Station for applications in land surveying. *J. Earth Syst. Sci.*, *120*(2), 215–221. https://doi.org/10.1007/s12040-011-0044-y

Krzyżek, R., & Kudrys, J. (2022). Accuracy of GNSS RTK/NRTK height difference measurement. *Appl. Geomat.*, *14*(3), 491–499. https://doi.org/10.1007/s12518-022-00450-2

Lestari, R., Bramanto, B., Prijatna, K., Pahlevi, A. M., Putra, W., Muntaha, R. I. S., & Ladivanov, F. (2023). Local geoid modeling in the central part of Java, Indonesia, using terrestrial-based gravity observations. *Geod. Geodyn.*, *14*(3), 231–243. https://doi.org/10.1016/j.geog.2022.11.007

Martinec, Z., Matyska, C., Grafarend, E. W., & Vanicek, P. (1993). On Helmert's 2nd condensation method. *Journal of Geodesy*, *18*(August 2019), 417–421.

Matsuo, K., & Kuroishi, Y. (2020). Refinement of a gravimetric geoid model for Japan using GOCE and an updated regional gravity field model. *Earth, Planets and Space*, *72*(1). https://doi.org/10.1186/s40623-020-01158-6

Omang, O. C. D., & Forsberg, R. (2000). How to handle topography in practical geoid determination: Three examples. *Journal of Geodesy*, *74*(6), 458–466. https://doi.org/10.1007/s001900000107

Pavlis, N. K., Holmes, S. A., Kenyon, S. C., & Factor, J. K. (2012). The development and evaluation of the Earth Gravitational Model 2008 (EGM2008). *Journal of Geophysical Research: Solid Earth*, *117*(4), 1–38. https://doi.org/10.1029/2011JB008916

Schwarz, K. P., Sideris, M. G., & Forsberg, R. (1987). Orthometric heights without leveling. *J. Surv. Eng.*, *113(1)*, 28–40. https://doi.org/10.1061/(ASCE)0733- 9453(1987)113:1(28)

Schwarz, K. P., Sideris, M. G., & Forsberg, R. (1990). The Use of FFT Techniques in Physical Geodesy. *Geophys. J. Int.*, *100*, 485–514.

Sideris, M. G. (2013). Geoid determination by FFT techniques. *Lecture Notes in Earth System Sciences*, *110*, 453–516. https://doi.org/10.1007/978-3-540-74700-0_10

Sideris, M. G. (2021). *Geoid Determination, Theory and Principles* (H. K. Gupta, Ed.; pp. 476–482). Springer. https://doi.org/10.1007/978-3-030-58631-7_154

Sideris, M. G., & Forsberg, R. (1991). *Review of Geoid Prediction Methods in Mountainous Regions*. *March*, 51–62. https://doi.org/10.1007/978-1-4612-3104-2_8

Sjoberg, L. E. (1984). Least Squares Modification of Stokes and Venning–Meinesz Formulas by Accounting for Errors of Truncation, Potential Coefficients and Gravity Data. In *Technical Report*.

Sjöberg, L. E. (1991). Refined least squares modification of Stokes' formula. *Journal of Geodesy*, *16*(9), 367–375.

Sjöberg, L. E. (2003). A general model for modifying Stokes' formula and its least-squares solution. *Journal of Geodesy*, *77*(7), 459–464. https://doi.org/10.1007/s00190-003-0346-1

Sjöberg, L. E. (2020). Unbiased least-squares modification of Stokes' formula. *Journal of Geodesy*, *94*(9), 1–5. https://doi.org/10.1007/s00190-020-01405-4

SRTM. (2015). *The Shuttle Radar Topography Mission (SRTM) Collection User Guide*. 1–17. https://lpdaac.usgs.gov/documents/179/SRTM_User_Guide_V3.pdf

Tozer, B., Sandwell, D. T., Smith, W. H. F., Olson, C., Beale, J. R., & Wessel, P. (2019). Global Bathymetry and Topography at 15 Arc Sec: SRTM15+. *Earth and Space Science*, *6*(10), 1847–1864. https://doi.org/10.1029/2019EA000658

Vanicek, & Kleusberg. (1987). The Canadian geoid - Stokesian approach. *Manuscr Geod*, *12*, 86–98.

Vaníček, P., Kingdon, R., Kuhn, M., Ellmann, A., Featherstone, W. E., Santos, M. C., Martinec, Z., Hirt, C., & Avalos-Naranjo, D. (2013). Testing Stokes-Helmert geoid model computation on a synthetic gravity field: Experiences and shortcomings. *Studia Geophys. et Geod.*, *57*(3), 369–400. https://doi.org/10.1007/s11200-012-0270-z

Vu, D. T., Bruinsma, S., & Bonvalot, S. (2019). A high-resolution gravimetric quasigeoid model for Vietnam. *Earth, Planets and Space*, *71*(1). https://doi.org/10.1186/s40623-019-1045-3

Wang, Y. M., Sánchez, L., Ågren, J., Huang, J., Forsberg, R., Abd-Elmotaal, H. A., Ahlgren, K., Barzaghi, R., Bašić, T., Carrion, D., Claessens, S., Erol, B., Erol, S., Filmer, M., Grigoriadis, V. N., Isik, M. S., Jiang, T., Koç, Ö., Krcmaric, J., … Zingerle, P. (2021). Colorado geoid computation experiment: overview and summary. *J. Geod.*, *95*(12), 127. https://doi.org/10.1007/s00190-021-01567-9

Wong, L., & Gore, R. (1969). Accuracy of Geoid Heights from Modified Stokes Kernels. *Geophysical Journal International*, *18*(1), 81–91. https://doi.org/10.1111/j.1365-246X.1969.tb00264.x

Wu, Q., Wang, H., Wang, B., Chen, S., & Li, H. (2020). Performance Comparison of Geoid Refinement between XGM2016 and EGM2008 Based on the KTH and RCR Methods: Jilin Province, China. *Remote Sens.*, *12*(2), 324. https://doi.org/10.3390/rs12020324

Yang, M., Hirt, C., & Pail, R. (2020). TGF: A new MATLAB-based software for terrain-related gravity field calculations. *Remote Sensing*, *12*(7). https://doi.org/10.3390/rs12071063

Yang, M., Hirt, C., Wu, B., Deng, X. Le, Tsoulis, D., Feng, W., Wang, C. Q., & Zhong, M. (2022). Residual Terrain Modelling: The Harmonic Correction for Geoid Heights. *Surveys in Geophysics*, *43*(4), 1201–1231. https://doi.org/10.1007/s10712-022-09694-4

Yildiz, H., Forsberg, R., Ågren, J., Tscherning, C. C., & Sjöberg, L. E. (2012a). Comparison of remove-compute-restore and least squares modification of Stokes' formula techniques to quasi-geoid determination over the Auvergne test area. *J. Geod. Sci.*, *2*(1), 53–64. https://doi.org/10.2478/v10156-011-0024-9

Yildiz, H., Forsberg, R., Ågren, J., Tscherning, C., & Sjöberg, L. (2012b). Comparison of remove-compute-restore and least squares modification of Stokes' formula techniques to quasi-geoid determination over the Auvergne test area. *Journal of Geodetic Science*, *2*(1), 53–64. https://doi.org/10.2478/v10156-011-0024-9

Zaki, A., & Mogren, S. (2022). A high-resolution gravimetric geoid model for Kingdom of Saudi Arabia. *Survey Review*, *54*(386), 375–390. https://doi.org/10.1080/00396265.2021.1944544

THE CONTRIBUTION OF REMOTE SENSING IN HIGHLIGHTING THE RESILIENCE OF RANGELANDS THROUGH INDICATORS OF LAND SURFACE TEMPERATURE AND THE NORMALIZED DIFFERENCE VEGETATION INDEX IN THE TIHAMA ALLUVIAL PLAIN

Azaiez NAIMA [1] ⓘ

ABSTRACT

The rangelands form a precious heritage of an ancient agro-pastoral system in Saudi Arabia, known for its livestock based on camel. The extensive rangelands in the Tihama alluvial plain are facing a deterioration in climatic conditions. In the past, the monitoring of these rangelands, in general, was done by direct vegetation surveys in the field. Currently, researchers have greatly benefited from the contribution of remote sensing, especially with the eighth generation of Landsat satellite images, making it possible to provide values relating to the thermal emissivity of the ground surface, obtained in the two bands 10 and 11. This method allows the calculation of algorithms and the creation of advanced models. The creation of a multi-source database established on the exploitation of the Geographic Information System and remote sensing was necessary to identify the local conditions that have favored the resilience of the plant cover, and the identification of multiple intervention methods appropriate to each sector according to its state of resilience. The results revealed a reduction in soil temperature average, increasing from 29.5 - 42.5°C in 2013 to 38.2 - 25.3°C in 2022. These changes are accompanied by a significant expansion of the vegetation cover, estimated at 26% over the same period despite the substantial climate changes the region has experienced. In the Tihama plain the LST index is significantly influenced by the type of deposit, soil salinity, soil moisture, as well as the density of soil benches. On the adjacent eastern and north-eastern slopes, the values are much lower due to the altitude, the sheltered position, the inclination of the angle of incidence of the sun's rays and the disparity in the colours of the rocky outcrops.

Key-words*: LST index, NDVI index, thermal comfort, plant resilience, rangelands, surface humidity.*

1. INTRODUCTION

In the present study, attention will be focused on the alluvial plain of the Hili and Yabbah wadis, which has undergone complex geomorphological dynamics in which forms of hydric origin mingle with those of eolian origin to give rise to a green space in an arid zone, despite the climatic changes that are in vigour. Although the scientific communities agree on the role of the mountains as the driving force behind the major local climatic constraints, certain disparities are sometimes noted in the plains, where local climatic and edaphic conditions are very favourable for the rehabilitation of natural plant cover. In the same perspective, the Tihama plain constitutes a real experimental laboratory to identify the different facets of landscape changes that have occurred during the last decade. The study area has special morphoclimatic characteristics due to its position between the sea and the Sarawat mountain range, which have largely conditioned a geomorphological dynamic controlled by the combined effects of water flow and wind. In order to enhance our understanding of these recent vegetation dynamics, it was necessary to accurately identify the contribution of the associated geomorphological forms and the role of different natural and anthropogenic factors in enhancing the state of the vegetation cover. Thus, a number of remote sensing indices were developed by multidisciplinary researchers to determine the behaviour of the soil related to hydro-climatic and human factors. The two most widely used indices are the Normalized Difference Vegetation Index (NDVI) and the Normalized Difference Water Index (NDWI).

---
[1] *King Khalid University, Department of Geography, Abha 62521, Saudi Arabia, azaieznaima@yahoo.fr*

Recently, several studies have been carried out investigating the identification of the LST parameter, which is mainly used in the estimation of thermal comfort in urban and peri-urban areas, in the delimitation of urban land and in the determination of the role of vegetation cover in the restoration of living conditions in large cities (Sobrino et al., 2004; Tahouri et al., 2017). Many others fields of investigation are particularly relevant to LST index as a crucial input parameter, such as drought, forestry, pasture monitoring, climate comfort studies, urban heat islands and so on (Ivan and Benedek, (2017), Roy and Bari, 2022; Varamesh et al., 2022; Degefu et al. 2023). There for, many researchers have explored this research area and they have provided valuable insights into the LST index and how it affects pasture conditions (Gleyce et al., 2019). Guha and Govil (2020) have revealed an inverse relationship between LST and NDVI values using the principal components statistics method. They have also shown that the LST index is strictly controlled by surface characteristics and seasonal changes. The accuracy of this key parameter was judged in order to achieve an optimum improvement in the results, so (García-Santos et al., 2018) tried to test a correction algorithm on band 11 of Landsat 8 satellite images to reduce the error caused by stray light.

Three algorithms (mono-window algorithm, split window algorithm (SWA) and single-channel (SC)), were tested to extract the LST map from the Landsat 8. The results showed that the split window algorithm (SWA) was the least sensitive to error (Gerace and Montanaro, 2017; Jiang and Lin, 2021). In the present research, this index will be used to understand the causes of the increase in humidity and the proliferation of usable water reserves in the soil, despite the decrease in rainfall in terms of quantity and seasonal distribution. Moreover, the alluvial plain of wadis Hili and Yabbah has not been the subject of detailed scientific reflection using similar techniques.

Fig. 1. Location map of the study area.

2. STUDY AREA

The study area extends over a 50 km long and 30 km wide strip in the west of Saudi Arabia. It lies between the El Gonnaa-El Msherif sector in the north, the Saida Soualha plain in the south, Khamis Harb in the north-west and the Wadi Hili dam in the south-west. Its altitudes range from 0 m in the west to 210 m in the east. It is characterized by a variable climate throughout the year (**Fig. 1**).

It is hot and moist in summer, hot and dry in winter, and winter rains are rare. Dusty winds are very frequent in autumn. With no topographical obstacles on the seaside, the alluvial plain is widely open to the prevailing winds blowing from the west-southwest with a speed between 10 and 20km/hour (Meteoblue, 2022). The sand and fine alluvium are constantly swept over short distances by a modest, almost monodirectional wind.

Several studies that are interested in wind activity show that gusty winds seem to be very rare in the region. Thus, microbursts and calm winds were the most frequent winds with 26 occurrences for wind blowing from 5 to 10 km/hour and 9 occurrences for 15 to 20 km/hour on an annual scale (Yu et al, 2015; Albugami et al, 2019). A detailed study of wind in Saudi Arabia over a long period (1978-2013 series), shows a trend towards a noticeable decrease in wind speed (**Fig. 2**).
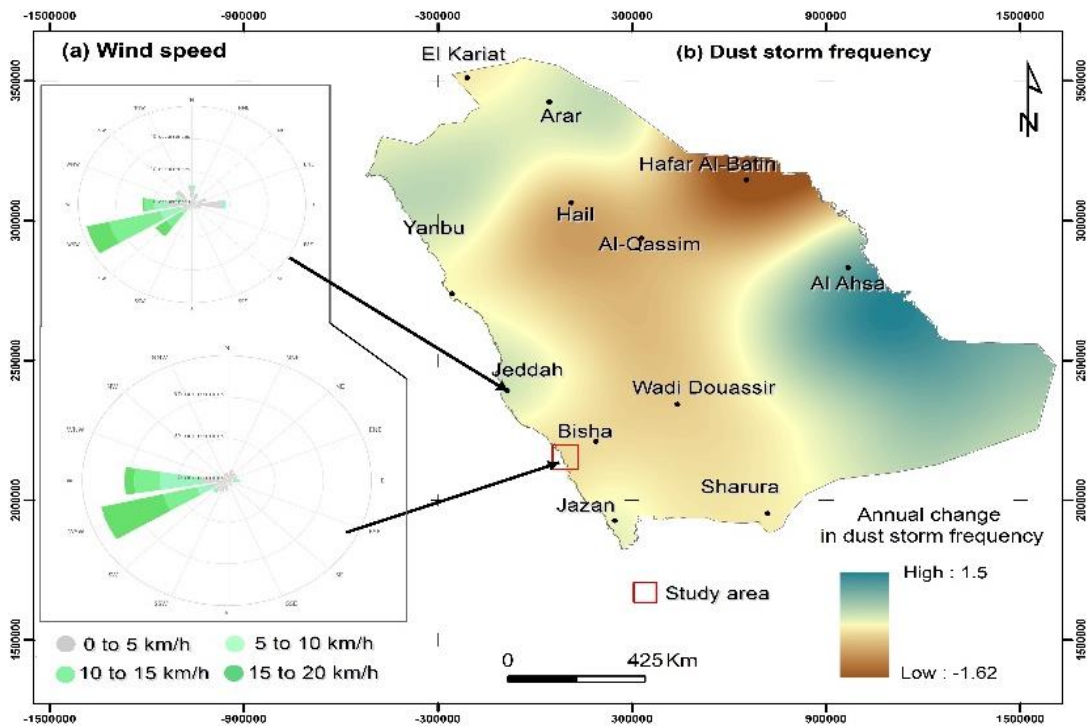
Fig. 2. Annual change in dust storm frequency (number of events/year) (b) and wind speed (a) over Saudi Arabia between 2000/2017. (*Source: Saudi Meteorological Authority and Meteoblue, 2022*).

For the sake of conciseness, this study is based on the above results, insofar as it took into consideration the winds measured near the ground, which can have a direct effect on the mobilisation of medium to coarse sand. Indeed, this study found almost consistent results with another study conducted on the annual evolution of dust storms. The negative relationship observed between light and gusty winds implies that sand winds have become increasingly weaker especially during spring and summer due to the increased humidity caused by the high evaporation in the Red Sea. The situation is closely related to seasonal maximum temperatures occurring between July and September which coincide with a reduction in precipitation, yet dust storms remain less frequent over the western

coastal strip of Saudi Arabia due to the high humidity (Albugami et al, 2019). Dust clouds can only be generated by microbursts or by adiabatic upwelling of dry continental air. All these facts explain a certain stabilization of the dunes, especially those close to the sea, promoting the growth of a basic vegetation that has adapted very quickly to give rise to a vegetation cover with a great pastoral potential. In contrast to this western wind dynamic, the study area is constantly confronted with a hydric dynamic, which becomes apparent in rainy years (Shi, 2014; Azaiez, 2021).

The inhabitants are prepared for untimely floods and are called upon to manage huge quantities of water from temporary torrents. These torrents flow down the mountain in deep valleys to the alluvial plain in the form of a large pool (Shi, 2014). The flood waters are diverted from the main channel and then directed towards the farming plots and rangelands by a system of benches which favours the storage of water in the soil. (Mollard et al, 2008). By slanting ditches oriented upstream diagonally with the channel, the farmers seek to create a counter-slope of the water upstream to favor a maximum lateral submersion of the land located on both sides of the watercourse, sometimes, quite far from it. The diagonal shape of the dikes avoids any direct position with the main flow that could cause their breach. On the upstream limits, several shallow channels guide the slow-moving water towards the various cultivated plots and rangelands. The main problem lies in the unpredictability of the magnitude of the floods. When they are strong, they wash away the dikes of the closest plots but properly submerge the more distant ones. By contrast, a weak flood correctly irrigates the upstream plots, close to the waterway, but plots located further downstream are deprived of water. In fact, the choice of water mobilization in the spreading plain would not be without consequences because of the sporadic character of the floods. The farming practices in the study area depend on rainfall and the distribution of fertile clay soils, or slightly sandy soils. (Shi, 2014).

3. METHODOLOGY AND TOOLS

There are many options for studying changes in rangelands landscapes. Remote sensing indices are a complementary tool to the traditional prospective method based on fieldwork. They have made a useful contribution to monitoring soil surface temperature since the appearance of the new generation of high-resolution Landsat (8 and 9) satellite images (Oguz, 2013; Bindajam et al, 2020). These images make it possible to study the functioning of the Soil-Atmosphere-Vegetation system and to focus on salinisation processes in relation to a new environmental trend and attempts by local populations to benefit from flood spreading. To explain the improvement in pastoral conditions in the Tihama plain, a multi-source approach based on remote sensing, statistical analysis and cartographic method was used. As a result, the two red and near infrared bands (5 and 4) were used to calculate NDVI and soil moisture indices. Bands 10 and 11 were used to estimate the LST index.The maps produced represent changes in thermal conditions and, consequently, variations in vegetation cover in terms of quantity and quality. The analysis was based on a diachronic approach with reference to Landsat 8-9 OLI/TIRS C2 L2 images of 2013 and 2022. Three parameters (LST, NDVI and soil moisture index) were calculated to obtain a more reliable estimations of the rangeland's aspects.

3.1. Land Surface Temperature changes between 2013-2022 depending on the NDVI index

The Land Surface Temperature (LST) index is considered a parameter of paramount importance. The good results have aroused great interest for geographers. Amongst others, it allows us to identify changes in land use and to improve our knowledge of the water status of the soil before and after the installation of embankments and flood control channels. The objective is to develop flexible solutions and to think about the possibility of generalizing this experiment to regions with similar environmental conditions (Oguz, 2013; Bindajam et al, 2020; Mallick et al, 2020). As a first step, two satellite images 2013 and 2022, taken during the spring, were selected. Then geoprocessing is performed in Arc GIS, starting with a composition of the bands under the "raster processing" tool. It should also be noted that both images have undergone an atmospheric correction to get rid of the potential effects of the different atmospheric components (cloudiness, aerosols...).

-Top of Atmosphere Radiance TOA (L) = ML * Qcal + AL $\qquad$ (1)

with:
Qcal = quantized and calibrated standard product pixel values;
ML= Band-specific multiplicative rescaling factor from the metadata (Reflectance_Mult_Band_X);
Al = Band-specific additive rescaling factor from the metadata (Reflectance_Add_Band_X).

Brightness Temperature (BT) defined as a radiation luminance and was transformed in (°C), using the following equation:

$$BT = \frac{K2}{(\ln (K1 / L) + 1)} - 273.15 \qquad (2)$$

-Normalized Difference Vegetation Index (DVI) = $\frac{(\text{Band 5} - \text{Band 4})}{(\text{Band 5} + \text{Band 4})}$ $\qquad$ (3)

-Portion Vegetation (PV) = $\frac{((\text{NDVI} - \text{NDVImin})}{(\text{NDVImax} - \text{NDVImin}))}$ $\qquad$ (4)

With Surface Emissivity Retrieval (ε) = 0.004 * Pv + 0.986 $\qquad$ (5)

-Land Surface Temperature (LST) index = $\frac{BT}{(1 + (0.00115 * BT / 1.4388) * \text{Ln}(\varepsilon)))}$ $\qquad$ (6)
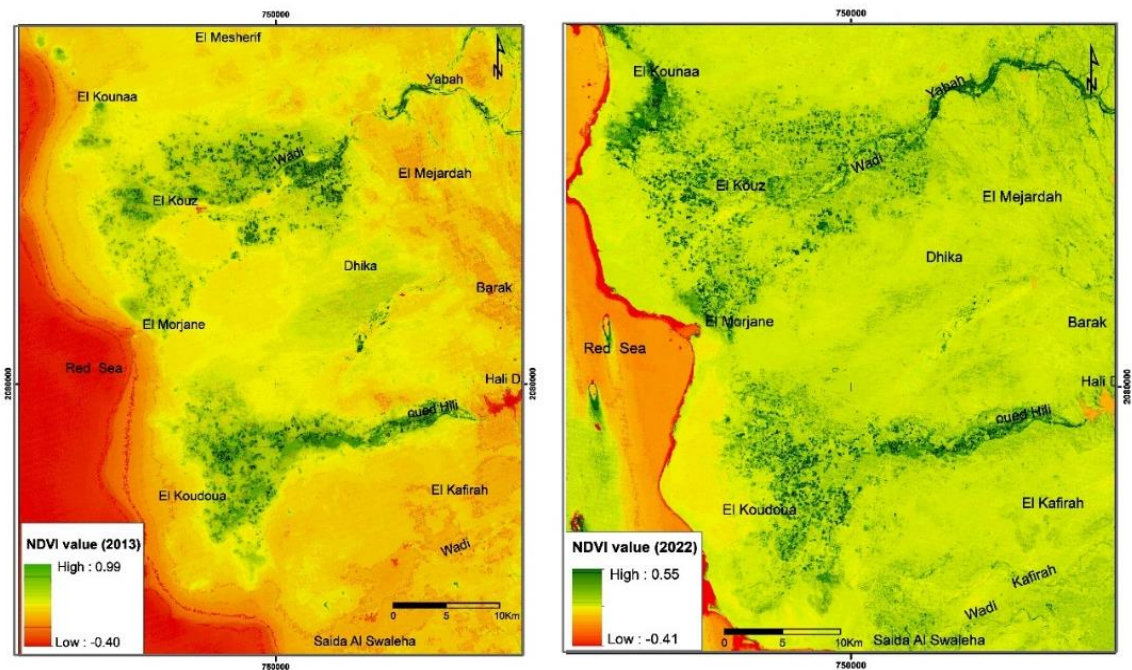
Fig. 3. Normalized difference vegetation index (NDVI) maps at the southern part of the alluvial plain of Tihama in 2013 (A) and 2022 (B). (*Source: Landsat 8-9 satellite images*).

The detailed mapping of this parameter reveals that LST values differ significantly according to land use patterns. The highest value was found in the bare land and the lowest LST was in pasture areas. The modelling of two parameters, the LST and NDVI indices, illustrates that they are closely related.

The (LST) values are inversely proportional to the NDVI values for the year 2013 as for the year 2022. Good soil cover results in lower soil surface temperature. The NDVI values are higher in 2022, although spring 2013 was wetter (**Fig. 3**). This situation clearly confirms the improvement in soil moisture conditions.

3.2. Land use changes between 2013 and 2022

One of the main observations obtained from the modeling is the proliferation of vegetation covering, which contrasts with the regional aridity. An increase of 26% in the planted area occurred in less than 10 years (**Fig. 4**). These are the coastal plains and the alluvial plain of the wadi Hili which have benefited the most from this new situation. A second highly localized proliferation in the intermediate sectors has accompanied the reforestation programs. Detailed mapping on a more accurate scale will undoubtedly be interesting for identifying the relationship between the ground temperature index (GTI), salinization and the changes in the vegetation cover. The surface skin temperature of the soil is of primary importance. It conditions the rhythm of heat and water exchanges with the atmosphere and determines the length of the vegetation season and the water balance in the soil. However, the involvement of other geographical and atmospheric factors should not be overlooked. The bay's position allows for more pronounced warming of the water, which causes additional evaporation along the shoreline. Thus, a sea breeze loaded with moisture can travel several kilometers inland during the day through the bay El Morjane and that of Saida Swaleha. In bad weather, this breeze can contribute to the onset of rains and thunderstorms in the hinterland in the plain of El Kouz-el Koudoua (spreading plain of Hili and Yabbah). Through earth levees and benches, farmers were able to create a traditional system of conducting water from the wadis Hili and Yabbah coming from the high mountain peaks of Sarawt and crossing extremely steep slopes to reach a depressed plain, where the flow was slow and difficult, due to the low slope and the presence of alluvial fans. The wind deflation causes a strong mobility of the dunes that are repeatedly carried away by an active wind. Almost all the rangelands of the Tihama plain are exposed to the combination of two phenomena that are likely to produce devastating effects.
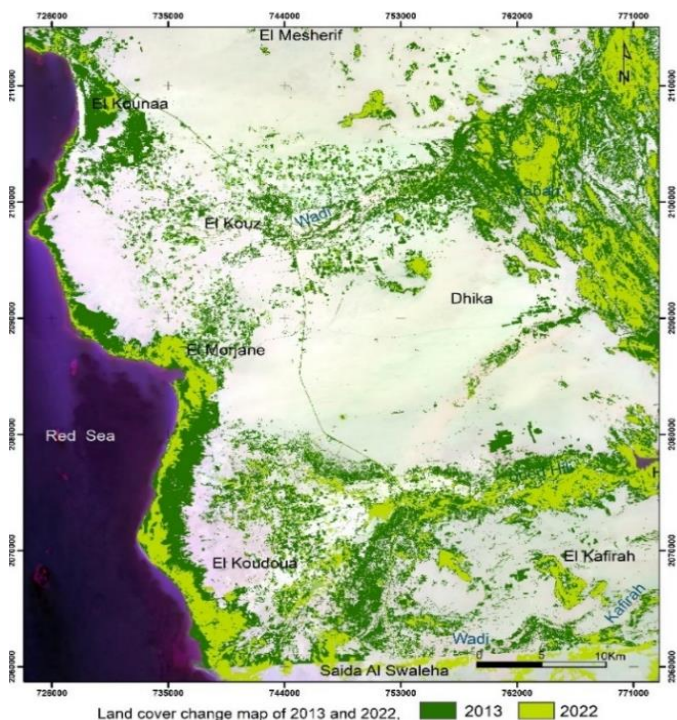
Fig. 4. Vegetation Change between 2013-2022. (*Source: Landsat 8-9 satellite images (2013/2022)*).

Dust storms and sandstorms on the one hand and occasional floods on the other. Thus, some rainfall events are difficult to manage because of the peculiarity of the study area and the unpredictability of floods, although ordinary floods have been beneficial for the most part. The study area has recorded dust storms respectively between 1and 2 in spring and winter and autumn and between 4 and 5 storms in summer between 2000 and 2017 (Albugami et al, 2019). These recorded values are among the lowest recorded in the country since the year 2000. This clear decrease is closely related to low wind speeds. The prevailing wind is essentially from the west-southwest. It follows a maritime trajectory which is the source of the high humidity. The most dust storms occurring during the summer season come from the Sudano-Egyptian desert. The influence of these dust storms increases on the western shore of the Red Sea and gradually fades on the eastern coast (**Fig. 5**).

The notable decrease in wind speed and the number of dust storm days may be the reason for the recent stability of the dunes and the rehabilitation of the natural vegetation cover that acted as a windbreaker. Indeed, these results underline the community efforts to manage water resources and combat desertification. In the same perspective, Saudi Arabia is distinguished by its commitment in an ambitious program to improve rangeland and dune fixation in two pilot areas (Douassir and El Quenfudah).

Based on the available water resources, coming from the wadis, the local authorities with the help of farmers, have been able to set up an adequate drainage system based on ridges and benches allowing a more balanced redistribution of water availability based on the spreading of flood waters, by helping the vegetation cover to develop in areas formerly subject to a very strong wind deflation. Thus, a fixation of dunes can be established in the short and medium terms.
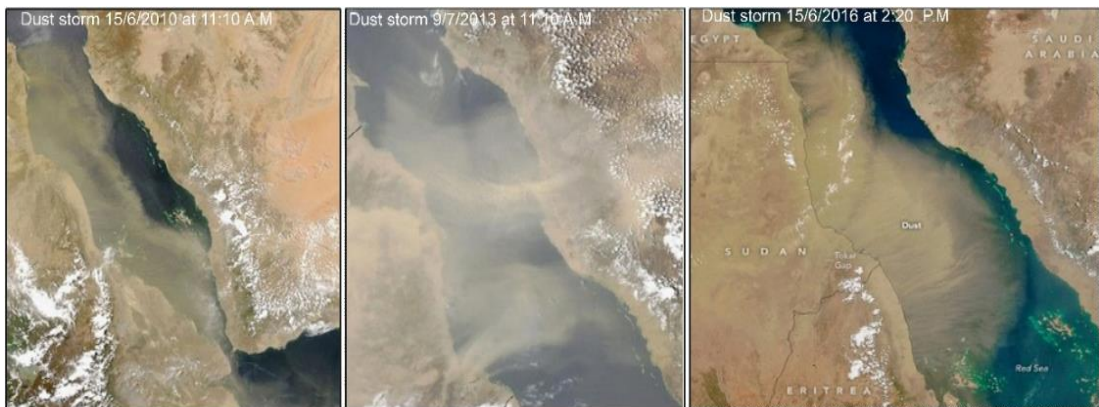
Fig. 5. Direction of dust storms spread from the Sudan-Egyptian desert towards Saudi Arabia for some key dates selected. (*Source: These top images were acquired by the Moderate Resolution Imaging Spectroradiometer (MODIS) on NASA's Terra satellite at 11:10 a.m. The lower image is from the MODIS sensor on NASA's Aqua satellite, acquired at 2:20 p.m.*).

4. RESULTS AND DISCUSSION

According to the comparative study of natural vegetation cover through the modelling of certain remote sensing parameters, it was found that a resilience of vegetation cover is confirmed, despite the deterioration in climatic conditions and the increase in the frequency of extreme climatic events during the last decades globally and locally. The direct interpretation of the (LST) maps from the modeling reveals two gradients. A first main latitudinal gradient ascending south-north that follows in accordance with the increase in the incidence angle of solar radiation and the duration of sunshine with a gradient starting from 34 °C to 38.5 °C in 2022 (**Fig. 6**).
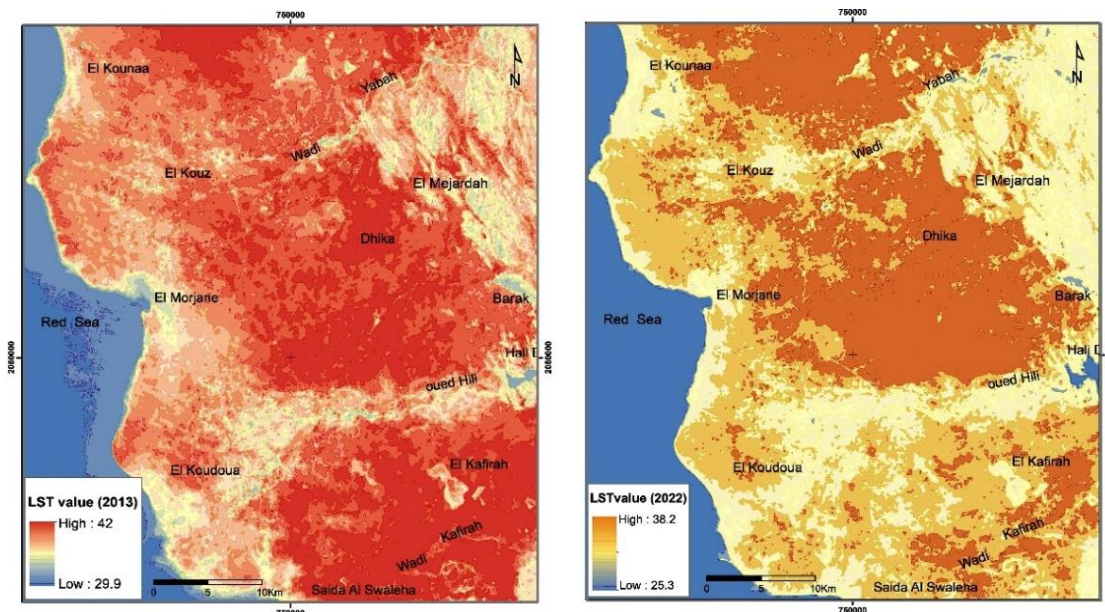
Fig. 6. The Land surface temperature (LST) maps of the study area in 2013 (A) and 2022 (B).
(*Source: Landsat 8-9 OLI/TIRS C2 L2 images of 2013*).

A second altitudinal gradient ascending from east to west from 25.3°C in the mountain sectors to 38.5 °C at the coastal plain for the same year. A meticulous interpretation of the research results carried out at a finer scale in the Tihama plain, showed that the LST index is significantly influenced by the type of deposit (alluvial or aeolian), the salinity of the soil, its humidity, as well as the density of the soil benches and ridges (Azaiez, 2021). However, the hottest sectors are in the intermediate zone between two spreading cones, considered the zone least supplied with runoff water. A clear drop in temperature occurred on the outskirts of the spreading plain with the establishment of plant cover, under the effect of shading and partial absorption of the sun's rays during the operation of photosynthesis. This decrease is illustrated by the trend curve of 3 simulated indices (**Fig. 7**).

On the adjacent slopes on the east and northeast side, the values are much lower due to the altitude, the sheltered position of some slopes, the inclination of the angle of incidence of solar radiation and the disparity of colors of the rocky outcrops.
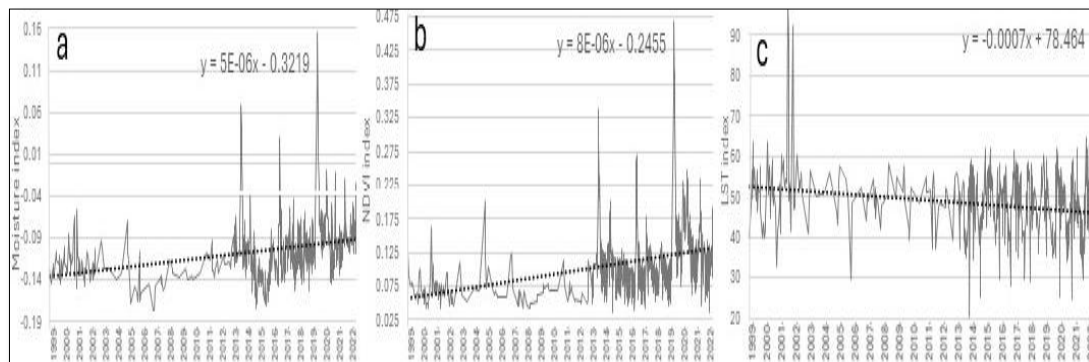
Fig. 7. Changes in soil moisture (a), NDVI index (b) and LST index (c) in the alluvial plain of wadi Hili between 1999 and 2022. (*Source: Processing of data available on the climate Engine website*).

The typical vegetation cover of the study area is characterized by trees with a broad and very branched framework, which provide permanent shade and continuous storage of moisture in the soil over a long period, which explains the persistence of the vegetation cover and its proliferation. However, the beneficial effect of some windbreakers formed by Salvadora persica and Gasuarina should not be overlooked. Their implementation comes as a state response to the specific requirements of windbreaks to fight against desertification. This state intervention has been limited to sectors in intermediate positions in relation to the two alluvial plains of the wadis Hili and Yabbah. In these sectors, the wind dynamics are even more active because the soil lacks moisture, which gives a more free and devastating wind action. Since 2004, the implementation of a single windbreak curtain arranged in a zigzag pattern over 1.5 km in the Al Konnaa plain to limit the effect of wind blowing from the west and west-southwest, has shown encouraging results and exceeded expectations within a decade. In the Al Konnaa plain, the vegetation cover increased to 92.5% within a decade (**Fig. 8**). Farmers responded by developing stepped sills along the Hili and Yabbah streams to slow the flow and by raising multi-directional soil ridges on both sides of the streams to counteract the adverse effects of flooding and to ensure a more balanced distribution of floodwaters among the different agricultural plots and rangelands.
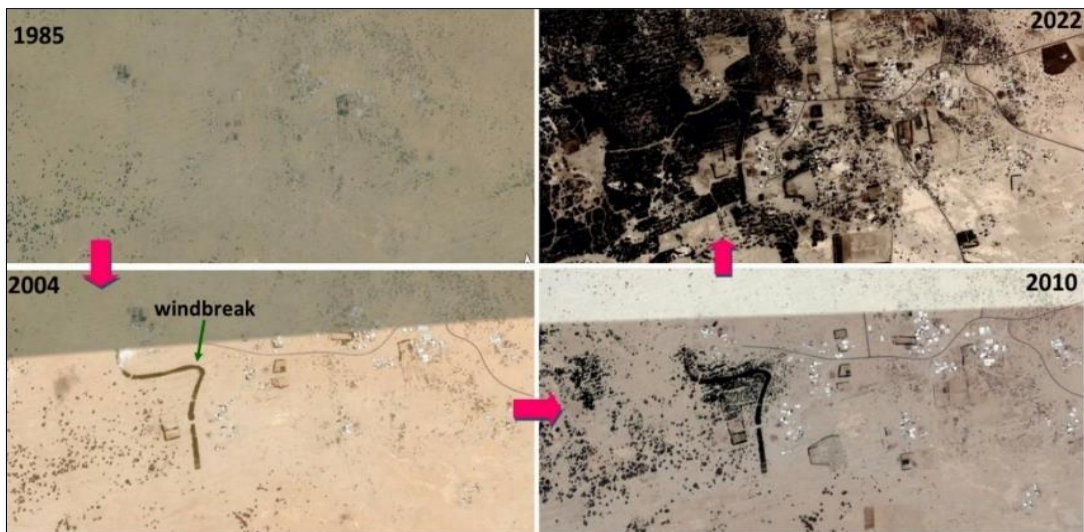
Fig. 8. Proliferation of vegetation cover following reforestation efforts in the Kounaa sand dunes between 1985-2022. (*Source: Image Google Earth Pro).*

A survey of some farmers confirms a significant increase in soil water potential and a stabilization of moisture in fine-textured soils during periods of low water. A new vegetation has developed spontaneously to give rise to small livestock in the village settlements around the El Quenfudah area. The improvement in environmental conditions is attributable to the serious commitment of the state to a strategy of collaborative efforts with local communities to combat desertification. This is indeed a very ambitious program that meets the medium and long-term objectives of local communities in the field of agriculture and livestock farming in the region of El Quenfudah and its surroundings. In addition, the problem of water scarcity is expected to be aggravated with the increasing pressures on water resources, especially in the context of conflict between domestic, tourism, and agricultural uses. The program requires additional monitoring and more detailed data collection on soil moisture variation. The normalized humidity difference modeling shows a close relationship between humidity and canopy density, with a slight difference between the alluvial plain of Hili and that of yabbah. The latter showed less moisture retention,

although wadi Hili is blocked by a dam located 10 km upstream of the plain. (**Figs 4** and **8**). Indeed, the seasonal monitoring of soil moisture is a key parameter in identifying periods of water stress. These regions are home to a significant portion of Saudi Arabia's rangelands. A comparison between the two situations of 2013 and that of 2022 shows an improvement in soil moisture and NDVI index in terms of value and distribution (**Figs 3,7** and **9**).
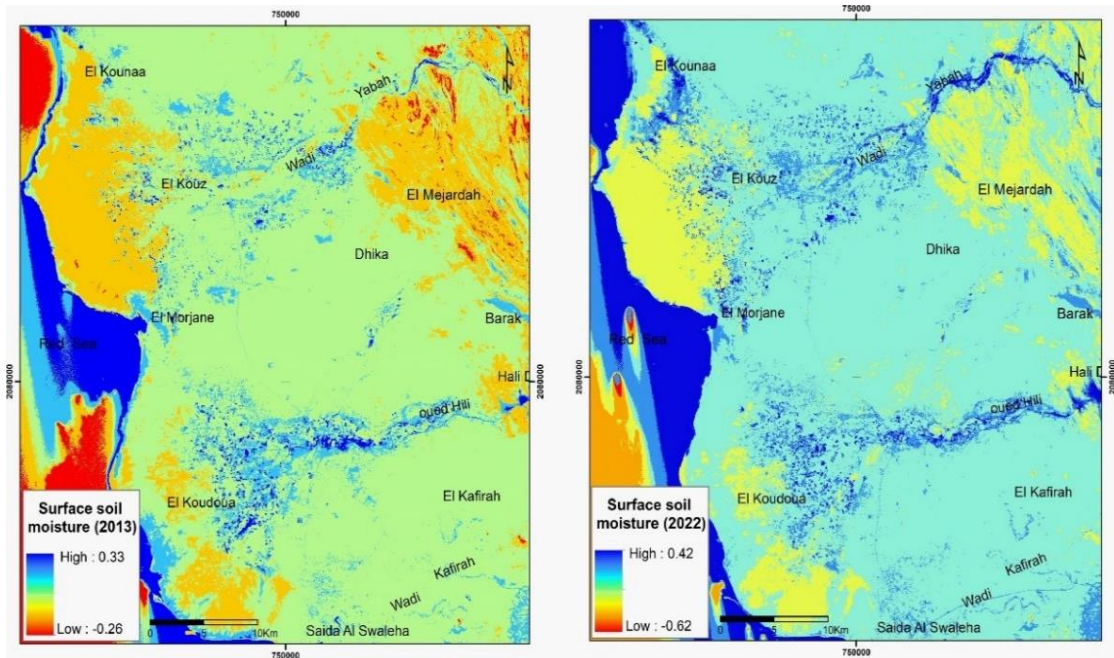
Fig. 9. Maps of the surface soil moisture distribution for the month of April, estimated from the Landsat 8-9 satellite images 2013 (A) and 2022 (B). (*Source: Landsat 8-9 satellite images).*

The sediments are deposited in separate spreading cones, having partially coalesced towards the extreme west of the Tihama plain. These outwash plains are characterized by varied deposits representative of former, sometimes contradictory, climatic periods. This conical arrangement allows an equitable distribution of humidity between the different compartments of the alluvial plain thanks to the good circulation of water in the surface horizon of the soil in the alluvial plain. Within this framework, special attention must be paid to the dunes for two reasons that are deemed fundamental (Azizov and Atbayev 1987) The first is the importance of dunes in terms of extension. They are the main component of the geomorphological landscape of the region of El Kouz and El Koudoua. The second is related to the exploitation of their possible water potential in the region. Thus, there is still work to be done to develop our knowledge on the distribution of the vegetation cover according to the vertical and lateral variation of the soil surface moisture (Guerf and Amriche, 2015). The monitoring of percolation, internal circulation and storage of flood water should be done sequentially and seasonally with a step of 30cm to a depth of 3.5m to 4m to better estimate its distribution and optimize the use of available water resources, choosing plants that adapt more easily with the local conditions of the region (Zribi et al, 2014; El Garouani et al., 2021). The correlation between vegetation and soil water conditions is also demonstrated by statistical analysis based on 500 random points, resulting in a positive correlation between the NDVI and moisture indices. However, the correlation is inverse between (LST) and NDVI values (**Tab. 1**). The evaluation of existing plant species remains a concern, especially for species that are favored by livestock. This study must be accompanied by a proposal of a wide range of plant species capable of establishing a better adaptation to the edaphic conditions and to overcome the climatic accidents that limit their growth. In many areas, the problem of degradation is essentially related to the distribution of livestock, in terms of the

number and type of livestock and the type of breeding practiced, as well as the grazing behaviour of the livestock. The consideration of all these aspects will allow the development of adequate strategies for the improvement and preservation of these rangelands. Thus, the creation of a working team involving young multidisciplinary researchers is a vital element to achieve the objectives of Saudi Arabia's 2030 vision in terms of biodiversity conservation and rehabilitation of fragile natural environments that are sensitive to climate change (Getachew, 2017).

Tab. 1.
Relationship between LST, NDVI and Soil Moisture indices.

Variables	LST index	moisture index	NDVI index
LST index	1		
moisture index	-0.71	1	
NDVI index	-0.679	0.899	1

The carrying out of a survey among farmers in pilot areas remains a very good method to know their habits in the rangelands and to highlight other facts acting on the evolution of the landscape. This is a crucial step to take decisive environmental actions in these rangelands that are recovering, but it is not yet at a perfect pace. Through multiple comparisons with other study areas, we can estimate the regional representativeness of the results to follow a rational intervention that respects the local and regional characteristics of each geographical unit in Saudi Arabia. Experimental results conducted at the College of Engineering in Saoud University showed a clear improvement in the engineering properties of sand dunes and their geotechnical properties after treating it from the surface by adding bentonite mineral, which made the treated dunes not move unless the wind speed exceeded 100 km/h.

The importance of this research comes from the specific nature of the Tihama coastal plain which constitutes a typical morphogenic system formed by coalescing alluvial fans in the north and individual ones in the south, where the accumulations are rapidly redistributed and reshaped by the different floods and rearranged by the wind. Another comparison of the LST index in the middle part of two alluvial plains showed lower LST values in the Wadi Hili plain than in the Wadi Yabbah plain. This variation is attributed to the phenomenon of bleaching of the surface soil horizon, which leads to a reflection of solar radiation and a reduced radiation balance. This different dynamic between the two plains is related to the large volumes of water drained and a specific mineralogical evolution in the plain of Wadi Hili, which deserves to be better analyzed in detail. The results in terms of tracing salinity have shown a concentration of salinity increasingly accentuated at the outlet of Wadi Hili compared to that of Yabbah.

In addition, the paper offers a useful information on environmental monitoring through a judicious mix of methods such as GIS and RS (Gomes and Caracristi, 2021; Hussain et al., 2023). New insights into the effectiveness, combination and implementation of the tools used for the novelty of rangeland monitoring in the context presented and this is provided by the detailed information offered on rangeland monitoring. It would be advantageous to extend the study area and incorporate a wider range of indices to provide more conclusive results and a more provide a more comprehensive perspective.

5. CONCLUSION

At the end of this research, monitoring the evolution of rangeland vegetation by evaluating the values of the (LST) and (NDVI) indices revealed a spatial variation in the distribution of plant cover that is closely linked to surface temperature variations. Obtaining LST values by using algorithms based on the integration of biophysical parameters and the exploitation of multispectral images is only one step among others. It has opened new paths of research that were previously uncommon and used for very strictly limited purposes.

The climatic index (LST) compared to a plant physiology index (NDVI) has shown the cooling effect of the vegetation cover and the shading effect in reducing evaporation. This fact is largely favored by water bodies, soil moisture and vegetation. However, the improvement of the water reserve in the alluvial plain still depends on the implementation of soft hydraulic techniques. The remote sensing makes a valuable contribution to the knowledge of the natural environment. The results showed very variable values of the LST index even within the vegetated sectors. The (LST) values are inversely proportional to the (NDVI) values and the density of the vegetation cover. Thus, with increasing (NDVI) values, the LST index decreased considerably to its lowest values in the alluvial plains that have dense vegetation cover, high humidity and intense agricultural activity.

The different vegetation composition probably influences the radiation balance of rangelands and agricultural plots (Gleyce et al., 2019). Vegetated areas with grass, bushes and trees do not necessarily have the same (LST) value because the rate of water consumption differs in accordance with the structure of the plant itself. The choice of the spring season of 2013 and 2022, is justified by similar climatic characteristics. Without denying the importance and validity of remote sensing, it does have its flaws. It is necessary to test the model several times, considering the season and time of acquisition of satellite images, because soil moisture and temperature are closely related to the solar radiation, water circulation, water exchanges between the water table and the topsoil and the speed and direction of wind.

The detailed study of these different elements of the natural environment and the comparison of the results will make it possible to partially overcome the shortcomings of the modeling and the algorithms obtained. Other studies have shown a strict relationship between the decrease of the LST value in the intermediate sector between two alluvial plains and the lowering of the water table each time we move away from the wadi axes. This hypothesis remains to be verified in the study area. The results may be improved by studying the vegetative cycle of annual plants, which are considered an additional source of fodder.

ACKNOWLEDGEMENT

R E F E R E N C E S

Azaiez, N. (2021) Contribution of the adjusted empirical analysis of the RSULE and FAO Models in the estimation of soil losses in the watershed of wadi El Hayat, (Saudi Arabia), Arabian Journal of Geosciences, 14 (2185), pp 1-18.

Azizov, A. and Atbayev, B. (1987) Influence of windborne sand on erosion resistance of soils treated with various preparations, Problems of Desert Development, (2), pp 85-90.

Bindajam. A. A, Mallick, J. AlQadhi, S. Kumar Singh, CH. and Thi Hang, H. (2020) Impacts of Vegetation and Topography on Land Surface Temperature Variability over the Semi-Arid Mountain Cities of Saudi Arabia, Atmosphere 2020, 11(762), pp 1-28.

García-Santos, V., Cuxart, J., Martínez-Villagrasa, D., Jiménez A.M. and Simó G. (2018) Comparison of Three Methods for Estimating Land Surface Temperature from Landsat 8-TIRS Sensor Data. Remote Sens,10 (1450), pp 2-13.

Degefu, M.A. D., Argaw, M., Legese Feyisa, G. and Degefa, S. (2023) Dynamics of green spaces- Land surface temperature intensity nexus in cities of Ethiopia, Heliyon, 9, pp 1-18.

El Garouani, M. Amyay, M., Lahrach, A. and Oulidi, H.J. (2021) Land Surface Temperature in Response to Land Use/Cover Change Based on Remote Sensing Data and GIS Techniques: Application to Saïss Plain, Morocco, Journal of Ecological Engineering, 22(7), 100–112.

Gerace, A. and Montanaro, M. (2017) Derivation and validation of the stray light correction algorithm for the thermal infrared sensor onboard Landsat 8. Remote Sens. Environ, 191, pp 246–257.

Getachew, B. F. (2017) the effect of climate change on range land and biodiversity: a review, International Journal of Research - Granthaalayah, 5(1), pp 172-182

Gleyce, K. D. A., Figueiredo, Roberto B., Santos, Julianne C., Oliveira and Rubens A. C. Lamparelli (2019) Analysis of land surface temperature on pastureland areas with different management using Landsat 8 data", Proc. SPIE 11149, Remote Sensing for Agriculture, Ecosystems, and Hydrology XXI, 111491B.

Gomes, YB. and Caracristi, I. (2021) Seasonal analysis on land surface temperature (LST) and normalized difference vegetation index (NDVI) variations in the Iguatu semi-arid hinterland, ceará. Int J Hydro, 5(6).

Guha, S. and Govil, H. (2020) Land surface temperature and normalized difference vegetation index relationship: a seasonal study on a tropical city. SN Appl. Sci, 2 (1661), pp 1-14.

Hussain, S., Raza, A., Abdo, H.G. et al. (2023) Relation of land surface temperature with different vegetation indices using multi-temporal remote sensing data in Sahiwal region, Pakistan. *Geosci. Lett,* **10** (33), https://doi.org/10.1186/s40562-023-00287-6.

Ivan, K. Benedek, J. (2017) The assessment relationship between land surface temperature (LST) and built-up area in urban agglomeration. Case study: Cluj-napoca, Romania, Geographia Technica, 12 (1), pp 64-74.

Jiang, Y. and Lin, W. (2021) A Comparative Analysis of Retrieval Algorithms of Land Surface Temperature from Landsat-8 Data, vol. 18, A Case Study of Shanghai, China, 2021, p. 5659.

Mallick, J., Bindajam, A. A., Al Qadhi, S., Ahmed, M., Hang, H. T., & Thanh, N. V. (2020) A comparison of four land surface temperature retrieval method using TERRA-ASTER satellite images in the semi-arid region of Saudi Arabia. *Geocarto International*, *37*(6), 1757–1781.

Oguz, H. (2013) LST calculator: a program for retrieving land surface temperature from LANDSAT TM /ETM + IMAGERY, Environmental Engineering and Management Journal, 12 (3), pp 549–555.

Roy, B. Bari, E. (2022) Examining the relationship between land surface temperature and landscape features using spectral indices with Google Earth Engine, Heliyon, 8 (9), pp 1-8.

Shi, Q. (2014) Flood Hazard Assessment along the Western Regions of Saudi Arabia using GIS-based Morphometry and Remote Sensing Techniques, Thesis of master, KAUST Research Repository, 103p.

Sobrino, J.A., Juan C., Muñoz, J. and Paolini, L. (2004) Land surface temperature retrieval from LANDSAT TM 5, Remote Sensing of Environment, 90(4), Pages 434-440.

Tahouri, J. Khalis, H., Boualla, S., Mesrar, H. and Sadiki, A. (2017) Surveillance de la température de surface des sols (LST) et de l'indice de végétation par différence normalisée (NDVI) pour l'étude de l'impact des activités anthropiques et du changement climatique sur le sol et la couverture végétale dans la région de Nador (Rif Oriental, Maroc), CIJC 2017, p 151-153.

Varamesh, S., Mohtaram Anbaran, S., Shirmohammadi, B., Al-Ansari, N., Shabani, S. and Jaafari, A. (2022) How Do Different Land Uses/Covers Contribute to Land Surface Temperature and Albedo? *Sustainability* **2022**, *14* (16963).

Zribi M., F. Kotti, R. Amri, W. Wagner, M. Shabou, Z. Lili-Chabaane, and N. Baghdadi. (2014) Soil moisture mapping in a semi-arid region, based on ASAR/Wide Swath satellite data. Water Resources Research, 50, pp 823–835.

COMPARISON OF DROUGHT INDICES FOR EVALUATING AGRICULTURAL DROUGHT RISK IN HIGHLAND REGIONS

Teerawong LAOSUWAN [1,4] 🆔 **, Yannawut UTTARUK[2]** 🆔 **, Phaisarn JEEFOO[3]** 🆔 **, Jumpol ITSARAWISUT[1,4]*** 🆔

ABSTRACT
The impact of drought on human livelihoods is significant, as it is a natural disaster that affects various aspects of life. This research aims to evaluate suitable drought indices for assessing agricultural drought risk in highland regions, focusing on the Nan Watershed in Northern Thailand. The study analyzed three types of drought indices: Normalized Monthly Precipitation Anomaly Percentage (NPA), Vegetation Health Index (VHI), and Normalized Vegetation Supply Water Index (NVSWI). Rainfall data from the Tropical Rainfall Measuring Mission (TRMM) TRMM 3B42 product was used to assess the suitability of these indices for evaluating agricultural drought risk over a ten-year period (2013-2022). The study found that ground-based rainfall data and TRMM3B42 satellite data have a very high statistical correlation, with a correlation coefficient of 0.8945. Analyzing the statistical correlation of suitable drought indices for assessing agricultural drought risk revealed that NVSWI had the highest statistical correlation with a coefficient of 0.956.VHI had a correlation coefficient of -0.8179, and NPA had a correlation coefficient of 0.867. For evaluating the suitability of drought indices affecting the assessment of agricultural drought risk in high areas, focusing on the Nan Watershed in Northern Thailand, this study concludes that NVSWI is the most suitable index for assessing agricultural drought risk in high areas.

Key-words*: Remote Sensing, Drought Indices, NPA, VHI, NVSWI, TRMM*

1. INTRODUCTION

Drought is a natural disaster that significantly impacts human livelihoods by causing dry conditions and a noticeable decline in quality of life (Rotjanakusol & Laosuwan, 2018; Rotjanakusol & Laosuwan, 2019). It is a phenomenon that takes time to reveal its effects (Uttaruk & Laosuwan, 2019), which can persist for extended periods as drought encroaches slowly. This contrasts with phenomena like floods, where impacts are immediately evident through rising water levels (Lloyd-Hughes & Saunders, 2002; Wang et al., 2020). Several factors contribute to drought, such as lower-than-normal rainfall (drought), uneven distribution of rainfall, prolonged dry spells, low soil water retention, insufficient water storage capacity, and the silting up of existing water sources leading to runoff into major rivers and ultimately the sea (Nanzad et al., 2019; Chen et al., 2020). These causes result in varied impacts depending on the nature of the affected area and the specific causes of drought in that area (Cui et al., 2021; Iamampai et al., 2023).

[1]*Department of Physics, Faculty of Science, Mahasarakham University, Maha Sarakham, Thailand, teerawong@msu.ac.th, jumpol.s@msu.ac.th*
[2]*Department of Biology, Faculty of Science, Mahasarakham University, Maha Sarakham, Thailand, yannawut.u@msu.ac.th*
[3]*Geographic Information Science Field of Study, School of Information and Communication Technology, University of Phayao, Phayao, Thailand, phaisarn.je@up.ac.th*
[4]*Space Technology and Geo-Informatics Research Unit, Faculty of Science, Mahasarakham University, Maha Sarakham, Thailand*
*Corresponding author: jumpol.s@msu.ac.th

Drought has different meanings (Prabnakorn et al., 2018). Generally, it refers to periods of significantly lower-than-average rainfall and is considered a permanent feature of regional climates, such as deserts with annual rainfall below 100 mm. In contrast, temporary droughts feature lower-than-normal precipitation, influenced by climatic variability such as higher temperatures, lower humidity, and strong winds (Magyari-Saska & Haidu 2009; Haidu & Magyari-Saska, 2010; Raksapatcharawong et al., 2020). Drought lacks a precise definition and can occur in any region of the world. Simply put, it means no rain in a particular area for an extended period, inhibiting plant and life growth (Fussel & Klein, 2006; Hannaford, 2018). Arid conditions exist on every continent, with local life adapting to these environments or maintaining natural balances, such as in African deserts (Muyambo et al., 2017). Drought can also occur anywhere, with severity depending on various factors, including physical, ecological, and human activities (Kamanga et al., 2020). Drought characteristics can be classified in several ways, with different definitions as follows: 1) meteorological drought, referring to low rainfall in the studied area; 2) agricultural drought, describing insufficient soil moisture for crops due to low rainfall; 3) hydrological drought, concerning low reserves of surface and groundwater; and 4) socioeconomic drought, which considers resource availability and demand, leading to scarcity when demand exceeds supply. This last type focuses on human needs and resource limitations (Copernicus, 2020). Agricultural drought specifically concerns inadequate water supply for agriculture due to insufficient rainfall or prolonged dry spells during critical growth periods or high evapotranspiration rates, resulting in soil moisture deficits (Wongtui & Nilsonthi, 2024).

Satellite remote sensing has demonstrated its effectiveness as a valuable and dependable tool for monitoring drought conditions (Rotjanakusol & Laosuwan, 2020; Meena & Laosuwan; 2021; Laosuwan et al., 2022; Itsarawisut et al., 2024). Additionally, it excels in analyzing the progression of drought over temporal and spatial (Nakapan & Hongthong, 2022; Yu et al., 2022; Hongthong & Nakapan, 2023). Satellite remote sensing for operational drought monitoring has mainly relied on the use of Normalized Difference Vegetation Index (NDVI) data from the National Oceanic and Atmospheric Administration (NOAA) Advanced Very High Resolution Radiometer (AVHRR). The NDVI, created in the early 1970s by Rouse et al. (1974), is a straightforward mathematical transformation of data from two commonly available spectral bands on most satellite-based sensors, the visible red and near infrared (NIR). AVHRR NDVI-based metrics have been utilized for monitoring drought for over two decades, with roots in the pioneering studies of Tucker et al., (1986), Kogan (1990), Burgan et al., (1996), Unganai and Kogan (1998). Drought indices are metrics indicating the dryness of an area based on influential factors such as agricultural land (Liu et al., 2023; Li et al., 2024; Wu et al., 2024). These indices have been developed and refined using various variables (Zargar et al., 2011; Zhou et al., 2021). Additionally, the application of satellite data products enhances the accuracy of drought assessments, as evidenced by research in multiple countries utilizing remote sensing technology for this purpose (Ndayiragije & Li, 2022). According to the Office of Water Resources (Region 9), the Nan Watershed is a major watershed in Northern Thailand, covering parts of Nan, Uttaradit, Phitsanulok, Phichit, and Nakhon Sawan provinces. This basin continues to experience recurrent drought (Ministry of Natural Resources and Environment, 2011). This research aims to evaluate appropriate drought indices for assessing agricultural drought risk in highland regions, focusing on the Nan Watershed in Northern Thailand.

2. MATERIALS AND METHODS

2.1. Study Area

The Nan Watershed (**Fig.1**) is located in Northern Thailand, covering a total area of 34,682.04 km². The basin extends in a north-south direction, situated between latitudes 15° 42′ N and 18° 37′ N and longitudes 99° 51′ E and 101° 21′ E. The topography of the Nan Watershed is predominantly mountainous, influenced by the southwest and northeast monsoons.

Additionally, occasional depressions and typhoons from the South China Sea pass through, resulting in distinct seasons: the rainy season from May to October, the winter from late October to February, and the summer from March to April. The basin has an average annual temperature of 26.3°C, with the highest average temperature of 36.6°C recorded in April and the lowest average temperature of 15.3°C in December. The monthly average temperature ranges from 22.1°C to 29.3°C. The average annual rainfall is 1,371.0 mm, with monthly averages ranging from 5.9 mm to 280.9 mm.
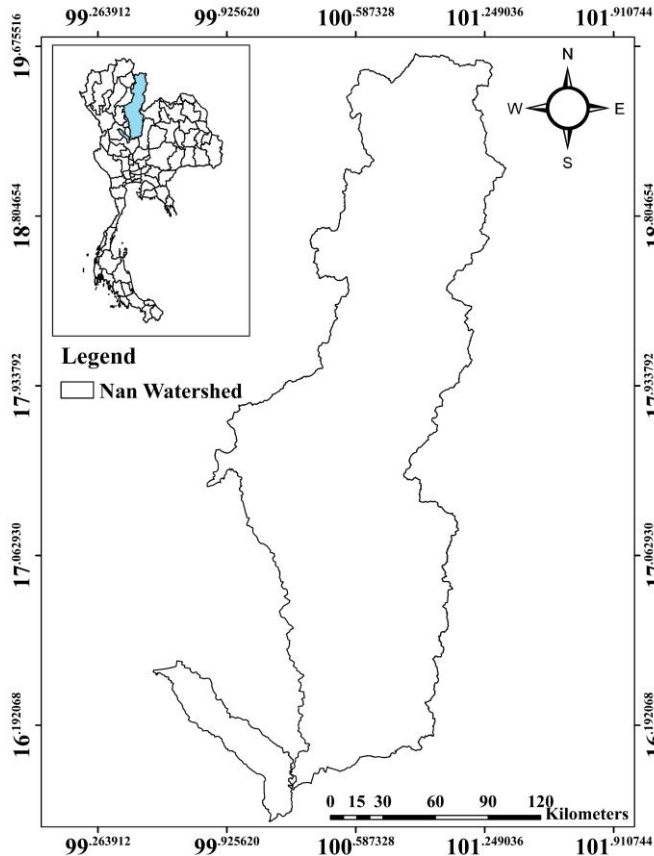
Fig. 1. Nan Watershed.

2.2. Data Acquisition and Pre-processing

2.2.1. MODIS NDVI and LST Products

The NDVI and LST products from MODIS (MOD13C2 and MOD11C3, respectively) for the period 2012-2022 were used in this study. Both products were downloaded from the website https://ladsweb.modaps.eosdis.nasa.gov/, the quality of the MOD13C2 satellite data was transform the NDVI values into real values by multiplying the fixed pixel values with a scaling factor of 0.0001, and the MOD11C3 data was Calculate the actual value by multiplying the pixel value by 0.02, then subtracting 273.15 to convert from Kelvin to Degrees Celsius.

2.2.2. TRMM 3B43 Precipitation Product

Monthly precipitation data from the TRMM 3B43 product, from January to December for the years 2013-2022, was downloaded from http://reverb.echo.nasa.gov, to calculate the monthly average rainfall in the Nan Watershed, Northern Thailand.

2.2.3. Rainfall Data

Daily rainfall data was collected from the Upper Northern Region Irrigation Hydrology Center, Thailand in the five provinces within the Nan Watershed, Northern Thailand, over a 10-year period (2013-2022) from seven stations. The data included details such as province, period, station name, station code, and rainfall amount. The annual accumulated rainfall average and the maximum and minimum rainfall were calculated to observe the correlation and variability of rainfall, whether increasing or decreasing.

2.3. Methodology

2.3.1. Normalized Monthly Precipitation Anomaly Percentage (PA)

This measures the deviation of rainfall from the average over a specified period and can be analyzed using Equations 1 and 2 (Shao-E & Bing-Fang, 2010).

$$PA = \frac{P - \bar{P}}{P} *100\% \tag{1}$$

The current precipitation, denoted as P, and the mean precipitation during the same period, denoted as P, are used to calculate the Precipitation Anomaly (PA). This PA can be utilized to assess drought conditions based on the deviation from the average rainfall. The PA values may be either positive or negative. An alternative approach is to derive a Monthly Precipitation Anomaly Percentage (NPA) with values ranging from 0 to 1 using the Equation 2.

$$NPA = \frac{PA - PA_{min}}{PA_{max} - PA_{min}} \tag{2}$$

The minimum and maximum values of the NPA are denoted as PAmin and PAmax, respectively.

2.3.2 Vegetation Health Index (VHI)

VHI considers the biophysical and climatic conditions of the local area and can be used to monitor actual plant drought in different agrometeorological regions. The basic principle of VHI is that low NDVI and high LST indicate poor plant health. VHI can be analyzed using Equations 3-5 (Kogan, 1998).

$$VCI = \frac{NDVI - NDVI_{min}}{NDVI_{max} - NDVI_{min}} \tag{3}$$

$$TCI = \frac{LST - PA_{min}}{LST_{max} - LST_{min}} \tag{4}$$

$$VHI = a*VCI + b*TCI \tag{5}$$

NDVImin and NDVImax represent the minimum and maximum values of NDVI, while LSTmin and LSTmax represent the minimum and maximum values of LST. The weight coefficients of VCI and TCI are denoted as a and b. Given the current lack of knowledge regarding the contribution of moisture and temperature during the vegetation cycle, it is assumed that the share of VCI and TCI is equal (a= b= 0.5). The VHI for the study area was calculated from January to December over the entire period from 2001 to 2014.

2.3.3. Normalized Vegetation Supply Water Index (NVSWI)

During periods of drought, plants close their stomata to conserve water, which in turn reduces transpiration as leaf surface temperature (LST) rises. This phenomenon is evident in smaller plants as a result of lower soil evaporation. Equations 6-7 can be utilized to analyze NVSWI (Carlson et al., 1994).

$$VSWI = \frac{NDVI}{LST} \tag{6}$$

The VSWI is limited to representing relative spatial location and cannot be compared over time series. Therefore, the NVSWI was introduced, calculated using the formula provided by Abbas et al., (2014).

$$NVSWI = \frac{VSWI - VSWI_{min}}{VSWI_{max} - VSWI_{min}} \tag{7}$$

VSWImin and VSWImax represent the minimum and maximum values of VSWI for the pixel over the study period. The NVSWI for the Nan Watershed from January to December for the entire period of 2012-2022 was computed.

2.4. Correlation and Simple Linear Regression Analysis

This involves Correlation (Equations 8) and Simple Linear Regression Analysis (Equations 9) between the TRMM 3B43 product and ground-based rainfall data and the three types of droughts indices.

$$r = \frac{\sum (x_i - \bar{x})(y_i - \bar{y})}{\sqrt{\sum (x_i - \bar{x})^2 \sum (y_i - \bar{y})^2}} \tag{8}$$

r represents the correlation coefficient. x_i denotes the values of the x-variable within a sample. $\bar{x}$ signifies the average of the x-variable values. y_i indicates the values of the y-variable in a sample, while $\bar{y}$ represents the mean of the y-variable values.

$$y = ax + b \tag{9}$$

In this context, Y signifies the dependent variable, a indicates the slope of the regression equation, X refers to the independent variable, and b represents a constant term.

3. RESULTS AND DISCUSSION

3.1. NDVI and LST Analysis Results

The analysis results of NDVI are shown in **Table 1**, which presents the NDVI values in the Nan Watershed. **Table 1** indicates that NDVI values are highest in October, with a maximum value of 0.758, and lowest in April, with a value of 0.488. This suggests that NDVI values are high during the rainy season and low during the summer due to insufficient water or drought conditions. The central and lower parts of the Nan Watershed have higher NDVI values due to irrigation water, promoting better plant growth.

Table 1.

Analysis result of NDVI.

NDVI	2013	2014	2015	2016	2017	2018	2019	2020	2021	2022
Jan	0.593	0.595	0.684	0.626	0.632	0.593	0.593	0.595	0.684	0.632
Feb	0.570	0.543	0.575	0.585	0.627	0.570	0.543	0.543	0.575	0.627
Mar	0.618	0.532	0.516	0.620	0.581	0.618	0.635	0.532	0.516	0.581
Apr	0.565	0.494	0.488	0.657	0.715	0.565	0.596	0.494	0.488	0.715
May	0.553	0.628	0.516	0.691	0.634	0.553	0.632	0.628	0.516	0.634
Jun	0.687	0.737	0.575	0.687	0.554	0.687	0.687	0.737	0.575	0.554
Jul	0.698	0.752	0.691	0.748	0.590	0.698	0.654	0.752	0.691	0.590
Aug	0.717	0.723	0.739	0.767	0.751	0.717	0.654	0.753	0.739	0.751
Sept	0.705	0.750	0.729	0.675	0.752	0.705	0.659	0.750	0.729	0.752
Oct	0.694	0.746	0.758	0.714	0.664	0.694	0.657	0.746	0.748	0.697
Nov	0.693	0.698	0.688	0.688	0.697	0.693	0.752	0.698	0.688	0.697
Dec	0.632	0.616	0.631	0.645	0.706	0.632	0.658	0.616	0.631	0.706

In contrast, the upper part of the basin, which is mountainous and far from irrigation sources, shows lower NDVI values. **Fig.2(a)** illustrates that the upper basin, shown in yellow to orange (low NDVI), and the lower basin, shown in green (high NDVI), do not face severe drought due to irrigation water mitigating drought effects. LST analysis results are presented in **Table 2** and **Fig.2(b)**.

Table 2.

Analysis result of LST.

NDVI	2013	2014	2015	2016	2017	2018	2019	2020	2021	2022
Jan	27.55	27.55	26.54	28.37	27.98	27.60	26.33	28.56	27.60	28.52
Feb	30.69	30.69	30.27	29.38	30.72	31.17	30.65	29.08	31.17	29.08
Mar	32.76	32.76	33.61	34.65	33.69	33.49	32.64	32.62	33.49	32.63
Apr	33.75	33.75	34.77	38.29	34.62	36.73	33.87	34.61	36.73	32.65
May	34.33	34.33	34.99	36.99	33.30	33.59	32.61	32.59	33.21	29.77
Jun	29.56	29.56	32.71	31.33	29.76	29.56	27.36	29.77	31.01	28.37
Jul	28.96	28.96	29.39	28.62	28.42	28.62	28.36	28.37	29.13	28.25
Aug	27.45	27.45	28.73	29.13	28.19	27.54	28.77	28.25	27.24	28.06
Sept	27.43	27.43	28.39	26.72	28.37	27.43	27.70	28.06	26.51	27.62
Oct	28.49	28.49	28.41	27.77	27.50	28.65	27.63	27.62	27.16	27.36
Nov	28.42	28.42	27.88	28.28	27.37	28.64	27.66	25.49	27.63	25.49
Dec	27.92	24.65	27.18	27.68	26.49	27.99	27.65	27.36	26.69	26.12

Figure 2(b) shows that the central and lower parts of the Nan Watershed, being urban areas, have moderate to high LST values (yellow to red), caused by heat emissions from human activities. The upper part, being mostly mountainous and forested, has low LST values. **Table 2** shows that LST is highest in April (summer), reaching 36.73°C, and lowest in December at 24.65°C.

3.2. Verification of TRMM 3B42 Product with Ground Station Data

The accuracy verification of the TRMM 3B42 product with ground-based rainfall data in this study is shown in **Fig. 3**. The **figure 3** shows a high correlation between TRMM 3B42 data and ground-based rainfall data, with a correlation coefficient of 0.894. Therefore, the TRMM 3B42 product can be used to determine rainfall patterns in the Nan Watershed.
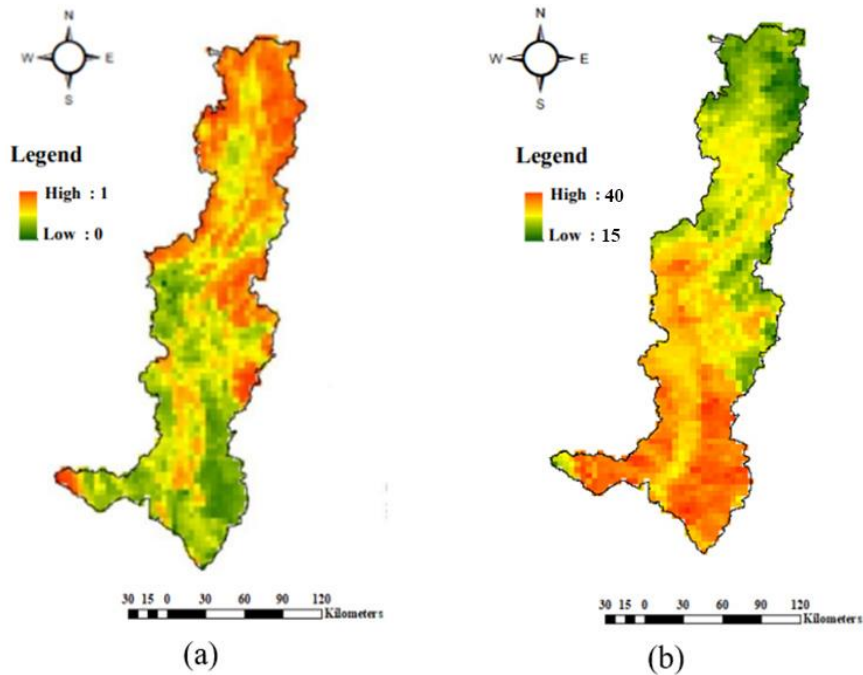
Fig. 2. (a) NDVI and (b) LST.
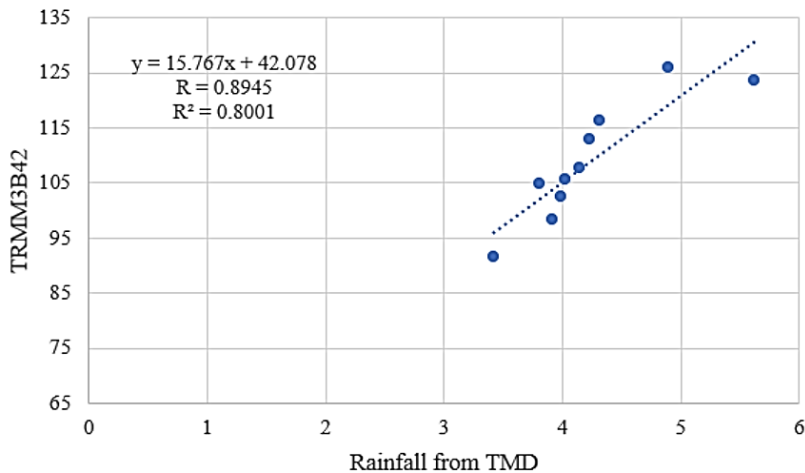
Fig. 3. Correlation between TRMM 3B42 data and ground-based rainfall data.

3.3. Evaluation of Suitable Drought Indices

To select the most appropriate index for the Nan Watershed, the indices used in this study (NPA, VHI, and NVSWI) were evaluated for correlation using the TRMM 3B42 product. To assess the suitability of drought indices for evaluating agricultural drought risk in high areas, the study categorized drought levels into five levels, as shown in **Table 3**. The suitable drought index was determined by comparing each calculated index to the criteria, then analyzing the correlation of the three indices with the TRMM 3B42 product.

Table 3.

Drought levels into five levels.

Degree of Drought	level of drought
0 - 0.20	Severe drought
0.21 – 0.40	Moderate drought
0.41 – 0.60	Low drought
0.61 – 0.80	Normal
0.81 - 1	Humid

- NPA Index: This index calculates the monthly deviation percentage of rainfall, using rainfall data from ground stations in the Nan Watershed, as shown in **Table 4**. **Table 4** indicates that NPA values are relatively low from January to March, increase from April to September, and then decrease until December (maximum NPA value of 1 and minimum of 0). The highest NPA values occur in June and July. The average NPA index from 2013-2022 shows low values in 2013-2014, an increase in 2015, and little variation in subsequent years, with a maximum value of 1.000 in 2016 and a minimum of 0.000 in 2013. A limitation of this index is its inability to assess spatial distribution, as NPA only considers rainfall, causing some monthly discrepancies in analysis results. Despite this, a statistical correlation analysis between TRMM 3B42 and NPA shows a high correlation, with a coefficient of 0.867, indicating a strong relationship between the two variables.

Table 4.

Exhibits the mean value of the NPA index.

NPA	2013	2014	2015	2016	2017	2018	2019	2020	2021	2022
Jan	0	0.512	1	0.569	0	0	0.011	0.194	0.633	0
Feb	0.201	1	0.032	0.009	0	0.110	0.845	0	0.379	0.110
Mar	0.147	0.246	0.016	0.199	0	0.084	1	0.176	0.019	0.084
Apr	0.612	0.692	0.529	0	1	0.204	0.194	0.578	0.194	0.265
May	0.368	0.398	0.264	0.588	1	0.068	0.184	0.599	0	0.596
Jun	0.981	0.656	0.292	1	0.839	0.138	0.471	0.298	0.138	0.194
Jul	0.560	0.482	0.351	0.687	1	0.205	0.510	0.766	0.205	0.184
Aug	0.429	0.753	0.292	1	0.860	0.307	0.387	0.387	0.307	0.068
Sept	0.707	0.316	0.267	0.311	0.626	0.005	1	0.984	0.005	0.766
Oct	0.416	0.364	0.401	0.571	0	0.220	1	0.158	0.220	0.17
Nov	0.546	0.341	0.679	0.459	0.133	0.006	0	0.442	0.006	1
Dec	0.362	0.003	0.435	0.001	0	0	1	0.041	0.003	0

- VHI Index: The VHI Index is calculated by analyzing NDVI and LST data to create a drought monitoring index that reflects normal NDVI conditions. According to the VHI analysis results presented in **Table 5**, the highest VHI values are observed in March and November, reaching a value of 1, while the lowest values are recorded in January, with a value of 0.027. The VHI generally shows an increasing trend over the years, except for 2013 and 2016 when low values were observed. A statistical correlation analysis between TRMM 3B42 and VHI indicates a strong inverse correlation, with a coefficient of -0.8179. This study highlights significant monthly variations in NDVI and LST, leading to an overestimation of drought severity in the analysis results.

- NVSWI Index: This index factors in plant transpiration affected by changes in LST. As LST increases, plant stomata close to conserve water, reducing transpiration. NVSWI analysis results (**Table 6**) show the highest value of 0.031 in October 2016 and the lowest of 0.020 in February 2015. The average NVSWI index from 2013-2022 shows little yearly variation. Spatial analysis divides the basin into three parts: the upper basin, being high and natural, faces more severe drought due to lack of irrigation; the central basin, between natural and irrigated areas, faces moderate drought; and the

lower basin, mostly irrigated, faces minimal drought impacts due to irrigation water. A statistical correlation analysis between TRMM 3B42 and NVSWI shows a high correlation, with a coefficient of 0.956.

Table 5.

Exhibits the mean value of the VHI index.

VHI	2013	2014	2015	2016	2017	2018	2019	2020	2021	2022
Jan	0.315	0.728	0.047	0.662	0.877	0.517	0.726	0.222	0.027	0.475
Feb	0.885	0.655	0.417	0.123	0.614	0.136	0.664	0.331	0.416	0.707
Mar	0.585	0.399	0.416	1.000	0.654	0.625	0.393	0.408	0.356	0.532
Apr	0.455	0.515	0.370	0.500	0.458	0.488	0.522	0.405	0.299	0.865
May	0.533	0.348	0.682	0.622	0.584	0.395	0.578	0.500	0.558	0.756
Jun	0.379	0.578	0.519	0.514	0.609	0.533	0.557	0.389	0.500	0.239
Jul	0.588	0.877	0.495	0.486	0.559	0.499	0.812	0.692	0.500	0.237
Aug	0.467	0.574	0.379	0.997	0.350	0.487	0.844	0.673	0.764	0.581
Sept	0.578	0.413	0.734	0.500	0.755	0.493	0.465	0.176	0.914	0.589
Oct	0.839	0.804	0.883	0.817	0.530	0.377	0.426	0.426	0.561	0.500
Nov	1.000	0.461	0.725	0.696	0.769	0.056	0.236	0.365	0.492	0.605
Dec	0.681	0.072	0.886	0.661	0.532	0.333	0.361	0.395	0.399	0.457

Table 6.

Exhibits the mean value of the NVSWI index.

NVSWI	2013	2014	2015	2016	2017	2018	2019	2020	2021	2022
Jan	0.022	0.028	0.023	0.024	0.027	0.023	0.024	0.028	0.023	0.023
Feb	0.022	0.021	0.002	0.019	0.020	0.017	0.020	0.018	0.022	0.017
Mar	0.019	0.016	0.016	0.021	0.018	0.017	0.021	0.016	0.017	0.017
Apr	0.018	0.015	0.014	0.010	0.016	0.016	0.023	0.013	0.025	0.014
May	0.017	0.011	0.018	0.013	0.019	0.014	0.024	0.015	0.019	0.020
Jun	0.022	0.021	0.017	0.020	0.024	0.017	0.026	0.017	0.016	0.026
Jul	0.025	0.024	0.023	0.024	0.023	0.023	0.028	0.026	0.018	0.027
Aug	0.026	0.026	0.022	0.026	0.024	0.024	0.026	0.028	0.027	0.027
Sept	0.029	0.026	0.025	0.028	0.026	0.024	0.022	0.023	0.022	0.025
Oct	0.028	0.028	0.027	0.031	0.027	0.024	0.026	0.026	0.024	0.023
Nov	0.027	0.025	0.025	0.025	0.027	0.028	0.025	0.025	0.024	0.024
Dec	0.023	0.026	0.025	0.024	0.026	0.025	0.025	0.025	0.026	0.018

4. CONCLUSIONS

The growth of crops, global food prices, and political unrest are all influenced by drought. The upper Nan Watershed faces severe drought due to mountainous terrain and distance from irrigation, while the central and lower basin areas experience less severe drought due to irrigation. The highest drought occurred in 2013, with the lowest in 2015. Annual droughts are normal, with severity depending on rainfall and climatic variability. The Nan Watershed shows an increasing drought trend. This study aims to evaluate suitable drought indices for assessing agricultural drought risk in highland regions, focusing on the Nan Watershed in Northern Thailand. The analysis of three drought indices (NPA, VHI, and NVSWI) with the TRMM 3B42 product finds NVSWI to have the highest correlation (0.956), indicating its suitability for monitoring agricultural drought in high area highland regions s of the Nan Watershed.

REFERENCES

Abbas, S., Nichol, J.E., Qamer, F.M., & Xu, J. (2014). Characterization of drought development through remote sensing: A case study in central Yunnan, China. Remote Sensing. 6(6), 4998–5018. DOI: 10.3390/rs6064998

Burgan, R.E., R.A. Hartford, & J.C. Eidenshink. (1996). Using NDVI to Assess Departure from Average Greenness and Its Relation to Fire Business, Gen. Tech. Rep. INT-GTR-333, U.S. Department of Agriculture, Forest Service, Intermountain Research Station, Ogden, Utah, 8 p.

Carlson, T. N., Gillies, R. R., & Perry, E. M. (1994). A method to make use of thermal infrared temperature and NDVI measurements to infer surface soil water content and fractional vegetation cover. Remote Sensing Reviews, 9(1–2), 161–173. DOI: 10.1080/02757259409532220

Chen, S., Zhong, W., Pan, S., Xie, Q., & Kim, T. W. (2020). Comprehensive drought assessment using a modified composite drought index: A case study in Hubei Province, China. Water, 12(2), 462. DOI: 10.3390/w12020462

Copernicus. (2020). OBSERVER: What impact does drought have on vegetation, and how does Copernicus help? Available online: https://www.copernicus.eu/en/news/news/observer-what-impact-does-drought-have-vegetation-and-how-does-copernicus-help (Accessed on 20 March 2024)

Cui, A., Li, J., Zhou, Q., Zhu, R., Liu, H., Wu, G., & Li, Q. (2021). Use of a multiscalar GRACE-based standardized terrestrial water storage index for assessing global hydrological droughts. Journal of Hydrology. 603, p.126871. DOI: 10.1016/j.jhydrol.2021.126871

Fussel, H. M., & Klein, R. J. T. (2006). Climate change vulnerability assessments: An evolution of conceptual thinking. Climatic Change, 75(3), 301-329. DOI: 10.1007/s10584-006-0329-3

Haidu, I., & Magyari-Saska, Z. (2010). Drought and Extreme Moisture in Small Mountainous Basins. Geographia Technica, 5(2), 51-58.

Hannaford, M. J. (2018). Long-term drivers of vulnerability and resilience to drought in the ZambeziSave area of southern Africa, 1505–1830. Global and planetary change, 166, 94-106. DOI: 10.1016/j.gloplacha.2018.05.001

Hongthong, A., & Nakapan, S. (2023). Assessing the impact of a waste incinerator on the environment using the MAIAC-AOD and AERMOD models. Frontiers in Environmental Science, 11, 1240705.

Iamampai, S., Kanasut, J., Kantawong, B., & Rangsiwanichpong, P. (2023). Drought Hazard Assessment Using Anomaly Drought Index and Geographic Information System in The Chi River Basin, Thailand. Geographia Technica. 18(1), 39-55. DOI: 10.21163/GT_2023.181.04

Itsarawisut, J., Puckdeevongs, A., & Laosuwan, T. (2024). Environmental Monitoring on the Surface of The Andaman Sea Over the Southwestern Coast of Thailand: A Case Study of Spatial and Temporal Variability of Chlorophyll-A. Geographia Technica, 19(2), 57-69. DOI: 10.21163/GT_2024.192.05

Kamanga, T.F., Tantanee, S., Mwale, F.D., & Buranajarukorn, P. (2020). A Multi Hazard Perspective in Flood and Drought Vulnerability: Case Study of Malawi. Geographia Technica. 15(1), 132-142. DOI: 10.21163/GT_2020.151.12

Kogan, N. (1990). Personality and aging. In J. E. Birren & K. W. Schaie (Eds.), Handbook of the psychology of aging (3rd ed., pp. 330–346). Academic Press. DOI: 10.1016/B978-0-12-101280-9.50026-7

Kogan, F.N. (1998). Global drought and flood-watch from NOAA polar-orbiting satellites. Adv. Space Res. 21 (3), 477–480.

Laosuwan, T., Uttaruk, Y., & Rotjanakusol, T. (2022). Analysis of Content and Distribution of Chlorophyll-a on the Sea Surface through Data from Aqua/MODIS Satellite. Polish Journal of Environmental Studies, 31(5), 4711-4719. https://doi.org/10.15244/pjoes/150731

Lloyd-Hughes, B., & Saunders, M.A. (2002). A drought climatology for Europe. International Journal of Climatology, 22(13), 1571–1592. DOI: 10.1002/joc.846

Li, H., Yin, Y., Zhou, J., & Li, F. (2024). Improved Agricultural Drought Monitoring with an Integrated Drought Condition Index in Xinjiang, China. Water, 16(2),325. DOI: 10.3390/w16020325

Liu, W., Ma, S., Feng, K., Gong, Y., Liang, L., & Tsubo, M. (2023). The Suitability Assessment of Agricultural Drought Monitoring Indices: A Case Study in Inland River Basin, Agronomy, 13(2), 469. DOI: 10.3390/agronomy13020469

Magyari-Saska, Z. & Haidu, I., (2009). Drought and Extreme Moisture Evaluation and Prediction with GIS Software Module. In Proceedings of the ITI 2009, 31st International Conference on Information Technology Interfaces (editors: LuzarStiffler, V; Jarec, I; Bekic, Z.), page 553-+, Univ Zagreb & IEEE Reg 8, DOI:10.1109/ITI.2009.5196146.

Meena, P., & Laosuwan, T. (2021). Spatiotemporal Variation Analysis of Atmospheric Carbon Dioxide Concentration using Remote Sensing Technology. International Journal on Technical and Physical Problems of Engineering, 13 (3), 7-13.

Ministry of Natural Resources and Environment. (2011). Nan Watershed. Available online: http://lib.mnre.go.th/lib/report/reo3_54.pdf (Accessed on 28 March 2024)

Muyambo, F., Jordaan, A. J., & Bahta, Y. T. (2017). Assessing social vulnerability to drought in South Africa: Policy implication for drought risk reduction. Jàmbá: Journal of Disaster Risk Studies, 9(1), 1-7.

Nakapan, S., & Hongthong, A. (2022). Applying surface reflectance to investigate the spatial and temporal distribution of PM2.5 in Northern Thailand. ScienceAsia, 48, 75-81.

Nanzad, L., Zhang, J., Tuvdendorj, B., Nabil, M., Zhang, S., & Bai, Y. (2019). NDVI anomaly for drought monitoring and its correlation with climate factors over Mongolia from 2000 to 2016. Journal of arid environments. 164, 69-77. DOI: 10.1016/j.jaridenv.2019.01.019

Ndayiragije, J.M., & Li, F. (2022). Effectiveness of Drought Indices in the Assessment of Different Types of Droughts, Managing and Mitigating Their Effects. Climate, 10(9), 125. DOI: 10.3390/cli10090125

Prabnakorn, S., Maskey, S., Suryadi, F. X., & de Fraiture, C. (2018) Rice yield in response to climate trends and drought index in the Mun River Basin, Thailand. Science of the Total Environment. 621, 108-119. DOI: 10.1016/j.scitotenv.2017.11.136

Raksapatcharawong, M., Veerakachen, W., Homma, K., Maki, M., & Oki, K. (2020). Satellite-based drought impact assessment on rice yield in Thailand with SIMRIW− RS. Remote Sensing. 12(13), p. 2099. DOI: 10.3390/rs12132099

Rotjanakusol, T., & Laosuwan, T. (2018). Remote Sensing Based Drought Monitoring in The Middle-Part of Northeast Region of Thailand. Studia Universitatis Vasile Goldis: Seria Stiintele Vietii, 28(1), 14-21.

Rotjanakusol, T., & Laosuwan, T. (2019). Drought Evaluation with NDVI-based Standardized Vegetation Index in Lower Northeastern Region of Thailand. Geographia Technica, 14(1), 118-130. DOI:10.21163/GT_2019. 141.09

Rotjanakusol, T., & Laosuwan, T. (2020). Model of Relationships between Land Surface Temperature and Urban Built-Up Areas in Mueang Buriram District, Thailand. Polish Journal of Environmental Studies, 29(5), 3783-3790. DOI: 10.15244/pjoes/116384

Shao-E, Y., & Bing-Fang, W. (2010). Calculation of monthly precipitation anomaly percentage using web-serviced remote sensing data. Advanced Computer Control (ICACC), 2010 2nd International Conference. vol. 5. IEEE, pp. 621–625

Tucker, C. J., & Sellers, P. (1986). Satellite Remote Sensing of Primary Production. International Journal of Remote Sensing, 7, 1395-1416. DOI: 10.1080/01431168608948944

Rouse, J.W., Haas, R.H., Schell, J.A. & Deering, D.W. (1974). Monitoring Vegetation Systems in the Great Plains with ERTS. Third ERTS-1 Symposium NASA, NASA SP-351, Washington DC, 309-317.

Unganai, L.S., & Kogan, F.N. (1998). Drought monitoring and corn yield estimation in southern Africa from AVHRR data, Remote Sensing of Environment, 63, 219-232.

Uttaruk, Y., & Laosuwan, T. (2019). Drought Analysis Using Satellite-Based Data and Spectral Index in Upper Northeastern Thailand. Polish Journal of Environmental Studies, 28(6), 4447-4454. DOI:10.15244/pjoes/94998

Wang, X., Zhuo, L., Li, C., Engel, B.A. Sun, S., & Wang, Y. (2020). Temporal and spatial evolution trends of drought in northern Shaanxi of China: 1960–2100. Theoretical and Applied Climatology, 139(2), 965–979. DOI: 10.1007/s00704-019-03024-2

Wongtui, B., & Nilsonthi, P. (2024). Analysis of Agricultural Drought Risk Areas and Influencing Factors in the Mae Wang River Basin, Chiang Mai Province. Life Sciences and Environment Journal, 25(1), 212–224. DOI: 10.14456/lsej.2024.17

Wu, X., Xu, H., He, H., Wu, Z, Lu G, Liao T. (2024). Agricultural Drought Monitoring Using an Enhanced Soil Water Deficit Index Derived from Remote Sensing and Model Data Merging. Remote Sensing, 16(12),2156. DOI: 10.3390/rs16122156

Yu, Z., Wang, T., Wang, P., Yu, J. (2022). The Spatiotemporal Response of Vegetation Changes to Precipitation and Soil Moisture in Drylands in the North Temperate Mid-Latitudes. Remote Sensing, 14(15), 3511. DOI: 10.3390/rs14153511

Zargar, A., Sadiq, R., Naser, B., Khan, F.I. (2011). A review of drought indices. Environmental Reviews,19, 333–349.

Zhou, Z.Y., Long, Q.B., Bai, P. (2021). Scale of meteorological drought index suitable for characterizing agricultural drought: A case study of hunan province. J. South–North Water Transf. Water Sci. Technol, 19, 119–128.

CHOLNOKY MAP COLLECTION'S WEB SERVICES WITH ONLINE CATALOGUE AND SEARCH ON INTERACTIVE MAP

Zsombor BARTOS-ELEKES[1]* , *Zsolt MAGYARI-SÁSKA[2]*

ABSTRACT
The library of the Institute of Geography at the university of Cluj / Kolozsvár, including cartographic materials, was founded in 1884. The maps and atlases of the library were hided around 1950. The remains, found in 2001, are the core of the Cholnoky Map Collection, one of the most important collections of old maps in Romania, with more than 6,600 items (map sheets, atlases), the earliest dating from the 17th century, including valuable manuscripts. Digitization is the key to the survival of this long-suffering collection, so it has always tried to be a pioneer in digitization and dissemination. The topic of this paper is the digitization and visualization of the cartographic heritage: how to realize a digital catalogue and online dissemination of a map collection. With this paper, the authors report on the approaches they applied: they realized the automatic update of the website from the online catalogue, and based on this database, a web search of the maps by their metadata and by their bounding coordinates. The paper presents the map collection: its history, its structure and the features of its previous website (https://hagyatek.cholnoky.ro/terkeptar). It provides an overview of the websites and online map-based search engines of major map libraries in the neighborhood and around the world. It describes how was completed the catalogue with geolocation data; how the back-end IT system enables the automatic updates of online content based on the continuously upgraded catalogue. The front-end interface, the new webpage (http://cholnokymaps.gis-it.ro/) allows users to search for maps by text matching in metadata, and to obtain the corresponding results depending on the actual map bounding box of the OpenStreetMap (OSM). The selected map is visualized using magnifier and panning tools and can be downloaded in high-resolution.

Key-words: *cartographic heritage, visualization, automated data update, geolocation, Jenő Cholnoky, Cluj-Napoca*

1. INTRODUCTION: theoretical background

The digital approaches to cartographic heritage have been at the focus of research in the last decades. The International Cartographic Association set up as a forum for such researchers a working group in 2005, which was upgraded to a commission in 2007. This forum has organized annual workshops, international conferences since 2006 (including one in Cluj-Napoca, where the Cholnoky Map Collection exhibited maps). Among the topics of the Commission on Cartographic Heritage into the Digital (http://cartography.web.auth.gr/ICA-Heritage/) are the visualization of cartoheritage and the web providing issues. Only a selection of recent papers is presented below. Fleet (2019) describes viewers and tools for delivering maps online. Tegeler & Bauer (2019) reports on trends in enabling spatial information retrieval of maps in libraries. Žabička & Pacek (2019) relates online tools for cataloguing and presenting old maps. Arevalo (2021) compares the quality of websites providing access to cartoheritage. Novak & Ostash (2022) lists websites of the online map collections. Appel (2022) presents a digital geographic index map standard. Ungvári et al (2023) introduces an interactive gazetteer on a virtual globe collection. The authors of this paper were inspired by the work of this commission.

[1*] *Department of Geography in Hungarian, Faculty of Geography, Babeş–Bolyai University, 400006, Cluj-Napoca, Romania,* zsombor.bartos@ubbcluj.ro *(corresponding author)*
[2] *Geography Department of Extensions - Gheorgheni Extension, Faculty of Geography, Babeş–Bolyai University, 535500, Gheorgheni, Romania,* zsolt.magyari@ubbcluj.ro

2. SOURCES: the Cholnoky Map Collection

2.1. History and structure

The nucleus of the collection is the library of the Institute of Geography at the former Hungarian-language Francis Joseph University of Kolozsvár (at that time Austria–Hungary, now Cluj-Napoca, Romania). This library was founded in 1884 and from 1895 it was the library of the Institute of Geography. The first director of the collection was Adolf Terner, who did not gather a significant map collection. At the time of his retirement, in 1904, the collection consisted of only 14 atlases and 755 map sheets, the latter probably being sheets of the 1:75,000 topographic map series of the dual monarchy (Magyar Minerva, 1904: 377; Cholnoky, 1998: 255).

From 1905, Jenő Cholnoky, an outstanding Hungarian geographer, became the professor of geography at this university until 1919. The most important development took place under his directorship; he was the main contributor to the map collection. By 1919 the collection had at least 951 maps, but in this calculation, the previously mentioned topographic map series was counted only as a single map (Cholnoky, 1998: 276), so the number of map sheets could be measured in thousands. Note, we obtain different numbers on the size of map collections when counting maps or map sheets, since a map may be kept in several copies or a map series may consist of several map sheets. The catalogue of the library has not been left behind, the sources for the amounts are: Magyar Minerva, 1912: 470; Magyar Minerva, 1915: 335; Cholnoky, 1917: 445.

The collection was taken over and slightly enlarged between the two world wars by the Romanian-language Ferdinand University, and then during the Second World War by the returning Francis Joseph University. The importance of the map collection at the time is illustrated by the fact that Vasile Meruțiu, the professor in the interwar period, when compiling a list of old maps of Transylvania, rather relied on the institute's collection than on the university's central map collection. The continuity of the map collection is indicated by the fact that he used the catalogue numbers of Jenő Cholnoky (Meruțiu, 1929: 204–207).

Under communism, presumably in the early 1950s, this collection and other similar institutional map collections were eliminated, and for half a century they were in an unknown location, presumed lost (Bartos-Elekes, 2015; Bartos-Elekes, 2022).

In 2001, by chance, a few cubic meters of maps, atlases and photographs were discovered in a storage room of the Faculty of Geography at the multilingual Babeș–Bolyai University (Cluj-Napoca), which quickly proved to be the remains of the disappeared collection. Old Austrian topographic map sheets no longer in use were added to them, most of which had previously also been in the collection of the Institute of Geography or other institutes. The collection is currently kept at the Faculty of Geography and is managed by the Cholnoky Geographical Society. This material consists of two parts: the photo and the map collection, containing about 5,300 photographs and 6,600 map sheets and atlases. The Cholnoky Map Collection consists of three collections from three different sources: a map collection (general, thematic and topographic maps: 4,383 map sheets), an atlas collection (133 atlases, 31 albums and 9 books) and a topographic map collection (2,111 topographic map sheets). The oldest maps are from the 17th century, the most recent from the mid-20th century, including several valuable manuscript maps (Bartos-Elekes, 2015; Bartos-Elekes, 2022; Imecs, 2004).

Thus, the collection started as a provincial university departmental collection in 1884, which was developed into a significant collection by its outstanding director in the 1910s, then locked away from the public during the years of communism from 1950, and has been available for use again since 2001. Among collections with a similar history is the Justus Perthes Collection in Gotha: founded in 1785, the publishing house was one of the world's leading geographic and cartographic institutions from mid-19th century until the mid-20th century, when the family business was expropriated in East Germany in 1953. Their collection, including 185,000 maps, 120,000 volumes and 800 linear meters of archival material, was acquired by the state in 2003 and integrated into the Gotha Research Library, and after 50 years of isolation now is made accessible for future generations (Ormeling, 1986;

Demhardt, 2006; Weigel, 2011). Besides the similar history, the two collections are also connected by the fact that only two copies of the 1858 manuscript map of an explorer of Africa, László Magyar are known in the world, and these were found in these two collections, which were previously unsearchable (Bartos-Elekes & Nemerkényi, 2014).

2.2. Catalogue and former web service

The catalogue and the website (https://hagyatek.cholnoky.ro/terkeptar) have not yet formed a coherent system.

The work on the catalogue started in 2006, until 2008 the most important metadata from maps, atlases and topographic sheets were entered quickly into an Excel spreadsheet. The scanning process started afterwards (since 2012 the collection has its own roll scanner), during which the metadata entered in the first step in the Excel spreadsheet are completed. Until now, 2458 image files have been digitized (2181 scanned map sheets, 270 photographed atlas pages and 7 scanned topographic sheets). With the former web service 672 images of the digitized material are available (395 of the scanned map sheets, plus the digitized atlas pages and topographic sheets). The items are visualized in low-resolution, with their most important metadata and, in a limited number of cases, with the option to download the high-resolution image.
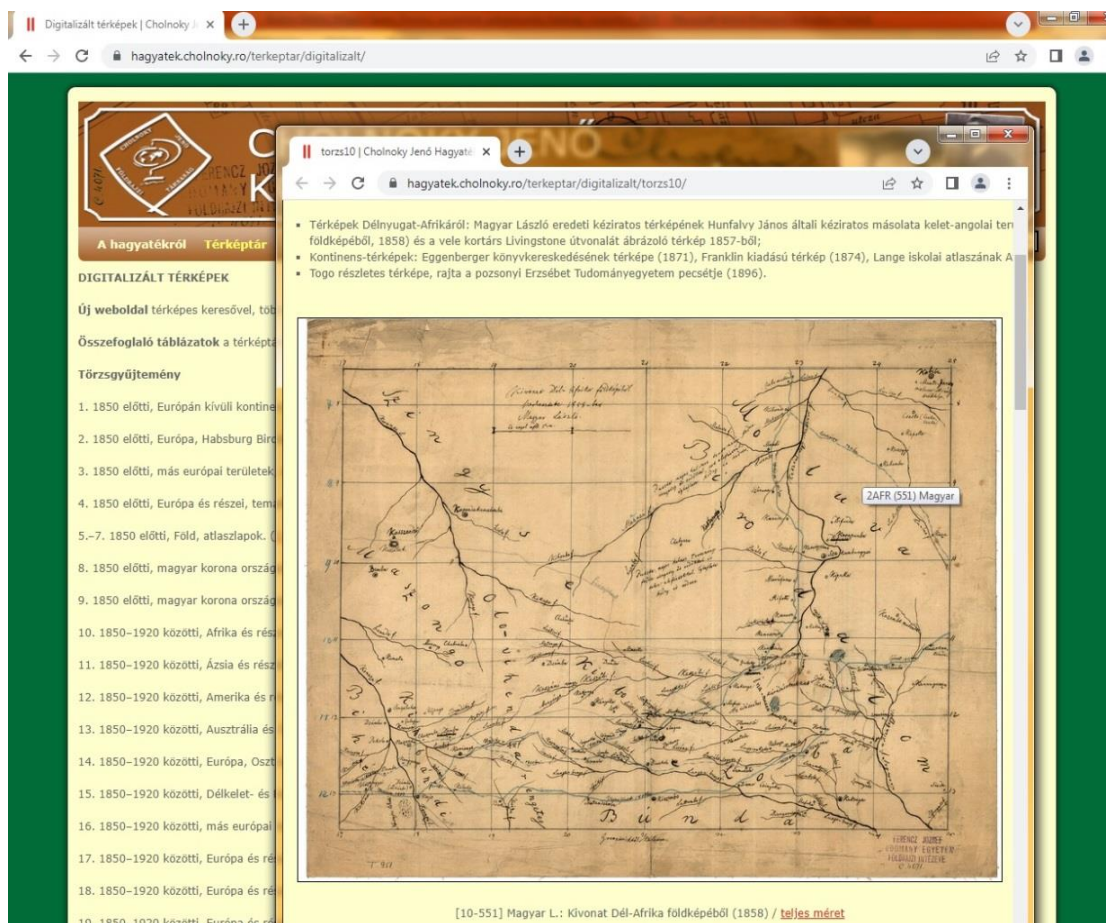

Fig. 1. The former website: the manuscript map of the inner parts of Angola from 1858 by László Magyar, explorer of Africa.

The website was edited as a WordPress blog. Adding newly digitized items to the website required manual editing. This limitation slowed down the dissemination of the digitized material, which led to the necessity of modernizing the website (**Fig. 1**, https://hagyatek.cholnoky.ro/terkeptar/digitalizalt/).

3. OBJECTIVES AND METHODS

3.1. Objectives

One of our objectives was to develop a back-end IT system that would be able to automatically update the online content, based on the constantly evolving catalogue. The other objective was to add geolocation data for each map in the catalogue, so that the cartographic items could be found on an interactive map in the online front-end environment. During the research, we overviewed the websites of the important map collections, the key elements of their online map-based search systems.

3.2. The web services of some important map collections

We visited the websites of some important Romanian and foreign (American, Austrian, British, French, German and Hungarian) map collections, looking for the examples that could be used as a model for our website.

The largest map collection in Romania is the Maps Department at the Academic Library in Bucharest, which has 16,606 maps, 3,786 estate plans, 552 atlases, 250 wall maps, relief maps and world maps. It has a traditional catalogue, so it can be researched on the spot. On its webpage, there is only a short description of the map collection (https://biblacad.ro/eng_harti.html). A search in the whole library's online catalogue of maps ("hărți") in the field "subject" returns the metadata of 2,290 results (http://aleph23.biblacad.ro:8991/F), but we have no information on how much of these are kept in the map department.

Another important national map collection is the National Library's Map Collection in Bucharest, which contains some 5,300 maps and atlases. Until recently, it only had a handwritten inventory book, making research even more difficult. On its webpage, there is only a description of the map collection (https://www.bibnat.ro/Cartografie-s68-ro.htm). A search in the whole library's online database for map-type documents returns metadata for 687 results (https://aleph.bibnat.ro/F), but we have no information on how much of these are kept in the map collection. A significant progress is that the high-resolution images of 307 maps and of all pages of 11 atlases can be downloaded from the digital library (http://digitool.bibnat.ro/R).

Among the domestic university collections, we can highlight the Map and Atlas Collection at the Central University Library of Cluj-Napoca. It contains 580 atlases (in 698 volumes), at least 4,710 maps (as 9,669 map sheets), 103 wall maps and 202 guidebooks. An advantage compared to the previous collections is that the 8,453 cards of the traditional catalogue (which were managed until 2005) are available in scanned form on the website: https://www.bcucluj.ro/ro/resursele-bibliotecii/cat/csh. A search in the whole library's online catalogue of maps ("hărți") in the field "subject" returns the metadata of 878 results (http://aleph.bcucluj.ro:8991/F), but in this case we know that from these only 69 atlases and 56 maps are kept in the map collection. Some of these are available for downloading as digital copies.

The Cholnoky Map Collection contains mostly cartographic material related to Transylvania. As the largest number of old maps related to Transylvania is kept in Hungary, these collections are presented below. The two largest Hungarian map collections are in Budapest.

The backbone of the Map Collection at the Military History Institute and Museum in Budapest was the map sheets from the War Archives in Vienna that were allocated to Hungary after the First World War, so its main collection is of topographic maps. Today it contains nearly half a million items. The most relevant items of these are available on two websites. Hungaricana, the portal of Hungarian

public collections, contains 77,823 maps and 42,652 plans (https://maps.hungaricana.hu/hu/). On this website this map collection appears with 20,285 digitized maps, where one map can contain several sheets. The website provides a table of contents of the collection. Hits within a category can be filtered or sorted by their metadata. The map view uses Google Maps, with around 30,000 maps searchable by represented area. The selected map is displayed with detailed metadata and is visualized with magnifying and panning tools, but downloading is not possible. The most important part of the collection (together with the material from the Viennese twin collection), that is the former topographic map sheets are available on a separate website. Arcanum Maps (https://maps.arcanum.com/hu/) is one of the world's leading digital historical map sites. Among other map series, it presents the three Habsburg military topographic surveys and former Hungarian topographic maps, tens of thousands of sheets. They are depicted together and thus visualized as a geo-referenced, interactive mosaic of maps: with the possibility to overlay multiple (historical and modern) maps, to adjust their transparency.

While the previous collection collects mainly topographic maps, the Map Collection of the National Széchényi Library in Budapest collects Hungarian maps and atlases of any type; today it has more than three hundred thousand items. On its webpage, there is some general information (https://www.oszk.hu/terkepek). A search in the whole library's online catalogue of maps ("térkép") in the field "subject keyword" returns the metadata of at about 52,000 results (https://nektar2.oszk.hu/librivision_eng.html). Of the printed maps, 1,183 can be viewed and downloaded in medium resolution on the map collection's website (https://foldabrosz.oszk.hu/). Among the manuscript maps, 2,314 are included in the Hungaricana website.

Some of the world's leading map collections are described briefly below, just for comparison with the above.

The world's largest map collection is considered to be that of the Library of Congress in Washington, D.C., with 5.6 million maps. Their website (https://www.loc.gov/maps/) contains 418,000 searchable maps, of which 57,000 are available online, for viewing and downloading.

Another major US map collection is the map collection of the American Geographical Society Library in Milwaukee, which contains 520,000 maps, 21,000 of which are available online, for viewing and downloading (https://uwm.edu/lib-collections/agsl-digital-map-collection/).

The David Rumsey Map Collection (https://www.davidrumsey.com/) in Stanford, California contains 150,000 maps, of which 130,000 are now digitized and available on their website, making it a reference in terms of digitization. The website has many tools for searching (by period, area and content keywords), visualizing (compare and overlaying in geo-referencing) and downloading (at various resolutions).

Besides the one in Washington, the other largest map collection in the world is in London: the British Library contains 4.5 million cartographic items (https://blogs.bl.uk/magnificentmaps/about-this-blog.html), and has an online catalogue on its website, but the amount of scanned maps is not significant.

The National Library of France contains 950,000 maps, of which nearly 70,000 are now available online, which can be listed by different criteria (e.g. by century), searched in the catalogue, downloaded (https://gallica.bnf.fr/html/und/cartes/cartes). Maps are accompanied by a pair of coordinates, which shows approximately where the center of the map is.

The Bavarian State Library in Munich has 430,000 maps, 260,000 of which can be searched in its online catalogue (https://www.bsb-muenchen.de/), some of which can be viewed and downloaded at a limited resolution.

The Austrian National Library in Vienna has a map collection of 300,000 maps, which can be searched in the online catalogue on its website, and a small number of maps can be viewed (https://www.onb.ac.at/en/departments/map-department).

In conclusion, the world's largest map collections contain around five million maps (Washington, London), but in major European cities even collections with a few hundred thousand cartographic items are outstanding (e.g. Vienna, Budapest). In Romania, the largest collections are with around ten thousands of maps (Academic Library, Central University Library of Cluj-Napoca), among which

Cholnoky is considerable. Libraries are working on making their collections available in their online catalogue, searchable by their metadata, but in many cases this is still only partially or even fragmentarily implemented. At best, around one hundred thousand maps can be explored online (e.g. David Rumsey, Hungaricana), in better case using magnifier and panning tools, and more rarely the maps can be downloaded. Among the collections in Romania, Cholnoky leads in this respect with more than two thousand digitized map sheets which are visualized and can be downloaded. The search by represented area using an interactive map is a rarity (e.g. Hungaricana). The American David Rumsey and the Hungarian Arcanum sites are outstanding in their special tools (overlay, transparency, geo-referenced mosaic).

3.3. The structure of the catalogue, addition of geolocation data

The digital catalogue (an Excel file) has been revised to allow easy automatic updating and data columns for the geolocation of the items have been added.

As a result of this upgrade, the catalogue of the map collection has the following data columns (fields) available online:

Bibliographic data:
- Title/map (*Mű címe*, e.g. *Map of North America*)
- Title/sheet (*Lap címe*, in the case of a map series with several sheets)
- Author (*Szerző*)
- Publisher (*Kiadó*, e.g. *United States Geological Survey*)
- Pub location (*Kiadás helye*)
- Pub date (*Kiadás éve*, e.g. *1912*)
- Scale (*Méretarány*, e.g. *1:5000000*)
- No. of sheets (*Lapok száma*, number of map sheets for this database row, e.g. *1*)

Categories, reference codes, digitization:
- Category (*Csoport*, e.g. *1850–1920, Amerika és részei térképek: általános, földrajzi, közigazgatási*, '1850–1920, America, general maps')
- List No. (*Tételszám*, e.g. *579*, physical identifier, the list number of the map sheet)
- Call No. (*Jelzet*, e.g. *12-0579*, logical identifier, it is located in folder 12 and has the call number 579. The call number is usually the same as the list number. If the sheets/copies of the same map were entered in more than one row, these rows have the same call numbers, which links them together)
- Year of dig. (*Digitalizálás éve*, e.g. *2011*)
- No. of images (*Fájlok száma*, number of images for this database row, e.g. *1*)

Former reference codes:
- FJTE-T (*FJTE-T*, e.g. *T608*, the 608th map in the Institute of Geography's library at Francis Joseph University)
- FJTE-C (*FJTE-C*, e.g. *C2640*, the 2640th catalogued item in the Institute of Geography's library at Francis Joseph University)
- IG (*IG*, e.g. *79*, the 79th map in the Institute of Geography's library of the Ferdinand University)

Notes:
- Area (*Terület*, e.g. *Észak-Amerika*, 'North America', the map represents approximately the area of these nowadays countries, regions or continents)
- Map type (*Műfaj*, e.g. *közigazgatási*, 'administrative map')
- Notes (*Megjegyzés*, e.g. *Souvenir of the visit of the geographers of the Transcontinental excursion*)

Besides the addition and organization of the existing database, a real novelty was the matching of the data rows with map bounding box data similar to Google Maps and OpenStreetMap. Three

columns were used to specify where the center of the map is located and at what zoom level the full map is displayed by the above mentioned web map services.

- Lat (e.g. *40*, latitude of the center of the map/sheet)
- Lon (e.g. *-100*, longitude of the center of the map/sheet)
- Zoom (e.g. *4*, the area represented on the map corresponds to this zoom level in web maps. Zoom 1 is for astronomical maps, 2 for world maps, 3–4 for a continent, 5–9 for a country, 10–11 for city maps).

The rows in the catalogue (records) can refer to a single map sheet (for which we may have one image file, or even front and back, so multiple image files can be associated with it), or a multi-sheet map series can be included in a single row (which can also have multiple image files associated with it). If just one image file is associated with a call number, the image file name is the same as the call number (*12-0579.JPG*). If there are multiple images associated with the same call number, the image file name will contain the call number, but will continue for identification purposes.

3.4. Implementation of the IT system and website

The digitization of the map collection is a continuous process that takes several years. We wanted to make the already processed, digitized content easily accessible to the public on the website, and to make the new results of the ongoing digitization work easily, automatically and efficiently incorporated as possible.

Accordingly, the IT implementation of the project was divided into two parts: the creation of visualization and browsing interface, and the development of a data uploading system. The two modules share a common database (the catalogue of the collection), so that when the database is upgrading through the data uploading module, its content is already available in real time on the visualization interface. The data flows are shown in **figure 2**. Since the beginning, the data was recorded in Excel spreadsheets, so the metadata of the image files is uploaded as XLSX file.

We used MariaDB database as data warehouse management system, PHP for the back-end and JavaScript for the front-end development. The map collection is currently available under the following domain: http://cholnokymaps.gis-it.ro/
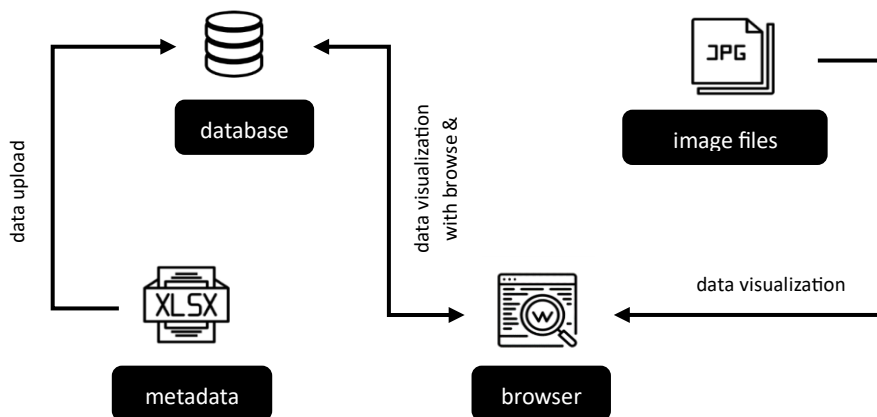
Fig. 2. – Data flows in the system

The upload of the catalogue including newly digitized data is done in two steps. Both the JPG image data files and the XLSX file containing their metadata have to be uploaded. The uploading of image files, accounting for their size of several 10MB each, should not be done using a web upload interface, but via FTP connection provided by the hosting provider. However, as the catalogue, including metadata is integrated in the database used by the visualization interface, a separate interface has been developed for uploading them.

4. RESULTS

4.1. Data upload

The user interface of the data upload module is simple. In addition to browsing the Excel metadata file from the local machine and providing the appropriate password a button activates the authentication check, the connection and the upload processes. In the upload window, the data uploader will receive continuous feedback on the success or failure of the steps. The access link to this interface is not public and is only available to those involved in the digitization and data management process of the map.

A key element of data uploading is that, although it is done from a public web interface, it can only be done with the appropriate authorization. For this purpose, we have chosen an authentication method that has a fixed – possibly modifiable – and a variable component that depends on external but easily accessible factors. Thus, using both components together the authentication is more secure than using a single keyword.

After the selected file is uploaded to the server, the password is checked. This is followed by the verifying of the availability of the database and the access rights on it, and afterwards the contents of any previously existing data table are deleted in their entirety. Once a new data table is created, its entries are populated with the individual columns of the corresponding data sheet of the uploaded XLSX file. It is therefore important that the Excel file has the same internal structure for each upload. It is also noticeable that the user receives continuous feedback on the success or failure of each step, so that any errors that may occur can be easily identified.

4.2. Data visualization and browsing

Three versions of data view and browsing have been implemented. The first option is to navigate in the table of contents (categories and folders) of the map collection: e.g. *1850 előtti térképek* ('Maps before 1850'), within that *Európán kívüli kontinensek* ('Continents other than Europe'). The second option is to search by text matching in metadata, next to the magnifying glass icon, where it is possible to specify the search field *(Keresés mezője)*. The third option is based on geolocation: this is an interactive search on a map, depending on its current bounding box; the displayed results are the maps whose geographical area is within the bounding box of the map.

During the implementation, different client-side and server-side programming languages and techniques have been used to create a system that works in a unified way. MariaDB and PHP were used on the server side, while HTML, CSS and JavaScript were used on the client side.

The user interface is depicted to follow the design of today's modern web content, being easy to understand, simple and intuitive (**Fig. 3**). The results can be searched by table of contents or metadata, respectively on map. Switching between these two is made possible by icons in the top right corner of the interface. When navigating in table of contents, if the user navigates to the lowest level, the results corresponding to that category will appear in the list on the right. In all cases, the list of results will display the number of results after the word *Találatok* ('Results').

If the user wants to search by metadata, they can start by typing it in the field above the table of contents. It is possible to search for the totality of the metadata (*Összes,* 'All Fields', this is the default) or to select the field to be searched, from the drop-down list of the fields (*Cím, Szerző,* etc. for 'Title', 'Author'), which can be done by pressing Enter or clicking on the search icon. Whether the results displayed on the right are the result of a content category selection or a text search is made clear by the note under the word *Találatok* ('Results'): in the case of a content category, the name of the category is displayed (e.g. *1850 előtti térképek,* 'Maps before 1850'), while in the case of a search, the searched text is displayed (e.g. *Keresett szó: Amerika,* 'Searched text: America'). The search is performed on metadata except the last option, *Fájlnév* ('Filename'), when the search is conducted for existing filenames in the data folder. In this case the search field must contain at least the first seven characters of the filename (in the format ??-????-*). If files with the specified prefix are identified, metadata for them will be extracted from catalogue.
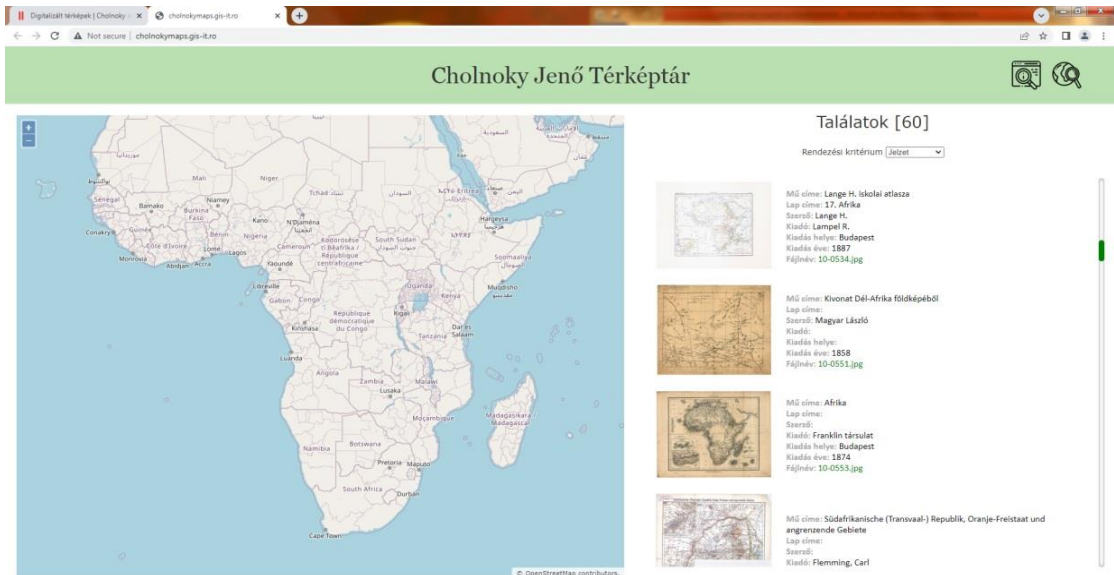
Fig. 3. The new webpage: the map-based search and the results with similar bounding coordinates.

The results list will display, at each position, a thumbnail image of the map, accompanied by the most important metadata for identification (Title, Author, etc.). If the result does not yet have a thumbnail image, a replacement image will be displayed to indicate this status. When positioned on an item in the results list, the mouse cursor also indicates whether a high-resolution image of the content is available or not. In the former case a magnifying glass is displayed, in the latter a question mark icon, but in both cases, it is possible to click on it and thus select the detailed data display.

The third search option is map-based, and its implementation has meant the appearance of a new option in the interface, represented by an icon with a magnifying glass over a map. By selecting this option, the OpenStreetMap is displayed in the browser, and those results are displayed whose geo-locations are similar to the current bounding coordinates. The geo-localized search is performed based on catalogue data. In order to make this map-based search feasible, the catalogue includes three new columns containing the geographic coordinates of the center of each map and a zoom level. If the center of the map is located between the bounding coordinates and the OSM zoom level is less than or equal to the value existing in the catalogue, the map will be listed as a result. This map-based search is activated by panning and magnifier tools. After each of these operations, the values of the corner points are read and converted from Google Web Mercator projection (which is the projection of the OSM) to a geographic coordinate; these values are used to call the search function.

Whatever the search method is selected, clicking on each item of the results will open a window displaying the detailed content that will fill the screen. In the left part of this window, a high-resolution version of the map will be displayed, while on the right, the associated metadata will be displayed.

In the detailed image part of the window, it is possible to zoom in and out of the content using the mouse scroll wheel, and panning by holding down the left mouse button. Double-clicking will reset the image zoom. There are two actions available in this view: downloading the map (clicking the icon in the top left corner) or returning to the previous search interface (clicking the icon in the top right corner). Returning can also be achieved by using the icons in the top right corner of the browser interface to select the search mode.

When displaying a high-resolution image, a large amount of data has to arrive from the server to the client computer, which can take a few seconds, during which time an animated icon informs the user on the ongoing data transfer. By default, when downloaded, the file name will match the file name stored on the server, created during digitization.

5. CONCLUSION

This paper reports on how the Cholnoky Map Collection website (http://cholnokymaps.gis-it.ro/) has been developed recently:

- previously, the updating from the digital catalogue was done manually, now it has become automatic,
- previously, the maps could only be searched indirectly by the most important metadata, but now it is possible to search quickly and directly by all metadata,
- the new feature is the search by map bounding box, which is a great help in the case of maps representing different areas,
- previously, only a few maps could be downloaded in high-resolution, now any user can do this for any map.

The Cholnoky Map Collection, located in a store-room in the building of the Faculty of Geography, Babeş–Bolyai University, Cluj-Napoca has no staff: it is managed by a teacher of the university, with the help of a rotating team of students. The current level of digitization is as follows:

- it has a digital catalogue (an Excel file) of its entire contents (4,383 map sheets, 133 atlases, 31 albums, 9 books and 2111 topographic map sheets), with a wide range of data fields per records (bibliographic data, reference codes, notes, geolocation data, etc.),
- its website (https://hagyatek.cholnoky.ro/terkeptar/) is maintained by the Cholnoky Jenő Geographical Society, the site is mostly in Hungarian (with Romanian and English introductions), presenting studies and news,
- an old page of the website (https://hagyatek.cholnoky.ro/terkeptar/digitalizalt/) contains the low-resolution images and the most important metadata of 395 map sheets, 270 pages of 9 atlases and 7 topographic map sheets, grouped by categories, almost half of them can be downloaded in high-resolution,
- on a new page of the website (http://cholnokymaps.gis-it.ro/), the metadata of the 2,181 map sheets digitized so far have been made online from the digital catalogue: they can be browsed by categories, searched by text matching and by bounding box of an interactive map; the results are visualized (with magnifying and panning tools) and can be downloaded in high-resolution; the 395 map sheets of the old webpage are included here too, but the 270 pages of atlases and the 7 topographic map sheets can be browsed only on the old webpage.

The unfair history of the collection (its existence was unknown for half a century) is a strong warning of the importance of its survival. Given its limited physical space (only one store-room available), this preservation is only possible by promoting it in the online space. This is the key to making this fund of old maps accessible to potential researchers. Searching is facilitated by implementing location-based search in a map-specific graphical interface. The aim of this paper was to highlight these issues describing the web system analytically, thus providing examples for other solutions.

REFERENCES

Appel, S. (2022). OpenIndexMaps: A New Iteration of Collaborative Digital Index Mapping. *e-Perimetron* 17/4, pp. 181–191.

Arevalo, E. (2021). Quality assessment criteria for cartographic heritage dissemination: a preliminary analysis of 300 websites. *e-Perimetron* 16/3, pp. 141–155.

Bartos-Elekes Zs. & Nemerkényi Zs. (2014). Petermann's Map of László Magyar's Travels in Angola: Its Sources, Compilation and Contents. In Liebenberg, E., Collier P. & Török Zs. Gy. eds. *History of Cartography. International Symposium of the ICA, 2012.* Springer, Heidelberg. pp. 195–209.

Bartos-Elekes Zs. (2015). *A kolozsvári Cholnoky Jenő Térképtár.* https://hagyatek.cholnoky.ro/terkepek/tanulmanyok/BEZs-terkeptar-2015-04.pdf

Bartos-Elekes Zs. (2022). A kolozsvári magyar nyelvű felsőfokú földrajzoktatás története. In Szenkovits F. & Soós A. eds. *Szemelvények a 150 éve alapított kolozsvári egyetem Matematikai és Természettudományi Karának történetéből.* Presa Universitară Clujeană, Cluj-Napoca. pp. 279–326.

Bartos-Elekes Zs. & Magyari-Sáska Zs. (2022): *A Cholnoky Jenő kolozsvári hagyatéka adatbázis és weblap korszerűsítése.* http://hagyatek.cholnoky.ro/terkepek/tanulmanyok/BEZS-MSZS-weblap-2022.pdf

Cholnoky J. (1917). Geográfus tanárképzés a kolozsvári egyetemen. *Földrajzi Közlemények* 45/9–10. pp. 444–453.

Cholnoky J. (1998). Cholnoky Jenő önéletrajza. In Géczy J. ed. Cholnoky Jenő. *Vár ucca tizenhét* VI/2.

Demhardt, I. J. (2006). Der Erde ein Gesicht geben. Petermanns Geographische Mitteilungen und die Anfänge der modernen Geographie in Deutschland. Katalog zur Ausstellung der Universitäts- und Forschungsbibliothek Erfurt/Gotha im Spiegelsaal auf Schloß Friedenstein in Gotha, 23. Juni bis 9. Oktober 2005. *Veröffentlichungen der Forschungsbibliothek Gotha*, 42. Gotha.

Fleet, C. (2019). An open-source web-mapping toolkit for libraries. *e-Perimetron* 14/2, pp. 59–76.

Imecs Z. (2004). Cholnoky Jenő fényképi hagyatéka a kolozsvári egyetemen. *Földtani Kutatás* 41/3–4. pp. 18–24.

Magyar Minerva (1904). *Magyar Minerva. A magyarországi múzeumok és könyvtárak czímkönyve III.* Közrebocsájtják a Múzeumok és könyvtárak országos tanácsa és országos főfelügyelősége. Atheneaum, Budapest.

Magyar Minerva (1912). *Magyar Minerva. A magyarországi múzeumok és könyvtárak czímkönyve IV.* Közrebocsájtják a Múzeumok és könyvtárak országos tanácsa és országos főfelügyelősége. Atheneaum, Budapest.

Magyar Minerva (1915). *Magyar Minerva. A magyarországi múzeumok és könyvtárak czímkönyve V.* Közrebocsájtják a Múzeumok és könyvtárak országos tanácsa és országos főfelügyelősége. Atheneaum, Budapest.

Meruţiu, V. (1929). *Judeţele din Ardeal şi din Maramureş până în Banat. Evoluţia teritorială.* Institutul de Arte Grafice „Ardealul", Cluj.

Novak, A. & Ostash, V. (2022). Digitizing Historical Maps and their presentation in Online Map Collections. *e-Perimetron* 17/1, pp. 33–44.

Ormeling, F. J. Sr. (1986). Tribute to Justus Perthes. *GeoJournal,* 13, 413–416 doi: 10.1007/BF00224596

Tegeler, T. & Bauer, H. (2019). Introduction: Maps in Libraries. Trends in Enabling Spatial Information Retrieval. *e-Perimetron* 14/3, pp. 110–116.

Ungvári Zs., Rapcsán K., Krizsán H., Kuris Z., Beszkid A. & Gede M. (2023). Interactive name index of old virtual globes. *e-Perimetron* 18/4, pp. 171–180.

Weigel, P. (2011). Die Sammlung Perthes Gotha. *Patrimonia 254.* Kulturstiftung der Länder, Berlin.

Žabička, P. & Pacek, M. (2019). Cataloguing and Presentation Tools for Old Maps and Map Series. *e-Perimetron* 14/4, pp. 203–214.

SPATIAL AND TEMPORAL VARIATIONS IN SURFACE WATER QUALITY: A CONTINENTAL REVIEW

Mary NGATIA [1], Shadrack M. KITHIIA [1] (iD), Mihai VODA [2,3]* (iD) and Ronald SSEMBAJWE [4,1] (iD)

ABSTRACT
Surface water quality is a critical component of environmental health and sustainability. Its variations across space and time are influenced by numerous factors, including natural processes, human activities, and climate change. While the water quality is a critical issue, it is important to understand the spatial, temporal variations and the pollution sources that contribute to the variations. This review aims to provide a comprehensive overview of the spatial and temporal variations in surface water quality on a continental scale: Europe, Asia, North America, South America and Africa. This study used cluster analysis for a comparative approach based on papers published between 2002 and 2022. Our findings prove that domestic effluent discharges, agricultural runoffs and industrial discharges on the river basins represent the main contributors of water quality variations observed and consequently water pollution.

Key-words: Multivariate techniques, Cluster Analysis (CA), Water pollution

1. INTRODUCTION

Water quality of rivers is a major global environmental concern because rivers are the most available fresh water resources for human consumption. However, rivers across different continents have been heavily polluted due to their easy accessibility to waste disposal.

Water pollution refers to the presence of toxic contaminants in the water bodies that render the water unfit for domestic, industrial and agricultural use. As such, water quality degradation owing to anthropogenic activities is a global concern resulting in significant water management challenges for both developed and developing countries (Hussein & Bomola, 2011; Voda et al., 2019). A plethora of authors have documented water quality related research (Daoji and Daler, 2004; Ismail and Robescu, 2019; Kithiia, 1992 and 2006; Voza, Vuković, et al., 2015). For Instance, Daoji and Daler. (2004), Hussein and Bomola (2011), Mehmood et al. (2017), Rodrigues et al. (2018) and recently Bhat et al. (2021) reported water quality degradation in Asian rivers especially within the Yangtze River basin (Yang et al., 2021), Euphrates and Tigris rivers (Hussein & Bomola, 2011) and Sukhnang river (Mehmood et al., 2017).

The huge pollution stresses affecting these rivers were attributed to human activities that discharge wastes rich in inorganic nitrogen, phosphate, oil hydrocarbons, organic matters and heavy metals. Excess nutrient loads cause eutrophication of the coastal waters and estuarine area often experiences red tides. The pollution of the Yangtze river basin for example consequently influences

---

[1] *University of Nairobi, Department of Geography, P.O. Box 30197-00100 GPO, Nairobi, Kenya, maryngatia88@gmail.com, shadrack.mulei@uonbi.ac.ke*

[2]* *Dimitrie Cantemir University, Geography Department, 540545 Targu Mures, Romania, mihaivoda@cantemir.ro (corresponding author)*

[3] *Geography Doctoral School, Faculty of Geography, Tourism and Sport, University of Oradea, 410087 Oradea, Romania;*

[4] *College of Agricultural and Environmental Sciences, Makerere University, P.O. Box 7062 University Rd, Kampala, Uganda, ronaldnazirite@gmail.com*

the marine environment of the East China Sea(ESC) (Daoji and Daler, 2004). Similar consequences have been reported in Europe especially in the Danube River. Europe's second longest river has remarkably been experiencing water quality degradation as a result of anthropogenic pressure. For example, Mănoiu and Crăciun (2021) have attributed this degradation to mainly organic pollution downstream of major cities and in some major tributaries. While, Georgescu et al. (2023) have further linked it to more factors such as changes in river flow patterns and sediment transport regimes.

In Africa, water pollution has been a longstanding issue (Chen et al., 2022). Studies including Elnazer et al., (2018) over the Nile river in the North, Madonsela et al., (2024) over river Mpumalanga in the south, Mustapha et al., (2014) over Kano river in the West and recently Chen et al., (2022) over east African Urban rivers have reported significant deteriorations in water quality owing to anthropogenic activities especially urbanization and agriculture. Other rivers source pollution from mining operations, oil spills and solid waste. Such rivers include Niger River, Zambezi River, Nile River and Congo River given their strategic location in mining Africa's mineral rich zones. The Zambezi River, known for its iconic Victoria Falls for example has been affected by pollution from both mining activities, agricultural runoff, and industrial waste. The same is true for Africa's second largest river: Congo river. The Nile River on the other hand has faced pollution issues due to industrial discharges, agricultural runoff, and domestic waste. While significant progress has been made, water pollution remains a challenge in many rivers across the globe. Continued efforts are needed to protect these vital ecosystems and ensure the health and well-being of future generations.

In East Africa, emphasis has been drawn to rivers whose basins are centered or bordered by major cities such as Nairobi, Jinja, Arusha among others, where, industrial waste, agricultural runoff, domestic sewage and deforestation are rampant and increasing over time (Voda et al., 2019). These issues have significant implications for public health, as contaminated water can lead to various diseases.

In Kenya, the earlier studies by Kithiia, (2007) within the Nairobi and Athi river basins indicated a downstream increase in water pollutants and water quality degradation. Sediments and heavy metals within the basins were observed to increase downstream the river courses which was attributed to industrialisation and urbanisation. Additionally, Njuguna et al. (2017) reported increased nutrient loads and heavy metal concentrations; Fe, Cr, Pb, Mn above the World Health Organization (WHO) macrophytes tolerable limits in the Nairobi River basin. In the same basin, Musyoki et al. (2013) reported high microbiological contamination of the river basin levels above the WHO standards for safe water for agriculture use and human consumption. As such, continuous monitoring of the surface water bodies and the pollution sources so as to minimise the observed pollution trends is recommended (Chen et al., 2022).

In North America especially Canada and the United States, improving water quality is one of the key focus of integrated water shed management project (Line, 2002; St-Hilaire et al., 2004) with water quality monitoring being a key component in water quality management. Similarly, various water quality management programmes have been initiated elsewhere to aid in assessing spatial and temporal variation which are important aspects of water management and pollution control (Melo et al., 2020). In Eastern Canada and especially New Brunswick province, the Sustainable Development program and the Water Classification program water quality management programs have been initiated with the Richibucto River being one of the focus of such program (St-Hilaire et al., 2004). Well planned and well managed water quality monitoring system is essential to signal, control or predict changes in water quality of a certain water body. This however cannot be achieved without continuous collection of water samples, analysis of the physico-chemical parameters and analysis of the water quality data. Oddly, long-term survey and monitoring programmes however produce large complex datasets which are difficult to analyse and interpret (Ismail and Robescu, 2019; Ngatia, 2022; Voza et al., 2015a; Zhang et al., 2011). Due to complexity of water quality data, application of multivariate statistics has proven useful in provision of meaningful information through reduction of data sets and interpreting various parameters in pollution monitoring.

Multivariate analysis techniques help in reducing the complexity of a large scale data set and are widely used in environmental impact studies (Voza et al., 2015a; Voda et al., 2018). Cluster analysis (CA) is one such technique used for classification of objects into clusters to indicate their intrinsic characteristics on the basis of their similarity or nearness (Bu et al., 2010). Cluster analysis is useful in solving classification problems by placing variables into groups such that the association level is strong between the same cluster members and weak between different cluster members (Bhat et al., 2014). Hierarchical clustering analysis (HCA) is the widely used approach that uses the Euclidean distances as a measure of similarity to form higher clusters. The cluster results is usually demonstrated using a dendrogram which gives a visual summary of clustering processes, showing high internal (or within cluster) homogeneity as well as high external (or between clusters) heterogeneity (Bu et al., 2010). Several successful applications of CA to water quality assessments have been reported in recent studies (Bhat *et al.,* 2014; Bu *et al.,* 2010; Voza *et al.,* 2015). The analytical results in this study indicate that this technique is useful in offering reliable classification of surface waters. The present findings are consistent with the recent studies on Hindawi River, Jonshui and Marova river systems as reported by (Bhat *et al.,* 2014; Bu *et al.,* 2010; Voza *et al.,* 2015). The application of multivariate techniques helps in the interpretation of complex data matrices, provides a clear indication of water quality and ecological status of study areas (**Fig.1**), allows for identification of possible sources of pollution and eventually offers a rapid solution to the pollution problem thus an important tool to water quality monitoring managers.

Fig. 1. Location of the study Rivers on the world map.

2. STUDY AREA

The study relied heavily on publications on Rivers in selected continents. In Europe, the study was conducted on Danube River which is Europe's second-longest river. Danube river flows through Romania for a significant distance and its a major transportation artery in Romania. The Danube also flows through Serbia, where it forms a natural border with Romania and Hungary. It's a vital source of water and supports a diverse ecosystem. Sukhnag a small stream located in the Indian state of Jammu and Kashmir also formed part of this study. This stream is known for its scenic beauty and is a popular destination for trekking and fishing. Elsewhere in Iraq, the Euphrates River which is one of the most important rivers in the Middle East, flowing through Iraq was studied. It's a vital source of water for agriculture and irrigation, and its basin has been a center of human civilization for millennia in Iraq. Richibucto River located in New Brunswick, Canada in North America was also studied. Richibucto flows into the Northumberland Strait and is known for its fishing and recreational opportunities. In South America Pianbaha River in Brazil located in the state of Mato Grosso also contributed in this research. It's a tributary of the Xingu River and flows through a region known for its biodiversity. In Africa, Ngong river in Kenya flows from the Ngong forest through Kibera slums and along the Nairobi city boundary and later traverses into the industrial area. Its a major tributary of the Nairobi River which drains Nairobi city and its environs. It's a vital source of water for wildlife and is known for its scenic beauty. The Pangani River is a major river in Tanzania and is important for agriculture, hydropower, and fisheries. Water quality is a significant concern in many river basins around the world, and monitoring and management are essential for protecting these valuable resources.

3. DATA AND METHODS

The present study was aimed at identifying and reviewing findings from research work published between 2002 to 2022, a period of 20 years, in which multivariate analytical techniques in "spatial and temporal variations of water quality in rivers" was used. The target research publications were based on different rivers in five continents: Africa, Europe, Asia, North America and South America. The research articles were chosen as case studies regarding water pollution as they revealed the benefits of application of multivariate techniques such as PCA and Cluster analysis in pollution monitoring of surface water quality in different continental contexts. Google scholar search engine was used to identify papers for inclusion and exclusion for this study. The reviewed papers were obtained using key words" multivariate analysis of water quality of rivers" in different combinations. The last search was conducted on 4th April, 2023. From the search, an inclusion and exclusion criteria were applied where by all papers published between 2002 and 2022 were selected. The second criteria was to obtain papers with open access, in English language and studies that used multivariate techniques in Water Quality (WQ) analysis were selected. Papers that did not have open access were excluded. Studies with no evidence of multivariate analysis were also excluded. Finally, eight papers were selected from Europe, Asia North and South America and Africa continents as case studies. Relevant studies from most recent publications whose research used Cluster Analysis were given priorities for inclusion.

The following eight papers were closely reviewed; WQ analysis of Danube River in Romania published in 2019, WQ of Danube River in Serbia published in 2015, WQ of Sukhnag stream in India published in 2014, WQ analysis of Euphrates River in Iraq published in 2012, WQ analysis of Richibucto River in Canada published in 2004, WQ in Pianbaha River in Brazil published in 2019, WQ analysis of Ngong River in Kenya published in 2022 and WQ in Pangani River Basin in Tanzania published in 2013. The full texts of the eight papers were retrieved and an in-depth review conducted. The review's results considering the scientific contribution in multivariate analytical techniques for water quality data of the rivers in various continents have been presented and discussed in this study (**Tab. 1**).

Table 1.

The google scholar review process on WQ analysis of Rivers using Multivariate techniques in different continents

River/Lake subjected to WQ analysis	Country	Continent	Reference
Danube River	Romania	Europe	(Ismail and Robescu, 2019)
Danube River	Serbia	Europe	(Voza et al., 2015b)
Sukhnag River	India	Asia	(Bhat et al., 2014)
Euphrates River	Iraq	Asia	(Emad AM et al., 2012)
Richibucto River	Canada	N.America	(St-Hilaire et al., 2004)
Pianbaha River	Brazil	S.America	(de Andrade Costa et al., 2020)
Ngong River	Kenya	Africa	(Ngatia, 2022)
Pangani River	Tanzania	Africa	(Hellar-Kihampa et al., 2013)

4. RESULTS AND DISCUSSION

Research papers by the nine authors (table 1) whose research work was in the five continents (Africa, Europe, Asia, North America and South America) selected for this study were reviewed and are presented below.

4.1. Multivariate statistical techniques and Water Quality (WQ) aspects of the reviewed rivers

Danube River is the second longest river in Europe with a length of 2860 km. It's a transboundary water body originating from Germany and draining into the Black Sea (Ismail and Robescu, 2019; Voza et al., 2015b). Over the decades, Danube River has been experiencing high pollution levels due to the agricultural, urban settlements and industrial establishments along its course thus attracting scientific research projects that look into its water quality (Ismail and Robescu, 2019; Radu et al., 2022; Voza et al., 2015b). A study conducted along a 13km stretch on Danube River in Romania from Gura Vaii, 2 km downstream of Iron Gate 1 up to Drabeta-Turnu Severin City revealed that the water quality of Danube River was influenced by both point and non-point sources of pollution (Ismail and Robescu, 2019). The study area is characterised by industrial effluent discharges coupled with human settlements that lack proper sewer treatment facilities (Andrița, 2012). Water quality data sets from Danube river gathered for a period of 1 year were subjected to Multivariate Statistical methods Factor analysis and Cluster Analysis was applied to evaluate the spatial and temporal variations among the study sites and monitoring periods (Ismail and Robescu, 2019).

In this study Hierarchical agglomerative clustering using Ward's method of linkage and squares Euclidean distance determined the spatial similarity distance and results illustrated using a dendrogram.

In cluster analysis, locations within the same cluster infer similar characteristics hence for a rapid water quality assessment, only one site from each cluster acts as an indicator of the whole cluster Singh *et al.*, (2004); Voza, Vukovic, *et al.*, (2015) so the number of sampling sites can be reduced hence cost without losing any significance of the outcome (de Andrade Costa et al., 2020). The four sampling sites were clustered into two significant groups (Group A and B). Group A corresponded to less polluted sites which were located upstream of Drobeta Turnu Severin City whose pollution sources were attributed to non-point sources mainly agricultural. Group B sites were considered to be moderately polluted in comparison with Group A which was attributable to their location within the Drobeta Turnu Severin's city industrial area which contribute to industrial and domestic effluents to Danube River. CA further grouped the 12 months in to two groups indicating that temporal variation in the Danube WQ was not determined by local climate (spring, summer, winter, autumn) but rather the discharge (Q) was the main factor (Ismail and Robescu, 2019).

Similar to the Danube stretch in Romania, a recent study was also conducted on the same river in Serbia (Voza et al., 2015b). Danube River flows through Serbia over a distance of 588km stretching from Bezdan to Prahovo. The river in this stretch hosts two main cities located on its banks; Belgrade city with a population of 1.7 million people (3rd largest city on Danube River) and Novi sad with a population of 300,000 people. Several other smaller towns are also located in Danube Serbia basin. Similar to the Danube River in Romania's Drobeta Turnus Severin city, the settlements along the river banks lack adequate waste water treatment system contributing to water quality degradation of the River (Voza et al., 2015b). To evaluate the WQ in Danube River Serbia basin, 17 water quality monitoring stations were sampled and monitored for a duration of one year (January-December,2011) by Voza in 2011. Cluster Analysis was performed on the obtained data sets after performing basic statistics to determine similarities between sampling stations.

In reference to Voza, Vukovic 2015, cluster 1 consisted of 7 sampling stations on Danube Serbia River. These stations were; Apatin, Bezdan, Bogojevo, Centa, Backa, Palanka, and Novi sad while cluster 2 had two stations; Banatska Palanka and Pancevo. Cluster consisted of eight sampling stations; Belgrade-Vinča, Dobra, Zamun, Brza Palanka, Tekija, Smederevo, V. Gradište, and Radujevac. Cluster 1 consisted of sampling stations that are highly polluted while cluster 2 and cluster 3 had stations with moderate and low pollution, respectively. The observation on temporal similarities of Serbia's Danube by Voza, 2105 were similar to those of Ismail and Robescu 2019 whereby the temporal similarities were clustered into two groups; group 1 (January, February, March, April, November and December) and group 2 (May, June, July, August, September and October) inferring that the water quality in Danube River in Serbia is not influenced by the four seasons (Spring, Summer, Autumn and Winter) but by other factors such as discharge (Q).

Comparable to the Danube River in Romania and Serbia located in Europe, the Asian continent is also grappling with the issue of water pollution in various rivers. This clearly depicts the global challenge of water quality management that continuously need monitoring to evaluate pollution levels that occur due to continuous anthropogenic pressures. In India, water quality assessment of Sukhnag stream in Kashmir Himalaya was carried out in February 2011 to January 2022 on five sampling stations (Bhat et al., 2014). Sukhnag stream originates from Pir Panjal mountain range located in the southwest of Beerwah town (Bhat et al., 2014). The stream is 51 kms in length and drains in to lake Wular which is the second largest lake in the Indian Subcontinent and a Ramsar site (Bhat et al., 2014). The Sukhnag stream drains an area characterised by various economic activities of importance to North Kashmir (Bhat et al., 2014). The stream is an important source of water for both domestic and agricultural purposes. CA was applied on the WQ data set obtained from the five sampling sites and resulted to three clusters based on similarities and dissimilarities of the WQ parameters. Spatially, site IV and V revealed 96% and 94% similarity, respectively, while site II and III showing 94% similarity. Site I located on the upstream of Sukhnag, was the most dissimilar site indicating low influence by anthropogenic activities (Bhat et al., 2014).

Contrary to Ismail & Robescu, 2019 and Voza, Vukovic, *et al.*, (2015), the temporal variations in Sukhnag stream were due to higher inorganic and organic loads during spring and autumn season indicating that temporal variations are due to seasonal variations (Bhat *et al.*, 2014) as opposed to discharges (Q) as observed in Danube River in Romania and Serbia.

Furthermore, in the study on the WQ of the Euphrates River in Iraq, CA revealed that the temporal variations in the water quality was not influenced by the wet and dry seasons (Emad AM et al., 2012) but other factors. The month of April had the highest dissimilarity as compared to other months, which was attributed to high Total Dissolved Solids values (Emad AM et al., 2012). The study used cluster analysis to classify sampling sites based on standardized mean values of 16 measured parameters. The dendrogram produced from this analysis indicated two distinct clusters: Cluster I which Included only sampling site 7 (S7) and cluster 2 Comprised sampling sites 1-6 and 8-11. Further, the results suggested that sampling site 7 had the lowest pollution levels, while the other sites had higher levels of pollution. This was consistent with the observed variations in water quality parameters among the sites (Emad AM et al.,2012). The study concluded that cluster analysis is a valuable tool for classifying river water in the study region. It can help reduce the number of sampling sites and associated monitoring costs without sacrificing significant information. This finding aligns with the results of previous studies conducted in other rivers.

In the North American Continent, CA analysis applied on the WQ analysis of Richibucto River in Canada revealed that high phosphorus and nitrate concentrations were attributed to run offs from peats, tributaries receiving treated municipal effluent and lentic zones upstream of culverts (St-Hilaire et al., 2004). Moreover, peat runoff was found to be acidic whether from a harvested area or a natural bog which prompts continuous monitoring of the water quality of Richibucto River. In this study, 36 water quality stations were sampled during ice free periods from 1996-2001 which generated huge sets of data (St-Hilaire et al., 2004). The study used cluster analysis to identify distinct groups of freshwater and estuarine stations based on their water quality parameters. The results showed that Stations 31, 3, and 1, located in the upper reaches of tributaries, clustered together due to their high pH values and low TC concentrations. These stations formed the fresh water stations. Moreso, stations draining the St. Charles Plain formed two distinct clusters based on their pH values while Stations 18 and 16, located on tributaries of Mill Creek, were characterized by high P_{tot} and NO_3 concentrations and formed a separate cluster. On the other hand, estuarine stations located on the main Richibucto River and those in the downstream reaches of tributaries formed two distinct groups based on their physical parameters (SpCond, Q, and TC). Station 36, receiving treated sewage, was isolated due to its high P_{tot} and NO_2NO_3 concentrations. The remaining estuarine stations were clustered together based on their nutrient and DO levels. The most significant difference between freshwater and brackish water was the primary factor that accounted for the majority of variations in water quality within the Richibucto system. Overall, the cluster analysis provided valuable insights into the spatial variability of water quality parameters within the study area (St-Hilaire et al., 2004).

Over south America, similar studies were conducted in the Piabanha River basin in Brazil. This river basin forms a sub basin of the Paraiba do Sul river and is characterized by a combination of urban, industrial, rural characteristics together with large conserved fragments of the Atlantic forest (de Andrade Costa et al., 2020). In this study 40 years of monitoring were studied so as to provide an in-depth understanding of the water quality trends of the Piabanha River and support its steering committee in the application of public policies (de Andrade Costa et al., 2020). Due to the huge sets of data involved in this study, multivariate techniques were used to conduct an update diagnosis of the WQ of Piabanha River. The CA clustered Piabanha River into three clusters according to the stretches of the river with similar WQ. In cluster 1 (S1,S6,S4,S5) stations corresponded to Petropolis urban centre and the main sources of pollution were identified as industrial and sewer effluents (de Andrade Costa et al., 2020). Additionally, S6 traverses Teresopolis city also characterised by industrial and other economic activities such as mining which have an impact on its WQ. Similarly, station S4 and S5 also receive negative impacts from mines. S2 and S3 fall within the most urbanised section of the river

however it is less polluted due to dilution effects from Araras River on the left bank and Poco do Ferreira River on the right bank. The third cluster also was low polluted due to its location near the mouth of the river (de Andrade Costa et al., 2020) study revealed that the pollution levels in some sections of the river are high comparable with class 4 of the Brazilian Regulation for coliforms and Biological Oxygen Demand parameters rendering the water not suitable for agriculture, human or animal consumption further recommending continuous monitoring.

In the African continent, Multivariate Analysis (Cluster Analysis) was applied to evaluate the effects of human activities on the WQ of Ngong River (Ngatia, 2022). CA clustered the river into three distinct clusters according to the levels of pollution (Low level, moderate level and high level of pollution) reflecting the different pollution levels for both wet and dry seasons. In the wet season, CA clustered the 12 sampling sites into three distinct clusters. The sampling sites of Cluster 1 (site 1, 5, 4, 9, 8, 7, 11, 12, 6 and 10) were located on the upstream, middle reaches and downstream of Ngong River basin. The sites showed a strong similarity, indicating the dilution effects on anthropogenic pollutants due to increased volume of water in the river as a result of surface runoff during the rainy season. The sampling site in cluster 2 (site 3) was less similar to the other sites probably due to the agricultural runoff from the farming activities carried out on the encroached part of the Nairobi dam. Contrary to these sites, Site 2 in Cluster 3 showed the maximum dissimilarity with other sites during the wet season. Site 2 (Lindi Mosque) is located downstream of site 1. This site receives sewer effluents and other forms of waste from the highly populated Kibera informal settlement. The dendrogram therefore, clearly indicates that the water quality degradation of site 2 is attributed to anthropogenic impacts including the sewer discharge which was revealed by the highest *Escherichia coli* Levels (214×10^6 MPN/100ml) recorded for the wet season. This also indicated that site 2 is highly polluted above the dilution capacity of the river during the wet season.

Contrary to other reviewed studies for Danube River in Romania and Serbia (Ismail and Robescu, 2019; Voza et al., 2015b), temporal variations on Ngong River +6 were found to be influenced by the wet and dry season. The CA for the dry season indicated a spatial and temporal variation of pollution factors suggesting the effects of human activities on water quality of Ngong River. The pollution levels were observed to be high during the dry season owing to high concentration of contaminants due to evaporation effect. The CA produced 3 distinct clusters. Sampling sites in Cluster 1 were site 6, 12, 3, 4, 8, 9, 2, 7, 10 and site 5. These sites are located in the middle and downstream stretch of Ngong River Basin. Site 2 which is Lindi Mosque in Kibera is located just after the forest and is highly populated, lacking basic sanitary provisions hence domestic effluent discharge into Ngong River and solid waste dumping. Sites 5, 6 and 7 (Enterprise Road, Likoni Road Bridge and Mukuru Kayaba) are all located within the Nairobi's industrial hub. These sites receive industrial waste, sewer discharge and other domestic effluents from the existing industries and the highly populated Mukuru slums. Dumpsites are also common on all the sites located along this stretch. Sites 4, 8 and 9 (Outering road, Embakasi and Kayole) are located downstream of the industrial area hence the impacts of industrial activities upstream and the existing human settlements along Ngong River in this section are revealed. Dump sites were also evident in these sampled sites while direct sewer discharge was evident at site 9-Kayole. Site 12 (Mong'etho) is located downstream of Ngong River just before confluence with the Nairobi River. The site also shows a similarity with the other middle stream sites indicating the impacts of anthropogenic activities in the downstream of the river. Small scale farming, informal settlements lacking proper domestic and sewer disposal, dumpsite and pig farming were evident in this site making it similar to the other sites due to pollution.

Contrary to these sites, Ngong Forest site 1 which formed Cluster 3 indicated maximum dissimilarity with the other sites during dry season as it's located on the headwater section of the stream. This indicates that anthropogenic activities on the Ngong River at site 1 is relatively low resulting to minimal pollution. The concentrations of all monitored pollutants were relatively low at the Ngong Forest boundary site as compared to other sites indicating less anthropogenic sources of pollution (**Fig. 2**).
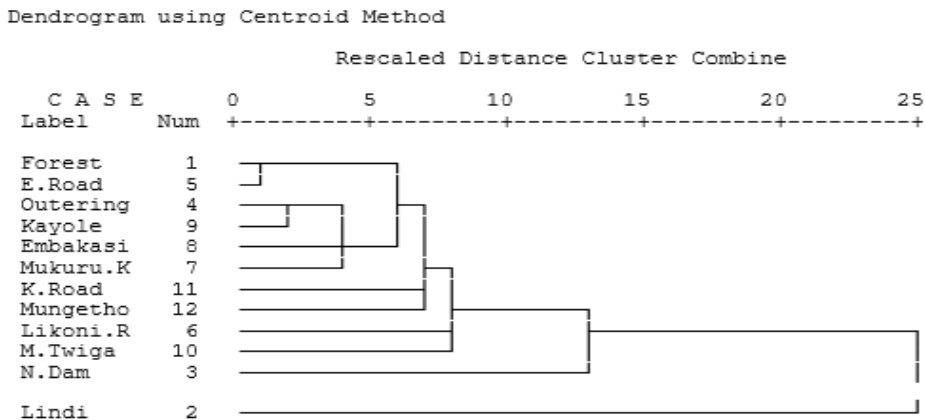
Fig. 2. Dendrogram of the cluster analysis for 12 sampling sites based on water quality parameters of Ngong River, Kenya for the wet season (The sample sites were represented as follows: Forest Boundary (1), Lindi Mosque (2), Nairobi dam (3), Outering bridge (4), Enterprise Road (5), Likoni road (6), Mukuru Kaiyaba (7), Embakasi bridge (8), Kayole (9), Matopeni Twiga (10), Kagundo Road bridge (11), and Mungetho-Njiru (12).

Source (Ngatia,2022).

In Tanzania, (Hellar-Kihampa et al., 2013) assessed using CA the natural and anthropogenic influences on the ions concentrations of Pangani River located in North Eastern part of Tanzania. Pangani River is one of the longest River basins in Tanzania and highly depended on for agricultural activities. CA applied in the analysis ions concentrations of this river revealed that the water quality is influenced by both natural and anthropogenic pressures which contributed to the variations in ionic concentrations of the river water.

5. CONCLUSION

The reviewed studies discussed here demonstrate the usefulness of multivariate statistical tools such as Cluster Analysis in investigating both the underlying processes and the spatial variation of water quality which are both critical aspects in developing the best river basins integrated management practices for water managers. Cluster analysis has proved to be a useful tool in obtaining maximum amount of information from a minimum number of sampling stations and consequent optimization of regional water quality sampling network which reduces on the costs that are usually incurred in water quality monitoring and evaluation programs. The present study analysed the spatial and temporal fluctuations of water quality in rivers from Europe, Asia, America and Africa. Our results show that industrial effluent discharges and agricultural runoffs constitute the principal influence on water quality variations.

Further studies on the application of multivariate techniques in water quality data management are recommended. These techniques are contributing to the identification of pollution sources as well as giving a comprehensive understanding of the spatial and temporal changes in surface water quality.

REFERENCES

Adeogun, A.O., Babatunde, T.A., Chukwuka, A.V., (2012). Spatial and temporal variations in water and sediment quality of Ona River, Ibadan, Southwest Nigeria. *European Journal of Scientific Research* 74, 186–204. http://www.europeanjournalofscientificresearch.com

Andriţa, V., (2012). Water Quality in the Urban Ecosystem of Drobeta–Turnu Severin. Presented at the International Conference: Water Resources and Wetlands, Selected Paper, Gâştescu P., Lewis W., Breţcan P.(Eds.), pp. 14–16. https://www.limnology.ro/water2012/Proceedings/102.pdf

Bhat, S.A., Meraj, G., Yaseen, S., Pandit, A.K., (2014). Statistical assessment of water quality parameters for pollution source identification in Sukhnag stream: an inflow stream of lake Wular (Ramsar Site), Kashmir Himalaya. *Journal of Ecosystems* 2014. https://doi.org/10.1155/2014/898054

Bhat, S. U., Khanday, S. A., Islam, S. T., & Sabha, I. (2021). Understanding the spatiotemporal pollution dynamics of highly fragile montane watersheds of Kashmir Himalaya , India ☆. *Environmental Pollution*, *286*(November 2020), 117335. https://doi.org/10.1016/j.envpol.2021.117335

Bu, H., Tan, X., Li, S., Zhang, Q. (2010). Water quality assessment of the Jinshui River (China) using multivariate statistical techniques. *Environmental Earth Sciences* 60, 1631–1639. https://doi.org/10.1007/s12665-009-0297-9

Chen, S. S., Kimirei, I. A., Yu, C., Shen, Q., & Gao, Q. (2022). Assessment of urban river water pollution with urbanization in East Africa. *Environmental Science and Pollution Research*, *29*(27), 40812–40825. https://doi.org/10.1007/s11356-021-18082-1

Daoji, L., Daler, D. (2004). Ocean Pollution from Land-based Sources: East China Sea, China. AMBIO: A *Journal of the Human Environment* 33, 107–113. https://doi.org/10.1579/0044-7447-33.1.107

De Andrade Costa, D., Soares de Azevedo, J.P., Dos Santos, M.A., dos Santos Facchetti Vinhaes Assumpção, R., (2020). Water quality assessment based on multivariate statistics and water quality index of a strategic river in the Brazilian Atlantic Forest. *Scientific reports* 10, 22038. https://doi.org/10.1038/s41598-020-78563-0

Elnazer, A. A., Mostafa, A., Salman, S. A., Seleem, E. M., & Al-Gamal, A. G.-A. (2018). Temporal and spatial evaluation of the River Nile water quality between Qena and Sohag Cities, Egypt. *Bulletin of the National Research Centre*, *42*(1). https://doi.org/10.1186/s42269-018-0005-6

Emad AM, S., Ahmed M, T., Eethar M, A.-O. (2012). Assessment of water quality of Euphrates River using cluster analysis. *Journal of Environmental Protection* 2012. DOI:10.4236/jep.2012.312180

Hellar-Kihampa, H., De Wael, K., Lugwisha, E., Van Grieken, R. (2013). Water quality assessment in the Pangani River basin, Tanzania: natural and anthropogenic influences on the concentrations of nutrients and inorganic ions. *International journal of river basin management* 11, 55–75. https://doi.org/10.1080/15715124.2012.759119

Hussein, A., & Bomola, A. (2011). *Temporal and spatial changes in water quality of the euphrates river - Iraq.* LundUniversitty. https://lup.lub.lu.se/luur/download?func=downloadFile&recordOId=2341931&fileOId=2341934

Ismail, A.H., Robescu, D. (2019). Application of multivariate statistical techniques in water quality assessment of Danube River, Romania. *Environ. Eng. Manag. J* 18, 719–726. http://www.eemj.icpm.tuiasi.ro/pdfs/vol18/full/no3/15_90_Ismail_16.pdf

Kithiia, S.M. (1992). Effects of industries and other land use systems on the water Quality within the Nairobi River sub-catchments, Kenya. (Thesis). http://erepository.uonbi.ac.ke/handle/11295/19544

Kithiia, S.M. (2012). Water quality degradation trends in Kenya over the last decade. Water quality monitoring and assessment 509. https://www.intechopen.com/chapters/35067
https://web.archive.org/web/20170815224953id_/http://cdn.intechopen.com/pdfs/35067/InTech-Water_quality_degradation_trends_in_kenya_over_the_last_decade.pdf

Kithiia, S.M. (2007). An assessment of water quality changes within the Athi and Nairobi River basins during the last decade. IAHS publication 314, 205. https://www.cabidigitallibrary.org/doi/full/10.5555/20093064978

Line, D.E. (2002). Changes In Land Use/Management and Water Quality In The Long Creek Watershed 1. Jawra *Journal of the American Water Resources Association* 38, 1691–1701. https://doi.org/10.1111/j.1752-1688.2002.tb04374.x

Mănoiu, V.-M., Crăciun, A.-I. (2021). Danube river water quality trends: A qualitative review based on the open access web of science database. *Ecohydrology & Hydrobiology* 21, 613–628. https://doi.org/10.1016/j.ecohyd.2021.08.002

Mehmood, M. A., Rashid, A., & Ganie, S. A. (2017). *Spatio-Temporal Changes in Water Quality of Jhelum River , Kashmir Himalaya*. *12*(1), 1–29.

Melo, D.C., Anache, J.A., Almeida, C. das N., Coutinho, J.V., Ramos Filho, G.M., Rosalem, L.M., Pelinson, N.S., Ferreira, G.L., Schwamback, D., Calixto, K.G. (2020). The big picture of field hydrology studies in Brazil. *Hydrological Sciences Journal* 65, 1262–1280. https://doi.org/10.1080/02626667.2020.1747618

Mustapha, A., Aris, A. Z., Yusoff, F. M., Zakaria, M. P., Ramli, M. F., Abdullah, A. M., Kura, N. U., & Narany, T. S. (2014). Statistical Approach in Determining the Spatial Changes of Surface Water Quality at the Upper Course of Kano River, Nigeria. *Water Quality, Exposure and Health*, *6*(3), 127–142. https://doi.org/10.1007/s12403-014-0117-7

Musyoki, A.M., Abednego, M., Suleiman, M.A., Mbithi, J.N., Maingi, J.M. (2013). Water-borne bacterial pathogens in surface waters of Nairobi River and health implication to communities downstream Athi river. http://ijlpr.com/admin/php/uploads/163_pdf.pdf

Ngatia, M.W. (2022). Effects of Anthropogenic Activities on Water Quality of Ngong River, Nairobi County, Kenya. Thesis. http://erepository.uonbi.ac.ke/handle/11295/162506

Njuguna, S.M., Yan, X., Gituru, R.W., Wang, Q., Wang, J. (2017). Assessment of macrophyte, heavy metal, and nutrient concentrations in the water of the Nairobi River, Kenya. *Environmental monitoring and assessment* 189, 1–14. https://doi.org/10.1007/s10661-017-6159-0

Radu, C., Manoiu, V.-M., Kubiak-Wójcicka, K., Avram, E., Beteringhe, A., Craciun, A.-I. (2022). Romanian Danube River Hydrocarbon Pollution in 2011–2021. *Water* 14, 3156. https://doi.org/10.3390/w14193156

Rodrigues, M. O., Abrantes, N., Gonçalves, F. J. M., Nogueira, H., Marques, J. C., & Gonçalves, A. M. M. (2018). Science of the Total Environment Spatial and temporal distribution of microplastics in water and sediments of a freshwater system (Antuã River , Portugal). *Science of the Total Environment*, *633*, 1549–1559. https://doi.org/10.1016/j.scitotenv.2018.03.233

Singh, K.P., Malik, A., Mohan, D., Sinha, S. (2004). Multivariate statistical techniques for the evaluation of spatial and temporal variations in water quality of Gomti River (India)—a case study. *Water Research* 38, 3980–3992. https://doi.org/10.1016/j.watres.2004.06.011

St-Hilaire, A., Brun, G., Courtenay, S.C., Ouarda, T.B., Boghen, A.D., Bobée, B. (2004). Multivariate Analysis of Water Quality In The Richibucto Drainage Basin (New Brunswick, Canada) 1. JAWRA *Journal of the American Water Resources Association* 40, 691–703. https://doi.org/10.1111/j.1752-1688.2004.tb04453.x

Voda, A. I., Sarpe, C. A., & Voda, M. (2018). Methods of maximum discharge computation in ungauged river basins. Review of procedures in Romania. *Geographia Technica*, 13(1), 130-137. DOI: 10.21163/GT_2018.131.12

Voda, M., Kithiia, S., Jackiewicz, E., Du, Q., & Sarpe, C. A. (2019). Geosystems 'pathways to the future of Sustainability. *Scientific Reports*, 9(1), 14446. https://doi.org/10.1038/s41598-019-50937-z

Voda, M., Sarpe, C. A., & Voda, A. I. (2019). Romanian river basins lag time analysis. The SCS-CN versus RNS comparative approach developed for small watersheds. *Water Resources Management*, 33(1), 245-259. https://doi.org/10.1007/s11269-018-2100-8

Voza, D., Vuković, M., Takić, L., Arsić, M. (2015) a. Spatial and seasonal variations in the water quality of the Morava River system, Serbia. *Fresenius Environmental Bulletin* 24, 1119–1130. https://www.prt-parlar.de/

Voza, D., Vukovic, M., Takic, L., Nikolic, D., Mladenovic-Ranisavljevic, I. (2015) b. Application of multivariate statistical techniques in the water quality assessment of Danube River, Serbia. *Archives of Environmental Protection*. DOI 10.1515/aep-2015-0044

Yang, X., Meng, F., Fu, P., Zhang, Y., & Liu, Y. (2021). Spatiotemporal change and driving factors of the Eco-Environment quality in the Yangtze River Basin from 2001 to 2019. *Ecological Indicators*, *131*, 108214. https://doi.org/10.1016/j.ecolind.2021.108214

Zhang, X., Wang, Q., Liu, Y., Wu, J., Yu, M. (2011). Application of multivariate statistical techniques in the assessment of water quality in the Southwest New Territories and Kowloon, Hong Kong. *Environmental monitoring and assessment* 173, 17–27, https://doi.org/10.1007/s10661-010-1366-y.

THE USE OF OPENSTREETMAP AND GIS SOFTWARE TO IDENTIFY MASONRY BRIDGE IN A SPECIFIC REGION AND TO BUILD A DATABASE TO PRESERVING HISTORICAL STRUCTURES

Ahmed Kamal Hamed DEWEDAR[1]* ⓘ *, Massimiliano PEPE[1]* ⓘ

ABSTRACT

This research investigates the efficacy of OpenStreetMap (OSM) and Geographic Information Systems (GIS) for rapidly identifying and cataloging masonry bridges in specific regions integrating modern technology with historical data to enhance the mapping and preservation of these critical structures. The methodology developed is based on the use of OSM, Google Street View (GSV), and the Overpass API. It includes data extraction, processing, and validation through intrinsic and extrinsic quality measures, highlighting the robustness of masonry bridges, particularly in historical areas where traditional construction techniques prevail. The experimentation was carried out on an area of 1.225 km^2 in the province of Pescara (Italy). The results showed an accuracy rate of 74.35% in identifying bridge types from street-level images, despite the crowd-sourced nature of the data demonstrating the potential of combining open-access geospatial data with modern verification tools to support infrastructure mapping and preservation efforts, providing a comprehensive and cost-effective approach, especially in regions with deficient geospatial data.

Key-words: *OpenStreetMap, GIS, Masonry Bridges, Google Street View, Quality Assessment.*

1. INTRODUCTION

OpenStreetMap (OSM) is a user-generated platform that provides a detailed and editable map of the world, created and maintained by a community of volunteers and enthusiasts. The platform's extensive database includes a variety of geospatial data points such as roads, buildings, natural features, and critical infrastructure elements like bridges (Grinberger, 2022). The collaborative nature of OSM ensures that the data is continuously updated, making it a dynamic and valuable resource for researchers, urban planners, and policymakers. Given the resource-intensive nature and data volume of High-Definition Maps, recent research has turned towards OSM-based navigation methods. OSM offers a publicly accessible map that is easier to access and modify, requiring less storage while encompassing crucial road semantic information essential for global path planning. However, OSM suffers from lower geometric accuracy compared to proprietary maps. Haklay et al. (2010) noted an average 6-meter discrepancy between Ordnance Survey (OS) data and corresponding OSM locations across various London regions. While navigation methods based on OSM reduce map construction costs (Naik, 2019), the accuracy of Global Navigation Satellite System (GNSS) coordinates within OSM can be insufficient for precise navigation, posing risks. To mitigate this, researchers advocate for multi-sensor fusion to enhance accuracy in positioning, mapping, and environmental data acquisition. Zaman et al. (2013) proposed an outdoor navigation approach leveraging OSM, which integrated GNSS, IMU, and wheel encoder data to improve robot positioning relative to the map. However, this method primarily addresses robot positioning errors without fully addressing the accuracy limitations of OSM itself.

[1*]*Department of Engineering and Geology, "G. d'Annunzio" University of Chieti-Pescara, 65127 Pescara, Italy;* ahmedkamalhamed.dewedar@phd.unich.it *(corresponding author),* massimiliano.pepe@unich.it

Technical Geography is an emerging field within Geography that focuses on the integration of statistical methods and modern technologies. It plays a crucial role in supporting geo-information management and decision-making systems. With ongoing research and the growing number of applications in this field, it is expected that all branches of Geography will eventually adopt technical approaches and continue to evolve in this direction (Haidu, 2016).

Spatial data quality is a well-explored domain, governed by international standards that encompass various elements such as completeness, commission/omission errors, logical consistency, and spatial, temporal, and thematic accuracy. Over the past two decades, the concept of 'fitness-for-use' has emerged as a crucial yet subjective parameter of data quality, essential for numerous applications (Veregin, 1999). Evaluating the quality of OSM data remains a vibrant area of research for two primary reasons. Firstly, the volume of contributions to OSM is continually growing, with some European cities now extensively mapped. Secondly, the lack of standardized data production methods given that anyone can contribute necessitates evaluating how well Volunteered Geographic Information (VGI) reflects reality. Despite the presence of international standards such as ISO 19113 and ISO 19157, researchers generally employ two main strategies to assess OSM data quality: intrinsic and extrinsic measures (Barron et al., 2014). Intrinsic measures do not depend on a reference dataset; instead, they assess quality based on the development of a geographical object. This method is often favored due to the high costs or restrictive licenses associated with reference datasets. Researchers examine the data and its historical records to estimate quality. For instance, Haklay et al. (2010) validated 'Linus′ Law' in the context of spatial accuracy, suggesting that spatial accuracy improves with the number of volunteers mapping an object or region. Another study used the ratio of buildings with a house number or name to the total number of buildings as a proxy for attribute completeness. However, as Barron et al. (2014) noted, absolute quality assessments require a high-quality reference dataset for comparison. Extrinsic measures assume the availability of reference datasets. Extensive research has compared OSM datasets with authoritative datasets, typically generated by legal entities and presumed to have superior quality. Recent studies advocate for combining intrinsic and extrinsic measures to mitigate the limitations inherent in each approach (Touya et al., 2017). Nicoară and Haidu (2011) conducted a study aimed at modeling the shortest path and closest facility problems for ambulances navigating a road network. They developed a system based on GIS technology, applying it to the city of Cluj-Napoca, Romania.

Bridges are pivotal components of transportation networks, enabling the passage over obstacles such as rivers, valleys, and other roadways. Their strategic importance in connecting regions, facilitating trade, and supporting emergency response efforts underscores the necessity of accurate mapping and identification. Traditional methods of mapping bridges often involve extensive field surveys and expensive remote sensing technologies. However, the advent of collaborative mapping platforms like OSM presents an innovative and cost-effective alternative.

OSM has become a vital resource in various fields due to its collaborative nature and open-access policy. Numerous studies have evaluated its data quality, application potential, and the dynamics of its contributor community. Borkowska et al. (2022) conducted an assessment of OSM as a geospatial open data source for monitoring Sustainable Development Goals (SDG) indicators, comparing it with national official data from a 1:10,000 scale topographic objects database. Salvucci and Salvati (2022) directed a study on Official Statistics, Building Censuses, and OSM Completeness in Italy providing a streamlined framework for assessing the coverage and completeness of settlement maps derived from the OSM database on a national scale, with potential applications in official statistics. Benjamin et al. (2021) explored the utilization of OSM collaborative maps over the past decade to support humanitarian efforts globally and address critical data deficiencies necessary for implementing major development frameworks such as the Sustainable Development Goals. Cerri et al. (2021) explored using OSM to build data for flood vulnerability modeling; in this latter case study the authors found that models outperformed simple stage-damage functions but often struggled outside their development areas. Klinkhardt et al. (2021) introduced a methodology for extracting points of interest (POIs) data from OSM for use in travel demand models. Jing et al. (2022) highlight OSM's utility in outdoor navigation due to its public availability and detailed road information. Xiang et al. (2024)

explored the sustainability of OSM by tracking individual editing behaviors from 2005 to 2021; this latter research investigated whether OSM can reliably provide its services in the long term, proposing an "inner cycle of career stages" to monitor sustainable status and applying critical mass theory to identify sustaining factors.

The proposed research focuses on assessing the quality of bridge attributes, comprehensively capturing their integrity and enabling an understanding of their fitness for accuracy purposes. This assessment follows frameworks and definitions established in the GIS science literature. Accuracy evaluates whether the value of an attribute is correct. Our approach to assessing accuracy involves using an external data source and concentrates on a subset of bridges, as it is not feasible to scale this method to the entire dataset. Additionally, the paper aims to develop an easily applicable method to analyze masonry bridges from OSM. The research provides a straightforward and efficient approach for identifying and evaluating masonry bridges, facilitating better data accuracy and usability for researchers and practitioners working with OSM data.

2. DATA AND METHOD

2.1. Study Area

Masonry arch bridges are part of Italy's infrastructure heritage and are often held up as examples for their consistency and resistance to the inexorable passage of time. This type of infrastructure also needs maintenance and checking even non-structural aspects can make a difference (Pepe et al., 2024). The study area covers the province of Pescara and is located in the Abruzzo region (Italy) and covers an area of about 1.225 km^2.

2.2. Method

This section will detail a generic step-by-step process that can be applied to various contexts. The method can be summarized in the following main steps: i) Data Collection, ii) Data Processing, iii) Data Validation, iv) Data Analysis, and v) Data Correction and Documentation.

The first step in this methodology is **Data Collection**, where the goal is to gather relevant geospatial data from a variety of sources. To begin, it is crucial to identify appropriate data sources. OpenStreetMap (OSM) serves as a primary resource due to its extensive, community-contributed geospatial data. Additional sources such as GSV or Overpass API can be leveraged for supplementary information. Tools like Geofabrik are particularly useful for obtaining region-specific OSM data extracts, while Overpass Turbo provides a powerful web-based interface for querying OSM data.

Once the data sources have been identified, the next task is to extract the relevant data. This involves downloading region-specific datasets, and ensuring that the correct geographic area and data layers (such as roads or bridges) are included. Overpass Turbo queries are then crafted to extract specific features of interest, like bridges or masonry structures, using appropriate tags such as highway=bridge or building=masonry. After extraction, the data must be prepared for analysis. This involves converting the data into compatible formats (e.g., GeoJSON or Shapefile) for use in Geographic Information System (GIS) software (Alcaras et al., 2023; Alfio et al., 2024), followed by a cleaning process to remove irrelevant features and focus on the study area.

The **Data Processing** phase involves isolating the relevant features from the collected data to facilitate detailed analysis. The first part of this step is data querying, where precise Overpass Turbo queries are employed to filter out the desired geospatial features from the dataset. These queries are designed to target specific characteristics, such as materials or structural types relevant to the study. Once the queries are executed, the resulting data is exported in formats suitable for further analysis.

In some cases, it may be necessary to enrich the dataset with additional attributes or by integrating data from other sources. This enrichment process can involve manually adding new attributes—such as the height, age, or structural type of a feature—or merging the dataset with other authoritative data sources.

Following data processing, the next step is **Data Validation**. This is a critical phase where the accuracy of the processed data is verified by cross-referencing it with authoritative sources. The first task is to identify and obtain these authoritative datasets, which may include government maps, official registries, or other reliable sources relevant to the study area. Using GIS software, the processed OSM data is overlaid with these authoritative datasets, and discrepancies in location, attributes, or completeness are meticulously checked. Field verification enhances data accuracy by involving site visits to physically check selected features, such as bridge materials or structures. Tools like GNSS devices or mobile mapping apps (e.g., OSMTracker) are used to collect field data, which is then compared with the dataset. Any discrepancies are corrected using GIS software or OSM editing tools like JOSM. If major errors are found, the data may need to be reprocessed to ensure reliability.

Once the data has been validated, the **Data Analysis** phase begins, where the dataset is thoroughly examined to draw meaningful insights. This process often starts with spatial analysis, which involves using GIS tools to perform operations like spatial joins, overlays, and proximity analyses. These techniques help reveal relationships between different features, such as the proximity of bridges to roads or rivers. Additionally, hotspot analysis can be employed to identify patterns or clusters within the data, such as areas with a high concentration of specific types of bridges.

The final step is **Data Correction and Documentation**. This step involves addressing any remaining discrepancies and making necessary adjustments to ensure accurate data representation. For OSM projects, corrections can be uploaded to improve community data quality. Documentation is crucial for transparency, requiring a detailed report on the methodology, tools used, challenges, and analysis results. This documentation, including maps and recommendations, should be shared with stakeholders or the public through publications, websites, or presentations, ensuring accessibility and usability for others. The methodology can be summarized as **(Fig.1)**:
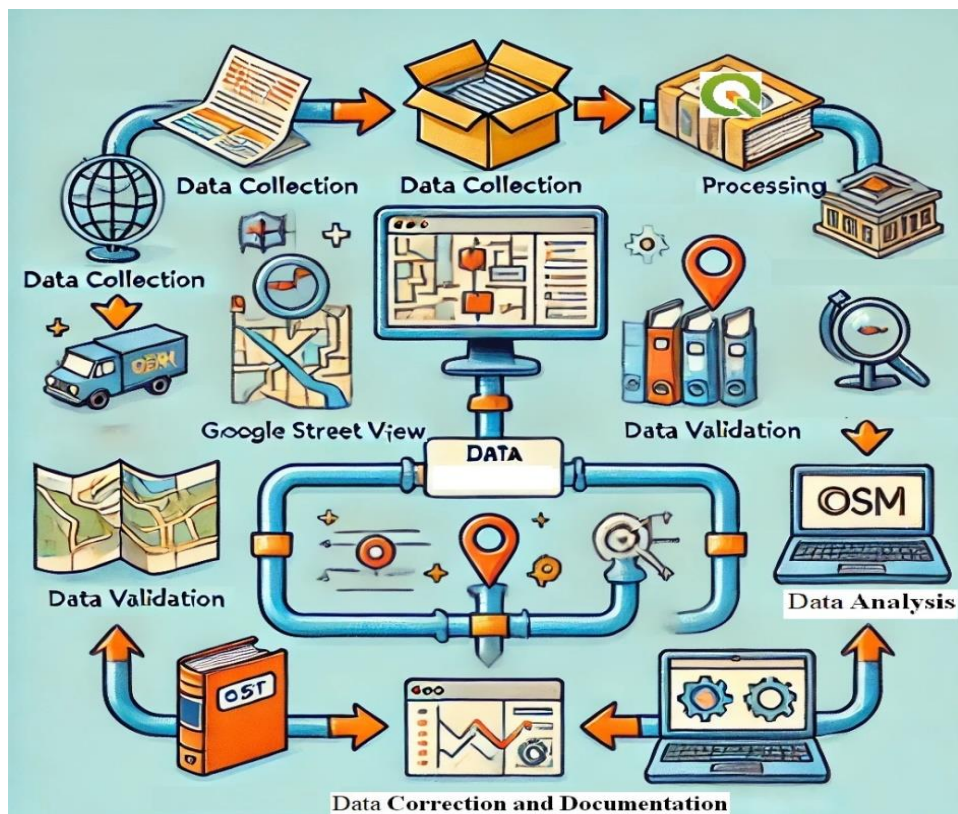

Fig. 1. Details of the Methodology Flow chart.

• Data Collection: Represent sources such as OpenStreetMap (OSM), Google Street View (GSV), and the Overpass API.

• Data Processing: Show the conversion of extracted data into formats for GIS software.

• Data Validation: Indicate cross-referencing with authoritative datasets.

• Data Analysis: Highlight GIS tools used for spatial joins and hotspot analysis.

• Data Correction and Documentation: Demonstrate uploading corrections to OSM and generating reports.

To evaluate the accuracy of the bridge classification method, the F1 Score was incorporated as a key metric. The F1 Score is a comprehensive measure that balances precision and recall, offering a nuanced understanding of the model's performance, particularly when handling imbalanced datasets. Precision quantifies the number of true identifications relative to the total instances identified as positive, while recall measures the number of true positives relative to the actual number of positives in the dataset. The precision (P) and recall (R) are defined as equations 1 and 2 (Alberg et al., 2004, Dewedar et al., 2024):

$$P = \frac{TP}{(TP + FP)} \tag{1}$$

$$R = \frac{TP}{(TP + FN)} \tag{2}$$

where   *P* is Precision,

TP is True Positives

FP is False Positives,

R is Recall

FN is False Negatives.

The F1 Score (F1) is then calculated as the harmonic mean of precision and recall, using the formula (equation 3):

$$F1 = 2 \cdot \frac{P \times R}{P + R} \tag{3}$$

This metric provides a single value that accounts for both false positives and false negatives, ensuring a balanced evaluation of our model's performance. This is especially relevant in our context, where subjective interpretation and the inherent limitations of crowd-sourced data can lead to misclassifications. Employing the F1 Score in our methodology ensures a balanced evaluation, highlighting the effectiveness of our approach and identifying areas for further refinement. This metric not only validates the reliability of our classification but also guides improvements in integrating advanced imagery and enhancing the accuracy of our infrastructure mapping efforts.

3. CASE STUDY: (Identification of Masonry Bridges)

To download OSM data for a study area, such as Pescara, visit a site like Geofabrik, which provides regional OSM extracts. After downloading the relevant data from Geofabrik's Europe section, you can use the Overpass API to query specific map features, such as bridges. Bridges are categorized under the building tag in OSM. For easier interaction, Overpass Turbo, a web-based tool, can be used to run queries and visualize the results on a map for detailed analysis. To effectively process data with the Overpass API, it's crucial to understand the relevant map features **(Fig. 2)**.

```
 1    /*
 2    This has been generated by the overpass-turbo wizard.
 3    The original search was:
 4    "bridge=* in "Pescara""
 5    */
 6    [out:json][timeout:25];
 7    // fetch area "Pescara" to search in
 8    {{geocodeArea:Pescara}}->.searchArea;
 9    // gather results
10    nwr["bridge"](area.searchArea);
11    // print results
12    out geom;
```

Fig. 2. Details of the Overpass Turbo interface displaying the query for bridges in the investigated region.

Start by researching bridge-related tags on the OSM Wiki. These tags help identify and categorize bridges within the OSM data. A good resource for this information is the bridge tag page on the OSM Wiki. This page provides comprehensive details on how bridges are tagged in OSM, including examples and common usage patterns. Overpass Turbo wizard was used to generate a query to extract bridge data. Once pasted the script into the Overpass Turbo interface and then executed, it was possible to obtain data on tagged bridges **(Fig. 3)**.
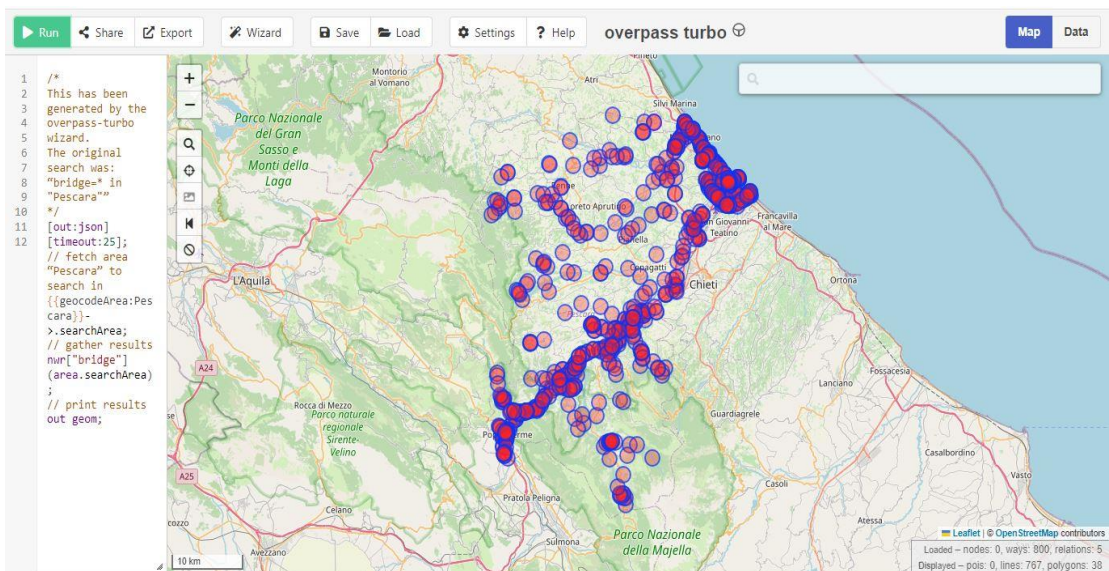
Fig. 3. Locations of bridges in the investigated region (multiple bridge locations marked with red circles outlined in blue).

Once the bridge data for the area under investigation has been exported (e.g. in GeoJSON format), a thorough analysis was performed to ensure the accuracy and completeness of the data. This analysis involved several steps:

a) **Data Loading and Initial Review**: Load the exported bridge data into GIS software (e.g., QGIS, ArcGIS) and review the data structure to ensure all necessary attributes are included. Use spatial queries to isolate bridge data and create a dedicated layer for further analysis.

b) **Data Comparison and Verification**: Obtain official GIS datasets for the Pescara region and perform a spatial join or overlay analysis to compare them with the OSM bridge data. Identify discrepancies and investigate inconsistencies through attribute comparison and satellite imagery integration.

c) **Manual Inspection and Data Correction**: Conduct a manual inspection of bridge locations using satellite imagery and OSM editing tools (e.g., JOSM). Verify the accuracy of bridge data, make necessary corrections, and document the process. Generate reports and maps to summarize the findings and share them with relevant stakeholders.

Begin The process of verifying and enhancing OSM bridge data begins by loading the extracted GeoJSON files into GIS software like QGIS or ArcGIS for visualization and analysis. After reviewing the data structure to ensure the inclusion of key attributes such as bridge type and material, spatial queries and filters are applied to isolate bridge data from other features. Next, official GIS datasets from local authorities are integrated through spatial joins or overlay analyses to compare the OSM bridge data and identify discrepancies. High-resolution satellite imagery is also overlaid for visual verification of bridge locations and attributes. Tools like JOSM are used for detailed inspection and corrections based on the findings. The verification process is meticulously documented, and reports are generated to highlight areas of accuracy and needed improvements. Finally, these findings are shared with the OSM community and local authorities to enhance the overall quality of the bridge data in the study area. Street-level imagery is also employed to manually inspect and verify bridge details, ensuring a high level of data accuracy.

4. RESULTS AND DISCUSSIONS

OSM mapping helps mappers develop a range of vital skills and expand their knowledge in various areas. These include deepening civic engagement, developing social identity, expanding geographic knowledge, enhancing spatial awareness, and increasing happiness and satisfaction. Remarkably, mappers retain most of these skills over the long term, regardless of their academic or professional backgrounds.

However, there remains significant scope for further investigation in this area. Ideally, this should be pursued through a longitudinal study with a larger and more diverse sample, as well as comparisons between different program designs. Such research would help fully understand the wide array of effects OSM mapping has on mappers and explore the potential to enhance positive outcomes through associated youth learning and leadership programs.

To design a balanced global sample, several 267 bridges were selected from OSM, focusing on those with existing attributes. The research aimed to inspect their street-level imagery using GSV. First, it was checked if GSV was available for the location and then determined if the bridge was visible (some might be obstructed by structures or vegetation). If the bridge was visible, a few visually verifiable attributes was inspected.

The analysis revealed that 74.35% of the sampled bridges are located in areas covered by GSV. Among these, a various types of bridge materials were identified: 6 bridges were constructed from steel, 7 from wood, and an impressive 150 from masonry, indicating the prevalence of masonry bridges in our sample. The classification process also identified 5 bridges using other unspecified materials. For bridges in OSM where the material type was available and could be inferred from the street-level imagery, it was achieved an accuracy of 74.35%.

This level of accuracy is noteworthy, particularly considering the crowd-sourced nature of the data on OSM. However, it is essential to acknowledge the inherent subjectivity in evaluating these values. The variability in user contributions and the diverse interpretations of bridge characteristics can impact the consistency and reliability of the data. Standardizing bridge identification and classification on a global scale remains a complex challenge due to these subjective elements. Despite these challenges, the relatively high accuracy of our findings underscores the potential of using crowd-sourced data for large-scale infrastructure analysis, while also highlighting the need for careful validation and standardization efforts to enhance data reliability and utility. Given these nuances and the fact that contributors might struggle with ambiguous cases (which do not significantly affect downstream analyses), the achieved accuracy is considered rather high.

After a thorough analysis of the bridges in Pescara, it was found that OpenStreetMap (OSM) represents bridges as either polygons or lines when opened with GIS software. To refine the results, a filter was applied in the attribute table to only include bridges longer than 50 meters. Initially, 267 bridges were analyzed after applying this filter, though this number was reduced by multiple iterations of filtering based on length. Additionally, many bridges initially represented by multiple lines **(Fig. 4 a)**, were consolidated into a single line. However, several discrepancies were observed, as described below.

- Incorrect Bridge Identifications: Some locations marked as bridges were, upon GSV inspection, identified as buildings **(Fig. 4 b)**. For instance, a building with a tunnel and parking ramp was labelled as a bridge.
- Vegetation and Forests: Numerous bridges were located in areas with dense vegetation or forests, making them invisible in GSV **(Fig. 4 c)**.
- Normal Roads Misidentified as Bridges: OSM occasionally misidentified regular roads as bridges, with no elevation difference discernible at ground level.
- Tunnels Misclassified as Bridges: Several tunnels were inaccurately classified as bridges.
- Footpaths and Small Paths: Footpaths, small pedestrian pathways, and bicycle paths were often erroneously tagged as bridges.

(a)   (b)   (c)
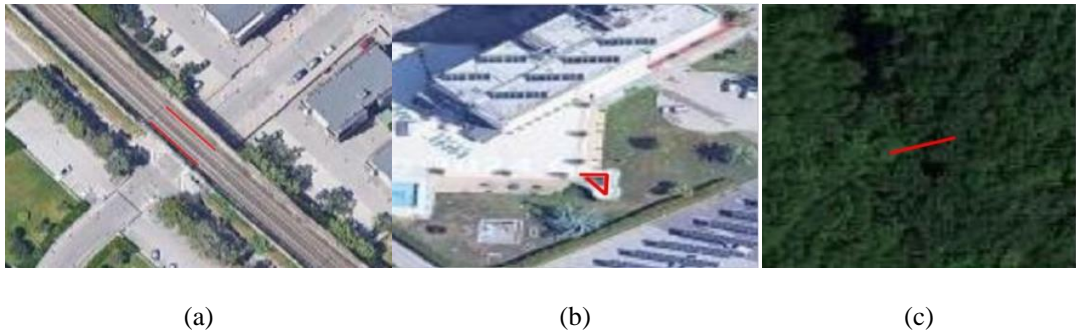
Fig. 4. Some examples of errors in bridge recognition: Bridge on Google Maps but has 2 lines that were identified twice at OSM (a), Detection of a Bridge Over a Triangular Architectural Structure (b), bridge was located with dense vegetation (c).

Overall, the study highlights the need for meticulous review and verification of bridge data in OSM to ensure accuracy and reliability. The results underscore the complexities and challenges of using crowd-sourced data for precise applications like infrastructure mapping.

The widespread presence of masonry bridges in Italy's historic regions highlights the nation's dedication to preserving its architectural heritage. Many of these bridges are protected as cultural heritage sites, attracting global attention for their historical and aesthetic value. Constructed using local stone and traditional techniques, they reflect a deep connection to regional resources (Crisan et al., 2024). The ongoing maintenance and restoration of these bridges are crucial to ensuring their functionality within modern infrastructure while preserving their historical significance. In this study, five masonry bridges, comprising 2.5% of the 200 sampled, were identified using GSV imagery, showcasing the blend of modern technology with historical preservation efforts.

This F1 Score of approximately 0.666 reflects the model's balanced accuracy in classifying masonry bridges. While this score is relatively high, indicating a good level of precision and recall, it also highlights areas for improvement, particularly in minimizing false positives and false negatives. The integration of advanced imagery and more robust validation techniques could further enhance the accuracy of our classification method, thereby improving the F1 Score and the overall reliability of the data. For instance, of the 200 bridges analyzed, the precision achieved was 0.625, recall 0.714 and F1 Score 0.666.

After setting up the QGIS environment, the OSM Downloader plugin was used to download relevant OSM data for the area of interest. The data, including roads, buildings, natural features, and

bridges, was loaded into QGIS. Bridges were filtered using attributes like "bridge=yes" and refined further by isolating masonry bridges with tags such as "bridge = masonry." A new point or polygon layer was created to represent these masonry bridges, with an attribute table that included fields for ID, Name, Material (Masonry), Condition, Year Built, OSM ID, and Photo. Images of the bridges were linked to the dataset through a Photo field or the built-in attachment feature in QGIS, allowing pop-ups to display detailed information and images.

The masonry bridges were visually symbolized with custom icons or styles, distinguishing them from other bridge types. The completed database was integrated with broader OSM data in QGIS for advanced spatial analysis and map creation. It was then exported to formats like Shapefile or GeoJSON for sharing or further analysis. To make the data accessible, it could be published on a web map using plugins like QGIS2Web. This approach allowed for a visually rich and interactive spatial database, enhancing applications in academic research and heritage management. For instance, a masonry bridge named "Contrada San Clemente" was identified in the spatial database, and its attributes (ID: way/48998350, material: Masonry, structure: One Arc) were linked to a photo for better visualization and context **(Fig. 5)**. The photo of the 'Contrada San Clemente' bridge was linked to the spatial database, allowing its current state to be compared with historical records from the last century, enabling a detailed assessment of structural changes over time and ensuring the data remains up-to-date.
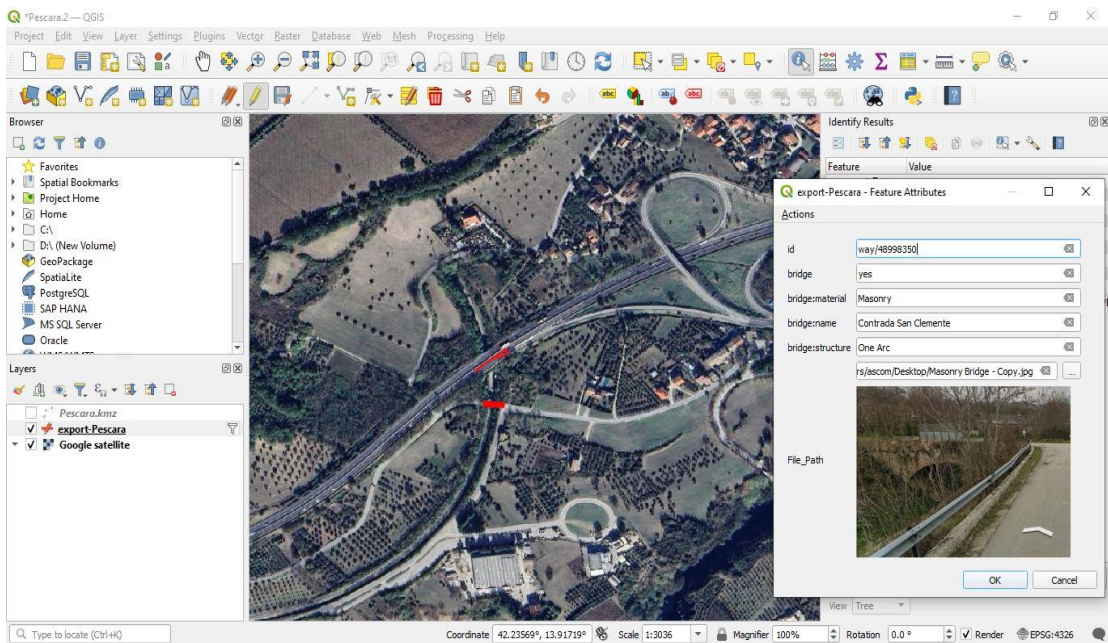

Fig. 5. Integration of Bridge Attributes with Visual Data in QGIS.

5. CONCLUSIONS

This study systematically analyzes the completeness of OpenStreetMap for 267 bridges in the case study. The focus was exclusively on bridges due to their relevance for applications such as urban planning and civil engineering. Data collection and management were carried out using QGIS with a visual comparison approach. Geospatial building information sourced from OSM, including both geometric and descriptive attributes, has gained a foothold in multiple domains across the built environment, thanks to its liberal license, growth in the completeness of the building stock mapped, and increasing awareness of this crowd-sourced platform of geospatial data.

This paper aimed to showcase the viability of using OpenStreetMap for bridge identification. By leveraging OSM's comprehensive and continually updated geospatial data, researchers and planners can obtain accurate bridge information more efficiently than traditional methods. The implications of this research extend beyond bridge identification, offering insights into the broader applications of collaborative mapping platforms in infrastructure management and urban planning. Currently, due to the lack of automated methods for acquiring essential parameters and the need for manual steps in certain aspects of conflation, the bridge identification cannot be considered a fully automated, one-click solution. Instead, this study highlights the importance of active user involvement in reviewing results step-by-step, leveraging the capabilities of both QGIS and JOSM toolsets to achieve optimal outcomes. Users are encouraged to undertake a Tasking Manager validation project after importing the data to ensure accuracy.

The main limitations of the method include its inability to handle multi-level roads such as overpasses, the frequent lack of accurate information on OSM street levels, and the uncertainty regarding the presence of bridges. Future iterations of the plugin could address these limitations by integrating satellite and/or terrestrial imagery. Plans also include extending the plugin's functionality to make it easily integrable as a QGIS processing provider algorithm with additional features such as drawing missing intersections and access points.

Another valuable lesson from this study is that comprehensively measuring the accuracy and correctness of OSM tag values by comparing them to street view imagery of real bridges is impractical and unscalable. However, the large and well-balanced sample of bridges used in this study provides a strong indication of the general accuracy of the data and highlights variations across different regions. Quantifying the accuracy of text-based tag values is also challenging as it is highly subjective and influenced by personal knowledge and opinions.

Scaling spatial data quality assessments and conducting them across multiple countries with diverse architectures and morphologies remains a significant challenge. Nevertheless, this study aims to advance this research area and set the stage for future work. As new buildings and bridges are continuously mapped and existing ones updated with additional information, the findings of this study will remain relevant for several years, as many of the identified advantages, trends, and challenges are likely to persist.

In addition to the findings discussed, the database obtained from OSM can be customized to meet specific research needs. By developing custom queries, relevant features like specific types of masonry bridges can be extracted and additional attributes such as construction materials or historical significance can be included. Integrating external data sources and validating against authoritative datasets can enhance the database's accuracy. This flexibility allows researchers to address unique project requirements and broadens the applicability of OSM data in fields like infrastructure management and cultural heritage preservation.

Finally, this approach is particularly useful in regions where there is a lack of geospatial information, such as the absence of numerical cartographies or thematic maps.

R E F E R E N C E S

Alberg, A. J., Park, J. W., Hager, B. W., Brock, M. V., & Diener-West, M. (2004) The use of "overall accuracy" to evaluate the validity of screening or diagnostic tests. Journal of general internal medicine, 19(5p1), 460-465.

Alcaras, E., Morale, D., Parente, C., & Prezioso, G. (2023) Integrating elevation and bathymetric data in GIS for a continuous 3D model of Ischia Island and surrounding seabed. In 2023 3rd International Conference on Innovative Research in Applied Science, Engineering and Technology (IRASET), pp. 1-6.

Alfio, V. S., Pepe, M., Costantino, D., & Baratin, L. (2024) GIS Approach for Mosaic Tesserae Recognition by Supervised Image Classification. Studies in Digital Heritage, 8(1), 22-35.

Barron, C., Neis, P., & Zipf, A. (2014) A Comprehensive Framework for Intrinsic OpenStreetMap Quality Analysis. Transactions in GIS, 18(6), 877‑895.

Benjamin, H., Sven, L., João, P., Jennings, A., Alexander, Z. (2021) The evolution of humanitarian mapping within the OpenStreetMap community. Scientific Reports, doi: 10.1038/s41598-021-82404-z.

Borkowska, S., Pokonieczny, K. (2022) Analysis of OpenStreetMap Data Quality for Selected Counties in Poland in Terms of Sustainable Development. Sustainability, 14, 3728. https://doi.org/10.3390/su14073728.

Cerri, M., Steinhausen, M ,& Kreibich, H. (2021) Are OpenStreetMap building data useful for flood vulnerability modelling?. Natural Hazards and Earth System Sciences, 21(2), pp. 643-662, Doi: 10.5194/nhess-21-643-2021.

Crisan, A., Pepe, M., Costantino, D., & Herban, S. (2024) From 3D Point Cloud to an Intelligent Model Set for Cultural Heritage Conservation. Heritage, 7(3), 1419-1437.

Dewedar, A. K. H., Palumbo, D., & Pepe, M. (2024) Hydraulic Risk Assessment on Historic Masonry Bridges Using Hydraulic Open-Source Software and Geomatics Techniques: A Case Study of the "Hannibal Bridge", Italy. Remote Sensing, 16(16), 2994.

Grinberger, A.Y., Minghini, M., Juhász, L., Yeboah, G., Mooney, P. (2022) OSM Science—The Academic Study of the OpenStreetMap Project, Data, Contributors, Community, and Applications. ISPRS Int. J. Geo-Inf.2022, 11, 230. https://doi.org/10.3390/ijgi11040230.

Haidu, I. (2016) What is Technical Geography. Geographia Technica, 11(1), 1-5. DOI: 10.21163/GT_2016.111.01.

Haklay, M., Basiouka, S., Antoniou, V., & Ather, A. (2010) How Many Volunteers Does It Take to Map an Area Well? The Validity of Linus' Law to Volunteered Geographic Information. The Cartographic Journal, 47(4), 315-322. Doi: 10.1179/000870410X12911304958827.

Jing, C., Hu, Y., Zhang, H., Du, M., Xu, S., Guo, X., & Jiang, J. (2022) Context-aware matrix factorization for the identification of urban functional regions with POI and taxi OD data. ISPRS International Journal of Geo-Information, 11(6), 351.

Klinkhardt, C., Woerle, T.,Briem, L., Heilig, M., Kagerbauer, M., Vortisch, P. (2021) Using OpenStreetMap as a Data Source for Attractiveness in Travel Demand Models . Transportation Research Record: Journal of the Transportation Research Board, doi: 10.1177/0361198121997415.

Naik, L., Blumenthal, S., Huebel, N., Bruyninckx, H., Prassler, E.(2019) Semantic mapping extension for openstreetmap applied to indoor robot navigation. IEEE Int. Conf. Robot. Autom, pp. 3839–3845.

Nicoară, M., Haidu, I. (2011) Creation of the roads network as a network dataset within a GEODATABASE. Geographia Technica, 6(2), 81-86. https://hal.univ-lorraine.fr/hal-02488216.

Pepe, M., Costantino, D., & Alfio, V. S. (2023) Topographic Measurements and Statistical Analysis in Static Load Testing of Railway Bridge Piers. Infrastructures, 9(1), 4.

Salvucci, G., Salvati, L. (2022) Official Statistics, Building Censuses, and OpenStreetMap Completeness in Italy. ISPRS Int. J. Geo-Inf. 11, 29. https://doi.org/10.3390/ijgi11010029.

Touya, G., Antoniou, V., Olteanu-Raimond, A.-M., & Van Damme, M.-D. (2017) Assessing Crowdsourced POI Quality: Combining Methods Based on Reference Data, History, and Spatial Relations. ISPRS International Journal of Geo-Information, 6(3), 80.

Veregin, H. (1999) Data Quality Parameters. In Geographical Information Systems: Principles and Technical Issues, 1,177-189. New York: John Wiley & Sons.

Xiang Zhang, Jiayan An, Yuchuan Zhou, Min Yang & Xi Zhao (2024) How sustainable is OpenStreetMap? Tracking individual trajectories of editing behavior. International Journal of Digital Earth, 17:1, 2311320, DOI: 10.1080/17538947.2024.2311320.

Zaman, S., Steinbauer, G., Maurer, J., Lepej, P., Uran, S. (2013) an integrated model-based diagnosis and repair architecture for ros-based robot systems. IEEE Int. Conf. Robot. Autom, pp. 482–489.

COUPLING COORDINATION RELATIONSHIP BETWEEN TOURISM DEVELOPMENT AND URBAN-RURAL INTEGRATION

Zhangxin YIN [1], Liuyan DAI [2], Chang GAN [3], Mihai VODA [4]*

ABSTRACT

Our research aims to explore the coupling coordination relationship between tourism development and the URI (urban-rural integration) and its obstacle factors in the western Hunan Province by adopting modified coupling coordination model, scissor difference model, and grey correlation model. Prime conclusions are as follows. First, the relationship among tourism development and urban-rural integration in western Hunan Province has experienced the evolution process of "moderately uncoordinated–slightly uncoordinated–nearly uncoordinated". Second, the level of tourism development still lagged behind the degree of urban-rural integration. Third, spatial integration, social integration, and tourism scale were main obstacle factors that affects this coupling coordination relationship. Compared with previous research, this study concentrates on the division of evolution periods and the obstacle factors of relationship among tourism development and urban-rural integration. It is of great importance for policy-makers to formulate policies of common prosperity in western Hunan Province, China.

Key-words: *Tourism development; urban-rural integration; Modified coupling coordination model; Coupling coordination; Scissor difference model*

1. INTRODUCTION

With the rapid urbanization, the dichotomy among the prosperity of urban region and the decline of rural region is widespread around the world (Bennett, Yuen, & Blanco-Silva, 2018; Liu & Li, 2017; Ernawati et al., 2018; Lakatos et al., 2023; Magyari-Saska & Dombay, 2016). In China, as relatively independent area, the overall efficiency of resource allocation is relatively low. Meanwhile, the siphoning effect, a phenomenon of the agglomeration of economic factors, is much greater than the radiation effect, a phenomenon of the expansion of economic factors (Yang, Bao, Wang, & Liu, 2021). External manifestations of the urban-rural dichotomy are gradually diversifying from economic to social, cultural and ecological fields, which further hinders sustainable development (Ma, Liu, Fang, Che, & Chen, 2020; Sheng, 2011). Along with the strategy of Rural Revitalization, the relationship among two areas in China is in a stage of restructuring (Chen, Zhou, Huang, & Ye, 2021; Yin et al., 2022). Therefore, boosting urban-rural integration (URI) is a crucial goal for realizing sustainable development goals (SDGs) in social fields.

As a modern service industry with strong integrated effect, wide radiation and large multiplier effect, tourism industry plays an increasing role in the URI as the industrial chain has accelerated and the scale of tourism demand has continued to expand (Buckley, Shekari, Mohammadi, Azizi, & Ziaee,

---

[1,2] *Business School of Hunan First Normal University, Changsha, 410205 China, nadineyin@hnfnu.edu.cn; dly2022@hnfnu.edu.cn.*

[3] *School of Management, Wuhan Polytechnic University, Wuhan, 430048 China, gzrycxwl@whpu.edu.cn.*

[4] *Geography Department, Dimitrie Cantemir University, Targu Mures, 540545 Romania, corresponding author*, mihaivoda@cantemir.ro.*

2019; Quevedo, Uchiyama, & Kohsaka, 2021; Voda et al., 2019). First, based on the multiplier effect, tourism development can improve the URI by strengthening the interaction, narrowing the income gap, promoting public service, and boosting the eco-environmental management (Gao & Cheng, 2020; Sun, Ling, & Huang, 2020). Second, on the basic of system theory, the URI has expanded the space in terms of tourism economic development through the resources' allocation, the promotion of brands, and the expansion of markets (Luo, Chu, & Gao, 2022; Xu & Cheng, 2019). Coupling coordination relationship means that there is good correlation, coordination and coordination among various sub-systems. Therefore, forming the coupling coordination relationship among tourism development and the URI cannot only realize the SDGs in social field (e.g., narrowing urban-rural gap), but also promote tourism economic development.

Along with tourism economic development, the role that tourism industry plays in the economic growth in areas becomes more important (Sokhanvar, Çiftçioğlu, & Javid, 2018; Gupta et al., 2018). The URI, a manifestation of socio-economic development, has received increasing attention from academic circle. Tourism industry possesses of inclusiveness and universality, exerting a positive influence on the URI. For example, some scholars reveal that tourism development is able to decrease the income gap (Gatti, 2013; Paniagua, 2002). In addition, Kim and Kang (2020) adopted the fixed effect models and revealed that the interaction effect of tourism and FDI can significantly reduce the income disparity. At the level of whole economy, Liu, Nijkamp, and Lin (2017) confirms that tourism growth is beneficial for the decrease of the URI. However, as the increase of gap, the inhibiting effect of tourism development will be weakened. Moreover, the urban-rural migration (Buckley et al., 2019; Sun et al., 2020), social reform (Chen, Clarke, & Hracs, 2022; Gao & Cheng, 2020), and the flow of product factor (Li, Zhang, Zhang, & Abrahams, 2019; Quevedo et al., 2021) induced by the tourism development comes into researchers' perspective. Although quite a few scholars have concentrated on the association among tourism development and the URI, the literature on this coupling coordination association is lack. Additionally, abundant attention needs to be paid for the division of evolution periods regarding association among tourism development and the URI. What's more, the influencing factors affecting the relationship among two system accept little attention from researchers yet.

Taking into account above-mentioned gaps, our research aims to solve these issues. What is the coupling coordination relationship in specific tourist destination? How to divide the evolution periods of relationship between tourism development and the URI? What are the factors influencing this coupling coordination relationship? Therefore, this study not only investigated the evolution trend and period of the coupling coordination relationship among two systems, but also explored the obstacle factors. The contribution of answering the above questions. First, this study captures the bidirectional association among two systems, which offers evidence that tourism development is beneficial for advancing the social welfare and fairness, and thus promoting the SDGs in social field. Second, our research provides an adaptive research framework that integrates the evaluation of coupling coordination degree, the analysis of evolution period, and the investigation of influencing factors, which can be applied to other research samples. Thirdly, this study examines the influencing factors that affect this coupling coordination relationship, offering the recommendation of common prosperity for the policy-makers.

2. THEORATICAL FRAMEWORK

Referring to synergy theory, this study takes "elements-structure-function" as the logical main line to sort out the coupling mechanism between tourism development and the URI. Area is the basic unit connecting tourism development and the URI (Tan & Wang, 2024). Tourism development includes two sub-systems, namely, tourism scale and tourism performance (Gan et al., 2021; Voda et al., 2014). The URI includes four sub-systems, namely, economic integration, spatial integration, social integration, and ecological integration (Luo et al., 2022). The specific framework can be seen in **Fig. 1.**

Tourism development exerts an effect on the URI by the flow of factor, structure change, as well as scale growth. The flow of factor means that capital, technology and information flow between urban and rural areas. The structure change represents that the optimization of industry structure and income structure. The scale growth shows that the economic value added grows. The URI exerts an influence on tourism development through coordinated plan, industrial integration, and fund support. The coordinated plan represents that urban-rural planning is coordinated. Industrial integration refers to the process of interpenetration and intersection in different industries. Fund support means that the economic growth caused by the URI can provide fund support for tourism economic development. In summary, the interaction impact of tourism development and the URI stems from each influencing paths.

In terms of the effect of tourism development on the URI. Firstly, the flow of factors lays the foundation for the URI. Tourism industry helps to accelerate the flow of factors and achieve the resources' allocation, and thus promoting the URI (Zhang, Wang, & Yang, 2023), especially for economic integration. Secondly, urban and rural learn from and exchange with each other in destination management, breaking down the barriers between urban and rural areas at the level of culture, thus promoting spatial integration (Li et al., 2019). Thirdly, the tourism development is beneficial for an increase in tax revenue, which in turn offers a material basis for the renovation of infrastructure and the enhancement of public services, and boosts the quality of education, medical and cultural resources to rural areas (Gong, Guo, Ma, & Li, 2021).

With respect to the effect of the URI on tourism development. Firstly, unified urban-rural planning optimizes the allocation and application of tourism resources, improves the spatial structure of scenic spots, concentrates development advantages, avoids blindness in development (Chen et al., 2022). Secondly, the mutual integration of different industries is beneficial for the integrated progress of tourism and agriculture, culture, education, recreation and other industries, the promotion of innovation in tourism products and business models, the cultivation of new tourism consumption hotspots, and thus promoting the expansion of the tourism industry chain (Dan, 2019; Fang, Cheng, Su, & Bao, 2021). Thirdly, with the socio-economic integration, there is greater support for tourism development from urban and rural residents (Lee, 2013). Especially, the URI can boost economic development, and thus providing fund support for tourism enterprises. At presents, the fund support plays in a crucial role in the recovery of tourism economy.
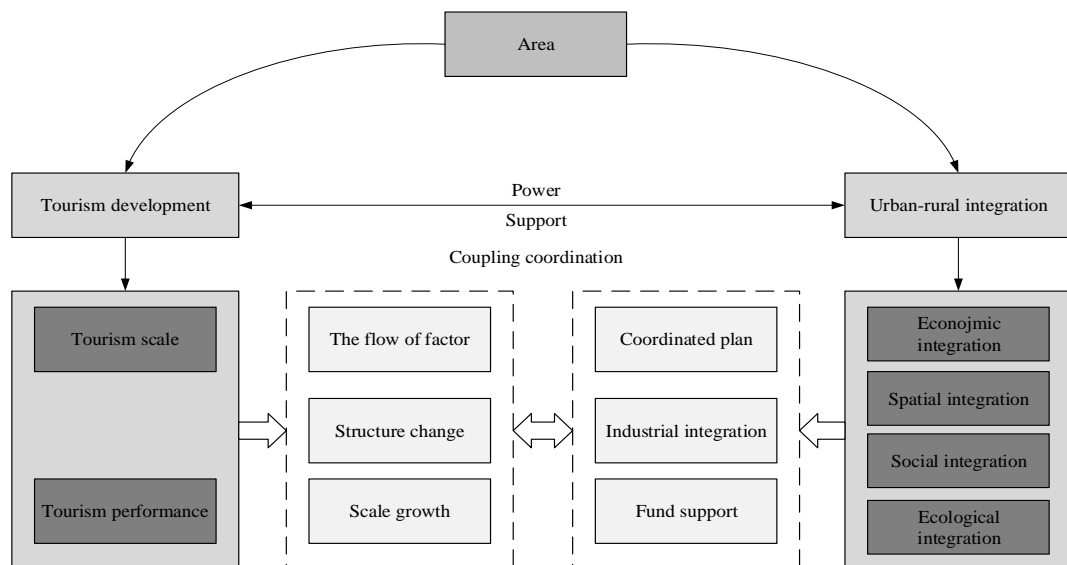

Fig. 1. The coupling coordination mechanism.

3. METHODOLOGY AND MATERIALS

3.1. Sample and data

The western Hunan Province, China mainly contains four cities, namely, Shaoyang, Zhangjiajie, Huaihua and Xiangxi (**Fig. 2**), which is an ethnic minority concentration area and underdeveloped area in Hunan Province. There are 41 attractions of 4A level and above in sample area, such as Wulingyuan Scenic and Historic Interest Area (World Natural Heritage) and Fenghuang Ancient City. Furthermore, tourism development is a crucial driving force enhancing the well-being of residents, accelerating economic development, and boosting the URI (Kai; Wang, Tan, & Gan, 2023). However, tourism industry was hit hard by the COVID-19, tourism revenues declined in 2020. In addition, the urban-rural income gap widened.
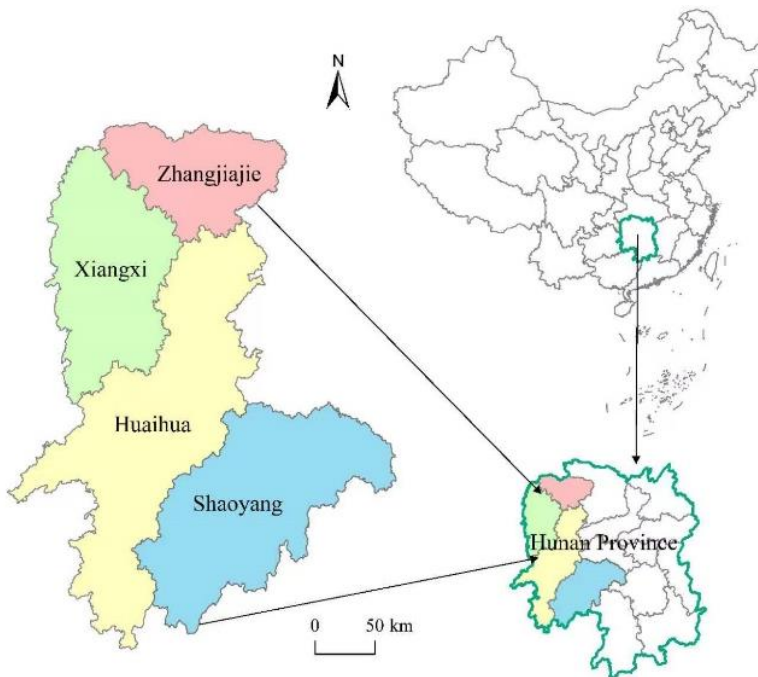
Fig. 2. The evolution trend of tourism development in western Hunan Province.

The data were received from the Hunan Statistical Yearbook (2011~2021), Shaoyang Statistical Yearbook (2011~2021), Zhangjiajie Statistical Yearbook (2011~2021), Huaihua Statistical Yearbook (2011~2021) and Xiangxi Statistical Yearbook (2011~2021). Quite a few data, such as consumption level, were obtained from the statistical bulletin (2010~2020) of various cities.

3.2. Study design with measures of variables

In this study, with reference to Gan et al. (2021) and Tang (2015), tourism development in western Hunan Province was comprehensively evaluated in tourism scale and performance (**Table 1**). specifically, tourism scale and tourism performance are an organically integrated system, with industry scale being the effectiveness of tourism development in terms of "quantity"; industry performance being the economic output of tourism development.

Referring to Luo et al. (2022) and Sun and Yang (2022), this study comprehensively evaluated the degree of the URI from four aspects, namely, economic integration, spatial integration, social integration, and ecological integration (**Table 1**). First, spatial integration lays the foundation for the flow of production factors. Second, economic integration is the use of urban areas to lead rural areas, promoting agriculture with industry and driving countryside's achievement. Third, ecological integration is the process of collaboratively promoting the comprehensive management of the urban-rural eco-environment.

Table 1.

The evaluation indexes of tourism development and the URI.

Object	Dimension	Indicator (Influence)	Unit	Weight
Tourism development	Tourism scale	Number of 4A and 5A attractions (+)	Number	0.045
		Number of travel agencies (+)	Number	0.051
		Number of star-rated hotel (+)	Number	0.031
		The total of tourists (+)	Million person-times	0.045
		Number of domestic tourists (+)	Million person-times	0.045
		Number of inbound tourists (+)	Person-times	0.084
	Tourism performance	Per capita spending of domestic tourists (+)	RMB Yuan	0.056
		The density of tourism economy (+)	Yuan/km^2	0.063
		Percentage of total tourism income in GDP (+)	%	0.056
		Percentage of total tourism income in the tertiary industry (+)	%	0.048
		Total of tourism income (+)	100 million Yuan	0.047
		Domestic tourism income (+)	100 million Yuan	0.202
		Inbound tourism income (+)	USD 10000	0.226
The URI	Economic integration	Per capita of GDP (+)	RMB Yuan	0.050
		Ratio of agricultural to non-agricultural industries (-)	%	0.032
		Consumption ratio between urban and rural (-)	%	0.057
		Income ratio between urban and rural (-)	%	0.045
	Spatial integration	Urbanization rate (+)	%	0.045
		Proportion of built-up area (+)	%	0.081
		Per capita highway mileage (+)	km	0.058
		Per capita road area (+)	m^2	0.067
		The number of mobile internet users (+)	Number	0.109
	Social integration	Per capita domestic water consumption (+)	t	0.082
		The rate of gas penetration (+)	%	0.030
		The rate of television coverage (+)	%	0.042
		The number of mobile phone users (+)	Number	0.070
		The number of collection books per 1000 persons (+)	Number	0.043
	Ecological integration	The rate of sewage treatment (+)	%	0.031
		Per capita park green space (+)	m^2	0.081
		Green coverage of built-up areas (+)	%	0.032
		Carbon emission intensity (-)	t/Yuan	0.044

3.3. Data analysis procedure

(1) The modified coefficient of variation method. So as to represent the evolution pattern of different periods, this study improves the coefficient of variation method by adding a time variable, which makes the corresponding results more reasonable. The relevant equation referred to Yin, Tang, Liu, and Dai (2023).

(2) The modified coupling coordination degree model. The results from traditional coupling coordination degree model (CCDM) is unbalanced, resulting in the coupling degree being concentrated around 1, which simplifies the CCDM assuming the same coefficients of the sub-systems, reduces the validity of the model (Wang, Kong, Zhi, & Dai, 2021).

$$C = \sqrt{\left[1 - \sqrt{(M_2 - M_1)^2}\right] \times \frac{M_1}{M_2}} \qquad (1)$$

$$T = \alpha M_1 + \beta M_2, D = \sqrt{C \times T} \qquad (2)$$

where

C is coupling degree

M_1 and M_2 are the level of tourism development

URI, respectively, T is the comprehensive index of two systems D is the CCD.

Combing with the situation in western Hunan Province, this study illustrates that the importance of two systems is equivalent (Luo et al., 2022). Consequently, α and β are 0.5, respectively.

(3) Relative development degree. Because the CCDM cannot reveal the gap between tourism development and the URI, this study used the relative development degree to measure the synergistic evolution state between tourism development and the URI.

$$E = M_1/M_2 \qquad (3)$$

where

E is relative development degree.

When E is in the interval $[1.2, +\infty)$, it means that tourism development is ahead and the URI is lagging behind. When E is in the interval $(0.8, 1.2)$, it represents that tourism development and the URI are in synchronous development. Referring to the research from Shao and Leng (2022), this study divided 8 primary types.

The eight primary types are severely uncoordinated $(0<D\leq0.2)$, moderately uncoordinated $(0.2<D\leq0.3)$, slightly uncoordinated $(0.3<D\leq0.4)$, nearly uncoordinated $(0.4<D\leq0.5)$, barely coordinated $(0.5<D\leq0.6)$, primary coordinated $(0.6<D\leq0.7)$, moderately coordinated $(0.7<D\leq0.8)$, and superiorly coordinated $(0.8<D\leq1)$. Each primary type has three sub-types, namely, Tourism development lags the URI $(0<M_1/M_2\leq0.8)$, Synchronous development $(0.8<M_1/M_2<1.2)$, and the URI lags tourism development $(M_1/M_2\geq1.2)$.

(4) Scissor difference model. The scissor difference model can capture the degree of difference between two trends. The angle α between the two tangents of the change curves of the two systems at a particular moment t. The smaller value, the smaller the degree of difference (Ma, Tang, & Dombrosky, 2022). The change rate of two systems can be reflected through the slope of the tangent of the change curve, namely, $\left[F'(x)\right]$ and $\left[F'(y)\right]$

$$V(x) = F'(x) = dx/dt$$
$$V(y) = F'(y) = dy/dt \qquad (4)$$
$$\alpha = \arctan\left|\frac{F'(x) - F'(y)}{1 + F'(x)F'(y)}\right|, \left(0 \le \alpha < 2/\pi\right)$$

where

$v(x)$ and $v(y)$ denote the rate of change from system x and system y, respectively

$F'(x)$ and $F'(y)$ represent the slope of tangent from system x and system y, respectively

dx/dt is the derivative of the system x with respect to the independent variable t

dy/dt is the derivative of the system y with respect to the independent variable t

α represents angle between two tangents.

(5) Grey correlation model. The grey correlation model uses system's variability elements to determine the influence force (Yuan, Yang, Tian, & Zhuang, 2020). The smaller the correlation, the smaller the influence of the system factors on the whole system.

4. RESULTS

4.1. The level of tourism development

During the sample period, the overall level of tourism development in western Hunan Province showed a fluctuating growth trend (**Fig. 3**), rising from 0.078 to 0.239, with an average annual growth rate of 20.4%. This indicates that with the multi-directional exploitation of attractions, the optimization of infrastructures and market environment, tourism economic development in the western Hunan Province was gradually boosting.
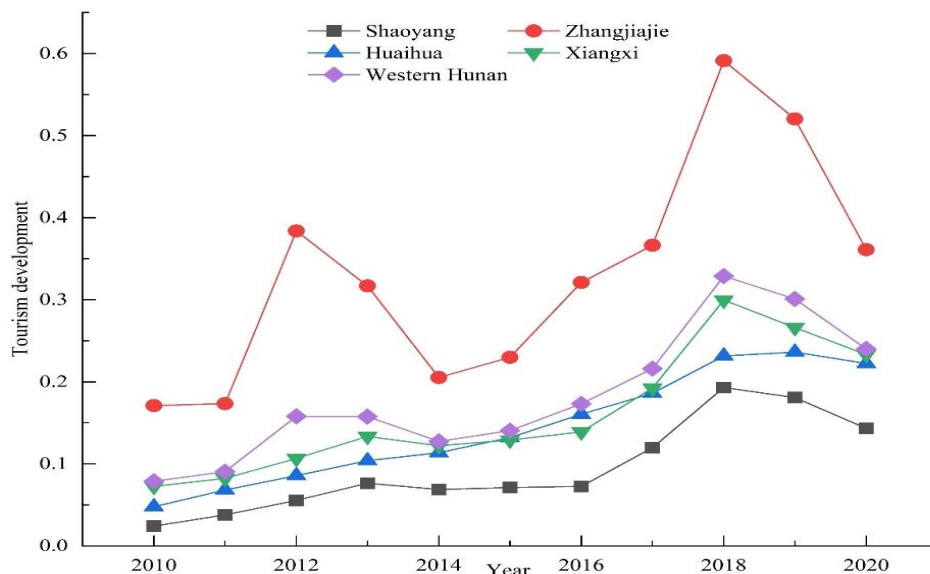
Fig. 3. The evolution trend of tourism development in western Hunan Province.

It is noteworthy that, given the distribution of the COVID-19, tourism economy in Xiangxi presented a declining trend in 2020, with a drop of 20.22% compared to 2010. This further confirms that the tourism industry is characterized by vulnerability. Regarding the spatial distribution, tourism development showed a spatial pattern of "Zhangjiajie > Xiangxi > Huaihua > Shaoyang", indicating that there was significant spatial heterogeneity in the western Hunan Province due to the differences in tourism resource endowment, tourism product innovation, and tourism market promotion.

In terms of each dimension, the average annual growth rates of tourism scale and tourism performance in the western Hunan Province were 13.5% and 35.2%, respectively. In 2020, tourism performance in each city was larger compared with tourism scale (**Table 2**), showing that the tourism industry in western Hunan Province has been steadily expanding in scale through innovation in tourism products and modes, while at the same time focusing on improving the "volume" of tourism development, effectively reducing the redundancy rate of inputs and improving the efficiency of tourism development.

Table 2.

The two dimensions of tourism development in western Hunan Province.

Area	2010		2020	
	Tourism scale	Tourism performance	Tourism scale	Tourism performance
Shaoyang	0.024	0.001	0.082	0.062
Zhangjiajie	0.113	0.058	0.157	0.204
Huaihua	0.039	0.009	0.142	0.081
Xiangxi	0.042	0.030	0.128	0.105
Western Hunan	0.054	0.025	0.127	0.113

4.2. The degree of the URI (urban-rural integration)

In the **Figure 4** we indicate that the overall level of the URI in western Hunan Province has continued to increase over the study period, from 0.213 to 0.675, with an average annual growth rate of 21.72%.
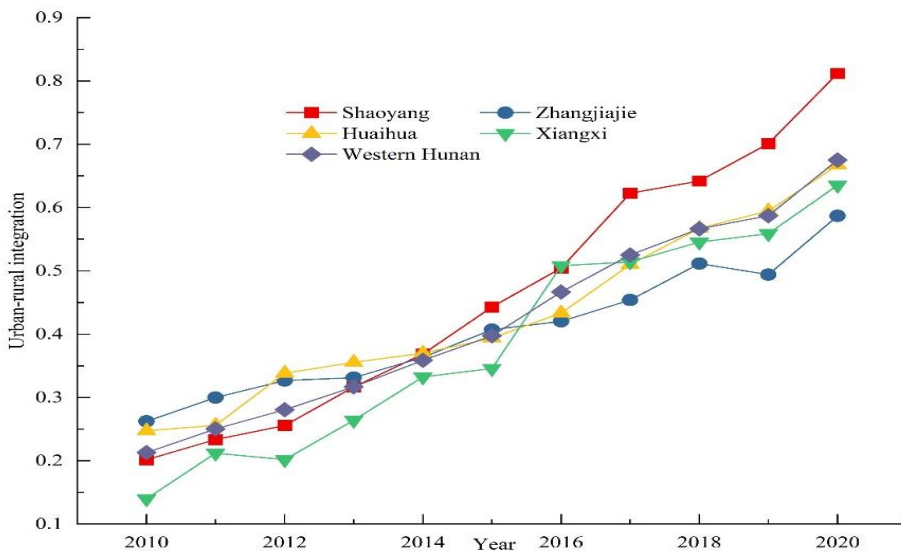
Fig. 4. The evolution trend of the URI in western Hunan Province.

This reason for the finding is that a series of strategies such as "Targeted Poverty Alleviation" and "Rural Revitalization", which have strongly promoted rapid rural development, and boosted the level of the URI. The growth rates of the URI in each city are, at descending order, Xiangxi > Shaoyang > Huaihua > Zhangjiajie. At the end of the study period, Shaoyang ranked first with regard to the URI instead of Zhangjiajie. The possible reason for this is that Shaoyang has a relatively strong economy and more funds are invested in rural economic and social construction, which has greatly improved infrastructure and public service, thus boosting the URI (**Fig. 4**).

On the subject of specific aspect (**Table 3**), the level of spatial integration as well as social integration was higher in western Hunan Province, reflecting that the removal of spatial barriers to the URI, and the accelerated circulating of social resource among urban area and rural area, as evidenced by the improving transport infrastructure, which has created the basic conditions for the URI. What is noteworthy is that the level of ecological integration was relatively low.

Table 3.

The sub-systems of the URI.

Area	2010				2020			
	Economy	Space	Society	Ecology	Economy	Space	Society	Ecology
Shaoyang	0.024	0.064	0.054	0.060	0.156	0.262	0.250	0.144
Zhangjiajie	0.053	0.093	0.082	0.035	0.149	0.183	0.163	0.093
Huaihua	0.040	0.068	0.106	0.034	0.122	0.208	0.231	0.106
Xiangxi	0.023	0.046	0.038	0.033	0.130	0.211	0.195	0.099
Western Hunan	0.035	0.068	0.070	0.040	0.139	0.216	0.210	0.111

4.3. The coupling coordination relationship

(1) The coupling coordination degree. As shown in Figure 5, the CCD of tourism development and the URI in the western Hunan Province presented a fluctuating growth trend from 2010 to 2020, with an average annual increase of 6.91%. The CCD of tourism development and the URI in Shaoyang, Huaihua, Zhangjiajie and Xiangxi remained consistent with the region as a whole. For example, the CCD of each city grew to varying degrees during the study period. In terms of growth trend, the relatively larger increases in Huaihua (81.59%) and Shaoyang (80.4%) indicate that these cities greater emphasis on the exploitation of tourism resource, the innovation of tourism product, and thus spurring tourism development and boosting the CCD. It is worth noting that the tourism economic slowdown in 2020, which results from the restrictions on trip caused by the COVID-19, led to a significant decline in the CCD among two systems.

In terms of municipal differences, Zhangjiajie had the highest CCD of tourism development and the URI, which resulted from that the level of tourism economy is highest in western Hunan Province. This promoted urban-rural economic development, improved urban-rural public services and raised rural residents' income. Accordingly, the URI promoted tourism development by improving the environment and securing the supply of production factors in reverse (**Fig. 5**).

(2) The types of coupling coordination. In starting year, the relationship between tourism development and the URI in the western Hunan Province was mainly uncoordinated, with Shaoyang being severely uncoordinated (**Table 4**). In 2015, although the relationship among tourism development and the URI was yet predominantly uncoordinated, the degree of incoordination had slowed down, with Huaihua and Xiangxi moving from moderately uncoordinated to slightly uncoordinated and Shaoyang moving from severely uncoordinated to moderately uncoordinated. In 2020, the CCD of two systems in western Hunan Province will be further optimized, with Zhangjiajie moving from being nearly uncoordinated in 2015 to barely coordinated in 2020. The other three cities have all improved their coupling coordination status to varying degrees.
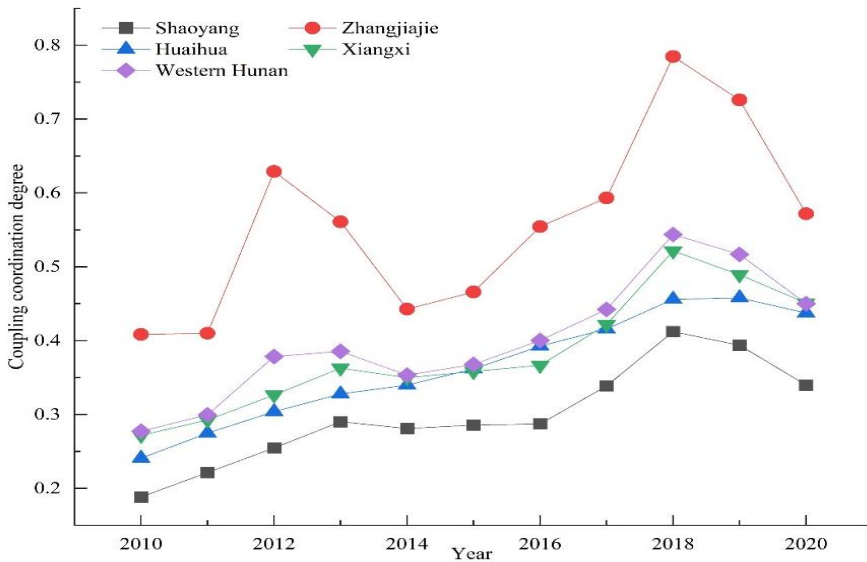
Fig. 5. The evolution trend of coupling coordination degree.

In terms of sub-type of the coupling coordination relationship, Shaoyang, Huaihua and Xiangxi was always "tourism development lags behind the URI". This indicates that the URI in these regions has accelerated; however, tourism development has not been promoted simultaneously. Zhangjiajie has improved tourism economy as well as the URI in the same frequency for some years. As a famous tourist city, Zhangjiajie's tourism image is well known both at home and abroad. Also, the expansion of the tourism market has accelerated urbanization, improving the public services in both urban, thus raising the level of the URI.

Table 4.
Types regarding coupling coordination relationship among tourism development and the URI.

Year	Shaoyang	Zhangjiajie	Huaihua	Xiangxi	Western Hunan
2010	I1	IV1	II1	II1	II1
2011	II1	IV1	II1	II1	III1
2012	II1	VI2	III1	III1	III1
2013	II1	V2	III1	III1	III1
2014	II1	IV1	III1	III1	III1
2015	II1	IV1	III1	III1	III1
2016	II1	V1	III1	III1	IV1
2017	III1	V2	IV1	IV1	IV1
2018	IV1	VII2	IV1	V1	V1
2019	III1	VII2	IV1	IV1	V1
2020	III1	V1	IV1	IV1	IV1
Average	III1	V2	III1	III1	IV1

Note: I, II, III, IV, V, VI, and VII represent severely uncoordinated, moderately uncoordinated, slightly uncoordinated, nearly uncoordinated, barely coordinated, primary coordinated, and moderately coordinated, respectively. 1, 2, and 3 mirror that tourism development lags urban-rural integration, synchronous development, and urban-rural integration lags tourism development.

4.4. Analysis of scissors difference

The composites indexes of tourism development and the URI were curve-fitted against time to obtain two well-fitted curves respectively. Meanwhile, the tangent equations of these two curves represent the evolution rate of tourism development and the URI, respectively, namely, $F'(x)$ and $F''(y)$. The fitted curves for the two systems are as follows

$$F(x) = 0.00004x^6 - 0.0014x^5 + 0.099x^4 - 0.137x^3 + 0.462x^2 - 0.665x + 0.401 (R^2 = 0.976)$$
$$F(y) = 0.00002x^6 - 0.0006x^5 + 0.004x^4 - 0.043x^3 + 0.128x^2 - 0.139x + 0.261 (R^2 = 0.999)$$

The slopes of two fitting curves regarding tourism development and the URI are as follows

$$F'(x) = 0.00024x^5 - 0.007x^4 + 0.079x^3 - 0.413x^2 + 0.925x - 0.665$$
$$F'(y) = 0.00012x^5 - 0.003x^4 + 0.029x^3 - 0.131x^2 + 0.257x - 0.139$$

Figure 6 shows that the evolution rate of tourism development in western Hunan Province increased from -0.08 in 2010 to 1.608 in 2020, and the evolution rate of the URI increased from 0.013 in 2010 to 1.561 in 2020, indicating that the change rate of two systems presented significant fluctuation. From 2010 to 2014, the evolution rate of two systems was relatively stable, while from 2015 to 2020, the change rate of two systems showed strong volatility. This shows that, although tourism development and the URI exhibited an overall trend of growth, the development trend is tortuous.
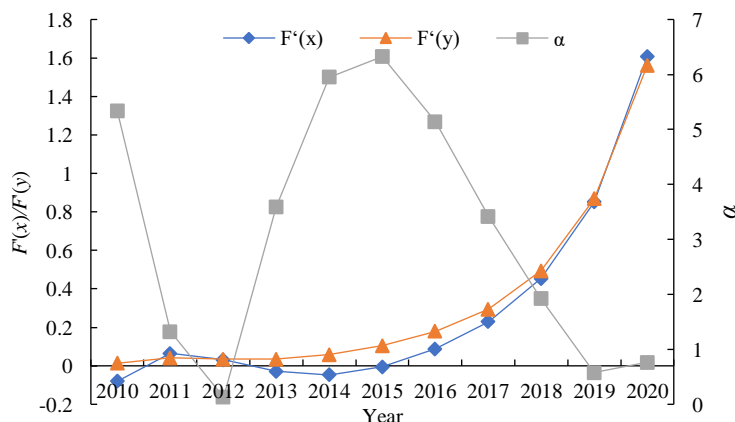
Fig. 6. Evolution rate and scissors differences of tourism development and the URI in western Hunan Province.

In the study period, the scissors difference among two systems in western Hunan Province showed a trend of fluctuation and decline. According to the value of scissors difference, the fluctuation cycle was divided into three stages, namely, 2010~2012, 2013~2015 and 2016~2020. From 2010 to 2012, the scissors difference decreased significantly, from 5.334 in 2010 to 0.128 in 2012, indicating that the positive externalities of coupling coordination were significantly enhanced. From 2013 to 2015, the scissors difference increased significantly, from 3.586 in 2013 to 6.325 in 2015, showing that the positive externalities of coupling coordination were not significant, which was consistent with the imbalance between tourism development and the URI in western Hunan Province at this stage. From 2016 to 2020, the scissors difference decreased significantly, from 5.140 in 2016 to 0.762 in 2020, which shows that under the strong promotion of the tourism poverty alleviation, the effect of coupling

coordination regarding tourism development and the URI was fully released, and tourism development and the URI in this stage jumped from low imbalance to near imbalance. It is worth noting that in 2020, the difference of scissors increased slightly, which may be related to the backward development of tourism caused by the COVID-19.

The above results show that the evolution trend of the scissors difference of two systems in western Hunan Province was highly consistent with the CCD in the three stages. Although the scissors difference among two systems exhibited a shrinking evolutionary trend on the whole, and the feed-effect of the synergistic improvement of the two systems showed an increasing fluctuation trend, the evolution rate of tourism development and the URI was not synchronized. Especially, under the impact of the COVID-19, the level of tourism economy declined greatly. Also, tourism development lagged behind the URI worsens. Consequently, tourism development and the URI were downgraded from barely coordinated to on the verge of imbalance (**Fig. 6**).

4.5. Analysis of influencing factors

To promote the CCD of tourism development and the URI in western Hunan Province, this study analyzed factors influencing the states of coupling coordination in different stages (2010~2012, 2013~2015 and 2016~2020). Various dimensions of tourism development and the URI were taken as influencing factors, this study adopted the grey correlation model to clarify key influencing factors (**Table 5**).

Table 5
Grey correlation analysis of influencing factors and coupling coordination degree in different stages.

System	Tourism development		The URI			
Dimension Period	Tourism scale	Tourism performance	Economic integration	Spatial integration	Social integration	Ecological integration
2010~2012	0.903	0.870	0.867	0.933	0.919	0.894
Rank	3	5	6	1	2	4
2013~2015	0.844	0.808	0.845	0.880	0.868	0.837
Rank	3	6	4	1	2	5
2016~2020	0.765	0.753	0.753	0.850	0.803	0.739
Rank	3	5	5	1	2	4

Spatial integration, social integration and tourism scale always exert a crucial effect on the coupling coordination relationship between two systems. First, spatial integration was the basis and direct form of the URI. The compression of spatial distance can boost tourism economic development through the scale effect. The effect of "integration of industry and city" produced by tourism economic development can also apparently promote the URI. Second, social integration reflected the further sharing of public services, which is beneficial for boosting the URI. The improvement of public service can also improve the service quality in tourist destinations. Therefore, social integration played a crucial role in the integration effect of two systems. Finally, the expansion of tourism scale can directly promote the tourism performance, while the prosperity of tourism economy can directly increase residents' income, improve infrastructure, optimize public services, and thus accelerating the urban rural integration. Especially, the ranking of the forces of economic integration showed an evolutionary trend of fluctuation decline. On the one hand, it shows that urban-rural residents concentrate on the equalization of public service and social welfare. On the other hand, this demonstrates that simple optimization of economic conditions is easy to lead to tourism leakage, thus narrowing the positive externalities (**Table 5**).

5. DISCUSSION

During the sample period, the level of tourism development in western Hunan Province showed a trend of fluctuating growth. However, at the end of the study period, given the impact of the COVID-19, the scale of the tourism market shrank sharply, and the level of tourism development presented a significant decline. This further illustrates the vulnerability of the tourism industry (Duro, Perez-Laborda, Turrion-Prats, & Fernández-Fernández, 2021). The overall level of the URI in western Hunan Province exhibited a trend of steady improvement. The main reasons are as follows. The implementation of such strategies as Targeted Poverty Alleviation, and Rural Revitalization has effectively boosted the socio-economic development of rural areas, narrowed the development differences, and thus promoting the URI in western Hunan Province (Kai Wang, Gan, Chen, & Voda, 2020).

The CCD of tourism development and the URI in western Hunan Province showed a fluctuating growth trend. Also, the CCD of each city also presented varying degrees of growth (Luo et al., 2022), showing that the coupling effect of tourism development and the URI was increasingly significant. To be more specific, the coupling coordination state of tourism development and the URI has experienced the evolution process of "moderately uncoordinated–slightly uncoordinated–nearly uncoordinated". Although the scissors difference between tourism development and the URI showed a shrinking evolutionary trend on the whole, and the mutual feed-effect of the synergistic improvement of the two systems presented an increasing fluctuation trend, the evolution rate of tourism development and the URI was not synchronized, and tourism development still lagged behind the URI.

Spatial integration, social integration and tourism scale have always played a key role in the coupling effect of tourism development and the URI in the western Hunan Province. However, the fluctuating downward in the ranking of the contribution of economic integration indicates that, on the one hand, residents in western Hunan Province were more concerned with the equalization of public services and social security; on the other hand, it shows that the mere optimization of economic conditions leads to tourism leakage, which, to a certain extent, tends to widen the gap between urban and rural economic development and thus discourages the URI.

The literature contributions of this study are as follows. First, this study analyzed the coupling coordination relationship between tourism development and the URI, which is conducive to enriching the literature on tourism impact and also providing a new perspective for studying the relationship between tourism development and the URI. Second, this study adopted a modified coupling coordination model to improve the validity of the CCD, so that the CCD can more reasonably reveal the measurement of coupling coordination relationship, which offers a methodological reference for studying the coupling relationship between tourism development and other systems. Third, this study follows the "Pattern-Process-Factor" research paradigm and analyses the spatiotemporal patterns of the coupling coordination relationship between tourism development and the URI. This analytical framework has good generalizability.

6. CONCLUSIONS

Taking the western Hunan Province of China as an example, this study used the modified entropy method, the modified coupling coordination degree model, the scissor difference model and the grey correlation model to examine the coupling coordination relationship between tourism development and the URI and its influencing factors. The main findings are as follows: First, the coupling and feedbacks between tourism development and the URI in the western Hunan Province have become increasingly prominent during the study period, and the coupling coordination state has evolved through a process of "moderately uncoordinated–slightly uncoordinated–nearly uncoordinated".

Second, tourism development and the URI in western Hunan Province were not evolving at the same pace, with tourism development still lagging behind the URI. Third, spatial integration, social

integration and the scale of the tourism industry have al-ways played a key role in the coupled and reciprocal feedback process of tourism development and the URI.

First, he relationship among tourism development and the URI was still uncoordinated. On the one hand, governments at all levels should make full use of the dividends of the various support policies introduced by the central government, actively promote innovation in products, thereby accelerating the degree of the URI. On the other hand, governments in the western Hunan Province should promote the urbanization of the migrant agricultural population so that residents are able to share quality infrastructure and public affluence, thereby accelerating tourism development.

Second, tourism development in the western Hunan Province has always lagged behind the URI; therefore, governments should promote the exploitation of tourism resources, the flow of tourism factors and the improvement of tourism efficiency through the urban-rural economic cooperation, infrastructure renovation and public service enhancement. Moreover, with the improvement of the URI, the relevant fund, talent, and technologies should be tossed into tourism industry.

Third, spatial integration, social integration and tourism scale have always played a key role in this coupling coordination relationship. Therefore, governments at all levels in the western Hunan Province should boost the urbanization at county in each city, and thereby enhancing the spatial integration. Furthermore, For the sake of spurring social integration, administrative barriers should be broken down and attention need be paid to the household registration system, social security system as well as optimization of public services. In addition, ecotourism should be promoted to accelerate the ecological integration among urban and rural areas.

Inevitably, this study also suffers from the following shortcomings. First, in order to verify the applicability of the research framework, future studies could extend the research territory to other regions across China or the world. Second, because of unavailable dataset, the comprehensive evaluation indicator system of tourism development and the URI are not comprehensive; therefore, future scholars need to optimize the two comprehensive evaluation indexes. Third, this study adopted grey correlation and revealed the different dimensions influencing the coupling coordination relationship; nevertheless, the influencing mechanism need to be investigated by the panel regression model or Geo-Detector.

ACKNOWLEDGMENT

REFERENCES

Bennett, K. J., Yuen, M., & Blanco-Silva, F. (2018). Geographic differences in recovery after the great recession. *Journal of Rural Studies, 59*, 111-117. doi: https://doi.org/10.1016/j.jrurstud.2018.02.008.

Buckley, R., Shekari, F., Mohammadi, Z., Azizi, F., & Ziaee, M. (2019). World Heritage Tourism Triggers Urban–Rural Reverse Migration and Social Change. *Journal of Travel Research, 59*(3), 559-572. doi:10.1177/0047287519853048.

Chen, M., Zhou, Y., Huang, X., & Ye, C. (2021). The integration of new-type urbanization and rural revitalization strategies in China: Origin, reality and future trends. *Land, 10*(2), 207. doi: https://doi.org/10.3390/land10020207.

Chen, P., Clarke, N., & Hracs, B. J. (2022). Urban-rural mobilities: The case of China's rural tourism makers. *Journal of Rural Studies, 95*, 402-411. doi:https://doi.org/10.1016/j.jrurstud.2022.09.017.

Dan, Z. (2019). On exploration of tourism resources based on urban-rural industries integration: A case study of border town Tacheng. *Modern Urban Research*(1), 111-117+136. doi: 10.3969/j.issn. 1009-6000.2019.01.

Duro, J. A., Perez-Laborda, A., Turrion-Prats, J., & Fernández-Fernández, M. (2021). Covid-19 and tourism vulnerability. *Tourism Management Perspectives, 38*, 100819. doi: https://doi.org/10.1016/j.tmp.2021.100819.

Ernawati, N. M., Torpan, A., & Voda, M. (2018). Geomedia role for mountain routes development. Mesehe and Pisoiu waterfall comparative study. *Geographia Technica*, 13(1). doi: 10.21163/GT_2018.131.05.

Fang, Y., Cheng, X., Su, X., & Bao, J. (2021). The spatial spillover effect of integration progress on tourism economy: A case study of the Yangtze River Delta urban agglomeration. *Scientia Geographica Sinica, 41*(9), 1546-1555. doi:10.13249/j.cnki.sgs.2021.09.006.

Gan, C., Voda, M., Wang, K., Chen, L., & Ye, J. (2021). Spatial network structure of the tourism economy in urban agglomeration: A social network analysis. *Journal of Hospitality and Tourism Management, 47*, 124-133. doi:https://doi.org/10.1016/j.jhtm.2021.03.009.

Gao, C., & Cheng, L. (2020). Tourism-driven rural spatial restructuring in the metropolitan fringe: An empirical observation. *Land Use Policy, 95*, 104609. doi:https://doi.org/10.1016/j.landusepol.2020.104609.

Gatti, P. (2013). Tourism, welfare and income distribution: The case of Croatia. *Tourism, 61, 53-71.* https://hrcak.srce.hr/file/149493.

Gong, Z., Guo, R., Ma, H., & Li, Z. (2021). Spatio-temporal evolution of the coupling coordination development of tourism economy-tourism public service-population urbanisation. *Statistics & Decision, 37*(9), 83-87(in Chinese). doi:10.13546/j.cnki.tjyjc.2021.09.019.

Gupta, S. K., Negru, R., & Voda, M. (2018). The Indian Himalaya's unique attributes: Hemkund Sahib and the Valley Of Flowers. *Geographia Technica, 13*(2). doi: 10.21163/GT_2018.132.05.

Kim, J. H., & Kang, K. H. (2020). The interaction effect of tourism and foreign direct investment on urban–rural income disparity in China: a comparison between autonomous regions and other provinces. *Current Issues in Tourism, 23*(1), 68-81. doi:10.1080/13683500.2019.1637826.

Lakatos, J., Magyari-Saska, Zs., Dombay, S. (2023) A GIS-based analysis for ecotourism suitability in a geological complex area of Carpathians, *Geographia Technica*, 18(1), 149-160 doi: 10.21163/GT_2023.181.11.

Lee, T. H. (2013). Influence analysis of community resident support for sustainable tourism development. *Tourism Management, 34*, 37-46. doi: https://doi.org/10.1016/j.tourman.2012.03.007.

Li, Y., Zhang, H., Zhang, D., & Abrahams, R. (2019). Mediating urban transition through rural tourism. *Annals of Tourism Research, 75*, 152-164. doi:https://doi.org/10.1016/j.annals.2019.01.001.

Liu, J., Nijkamp, P., & Lin, D. (2017). Urban-rural imbalance and Tourism-Led Growth in China. *Annals of Tourism Research, 64*, 24-36. doi:https://doi.org/10.1016/j.annals.2017.02.005.

Liu, Y., & Li, Y. (2017). Revitalize the world's countryside. *Nature, 548*(7667), 275-277. doi: https://www.nature.com/articles/548275a.

Luo, W., Chu, X., & Gao, Y. (2022). A research on the correlation between tourism industry development and urban-rural Integration: A case study of Hunan Province. *Tourism Science, 36*(4), 42-55(in Chinese). doi:10.16323/j.cnki.lykx.2022.04.001

Ma, L., Liu, S., Fang, F., Che, X., & Chen, M. (2020). Evaluation of urban-rural difference and integration based on quality of life. *Sustainable Cities and Society, 54*, 101877. doi: https://doi.org/10.1016/j.scs.2019.101877.

Ma, M., Tang, J., & Dombrosky, J. M. (2022). Coupling relationship of tourism urbanization and rural revitalization: A case study of Zhangjiajie, China. *Asia Pacific Journal of Tourism Research, 27*(7), 673-691. doi:10.1080/10941665.2022.2105158.

Magyari-Saska, Zs., Dombay, S. (2016) Mixed group hikers optimal resting place location along trails. Test area at Lacu-Rosu region (Romania), *Geographia Technica*, 11(2), 69-77 doi: 10.21163/GT_2016.112.07.

Paniagua, A. (2002). Urban-rural migration, tourism entrepreneurs and rural restructuring in Spain. *Tourism Geographies, 4*(4), 349-371. doi:10.1080/14616680210158128.

Quevedo, J. M. D., Uchiyama, Y., & Kohsaka, R. (2021). Linking blue carbon ecosystems with sustainable tourism: Dichotomy of urban–rural local perspectives from the Philippines. *Regional Studies in Marine Science, 45*, 101820. doi:https://doi.org/10.1016/j.rsma.2021.101820.

Shao, J., & Leng, J. (2022). Types and spatial pattern of coupling coordination between the new-type urbanization and eco-environment in Wuling Mountainous Area of Hunan. *Economic Geography, 42*(9), 87-95. https://kns.cnki.net/kcms2/article/abstract?v=QHiZY5KKB7ZSK0oTE1v7Amtofl0_Z_WDkdsnZeKuu Aknp9fOtrMgoPY3-ChxgYvOUAhu-D7iugbPaPWGSZ3MIXX746wIOX2Iouf8nFxJB2mlq3Eu-i1QHDGDkmMvFh1M&uniplatform=NZKPT&language=gb.

Sheng, Z. (2011). Towards China's urban-rural integration: Issues and options. *International Journal of China Studies, 2*(2), 345. doi: https://scholarbank.nus.edu.sg/handle/10635/126376.

Sokhanvar, A., Çiftçioğlu, S., & Javid, E. (2018). Another look at tourism- economic development nexus. *Tourism Management Perspectives, 26*, 97-106. doi:10.1016/j.tmp.2018.03.002.

Sun, J., Ling, L., & Huang, Z. (2020). Tourism migrant workers: The internal integration from urban to rural destinations. *Annals of Tourism Research, 84*, 102972. doi:https://doi.org/10.1016/j.annals.2020.102972.

Sun, Y., & Yang, Q. (2022). Study on Spatial–Temporal Evolution Characteristics and Restrictive Factors of Urban–Rural Integration in Northeast China from 2000 to 2019. *Land, 11*(8). doi:10.3390/land11081195.

Tan, J., & Wang, K. (2024). Coordination relationship and identification of obstacle factors between harmonious and beautiful rural construction and tourism urbanization: Take Wuling Mountain Area as an example. *Journal of Natural Resources, 39*(4), 768-787(in Chinese). doi:10.31497/zrzyxb.20240402.

Tang, Z. (2015). An integrated approach to evaluating the coupling coordination between tourism and the environment. *Tourism Management, 46*, 11-19. doi:https://doi.org/10.1016/j.tourman.2014.06.001.

Voda, M., Moldovan, L., Torpan, A., & Henning, A. (2014). Using GIS for mountain wild routes assessment in order to qualify them for tourism valorisation. *Geographia Technica*, 9(1), 101-108. http://technicalgeography.org/pdf/1_2014/10_voda.pdf.

Voda, M., Kithiia, S., Jackiewicz, E., Du, Q., & Sarpe, C. A. (2019). Geosystems 'pathways to the future of Sustainability. *Scientific Reports*, 9(1), 14446. https://doi.org/10.1038/s41598-019-50937-z.

Wang, K., Gan, C., Chen, L., & Voda, M. (2020). Poor Residents' perceptions of the impacts of tourism on poverty alleviation: From the perspective of multidimensional poverty. *Sustainability, 12*(18), 7515. doi: https://doi.org/10.3390/su12187515.

Wang, K., Tan, J., & Gan, C. (2023). Degree of synergy of regional tourism development and urban-rural integration and influencing factors in the Western Hunan region. *Progress in Geography, 42*(8), 1468-1485 (in Chinese). doi:10.18306/dlkxjz.2023.08.003.

Wang, S., Kong, W. R., Liang, Zhi, D., & Dai, B. (2021). Research on misuses and modification of coupling coordination degree model in China. *Journal of Natural Resources, 36*(3), 793-810. doi:10.31497/zrzyxb.20210319.

Xu, J., & Cheng, L. (2019). *Research on the residents' support for intercity railway in rural tourism destinations: multiple regression analysis and fsQCA findings.* Paper presented at the Proceedings of 2019 International Conference on Strategic Management (ICSM 2019), Francis Academic Press, Oxfordshire.

Yang, Y., Bao, W., Wang, Y., & Liu, Y. (2021). Measurement of urban-rural integration level and its spatial differentiation in China in the new century. *Habitat International, 117*, 102420. doi: https://doi.org/10.1016/j.habitatint.2021.102420.

Yin, Q., Sui, X., Ye, B., Zhou, Y., Li, C., Zou, M., & Zhou, S. (2022). What role does land consolidation play in the multi-dimensional rural revitalization in China? A research synthesis. *Land Use Policy, 120*, 106261. doi: https://doi.org/10.1016/j.landusepol.2022.106261.

Yin, Z., Tang, Y., Liu, H., & Dai, L. (2023). Coupling coordination relationship between tourism economy-social welfare-ecological environment: Empirical analysis of Western Area, China. *Ecological Indicators, 155*, 110938. doi:https://doi.org/10.1016/j.ecolind.2023.110938.

Yuan, G., Yang, Y., Tian, G., & Zhuang, Q. (2020). Comprehensive evaluation of disassembly performance based on the ultimate cross-efficiency and extension-gray correlation degree. *Journal of Cleaner Production, 245*, 118800. doi:https://doi.org/10.1016/j.jclepro.2019.118800.

Zhang, D., Wang, Q., & Yang, Y. (2023). Cure-all or curse? A meta-regression on the effect of tourism development on poverty alleviation. *Tourism Management, 94*, 104650. doi:https://doi.org/10.1016/j.tourman.2022.104650.

THE APPLICATION OF THE SWAT+ MODEL FOR WATERSHED MANAGEMENT SCENARIOS IN LAHAR FLOW AREAS OF MERAPI VOLCANO

Reza Fadilla **HAIKAL**[1] ⃝ *, Slamet* **SUPRAYOGI** [1][*] ⃝

ABSTRACT
This research aimed to analyze the surface runoff using the SWAT+ model and developed scenarios for watershed management that followed the environmental and community conditions. To achieve this objective, the analysis requires parameters such as land use, soil types, morphology, climatology, and hydrology, which were collected from primary data sources and supplemented by secondary data from relevant stakeholders. The SWAT+ method was employed to delineate watershed boundaries, construct a Hydrologic Response Unit (HRU), edit and input parameters, and perform calibration and validation. The watershed management scenario was developed by altering land use to define conservation areas and buffer zones. The results were then calibrated and validated using multiple tests. Calibration results yielded NSE= 0.52, PBIAS=7.38, and R2= 0.79, while validation showed NSE= 0.50, PBIAS= -5.45, and R2= 0.58. The values of this statistical test were greatly influenced by the quality and length of the data. The analysis also explored how changes in land use affect runoff values, considering factors like Curve Number (CN) values, recharge area classes, and land use patterns (e.g., clustered or dispersed). This analysis takes into account various hydrological parameters, including evapotranspiration and surface runoff, which are influenced by the land's ability to retain water. Additionally, values like lateral flow, return flow, and recharge are affected by the location of land conversion within the watershed (e.g., upstream, midstream, or downstream). The findings from this analysis allow for adjustments in watershed management efforts to align with the desired changes.

Key-words: *Physical Geography, Runoff, Scenario, SWAT+ Model, Curve Number (CN) values, Watershed management.*

1. INTRODUCTION

One of the functions of a watershed is to collect, store, and distribute runoffs from upstream to downstream areas. Unfortunately, this function is often disrupted by various factors, such as anthropogenic activities, erosion, and sedimentation processes, or natural phenomena that can change the characteristics and patterns of the river flow (Jayawardena 2015).

A real example of such disruptions can be seen in the sub-watershed of Blongkeng, located in the vulcanic areas of Mount Merapi. Eruption activities produce pyroclastic materials that can affect the shape and morphology of the river and impact the watershed system in general. These disruptions cause erosion, mass movement, and intense sedimentation in the Blongkeng Sub-Watershed, which in turn increases vulnerability to flood disasters due to the narrowing and sedimentation of the river-cross section (Solikha, Marfai 2012, Zulfahmi et al. 2016).

The variation in slope classes and soil types influences flow velocity. The predominance of steep topography indicates a higher rate of erosion, which is further exacerbated by sand mining and other anthropogenic activities that alter the natural characteristics of the river. The parent rock formations in the area, composed of both young and old volcanic deposits from Mount Merapi, generally exhibit varying porosity and permeability, which affect the capacity for groundwater storage and movement.

Watershed modelling is an effective tool to simulate the impacts of watershed's management and process on land and water resources. In this context, the Soil Water Assessment Tool Plus (SWAT+), an advanced version of the previous SWAT model, was used to analyse water flow and enhance the

---

[1] *Department of Environmental Geography, Gadjah Mada University in Yogyakarta, Indonesia:*
reza.fadilla.haikal@mail.ugm.ac.id ; corresponding author ssuprayogi@ugm.ac.id*

understanding of spatial relationships in watershed analysis (Armoa et al. 2023). Particularly for applications in volcanic areas, physical hydrological modeling, such as SWAT+, is more effective at modeling complex conditions than empirical and conceptual hydrological modeling (Gull & Shah, 2020). The use of the innovative SWAT+ method aims to develop sustainable watershed management strategies and achieve a balance between natural resources and human needs (Wang et al. 2016). By employing SWAT+, this study focuses on analysing runoff and developing watershed management scenarios to address issues identified in the Blongkeng Sub-Watershed, such as erosion, sedimentation, and changes in river morphology.

2. STUDY AREA

The Blongkeng Sub-Watershed (Sub-DAS) has an elevation ranging from 190 to 2,720 meters above sea level. Administratively, this area is located in Magelang Regency, Central Java Province, Indonesia. The Blongkeng Sub-Watershed is part of the Progo River Basin, situated between 110˚15'18" and 110˚26'39" East Longitude, and 7˚32'10" and 7˚38'41" South Latitude. This region falls under the Köppen climate classification Af, indicating a tropical rainforest climate.
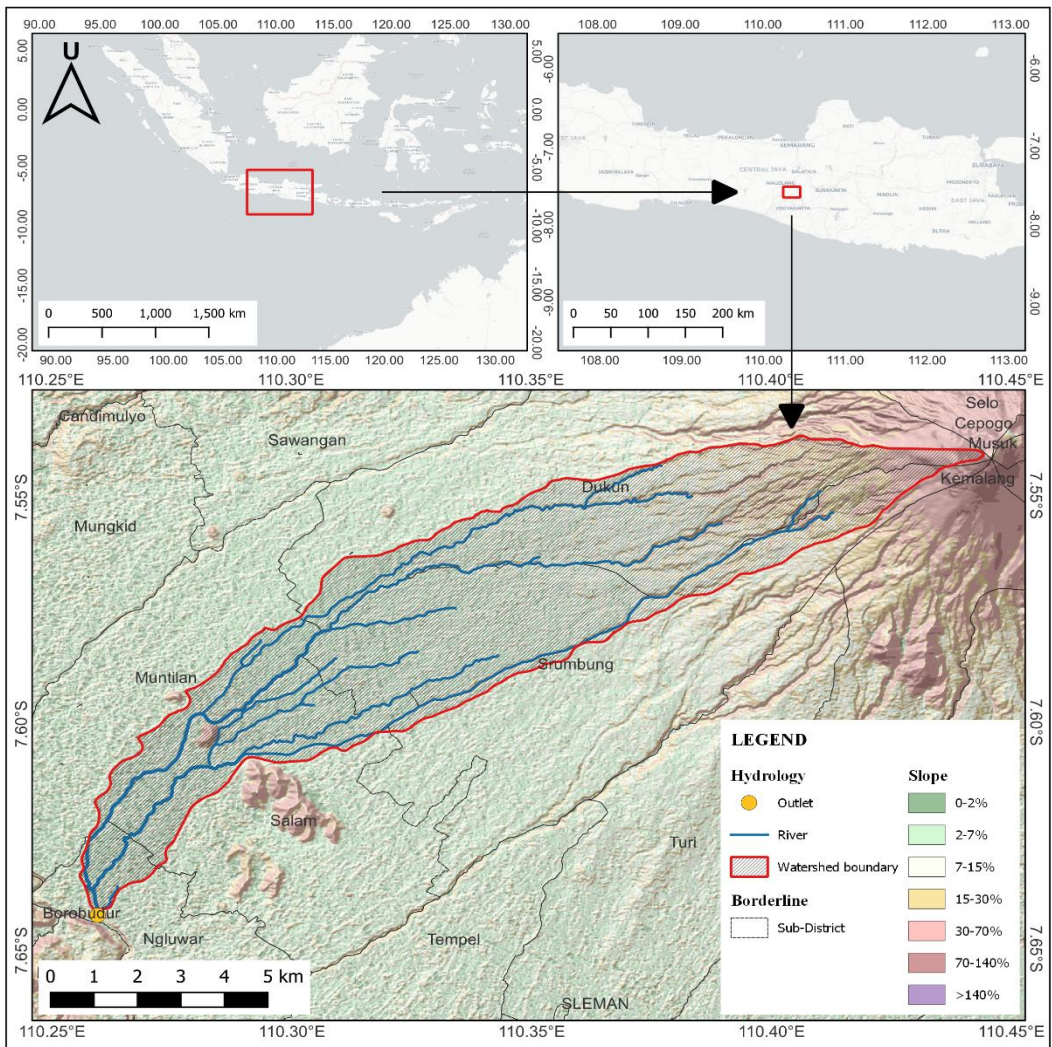
Fig. 1. Location Map of the Blongkeng Sub-Watershed.

As shown in **Fig. 1**, the Blongkeng Sub-Watershed exhibits high-risk factors concerning water resources but lacks sufficient field observation data. Therefore, runoff modeling using SWAT+ is crucial for developing a hydrological system that is suitable for the characteristics of the area and for formulating effective watershed management strategies (Morante-Carballo et al. 2022).

3. DATA AND METHODS

The Soil and Water Assessment Tool (SWAT+) is a physical hydrology model capable of analyzing runoff using complex data. This data includes climatological data (precipitation, humidity, temperature, solar radiation, and wind speed), soil data (texture, permeability, moisture, organic matter, coarse materials, and bulk density), land cover and land use data, and other data such as slope, morphology, and observation flow data.

3.1. Data

To support the analysis using the SWAT+ model, streamflow data were collected using an Automatic Water Level Recorder (AWLR) installed at the watershed outlet for one year. In addition to measurements with the TMA (Stage Height), direct observations of streamflow were recorded to establish a relationship between TMA and flow using a rating curve. This observation method involved the use of a float with the following formula:

-Flow Rate (Q), $Q = A \times V$

-Flow Velocity (V), $V = \frac{1}{n} R^{2/3} S^{1/2}$

-Hydraulic Radius (R), $R = A/P$

- A   = Cross-sectional area
- n   = Manning's roughness coefficient
- S   = Slope of the riverbed
- P   = Wetted perimeter

Furthermore, soil data were obtained by collecting soil samples using a pedo geomorphological approach, with landform unit scale as the classification unit (Christanto et al. 2019). The Blongkeng sub-shedwater has nine types of land such as upper slope, middle slope, lower slope, foot slope, valley, undulating plain, alluvial fan, hillock, and floodplain (BIG 209). The soil sample was gathered by taking into account the accessibility and activity of the volcano because the Merapi Mount is categorized into the Siaga level (watch) (BBD-DIY 2024). Thus, the soil data should be integrated into the global data of the DSOL Map (López-Ballesteros et al. 2023).

Another data required in this analysis was climatological data. These data were obtained from the records of an Automatic Rainfall Recorder (ARR), an Automatic Weather Recorder (AWR), and an ARR Logger installed around the Blongkeng sub-watershed areas. The SWAT+ model analysis utilized regional rainfall data, which was processed using the Thiessen Polygon method. Additionally, climatological data were classified based on elevation to account for orographic factors.

To ensure comprehensive analysis of the SWAT+ model, the study requires a range of data types, including land use data. Accurate and up-to-date land use data are essential for the SWAT+ analysis to reflect the current landscape conditions. In this study, land use data were based on the Indonesian Topographic Map (RBI) in accordance with the Indonesian Geographic Element Catalog (KUGI) (BIG 2019). This data was subsequently updated using Planetscope imagery with a spatial resolution of 5 meters to reflect the land cover conditions during the research year in 2021 (Planet Labs 2023).

3.2. SWAT+ method

With the land use data prepared, the next step in the SWAT+ analysis involved defining the characteristics of the study area and setting up the model for simulation. The SWAT+ model process began with determining the watershed's characteristics by delineating watershed boundaries and establishing HRU. The watershed boundaries, serving as the unit of analysis, were determined based on DEM data and river network data, while the HRUs were defined using land use, soil, and slope data. The simulation process included setting up a warming-up period, followed by calibration and validation, as shown in **Fig. 2**.
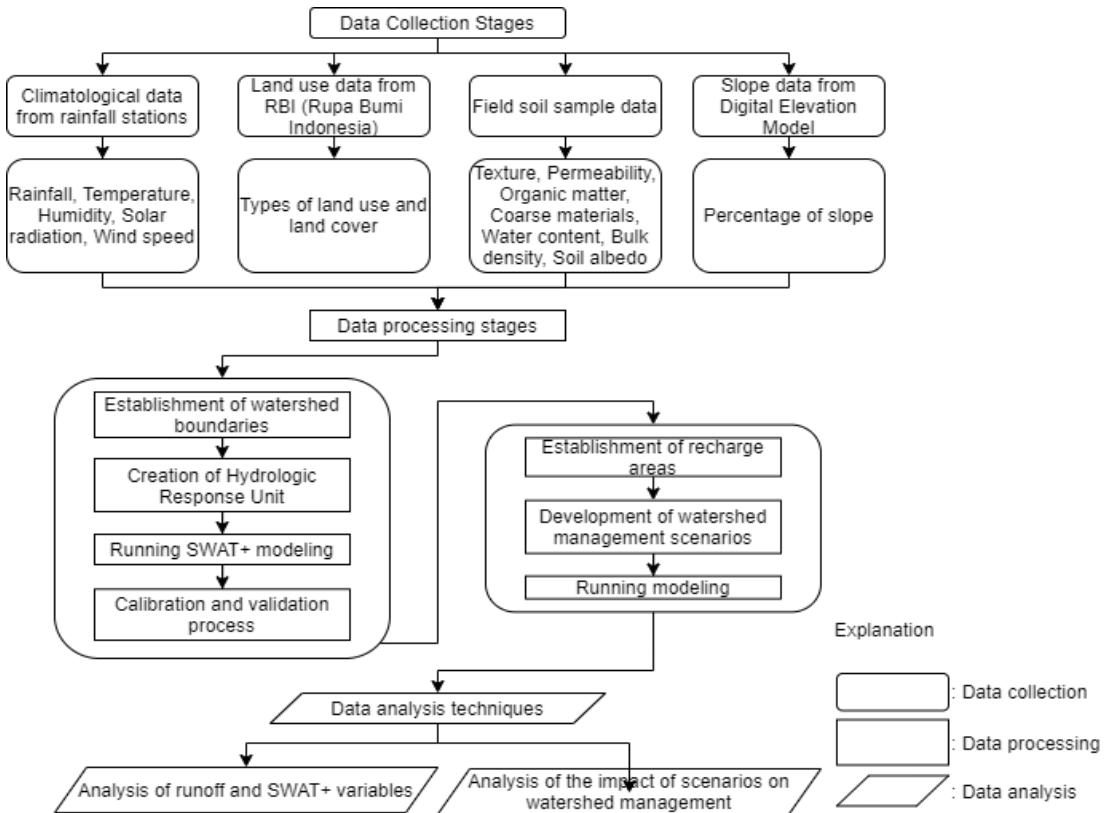
Fig. 2. SWAT+ modeling flowchart.

The calibration and validation steps were used to test the accuracy of the model results against observational data. The steps involved statistical tests over different time periods. Calibration and validation were processed using the SWAT+ Toolbox on 16 parameters. The tool also identified sensitivity parameters that influence the simulation process. The performance levels of the calibration and validation using the NSE, PBIAS, and R2 methods are shown in **Table 1**.

Table 1.

Results of statistical tests on performance levels.

Performance Level	NSE	(PBIAS) %	R^2
Very good	$0.75 - 1$	≤ 10	$0.7 - 1$
Good	$0.65 - 0.75$	$10 - 15$	$0.6 - 0.7$
Satisfactory	$0.5 - 0.65$	$15 - 25$	$0.5 - 0.6$
Unsatisfactory	≤ 0.5	> 25	≤ 0.5

Source : de Salis et al. (2019).

Building on the calibration and validation, the runoff analysis was conducted using Curve Number (CN) values, with simulations performed to assess how changes in land use impacted CN values. Many studies around the world have confirmed the efectiveness of integrating the SCS-CN method with hydrological modeling (Melesse et al., 2003; Melesse & Graham, 2004; Satheeshkumar et al., 2017). These impacts were further illustrated in flow hydrographs generated by the SWAT+ model. Land use changes involved altering the percentage of vegetative cover in recharge areas.

Following the runoff analysis and the creation of land use scenarios, the next step involved determining recharge areas. This was achieved using a hydrogeomorphological approach that considers parameters such as morphology, precipitation, geology, soil, and land cover (Suprayogi et al. 2013). These parameters were assessed and weighted, and the identification of recharge areas was carried out using the Weighted Method. The next step in watershed management involved creating scenarios to manage runoff. This stage focused on efforts to reduce runoff by adding vegetation areas designated as conservation zones for water and soil. The scenarios developed considered both environmental conditions and community needs.

4. RESULTS

This section presents the results obtained from the SWAT+ model simulations and the subsequent analysis of the data. We will discuss the key findings regarding streamflow (debit) data, soil data, climatological data, and other relevant parameters, including land use changes and their effects on hydrological processes. The discussion also explores the effectiveness of proposed management scenarios.

4.1. Data processing stage for the Blongkeng sub-watershed

Our first finding focuses on the streamflow data, which was obtained through precise measurements using the Automatic Water Level Recorder (AWLR). The logger requires observational data to calibrate the rating curve, and in this study, five sets of observation data were collected and presented in **Table 2**. The table indicates that the accuracy of the rating curve improves with the number of observations. The process of measuring streamflow began with recording the morphometric characteristics of the river segment: the river width was 16.7 meters, the wetted cross-sectional area was 20.1 meters, the riverbed slope was 0.113, and the Manning's roughness coefficient was 0.161.

Table 2.

Observational streamflow measurements.

Date	Water Flow	Q
8 December 2020	11 cm	0.022
15 January 2021	42 cm	2.344
19 May 2021	5 cm	0.886
11 October 2021	14 cm	1.656
23 November 2022	33 cm	1.772

The rating curve was derived from comparing the observational streamflow measurements with the water level data, resulting in the equation $y = e1.7103x$ and an R^2 value of 0.7952, as shown in **Fig. 3**. This equation was used to convert the water level data from the logger into streamflow data. **Fig. 4** shows the resulting streamflow data in 7 months (June 2021 - January 2022). However, it is important to note that this data includes only one rainy season and one dry season, which should be considered when utilizing and analyzing the data. The limited data period is due to constraints in field data recording. Collecting discharge and rainfall data poses challenges in extreme conditions like lahar flows. Therefore, this research requires the installation of measuring instruments. Issues of missing or unreadable data also affect the length of the dataset.
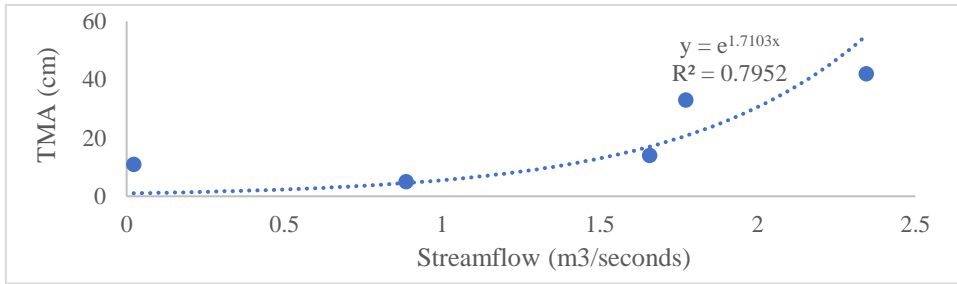
Fig. 3. Rating curve of water level and measured streamflow.

Fig. 4. Observed streamflow recorded by the logger.

The second finding relates to the soil conditions in the Blongkeng Sub-Watershed, which were distinguished based on landform analysis units. Soil data were obtained through field sampling at each landform type using a pedo geomorphological analysis. The sampling locations are shown in **Fig. 5a**, and the data represent the uppermost soil layer or the first layer. The sequence of soil samples is as follows: sample 1 = Floodplain, sample 2 = slope, sample 3 = alluvial fan, sample 4 = undulating plain, sample 5 = valley, sample 6 = foot slope, and sample 7 = lower slope. The soil characteristics are detailed in **Table 3**.

Table 3.

Soil data.

Sample	Permeabilitas (cm/jam)	Soil textures (%)			Water content (%)	Coarse materials (%)	Bulk density (gr/cm3)	Organic materials (%)
		Sand	Clay	Silt				
1	23.78	71%	19%	10%	1.00	0.10	1.17	0.34
2	26.33	54%	25%	21%	7.71	3.87	0.96	0.39
3	50.11	60%	24%	16%	1.83	8.58	1.34	2.14
4	22.51	57%	15%	27%	2.45	3.28	1.30	2.53
5	6.37	62%	17%	21%	0.80	11.43	1.87	2.61
6	22.51	64%	26%	10%	1.00	2.97	1.88	2.02
7	31.00	55%	41%	3%	1.00	7.63	1.67	2.69

The calculation of regional rainfall in the SWAT+ model is based on the Thiessen Polygon method, as illustrated in **Fig. 5b**. Climatological data were generated according to elevation to account for orographic factors. Although there were limitations in the availability of field data, the climatological data used in this study were still sufficiently representative.

Subsequently, **Fig. 5c** indicates that the types of land use significantly affect the amount of surface runoff. Specifically, vegetative land use types play a crucial role in retaining and storing rainfall as groundwater reserves through the process of infiltration. In contrast, built-up land use types result in high surface runoff because water cannot infiltrate the soil.

The next findings focus on the recharge area analysis. The analysis is identified in three classes: very low, low, and moderate (see **Fig. 5d**). The most influential parameters affecting the changes in recharge area classes in the Blongkeng Sub-Watershed are vegetation cover and slope gradient. Areas with vegetative cover tend to have higher recharge values, while flatter slope conditions also result in higher recharge values. These recharge area classes serve as indicators for evaluating the effectiveness of watershed management efforts, particularly through land use changes. The role of vegetation in conservation efforts is crucial as it helps retain rainfall, reduce immediate runoff, and allow water to be absorbed into the ground, thereby increasing groundwater reserves.
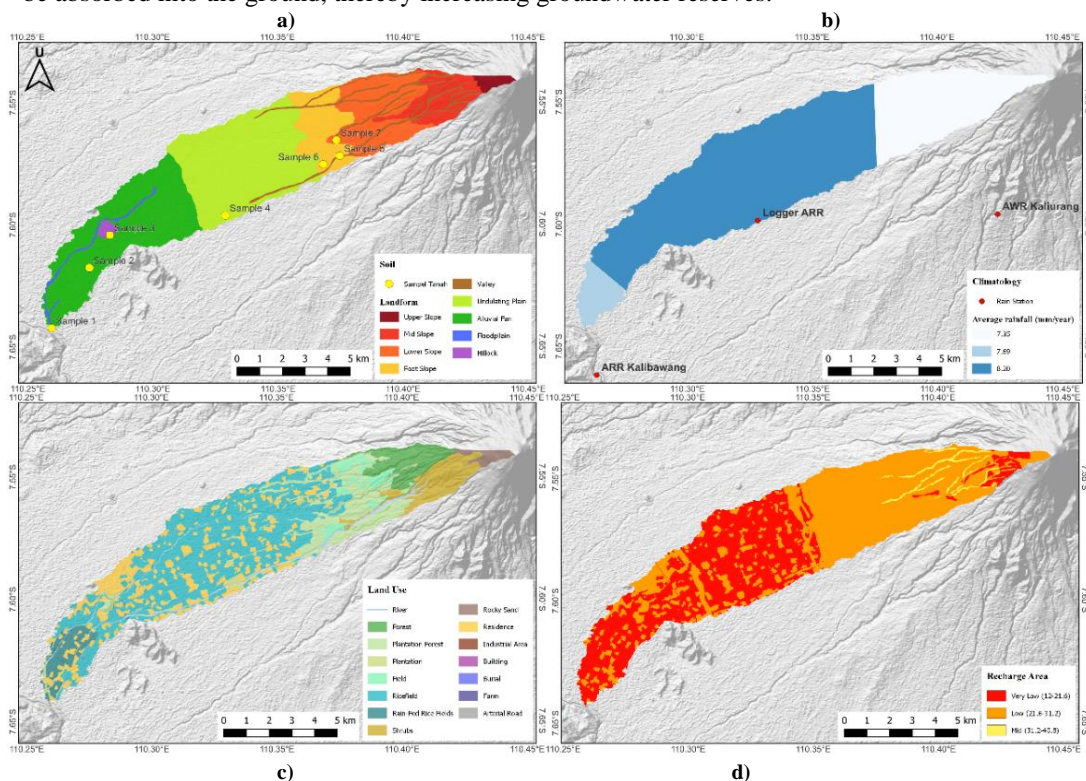
Fig. 5. (a) Pedo geomorphological map; (b) Regional rainfall map; (c) Land use map; (d) Recharge area map.

4.2. SWAT+ modeling based on Curve Number

Following the detailed analysis of various data types, including land use, soil characteristics, climatological data, and recharge areas, the next step was to run the SWAT+ model (Easton et al., 2008). The delineation of the watershed boundaries resulted in the Blongkeng Sub-Watershed covering 6,890.10 ha, divided into three subbasins and 25 channels. Additionally, the creation of Hydrologic Response Units (HRUs) produced a total of 1,147 HRUs. Each HRU represents the smallest unit of analysis in hydrology and is characterized by homogenous hydrological properties.

The use of Curve Number (CN) in hydrology, which relates surface runoff to land use and soil hydrological groups, is a critical component in this analysis (Chow 1988). The CN index which is the main parameter used for runoff estimation in ungauged basins is based on the physical characteristics of watersheds that influence the runoff, namely the land use, soil type, texture and the antecedent moisture conditions (Crăciun et al., 2009; Haidu and Ivan (2016a); Haidu and Ivan (2016b); Strapazan and Petruț, 2017). A high CN value indicates greater runoff and lower soil infiltration. Hydrological soil groups are classified as A, B, C, and D, with CN values increasing from lower to higher values for the same land use type, reflecting the soil's runoff potential.

4.2.1. Sensitivity Analysis and calibration

The next finding revolves around the sensitivity analysis. This analysis plays a crucial role in refining the SWAT+ model. By identifying which parameters have the greatest impact on model outcomes, this analysis helps prioritize which factors to focus on when adjusting scenarios and improving model accuracy. As detailed in **Table 4**, the results reveal that the parameter CN2 shows the highest sensitivity, indicating its significant role in modeling land use changes. Following CN2, parameters such as CN3_SWF (soil water adjustment factor) and AWC (available water capacity), related to soil properties, also show substantial influence, further guiding adjustments in model scenarios.

Table 5 shows the calibration period conducted from October to November 2021. In this study, CN values were obtained from the SWAT+ database, as detailed in **Table 6**. Although the dataset was relatively short due to the limited availability of observed streamflow data, the calibration yielded satisfactory results. The test produced an NSE value of 0.53, a PBIAS of 7.38, and an R^2 of 0.79 (**Fig. 6**). These values indicate a reasonable fit and meet the minimum required thresholds. The parameter values used during calibration were subsequently applied in the validation period.

Table 4.

Results of sensitivity analysis.

No	Group	Name	Change Type	Sensitivity
1	hru	cn2	Percent	0.506
2	hru	cn3_swf	Percent	0.470
3	hru	awc	Relative	0.120
4	aqu	epco	Percent	0.002
5	rte	revap_co	Replace	0.001

Table 5.

Calibration results.

No	Name	Change Type	Min	Best Value	Max	
1	cn2	Percent	-20.00	-39.000	20.00	
2	cn3_swf	Percent	-20.00	18.442	20.00	
3	epco	Relative	-500.00	4.025	1000	
4	revap_co	Percent	-20.00	12.596	20.00	
5	chn	Replace	0.50	1.475	2.00	
6	latq_co	Percent	-20.00	11.379	20.00	
7	esco	Replace	0.02	0.197	0.20	
8	lat_ttime	Replace	1.00	176.152	180.00	days
9	alpha	Replace	0.01	0.011	0.30	days
10	perco	Replace	0.30	0.994	1.00	fraction
11	flo_min	Replace	0.00	0.004	1.00	m
12	revap_min	Replace	0.60	0.616	1.00	m
13	bd	Percent	-20.00	-19.964	20.00	mg/m^3
14	canmx	Relative	-0.05	-0.050	0.05	mm/H2O
15	k	Replace	0.00	0.851	1.00	mm/hr
16	awc	Relative	-500.00	182.338	500.00	mm_H2O/mm

Table 6.

Land use areas.

No	SWAT+ Code	Land use	CN	Area (ha)	(%)
1	rice120	Paddy fields	78	3000.13	43.54
2	urml	Residential areas	98	1109.66	16.11
3	frst	Plantation forest	70	827.92	12.02
4	shrb	Shrubs	69	486.87	7.07
5	frse	Forest	52	442.59	6.42
6	rice180	Rain-fed paddy fields	65	268.15	3.89
7	agrl	Field/farm	71	245.94	3.57
8	orcd	Plantation	86	224.24	3.25
9	watr	River	98	172.04	2.50
10	bsvg	Rocky sand	61	103.21	1.50
11	Utrn	Arterial road	98	5.51	0.08
12	Urbn	Building	98	2.38	0.04
13	Uidu	Industrial area	98	0.83	0.01
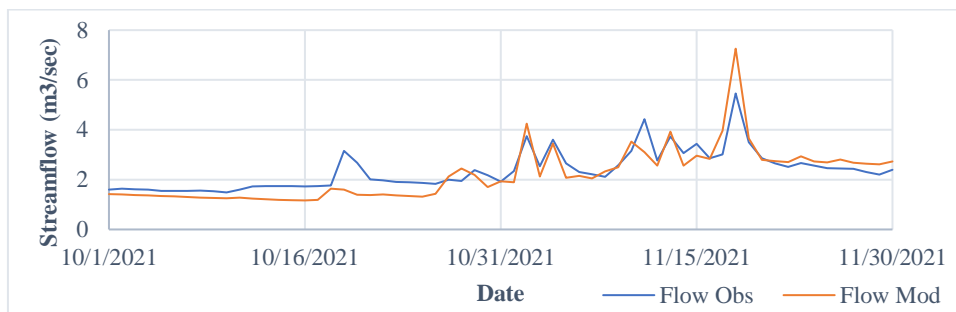
Fig. 6. Comparison chart of observed and calibrated streamflow.

4.2.2. Validation

Following the calibration process, which was conducted from October to November 2021, the validation was carried out during December 2021 and January 2022. The validation results produced statistical test values of NSE = 0.50, PBIAS = -5.45, and R^2 = 0.58, as provided in **Fig. 7**. These results indicate that the simulation is fairly consistent when applied across different time periods. However, it is important to note that the consistency of the data during the dry season was not tested, meaning that the simulation results are more suitable for runoff analysis during the rainy season.
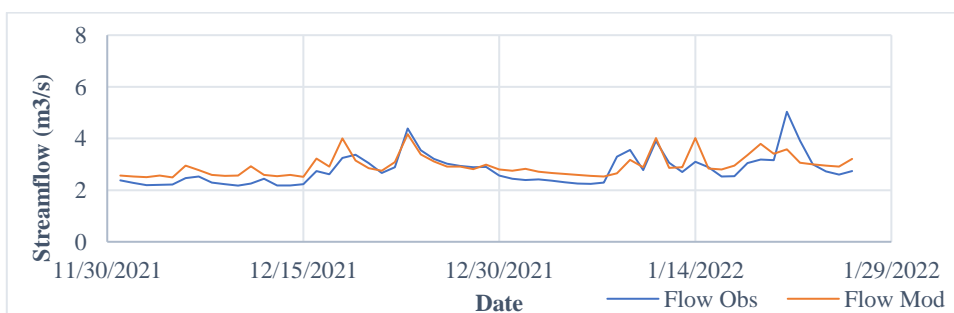
Fig. 7. Comparison graph of observed and validated streamflow.

5. DISCUSSION

5.1. Runoff Analysis

The statistical test values for NSE, PBIAS, and R^2 illustrate the reliability of the simulation results compared to field conditions. In this study, the statistical test results are deemed satisfactory, indicating that the simulation can effectively represent the actual conditions (Almeida et al. 2018).

Building upon this, the simulated streamflow in the Blongkeng Sub-Watershed shows significant fluctuations between the rainy and dry seasons, with a peak flow of up to 13.53 m³/day in May 2021. These simulations can be seen in **Fig. 8**. These runoff conditions are influenced by environmental factors and rainfall amounts. As a dynamic parameter, land use can change and produce varying runoff conditions. While land use affects evapotranspiration, infiltration, and runoff, soil type and morphology remain constant.

5.2. Watershed Management

This study will examine the impact of land use changes, particularly the conversion of areas into vegetation for conservation and buffer zones. **Table 6** presents the percentage of land use in the Blongkeng Sub-Watershed for 2021. With these land use proportions, it is necessary to create land use change scenarios to assess the extent of their influence. Land use changes are made by altering the types of land use that allow for transformations, such as rice fields, shrubs, fields, rocky sand, and settlements. The area of land use change is standardized to 50 hectares to facilitate comparisons between different types of land use. The locations for the changes in land use are selected based on visual interpretation adjusted to conservation objectives.
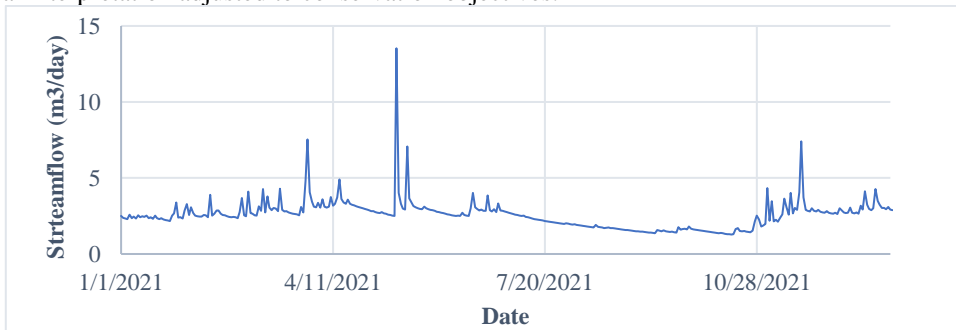
Fig. 8. Blongkeng sub-watershed streamflow.

5.3. Scenarios

Scenario 1. The first scenario involved changing land use by simulating the conversion of paddy fields along riverbanks into buffer zones. This land use change was primarily applied to the downstream area with a very low recharge area class, as shown in **Fig. 9a**. The results generally showed a decrease in maximum, minimum, and average runoff. Specifically, the Curve Number (CN) changed from 48 for paddy fields and 40 for rain-fed paddy fields to 43 for plantation forest areas. This scenario demonstrates how converting paddy fields to forested buffer zones impacts runoff characteristics.

Scenario 2. In the second scenario, the dominant change involved converting shrubland into very low and low recharge area classes (see **Fig. 9b**). This simulation resulted in a significant reduction in peak runoff, decreasing from 13.53 m³/day to 13.21 m³/day. Meanwhile, average and minimum runoff values remained relatively unchanged, and only minor adjustments were experienced. The reduction in peak runoff indicates that the conversion of scrubland to forested areas effectively enhances the retention of rainwater and reduces surface runoff. The Curve Number (CN) decreased from 42 for scrubland to 32 for forested areas (frse), reflecting this effective change.
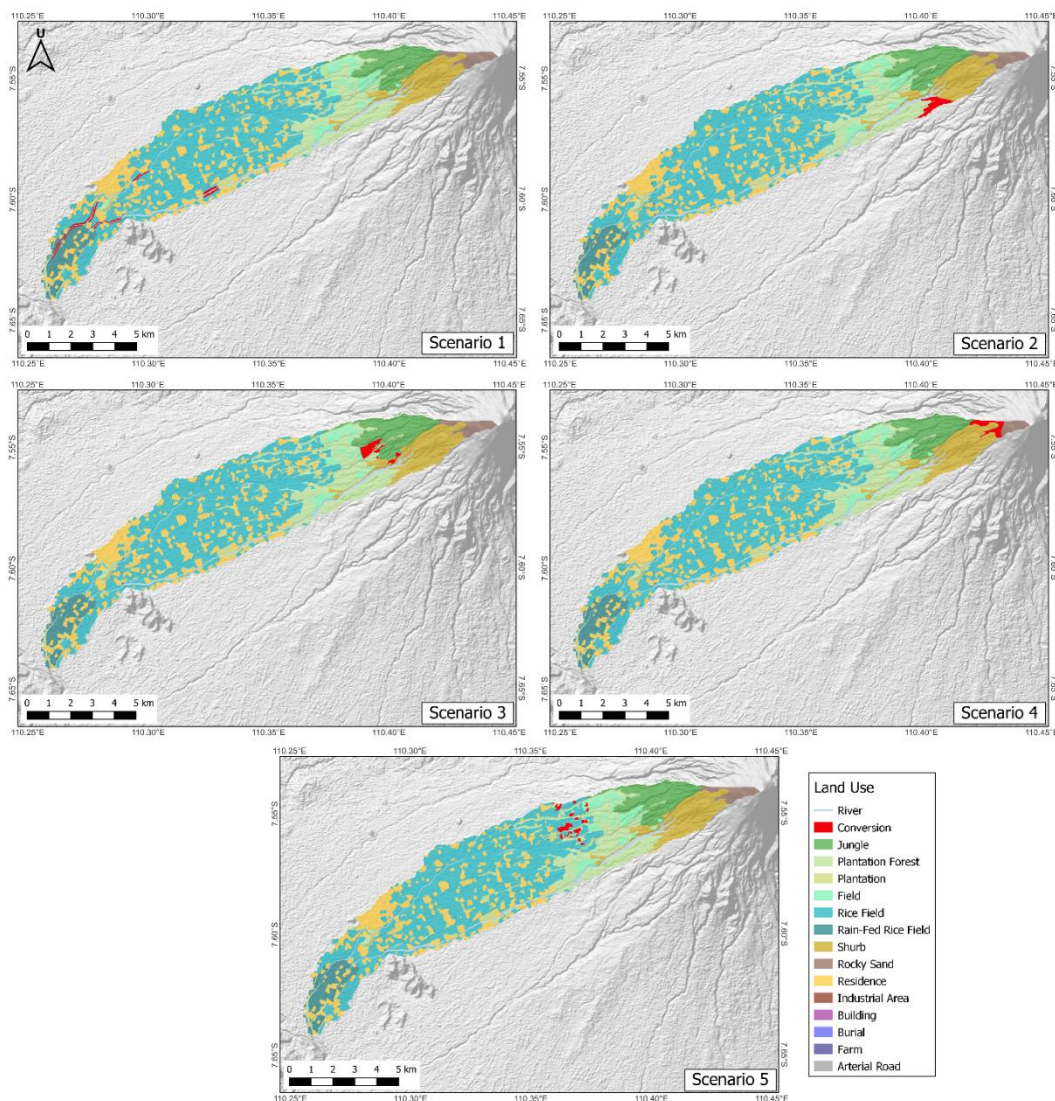
Fig. 9. (a) Scenario 1: Conversion of rice fields; (b) Scenario 2: Conversion of shrubs; (c) Scenario 3: Conversion of fields/farm; (d) Scenario 4: Conversion of rocky soil; (e) Scenario 5: Conversion of residential areas.

Scenario 3. In the third scenario, land use changes involved converting dryland farming areas to forested regions, with adjustments based on elevation factors (see **Fig. 9c**). This simulation resulted in a notable decrease in peak runoff, from 13.53 m³/day to 13.20 m³/day. The Curve Number (CN) also changed significantly, from an average of 43 for dryland farming to 32 for forested areas. The primary influence on this reduction was the dominant recharge area class, which was classified as medium in this scenario. This allows for greater groundwater storage, even though the CN value and the extent of land use change are similar to the previous scenarios.

Scenario 4. In the fourth scenario, land use changes were done by converting rocky sand areas (see **Fig. 9d**). This change was primarily applied to areas with very low and low recharge classes. The results of Scenario 4 showed a decrease in peak runoff that was relatively similar to Scenarios 2 and 3 but with a smaller reduction in peak flow. Meanwhile, the values for minimum and average runoff

remained relatively consistent. The Curve Number (CN) changed from 37 for rocky sand to 32 for forested areas. The differences in runoff values between Scenarios 2, 3, and 4 were influenced by the extent of the recharge area classes.

  Scenario 5. In this final scenario, the focus was on transforming residential areas into tree plantations (see **Fig. 9e**). The results of this land use change are detailed in **Table 7**, which shows a decrease in peak runoff that was not as significant but still lower compared to Scenario 1. These changes are influenced by factors such as changes in CN values, differences in recharge area classes, and patterns of land use change. Each scenario has its own characteristics; for example, in Scenario 1, the conversion of rice fields resulted in a decrease in maximum, minimum, and average discharge, although the values were not very significant. Meanwhile, in Scenario 3, the conversion of fields led to a significant decrease in maximum discharge, but the minimum and average discharge values remained the same. An important point to consider in land conversion for conservation purposes is to pay attention to recharge area classes, changes in CN values, and the patterns of land use change (clustered/scattered).

Table 7.

Comparison of scenarios

Streamflow (m³/day)	Blongkeng	Conversion				
		Paddy fields	Shrubs	Field/farm	Rocky sands	Residential areas
max	13.53	13.50	13.21	13.20	13.24	13.50
min	1.28	1.27	1.29	1.29	1.29	1.28
average	2.58	2.57	2.58	2.58	2.58	2.58

5.4. Water Balance

  The water balance conditions for the land use change scenarios are presented in **Table 8**. Building on the previous analysis of land use impacts, evapotranspiration values depend on land use types; converting to plantation forest increases evapotranspiration values while converting to dense forest results in lower values. Lateral flow, return flow, and recharge values decreased in Scenario 1, located in the downstream area, whereas conversions in the midstream and upstream areas tended to increase. Thus, the water balance in this study was also influenced by the location within the watershed. Meanwhile, surface runoff values decreased in Scenarios 2, 3, 4, and 5 but increased in Scenario 1. Rice paddies have the property of retaining water in irrigation, so when converted, the released water becomes a larger runoff. The most significant change in surface runoff occurred in Scenario 5 because the land was converted to conservation zones. An important note in this scenario change is that the land use changes were made over an area of 50 hectares. Although the changes that occurred are relatively small, the patterns of change between the scenarios can still be studied and analyzed.

Table 8.

Comparison of water balance.

Parameter (mm/year)	Blongkeng	1	2	3	4	5
Evapotranspiration	112.58	112.68	112.44	112.40	112.32	112.68
Lateral flow	3.23	3.17	3.23	3.23	3.23	3.23
Return flow	882.17	872.63	881.22	881.31	881.19	881.03
Recharge	1068.55	1058.69	1068.81	1068.91	1068.77	1068.56
Surface RO	143.48	146.59	143.27	143.18	143.11	140.89

6. CONCLUSIONS

The streamflow of runoff on the Blongkeng sub-watershed has test values as follows: NSE = 0.53, PBIAS = 7.38, and R2 = 0.79 during the calibration period, and NSE = 0.50, PBIAS = -5.45, dan R2 = 0.58 in the validation period. These results are deemed satisfactory, indicating the model performed adequately. The length of the data period and the quality of the observed streamflow data are crucial factors influencing the accuracy of the simulation results.

In exploring watershed management scenarios to improve runoff conditions, several strategies were evaluated, including the creation of conservation areas and buffer zones. For example, the conversion of rice field land showed a slight decrease in maximum, minimum, and average streamflow values, suggesting that rice fields, with their strong water retention capabilities, play a valuable role in reducing runoff. However, the impact on streamflow was not highly significant. On the other hand, the conversion of shrubland, fields, and rocky sand areas led to a decrease in maximum streamflow and an increase in minimum streamflow. Additionally, there was an increase in lateral flow, return flow, and recharge values while surface runoff decreased. These variations can be attributed to differences in Curve Number (CN) values and the classification of recharge areas between these land uses. Finally, the conversion of residential land to conservation areas resulted in a significant reduction in surface runoff. This emphasizes the potential benefits of such land conversions in managing runoff, particularly in reducing the impact of built-up areas.

R E F E R E N C E S

Almeida R.A., Pereira S.B., Pinto D.B.F. (2018). Calibration and validation of the SWAT hydrological model for the Mucuri river basin. *Engenharia Agricola*. 38(1): 55–63. DOI: https://doi.org/10.1590/1809-4430-eng.agric.v38n1p55-63/2018

Armoa B.O.L., Sauvage S., Houska T., Bieger K., Schürz C., Sánchez Pérez J.M. (2023). Representation of hydrological components under a changing climate—A case study of the Uruguay River Basin using the new version of the Soil and Water Assessment Tool model (SWAT+). *Water (Switzerland)*. 15(14). DOI: https://doi.org/10.3390/w15142604

Badan Informasi Geospasial. (2021). Inaland system. https://inaland.big.go.id/ (accessed 25 March 2024).

Badan Informasi Geospasial. (2019). Ina-Geoportal. https://tanahair.indonesia.go.id/portal-web/ (accessed 25 March 2024).

Badan Penanggulangan Bencana Daerah Daerah Istimewa Yogyakarta. (2024). Mengenal tingkatan status gunung api. https://bpbd.jogjaprov.go.id/berita/mengenal-tingkatan-status-gunung-api (accessed 10 April 2024).

Chow V.T., Maidment D.R., Mays L.W. (1988). Applied hydrology. *McGraw-Hill Book Company*, New York.

Christanto N., Setiawan M.A., Nurkholis A., Istikhomah S., Anajib D.W., Purnomo A.D. (2019). Rainfall-runoff and sediment yield modelling in volcanic catchment using SWAT, a case study in Opak Watershed. *IOP Conference Series: Earth and Environmental Science*. 256(1): 1-11. DOI: https://doi.org/10.1088/1755-1315/256/1/012015.

Crăciun A.I., Haidu I., Magyari-Sáska Zs., Imbroane A.I., (2009). Estimation of runoff coefficient according to soil moisture using GIS technique. *Geographia Technica*, 4(2), 01-10. https://technicalgeography.org/pdf/2_2009/gt_2_2009.pdf

Easton, M. Z., Fuka, R. D., Walter, M. T., Cowan, M. D., Schneiderman, M. E., Steenhuis, S. T. (2008). Re-conceptualizing the soil and water tool (SWAT) model to predict runoff from variable source areas. *Journal of Hydrology,* 348, 279-291.

Gull, S., & Shah, S. R. (2020). Watershed models for assessment of hydrological behavior of the catchments: A comparative study. *Water Practice and Technology*. 15(2): 261–291. DOI: https://doi.org/10.2166/wpt.2020.030

Haidu I., Ivan K. (2016a). The assessment of the impact induced by the increase of impervious areas on surface runoff. Case study the city of Cluj-Napoca, Romania. *Carpathian Journal of Earth and Environmental Sciences*, 11(2), 331-337. https://www.cjees.ro/viewTopic.php?topicId=621

Haidu I., Ivan K. (2016b). Évolution du ruissellement et du volume d'eau ruisselé en surface urbaine. Étude de cas : Bordeaux 1984-2014, France. *La Houille Blanche*, 5, 51-56. https://doi.org/10.1051/lhb/2016050

Melesse, A.,M., Graham, W.,D., Jordan, J.,D. (2003). Spatially distributed watershed mapping and modeling: GIS-based storm runoff response and hydrograph analysis. Part 2, *Journal of Spatial Hydrology*, 3,2 1-28.

Melesse, A.M., Graham, W.D. (2004). Storm Runoff Prediction Based on a Spatially Distributed Travel Time Method Utilizing Remote Sensing and GIS. *Journal of the American Water Resources Association*, 40,4, 863-879.

de Salis H.H.C., da Costa A.M., Vianna J.H.M., Schuler M.A., Künne A., Fernandes L.F.S., Pacheco F.A.L. (2019). Hydrologic modeling for sustainable water resources management in urbanized karst areas. *International Journal of Environmental Research and Public Health*. 16(14): 1-19. DOI: https://doi.org/10.3390/ijerph16142542.

Solikha D.A, Marfai M.A. (2012). Perubahan morfologi sungai Code akibat aliran lahar pasca erupsi gunungapi Merapi tahun 2010. *Jurnal Bumi Indonesia*. 1(3): 240-245. URL: https://core.ac.uk/download/pdf/295175925.pdf

Jayawardena A.W. (2015). Hydro-meteorological disasters: Causes, effects and mitigation measures with special reference to early warning with data-driven approaches of forecasting. *Procedia IUTAM*. 17: 3–12. DOI: https://doi.org/10.1016/j.piutam.2015.06.003.

López-Ballesteros, A., Nielsen, A., Castellanos-Osorio, G., Trolle, D., Senent-Aparicio, J. (2023). DSOLMap, a novel high-resolution global digital soil property map for the SWAT+ model: Development and hydrological evaluation. *Catena*. 231: 1-13. DOI: https://doi.org/10.1016/j.catena.2023.107339.

Morante-Carballo, F., Montalván-Burbano, N., Arias-Hidalgo, M., Domínguez-Granda, L., Apolo-Masache, B., Carrión-Mero, P. (2022). Flood models: An exploratory analysis and research trends. *Water (Switzerland)*. 14(16): 1-23. DOI: https://doi.org/10.3390/w14162488.

Planet Labs. (2023). Planetscope imagery. https://www.planet.com/ (accessed 10 March 2024).

Suprayogi, S., Purnama, I.L.S., Darmanto, D. (2013). Pengelolaan daerah aliran sungai. *Gadjah Mada University Press*, Yogyakarta.

Satheeshkumar S., Venkateswaran S., Kannan R. (2017). Rainfall–runoff estimation using SCS–CN and GIS approach in the Pappiredipatti watershed of the Vaniyar sub basin, South India. *Modeling Earth Systems and Environment*, 3:24.

Strapazan, C., Petruț, M. (2017). Application of Arc Hydro and HEC-HMS model techniques for runoff simulation in the headwater areas of Covasna Watershed (Romania). *Geographia Technica*, 12, 1, 95-107.

Wang, G., Mang, S., Cai, H., Liu, S., Zhang, Z., Wang, L., Innes, J.L. (2016). Integrated watershed management: Evolution, development and emerging trends. *Journal of Forestry Research.* 27(5): 967–994. DOI: https://doi.org/10.1007/s11676-016-0293-3.

Zulfahmi, Syam, N., Jufriadi. (2016). Jurnal dampak sedimentasi terhadap banjir Kota Makassar. *Jurnal Plano Madani*. 5(2): 180–191. DOI: https://doi.org/10.24252/jpm.v5i2.1581.

MAPPING SOIL ELECTRICAL CONDUCTIVITY AS AN INDICATOR OF SOIL SALINITY IN THE CITY OF NOUAKCHOTT (MAURITANIA)

Mohamed Mahmoud ABIDINE[1] , Mohamed Lemine BABA[1] ,*
Saleck Moulaye Ahmed CHERIF[2] , Zahra Ahmed BEDDI [1] , Youssef DALLAHI [3] ,
Mohamed Ould SIDINE [4] , Ahmedou SOULÉ [5] and Ahmedou VADEL [1]

ABSTRACT
The city of Nouakchott faces challenges linked to soil salinity, rising water tables and the absence of a sewerage system, leading to flooding during the rainy season. These conditions are disrupting urbanization and the greening of the city. All these phenomena inhibit plant growth and development due to soil hydromorphy and salinity. To remedy this situation, the Nouakchott region carried out a study to characterize soils and assess the adaptability of ornamental plants. The approach involves soil mapping. The parameters analyzed are: electrical conductivity (EC), pH, Calcium ($Ca^{2+)}$ Magnesium (Mg^{2+}) and Chloride (Cl^-). A total of 104 samples were collected from various representative sites in the city. GPS coordinates are well defined. Two spatial interpolation methods, Ordinary Kriging (OK) and Inverse Distance Weighting (IDW), were used to estimate unmeasured values. The results show that Nouakchott's soils are saltier in the west and more alkaline in the east. Calcium predominates in the west, while magnesium is evenly distributed but more present in the east. Chlorides are also concentrated in the west. The IDW method proved to be the most effective for characterizing soils in the city of Nouakchott, with a very high correlation coefficient ($R^2= 0.99$) and low errors (RMSE and MAE).

Key-words: Nouakchott, Mapping, Electrical conductivity, pH, Ions.

1. INTRODUCTION

Soil mapping is widely regarded as a rapid and reliable tool for diagnosing soil health (Tripathi et al. 2015; Abidine et al. 2018; Zarco-Perello et Simões 2017; Seyedmohammadi, Esmaeelnejad, et Shabanpour 2016; Poshtmasari et al. 2012). In the urban environment, soil salinization is a major factor not only in the deterioration of buildings but also in the creation of green spaces (Czaja, Kołton, et Muras 2020). The city of Nouakchott lies on the Atlantic Ocean coastline (Sidi Cheikh et al. 2007) ; it is separated from the ocean by a dune cordon dotted with preaches. Climate change has accentuated these effects (Mohamed et al. 2017). Global warming as the polar ice caps melt threatens to flood the city with ocean water. Estimates show that these floods could occur between 2050 and 2100. Thus, the city is subject to the combined effect of groundwater outcrops, soil salinization and flooding (Dubois et al. 2024). Over the past decade, the city has experienced several floods due to intense rainfall and poor soil drainage (Dubois et al. 2024).

----

[1] *Unit of Biodiversity and Valorization of Plant Resources, Faculty of Sciences and Technology, University of Nouakchott, Mauritania, corresponding author: abidinemohamedmahmoud@gmail.com (MMA); lemine827@gmail.com (MLB); zoz819313@gmail.com (ZAB); ahmedou.vadel@yahoo.fr (AV)*

[2] *Region de Nouakchott [Nouakchott City Hall], Nouakchott, Mauritania, ouldmoulayes@yahoo.fr (SMAC)*

[3] *Plant Physiology and Biotechnology Team, Center for Plant and Microbial Biotechnology, Biodiversity and Environment, Faculty of Sciences, Mohammed V University in Rabat, Morocco, dallahi.youssef@gmail.com (YD)*

[4] *Molecular Chemistry and Environment Unit, Department of Chemistry, Faculty of Sciences and Technology, University of Nouakchott, Nouakchott 880, Mauritania, medkh68@yahoo.fr (MOS)*

[5] *Ecology and Biodiversity Unit of Mauritania) Ecole Normale Supérieur de Nouakchott), ahmdous@yahoo.fr.*

To alleviate these problems, the Nouakchott region has embarked on approaches based on physical and biological systems. The biological approach aims to mitigate the rise in the water table by using adapted species. The choice of such species depends on their resistance to edaphic and climatic conditions. To our knowledge, no study of soil salinization in the city of Nouakchott has been carried out. The soils of Nouakchott, like those of other coastal towns, are mainly affected by sodium chloride salt (Okur et Örçen 2020). The presence of certain cations (Ca^{2+}, Mg^{2+}, etc.) in the soil can attenuate the harmful effect of Na^+ ions (Ismayilov et al. 2021). Cl^- anions are well tolerated in low concentrations (Pessoa et al. 2022).

The aim of this work is to map the distribution of Ca^{2+}, Mg^{2+} and Cl^- ions in soils. Soil salinity is estimated by measuring soil electrical conductivity; soil buffering capacity is defined by pH measurements. The various maps are produced using two interpolation methods: deterministic interpolation (IDW) and ordinary kriging.

2. STUDY AREA

Nouakchott, the capital of Mauritania, lies in the Sub-Saharan zone, serving as a transition between the Saharan climate to the north and the Sahelian climate to the south. The climate is dry, with low and very irregular rainfall in summer. The city's main feature is its flat topography, with areas just a few meters above sea level. The relief is almost uniform, not exceeding 30 meters above sea level. Land below sea level is therefore vulnerable to rising water tables, marine incursions and technical challenges in drainage and sanitation. The sebkha's brackish water table is sub-surface, at a depth of 2 to 4 meters, causing flooding during heavy rainfall. These conditions are generally unfavorable to the installation of trees intended for the city's green landscape. The study covered a transect (**Fig. 1**) representative of the city's three wilayas divided into Moughataa (Tevragh Zeina, Sebkha, Ksar, Teyarett, Dar Naïm, Toujounine, Arafat, Riadh and El Mina).
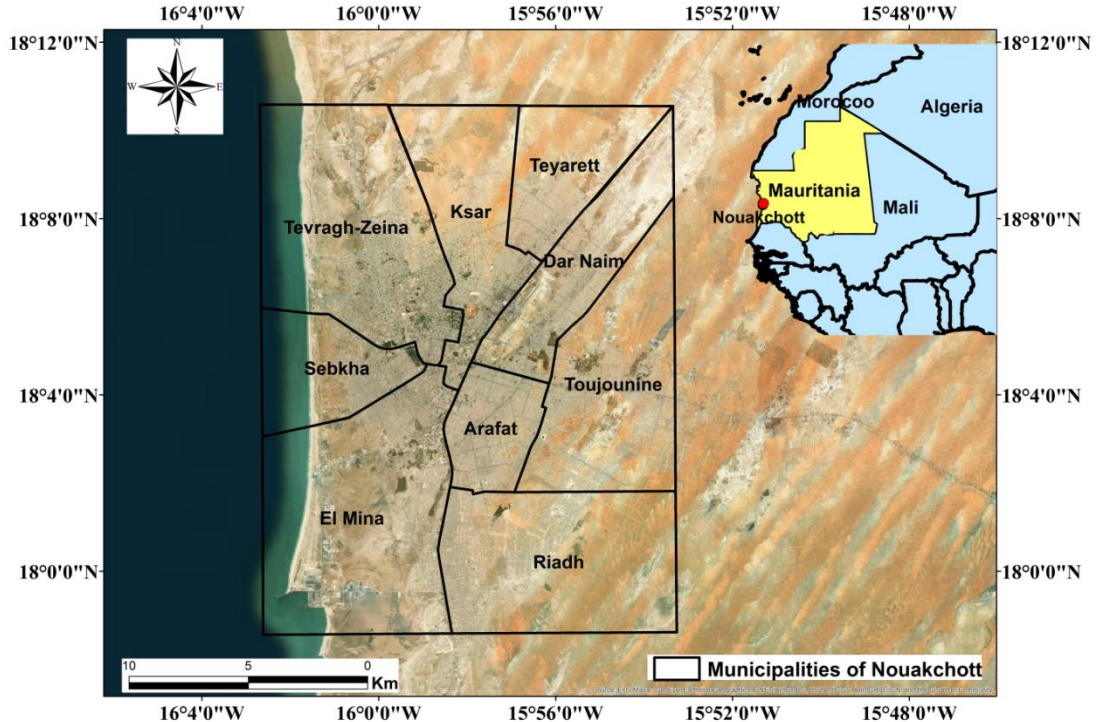
Fig. 1. Location of the Nouakchott region.

3. SOIL SAMPLING AND LABORATORY ANALYSIS

Site identification and sample collection were carried out over a two-week period. The choice of sampling sites was guided by the use of a SPOT image covering a large part of the city. The study area was sampled to a depth of 25 cm. A total of 104 samples were taken from 105 different sites. The GPS coordinates of each site were recorded. The soil samples were placed in plastic bags and kept cool. In the laboratory, they were dried in an oven at 105°C for 12 hours. They were then carefully ground in a mortar and sieved to 2 mm before the various protocols and measurements were applied. The various parameters studied are analyzed in the laboratories of the Biodiversity and Plant Resource Development Unit-Faculty of Science and Technology. pH and EC measurements were carried out using a multifunctional instrument. The protocol involves mixing 20g of crushed and sieved dry soil sample with 100ml of distilled water. The mixture is stirred for 1h30 min on a Hanna shaker, then left to settle and filtered on filter paper. The filtrate obtained is used for pH, EC and exchangeable ion measurements.

4. PREDICTION OF ELECTRICAL CONDUCTIVITY, PH AND SOIL IONS

Two spatial interpolation methods (OK and IDW) were used. They enable unknown values of electrical conductivity, pH and ions to be estimated from measured values. Correlation coefficients and performance criteria are used to validate the appropriate method for the study area.

4.1. Ok method prediction

The prediction of conductivity and pH by the ok method is calculated by the following equation (Tripathi et al. 2015)

$$y(h) = \frac{1}{2N} \sum_{i=}^{N(h)} [z(x_i) - z(x_i + h)]^2 \tag{1}$$

where: N(h) is the number of data pairs in a given distance and direction class.

4.2. Prediction using the IDW method

The prediction of conductivity and pH by the IDW method is calculated by the following equation

$$z(x_o) = \frac{\sum_{i=}^{n} \frac{x_i}{h_y^\beta}}{\sum_{i=1}^{n} \frac{1}{h_y^\beta}} \tag{2}$$

where, $Z(x0)$ is the interpolated value, n representing the total number of sample data values xi is the measured data value, hi is the separation distance between the interpolated value and the sample data value, and β denotes the weighting power.

4.3. Performance evaluation criteria

Three types of standard statistical performance evaluation criteria were used to assess the accuracy of the predictive ability of the models developed. These criteria include correlation coefficient (R), root mean square error (RMSE) and mean error (ME). The performance evaluations in our study are determined using the following equations:

$$R = \sqrt{1 - \left[\frac{\sum_{i=1}^{n}(y_i - \hat{y}_i)^2}{\sum_{i=1}^{n}(y_i - \overline{y})^2} \right]} \tag{3}$$

$$RMSE = \sqrt{\frac{1}{n} \sum_{i=1}^{n}(y_{i-} \hat{y}_i)^2} \tag{4}$$

$$MAE = \frac{1}{n}\sum_{i=1}^{n}|y_i - \hat{y}_i| \tag{5}$$

where y_i indicates the measured value; $\hat{y}_i$ the predicted value, $\overline{y}_i$ the mean of the measured value and n the total number of observations.

5. RESULTS

5.1. Explanatory statistics

The data in **Table 1** presents the descriptive statistics for the EC, pH, major cations (Mg^{2+} and Ca^{2+}) and predominant anion (Cl^-) data sets for the 104 soil samples analyzed. The average electrical conductivity (EC) of the soil is 1.97 dS m-1. It ranges from 0.15 to 3.99, implying that the area has been affected by salinization (Richards, 1954). The average pH of the soil varies between 3.46 and 8.78, and the soils are mainly alkaline (Soltner, 1989). Calcium ranged from 16.05 to 258.11 mg/l. Magnesium ranged from a low of 15.11 to 291.6 mg/l. Soil-available chloride ranged from 23.43 to 497 mg/l.

Table 1.

Descriptive statistic for soil pH and EC data sets in the Nouakchott study area.

Soil properties	Depth (cm)	Mean ± SD	Min	Max	CV (%)	Kurtosis	Skewness
EC (dS m−1) (n = 104)	0–40	1,97± 1,56	0,15	3,99	79	-1,70	0,33
pH (n = 104)	0–40	7,84±0,56	3,46	8,78	8,2	34,21	-4,47
Cl^- (mg/l)(n = 104)	0–40	133,75±131,79	23,43	497	98	3,41	2,05
Ca^{2+} (mg/l)(n = 104)	0–40	89,12±81,47	16,05	258,11	91	-0,55	1,02
mg^{2+} (mg/l)(n = 104)	0–40	84,50±63,27	15,11	291,6	74	4,42	1,78

Notes: SD, standard deviation; CV, coefficient of variation.

Coefficients of variation (CV) denote the variability of properties for soil parameters (Emadi et Baghernejad 2014). According to Wilding (1985), the variability of measured electrical conductivity (EC) is significant when CV exceeds 35%. Our results show this heterogeneity. Abidine et al. (2018) found the same results for Diawling soil. In contrast, soil pH CVs show little variability (8.2). The results of the EC and pH CVs corroborate those of Tripathi et al. (2015) in Odisha, India. The coefficients of variation (CV) are 62.5% for electrical conductivity (EC), 4.43% for pH.

5.2. Cross-validation

The variograms of the various parameters studied according to the two methods used (IDW and OK) showed a lower uncertainty (RMSE, MAE) and a very high R (0.99) for IDW (**Tab. 2**). Thus, the IDW method is the most appropriate in this study. It seems that this method is more valid in arid regions (Karydas et al. 2009; Attaeian et al. 2015;. Abidine et al. 2023 ; Abidine et al. 2018).

Table 2.

Validation criteria for two methods (IDW and OK) in the study area

	CE		pH		Cl-		Ca2+		Mg2+	
	IDW	OK	IDW	OK	IDW	OK	IDW	OK	IDW	OK
R	0,99	0,55	0,99	0,56	0,99	0,99	0,99	0,03	0,99	0,81
RMSE	0,0037	1,298	-0,00011	-0,00816	0,11	1,54	0,15	61,02	0,032	40,24
MAE	0,00012	0,012	0,00011	0,0082	0,002	0,22	0,004	1,24	0,005	1,24

R^2= coefficient of determination, RMSE=root mean square error, MAE=mean absolute error.

5.3. Interpolation using IDW

Figures (2, 3, 4, 5 and **6)** show the interpolation maps for the various parameters studied using the IDW method. **Figure 2** shows the soil pH in the study area. pH values are lower in the west, in the Tevragh-Zeina region (5.31-7.65). In the other areas (Ksar and Dar Naim), values are higher (7.65-8.77). Soils in the city of Nouakchott thus seem to have an alkaline tendency.
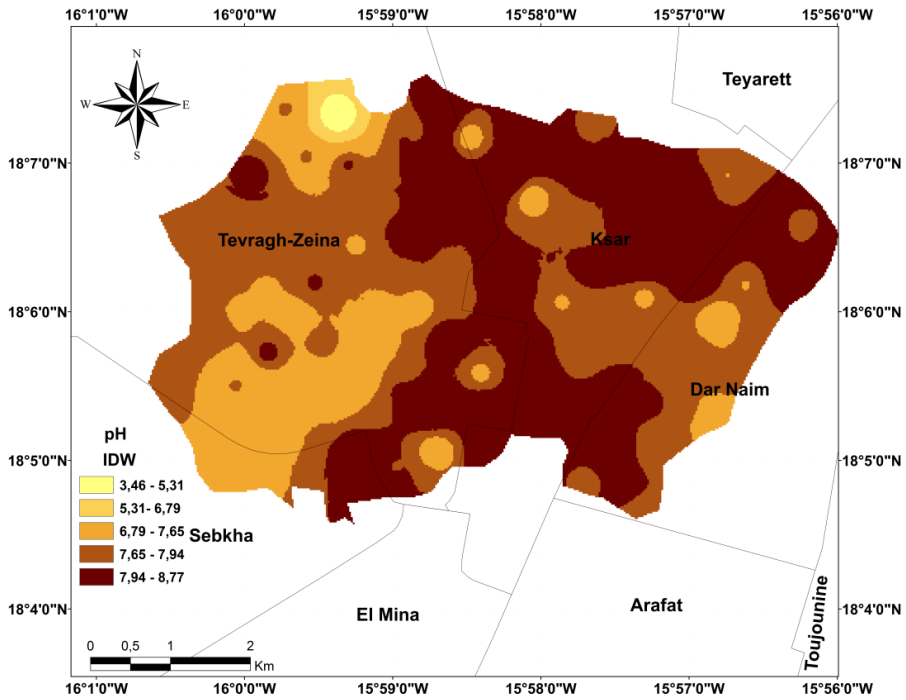
Fig. 2. IDW pH interpolation map.

Figure 3 shows that electrical conductivity (CE) follows a gradient from west to east. It is highest in the Tevragh-Zeina region (2.42-3.98 ds/m). It is lower in the Kasr and Dar Naim regions (0.15-2.42 ds/m).
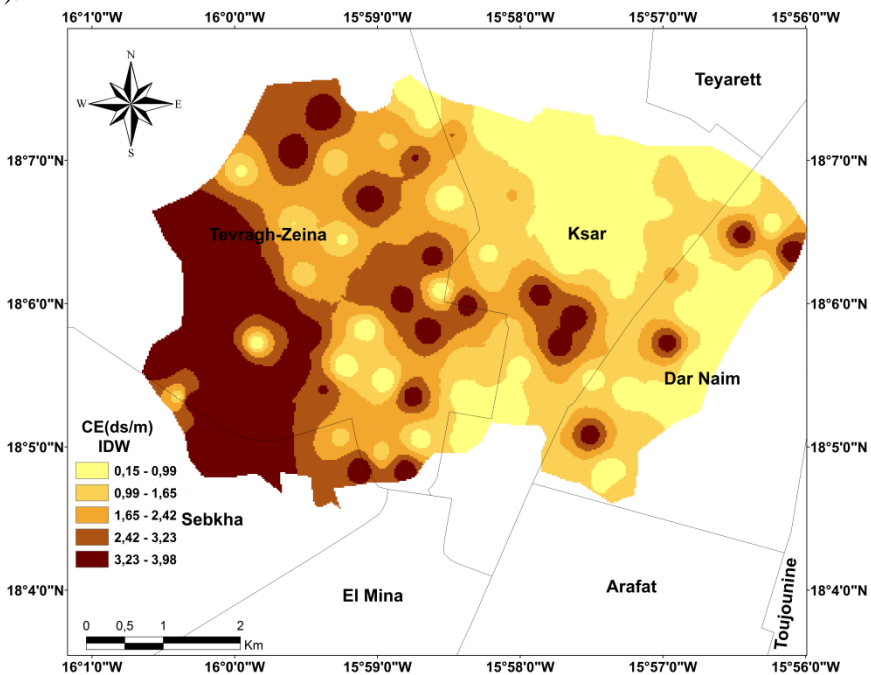

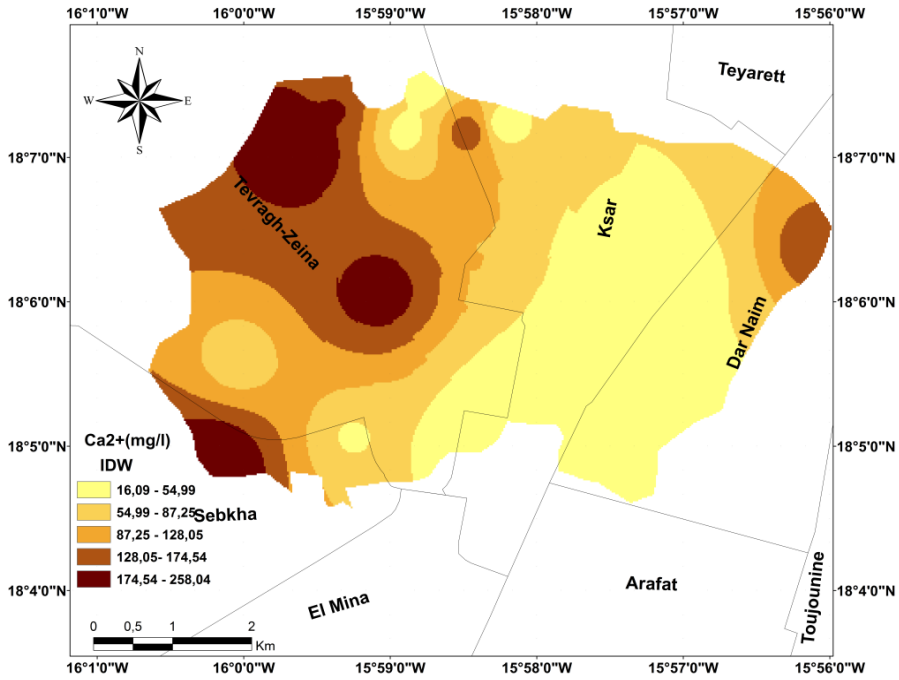
Fig. 3. CE interpolation map by IDW.

Fig. 4. IDW Calcium interpolation map.

Interpolation maps for two major cations (Ca^{2+} and Mg^{2+}) and anion (Cl^-) show contrasting behavior. The distribution of the Ca^{2+} ion shows a gradient from west to east. The highest concentration (87.25-258.04 mg/l) is found in Tevragh Zeina, while concentrations are only 16.09 to 54.99 mg/l in Ksar and Dar Naim (**Fig. 4**).
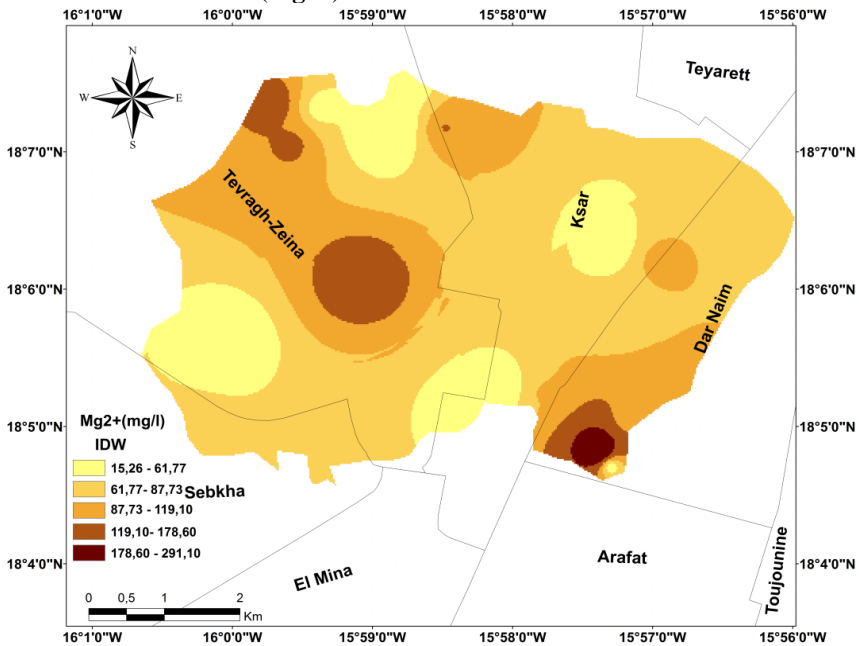
Fig. 5. IDW Magnesium interpolation map.

The Mg^{2+} cation shows a more even distribution. **Figure 5** illustrates the concentrations of this ion in the study area. Values range from 61.77 to 78.73 mg/l. No significant differences between the different zones (Tevragh Zeina, Ksar and Dar Naim).

Figure 6 shows the distribution of the anion (Cl^-). Concentrations are slightly higher in the west, in the Tevragh Zeina zone (251.82-496.89 mg/l). Ksar and Dar Naim have the lowest Cl^- concentrations (23.45-251.82 mg/l).
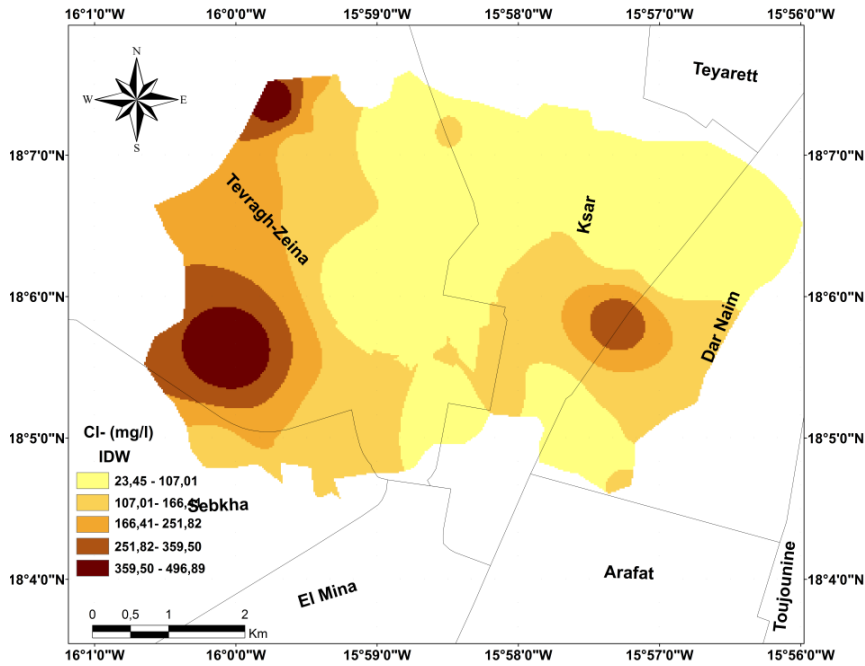
Fig. 6. IDW Chloride Interpolation Map.

6. DISCUSSION

Green spaces are considered the lungs of cities. Urban planning is heavily dependent on public gardens and street trees. The choice of species used depends on climatic and, above all, edaphic conditions. The ground in the city of Nouakchott (Mauritania) is characterized by sebkas and puddles. Salt crusts (especially NaCl) are frequently observed in certain parts of the city. The absence of sanitation infrastructures and the rising water table, which is very close to the surface, accentuate the problems of soil salinization.

Physico-chemical characterization of the soils in the city of Nouakchott is an important approach in any city vegetation program. In this study, we set out to map the distribution of salinity in the city using electrical conductivity (EC). The results show high salinity in the Tevragh Zeina area (EC=3.9 ds.m-¹). According to the scale established by Durand, (1983), this soil is considered very salty. In contrast, Ksar and Dar Naim (EC=1.6 ds.m-¹) have moderately saline soils, according to the same scale. The pH of Nouakchott soils is 8.7. According to Soltner (1989), this soil is considered alkaline.

Soil pH affects plant nutrition; certain ions are only available for absorption when the pH is basic. In alfalfa, a pH higher than 7 increases the harmful effect of Nacl 200mM on plant growth and development (Kaiwen et al. 2020). High salt concentration in alkaline soil reduces nutrient availability (He et al. 2017). Thus, plant nutrition in saline soils depends on the soil's nutritional status in terms of major and minor ions.

The beneficial effect of Ca^{2+} and Mg^{2+} on plant growth and development in saline conditions (rich in Na^+) has been well demonstrated in several studies. At soil level, Ca^{2+} competes with Na^+ at the same binding site, thus improving K^+ uptake (Taieb Tounekti et al. 2010).

K^+ ion improves plant water status (Taïeb Tounekti et al. 2011). The uptake of Ca^{2+} and Mg^{2+} by plant roots is proportional to their availability in the soil. However, the most sensitive species absorb major cations less efficiently than salinity-resistant species (Walker et al. 1955). In other species, Secale (Rajakaruna et al. 2003), Helianthus bolanderi ssp. exilis A. Gray and the sunflower (Walker et al. 1955), their ability to tolerate salinity depends on maintaining high Mg^{2+}/Ca^{2+} and K^+/Na^+ ratios.

The results observed in Lasthenia californica growing on different soils postulate that the salinity resistance of different populations is not due to a single mechanism (Rajakaruna et al. 2003). Resistance operates at several levels, including root morphology, uptake, translocation and cation interactions. One of the key elements of salinity tolerance is the ability to maintain a high level of cytosolic K^+/Na^+ independently of external concentrations of these two ions. Cl^- is a trace element, which is only toxic in relatively high concentrations (Rejili et al. 2007).

The soil of Nouakchott has a relatively homogeneous distribution of this ion. The exceptionally high content is localized in small pockets at Tevregh Zeina. We can understand its presence in such high concentrations in the context of its accompanying anion behaviour of Na^+, Ca^{2+}, Mg^{2+}. Abdelaal et al. (2021), have shown that the predominance of chloride salts in saline soils in Egypt disrupts the soil's biological processes and reduces its capacity for natural regeneration. As a result, the addition of certain cation-rich fertilizers improves soil quality to the extent that it does not lead to further soil salinization.

Halophytes are species adapted to these types of soil, where chloride salts predominate (Zhao et al. 2022). It thus seems to us that a judicious choice of halophytic species can be considered the most plausible approach in gardening programs in Nouakchott. Soil physico-chemical parameter maps for the city of Nouakchott are drawn up using the IDW method. This method showed very low error values and a high correlation coefficient, making it the most suitable for studying soils in desert regions. The effectiveness of the IDW method in arid environments has been endorsed by Lotfinasabasl et al. (2018) in Iran and Bashir et Fouli (2015) in Saudi Arabia.

7. CONCLUSION

Soil mapping in the city of Nouakchott has shown that soils tend to be basic, with Tevregh Zeina being the most saline. Chloride salt levels are very high and have a generally homogeneous distribution in the areas studied. Nevertheless, Tevregh Zeina showed pockets with exceptionally high concentrations.

The two major cations Ca^{2+} and Mg^{2+} show different edaphic behavior. Ca^{2+} ions are concentrated in the Tevregh Zeina area, while Mg^{2+} ions are more or less evenly distributed across the different regions studied. Vis the very high salinity of the soil, additional fertilizers can lead to salinization of the soil by total salts. So, the choice of species adapted to aridity conditions (salinity, heat and drought) seems to be the most appropriate strategy.

The IDW method is the most suitable for mapping soil physico-chemical parameters in these arid edaphic situations.

REFERENCES

Abdelaal, Samah M. S., Karam F. Moussa, Ahmed H. Ibrahim, Elsayed Said Mohamed, Dmitry E. Kucher, Igor Savin, et Mohamed K. Abdel-Fattah. 2021. « Mapping Spatial Management Zones of Salt-Affected Soils in Arid Region: A Case Study in the East of the Nile Delta, Egypt ». *Agronomy* 11 (12): 2510. https://doi.org/10.3390/agronomy11122510.

Abidine, Mohamed Mahmoud, Lemane Mohamed Cheikh, Youssef Dallahi, Mohamed Lemine Baba, El Weila Mohamed Mahmoud, Ahmedou Soulé, et Ahmedou Vadel. 2023. « The Study of the Germination Behavior of Forage Species on Substrates Taken from the Soil of Awleigatt National Park in Mauritania ». *Ecological Engineering & Environmental Technology* 24 (6): 257‑67. https://doi.org/10.12912/27197050/168453.

Abidine, Mohamed Mahmoud Ould, Ahmed El Aboudi, Aminetou Kebd, Brahim Baba Aloueimine, Youssef Dallahi, Ahmedou Soulé, et Ahmedou Vadel. 2018a. « Modeling the Spatial Variability of the Electrical Conductivity of the Soil Using Differents Spatial Interpolation Methods: Case of the Dawling National Park in Mauritania ». *Geographia Technica* 13 (2): 1‑11. https://doi.org/10.21163/GT_2018.132.01.

Attaeian, Behnaz, Behnoush Farokhzadeh, Davoud Akhzari, Mohammad Mahdi Artimani, et Mahshid Souri. 2015. « Comparing Interpolation Methods for Estimating Spatial Distribution of Topsoil pH and EC (Case Study: Karimabad Rangelands, Hamadan Province, Iran) » 3.

Bashir, Bashar, et Hesham Fouli. 2015. « Studying the Spatial Distribution of Maximum Monthly Rainfall in Selected Regions of Saudi Arabia Using Geographic Information Systems ». *Arabian Journal of Geosciences* 8 (11): 9929‑43. https://doi.org/10.1007/s12517-015-1870-z.

Czaja, Monika, Anna Kołton, et Piotr Muras. 2020. « The Complex Issue of Urban Trees—Stress Factor Accumulation and Ecological Service Possibilities ». *Forests* 11 (9): 932. https://doi.org/10.3390/f11090932.

Dubois, Emmanuel, Saleck Moulaye Ahmed Cherif, Mohamed Mahmoud Abidine, Mohamed Fall Ould Bah, Jerome Chenal, Montana Marshall, Wague Oumarou, Charlotte Grossiord, et Paolo Perona. 2024. « Nature-based solution enhances resilience to flooding and catalyzes multi-benefits in coastal cities in the Global South ». *The Science of The Total Environment* 928:172282.

Durand, J.H. 1983. *Les Sols Irrigables; Etude Pedologique; Presses Universitaires de France: Paris, France.*

Emadi, Mostafa, et Majid Baghernejad. 2014. « Comparison of Spatial Interpolation Techniques for Mapping Soil pH and Salinity in Agricultural Coastal Areas, Northern Iran ». *Archives of Agronomy and Soil Science* 60 (9): 1315‑27. https://doi.org/10.1080/03650340.2014.880837.

He, Honghua, Qi Peng, Xia Wang, Chenbin Fan, Jiayin Pang, Hans Lambers, et Xingchang Zhang. 2017. « Growth, Morphological and Physiological Responses of Alfalfa (Medicago Sativa) to Phosphorus Supply in Two Alkaline Soils ». *Plant and Soil* 416 (1‑2): 565‑84. https://doi.org/10.1007/s11104-017-3242-9.

Ismayilov, Amin I., Amrakh I. Mamedov, Haruyuki Fujimaki, Atsushi Tsunekawa, et Guy J. Levy. 2021. « Soil Salinity Type Effects on the Relationship between the Electrical Conductivity and Salt Content for 1:5 Soil-to-Water Extract ». *Sustainability* 13 (6): 3395. https://doi.org/10.3390/su13063395.

Kaiwen, Guo, Xu Zisong, Huo Yuze, Sun Qi, Wang Yue, Che Yanhui, Wang Jiechen, Li Wei, et Zhang Huihui. 2020. « Effects of Salt Concentration, pH, and Their Interaction on Plant Growth, Nutrient Uptake, and Photochemistry of Alfalfa (*Medicago Sativa*) Leaves ». *Plant Signaling & Behavior* 15 (12): 1832373. https://doi.org/10.1080/15592324.2020.1832373.

Karydas, Christos G, Ioannis Z. Gitas, Eirini Koutsogiannaki, Nikolaos Lydakis-Simantiris, et Georgios N. Silleos. 2009. « Evaluation of Spatial Interpolation Techniques for Mapping Agricultural Topsoil Properties in Crete ». *EARSeL eProceedings* 8.

Lotfinasabasl, Sakineh, V.R. Gunale, et Mohammad Khosroshahi. 2018. « Applying Geographic Information Systems and Remote Sensing for Water Quality Assessment of Mangrove Forest ». *Acta Ecologica Sinica* 38 (2): 135‑43. https://doi.org/10.1016/j.chnaes.2017.06.017.

Mohamed Ahmed Ould Sidi Cheikh, Pierre Ozer, et André Ozer. 2007. « Flood risks in the city of Nouakchott (Mauritania) ». *Geo-Eco-Trop* 31:19‑42.

Mohamed, Ahmed-Salem, Christian Leduc, Christelle Marlin, Oumar Wagué, et Mohamed-Ahmed Sidi Cheikh. 2017. « Impacts of climate change and anthropization on groundwater resources in the Nouakchott urban area (coastal Mauritania) ». *Comptes Rendus Geoscience*, Vulnerability of inter-tropical littoral areas, 349 (6): 280‑89. https://doi.org/10.1016/j.crte.2017.09.011.

Okur, Bülent, et Nesrin Örçen. 2020. « Soil Salinization and Climate Change ». In *Climate Change and Soil Interactions*, 331‑50. Elsevier. https://doi.org/10.1016/B978-0-12-818032-7.00012-6.

Poshtmasari, Hossein Kazemi, Zeynolabedin Tahmasebi Sarvestani, Behnam Kamkar, Shaban Shataei, et Sohrab Sadeghi. 2012. « Comparison of interpolation methods for estimating pH and EC in agricultural fields of Golestan province (north of Iran) ». *International Journal of Agriculture and Crop Sciences* 4 (4): 157‑67.

Rajakaruna, Nishanta, M. Yaeesh Siddiqi, Jeannette Whitton, Bruce A. Bohm, et Anthony D. M. Glass. 2003. « Differential Responses to Na^+/K^+ and Ca^{2+}/Mg^{2+} in Two Edaphic Races of the *Lasthenia Californica* (Asteraceae) Complex: A Case for Parallel Evolution of Physiological Traits ». *New Phytologist* 157 (1): 93‑103. https://doi.org/10.1046/j.1469-8137.2003.00648.x.

Rejili, M., A.M. Vadel, A. Guetet, et M. Neffatti. 2007. « Effect of NaCl on the Growth and the Ionic Balance K+/Na+ of Two Populations of Lotus Creticus (L.) (Papilionaceae) ». *South African Journal of Botany* 73 (4): 623‑31. https://doi.org/10.1016/j.sajb.2007.06.006.

Richards, L.A. 1954. *Diagnosis and improvement of saline and alkali soils. USDA Agriculture Handbook, p. 60.*

Seyedmohammadi, Javad, Leila Esmaeelnejad, et Mahmood Shabanpour. 2016. « Spatial Variation Modelling of Groundwater Electrical Conductivity Using Geostatistics and GIS ». *Modeling Earth Systems and Environment* 2 (4): 1‑10. https://doi.org/10.1007/s40808-016-0226-3.

Soltner D. 1989. *Les bases de la production végétal. Tome I: Le sol, 17ème Ed. C.S.T.A., Angers, 468 p.*

Tounekti, Taieb, Sergi Munné-Bosch, A.M. Vadel, Chaker Chtara, et Habib Khemira. 2010. « Influence of Ionic Interactions on Essential Oil and Phenolic Diterpene Composition of Dalmatian Sage (Salvia Officinalis L.) ». *Plant Physiology and Biochemistry* 48 (10‑11): 813‑21. https://doi.org/10.1016/j.plaphy.2010.08.007.

Tounekti, Taïeb, Ahmedou Mohammed Vadel, Mustapha Ennajeh, Habib Khemira, et Sergi Munné-Bosch. 2011. « Ionic Interactions and Salinity Affect Monoterpene and Phenolic Diterpene Composition in Rosemary (*Rosmarinus Officinalis*) ». *Journal of Plant Nutrition and Soil Science* 174 (3): 504‑14. https://doi.org/10.1002/jpln.201000213.

Tripathi, Rahul, A. K. Nayak, Mohammad Shahid, R. Raja, B. B. Panda, S. Mohanty, Anjani Kumar, B. Lal, Priyanka Gautam, et R. N. Sahoo. 2015a. « Characterizing Spatial Variability of Soil Properties in Salt Affected Coastal India Using Geostatistics and Kriging ». *Arabian Journal of Geosciences* 8 (12): 10693‑703. https://doi.org/10.1007/s12517-015-2003-4.

Walker, Richard B., Helen M. Walker, et P. R. Ashworth. 1955. « Calcium-Magnesium Nutrition with Special Reference to Serpentine Soils 1 ». *Plant Physiology* 30 (3): 214‑21.

Wilding LP. 1985. « Spatial variability: its documentation, accommodation and implication to soil surveys. » *In: Nielsen DR, Bouma J, editors. Soil spatial variability. Wageningen: Pudoc*, 166‑94.

Zarco-Perello, Salvador, et Nuno Simões. 2017. « Ordinary Kriging vs Inverse Distance Weighting: Spatial Interpolation of the Sessile Community of Madagascar Reef, Gulf of Mexico ». *PeerJ* 5 (novembre):e4078. https://doi.org/10.7717/peerj.4078.

Zhao, Yinghan, Tian Li, Junhan Liu, Jingkuan Sun, et Ping Zhang. 2022. « Ecological Stoichiometry, Salt Ions and Homeostasis Characteristics of Different Types of Halophytes and Soils ». *Frontiers in Plant Science* 13 (octobre):990246. https://doi.org/10.3389/fpls.2022.990246.

SAR SENTINEL-1 DATA, NDFI AND NDFVI FOR DETECTING AND MAPPING THE FLOOD HAZARD IN OUED SAKIA-EL HAMRA (LAAYOUNE, SOUTH MOROCCO)

Mohammed MOURJANE [1] , Naoual EL HAMMOUCH [1], Hassan TABYAOUI [1] , Fatima EL HAMMICHI [1], Fatima-Zahra LAAREJ [1], Nassareddine AZZOUZI [1], Ahmed GABER [2]*

ABSTRACT

A new automated approach for flash extent delineation and mapping and risk assessment was applied in the context of the Oued Sakia-Al Hamra flood (Laayoune, southern Morocco) of October 2016. Normalized Difference Flood Index (NDFI) mapping was employed to distinguish between flood-prone and non-flood-prone areas across an extensive region, leveraging the Bragg backscattering properties of active radar pulses on flat water surfaces, which exhibit minimal signal reflection. The study utilized Sentinel-1 satellite SAR images in Wide Swath (IW) interferometric mode and Ground Range Detected (GRD) product type. Pre-processing and processing chain, which combines water classification, multi-temporal and contextual filtering, topographic correction of a total number of 2 images: before and after the flood event. Consequently, a high classification accuracy of 99.05% using Sentinel-1 C-band images for the flooded area of Oued Sakia-El Hamra was obtained after validation using both optical images of Landsat-8 and Google-Earth. The results demonstrate the effective utilization of SAR data for identifying flooded areas, assessing their extent, evaluating associated hazards, and subsequently recommending appropriate mitigation measures as needed.

Key-words: SAR data, scattering response, natural flooding, Sakia-Al Hamra River, Morocco.

1. INTRODUCTION

Flash floods occur in numerous regions worldwide, causing substantial annual losses (White, 2023). They represent the most common natural disaster and are recognized as a significant threat, particularly in urban areas across sub-Saharan Africa (Tiepolo, 2014). Since, accurately mapping the flooded water extent areas is very important to be used to validate the hydraulic models and quantify the flood risk consequences in the context of land use planning and coverage.

Floods frequently inundate expansive regions that are challenging to survey and monitor on the ground. Spatial remote sensing data serves as an ideal source for efficiently and cost-effectively monitoring large-scale flood events from a bird's-eye view. Optical satellite imagery, including platforms like QuickBird, RapidEye, Planet, Landsat, SPOT, ASTER, Sentinel-2, and MODIS, has proven effective in previous studies for generating water masks of flooded areas. These optical sensors represent the most favored source of information due to their spectral component and simplicity of interpretation (Smith, 1995). Usually, such optical satellite data are suffered from cloud covers, especially of those which are accompany the heavy rains and cause flooding (Henshaw et al., 2013; Schumann et al., 2018). Meanwhile, synthetic aperture radar (SAR) systems emerge as robust tools for flood monitoring in near-real-time (NRT), owing to their ability to operate effectively in diverse

[1]*Natural resources and Environment Laboratory, Polydisciplibary Faculty of Taza, Sidi Mohamed Ben Abdellah University, Fez, Morocco, corresponding author[*] mourjanemohammed@gmail.com, naouallelhammouch@gmail.com, hassan.tabyaoui@usmba.ac.ma, Fatima.elhammichi@usmba.ac.ma, laarej.fatimazahra96@gmail.com, Nassareddine.azzouzi@usmba.ac.ma.*

[2] *Faculty of Science, Port Said University, Egypt, ahmedgaber_881@hotmail.com*

weather conditions (Mertes, 2002; Alsdorf et al., 2007) and around the clock (Franceschetti & Lanari, 1999; Schumann & Moller, 2015). SAR technology has demonstrated proficiency in detecting water surfaces, estimating flood depths, and identifying submerged areas under canopy cover. Significant efforts have been devoted to development of algorithms for accurately delineating flood extents from radar imagery. Common methodologies for SAR-based flood mapping encompass simple visual interpretation, supervised classification, image texture analysis, threshold segmentation, histogram-based thresholding, multi-temporal change detection techniques, active contour models, and interferometric SAR approaches (Arnesen et al., 2012 ; Borghys et al., 2006 ; Brivio et al., 2002 ; Dellepiane & Angiati, 2012 ; Dellepiane et al., 2000 ; Di Baldassarre et al., 2011 ; Dong et al., 2015 ; Horritt et al., 1999 ; 2001 ; Hostache el al., 2012 ; Martinez & Le Toan, 2007 ; Martinis et al. 2011 ; Mason et al., 2007 ; Nico et al., 2000 ; Pierdicca el al., 2012 ; Pulvirenti el al., 2011 ; 2013 ; Schumann et al., 2009 ; Smith, 1997).

Change Detection (CD) method involves technology that compares backscatter intensity before and during flooding to identify pixel change (Mertes, 2002; Alsdorf et al., 2007; Lu et al., 2014). The main water body thus identified from the reference image is used on the flood image to isolate water pixels within these bodies, facilitating the derivation of statistical curves that describe them.

By combining the strengths of change detection (CD) and thresholding, Long et al. (2014) computed the absolute difference between flood and reference images and applied two thresholds to distinguish flood areas and shallow water within short vegetation. To enhance objectivity and reduce user influence, threshold values were derived by analyzing the histogram of the difference image through a mathematical formula. In a similar vein, Cian et al, (2018) have devised two flood indices based on the methodology introduced by Long et al. (2014). The Normalized Difference Flood Index (NDFI) and the Normalized Difference Flood in Short Vegetation Index (NDFVI) function primarily as change detection techniques (Cian et al., 2018). They offer advantages such as reduced reliance on manual intervention and swift flood mapping capabilities (Xue et al., 2022). Specifically, NDFI categorizes flooded regions based on the disparity between the mean and minimum backscatter coefficient values across a time series (Álvarez-Mozos et al., 2005). However, NDFVI is tailored to highlight shallow water within areas of short vegetation, assuming sufficient revisit times for each pixel under dry conditions. This differentiation is crucial given the influence of factors like wind, vegetation, and environmental variability arising from satellite system parameters. The overarching goal of this study is to document and assess temporal and spatial changes in surface conditions of streams before and after flooding in the desert environment of the Moroccan Sahara. Like Cian et al. (2018), the approach prioritizes robustness and simplicity, requiring minimal user input and demonstrating effective applicability across diverse environments using data from various sensors. Additionally, it excels in delineating shallow water within short vegetation and identifying flooded open areas.

2. ENVIRONMENTAL SETTING OF THE STUDY SITE

The study area lies in the interior of the Moroccan Sahara (**Fig. 1A**), in particular the Oued Sakia El Hamra, which flows through one of the largest cities in the Moroccan Sahara (Laayoune Town). The area stretches from the foot of the Anti-Atlas massif to the town of Lagouira in the south and the Atlantic coast in the west (**Fig. 1B**). It is physically remarkably homogeneous, with a large desert zone characterized by the presence of the hammada, essentially made up of immense desert plateaus. The relief is very flat. Its monotony is interrupted only by a few sabkhas (depressions), limited dune belts and the remnants of a fairly small hydrographic network. The geological bedrock consists of Upper Cretaceous limestones and sandstones, dipping very gently to the west and overlain by powerful Oligocene and Miocene unconformable beds (Ratschiller, 1970). The top of the series is composed of lithological formations of Tertiary to Quaternary age, consisting of dunes, sands, evaporated silts and carbonate sandstones.

The area is crossed by the Sakia Hamra wadi, which is the source of numerous dry tributaries, highly parched valleys. In normal periods, the flow of the wadi is considered negligible, due to the

obstruction of its lower valley by a corridor of sand dunes moving from south to north, associated with landslides, the presence of the "Al Massira Al Khadra" hill dam built in 1995 at the town of Laayoune, and the absence of floods that have reached the ocean for over fifty years. Further west, this watercourse is now marked on the edge of the town of Laayoune by linear tree vegetation supported by the water table in the shallow subsoil.

The study area experiences moderate temperatures influenced by its proximity to the Atlantic Ocean. Annual rainfall is minimal, averaging 59 mm at the Laayoune station, and occurs irregularly. Coastal temperatures range from 17 to 25°C throughout the year. Persistent winds prevail across the region, with monthly maximum speeds ranging from 15.4 to 19.2 m/s, and an annual average speed of approximately 17.6 m/s or 63.4 km/h (HCP, 2020). Due to its consistency and strength, wind plays a crucial role in generating silting phenomena, shaping dune landscapes, and influencing sand movement dynamics. The dunes near Laayoune are renowned for being among the fastest-moving in the world, averaging a migration rate of 32 meters per year for dunes that are 9 m high tall. The dune fields take the form of a river of sand running NNE-SSW over a length of 150 km. Geomorphologically, the barchan dune is the dominant dune form in the region (Amimi et al., 2017). Air circulation patterns are significantly shaped by the coastline's configuration, while the dune formations are intricately connected to loose sediments originating from the Sahara (**Fig. 1C**).

In October 2016, this region was hit by violent storms that caused impressive flooding and river flooding. The rainfall occurred over a ten-hour period (between October 28 and 29). The volume of water stored at the Al Massira Al Khadra dam, which is known to have a total storage capacity of 110 million m3. The flood's peak was reached over 3,000 m3/s, well above the spillway's storage capacity threshold (410 m3/s). The occurrence of this extraordinary flood resulted in the wadi overflowing the crest of the dam, causing damage to the downstream slope. The height of the two breaches then increased as the overflow gradually reached the level of the river. The flood of October 28-30, 2016 swept away the entire infrastructure in the lower valley and led to the failure of the dam by overflow, followed by the obliteration of the dunes in the lower valley and delta (Mazel et al., 2019).

The infrastructure of the city of Laayoune concerns a wide range of sectors, from transport to energy, water, education, health, urbanization, agriculture, fisheries and food (HCP, 2020). They have undergone further development with projects to set up a technopole in the dried-up mouth of the Sakia El Hamra wadi (Mazel et al., 2019). This phenomenon, combined with the higher intensity of floods, has led to an increase in losses and damages.
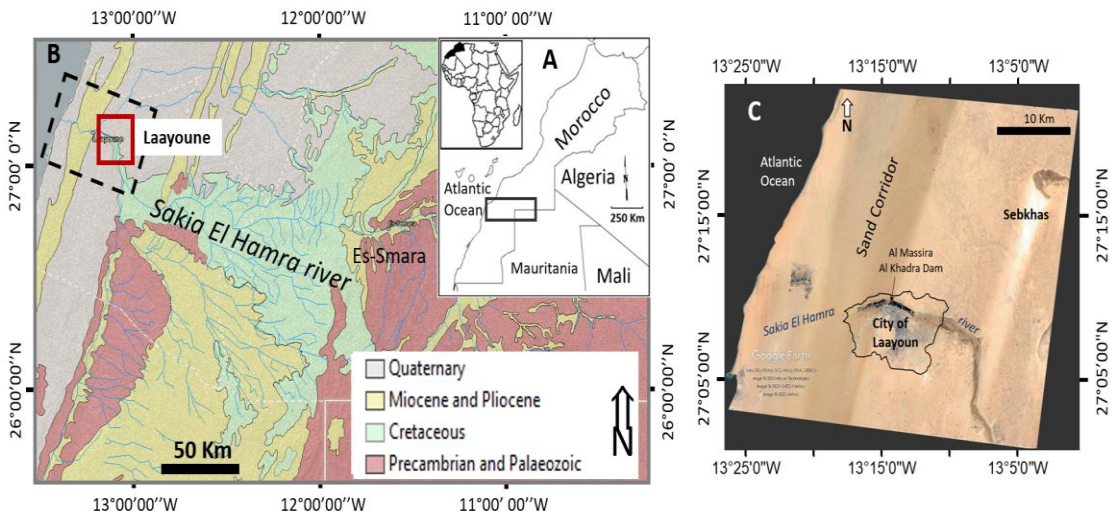

Fig. 1. A - Position of studied area in the south of Morocco, **B -** Simplified geological map of the study area from Geological map of Morocco at 1/1000000, and **C -** Situation of the study area in Google Earth image.

3. MATERIALS AND METHODS

Sentinel-1 mission represents a pivotal advancement, harnessing Earth Observation (EO) megadata with its provision of free, global SAR measurements through numerous repetitive observations. In this study, Sentinel-1 Level-1 Ground Range Detected (GRD) products were utilized. These products consist of focused, multi-look SAR data that have been geocoded onto the Earth's surface using a terrestrial ellipsoid model such as WGS84. The Sentinel-1 images employed in this study belong to the wide interferometric SAR category and operate within the C-band frequency range. They were accessed from the Sentinels Scientific Data Hub (https://scihub.esa.int/). the acquired images underwent processing using the Sentinel Application Platform (SNAP) software, which is an open-source framework developed by the European Space Agency (ESA) designed for the comprehensive exploitation and analysis of Earth Observation (EO) data (http://step.esa.int).

The methodology involves creating two sets of image stacks (**Fig. 2**) one comprising reference images and another incorporating flood images under investigation. Both stacks undergo radiometric calibration and terrain correction. Temporal statistics are computed thereafter to calculate the Normalized Difference Flood Index (NDFI) for detecting temporary open water bodies. The Normalized Difference Flood Index in Vegetated Areas (NDFVI) was computed to detect shallow water within short vegetation. Subsequently, a threshold is applied to the index values to isolate flooded areas, followed by additional filtering to eliminate clusters of erroneous pixels and enhance the precision of the final flood mapping results.
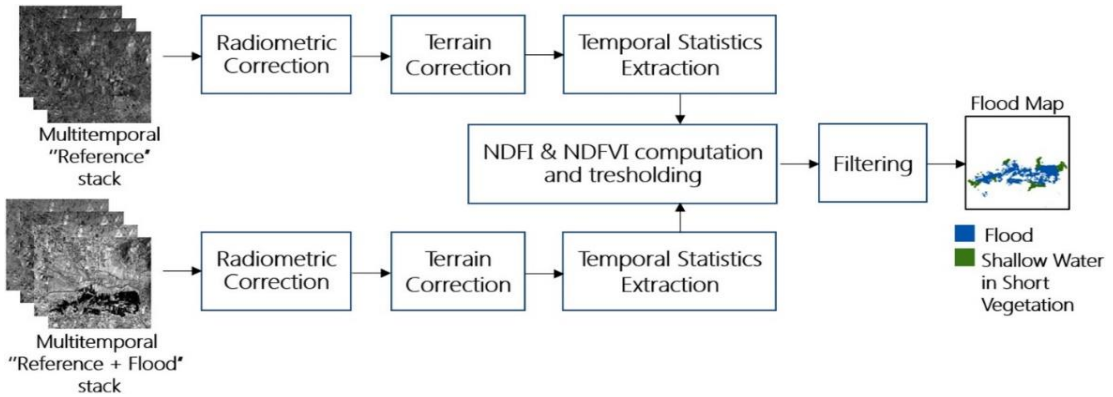
Fig. 2. Overview of method adopted in this study (after Cian et al., 2018).

The NDFI and NDFVI calculation formulas are as follows:

$$NDFI = \frac{\text{mean }(\sigma0\text{ reference}) - \text{min }(\sigma0\text{ reference} + \sigma0\text{ flood})}{\text{mean }(\sigma0\text{ reference}) + (\sigma0\text{ reference} + \sigma0\text{ flood})} \quad (1)$$

$$NDFVI = \frac{\text{mean }(\sigma0\text{ reference}) - \text{max }(\sigma0\text{ reference}, \sigma0\text{ flood})}{\text{mean }(\sigma0\text{ reference}) + \text{max }(\sigma0\text{ reference}, \sigma0\text{ flood})} \quad (2)$$

among these terms, "mean" ("reference") signifies the average backscatter coefficient of each pixel in the reference image, while "min" ("reference + flood") denotes the minimum backscatter coefficient of each pixel across all images.

We mention that in normal cases, Manjusree et al., (2012) show that backscatter of flood water in HV and VH polarizations are same, and both HV and VH polarizations are adequate for flood water mapping. From near range to far range, −8 to −12 dB, −15 to −24 dB and −6 to −15 dB can be used as optimal ranges for flood water classification in HH, HV and VV polarizations. This study can be the blueprint to define optimal threshold ranges of NDFI and NDFVI to produce flood maps within a short time from the onset of disasters and deliver these maps to the concerned agencies.

4. SURFACE ROUGHNESS ANALYSIS

The C-band, operating at a central frequency of 5.405 GHz and a wavelength of 5.7 cm, exhibits high sensitivity to surface water content as observed by radar. This characteristic means that this band can be utilized across various applications, such as soil moisture measurement and flood detection. In the filtered and geocoded reference image (**Fig. 3A**), the smoother surfaces appear very dark (Bragg scattering), attesting to the fact that the depth of penetration of radar waves into this bare dry soil can be quite deep. Radar waves can thus map bedrock and gravel surfaces beneath wind-blown sand several centimeters, or even meters, thick. This confirms that the highest soil layers detected can be considered as a homogeneous dielectric medium. Rough surfaces, which appear very bright on a radar image, correspond to SSW-NNE corridor of moving sand dunes. These have different geometric and dielectric properties, with backscattering on rough surfaces. With the same textural properties on the ground, image B (**Fig. 3B**) taken after the rainy flood period shows strong backscattering of the radar signal. This confirms that the dielectric properties of soil depend on its water content, and that the backscatter coefficient measured by radar instruments increases with increasing in soil moisture.
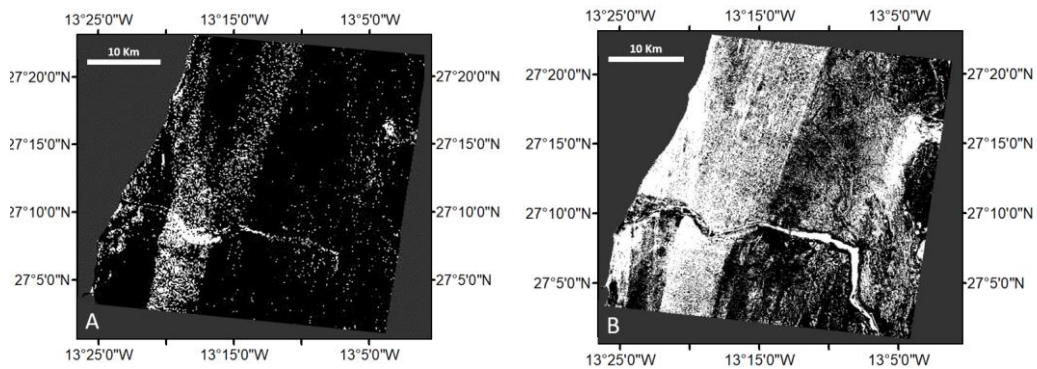
Fig. 3. Filtered and geocoded reference (**A**) and after flood event (**B**) of the study area.

Radar backscatter refers to the amount of radar signal redirected back to the sensor by the target (ESA, 2022). The backscatter coefficient, denoted as σ0 (Sigma0), is typically measured in decibels (dB) (Rosenqvist et al., 2018). In SAR imagery interpretation, a general principle states that rougher surfaces exhibit higher backscatter intensity in both cross-polarized and co-polarized orientations, resulting in brighter images (Liew 2001). Conversely, smooth surfaces tend to produce specular reflections, where radar signals are directed away from the sensor, leading to reduced radar return. Rough surfaces, on the other hand, scatter radar signals in various directions, resulting in greater radar return (IPR, 2022).

In semi-arid and arid landscapes, land surfaces are generally having low soil moisture content and making the radar backscattered return is mainly from the soil roughness, vegetation cover and rocks. Surface roughness is a dynamic geomorphic property. Radar signals vary considerably. In the study area, the radar signal returned varies significantly due to changes in terrain morphology, topography, and the predominance of sandy surface cover (**Fig. 4**).

On the reference corrected image centered on the course of Oued Sakia El Hamra (**Fig. 4A**), and for pixels with values σ0 less than 0.007dB (Points 1 to 6), water bodies are delineated with high precision, focusing on accurately detecting their outer boundaries. This is the case for pixels located in the middle of the dam (Points 1 and 2). These values are also detected in the target image (**Fig. 4B**). For σ0 values between 0.009 and 0.012, backscattering from the sand dunes on the bed of the main watercourse is expected (Points 9 to 12). For σ0 values between 0.012 and 0.0135, the water mass limits are included (Points 13 to 17). Values of σ0 between 0.062 to 0.067 (Points 20 to 23) attest to a smooth surface and the image are dark. By increasing this threshold (σ0 > 0.138) (Points 7,

8, 18 and 19), dry pixels of bare soil in watercourses begin to be included. Once the watercourse is fed, these pixels give values of σ0 around 0.0034 (Point 7, **Fig. 4B**).

Sabkhas are mainly found in inland desert basins and nearby coasts with semi-arid and arid climates. These depressions mark the desert landscape of southern Morocco. Most of them cover less than 5 square kilometers. They are seasonally covered by water that gradually seeps into the underlying aquifers or evaporates, causing salt and sediment deposits to form at the bottom and edges, and shaping their surface properties. Deposited sediments are exposed to shrinkage and drying, and the clay layers contained control changes in sediment volume, as clay-rich layers cause deep sediment shrinkage and drying during long-term droughts.

Changes in their surface area are controlled by changes in groundwater supply and evapotranspiration. These regions show low backscatter on the radar signal from the dry period and, on the contrary, very high backscatters of the radar signal on the image taken during the wet period (Point 25, **Fig. 4A & 4B**). This suggests that the sensitivity of the radar backscatter coefficient to salinity is influenced by moisture content. The strong dependence of the backscatter coefficient on salinity for low humidity values is an important result for applications involving the detection of low water resurgence, and confirms the work of Lasne et al, (2009).
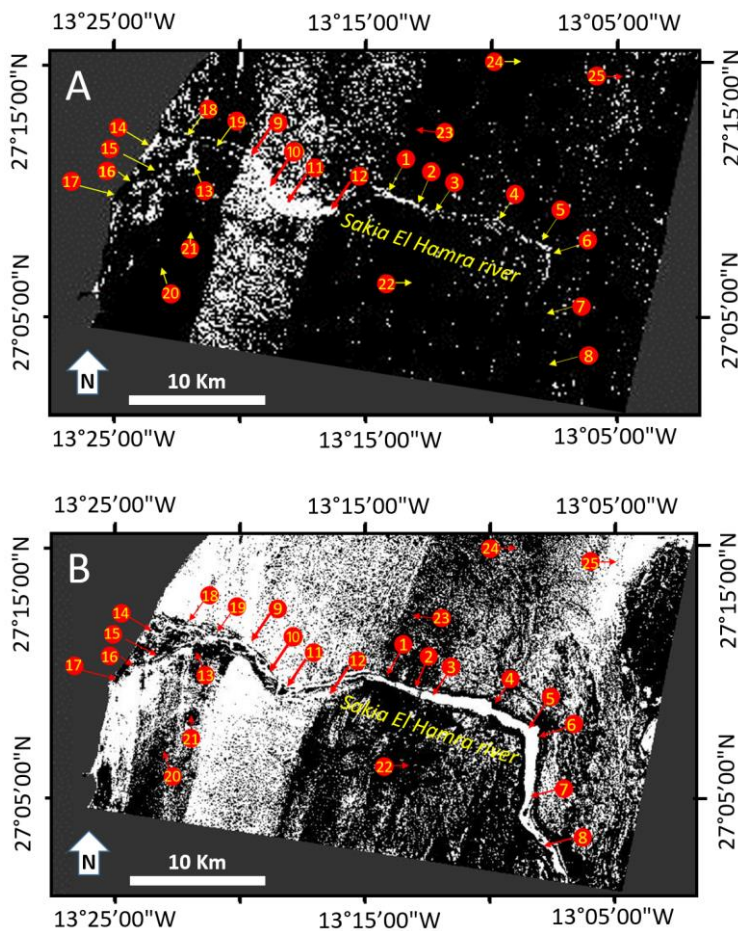
Fig. 4. Position of points with σ0 values in the filtered and geocoded reference image (**A**) and after flood event (**B**) of the study area.

5. INDEX ANALYSIS

Fig. 5 displays the outcomes of the index analysis on the Google Earth image (A) the corresponding NDFI image and (B) the resulting NDFVI image. The blue color of the NDFI image is the water bodies that flood the city of Laayoune (σ0 is around -0.93), in addition to the rivers that find their main beds under the moving sand dunes (σ0) (**Fig. 5A**). The same map reports water bodies on bare soil. Pixels take on σ0 values between -0.33 and 0.55. These pixels can be removed from the final maps, which is generally appropriate except in proximity to flooded areas where they may need to be included in the final flood map. The dilation filter helps mitigate this potential error, which remains within acceptable limits. On sand dunes, water bodies are barely distinguishable and σ0 is around -0.20. This supports the idea that dunes fossilize impermeable layers and recharge water to deep aquifers.
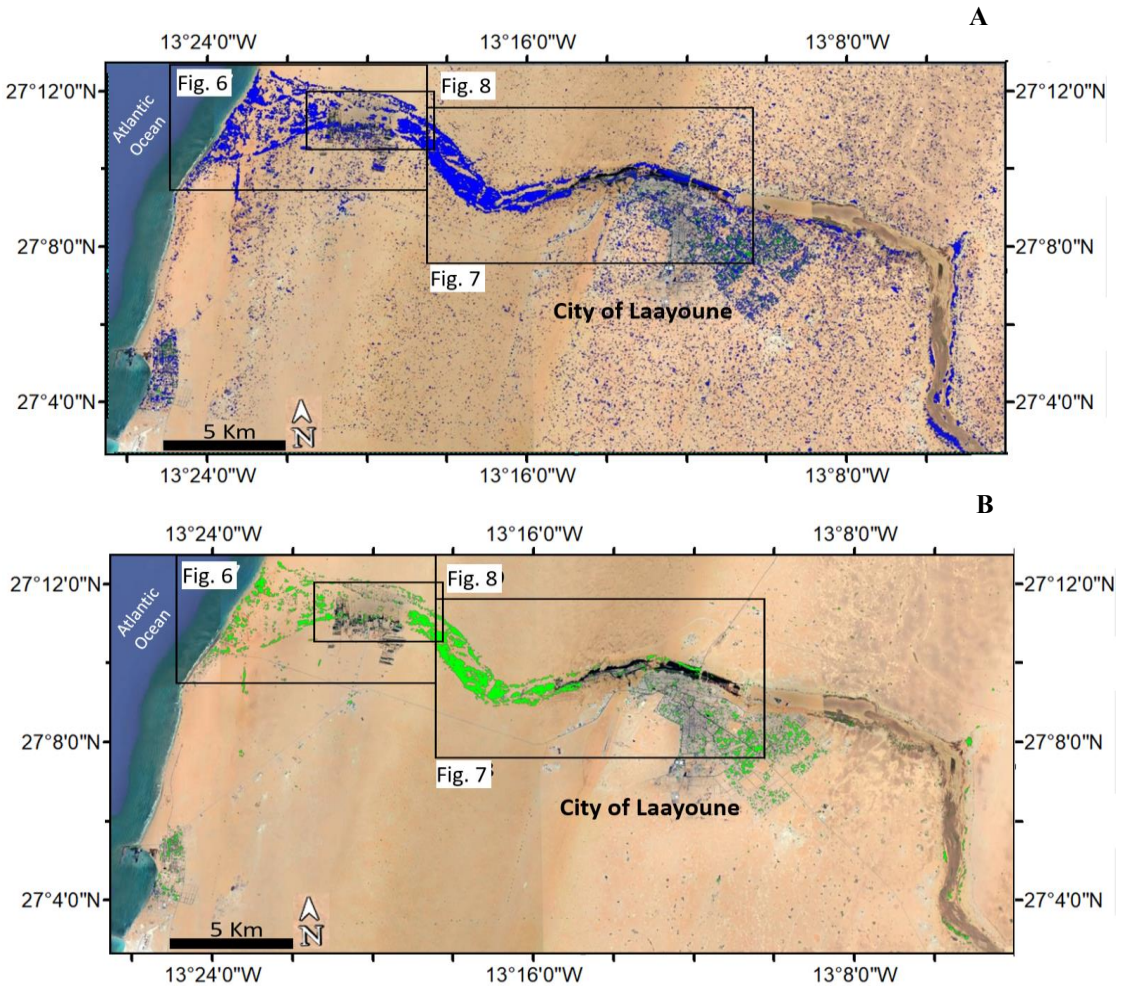
Fig. 5. Successively resulting analysis of NDFI and NDFVI on Google-Earth image of the study area (frames show positions of **Fig. 6, 7 and 8**).

The findings exhibit strong agreement with flooded areas identified by Hakdaoui et al., (2019) through their analysis of multi-spectral data in the same region. These researchers utilized four spectral indices (Normalized Difference Water Index "NDWI", Normalized Difference Moisture Index "NDMI", Normalized Difference Drought Index "NMDI", and Albedo "Al"), followed by

change detection using diachronic images data from Sentinel-2 MSI and Landsat-8 OLI acquisitions before and after the event. Their study underscores the value of integrating diverse sensor data for dynamic flood mapping purposes.

Fig. 5B illustrates the outcome of the NDFVI index analysis. Pixels aggregate prominently around the city, along the primary watercourse to the east, and at the river mouth, constituting more than 95% of all pixels classified as shallow water in short vegetation. In other areas, these pixels are scarcely discernible on the image.

6. RESULTS

Fig. 6 zooms in on a small area of the watercourse west of the town of Laayoune, where shallow water and short vegetation were detected by the NDFI and NDFVI indices. This is a time series of images from Google Earth referenced from the winter period from December 2010 to April 2023. The presence of bodies of stagnant water can be observed in numerous closed, endorheic depressions, generally limited by reliefs shaped by sand dunes. The latter occupy the route of the watercourse which is usually dry until the flood period. Depressions come from the dislocation of an organized hydrographic network, by capture, by exhaustion of flow or by drying out of the climate. They therefore depend on the climate and its variations over time. This zone gives an idea of the rate of accumulation of sand in depressions and lowlands. The rainy events that occurred in December 2016 were unusual and returned the main watercourse to its original path. This perfectly illustrates the interaction between aeolian and fluvial processes through the accumulation of sand resulting from an aeolian and fluvial process during dry conditions alternating with humid climatic episodes and the return of the fluvial system. Wind activities have led to the formation of a variety of dunes and sand sheets which promote the concentration of groundwater in humid periods. This is due to favorable circumstances often occurring in a desert environment.
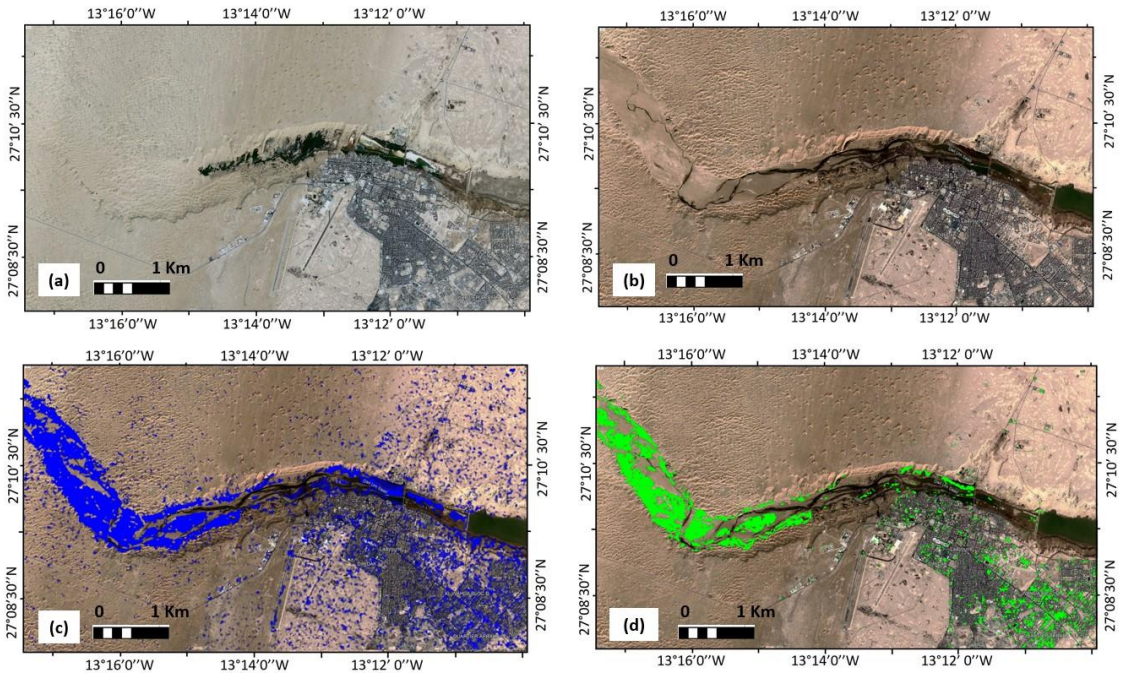
Fig. 6. Successively before (a) and after flood (b), NDFI (c) and NDFVI (d) along Sakia Al Hamra river and near Laayoune city.

The climate intervenes primarily in the specific profile of these bodies of water, which are all particular hydrological units. It regulates the abundance of rain, the primary source of water supply, and the evaporation, which counterbalances it. It also intervenes on the alternation regime between wet and dry periods. In addition to the direct contribution of rain, there are tributary contributions, diffuse runoff on the slopes and flooding in the rivers, when there is any, exsurgence and resurgence of groundwater.

Interpretation of spatial images at different scales provided the necessary indicators of the relationship between sand accumulations and fluvial processes. Sand accumulations would have been responsible for the concentration of groundwater in the substrate. Thus, the correlation between the likelihood of groundwater presence in depressions and substantial accumulations of sand emerges as a crucial consideration in the exploration of this progressively scarce resource.

Further west, near the mouth of Oued Sakia El Hamra, numerous drainage lines adjacent to the Foum El Oued aquifer were identified using NDFI and NDFI images. These dry waterways were covered in wind-blown sand. They generally reappear in sheet flood conditions with abundant surface water. Several of these large channels have small, braided streams in their layers, as revealed by enlargements of the Sentinel-1 data (**Fig. 7**). Braiding typically develops from small amounts of surface water, indicating multiple episodes of water flow. During the flood, the interior depositional basins would have accumulated significant volumes of fresh water. A large part of this water has been infiltrated in the deeper rocks under the sand. Field observations reveal that moisture starts to appear a few centimeters deep within the sand cover of shallow channels. Thus, areas that encompass large accumulations of sand may rely on vast groundwater resources.
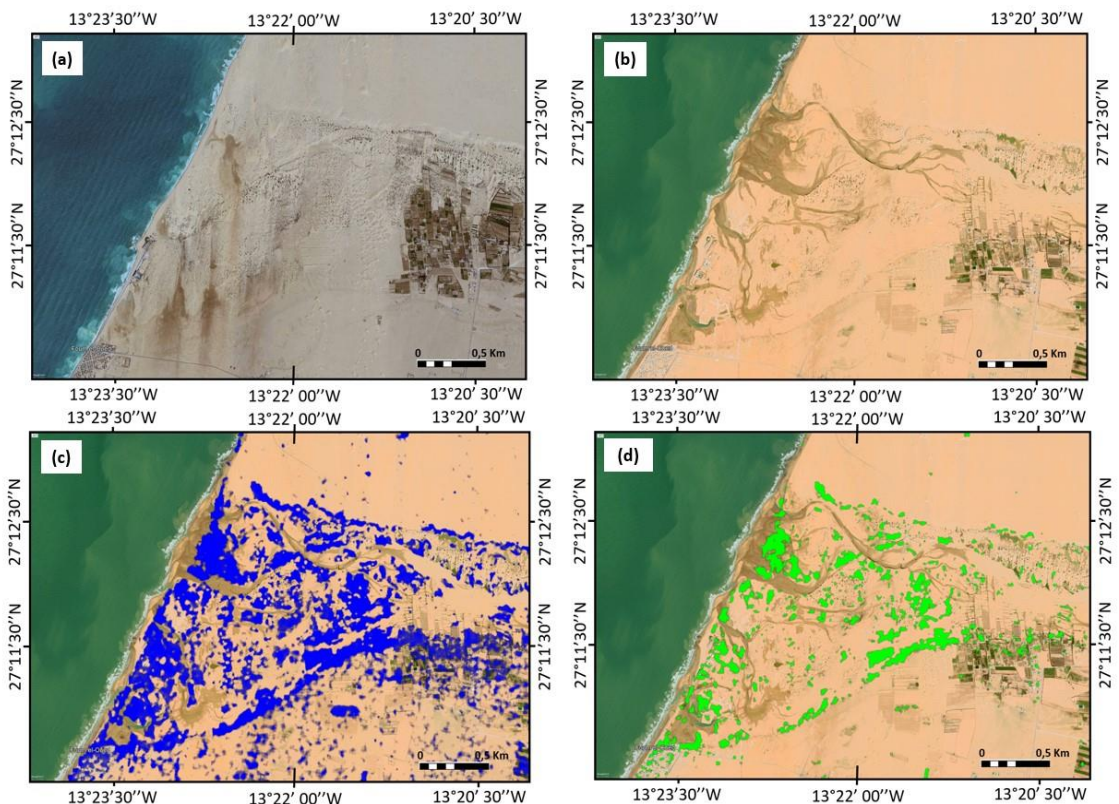
Fig. 7. Successively before (a) and after flood (b), NDFI (c) and NDFVI (d) at the mouth of Oued Sakia El Hamra in contact with the Atlantic Ocean.

In the collective imagination, the desert is synonymous with aridity. Researchers estimate the probability of urban flooding that could cause damage and threaten lives is less than 10% and the risk of flooding is considered very low or non-existent. To this end, many constructions are installed in areas prone to flooding. Due to its relatively flat topography, gentle slopes, and clay-rich layers, the torrential rains resulted in significant economic losses and material damage.
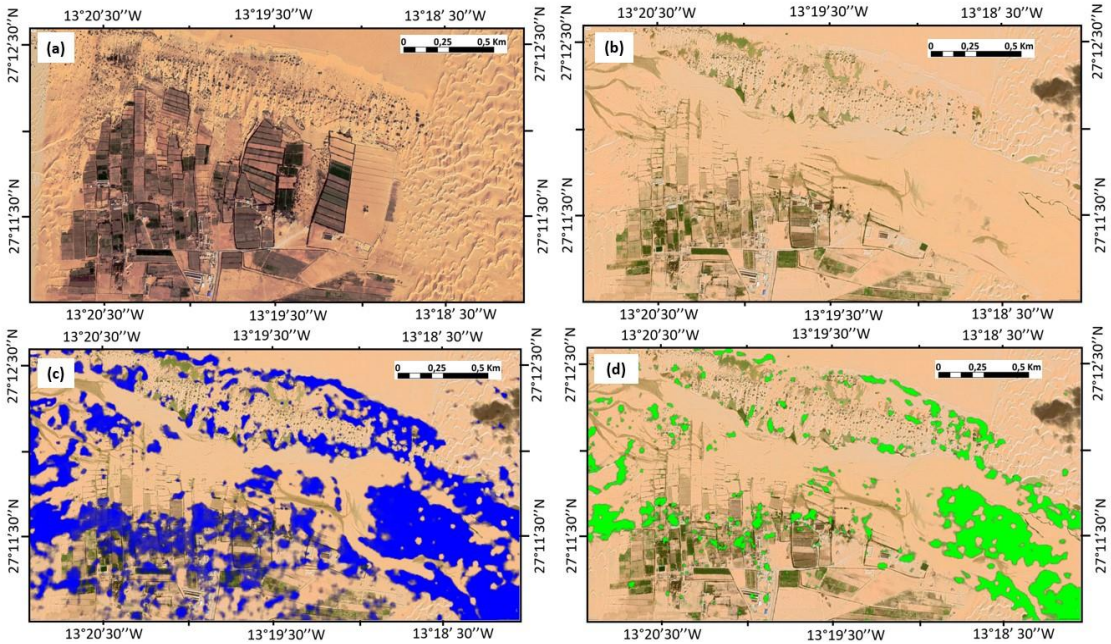

Fig. 8. Successively before (a) and after flood (b), NDFI (c) and NDFVI (d) showing flood damage near the city of Laayoune.

7. CONCLUSION

In this study, we applied a mapping methodology based on statistical analysis of time series for flood mapping in the Saharan environment. We used Sentinel-1 data and processed them with methods based on open-source software easily achievable also by the community of non-specialized experts in remote sensing of the flooded area in 2016, the city of Laayoune, southern Morocco (**Fig. 8**). The C band of Sentinel-1, operating at a wavelength of 5.7 cm, has a high sensitivity to surface water content as observed by radar. This band was used to measure soil moisture and flood detection. In the filtered and geocoded reference images, the smoothest surfaces appear very dark (Bragg scattering), attesting to the fact that the penetration depth of radar waves in this bare and dry soil can be quite deep. The rough surfaces appear very bright, corresponding to a corridor of moving sand dunes. These have different geometric and dielectric properties, with backscattering on rough surfaces. With the same textural properties on the soil, images taken after the rainy flood period show a strong backscattering of the radar signal. This confirms first that the dielectric properties of the soil depend on its water content, that the backscattering coefficient measured by radar instruments increases with increasing soil moisture and that the optimal threshold ranges for SAR data used in this analysis, can be the outline of a classification of flooded areas in desert context.

Two indices are proposed for flooded area mapping: the Normalized Difference Flood Index (NDFI) allowed the mapping of open water and the Normalized Difference Flood Index in Vegetation (NDFVI) for mapping shallow water in short vegetation and generating flood maps. These methods have made it possible to highlight the course of the watercourse, which is usually dry until flood periods as well as the stagnant water bodies in many closed depressions. The position of the

depressions show that they come from the dislocation of an organized hydrographic network, by capture, by exhaustion of the flow or by drying of the climate. This also gives an idea of the rate of accumulation of sand in the depressions and lowlands. The accumulations of sand would have been responsible for the concentration of groundwater in the substrate. This perfectly illustrates the interaction between wind and fluvial processes through the accumulation of sand resulting from a wind and fluvial process during dry conditions alternating with humid climatic episodes and the return of the fluvial system. This analysis can be generalized for the Saharan regions where wind activities and the return of the fluvial system interact during flood periods for the purpose of modeling, which is highly requested by the intervention organizations concerned, managers and scientists. In these regions, the correlation between the probability of groundwater in depressions and substantial sand accumulations appears to be a crucial consideration in the exploration of progressively scarce water resources.

REFERENCES

Alsdorf DE., Rodríguez E., & Lettenmaier DP., (2007) Measuring Surface Water from Space. *Reviews of Geophysics*, 45, DOI:10.1029/2006RG000197.

Álvarez-Mozos J., Casalí J., González-Audícana M., & Verhoest N.E.C. (2005) Correlation between Ground Measured Soil Moisture and RADARSAT-1 Derived Backscattering Coefficient over an Agricultural Catchment of Navarre (North of Spain). *Biosystems Engineering,* 92, 119–133, DOI: 10.1016/j.biosystemseng.2005.06.008.

Amimi T., Ouhnine R., Chao J., Elbelrhiti H., & Koffi AS. (2017) Potentialités de l'écotourisme et géotourisme aux provinces de Tantan, Tarfaya et Layoune (Sahara Atlantique marocain). *European Scientific Journal*. Edition Vol.13, No.15 ISSN: 1857- 7881 (Print) e - ISSN 1857- 7431.

Arnesen AS., Silva TSF., Hess LL., Novo EMLM., Rudorff CM., Chapman BD., & McDonald KC., (2013) Monitoring Flood Extent in the Lower Amazon River Floodplain Using ALOS/PALSAR ScanSAR Images. *Remote Sensing of Environment.* 130, 51–61, DOI: 10.1016/j.rse.2012.10.035.

Borghys D., Yvinec Y., Perneel C., Pizurica A., & Philips W., (2006) Supervised Feature-Based Classification of Multi-Channel SAR Images. *Pattern Recognition Letters*. 27, 252–258, DOI: 10.1016/j.patrec.2005.08.006.

Cian F., Marconcini M., Ceccato P., (2018) Normalized difference flood index for rapid flood mapping: Taking advantage of EO big data. *Remote Sens. Environ*. 209, 712–730.

Dellepiane S., Bo G., Monni S., & Buck C., (2000) SAR Images and Interferometric Coherence for Flood Monitoring. In Proceedings of the IGARSS 2000. *IEEE 2000 International Geoscience and Remote Sensing Symposium*. Taking the Pulse of the Planet: The Role of Remote Sensing in Managing the Environment. Proceedings (Cat. No.00CH37120). Vol. 6, pp. 2608–2610 vol.6.

Dellepiane SG., & Angiati E., (2012) A New Method for Cross-Normalization and Multitemporal Visualization of SAR Images for the Detection of Flooded Areas. *IEEE Transactions on Geoscience and Remote Sensing*. 50, 2765–2779, DOI:10.1109/TGRS.2011.2174999.

Di Baldassarre G., Schumann G., Brandimarte L., & Bates P., (2011) Timely Low Resolution SAR Imagery To Support Floodplain Modelling: A Case Study Review. *Surv Geophys* 2011, 32, 255–269, DOI:10.1007/s10712-011-9111-9.

Dong Y. B., Li M. J., Sun Y., (2013) Research on Threshold Segmentation Algorithms. Advanced Materials Research, DOI:10.4028/www.scientific.net/AMR.860-863.2888.

ESA. (2022b). Mission ends for Copernicus Sentinel-1B satellite. [Online]. ESA. Last Updated: 3 August 2022. Available at: https://www.esa.int/Applications/Observing_the_Earth/Copernicus/Sentinel1/Mission_ends_for_Copernic [Accessed 12 August 2022].

Franceschetti G., & Lanari R. (1999) Synthetic Aperture Radar Processing. Taylor & Francis Group, 324 pp, ISBN 9780203737484, https://doi.org/10.1201/9780203737484

Hakdaoui S., Emran A., Pradhan B., Lee C.-W., & Nguemhe Fils, S.C., (2019) A Collaborative Change Detection Approach on Multi-Sensor Spatial Imagery for Desert Wetland Monitoring after a Flash Flood in Southern Morocco. *Remote Sens.* 2019, 11, 1042. https://DOI.org/10.3390/rs11091042

Henshaw, A.J.; Gurnell, A.M.; Bertoldi, W.; Drake, N.A. An Assessment of the Degree to Which Landsat TM Data Can Support the Assessment of Fluvial Dynamics, as Revealed by Changes in Vegetation Extent and Channel Position, along a Large River. *Geomorphology* **2013**, *202*, 74–85.

Horritt M.S., (1999) A Statistical Active Contour Model for SAR Image Segmentation. *Image and Vision Computing* 1999, 17, 213–224, DOI:10.1016/S0262-8856(98)00101-2.

Horritt M.S., Mason D.C., & Luckman A.J., (2001) Flood Boundary Delineation from Synthetic Aperture Radar Imagery Using a Statistical Active Contour Model. *International Journal of Remote Sensing* 2001, 22, 2489–2507, DOI:10.1080/01431160116902.

Hostache R., Matgen P., & Wagner W., (2012) Change Detection Approaches for Flood Extent Mapping: How to Select the Most Adequate Reference Image from Online Archives? *International Journal of Applied Earth Observation and Geoinformation* 2012, 19, 205–213, DOI: 10.1016/j.jag.2012.05.003.

IPR. (2022). Roughness and Brightness of SAR Image. [Online]. IPR: Quick Image Processing Research Guide. Last Updated: 5 February 2022. Available at: https://www.gofastresearch.com/2022/02/roughness-and-brightness-of-sar-image.html [Accessed 10 August 2022].

Lasne Y., Paillou P., Freeman A., Farr T., McDonald K., Ruffié G., Malezieux J.M., & Chapman B., (2009) Study of hypersaline deposits and analysis of their signature in airborne and spaceborne SAR data: Example of Death Valley, California. *IEEE Trans. Geosci. Remote Sens.* 2009, 47, 2581–2598. [Google Scholar] [CrossRef]

Liew S.C., (2001). SAR Images. [Online]. CRISP: Centre for Remote Imaging, Sensing and Processing. Available at: https://crisp.nus.edu.sg/~research/tutorial/sar_int.htm [Accessed 10 August 2022].

Long S., Fatoyinbo T.E., & Policelli F., (2014) Flood Extent Mapping for Namibia Using Change Detection and Thresholding with SAR. Environ. Res. Lett. 2014, 9, 035002, DOI:10.1088/1748-9326/9/3/035002.

Lu J., Giustarini L., Xiong B., Zhao L., Jiang Y., & Kuang G., (2014) Automated Flood Detection with Improved Robustness and Efficiency Using Multi-Temporal SAR Data. *Remote Sensing Letters* 2014, 5, 240–248, DOI:10.1080/2150704X.2014.898190.

Manjusree, P., Prasanna Kumar, L., Bhatt, C.M., Rao G.S., & Bhanumurthy V., (2012) Optimization of threshold ranges for rapid flood inundation mapping by evaluating backscatter profiles of high incidence angle SAR images. *Int J Disaster Risk Sci* **3**, 113–122. https://doi.org/10.1007/s13753-012-0011-5.

Martinez J.-M., & Le Toan T., (2007) Mapping of Flood Dynamics and Spatial Distribution of Vegetation in the Amazon Floodplain Using Multitemporal SAR Data. *Remote Sensing of Environment* 2007, 108, 209–223, DOI: 10.1016/j.rse.2006.11.012.

Martinis S., Twele A., & Voigt S., (2011) Unsupervised Extraction of Flood-Induced Backscatter Changes in SAR Data Using Markov Image Modeling on Irregular Graphs. *IEEE Transactions on Geoscience and Remote Sensing* 2011, 49, 251–263, DOI:10.1109/TGRS.2010.2052816.

Mason D.C., Horritt M.S., Dall'Amico J.T., Scott T.R., & Bates P.D., (2007) Improving River Flood Extent Delineation from Synthetic Aperture Radar Using Airborne Laser Altimetry. *IEEE Transactions on Geoscience and Remote Sensing* 2007, 45, 3932–3943, DOI:10.1109/TGRS.2007.901032.

Mazel D., Fernez M., Meunier C., (2019) Protection contre les inondations du projet de la Technopole de Foum El Oued (Maroc), une évidence ?. Digues Maritimes et Fluviales de Protection contre les Inondations, 2019 Version finale DOI : 10.5281/zenodo.2558162.

Mertes L. A. K., (2002) Remote Sensing of Riverine Landscapes -" Freshwater Biol., Vol. 47, No. 4, 2002, 799-816.

Monographie de la région Laayoyne-Sakia-El Hamra. Direction Régionale de Laayoune. Haut-Commissariat au Plan. 2020. https://www.hcp.ma/region-laayoune/attachment/2258177/

Nico G., Pappalepore M., Pasquariello G., Refice A., & Samarelli S., (2000) Comparison of SAR Amplitude vs. Coherence Flood Detection Methods - A GIS Application. *International Journal of Remote Sensing* 2000, 21, 1619–1631, DOI:10.1080/014311600209931.

Pierdicca N., Pulvirenti L., Chini M., Guerriero L., & Candela L., (2013) Observing Floods from Space: Experience Gained from COSMO-SkyMed Observations. Acta Astronautica 2013, 84, 122–133, DOI: 10.1016/j.actaastro.2012.10.034.

Pulvirenti L., Pierdicca N., Chini M., & Guerriero L., (2011) An Algorithm for Operational Flood Mapping from Synthetic Aperture Radar (SAR) Data Using Fuzzy Logic. *Natural Hazards and Earth System Sciences* 2011, 11, 529–540, DOI:10.5194/nhess-11-529-2011.

Pulvirenti L., Pierdicca N., Chini M., & Guerriero L., (2013) Monitoring Flood Evolution in Vegetated Areas Using COSMO-SkyMed Data: The Tuscany 2009 Case Study. *IEEE Journal of Selected Topics in Applied Earth Observations and Remote Sensing* 2013, 6, 1807–1816, DOI:10.1109/JSTARS.2012.2219509.

Ratschiller L.K., (1970) Lithostratigraphy of the Northern Sahara Spanisch. Memoria Museo Tridentino Di Scienze Naurali Trento, 1970, 18, 9–78.

Rosenqvist A., Perez A., & Olfindo N., (2018). A Layman's Interpretation Guide to L-band and C-band Synthetic Aperture Radar data. Comittee on Earth Observation Satellites: Washington, DC, USA.

Schumann G., Bates P.D., Horritt M.S., Matgen P., & Pappenberger F., (2009) Progress in Integration of Remote Sensing–Derived Flood Extent and Stage Data and Hydraulic Models. *Reviews of Geophysics* 2009, 47, DOI:10.1029/2008RG000274.

Schumann G.J.-P., & Moller D.K., (2016) Microwave Remote Sensing of Flood Inundation. Physics and Chemistry of the Earth, Parts A/B/C 2015, 83–84, 84–95, DOI: 10.1016/j.pce.2015.05.002.

Smith L.C., (1997) Satellite Remote Sensing of River Inundation Area, Stage, and Discharge: A Review. Hydrol. Process., 11 (10) (1997), 1427-1439, 10.1002/(Sici)1099-1085(199708)11:10<1427: Aid-Hyp473>3.0. Co;2-s 1997.

Tiepolo M., (2014) Flood Risk Reduction and Climate Change in Large Cities South of the Sahara. In Climate Change Vulnerability in Southern African Cities: Building Knowledge for Adaptation; Macchi, S., Tiepolo, M., Eds, Springer Climate; *Springer International Publishing: Cham*, 2014; pp. 19–36 ISBN 978-3-319-00672-7.

White I., (2013) Water and the City: Risk, Resilience and Planning for a Sustainable Future; Routledge, 2013; ISBN 978-1-136-94749-0.

Xue F., Gao W., Yin C., Chen X., Xia Z., Lv Y., Zhou Y., & Wang M., (2022) Flood Monitoring by Integrating Normalized Difference Flood Index and Probability Distribution of Water Bodies. *IEEE Journal of Selected Topics in Applied Earth Observations and Remote Sensing* 2022, 15, 4170–4179, DOI:10.1109/JSTARS.2022.3176388.

THE CORRELATION OF LIMESTONE PHYSICAL/MECHANICAL PROPERTIES AND KARST GEOMORPHOLOGY, KARANGASEM AREA, PALIYAN DISTRICT, GUNUNGKIDUL REGENCY, INDONESIA

Sari Bahagiarti KUSUMAYUDHA[1] , Gunawan NUSANTO[2], Tuti SETYANINGRUM[3] ,
Heti HERASTUTI[3], A.Y.N. WARSIKI[4] and Istiana RAHATMAWATI[4]*

ABSTRACT

Karangasem Village, Paliyan District, Gunungkidul Regency, Indonesia is located in the Gunungsewu area, which has been designated as a Global Geopark by UNESCO (UGG = Unesco Global Geopark). This village has an interesting natural landscape, in the form of karst geomorphology which is reflected in the presence of dome and conical hills, dolines, uvala, locva, and caves, which can be promoted as one of the geosites in the Gunungsewu geopark. One aspect of a geopark is science. Thus, geomorphology in the Karangasem area needs to be elaborated from a scientific perspective. The aim of this study is to characterize the relationship between geomorphology and limestone physical/mechanical properties that make up this landform. The methods applied are surface mapping, geomorphological and petrological assessment, physical/mechanical properties testing, and correlation analysis. The research results show that there are three units of lithology, namely reef limestone unit, bedded limestone unit, and marl unit. The three rock units are characterized by their different values of unified compressive strength (UCS), Schmidt hammer hardness, and Mohs scale hardness. Landforms of the study area can be classified into karst hills, karst undulating, and karst plain. This geomorphology is very strong correlated with physical/mechanical properties and lithological units, with correlation coefficient (R^2) > 0.9. The strong, hard, and resistant rocks form rough relief, while weak, soft, and not resistant rocks produce smooth relief.

Key-words: *Geomorphology, Karst, Geopark, Limestone, Physical/Mechanical properties, Correlation*

1. INTRODUCTION

Karangasem in one of the villages included in the Paliyan District, Gunungkidul Regency, Indonesia. This area is located in the Gunungsewu karst range, which has been designated as a Global Geopark by UNESCO (UGGps = Unesco Global Geopark). This village has an interesting natural landscape, in the form of karst geomorphology which is reflected in the presence of domes, cones, dolines, uvala, polje, locva, and caves (Ford & Williams, 1989, White, 1988). This exotic scenery is very potential to be developed and promoted as one of the geosites in the Gunungsewu geopark area.

A geopark should provide scientific educational aspect, especially from earth sciences points of view. This is intensely relevant since education roles as one of the three principal pillars of UGGps (Henriques & Brilha, 2017; Catana & Brilha, 2020; Lakatos et al., 2023; Nyulas et al., 2024). Moreover, in the Karangasem area, there are specific landscape features, namely karst, which is a valuable subject to explore its scientific aspects for academic purposes (Masilela & Beckedahl, 2022).

----

[1]Geological Engineering Department, FTM, Universitas Pembangunan Nasional Veteran Yogyakarta, Indonesia; corresponding author* saribk@upnyk.ac.id

[2]Mining Engineering Department, FTM, Universitas Pembangunan Nasional Veteran Yogyakarta, Indonesia, gunawan.nusanto@upnyk.ac.id

[3]Agrotechnology Department, FP, Universitas Pembangunan Nasional Veteran Yogyakarta, Indonesia, Setyaningrumtuti@gmail.com

[4]Management Department, FEB, Universitas Pembangunan Nasional Veteran Yogyakarta, Indonesia, hetti.herastuti@upnyk.ac.id, warsiki@upnyk.ac.id

It is supposed that there a relationship between the forms of karst morphology and the physical/mechanical properties of the rocks that make it up. Thus, the association among geomorphology and physical rock properties in the Karangasem area needs to be elaborated from a scientific perspective.

The objectives of this study are to characterize the relationship between limestone physical/mechanical properties that make up the landform and karst geomorphology of the area. What is meant by physical/mechanical properties in this study is unified compressive strength (UCS), Schmidt hammer rebound hardness (SH), and Mohs scale scratches hardness (MS) of the rocks.

Location of the study area is in the coordinate of X: 445500 – 451000 E, and Y: 9118000 – 9109000 S, or latitude of 107°26'30"– 107°50'5.5" E, and longitude of 82°01'21" – 82°06'21" S. Administratively the study area belongs to Paliyan district, Gunung Kidul regency, Yogyakarta Special Region, can be reach easily, about 120 km distant from Yogyakarta city by riding either motorcycle or mobile car (**Fig. 1**).
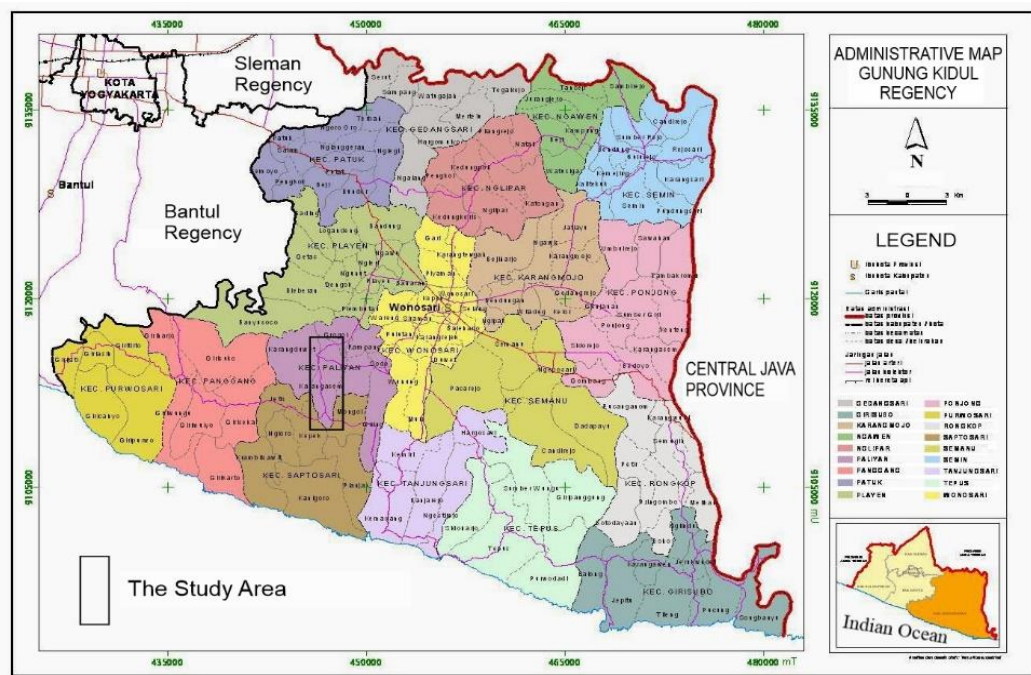
Fig. 1. Location map of the study area.

2. STUDY AREA

2.1. Geography and Geology

Karangasem village have an area of 1,268 Ha (Anonymous, 2022; Anonymous, 2018). Physiographically, Karangasem village, is situated in the Southern Zone of the Southern Mountains of Western East Java (Van Bemmelen, 1949). This zone is known as *Gunungsewu* (Javanese: A thousand mountains). It is a karst topography with a height ranges 120 m - 300 meters above sea level. As mentioned above, Gunungsewu has been designated as a UNESCO Global Geopark in 2015 (Cahyadi, 2017). It is a classic tropical karst that is built by limestone formations. In relation with that, the karst features of this area need to be protected by such a geoscientific study and geoconservation activities (Kubalíková, 2016). Karangasem Village has a tropical climate, the average rainfall from the years 2010 to 2022 is 1,954.43 mm/year with an average number of rainy

days is 130 days per year. Wet months are 7 months, while dry months are around 5 months. The average daily air temperature is 27.7°C, the minimum temperature is 23.2°C and the maximum temperature is 32.4°C. The relative humidity of the air ranges from 80%−85% (https://id.wikipedia.org/wiki/Kabupaten_Gunungkidul).

The Gunungsewu karst topography shows orientation axis of west-east, with a height difference of 10 m to more than 100 m, comprises about 45,000 small and large hills of 50 m - 300 m diameter (Kusumayudha, 2005). Limestone that experiences karstification is characterized by the presence of dissolution cavities, caves, and underground drainage systems. On the surface, there can be found many closed depressions (dolines) and dome-shaped or cone-shaped hills (cone karst) (**Fig. 2**, **Fig. 3**). If the depressions in this karst are covered with an impermeable layer, they will be able to hold water, forming a locva. In Karangasem village there are several lakes, namely Berok Lake, Boromo Lake, Jambeanom Lake, Namberan Lake and Tongtong Lake. Limestone that experiences karstification often leaves rough and sharps rock reliefs, called lapies, or microkarst.
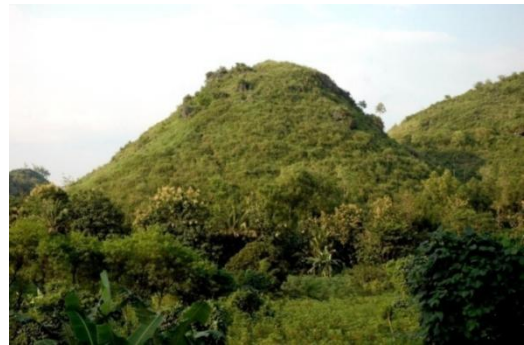
Fig. 2. Cone karst (left).   Convex cone karst (right), (Kusumayudha et al, 2018.
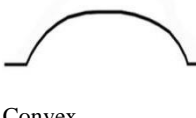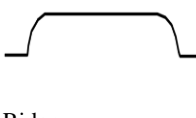
Fig. 3. Dome karst (left), Ridge karst (right), (Kusumayudha et al, 2018).

Geologically, Karangasem and the surrounding area are composed of the Wonosari Formation, which consists of reef limestone and bedded bioclastic limestone, The limestone experiences karstification, which is resulted from the interaction between limestone and meteoric water over millions of years (Kusumayudha, 2018; Kusumayudha, et al, 2022). There are two (2) lithofacieses of the limestone included in *boundstone* and *packstone* of reef limestone, and *wackestone* of bedded limestone, deposited from the middle Miocene to the late Miocene epoch. Limestone has a main mineralogical composition consisting of more than 90% calcite ($CaCO_3$), and dolomite ($CaMg(CO_3)_2$). The distribution of the lithofacies is relatively northwest - southeast, with geological tructure shows a homoclinic with an inclination of less than 15°, to the south and southwest (Kusumayudha, 2018).

2.2. Geomorphology

Geomorphologically, the study area displays a hilly karst topography, with a height difference of 10 m - 30 m, and the hills diameter ranges from 50 m - 200 m. Macro karst is found in the form of conical to dome-shaped hills, dolines, uvalas, and locvas, while micro karst and lapies which classified as exokarst are also found in the study area.

Table 1.

Model of the influence of lithologic physical-mechanical properties and geologic structures to positive relief karst morphology (Kusumayudha, et.al, 2015).

| Lithology | Morphology | | | Morphogenesis | | |
	Morphographic	Morphometric	Active morphostructure (geologic structures)	Passive morphostructure (physical properties)	Morphodynamic (exogenic processes)
Dominated by bedded limestone, grainstone and packstone	Cone	-Steep slope -Slope: 30°-45° -Relatively top sharp -Height: 30-90 m	-Joint -Thin bedded: < 1 m -Bedding plane inclination: > 5°	hard, cavernous, lapies, $\varphi = 32\text{-}50$	Karstification
Dominated by reef limestone, boundstone	Convex-cone	-Steep slope -Slope: 35°-45° -Top convex -Height: 30-70 m	-Joint -Massive, or thick bedded: > 1m -Bedding plane inclination > 5°	hard, cavernous, lapies, $\varphi = 32\text{-}50$	Karstification
Caliche limestone, wackestone	Dome (Sigmoid, Mogote)	-Steep slope -Slope: 30°-45° -Height: 20-50 m	-Joint -Massive or bedded -Relatively horizontal bedding plane: < 5°	hard, cavernous, lapies, $\varphi = 32\text{-}50$	Karstification Calichification
Caliche limestone, wackestone	Convex	-Gentle slope -Slope: 12°-20° -Height: 10-30 m	-Joint -With or without bedding plane -Relatively horizontal bedding plane: < 5°	weak, chalky, uncavernous $\varphi = 17\text{-}31$	Calichification
Bedded limestone, caliche limestone	Ridge	-Moderately inclined -To steep slope -Slope: 20°-35° -Top plane -Height: 10-30 m	-Joint -Thin bedded: < 1 m -Relatively horizontal: < 5°	hard, cavernous, lapies, $\varphi = 32\text{-}50$ Weak, chalky, uncavernous $\varphi = 17\text{-}31$	Karstification Calichification

Cone, dome and ridge shapes as modeled by Kusumayudha, et al., 2015 (**Table 1**) can be found in the Karangasem area. The karst geomorphology of Gunungsewu has been entering in the maturity

stage, marked by the intensiveness of carbonate dissolution process, resulting in the forms of caves with various ornaments such as stalactites, stalagmites, cinterflags, and flowstones. Referring to the model mentioned above (Kusumayudha, et.al, 2015), hills in the study area can be classified into cone, convex cone, and dome.

3. DATA AND METHODS

The research was applying analytical, descriptive field investigation and mapping, rock sampling, in situ rock physical testing, and laboratory rock mechanical testing. In the assessments, it utilizes two types of data, both secondary includes a variety of information from the results of existing research and studies, and primary data that were obtained through surveys, investigations, field mapping both geological and geomorphological (Korodi & Hofmann, 2016) and in situ or laboratory testing. Activities have been done including geomorphological mapping, lithological - stratigraphical identifications, and petrographic description to determine the limestone facieses. Rock sampling was also carried out for petrological and petrographical assessment, as well as 10 (ten) measurements for rock physical/mechanical properties. The method used to determine the strength of the rock, in this case limestone is unconfined compressive strength (UCS) test (Wang & Wan, 2019, Vračević, et.al, 2019). In situ physical properties testing was done by using *Schimdt hammer* for rebound hardness, and *Mohs scale* aparatus to determine the scratch hardness of the limestone (**Fig. 4, Fig. 5**). Furthermore, after UCS test has done, the UCS value was then used to estimate the value of internal friction angle using the following table (**Table 2**).

Fig. 4. Schmidt Hammer rebound chart (left) (Jumikis, 1983, Vračević, et.al, 2019), and **Fig. 5.** Mohs scale (right). (Perkins, 2020).

Compressive strength or compressive strength is the ability of rocks or materials to withstand pressure that tends to reduce their size (Bajpayee, et al., 2013). Compressive strength can also reflect the ability of rocks to withstand loads that can cause them to change shape and/or size (Goodman, 1989, Ning, et.al, 2018). Therefore, compressive strength can be used as one of the parameters in the discussion of rock geomorphology including its morphostructure (Suwarno, et.al, 2020). Another rock property taken into account in this study is the friction angle, which is defined as the slope formed between the resultant force exerted by an object and the surface on which the object rests (Goodman, 1989, Franklin & Dusseault, 1989). Of course, this will be related to how a material (rock) reacts to friction or erosion. So, this can also be used as a parameter when rocks experience friction during erosion. Rebound hardness (Schmidt) reflects the hardness of the rock surface, and the resistance of minerals and/or rocks to penetration (Goodman, 1989). On the other hand, scratch hardness is the resistance of minerals or rocks to scratches (Perkins, 2020). This is assumed to be effective in measuring the hardness of minerals/rocks to erosion. Pressure, friction, and scratches certainly influence geomorphological processes.

Table 2.
Correlation of friction angle and UCS (Mahdevari, et.al, 2020)

Rock types	Friction angle (deg.)	Applicable UCS Range (MPa)
Shale and Claystone	$\varphi = 0.090 \times UCS + 15$	10 – 80
Siltstone and Sandstone	$\varphi = 0.145 \times UCS + 25$	40 – 200
Limestone	$\varphi = 0.090 \times UCS + 33$	40 – 200

4. RESULTS AND DISCUSSIONS

Limestone Facieses and Physical/mechanical properties

Geologically, the rocks that make up the research area consist of Wonosari reef limestone units, Wonosari bedded limestone units, Kepek marl units. Referring to Dunham (1962) classification, the Wonosari reef limestone unit consists of *boundstone* and *grainstone*, while the Wonosari bedded limestone unit consists of *packsote* and *wackestone* (**Table 3**).

Tabel 3.
Description of the Gunungsewu limestone facies

| No.	Lithofacies (Dunham, 1962, Wilson & Lloyd, 1995)	Description
1	*Boundstone*	Consisting of fossil algae shells with a diameter of 3 - 7 cm and large foraminifera measuring 0.5 - 3 cm, coral, with a growing structure, contains carbonate mud <10%
2	*Grainstone*	Consisting of fossil algae shells with a diameter of 3 - 7 cm and large foraminifera measuring 0.5 - 3 cm, coral fragments, containing carbonate mud <10%
3	*Packstone*	Composed of large foraminifera fossil shells with a diameter of 0.5 - 3 cm, closed packaging, containing carbonate mud <10%
4	*Wackstone*	Consisting of fossil shells of large foraminifera with a diameter of 0.2 - 1 cm, containing between 30 and 50% granules, packed open with carbonate mud between 50 sd 70 %.
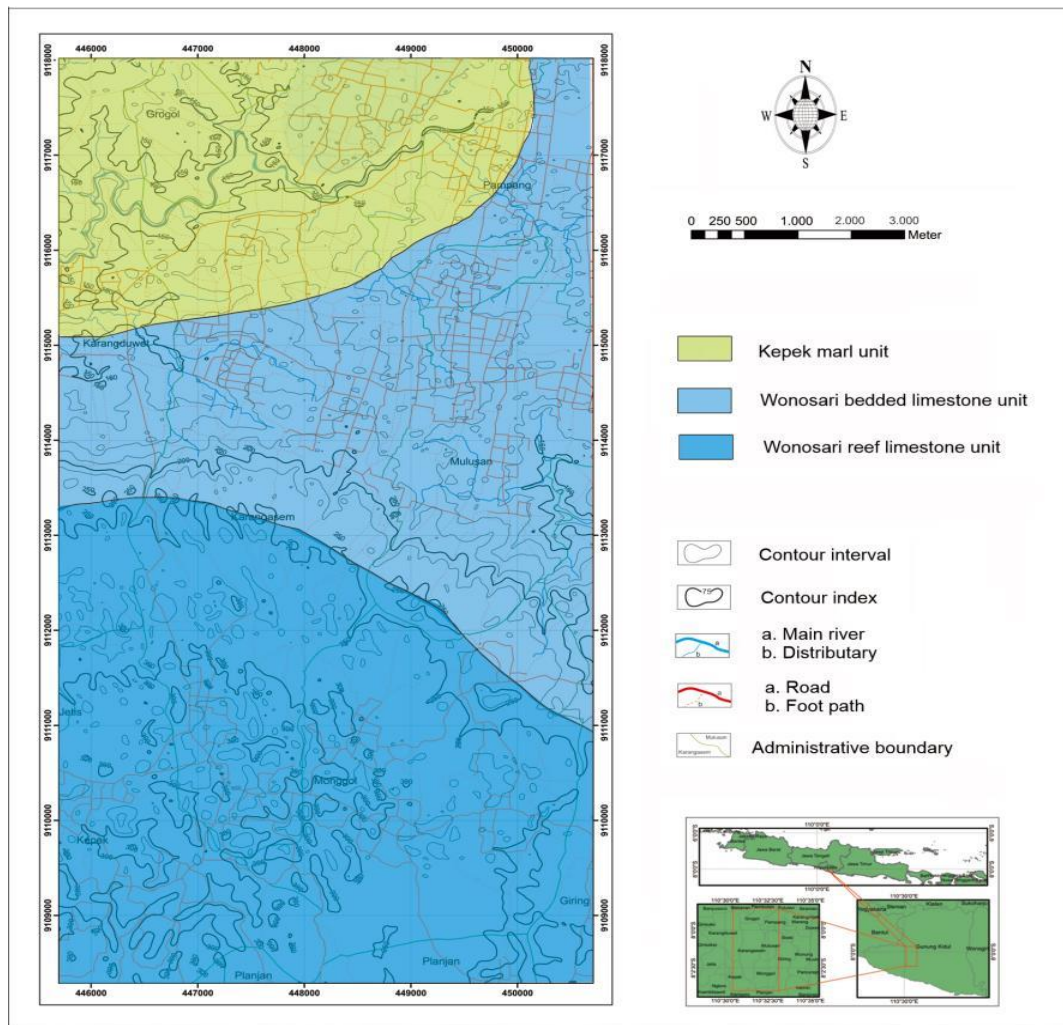
Fig. 6. Lithology distribution map of the Study Area.

The Wonosari reef limestone and Wonosari bedded limestone are Middle Miocene - Pliocene in age (Kusumayudha, 2005). The Kepek marl unit consists of marl, shale, mudstone and limestone, with an ideal layering structure. The layer thickness for each lithology ranges from 10 cm – 50 cm. The age of the Kepek marl unit is Pliocene – Pleistocene (Kusumayudha, 2005).

Stratigraphically, the relationship between the Wonosari reef limestone and Wonosari bedded limestone units is different facies, interfingering, as well as between the upper part of the Wonosari bedded limestone unit and the lower Kepek marl unit (Suyoto, 1994). The lithological distribution map of the study area is displayed in **Fig. 6.** The limestone facies in the study area, based on the results of physical-mechanical properties testing show different characteristics, between reef limestone units, layered limestone units, and marl units can be described as the following (**Table 4**).

Referring to **Table 2** (Mahdevari, et.al, 2020), the physical-mechanical properties of the rocks that make up the research area in dry conditions are as follows (**Table 4**). The results of this estimation are in accordance with the range of internal friction angle values for limestone in general, which is between 35º and 50º (Jumikis, 1983; Ning, et.al., 2018).

Table 4.

Physical and mechanical properties.

No.	Limestone Facies	Physical – Mechanical Properties							
		Compressive Strength (MPa)		Friction Angle (º)		Schmidt Hammer Hardness		Mohs Scale Hardness	
		Range	Mean	Range	Mean	Range	Mean	Range	Mean
1	Wonosari Reef Limestone unit	38-41	40.02	36.42-36.69	36.60	50-62	54.68	4-4.5	4.25
2	Wonosari Bedded Limestone unit	33-35	33.60	35.97-36.15	36.03	36-52	44.75	3.5-4.0	3.75
3	Kepek Marl unit	14 -15	14.12	27.03-27.18	27.05	20-35	25.33	2.25-2.5	2.35

Landforms

The landforms of the study area can generally can be categorized as a karst area, showing varied topography with slopes ranging from flat (0% - 2%) to very steep (40% - 140%) (**Fig. 7**). Likewise, the natural landscape varies, based on observations from North to South, including undulating karst plains in the North, karst plains in the middle, and karst hills in the South.
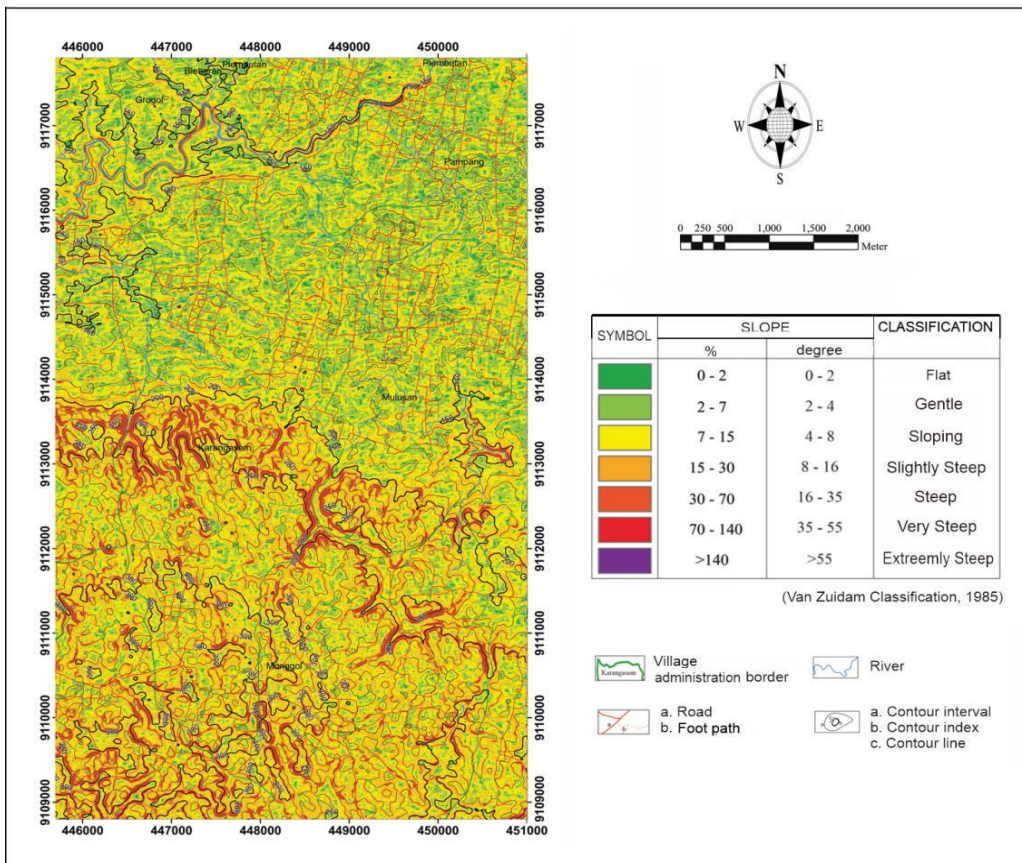

Fig. 7. Slope distribution map of the study area.

Landforms in the research area can be classified (Van Zuidam, 1983) into karst plain unit, karst undulating unit, and karst hills unit (**Fig. 8, Fig. 9**).
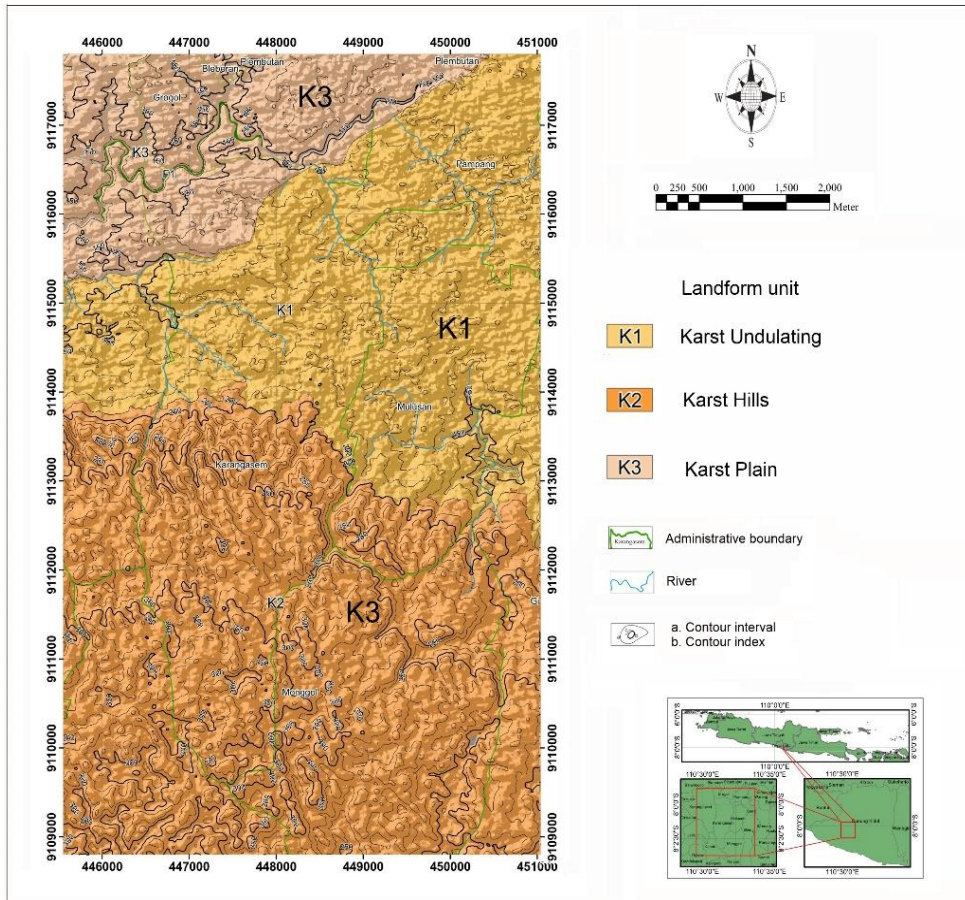
Fig. 8. Geomorphology map of the Karangasem Area.

GEOMORPHOLOGICAL ASPECTS / LANDFORM UNIT	MORPHOLOGY			MORPHOGENETICS			
	MORPHOGRAPHY	MORPHOMETRY		ACTIVE MORPHO - STRUCTURE	PASIVE MORPHO - STRUCTURE	DYNAMIC MORPHO - STRUCTURE	MORPHO - ASSOCIATION
		SLOPE	RELIEF				
		(%)	(°)				
K1 Karst - Undulating	Undulating, gently sloping	0–15	0–8	Low	Uplifting, fissures	Moderate resistance rock: bedded-limestone unit	Weathering, erosion	Karst - hills Karst- plains
K2 Karst - Hills	Hilly, conical, convex, dome	15–70	8–35	High	Uplifting, fissures	High resistance rock: reef limestone unit	Weathering, erosion	Karst - undulating
K3 Karst - Plain	Plain, relatively-flat	0–15	0–8	Low	Uplifting, fissures	Low resistance rock: marl unit	Weathering, erosion	Karst - undulating

Fig. 9. Description of the landform units.

Karst plain morphometric: has a relatively flat, sloping (0% - 15%, 0º - 8º), with a height difference of 0 to 2 meters. In this landform unit, surface flow is found, with a wide "U" shaped flow valley cross-section. The karst undulating Morphometric: has a flat to undulating slope level (0% - 15%, 0º - 8º), with a height difference of 0 to 3 meters. Plain landform unit is built bedded limestone. In this landform unit, surface flow is not found. Karst hills unit: Morphometric: has a steep slope level (15% - 70%) - sloping (8º- 35º), with a height difference of 30 -50 meters, and the developing flow pattern is multibasinal. The hills that make up this landform unit are cone-shaped, cone-shaped with a convex peak, and dome-shaped. The karst hill landform unit is composed of the Wonosari Formation reef limestone unit.

Correlation of physical rock properties and geomorphology

The Karangasem village area stretches along a relative North - South axis, as reflected in the topographic base map. The elevation in the research area ranges from 121 m to 300 m above sea level. Asmentioned previously, the geomorphology of the study area can be divided into karst hills landform unit, karst undulating landform unit, and karst plain landform unit.

As explained in the previous sub-chapter, the lithofacies in the research area consists of the Wonosari reef limestone unit, the Wonosari bedded limestone unit, and the Kepek marl unit, each with its own physical characteristics. Based on the physical and mechanical properties as shown in **Table 4**, the Wonosari reef unit has the highest UCS value compared to other lithofacies units, the Wonosari bedded limestone unit has medium physical/mechanical properties values, and the Kepek marl unit has the lowest physical/mechanical properties. Associated with the geomorphology occupied by each of these rock units, the Wonosari reef limestone unit is characterized by hilly geomorphology with cone-shaped hills, convex cones, and domes. The Wonosari bedded limestone occupies the undulating karst geomorphology, and the Kepek marl is located on the karst plain geomorphology.

Table 5.

Description of landform units in the study area

Description and Characteristics			Landform Unit		
			Karst Undulation	Karst Conical Hills	Karst Plain
Morphology	Morphometry		Undulating	Hilly, depressions	Plains, flat
	Morphometry	Slope	0%-15% (0º-8º)	15%-70% (8º-35º)	0%-15% (0º-8º)
		Relief	Low - moderate	High	Low
Morphogenesis	Active Morphostructure		Uplifting, Fissures	Uplifting, Fissures	Uplifting, Fissures
	Pasive Morphostructure		Bedded - limestone unit: packstone, wackestone	Reef -limestone unit: boundstone, grainstone	Marl, unit: marl, slate, clayston, limestone
	Dynamic Morphostructure		Weathering, erosion	Weathering, erosion	Weathering, erosion
	Morphoassociation		Karst plains, karst conical hills	Karst undulation	Karst undulation

In order to find the correlation of the physical-mechanical properties of limestone composing the landform, the maksimum, the mean, and minimum values of rock properties are plotted into line and x-y diagrams (**Fig. 10, Fig. 11, Fig. 12**).
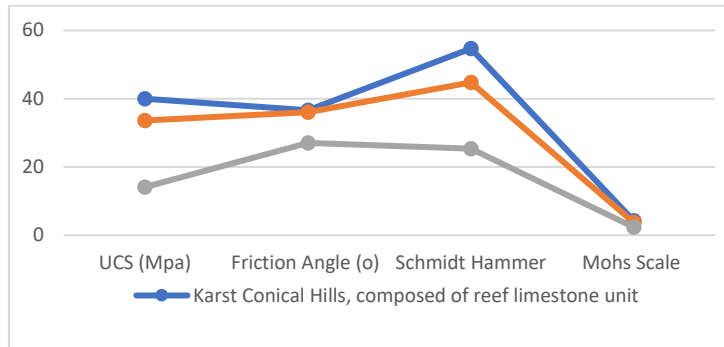
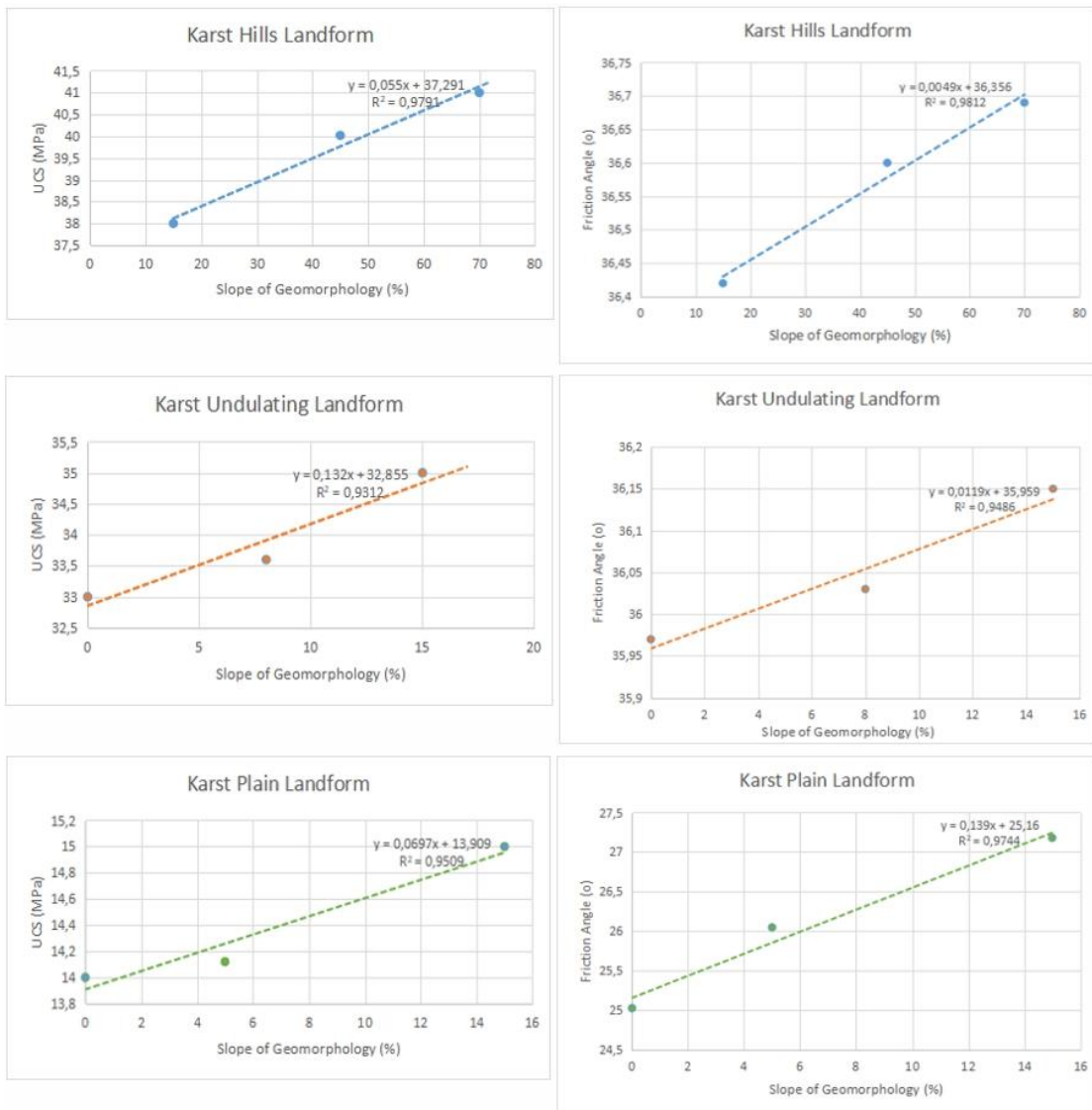**Fig..10.** Graphical plots of physical-mechanical characteristics of karst geomorphology.

Fig. 11. Correlation of unconfined compressive strength (UCS), friction angle of limestone and karst geomorphology.
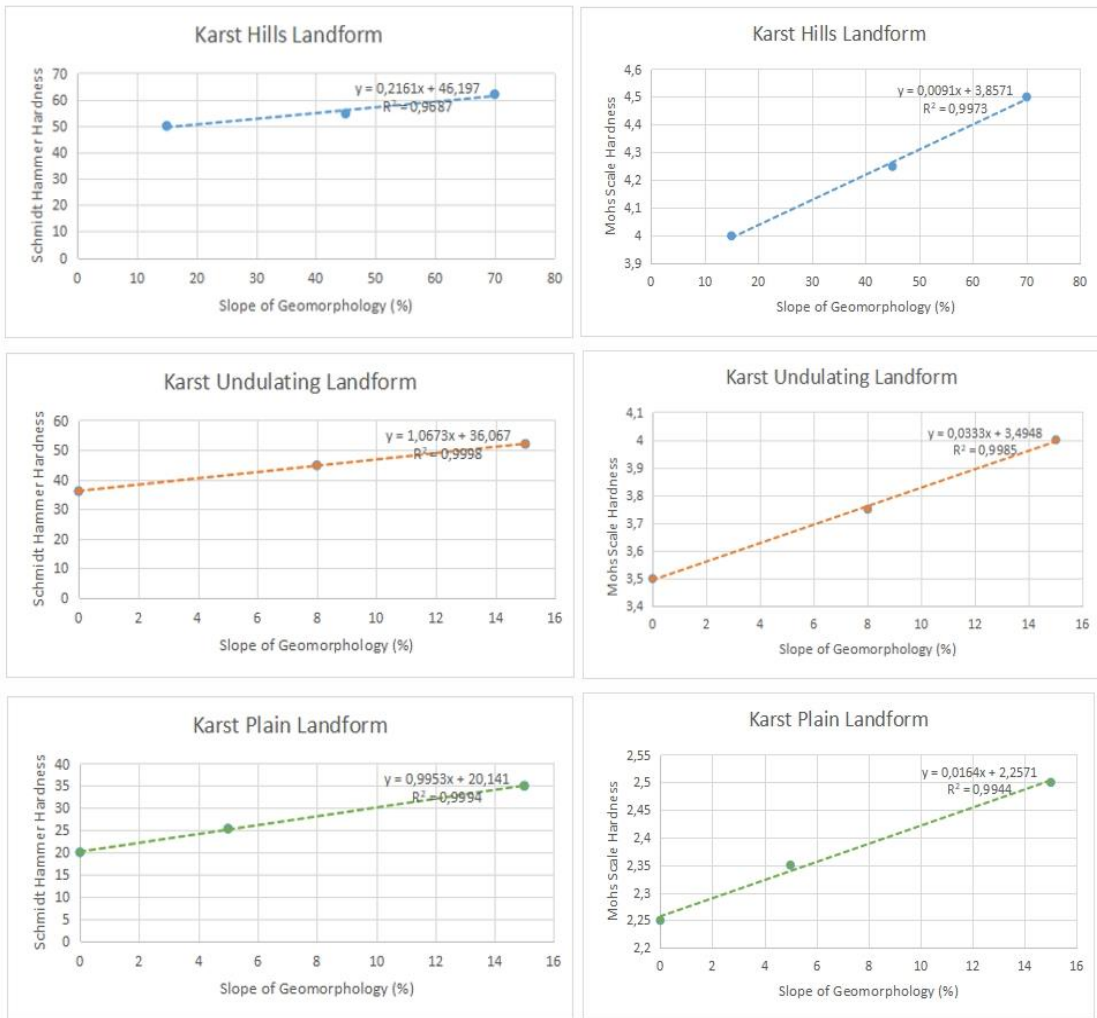
Fig. 12. Correlation of Schmidt Hammer hardness, Mohs Scale hardness of limestone and karst geomorphology.

Referring to **Table 4**, **Fig. 11** and **Fig. 12**, it can be stated that there is a very strong correlation between the physical/mechanical properties values of rocks and the landforms, with the correlation coefficient (R^2) of higher than 0.9 (Fig. 10). The higher the rock properties values (UCS, Friction angle, Schmidt hammer hardness, and Mohs scale hardness) the higher the morphological relief formed, reflected by their slope inclination distributions, and vice versa.

From the discussion above, it can be concluded that the *boundstone* and *grainstone* limestone facies which are reef limestones have the highest strength, hardness, and resistance compared to other lithofacies, forming dome and hill morphologies. *Packstone* and *wackestone* lithofacies which form layered (bedded) limestone units, have moderate strength, hardness, and resistance (intermediate) in morphology forming wavy (undulating) topography. Lithofacies of marl units, have low strength, hardness, and resistance in the exogenous process forming plain topography. Thus, this study supports that strong and hard rocks will form rough relief, while weak and soft rocks will produce smooth relief.

5. CONCLUSIONS

Some clear conclusions can be drawn from the research and discussions.

The lithology of the study area consists of Wonosari reef limestone unit, consists of *boundstone* and *grainstone*, Wonosari bedded limestone consists of *packstone* and *wackestone*, Kepek marl unit, consists of marls, shale, and sandy claystone with limestone intercalation.

Geomorphology of the study area can be classified into karst hills occupied by reef limestone unit, karst undulating compossed of bedded limestone unit, and karst plains consisted of marl unit.

The *boundstone* and *grainstone* have the highest strength, hardness, and resistance compared to other lithofacies, forming dome and hill morphologies. *Packstone* and *wackestone* lithofacies, have moderate hardness, strength, and resistance (intermediate) in morphology forming wavy (undulating) topography. Lithofacies of marl units, have low strength, hardness, and resistance in the exogenous process forming plain topography.

There is a very strong correlation with the coefficient of $R^2 > 0.9$ between physical-mechanical rock properties and karst geomorphology in the study area. The strong, hard, and resistant rocks will form rough relief, while weak, soft, and not resistant rocks will produce smooth relief.

ACKNOWLEDGEMENT

R E F E R E N C E S

Anonemous (2018) *Gunungkidul dalam Angka*. Central Statistics Agency of Gunungkidul Regency.

Bajpayee, G.S.T.S. Ellenberger, J.L. & Murphy, M.M. (2013) *Practical estimation of rock properties for modeling bedded coalmine strata using the Coal Mine Roof Rating Esterhuizen*, National Institute for Occupational Safety and Health, Pittsburgh, Pennsylvania, USA Copyright ARMA, American Rock Mechanics Association https://www.researchgate.net/publication/287380431.

Cahyadi,   A.   (2017)   *Sumberdaya   Lahan   Kawasan   Karst   Gunungsewu*, https://www.researchgate.net/publication/326114734_Sumberdaya_Lahan_Kawasan_Karst_Gunungsewu

Catana, M. M., & Brilha, J. B. (2020) The Role of UNESCO Global Geoparks in Promoting Geosciences Education for Sustainability. Geoheritage, 12(1). Scopus. https://doi.org/10.1007/s12371-020-00440-z.

Dunham, R.J. (1962) *Classification of carbonate rocks according to depositional texture. In: Classification of Carbonate Rocks* (Ed. W.E. Ham), Am. Assoc. Pet. Geol. Mem., 1, 108–121.

Ford, D.C. & Williams, P.W. (1989) *Karst Geomorphology and Hydrology*, Chapman & Hall, Springer Publisher.

Franklin, J.A. & Dusseault, M.B. (1989) *Rock Engineering*, McGraw Hill Publishing Company, New York.

Goodman, R.E. (1989) *Introduction to Rock Mechanics*, 2nd.Ed, John Wiley.

Henriques, M. H., & Brilha, J. (2017). UNESCO Global Geoparks: A strategy towards global understanding and sustainability. Episodes, 40(4), 349–355. https://doi.org/10.18814/epiiugs/2017/v40i4/017036.

Jumikis, A.R. (1983) *Rock Mechanics*, 2nd ed. Trans Tech Publications, Germany.

Korodi, E., & Hofmann, T. (2016). Historical cartographic overview and cartographic analysis of the geological map of TRANSYLVANIA by HAUER (1861). Geographia Technica, 11(1), 44–53. https://doi.org/10.21163/GT_2016.111.06.

Kubalíková, L. (2016) Geomorphological Heritage and Geoconservation in the Czech Republic. In T. Pánek & J. Hradecký (Eds.), Landscapes and Landforms of the Czech Republic (pp. 387–398). Springer International Publishing. https://doi.org/10.1007/978-3-319-27537-6_30.

Kusumayudha, S.B., Prastistho, B., Zakaria, M.F., Rahatmawati, I. , Setyaningrum, T. (2021) Rock mass rating and feassibility assessment of karst cave geo-ecotourism in Tanjungsari district, Gunungkidul regency, Yogyakarta Special Region, Indonesia, *Geographia Technica*, 16(2), 53 - 68, DOI: 10.21163/GT_2021.162.05.

Kusumayudha, S.B. Zakaria, M.F., Prastistho, B., Rahatmawati, I., Setyaningrum T. (2020) The Potencies of Cave Geo-Ecotourism Development in Tanjungsari District, Gunungkidul Regency, Yogyakarta Special Region, *LPPM UPN "Veteran" Yogyakarta Conference Series Proceeding on Political and Social Science (PSS),* 1(1), 309-322, http://proceeding.researchsynergypress.com/index.php/pss/article/view/208.

Kusumayudha, S.B. (2018) *Mengenal Hidrogeologi Karst* (*Introduction to Karst Hydrogeology*), penerbit Pohon Cahaya, Yogyakarta.

Kusumayudha, S.B., Setiawan J., Ciptahening, A.N., Dwi Septiana, P., (2015), Geomorphologic Model of Gunungsewu Karst, Gunung Kidul Regency, Yogyakarta Special Territory, Indonesia: The Role of Lithologic Variation and Geologic Structure, *Journal of Geologic Resource and Engineering*, 3(1), 1-7, DOI:10.17265/2328-2193/2015.01.001.

Kusumayudha, S.B. (2005) *Hidrogeologi Karst dan Geometri Fraktal di Daerah Gunungsewu*, Adicita Publisher, Yogyakarta.

Lakatos, J., Magyari-Sáska, Z., & Dombay, S. (2023). A GIS-Based Analysis for ecotourism suitability in a Geological Complex area of Charpathians. *Geographia Technica*, 18(1), 149–160. https://doi.org/10.21163/GT_2023.181.11.

Mahdevari, S. Moarefvand, P, Mohammadzamani, D. (2020) Considering the Effect of Block-to-Matrix Strength Ratio on Geomechanical Parameters of Bimrocks, *Geotech Geol Eng*, Springer Nature Switzerland AG, https://doi.org/10.1007/s10706-020-01304-7(0123456789.

Masilela , M. & Beckedahl, H. (2022) Karst geomorphology and related environmental problems in Southern Africa - A review, *Journal of African Earth Sciences*, 196, 104686, https://doi.org/10.1016/j.jafrearsci.2022.104686.

Ning, Z. Li, C Lu, A. Chen, X. Liu, D. & Zhu, E. (2018) Experimental Studies on the Basic Friction Angle of Planar Rock Surfaces by Tilt Test, *Journal of Testing and Evaluation,* DOI:10.1520/JTE20170308

Nyulas, J., Dezsi, Ș., Haidu, I., Magyari-Sáska, Z., & Niță, A. (2024). Attractiveness Assessment Model for Evaluating an Area for a Potential Geopark—Case Study: Hațeg UNESCO Global Geopark (Romania). *Land*, 13(2), 148. https://doi.org/10.3390/land13020148.

Perkins, D. (2020) *Mineralogy*, Second Edition, University of North Dakota, Word Press

Suyoto (1994) Sekuen Stratigrafi Karbonat Gunungsewu, *Pros PIT IAGI XXIII*, Vol I: 67-76, Yogyakarta

Suwarno, Misnah, & Mujiarto. (2020) Analysis of static morphostructure conditions with dynamic morphostructure (landslide type), *Geographia Technica,* 15(1), 70–79. https://doi.org/10.21163/GT_2020.151.06.

Van Bemmelen, R..W. (1949) *The Geology of Indonesia*, Vol. IA, Gov. Print. Office, The Hague Martinus Nijhoff.

Van Zuidam, R. A. (1983) Guide To Geomorphologic Aerial Photographys Interpretation and Mapping, ITC, Enschede The Netherlands.

Vračević, D., Dugonjić Jovančević, S., Peranić, J., & Hodanić, M. (2019) Determination of Uniaxial Compressive Strength of Limestone. *Zbornik Radova*, 22(1), 123–140. https://doi.org/10.32762/zr.22.1.8

Wang, M & Wan, a W. (2019) A new empirical formula for evaluating uniaxial compressive strength using the Schmidt hammer test, *International Journal of Rock Mechanics and Mining Sciences*, Volume 123, November 2019, 104094, https://doi.org/10.1016/j.ijrmms.2019.104094.

White, W.B. (1988) *Geomorphology and Hydrology of Karst Terrains*, Oxford University Press, New York.

Wilson, J. L. & Lloyd, R. M. (1995). "Robert J. Dunham (1924–1994)". *AAPG Bulletin*: 154.

MODELING FIRE HOTSPOTS IN KALIMANTAN, INDONESIA USING NESTED 3-COPULA REGRESSION BASED ON PRECIPITATION AND DRY DAYS DURING DIFFERENT ENSO PHASES

Teduh Wulandari MAS'OED[1] , **Sri NURDIATI**[1] , **Ardhasena SOPAHELUWAKAN**[2] ,
Mohamad Khoirun NAJIB[1] , **Ayudya SALSABILA**[1]

ABSTRACT
The persistent forest and land fires in Indonesia have piqued the interest of numerous social groups. Due to the huge number of losses caused by fires, fire prediction is an important part of fire prevention. This study focused on Kalimantan, which is one of the major contributors to fires in Indonesia. This article focuses on modeling the relationship between total precipitation, the number of dry days, and hotspots in Kalimantan, Indonesia for each ENSO phase using a nested 3-copula approach. Using the selected copula structure, the number of hotspots was estimated using nested 3-copula regression with two predictors. Copula regression offers more robustness to outliers and non-normality in the data compared to traditional regression techniques. The results reveal that the regression model based on ENSO phases has an RMSE of 1204 hotspots per month and can explain up to 70% of the variance in hotspots. These results outperform models without ENSO phases, highlighting the importance of ENSO phases in simulating hotspots in Kalimantan. From the regression plane, the ENSO phase has a small impact on the hotspots at low levels. When it comes to high or intense hotspots, the ENSO phase is very important. El Nino is the most dangerous phase for extreme hotspots, while La Nina is the least dangerous. The findings of this study can help researchers better understand the influence and dependence of local and global climate conditions on hotspots in Kalimantan, which can be evolved into an early warning model for forest fires in Indonesia in the future.

Key-words: Copula regression, Dry spells, Hierarchical copula, High-dimension, Multivariate copula, Uncertainty, Wildfire.

1. INTRODUCTION

Indonesia is known as a group of islands separated by vast oceans. Its location around the equator flanked by two continents (Asia and Australia) and two oceans (Pacific and Indian) makes the Indonesian region vulnerable to climate variability. The climate in Indonesia is strongly influenced by natural phenomena in the surrounding sea, such as the El Nino Southern Oscillation (ENSO) (Firmansyah et al., 2022; Kurniadi et al., 2021). Most of the natural disasters that have occurred in Indonesia are closely related to the ENSO phase, such as droughts (Lestari et al., 2018), floods (Rodysill et al., 2019), and forest fires (Zahra et al., 2023).

ENSO is a sea surface condition in the Pacific Ocean region that experiences an increase or decrease in sea surface temperature resulting in a shift in the seasons in Indonesia. There are three phases of ENSO: neutral, El Nino and La Nina phases. El Nino refers to warming the ocean surface, or above-average sea surface temperatures (SSTs), in the central and eastern tropical Pacific Ocean. It represents the warm phase of the ENSO cycle. On the contrary, La Nina refers to the cooling of the central and eastern tropical Pacific Ocean surface and is the cold phase of the ENSO cycle (Wahiduzzaman et al., 2022). In Indonesia, El Nino phase correlates to less rainfall and drought, while La Nina phase correlates to rainfall increase and floods (Nugroho, 2022). Several unforgettable forest fire events in Indonesia occurred during a very strong El Nino, such as in 1997 and 2015 (Fanin &

[1]*Department of Mathematics, Faculty of Mathematics and Natural Sciences, IPB University, Bogor, Indonesia. Teduhma@apps.ipb.ac.id (TWM), corresponding author*: nurdiati@apps.ipb.ac.id (SN), mohknajib@gmail.com (MKN), 13072001ayudya@apps.ipb.ac.id (ASo)*

[2]*Center for Applied Climate Information Services, Agency for Meteorology, Climatology, and Geophysics, Jakarta, Indonesia, ardhasena@bmkg.go.id (ASa)*

Van Der Werf, 2017). These forest fires impact various sectors from rampant deforestation (Adrianto et al., 2020) and alarming declines in air quality (Rahman et al., 2024) to the tragic loss of flora and fauna (Harrison et al., 2016; Wasis et al., 2018) and the health problems faced by affected residents (Hein et al., 2022; Uda et al., 2019). This phenomenon underscores the far-reaching consequences of forest fires, impacting every facet of ecosystems and human life.

Forest fires are a recurring environmental issue that has significant local, regional, and global implications. Forest and peatland fires during the 2015 El Nino drought were among the worst in Southeast Asia, contributing to carbon emissions across the region, with the haze causing an air pollution crisis affecting millions of people (Lee et al., 2017). Peatland fires in Indonesia also result in long-term health impacts causing premature mortality due to chronic respiratory, cardiovascular and lung cancer (Uda et al., 2019) . As a result, forest and peatland fires have become an issue that has attracted the attention of the government, communities and researchers.

Several researchers have explored the intricate relationship between global and local climate factors and their correlation with hotspots as indicators of forest and land fires. Yananto & Dewi (2016) highlighted how El Niño events significantly increased hotspots in Sumatra and Kalimantan, particularly between July and October 2015, when reduced rainfall coincided with a surge in fires. Aflahah et al. (2018) further examined forest fire indicators in Kalimantan, using multiple linear regression analysis to show the strong interconnection among visibility data, the number of hotspots, and temperature, underscoring their substantial influence on fire incidents. Nurdiati et al., (2022b) investigated the effects of ENSO and IOD conditions on the distribution of dry days and total precipitation in southern Sumatra, concluding that these factors significantly impacted the dry season but not the rainy season. Najib et al. (2022b) proposed a fire risk model for Kalimantan using copula regression, demonstrating that dry spells served as a better climatic predictor for fire risks than total precipitation. Collectively, these studies illuminate the complex dynamics of climate and fire activity, offering vital insights for effective forest fire management.

Copula regression is a statistical modeling technique that combines two important concepts: copulas and regression analysis. Copulas are mathematical functions used to describe the dependence structure between random variables, while regression analysis is a method for modeling the relationship between a dependent variable and one or more independent variables. Copula regression brings these two concepts together to provide a flexible and powerful approach for modeling complex dependencies and relationships in data (Czado et al., 2022; Kolev & Paiva, 2009).

One of the advantages of copula regression is its flexibility in modeling dependencies. Copula regression is often more robust to outliers and non-normality in the data compared to traditional regression techniques. Unlike traditional regression models that assume normality and linearity, copula regression can capture a wide range of dependency patterns, such as tail dependencies, asymmetry, and non-monotonic relationships. Copula regression has applications in various fields including environmental science (Najib et al., 2023), finance (Pan et al., 2023), medicine (Gayawan et al., 2023), and engineering (Ma et al., 2022).

Previous studies have shown that apart from decreasing rainfall due to the El Nino phase, a high number of days without rain (or dry days) is an important factor triggering forest and peatland fires, especially in Kalimantan, Indonesia. In Najib et al., (2022a), the two climatic factors are used separately to model hotspots using bivariate copulas. Both of these factors have their respective advantages in predicting hotspots in Kalimantan, although in general the number of dry days outperforms as a predictor of hotspots. Therefore, it is a challenge to model hotspots using both climatic factors using the copula trivariate. Multivariate copulas can be constructed based on bivariate copulas. Two commonly used approaches are nested copula (Serinaldi & Grimaldi, 2007) and vine copula (Heredia-Zavoni & Montes-Iturrizaga, 2019).

Nested and vine copulas are advanced techniques used to model complex multivariate dependencies, each of which has advantages and disadvantages. Here, we are interested in studying nested copula which has advantages, including a simple structure and less computational complexity (Saad et al., 2015), especially when dealing with a relatively small number of variables. Meanwhile, vine copulas can be advantageous when dealing with high-dimensional data, as they provide a

structured approach to managing the computational complexity of estimating multivariate dependencies.

Based on that description, this article focuses on modeling the relationship between total precipitation, number of dry days, and hotspots in Kalimantan, Indonesia for each ENSO phase using a nested 3-copula approach. There are several bivariate copula functions used in this article, both 1-parameter and 2-parameter copula. Using the selected copula structure, the number of hotspots was estimated using copula regression with two predictors using the Riemann sum discretization approach (Jha & Danjuma, 2020).

The article is organized as follows. Datasets are detailed in Section 2. Section 3 presents the methods, including copula functions, parameter estimation, and nested 3-copula regression. The results and discussion are reported in Section 4. Finally, Section 5 concludes this article.

2. STUDY AREA AND DATASETS

This research focuses on Kalimantan, the Indonesian section of the island of Borneo, the world's third-largest island. The island of Borneo is shared by three countries: Indonesia, Malaysia, and Brunei. Kalimantan is the Indonesian portion of Borneo, accounting for roughly three-quarters of the island's total area. West, Central, South, East, and North Kalimantan are the five provinces of Kalimantan (**Fig. 1a**). Each province has its unique culture, topography, and governance system.

Forest fires have been a reoccurring environmental and ecological hazard in Kalimantan, as well as other parts of Southeast Asia. These fires are frequently caused by a combination of factors and have far-reaching consequences for the region, including human activities, deforestation, infrastructure development, land management policies and climate changes. This study focuses on the climate factors that play a significant role in causing forest fires in Kalimantan, as they influence the environmental conditions that can lead to fire ignition and propagation, such as total precipitation and the number of dry days.
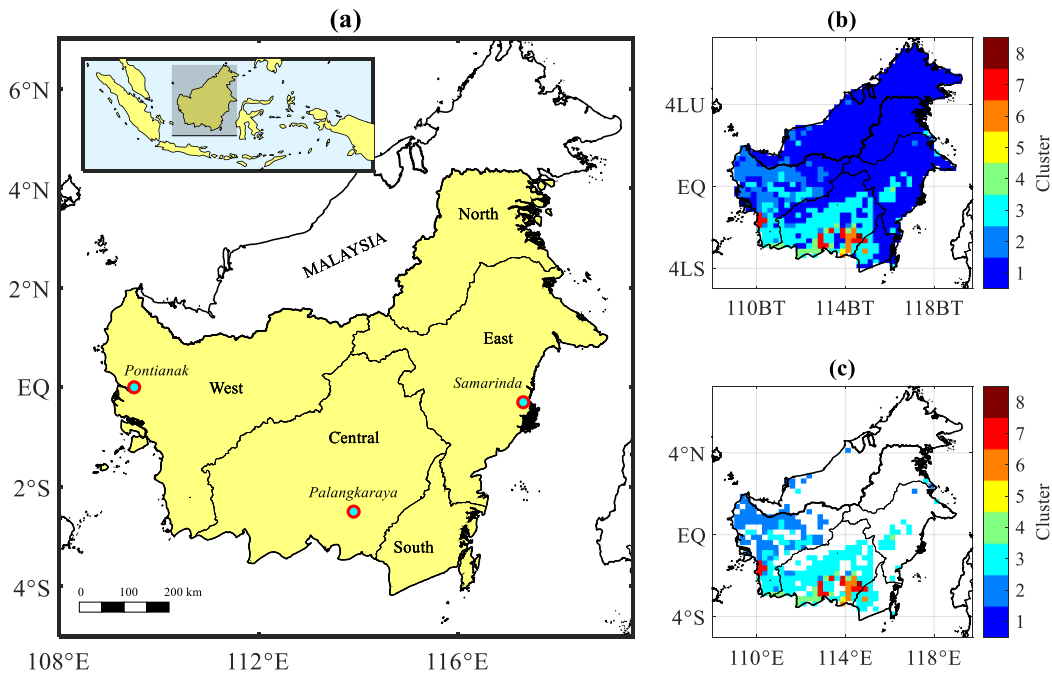

Fig. 1. (a) Map of Kalimantan, (b) clusters of hotspots in Kalimantan, and (c) selected areas for research.

This study makes use of numerous datasets. The information includes hotspots, total precipitation, the number of dry days (also known as dry spells), and the ENSO index (Nino 3.4). Hotspot data covers the Asia-Pacific region with a spatial resolution of 0.25° × 0.25°. The data was obtained from the Indonesian Agency for Meteorology, Climatology, and Geophysics (BMKG) in the 2001-2020 period. Precipitation and number of dry days were taken and derived from the CMORPH-CRT product. The acronym CMORPH stands for "CPC (Climate Prediction Center) MORPHing technique", while CRT stands for "Calibrated Rainfall Technique" (Xie et al., 2019). By incorporating satellite data and calibrating the estimates with ground-based measurements (Bruster-Flores et al., 2019), CMORPH-CRT provides a more comprehensive and accurate picture of precipitation patterns on a global scale. CMORPH-CRT is adjusted through matching the probability density functions (PDF) of daily CMORPH-RAW against that for the CPC unified daily gauge analysis at each month over land (Xie et al., 2017). The spatial resolution for the precipitation data used is 0.25° × 0.25°, while the temporal resolution used is the monthly resolution of precipitation and number of dry days.

According to Septiawan et al. (2019), forest fire patterns are generally divided into two characteristics, namely Sumatra and Kalimantan fires. In terms of temporal characteristics, Septiawan et al. (2019) also stated that fires in Sumatra have two characteristics (6-month and 12-month periods), while fires in Kalimantan generally have an annual period. Compared to Sumatra which is more affected by the Indian Ocean Dipole phenomenon, forest fires in Kalimantan are more affected by the El Nino-Southern Oscillation phenomenon (Nurdiati et al., 2022a). Thus, the general characteristics of fires in Kalimantan can be said to be the same. However, not all areas but only a few points in Kalimantan are affected by forest fires. Therefore, a classification needs to be carried out so that only areas that have a significant influence on forest fires in Kalimantan are considered.

The data used is the result of extraction from previous research by Najib et al. (2021) which classifies forest fires in Kalimantan into several clusters (**Fig 1b**). In general, cluster 1 is an area with very low fire incidence, has relatively high land topography (mountains) and has quite high rainfall. Thus, the area in cluster 1 can be ignored because it can interfere with the general characteristics of forest fires in Kalimantan. Only cluster 1 was removed from the study area due to its classification as a low fire-prone region, characterized by a maximum hotspot occurrence of only about 3.43 hotspots per grid point, i.e., in 2002. The selection criteria focused on hotspot frequency and geographic coverage, allowing for a more targeted analysis of higher-risk areas, while higher-level clusters exhibit more hotspots and reflect conditions conducive to increased fire risks. The datasets are then aggregated into fire-prone areas in Kalimantan, i.e., grid points with significant concentrations of hotspots (**Fig. 1c**) to generate general characteristics of the data. Moreover, data were taken in months with high hotspots: July to November (**Fig. 2**).
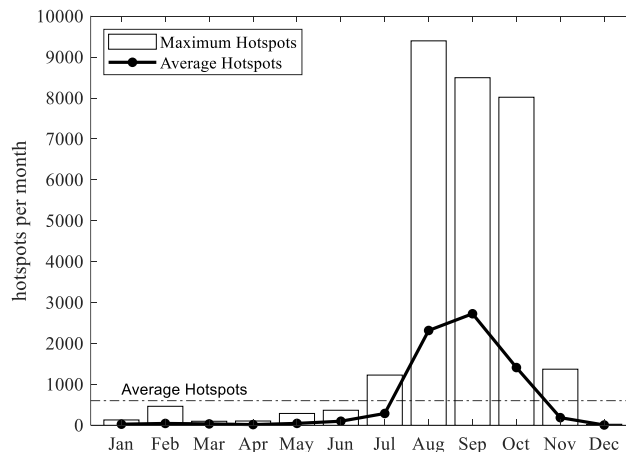

Fig. 2. Average and maximum monthly hotspots in 2001-2020 in fire-prone areas in Kalimantan.

According to Najib et al., (2021), the total precipitation that gives the strongest relationship is the two-month average, meaning that if the hotspots are in September, then the intended total precipitation is the average of the precipitation in August and September. If hotspots are detected in October, the total precipitation used for analysis would typically be calculated as a two-month average, encompassing the precipitation from September and October, and so on. Meanwhile, the number of dry days that is most correlated with hotspots is the three-monthly number of dry days, which is averaged over all fire-prone areas in Kalimantan. These data are used as predictors for hotspots in this study which will later be referred to as total precipitation and number of dry days.

3. METHODS

3.1. Copula Function

A copula function is a mathematical concept used in probability theory and statistics to describe the dependency structure between multiple random variables. Copula theory's basic concept is to separate the modeling of marginal distributions from the modeling of joint distributions, allowing for more flexible and complete representations of dependence patterns. Therefore, copulas provide a flexible way to model various types of dependencies between random variables, including linear, nonlinear, positive, negative, and tail dependencies. This flexibility allows them to capture complex relationships that may not be easily represented by traditional multivariate distributions. Traditional multivariate statistical techniques often assume normal distributions for variables, but real-world data frequently deviates from this assumption. Mathematically, a copula is defined as follows.

Definition 1. An n-dimensional copula (or n-copula) is a function C from $\mathbf{I}^n \rightarrow \mathbf{I}$ with the following properties:
1. For every $\mathbf{u} \in \mathbf{I}^n$, $C(\mathbf{u}) = 0$ if at least one coordinate of $\mathbf{u}$ is 0, and if all coordinates of $\mathbf{u}$ are 1 except u_k, then $C(\mathbf{u}) = u_k$
2. For every $\mathbf{a}, \mathbf{b} \in \mathbf{I}^n$ such that $\mathbf{a} \leq \mathbf{b}$, $V_C([\mathbf{a}, \mathbf{b}]) \geq 0$, where V_C is C-measure of a set.

Sklar's theorem is the core of the copula theory (Nelsen, 2006). Based on Sklar's theorem, copula is referred to as a function that links the multivariate joint cumulative distribution function to the corresponding univariate marginal cumulative distribution functions (Li et al., 2019).

Theorem 1. *Let F be a joint distribution function for a set of n continuous random variables $X_1, X_2, \ldots, X_n$ each with marginal distribution function $F_1, F_2, \ldots, F_n$. According to Sklar's theorem (1959), there exists a copula function C such that for any $x_1, x_2, \ldots, x_n \in \mathbb{R}$:*

$$F(x_1, x_2, \ldots, x_n) = C(u_1, u_2, \ldots, u_n) \qquad (1)$$

where $u_i = F_i(x_i)$ for $i = 1,2, \ldots, n$ and is called n-copula.
Proof: See (Nelsen, 2006)   □

In other words, the joint distribution function F can be expressed in term of the marginal distribution functions $F_1, F_2, \ldots, F_n$ and a copula function C, which characterizes the dependence structure between the variables. If marginal distributions are continuous, the copula function is unique. However, this assumption can easily extend to a mixture of continuous and discrete variables (Schölzel & Friederichs, 2008). A copula function C is uniquely determined on $Ran\ F_1 \times Ran\ F_2 \times \cdots \times Ran\ F_n$, if not all marginal distributions are continuous.

3.1.1. Nested Copula

In the context of multivariate dependence modeling, an exchangeable copula is a copula function that reflects the exchangeability property. This is a simple and elegant approach to constructing high dimensional copulas (Zhang & Singh, 2019b). It is assumed that the variable dependence structure remains constant regardless of the order in which the variables are analyzed. Exchangeable copulas

are frequently symmetric, which means they do not distinguish between variables based on their involvement in the dependent structure. This symmetry is an unavoidable result of the exchangeability property, so exchangeable copulas are also often called symmetric copulas. Therefore, they may not capture more complex or heterogeneous dependence structures that exist in real-world data, although exchangeable copulas offer simplification in modeling high-dimensional dependencies.

Following (Joe, 1997), (Whelan, 2004), and (Serinaldi & Grimaldi, 2007), n-copula can be written in a form called "fully nested" or "asymmetric" which is obtained from a generalization of 2-copula, since it takes into account the non-exchangeability of the variables. The nested copula approach outperforms the exchangeable copula approach significantly (Aas & Berg, 2009). Asymmetries, allowing for more realistic dependencies, are obtained by plugging in Archimedean copulas into each other (Segers & Uyttendaele, 2014). There are $n - 1$ bivariate copula functions for n-dimensional random variables modeled with fully nested copula, resulting in dependence structure with partial exchangeability. The fully nested copula structure is constructed with the following procedures (based on the degree of dependence between the pair variables):

1. As the first two variables (1 and 2), select the variables with the highest degree of dependence (rank-based).
2. Using variables 1 and 2, estimate the copula.
3. Evaluate the degree of dependence (rank-based) between empirical copula from step 2 with the remaining variables.
4. Select variable 3, which has the maximum degree of dependence (rank-based) with the copula constructed using variables 1 and 2.
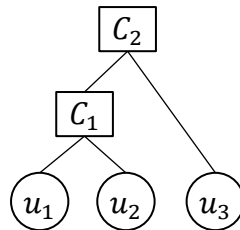5. Continue the process until the last variable is considered.

Fig. 3. Three-dimensional nested copula structure.

Figure 3 presents an example of a three-dimensional nested copula structure. Bivariate copulas are the foundation of nested copulas. Since $n = 3$, the nested 3-copula equation is given by

$$C(u_1, u_2, u_3) = C_2(C_1(u_1, u_2), u_3) \tag{2}$$

Figure 3 shows that two bivariate copulas are required to describe the dependence for three-dimensional random variables using nested copulas, as shown below. First, u_1 and u_2 are coupled by copula C_1, then the resulting variable is linked with u_3 by copula C_2. In general, the first two variables are coupled by a 2-copula, then the resulting copula is coupled with another variable by a second copula, and so on. The nested copula model makes it possible to construct joint distributions with different degrees of positive dependence within different bivariate margins (McNeil, 2008).

In the context of this research, u_1 represents the transformed cumulative distribution function (CDF) values of total precipitation, while u_2 corresponds to the transformed CDF values of the number of dry days. Additionally, u_3 signifies the transformed CDF values of hotspots. The function C_1 is the copula function that describes the dependence between the climate factors (total precipitation and number of dry days), while C_2 is the copula function that links these climate factors to the hotspots. This nested copula structure allows for a comprehensive analysis of the relationships and dependencies among the various variables, facilitating a deeper understanding of how climate factors influence hotspot occurrences.

3.2. Parameter Estimation and Hypothesis Tests

There are various types of copula functions, each with its own characteristics, properties and suitability for different dependencies. Different copulas differ in describing the dependence structures (Li et al., 2020). We use many types of copula functions, both 1-parameter and 2-parameter, including Gaussian, t-student, Clayton, Gumbel, Frank, Joe, Galambos, BB1, BB6, BB7, and BB8 copulas. Meanwhile, there are also many types of marginal univariate distribution that are used, including normal, lognormal, inverse gaussian, extreme value, generalized extreme value, logistic, loglogistic, exponential, gamma, and Weibull distributions for climate factors and negative binomial distribution for hotspots.

We use a 2-step method to estimate the copula parameters called the inference of function for margins (IFM), which estimates the parameters of the marginal distribution first before estimating the copula parameters (Joe, 1997). In summary, the process for constructing a nested 3-copula is as follows.

1. Estimate F_1, F_2, and F_3.
2. Estimate C_1 using u_1 and u_2.
3. Estimate C_2 using u_3 and $C_2(u_2, u_1)$.

Several statistics were used such as the Anderson Darling hypothesis test to select the most fit marginal distribution, while the copula function was selected using the Akaike Information Criterion (AIC) and tested based on the Cramer-von Mises hypothesis test. For more details, the parameter estimation process can be seen in Najib et al., (2022b).

The Anderson-Darling test departs with the null hypothesis that the data comes from a population with the selected distribution, where the test statistic is given by

$$A^2 = -\left(\sum_{t=1}^{N} \frac{2t-1}{N}\left[\ln F(x_t) + \ln\big(1 - F(x_{n+1-t})\big)\right]\right) - N \tag{3}$$

over the ordered sample values $x_1 \leq x_2 \leq \cdots \leq x_N$ (Anderson & Darling, 1954). Meanwhile, the Cramer-von Mises hypothesis test was performed to test the selected theoretical copula, with the null hypothesis that the data comes from the population with the selected theoretical copula, where the test statistic is given by

$$\hat{T} = \sum_{t=1}^{N}\left[C\big(F_1(x_1^t), F_2(x_2^t)\big) - \tilde{C}(x_1^t, x_2^t)\right]^2 \tag{4}$$

where $\tilde{C}$ is the empirical frequency (copula) estimated using the Gringorten formula (1963):

$$\tilde{C}(x_1^t, x_2^t) = \frac{\#(X_1 \leq x_1^t, X_2 \leq x_2^t) - 0.44}{N + 0.12} \tag{5}$$

where N is the sample size of data. The p-value is estimated, then with a significance level of 5%, if the p-value is greater than 5%, then the test fails to reject the null hypothesis.

3.3. Nested 3-Copula Regression Model

From Equations 1 and 2, it can be written that

$$F(x_1, x_2, x_3) = C_2(C_1(u_1, u_2), u_3) \tag{6}$$

Since $u_i = F_i(x_i)$ for $i = 1,2,3$, a joint probability density function f can be obtained by deriving both sides with respect to x_1, x_2, x_3, so that

$$f(x_1, x_2, x_3) = c_2(C_1(u_1, u_2), u_3) \cdot c_1(u_1, u_2) \cdot f_1(x_1) \cdot f_2(x_1) \cdot f_3(x_3) \tag{7}$$

where c_1 and c_2 are density functions of C_1 and C_2, respectively. A copula density c of a copula function C is given by its derivative with respect to each of its marginals:

$$c(u_j, u_k) = \frac{\partial^2}{\partial u_j \partial u_k} C(u_j, u_k) \tag{8}$$

where $u_j = F_j(x_j)$ and $u_k = F_k(x_k)$ for $j \neq k$. If F_j and F_k are continuous CDFs, then copula will uniquely determine the joint probability distribution of X_j and X_k. If F_j and F_k are a mixture of discrete and continuous CDFs, then copula will only uniquely determine the joint probability distribution of X_j and X_k over range $F_j \times$ range F_k (Pleis, 2018).

Let X_3 be the response variable while X_1 and X_2 are the explanatory variables, then the conditional probability density function of x_3 given x_1 and x_3 is defined by

$$f(x_3|x_1, x_2) = \frac{f(x_1, x_2, x_3)}{f(x_1, x_2)} = c_2(C_1(u_1, u_2), u_3) \cdot f_3(x_3) \tag{9}$$

due to $f(x_1, x_2) = c_1(u_1, u_2) \cdot f_1(x_1) \cdot f_2(x_1)$.

If we wish to predict the value of x_3, then we might take the expected value of the conditional density (Eq. 6), which is so-called conditional expectation. The conditional expectation value gives the minimum mean square error in the prediction for x_3, so it is also called the minimum-mean-square-error predictor. Using Equation 6, the conditional expectation value of x_3 given x_1 and x_2 is defined by

$$E(x_3|x_1, x_2) = \int_{-\infty}^{\infty} x_3 \cdot f(x_3|x_1, x_2)\, dx_3 = \int_{-\infty}^{\infty} c_2(C_1(u_1, u_2), u_3) \cdot f_3(x_3) \cdot x_3\, dx_3 \tag{10}$$

Since nested copulas are used to construct the conditional density, we call this formula a nested copula regression. Copula regression is often more robust to outliers and non-normality in the data compared to traditional regression techniques. It can handle data with heavy tails and non-standard distributions more effectively.

For computational convenience, we use the Riemann sum approach to estimate the value of the integral in Equation 7:

$$E(x_3|x_1, x_2) \approx \sum_{i=1}^{p} c_2(C_1(u_1, u_2), u_3^{(i)} \cdot f_3(x_3^{(i)}) \cdot x_3^{(i)} \cdot \Delta x_3^{(i)} \tag{11}$$

where p represents the number of partitions used (Jha & Danjuma, 2020).

3.4. Performance Metrics

We use several metrics to measure the performance of the resulting regression models, including root mean squared error (RMSE) and explained variance score (EVS). The RMSE is defined as:

$$\text{RMSE}(y, \hat{y}) = \sqrt{\frac{1}{N} \sum_{i=1}^{N} (y_i - \hat{y}_i)^2} \tag{12}$$

where y is the actual data and $\hat{y}$ is the predicted data. Meanwhile, the explained variance score is estimated by:

$$\text{EVS}(y, \hat{y}) = 1 - \frac{var(y_i - \hat{y}_i)}{var(y_i)} \tag{13}$$

Scores close to 1.0 are highly desired, indicating better squares of standard deviations of errors (Oyedele et al., 2023).

4. RESULTS AND DISCUSSION

Here, we use scenario 1 without observing the ENSO effect and scenario 2 by observing the ENSO effect. This study analyzed the ENSO data monthly, allowing for a detailed examination of its influence on precipitation and dry days throughout the year. The ENSO phases were then classified into neutral, El Niño (ENSO > 0.5), and La Niña (ENSO < -0.5) categories. Scenario 1 uses all data without splitting (100 rows), while scenario 2 split data based on the ENSO phase: neutral (51 rows), El Nino (23 rows), and La Nina (26 rows). This section presents the selected marginal distribution, nested copula construction, and nested copula regression results.

Table 1.

Kendall-tau correlation between variables.

Datasets	$X_1 - X_2$	$X_1 - X_3$	$X_2 - X_3$
No Split	**0.7119**	0.5972	0.6186
El Nino	0.6614	**0.6878**	0.6138
Neutral	**0.7396**	0.5069	0.5367
La Nina	**0.6857**	0.5871	0.5298

Suppose X_1, X_2, and X_3 are negative of total precipitation, number of dry days, and hotspots, respectively. We choose to use the negative of total precipitation as X_1 so that the two predictors (X_1 and X_2) have a positive dependence on hotspots. **Table 1** shows the Kendall-tau correlation between variables. Except in El Nino conditions, the pair of variables X_1 and X_2 produces the strongest Kendall-tau correlation. For equality, the copula structure chooses X_1 and X_2 to be coupled as the first pair of variables. Aside from that, the presence of correlation is a prerequisite for copula-based modeling. Because the correlation value is quite strong, copula modeling can be performed.

4.1. Marginal Distribution of Variables

Estimating the marginal distribution of all variables is the first procedure for copula modeling. For instance, **Table 2** shows the statistics of distribution fitting results for the number of dry days in scenario 1.

Table 2.

Statistics of Distribution Fitting Results for the Number Of Dry Days in Scenario 1.

Distribution	Anderson-Darling		AIC
	Statistics	*p-value*	
Generalized Extreme Value	0.27261	0.95711	776.38
Weibull	0.3138	0.92727	775.88
Normal	0.43073	0.81744	777.94
Logistic	0.58951	0.65754	784.07
Extreme Value	0.63162	0.6182	783.24
Gamma	0.85789	0.4408	781.98
Log-logistic	1.0708	0.322	789.67
Lognormal	1.2084	0.26427	786.42
Inverse Gaussian	1.2687	0.24271	786.42
Exponential	26.397	6e-06	978.94

A total of ten distributions were tested for the fitting of the marginal distributions of each variable. The results in **Table 2** indicate that the Generalized Extreme Value (GEV) distribution provided the most significant fit for the number of dry days in scenario 1, as evidenced by its high p-value of 0.95711 and the lowest Akaike Information Criterion (AIC) value of 776.38 among all distributions tested. These statistics suggest that the GEV distribution effectively captures the characteristics of the data, making it the optimal choice for modeling the number of dry days in this study. In contrast, other distributions, such as the Exponential distribution, exhibited poor fit with a low p-value (6e-06), indicating a significant deviation from the observed data. This selection process highlights the

importance of evaluating multiple distribution models to identify the most appropriate one for the given dataset.

The fitting process was subsequently carried out for each variable in both scenario 1 and scenario 2. This involved applying the same methodology of estimating marginal distributions and assessing the goodness-of-fit for various distributions across all relevant variables. By conducting this comprehensive fitting analysis, the study aimed to ensure that the selected distributions accurately represent the underlying characteristics of the data for both scenarios, facilitating a more robust copula modeling approach for understanding the relationships between the climate factors and hotspot occurrences.

Table 3 presents the marginal distributions that were determined to be the best fit for the data across different scenarios, with the p-values from the Anderson-Darling hypothesis test provided in brackets. These p-values serve as an indicator of how well each distribution fits the observed data, with a focus on testing the null hypothesis (H_0) that the data follows the specified distribution. In this case, all marginal distributions exhibited p-values greater than 0.05, which indicates that there is insufficient evidence to reject the null hypothesis. This result suggests that the observed data does not significantly deviate from the fitted distributions, implying that these distributions are suitable for accurately representing the characteristics of the data.

Consequently, since the p-values indicate a good fit, all identified marginal distributions can be confidently used in subsequent analyses and modeling processes. This is a crucial step in the copula modeling framework, as ensuring that the marginal distributions are appropriately fitted provides a solid foundation for understanding the dependencies and interactions between the variables in the study. The ability to utilize these distributions in further processing enhances the robustness of the research findings and the reliability of the conclusions drawn regarding the relationships among the climate factors and hotspot occurrences.

Table 3.

Fitting Results of Marginal Distributions with Anderson-Darling Test.

Datasets	X_1	X_2	X_3
No split	Generalized Extreme Value $k = -0.475,$ $\sigma = 78.826, \mu = -214.47$ AD p-value = 0.5129	Generalized Extreme Value $k = -0.381,$ $\sigma = 12.013, \mu = 45.105$ AD p-value = 0.9571	Negative Binomial $R = 0.42177,$ $P = 0.00030405$ AD p-value = 0.6772
Neutral	Generalized Extreme Value $k = -0.447,$ $\sigma = 72.164, \mu = -204.56$ AD p-value = 0.9113	Normal $\mu = 48.189,$ $\sigma = 9.6703$ AD p-value = 0.9985	Negative Binomial $R = 0.44483,$ $P = 0.00046452$ AD p-value = 0.9908
El Nino	Generalized Extreme Value $k = -0.721,$ $\sigma = 74.768, \mu = -176.82$ AD p-value = 0.9956	Generalized Extreme Value $k = -0.532,$ $\sigma = 9.2313, \mu = 55.484$ AD p-value = 0.9951	Negative Binomial $R = 0.64896,$ $P = 0.00022228$ AD p-value = 0.7666
La Nina	Generalized Extreme Value $k = 0.241,$ $\sigma = 40.913, \mu = -288.80$ AD p-value = 0.9668	Generalized Extreme Value $k = 0.0745,$ $\sigma = 7.8011, \mu = 32.976$ AD p-value = 0.9915	Negative Binomial $R = 0.4662,$ $P = 0.0012023$ AD p-value = 0.7158

The results show that generalized extreme value distribution is the dominant distribution for variables X_1 and X_2. Generalized extreme value distribution is a probability distribution used to model the extreme values of random variables, that includes three types of extreme value distributions as a special case: the Gumbel, Fréchet, and Weibull distributions (Boudrissa et al., 2017; Jenkinson, 1955). Since X_1 refers to negative values of total precipitation, the smaller the position parameter (μ) of the generalized extreme value distribution the wetter the climate conditions. Based on that, El Nino causes drier precipitation in Kalimantan, while La Nina causes wetter precipitation than the neutral phase. Moreover, El Nino causes more dry days while La Nina causes fewer dry days than the neutral phase based on the fittest distribution of X_2.

For X_3, the negative binomial distribution is chosen because of its data type which contains many zero values (Greene, 1994). In the context of data analysis with many zero values, the parameter P in the negative binomial distribution refers to the probability of a zero value (excess zeros component). The results show that El Nino has a smaller probability of zero hotspots than the neutral phase, which means that El Nino is more likely to have high hotspots. Conversely, La Nina has a greater probability of zero hotspots than the neutral phase, so it is safer from high hotspots. A comparison of the position parameters and the probability of a zero-value parameters is presented in **Figure 4**.

Using selected distributions, each variable is estimated with the cumulative distribution function (CDF) which is known as the probability transformation. Probability transformation refers to the process of converting probabilities from one distribution to another using a specific mathematical function. Here, we transform the selected distributed original data into uniformly distributed using the CDF value. The variables resulting from this transformation are denoted U_1, U_2, and U_3 which are used for the copula parameter fitting process.
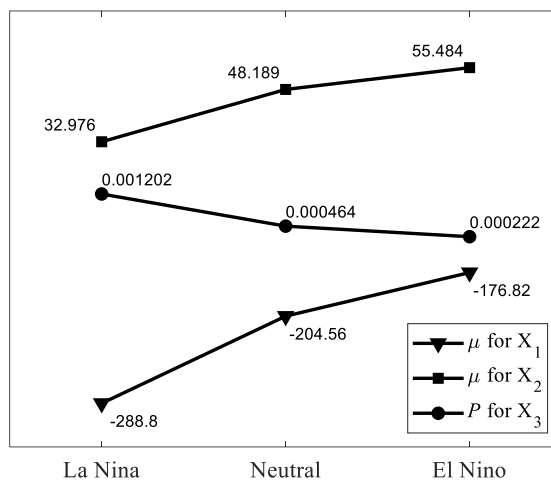

Fig. 4. Comparison of the position parameters and the probability of a zero-value parameters.

4.2. Selected Copulas and Its Parameters

The parameters of each copula function used are estimated using U_1, U_2, and U_3, then the fittest copulas are selected based on Akaike's Information Criterion (AIC). **Table 4** shows the fittest copula functions and their parameters for each condition, as well as the p-values of the Cramer-von Mises hypothesis test. Based on these p-values, all copulas have a p-value > 0.05, meaning that there is not enough evidence to reject H_0 (data comes from the selected copula). Thus, all these copulas can be used for further processing. Gaussian is the most preferred copula compared to other copula functions. The other copula functions selected are the copula functions of Galambos-180°, Gumbel, and Joe.

Table 4.
Fitting Results of Copula Functions With Cramer-Von Mises Test.

Datasets	C_1	C_2	CvM (p-value)
No split	Gaussian, $\rho = 0.89$	Gaussian, $\rho = 0.834$	0.059 ($p = 0.570$)
Neutral	Gaussian, $\rho = 0.9067$	Gaussian, $\rho = 0.7744$	0.040 ($p = 0.640$)
El Nino	Gaussian, $\rho = 0.8905$	Galambos-180°, $\theta = 1.7879$	0.028 ($p = 0.689$)
La Nina	Gumbel, $\theta = 3.4330$	Joe, $\theta = 3.1067$	0.028 ($p = 0.690$)

In the data without splits and in the neutral phase, the inner C_1 and outer C_2 copulas choose Gaussian as the fittest copula. A Gaussian copula can be understood as a member of the elliptical copula family. Elliptical copulas are a class of copula functions that encompass a broader range of

dependence structures beyond just the Gaussian (normal) distribution. By obtaining the Gaussian as the fittest copula, this means that there is no significant tail correlation in the constructed model. This is natural because during normal phases, climatic factors (conditions) and forest fires usually have no upper or lower extremes. However, the parameters of the Gaussian copula control the correlation or dependence between variables. Thus, due to the high value of ρ, a strong dependency is seen in the relationship between climatic factors as well as between climatic factors and hotspots.

For the El Nino phase, the Gaussian copula was chosen as the inner copula and Galambos-180° as the outer copula. The term 180° indicates that there is a rotation of the Galambos copula by 180°, also known as the survival Galambos copula (Liu et al., 2018). The Galambos copula is a specific type of copula that is often used to model extreme value dependencies. It is well-suited for capturing positive tail dependence, which means that extreme values of one variable are likely to be accompanied by extreme values of another variable.

For the La Nina phase, the Gumbel copula was chosen as the inner copula and Joe as the outer copula. Like the Galambos copula, the Gumbel copula is often used to model joint extreme events (Budiarti et al., 2018). Meanwhile, the Joe copula, is a family of copulas that generalizes the Gumbel and Clayton copulas. It allows for a smooth transition between these two copulas, providing flexibility in capturing different types of dependence structures.

4.3. Mean Regression

Using Eq. 8, the mean regression for hotspots is estimated based on the corresponding climate factor values. If the regression with one predictor is visualized using the regression line, then in the case of a two-predictor regression, the visualization uses the regression plane.

We plot the regression plane in a two-dimensional plane using a contour plot, while bubble plots are used to plot the actual hotspots. A contour plot, also known as a level plot or isoline plot, is a graphical representation used to visualize three-dimensional data on a two-dimensional surface. It is commonly used to show the variations and patterns in data that have two independent variables (represented on the x and y axes) and a dependent variable (represented through contour lines or color gradients). Here, the more yellow the color, the higher the estimated number of hotspots. Meanwhile, a bubble plot extends the concept of a scatter plot by introducing a third dimension using varying sizes of markers, usually represented as circles (or bubbles). This allows us to represent three variables in a two-dimensional space. We also provide color accents to emphasize the high and low number of hotspots that occur. Here, the larger the circle and the yellower the color, the higher the number of actual hotspots. **Figure 5** shows the regression plane for hotspots on the data without splitting based on the ENSO phases.
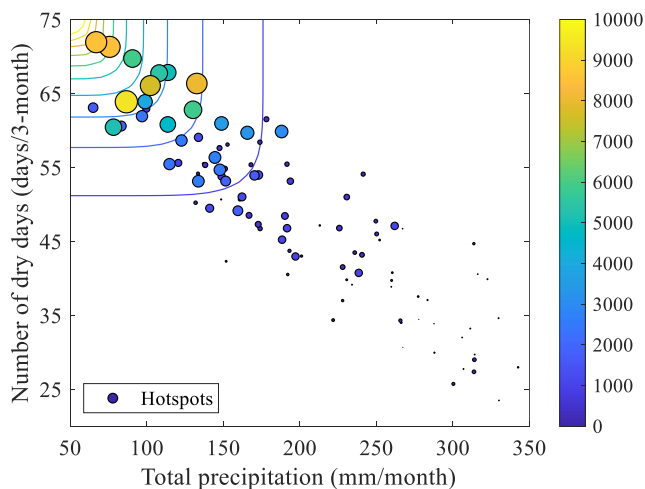

Fig. 5. Regression plane for hotspots on the data without splitting based on the ENSO phases.

Based on **Figure 5**, if the total precipitation value is smaller and the number of dry days is higher, then the number of hotspots is increasing. From the regression plane, hotspots start to appear more than 1000 hotspots in a month when the average 2-month total precipitation is less than 175 mm/month, and the number of dry days is more than 51 days in three months. The regression plane shows color gradations like the actual hotspots values indicated by the colors in the circles, indicating that the regression gives good results for estimating the number of hotspots. This is reinforced by its performance metrics which show an RMSE of 1340 hotspots and an EVS of 63.17%. This shows that the estimated hotspots can explain the variance of the actual hotspots by 63.17%. These results have not considered the ENSO phase in the modeling. Regression planes for hotspots based on ENSO phases are visualized in **Figure 6**.
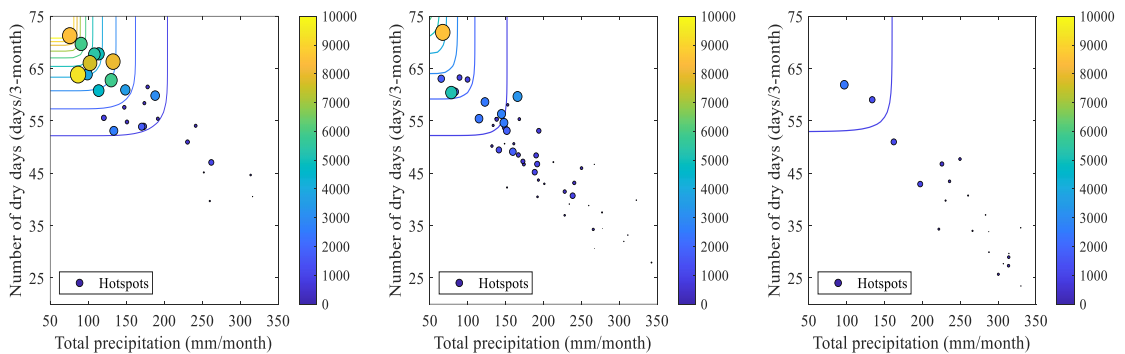

Fig. 6. Regression planes for hotspots based on ENSO phases: (a) El Nino, (b) neutral and (c) La Nina.

Figure 6 presents the regression results for hotspots in the El Nino, neutral and La Nina phases. It is interesting to note that the borders for hotspots above or below 1,000 hotspots/month emerge almost on the same line, i.e., when total precipitation is 150-200 mm/month and the number of dry days is approximately 50 days/3 months, based on the regression plane. This suggests that the ENSO phase has no impact on low hotspot situations with fewer than 1,000 hotspots/month. The significant difference can be noticed in hotspots above 1,000 hotspots/month. The regression plane, which only has one contour level at 1,000 hotspots/month, demonstrates that the La Nina phase will not touch the value of 2,000 hotspots/month. Meanwhile, in the neutral phase, this allows hotspots of up to more than 5,000 hotspots/month, though there was one event where hotspots reached up to 8,000 hotspots/month. This event occurred in 2019 during a very strong positive IOD phenomena, despite ENSO being under neutral conditions (Iskandar et al., 2022). More extreme hotspots appear during the El Nino phase. In this phase, there is a possibility that hotspots can reach more than 10,000 hotspots in a month when total precipitation is less than 80 mm/month, and the number of dry days is more than 70 days in 3 months.

Table 5 shows the performance metrics of regression model based on ENSO phases. The RMSE value describes that the El Nino phase has the greatest and the La Nina phase has the lowest. This number is proportional to the number of monthly hotspots that occur in each phase. Because the number of hotspots is so significant during the El Nino phase, the regression model's RMSE is also very high. Likewise, for the La Nina phase, the number of hotspots is relatively small.

Table 5.
Performance metrics of regression model based on ENSO conditions.

Phase	RMSE	EVS
El Nino	1789	66.74%
Neutral	1025	54.35%
La Nina	295	77.43%

Based on the EVS value, the regression model in the neutral phase is the lowest: 54.35%. This means that the regression model can explain the variance of the original data by 54.35%. This also implies that the neutral phase has high variance when compared to other phases. In this neutral phase, hotspots can be very high or very low with quite high extreme values as happened in 2019. Meanwhile, the La Nina phase produces the highest EVS values, which corresponds to the low variance in this phase. In this phase, monthly hotspots tend to be low and there have been no extreme hotspot events in this phase.

Finally, the regression model separated by ENSO phases yields an RMSE of 1204 hotspots and an EVS of 70.01%. This is an improvement compared to the previous model which did not differentiate based on ENSO phases, which only produced an EVS of 63.17%. This highlights the importance of ENSO phases in modeling hotspots in Kalimantan. In comparison to previous research by Najib et al. (2022b), the RMSE results are relatively close; that study, which also classified ENSO phases, reported an RMSE of 1189 hotspots when using total precipitation as a single predictor, while using the number of dry days as a predictor yielded an RMSE of 1110 hotspots. Therefore, the results obtained in this study remain highly acceptable when compared to those findings. However, there is still potential for further research to enhance the accuracy of this copula regression model, aiming to achieve an RMSE that approaches or surpasses that of the single-variable predictor copula regression models. One potential avenue for improvement is the implementation of more advanced structures, such as vine copulas, which could better capture the dependencies among the variables and enhance model performance.

5. CONCLUSIONS

This study focuses on modeling hotspots based on total precipitation and the number of dry days using nested 3-copula regression. Nested copulas offer a simple way to construct high-dimensional multivariate distributions. By estimating conditional probability values, the number of monthly hotspots in Kalimantan can be estimated. Even though there are many advantages offered by nested copulas, there are several notes that need to be considered in regression using copulas. One of them is the dependency between the predictors. In section 4 it was revealed that we used negative data from total precipitation rather than the original data. This is because if you use total precipitation data, it will result in the relationship between total precipitation and the number of dry days being negative. This means that the relationship between the predictor data and the response variable is different. Thus, cancellation of the response variable occurs when a joint distribution between the predictor data is formed. In other words, if the predictor has a negative relationship, then the relationship between the joint distribution of the predictor and the response variable will be low. This results in predictions being inaccurate. Therefore, the relationship between predictor data and response data is very important in nested copula-based regression models. This conclusion is supported by McNeil (2008) which states that the nested copula model allows to construct joint distributions with different levels of *positive dependence* in different bivariate margins.

Regression results for hotspots using nested copula regression show satisfactory performance where overall the model based on ENSO phases can explain the variance of hotspot data up to 70%. From the regression plane that is formed, the ENSO phase does not really affect the hotspots at low levels. The ENSO phase is very influential when talking about high or extreme hotspots, where El Nino is the phase that has the greatest opportunity for extreme hotspots to occur, even up to more than 10,000 hotspots per month. Meanwhile, La Nina is the safest phase for extreme hotspots. From the performance metrics, it can be concluded that the ENSO phase has a big influence on modeling hotspots in Kalimantan based on total precipitation and the number of dry days.

Although the nested copula approach significantly improves the symmetric copula approach, it is still insufficient to capture all possible interrelationships among n-dimensional random variables. Based on the multivariate density decomposition (Joe, 1997), other approaches such as Pair-Copula Construction (PCC) allow for the free specification of copulas that are hierarchical in nature. There are two main types of PCCs, canonical (C)-vines and drawable (D)-vines copula (Zhang & Singh,

2019a). This study can be developed further by applying a similar regression concept, with a copula model construction process using the vine copula approach. However, it should be noted that the construction of the vine copula model is more complicated than the nested copula model in the high-dimensional case.

ACKNOWLEDGEMENT

Code Availability

We use MATLAB for all computational processes conducted in this study. The codes can be downloaded from https://mkhoirun-najiboi.github.io/mycopula/.

Conflict of Interest

The authors declare that they have no conflict of interest for this research.

R E F E R E N C E S

Aas, K., & Berg, D. (2009). Models for construction of multivariate dependence - a comparison study. *European Journal of Finance*, *15*(7–8), 639–659. https://doi.org/10.1080/13518470802588767

Adrianto, H. A., Spracklen, D. V., Arnold, S. R., Sitanggang, I. S., & Syaufina, L. (2020). Forest and land fires are mainly associated with deforestation in Riau Province, Indonesia. *Remote Sensing*, *12*(1). https://doi.org/10.3390/RS12010003

Aflahah, E., Hidayati, R., Hidayat, R., & Alfahmi, F. (2018). Pendugaan hotspot sebagai indikator kebakaran hutan di Kalimantan berdasarkan faktor iklim. *Journal of Natural Resources and Environmental Management*, *9*(2), 405–418. http://dx.http//journal.ipb.ac.id/index.php/jpsl

Anderson, T. W., & Darling, D. A. (1954). A Test of Goodness of Fit. *Journal of the American Statistical Association*, *49*(268), 765–769. https://doi.org/10.1080/01621459.1954.10501232

Boudrissa, N., Cheraitia, H., & Halimi, L. (2017). Modelling maximum daily yearly rainfall in northern Algeria using generalized extreme value distributions from 1936 to 2009. *Meteorological Applications*, *24*(1), 114–119. https://doi.org/10.1002/met.1610

Bruster-Flores, J. L., Ortiz-Gómez, R., Ferriño-Fierro, A. L., Guerra-Cobián, V. H., Burgos-Flores, D., & Lizárraga-Mendiola, L. G. (2019). Evaluation of precipitation estimates CMORPH-CRT on regions of Mexico with different climates. *Water (Switzerland)*, *11*(8). https://doi.org/10.3390/w11081722

Budiarti, R., Wigena, A. H., Purnaba, I. G. P., & Achsani, N. A. (2018). Modelling the Dependence Structure of Financial Assets: A Bivariate Extreme Data Study. *IOP Conference Series: Earth and Environmental Science*, *187*(1). https://doi.org/10.1088/1755-1315/187/1/012003

Czado, C., Bax, K., Sahin, Ö., Nagler, T., Min, A., & Paterlini, S. (2022). Vine Copula Based Dependence Modeling in Sustainable Finance. *The Journal of Finance and Data Science*, *8*, 309–330. https://doi.org/10.1016/j.jfds.2022.11.003

Fanin, T., & Van Der Werf, G. R. (2017). Precipitation-fire linkages in Indonesia (1997-2015). *Biogeosciences*, *14*(18), 3995–4008. https://doi.org/10.5194/bg-14-3995-2017

Firmansyah, A. J., Nurjani, E., & Sekaranom, A. B. (2022). Effects of the El Niño-Southern Oscillation (ENSO) on rainfall anomalies in Central Java, Indonesia. *Arabian Journal of Geosciences*, *15*(24). https://doi.org/10.1007/s12517-022-11016-2

Gayawan, E., Egbon, O. A., & Adegboye, O. (2023). Copula based trivariate spatial modeling of childhood illnesses in Western African countries. *Spatial and Spatio-Temporal Epidemiology*, *46*. https://doi.org/10.1016/j.sste.2023.100591

Greene, J. (1994). Accounting for Excess Zeros and Sample Selection in Poisson and Negative Binomial Regression Models. *NYU Working Paper No. EC-94-10*, *9*, 265–265. http://ssrn.com/abstract=1293115

Gringorten, I. I. (1963). A plotting rule for extreme probability paper. *Journal of Geophysical Research*, *68*(3), 813–814. https://doi.org/10.1029/jz068i003p00813

Harrison, M. E., Capilla, B. R., Thornton, S. A., Cattau, M. E., & Page, S. E. (2016). Impacts of the 2015 fire season on peat-swamp forest biodiversity in Indonesian Borneo. *15Th International Peat Congress*, *2006*(August 2006), 713–717.

Hein, L., Spadaro, J. V., Ostro, B., Hammer, M., Sumarga, E., Salmayenti, R., Boer, R., Tata, H., Atmoko, D., & Castañeda, J. P. (2022). The health impacts of Indonesian peatland fires. *Environmental Health: A Global Access Science Source*, *21*(1). https://doi.org/10.1186/s12940-022-00872-w

Heredia-Zavoni, E., & Montes-Iturrizaga, R. (2019). Modeling directional environmental contours using three dimensional vine copulas. *Ocean Engineering*, *187*. https://doi.org/10.1016/j.oceaneng.2019.06.007

Iskandar, I., Lestari, D. O., Saputra, A. D., Setiawan, R. Y., Wirasatriya, A., Susanto, R. D., Mardiansyah, W., Irfan, M., Rozirwan, Setiawan, J. D., & Kunarso. (2022). Extreme Positive Indian Ocean Dipole in 2019 and Its Impact on Indonesia. *Sustainability (Switzerland)*, *14*(22). https://doi.org/10.3390/su142215155

Jenkinson, A. F. (1955). The Frequency Distribution of the Annual Maximum (or Minimum) of Meteorological Elements. *Quarterly Journal of the Royal Meteorological Society*, *81*, 158–171.

Jha, B. K., & Danjuma, Y. J. (2020). Unsteady Dean flow formation in an annulus with partial slippage: A riemann-sum approximation approach. *Results in Engineering*, *5*. https://doi.org/10.1016/j.rineng.2019.100078

Joe, H. (1997). *Multivariate Models and Dependence Concepts*. Chapman and Hall. https://doi.org/10.1201/9780367803896

Kolev, N., & Paiva, D. (2009). Copula-based regression models: A survey. *Journal of Statistical Planning and Inference*, *139*(11), 3847–3856. https://doi.org/10.1016/j.jspi.2009.05.023

Kurniadi, A., Weller, E., Min, S. K., & Seong, M. G. (2021). Independent ENSO and IOD impacts on rainfall extremes over Indonesia. *International Journal of Climatology*, *41*(6), 3640–3656. https://doi.org/10.1002/joc.7040

Lee, B. P. Y. H., Davies, Z. G., & Struebig, M. J. (2017). Smoke pollution disrupted biodiversity during the 2015 El Nino fires in Southeast Asia. *Environmental Research Letters*, *12*(9). https://doi.org/10.1088/1748-9326/aa87ed

Lestari, D. O., Sutriyono, E., Sabaruddin, & Iskandar, I. (2018). Severe Drought Event in Indonesia Following 2015/16 El Niño/positive Indian Dipole Events. *Journal of Physics: Conference Series*, *1011*(1). https://doi.org/10.1088/1742-6596/1011/1/012040

Li, H.-N., Zheng, X.-W., & Li, C. (2019). Copula-Based Joint Distribution Analysis of Wind Speed and Direction. *Journal of Engineering Mechanics*, *145*(5). https://doi.org/10.1061/(asce)em.1943-7889.0001600

Li, Z., Shao, Q., Tian, Q., & Zhang, L. (2020). Copula-based drought severity-area-frequency curve and its uncertainty, a case study of Heihe River basin, China. *Hydrology Research*, *51*(5), 867–881. https://doi.org/10.2166/nh.2020.173

Liu, J., Sirikanchanarak, D., Sriboonchitta, S., & Xie, J. (2018). Analysis of Household Consumption Behavior and Indebted Self-Selection Effects: Case Study of Thailand. *Mathematical Problems in Engineering*, *2018*. https://doi.org/10.1155/2018/5486185

Ma, M., Wang, X., Liu, N., Song, S., & Wang, S. (2022). Nested Copula Model for Overall Seismic Vulnerability Analysis of Multispan Bridges. *Shock and Vibration*, *2022*. https://doi.org/10.1155/2022/3001933

McNeil, A. J. (2008). Sampling nested Archimedean copulas. *Journal of Statistical Computation and Simulation*, *78*(6), 567–581. https://doi.org/10.1080/00949650701255834

Najib, M. K., Nurdiati, S., & Sopaheluwakan, A. (2021). Quantifying the joint distribution of drought indicators in Borneo fire-prone area. *IOP Conference Series: Earth and Environmental Science*, *880*. https://doi.org/10.1088/1755-1315/880/1/012002

Najib, M. K., Nurdiati, S., & Sopaheluwakan, A. (2022a). Copula-based joint distribution analysis of the ENSO effect on the drought indicators over Borneo fire-prone areas. *Modeling Earth Systems and Environment*, *8*(2), 2817–2826. https://doi.org/10.1007/s40808-021-01267-5

Najib, M. K., Nurdiati, S., & Sopaheluwakan, A. (2022b). Multivariate fire risk models using copula regression in Kalimantan, Indonesia. *Natural Hazards*, *113*(2), 1263–1283. https://doi.org/10.1007/s11069-022-05346-3

Najib, M. K., Nurdiati, S., & Sopaheluwakan, A. (2023). Prediction of hotspots pattern in Kalimantan using copula-based quantile regression and probabilistic model: a study of precipitation and dry spells across varied ENSO conditions. *Vietnam Journal of Earth Sciences*, *Early Access*. https://doi.org/10.15625/2615-9783/19302

Nelsen, R. B. (2006). *An introduction to copulas*. Springer.

Nugroho, A. R. (2022). *Teleconnections of El Niño–Southern Oscillation (ENSO) and Indian Ocean Dipole (IOD) to streamflow in Java, Indonesia* [Dissertation, Gifu University]. http://hdl.handle.net/20.500.12099/88935

Nurdiati, S., Bukhari, F., Julianto, M. T., Sopaheluwakan, A., Aprilia, M., Fajar, I., Septiawan, P., & Najib, M. K. (2022). The impact of El Niño southern oscillation and Indian Ocean Dipole on the burned area in Indonesia. *Terrestrial, Atmospheric and Oceanic Sciences*, *33*(15). https://doi.org/10.1007/S44195-022-00016-0

Nurdiati, S., Najib, M. K., & Thalib, A. S. (2022). Joint Distribution And Coincidence Probability Of The Number Of Dry Days And The Total Amount Of Precipitation In Southern Sumatra Fire-Prone Area. *Geographia Technica*, *17*(2), 107–118. https://doi.org/10.21163/GT_2022.172.10

Oyedele, A. A., Ajayi, A. O., Oyedele, L. O., Bello, S. A., & Jimoh, K. O. (2023). Performance evaluation of deep learning and boosted trees for cryptocurrency closing price prediction. *Expert Systems with Applications*, *213*. https://doi.org/10.1016/j.eswa.2022.119233

Pan, S., Joe, H., & Li, G. (2023). Conditional Inferences Based on Vine Copulas with Applications to Credit Spread Data of Corporate Bonds. *Journal of Financial Econometrics*, *21*(3), 714–741. https://doi.org/10.1093/jjfinec/nbab016

Pleis, J. R. (2018). *Mixtures of discrete and continuous variables: Considerations for dimension reduction* [Dissertation]. University of Pittsburgh.

Rahman, R. A., White, B., & Ma, C. (2024). The effect of growth, deforestation, forest fires, and volcanoes on Indonesian regional air quality. *Journal of Cleaner Production*, *457*. https://doi.org/10.1016/j.jclepro.2024.142311

Rodysill, J. R., Russell, J. M., Vuille, M., Dee, S., Lunghino, B., & Bijaksana, S. (2019). La Niña-driven flooding in the Indo-Pacific warm pool during the past millennium. *Quaternary Science Reviews*, *225*. https://doi.org/10.1016/j.quascirev.2019.106020

Saad, C., El Adlouni, S., St-Hilaire, A., & Gachon, P. (2015). A nested multivariate copula approach to hydrometeorological simulations of spring floods: the case of the Richelieu River (Québec, Canada) record flood. *Stochastic Environmental Research and Risk Assessment*, *29*(1), 275–294. https://doi.org/10.1007/s00477-014-0971-7

Schölzel, C., & Friederichs, P. (2008). Multivariate non-normally distributed random variables in climate research - Introduction to the copula approach. *Nonlinear Processes in Geophysics*, *15*(5), 761–772. https://doi.org/10.5194/npg-15-761-2008

Segers, J., & Uyttendaele, N. (2014). Nonparametric estimation of the tree structure of a nested Archimedean copula. *Computational Statistics and Data Analysis*, *72*, 190–204. https://doi.org/10.1016/j.csda.2013.10.028

Septiawan, P., Nurdiati, S., & Sopaheluwakan, A. (2019). Numerical Analysis using Empirical Orthogonal Function Based on Multivariate Singular Value Decomposition on Indonesian Forest Fire Signal. *IOP Conference Series: Earth and Environmental Science*, *303*. https://doi.org/10.1088/1755-1315/303/1/012053

Serinaldi, F., & Grimaldi, S. (2007). Fully Nested 3-Copula: Procedure and Application on Hydrological Data. *Journal of Hydrologic Engineering*, *12*(4), 420–430. https://doi.org/10.1061/(asce)1084-0699(2007)12:4(420)

Sklar, M. (1959). Fonctions de Répartition àn Dimensions et Leurs Marges. *Publications de L'Institut de Statistique de L'Université de Paris*, *8*, 229–231.

Uda, S. K., Hein, L., & Atmoko, D. (2019). Assessing the health impacts of peatland fires: a case study for Central Kalimantan, Indonesia. *Environmental Science and Pollution Research*, *26*(30), 31315–31327. https://doi.org/10.1007/s11356-019-06264-x

Wahiduzzaman, M., Cheung, K., Tang, S., & Luo, J. J. (2022). Influence of El Niño–Southern Oscillation on the long-term record of floods over Bangladesh. *Theoretical and Applied Climatology*, *147*(1–2), 173–184. https://doi.org/10.1007/s00704-021-03814-7

Wasis, B., Winata, B., & Marpaung, D. R. (2018). Impact of land and forest fire on soil fauna diversity in several land cover in Jambi Province, Indonesia. *Biodiversitas*, *19*(2), 660–666. https://doi.org/10.13057/biodiv/d190249

Whelan, N. (2004). Sampling from Archimedean copulas. *Quantitative Finance*, *4*(3), 339–352. https://doi.org/10.1088/1469-7688/4/3/009

Xie, P., Joyce, R., Wu, S., Yoo, S.-H., Yarosh, Y., Sun, F., & Lin, R. (2019). NOAA Climate Data Record (CDR) of CPC Morphing Technique (CMORPH) High Resolution Global Precipitation Estimates, Version 1. In *NOAA National Centers for Environmental Information*. NOAA National Centers for Environmental Information. https://doi.org/10.25921/w9va-q159

Xie, P., Joyce, R., Wu, S., Yoo, S. H., Yarosh, Y., Sun, F., & Lin, R. (2017). Reprocessed, bias-corrected CMORPH global high-resolution precipitation estimates from 1998. *Journal of Hydrometeorology*, *18*(6), 1617–1641. https://doi.org/10.1175/JHM-D-16-0168.1

Yananto, A., & Dewi, S. (2016). Analisis Kejadian El Nino Tahun 2015 dan Pengaruhnya Terhadap Peningkatan Titik Api di Wilayah Sumatera dan Kalimantan. *Jurnal Sains \& Teknologi Modifikasi Cuaca*, *17*(1), 11. https://doi.org/10.29122/jstmc.v17i1.544

Zahra, R. A., Nurjani, E., & Sekaranom, A. B. (2023). The Analysis of Fire Hotspot Distribution in Kalimantan and Its Relationship with ENSO Phases. *Quaestiones Geographicae*, *42*(1), 75–86. https://doi.org/10.14746/quageo-2023-0006

Zhang, L., & Singh, V. P. (2019a). Asymmetric Copulas: High Dimension. In *Copulas and their Applications in Water Resources Engineering* (pp. 172–241). Cambridge University Press. https://doi.org/10.1017/9781108565103.006

Zhang, L., & Singh, V. P. (2019b). Symmetric Archimedean Copulas. In *Copulas and their Applications in Water Resources Engineering* (pp. 123–171). Cambridge University Press. https://doi.org/10.1017/9781108565103

JAKARTA AND GREATER KUALA LUMPUR URBAN HEAT ISLAND DURING THE PANDEMIC OF COVID-19

Aditya SAPUTRA[1]*, **Mohd Hairy bin IBRAHIM[2]**, **Sharif Shofirun Sharif ALI[3]**, **Christopher GOMEZ[4]**, **Yuli PRIYANA[1]**, **JUMADI[1]**, **M. Iqbal Taufiqurrahman SUNARIYA[1]**, **DANARDONO[1]**, **Afif Ari WIBOWO[1]**, **Agus Anggoro SIGIT[1]**, **Choirul AMIN[1]**, **Hamim Zaky HADIBASYIR[1]**, **Kuswaji Dwi PRIYONO[1]**, **Khusna FLUORIDA[5]**, **Aditya SYAIFUDIN[5]**, **Ridwan HAFIDZIN[6]**

ABSTRACT

The Covid-19 outbreak rapidly became a global pandemic in December 2019, spreading through droplets, direct contact, and possibly airborne transmission. Southeast Asian nations like Malaysia and Indonesia experienced delayed outbreaks but saw a surge in cases. Analysing Covid-19 spatial patterns, especially concerning temperature and humidity, provides valuable insights. Utilizing remote sensing, allows studying the correlation between temperature conditions and Covid-19 outbreak patterns. This study focuses on investigating the impact of urban heat islands (UHIs) on Covid-19 outbreaks in Jakarta and Greater Kuala Lumpur, given their significant caseloads in Indonesia and Malaysia, respectively. The research integrates remote sensing, secondary data, and statistical analysis methods. Remote sensing was used to acquire land surface temperature (LST) and Normalized Difference Vegetation Index (NDVI). The analysis revealed that industrial and commercial areas were hotter than others during normal times, but during the pandemic, LST and UHI shifted from industrial to settlement areas due to large-scale social restrictions. This shift corresponded with the cessation of office, tourism, and industrial activities during lockdowns in March and July 2020 in Jakarta and Greater Kuala Lumpur, respectively. The concentration of people shifted from central business and industrial areas to residential areas during lockdowns, resulting in changes in UHI patterns.

Key-words: LST, UHI, Covid 19, NDVI, Urban climate, Social restriction

1. INTRODUCTION

In December 2019, the City of Wuhan which is located in Hubei, China developed into the epicentre of unknown pneumonia disease outbreaks. At the beginning, the number of the suspect increased both inside and outside China. At the same time, The China local government conducted rapid prevention to control the transmission of virus by conducting detail investigation of the virus, identification and insulated the positive suspect, continuous monitoring and medication the patient, also reconstruct the specific standard operational of patient diagnostic. As a result, at January 7, 2020, the China scientist successfully revealed the cause of unknown pneumonia outbreak in China. He found that the pneumonia was caused from a virus which later known as Corona Virus 2019 (Covid-19), (Heymann, 2020).

----

[1]*Geography Faculty, Universitas Muhammadiyah Surakarta, Indonesia; corresponding author* as105@ums.ac.id (AS), Yuli.Priyana@ums.ac.id (YP), Jumadi@ums.ac.id (J), iqbal.t.sunaria@ums.ac.id (ITS), dan115@ums.ac.id (D), aaw346@ums.ac.id (AAW), choirul.amin@ums.ac.id (CA), hamim.zaky.h@ums.ac.id (HZH), kdp130@ums.ac.id (KDP)*

[2] *Dept. Geography and Envirnment, Human Sciences Faculty, Universiti Pendidikan Sultan Idris, Malaysia; hairy@fsk.upsi.edu.my (MHI)*

[3] *School of Government, College of Law, Government & International Studies (COLGIS), Universiti Utara Malaysia; sshofirun@uum.edu.my (SSA)*

[4] *Graduate Program of Maritime Science, Kobe University, Japan; christophergomez@bear.kobe-u.ac.jp (CG)*

[5] *Remote sensing and Geographic Information System Laboratory, Geography Faculty, Universitas Muhammadiyah Surakarta, Indonesia; khusnaf@gmail.com (KF), aditya.saifuddin@mail.ugm.ac.id (ASN)*

[6] *Regional Planning Laboratory, Geography Faculty, Universitas Muhammadiyah Surakarta, Indonesia; ridwan.hafidzin@gmail.com (RH)*

At early stage of pandemic, Covid-19 started to infect the other countries who has close relationship with China such as Thailand, Japan, Korea, USA, Vietnam dan Singapore (China National Commission, 2020). The suspect of Covid-19 increased both in China and other countries. More than ten of thousands positive cases associated with Covid-19 were identified in several countries. The Covid-19 spread rapidly through droplet, direct contact to the positive suspect, and was able to spread airborne (Luo and Gao, 2020; Lu, Stratton and Tang, 2020; Wang, Tang, and Wei, 2020; Li et al., 2020).

Malaysia and Indonesia are Southeast Asia Countries that experienced spread of Covid-19 on Late January and early March 2020, respectively. It was slightly different with the other four neighbouring countries such as Thailand, Vietnam, Singapore, and Australia which started the Covid-19 spread on December 2019. Similar with other countries, the number of infected Covid-19 in Indonesia and Malaysia increased exponentially at the beginning stage of pandemic. On April 2020, the accumulative positive cases of Covid-19 reached 5,780 people with the number of death around 98 people. Meanwhile, in Indonesia there were 7,125 positive cases of Covid-19 with the number of death around 616 people. The distribution of Covid-19 cases in Malaysia and Indonesia until April 2020 is provided in **Figure 1 and 2** below.
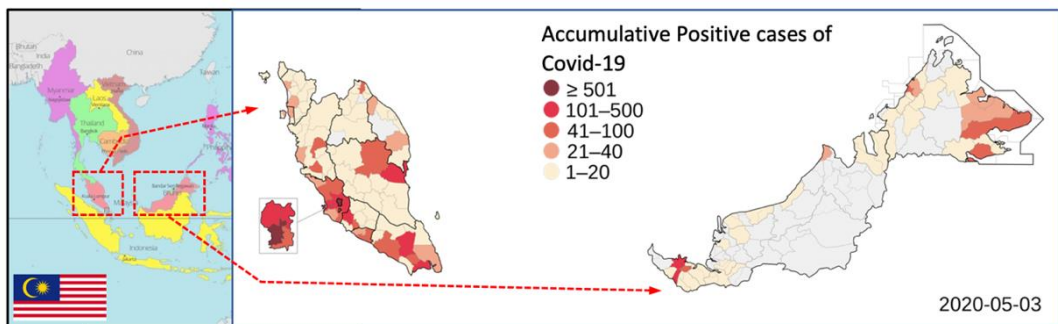

Fig. 1. The Covid-19 outbreak in Malaysia until 3 May 2020.
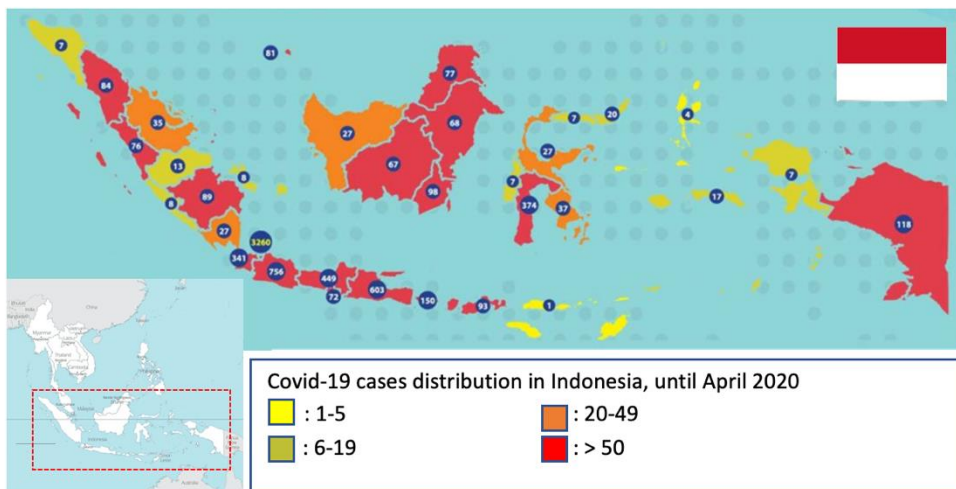*Source: Ministry of Health of Malaysia, 2020.*
.

Fig. 2. Distribution of Covid-19 outbreaks in Indonesia until 20 April 2020.
Source: Badan Nasional Penanggulangan Bencana (BNPB)/ National Disaster Management Agency, Indonesia, 2020.

In term of spatial pattern of Covid-19 outbreaks, there were some interesting facts that need to be observed further. At the beginning of outbreaks (December 2019-January 2020), the Covid-19 infected the country which is located in the high latitude such as US (Naeger & Murphy, 2020; Dutta et al., 2021), Italy (Bassani et al., 2021) and France (Kovacs & Haidu, 2021; Kovacs & Haidu, 2022). Araujo and Naimi (2020) found that based on the mathematical model, tropical climate with the high temperature is able to unstable the virus and make it easy to die. Previous researches also concluded the similar things. The temperature and humidity level affect the level of virus transmission in particular area. Thus in high latitude countries (low temperature and low humidity), the virus grow and spread rapidly across the country (Chen et al., 2020, Sajadi et al. 2020; Sun et al. 2020; dan Wang et al. 2020). The cold air temperature and low humidity condition are evidently helps the virus to last longer (Sun et al., 2020). Based on the spatial pattern analysis, the area with average surface temperature 5.810C and minimum-maximum temperature of -3.440C – 12.550C are closely associated with the location of Covid-19 infected people.

Indonesia and Malaysia which is located in tropical area have relatively high temperature and humidity comparing the other high latitude countries. Thus this condition can reduce the rate of the virus outbreaks. Based on the climate monitoring, in general, the temperature and humidity level in Indonesia and Malaysia increase in April to August 2020. However, the Covid-19 transmission still occur in several big cities in Indonesia and Malaysia such as Jakarta and Kuala Lumpur. Thus this phenomena need to be further observed to get the better understanding how far the climate element (temperature and humidity) inhibit the rate of virus outbreaks.

The temperature information can be easily obtained from remote sensing technology. Without any direct contact into research area, the temperature and humidity level can be precisely discovered. One of the satellite imageries that can be used to extract the temperature data is Landsat 8 OLI (Prohmdirek et al., 2020). Landsat provide 11 bands with 2 channels (10 and 11) which consists the thermal infrared (TIR). These channels able to record the surface temperature of the observed object. Thus it will interesting to conduct a research about the spatial analysis of relationship between temperature condition and the Covid-19 outbreak pattern. The urban heat island (UHI) will used as main parameter to characterise the temperature and humidity condition in Jakarta and Greater Kuala Lumpur. By identify the UHI pattern, the local temperature which affected by land use and air pollution can be identified accurately (Ibrahim, 2019). Thus, based on the aforementioned background above, this study aims to understand the urban heat island during the Covid-19 outbreak. Two big cities, The Greater Jakarta and Greater Kuala Lumpur, were chosen to conduct this research. In term of the number of the confirmed positive cases, both cities have the largest number of confirmed positive cases in Indonesia and Malaysia.

2. STUDY AREA

The two largest cities in Southeast Asia, Jakarta and Greater Kuala Lumpur, are presented in a comparative analysis in the present study. Those two cities is similar in terms of physical and human geography, the growth with respect to population size are in contrast to each other. Jakarta has around 9.61 million population, while Kuala Lumpur only 1.63 million population. Jakarta, is coastal city located in the north cost of west part of Java. Jakarta is the capital city of Indonesia and, therefore, is a centre of a large number of executive buildings and residential areas. Similar with Jakarta, Kuala Lumpur, is a coastal city and is the financial capital of the country. Kuala Lumpur located in the west coast of Malaysia close to the busiest strait in the world namely Malaka Strait. Gemorphologically, Kuala Lumpur is characterised as a huge valley known as "*Lembah Klang*" or Klang Valley which bordered by Titiwangsa mountainous area in the east, north and south and also bordered by the Malaka Strait in the west.

Jakarta expands into a Jakarta Metropolitan Region (JMR) or known as Jabodetabek (Jakarta-Bogor-Depok-Tangerang-Bekasi). This area develop into urban area which support the activities in the Jakarta as capitol city Indonesia. This area covers the sub-urban area in the west (Tangerang), south (Bogor and Depok), and the east (Bekasi) (Taki and Maatouk, 2018). Similar with Jakarta,

Kuala Lumpur expand rapidly to the east side (Hulu Langat) and north (Gombak) of the city (Boori et al., 2015). The west and the south side of the City Centre Commercial (CCC) Kuala Lumpur is bordered with the busy industrial area known as Petaling Jaya and Putra Jaya, respectively. There are also two important public facilities which are located in Petaling jaya and Putra Jaya, i.e., Klang Seaport in Petaling Jaya and international airport Kuala Lumpur in Putra Jaya. Kuala Lumpur also expand rapidly into Greater Kuala Lumpur which consists of Sabak Bernam, Kuala Selangor, Ulu Selangor and Gombak in the north part; Klang and Petaling in the west part; Kuala Langat and Sepang in the south part; and Ulu Langat in the east part of Kuala Lumpur City Centre,

In term of climate, Jakarta and Greater Kuala Lumpur has similar tropical climate. The average monthly temperature are between 26 to 28^0C (Masoudi et al., 2019). Both Jakarta and Greater Kuala Lumpur has dry and rainy season which affected by the monsoonal wind. **Figure 3** below shows that the Jakarta and Greater Kuala Lumpur have similar pattern of temperature, monthly average rainfall, humidity and daylight, because they are located in the same climatic zone and greatly influenced by the ocean (**Fig. 4**).
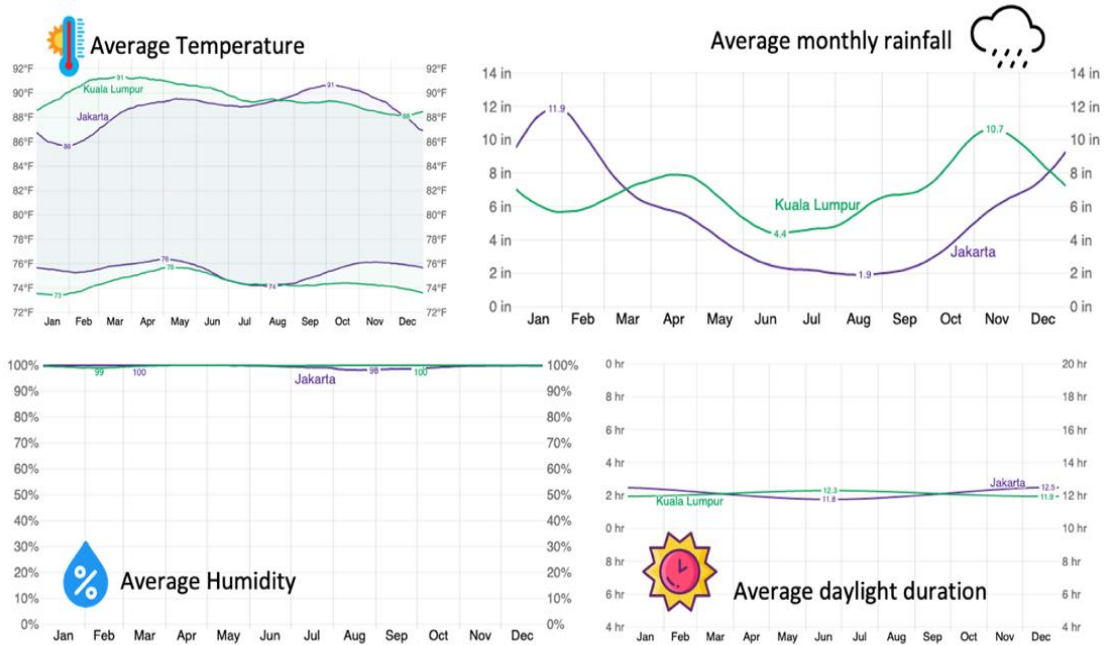

Fig. 3. Comparison of monthly average temperature, monthly rainfall, humidity, and daylight duration in Jakarta and Kuala Lumpur.
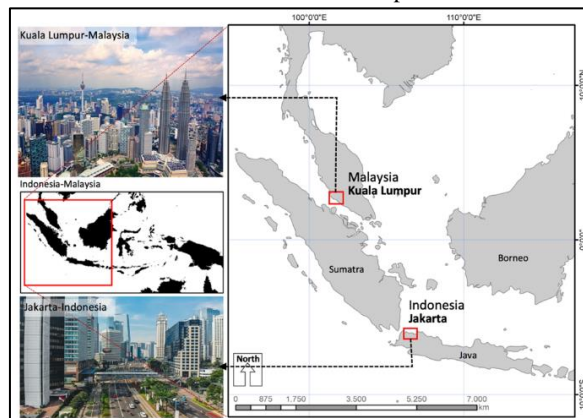

Fig. 4. Jakarta and Greater Kuala Lumpur map.

3. DATA AND METHODS

There are three main steps to conduct this study, first step is to know the covid-19 distribution in study area (Jakarta-Kuala Lumpur). The second step is two extract the surface temperature and the third step are to calculate the Urban Heat Island (UHI). The last step is to analyse the relationship between covid-19 distribution and UHI index. The LST will be extracted by using several equations through remote sensing software based on the image analysis of Landsat 8 OLI (Worachairungreung et al., 2023). Landsat 8 OLI or often called as L8 is the newest generation of Landsat after Landsat 7 ETM was stated experienced damage on one of the scanner sensors especially on Scan Line Corrector (SLC) on May 2003. Since that time, L8 was launched to work around 5 year. The main objective of L8 is to continue providing data which had been done by the previous generation. This project (L8) provides the satellite imagery which has faster temporal resolution (16 days) and also provides an open-source image base on the cloud platform. L8 carries several new innovations from the previous generation. The comparison between Landsat 7 and 8 can be seen in **Table 1**. The L8 was designed to have Sun-Synchronous with the altitude of 705 km. L8 has 16 days of temporal resolution with 98.9 minutes of orbital time travel. L8 carries 2 main sensors namely OLI and TIRS. OLI was made by BATC and TIRS was developed by NASA GSFC. Both of them have ability to records simultaneously, although they can operate individually if damage occurs on one of the sensors. Furthermore, there are also slightly different in term of the number of carried bands. The detail information of bands in Landsat 7 and 8 can be seen in **Table 2**.

Table 1.

The observation ability in L7 and L8.

	Landsat 7	Landsat 8
Scene per day	~450	~700
SSR size	378 Gbits, Block-based	3.14 Terabit, file-based
Type of Sensor	ETM+, Whisk-Broom	OLI/ TIRS, Push broom
Compression	No	~2:1 Variable rice compression
Data rate	150 Mbits/ second x 3 bands/ frequency	384 Mbits/ second, CCSDS bands virtual
Encoding	No all of CCSDS compliant	CCSDS, LDPC FEC
Range	S-band 2-way Droppler	GPS
Orbit	705 km Sun-syn. 98,2^0	705 km Sun-syn. 98,2^0
Crossing time	~10:00 AM ± 15 minutes	~10:00 AM ± 15 minutes

Source: USGS, 2019.

Table 2.

Comparison of bands between Landsat 7 and 8.

Bands (µm) of Landsat 7 ETM+			Bands (µm) of Landsat 8 OLI and TIRS		
			30 m Coastal/ Aerosol	0,435-0,451	Band 1
Band 1	30 m Blue	0,441-0,514	30 m Blue	0,452-0,512	Band 2
Band 2	30 m Green	0,519-0,601	30 m Green	0,533-0,590	Band 3
Band 3	30 m Red	0,631-0,692	30 m Red	0,636-0,673	Band 4
Band 4	30 m NIR	0,772-0,898	30 m NIR	0,851-0,879	Band 5
Band 5	30 m SWIR-1	1,547-1,749	30 m SWIR-1	1,566-1,651	Band 6
Band 6	60 m TIR	10,31-12,36	100 m TIR-1	10.60-11.91	Band 10
			100 m TIR-2	11.50-12.51	Band 11
Band 7	30 m SWIR-2	2,064-2,345	30 m SWIR-2	2,107-2,294	Band 7
Band 8	15 m Pan	0,515-0,896	15 m Pan	0,503-0,676	Band 8
			30 m Cirrus	1.363-1.384	Band 9

Source: USGS, 2019.

Urban Heat Island (UHI) can be defined as the urban temperature transformation in comparison to their surroundings area (Schwarz et al. 2011). Two common approaches to calculate the UHI are first, direct air temperature measurement, and second, measuring the surface temperature (Streutker, 2003). Today with the rapid enhancement of remote sensing technology, the land surface temperature can be obtained through satellite imagery analysis to support the UHI study around the globe. Several studies in different type of satellite imagery had been conducted to obtain the land surface temperature in order to support the UHI study. Schwarz et al. (2011), Tomlinson et al. (2012) and Miao et al. (2009), succeeded to extract the land surface temperature and to analyse the UHI through low-resolution sensor (MODIS). Meanwhile Chen et al. (2006), Zha et al. (2003), Liu & Zhang (2011) and Kaplan et al (2018), successfully utilized the middle resolution image such as Landsat 8 OLI and ASTER to study the UHI for particular cities and smaller area. Most of those previous study revealed that the different level of UHI is dominantly controlled by surface temperature which depends on the function of different land cover (Owen et al., 1998) especially the vegetation abundance (Chen et al., 2006; Gallo and Owen, 1999; Weng, 2001; and Weng et al., 2004). The recent study analysis the UHI phenomena during the pandemic Covid in two similar areas, i.e. greater Kuala Lumpur, Malaysia and Jakarta, Indonesia. Both areas are compared the UHI before and during the pandemic COVID-19. LANDSAT-8 on May, July, September, and December 2020 were used to obtain the LST and UHI. Meanwhile, Landsat 8 on March and August 2019 and 2020 were used to generate LST and UHI in Greater Kuala Lumpur. This recent study analysed also the relationship between the policy during the pandemic covid 19 and the UHI pattern.

In Malaysia, Covid-19 case started on Januari 25, 2020 (Hashim et al., 2021) and the government applied Lockdown in mid-March (Yusof, 2021). Meanwhile, In Indonesia first case of COVID-19 started on March 2, 2020 (Damaledo, 2021) and first lockdown in Indonesia as known as PSBB (Large-Scale Social Restrictions) which was applied in April 10, 2020. The data used represented 2 season, dry season and wet season in Jakarta and Kuala Lumpur. The data used is the Landsat 8 OLI with minimum cloud cover. The UHI identification consist of several steps such as calculating the radiance value of the satellite imagery, brightness temperature value conversion, and calculating the Land Surface Emissivity (LSE). The LSE was calculated by considering the Normalized Difference Vegetation Index (NDVI) and Proportion of Vegetation (PV) (Sobrino et al., 2004). The set of equation was used to generate the UHI index and the research flow can be seen in **Figure 5**.
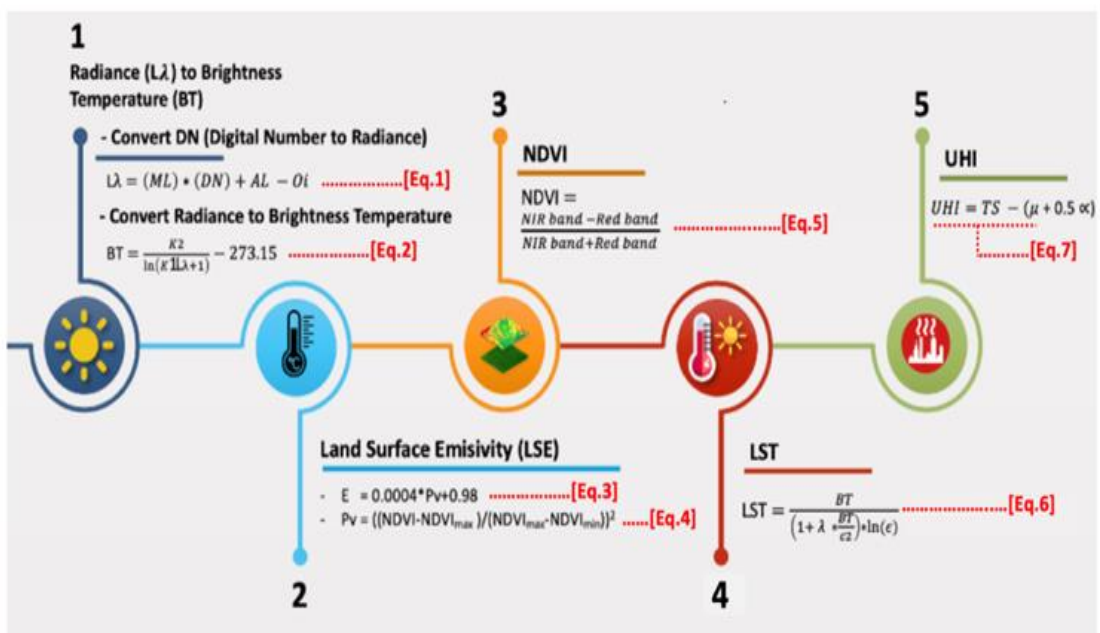

1

Radiance (Lλ) to Brightness Temperature (BT)

- Convert DN (Digital Number to Radiance)

$$L\lambda = (ML) * (DN) + AL - Oi \quad \text{[Eq.1]}$$

- Convert Radiance to Brightness Temperature

$$BT = \frac{K2}{\ln(K1/L\lambda + 1)} - 273.15 \quad \text{[Eq.2]}$$

3

NDVI

$$NDVI = \frac{NIR\ band - Red\ band}{NIR\ band + Red\ band} \quad \text{[Eq.5]}$$

5

UHI

$$UHI = TS - (\mu + 0.5 \propto) \quad \text{[Eq.7]}$$

Land Surface Emisivity (LSE)

- $E = 0.0004 * Pv + 0.98$ \quad [Eq.3]
- $Pv = ((NDVI - NDVI_{max})/(NDVI_{max} - NDVI_{min}))^2$ \quad [Eq.4]

2

LST

$$LST = \frac{BT}{\left(1 + \lambda * \frac{BT}{c2}\right) * \ln(\epsilon)} \quad \text{[Eq.6]}$$

4

Fig. 5. The workflow of the research.

Note. *Lλ: Radiance; ML and AL: factor value radiance from metadata; DN: digital number of each pixels; BT: Brightness Temperature; K1 and K2: Obtain from metadata of Landsat imagery is constant value; E: Emissivity; Pv: proportion vegetation value; NDVI: Normalised different Vegetation Index; LST: land surface temperature; C2 follow equation 7 below; UHI is urban heat island; TS is land surface temperature, μ is the average value of TS and α is standard deviation of TS.*
Equation 7.

$$C2 = h\frac{c}{s}$$

h = Planck constant value (1.38 x 10⁻²³ JK⁻¹); c is light speed vacuum (2,998 X 10-8 ^{Ms-1}); s = Boltzmann constant value (1.38 x 10⁻²³ JK⁻¹); C2 value is constant around 14,338 MK.

4. RESULTS

4.1. Land surface temperature (LST)

Air temperature and surface temperature is slightly different. Air temperature refers to the measurement of the temperature of the air in the Earth's atmosphere. It is typically measured at a certain height above the ground, often at around 1.5 to 2 meters (5 to 6.5 feet) above the surface. This measurement is commonly recorded using thermometers placed inside a weather station or other measuring devices. Air temperature is an important parameter in weather forecasting, climate studies, and various applications ranging from agriculture to energy consumption predictions. It plays a significant role in determining weather patterns, as variations in air temperature lead to changes in atmospheric pressure, wind patterns, and precipitation. (Good et al., 2017). Land surface temperature (LST) refers to the temperature of the actual land or ground surface itself. LST can be vary based on the factors such as land cover (forests, urban areas, deserts), moisture content, and solar radiation received by the surface. LST is commonly measured using remote sensing techniques, such as satellite sensors that detect infrared radiation emitted by the Earth's surface. These sensors can provide a comprehensive view of land surface temperatures across large geographic areas. LST data are crucial for studying urban heat islands, monitoring agricultural productivity, assessing environmental changes, and understanding the Earth's energy balance.

During the observation months (May, July, September and December 2020), there are strong heterogeneity of land surface temperature in Jakarta. The observed months refers to the dry and wet season in Indonesia. July-September represent the wet season, meanwhile December represent the wet season. The land surface temperature variation also occur in different type of land cover over the Jakarta. The minimum surface temperature in the observed month are 13.42⁰C, meanwhile, the highest surface temperature of study area is 35,73ᵒC. During the dry season which has low humidity and rainfall, the temperature near surface is vary between 13-34⁰C. Meanwhile, the rainy season which has high humidity and rainfall, the temperature near surface is vary between 13-35⁰C. The LST condition during the observation months can be seen in **Figure 6** below.

During the Pandemic Covid-19 LST in Greater Kuala Lumpur has similar pattern in Jakarta, Indonesia. There was a shift in LST distribution from industrial area (Pelabuhan Klang-Petaling Jaya) to settlement area in the east such as Wangsa Maju, Cheras, Hulu Langat and Puchong. In March 2020 (dry season), the LST in Kuala Lumpur range between 13.01 – 33.53⁰C. The hot temperature tends to distribute in industrial area in Centre part of Greater Kuala Lumpur from west side (Klang) to the east part of Hulu Langat. In general, the centre to south part of Greater Kuala Lumpur experienced higher LST comparing than the north part of Kuala Lumpur (**Fig. 7** (left)). Whereas, LST in Greater Kuala Lumpur slightly shifted to the west direction during the August 2020. The LST value in August 2020 range between 15.92-35.48⁰C.

The shifting LST mostly occurs because wind speed (Klysik & Fortuniak, 1999; Steeneveld et al., 2011; Wang et al., 2019), or water index variability (Binarti & Santoso, 2023). However, recently during the covid-19 pandemic, the population restriction policy indirectly affects the LST pattern (Hadibasyir et al., 2020; Saputra et al., 2022). The restriction policy forced the people to stay and work at home to decrease the covid-19 transmission. As a results, the LST pattern move to the settlement area due to high energy and electricity consumption in household level (Shofirun et al., 2023; Elvidge et al., 1997; Bessec et al., 2008).
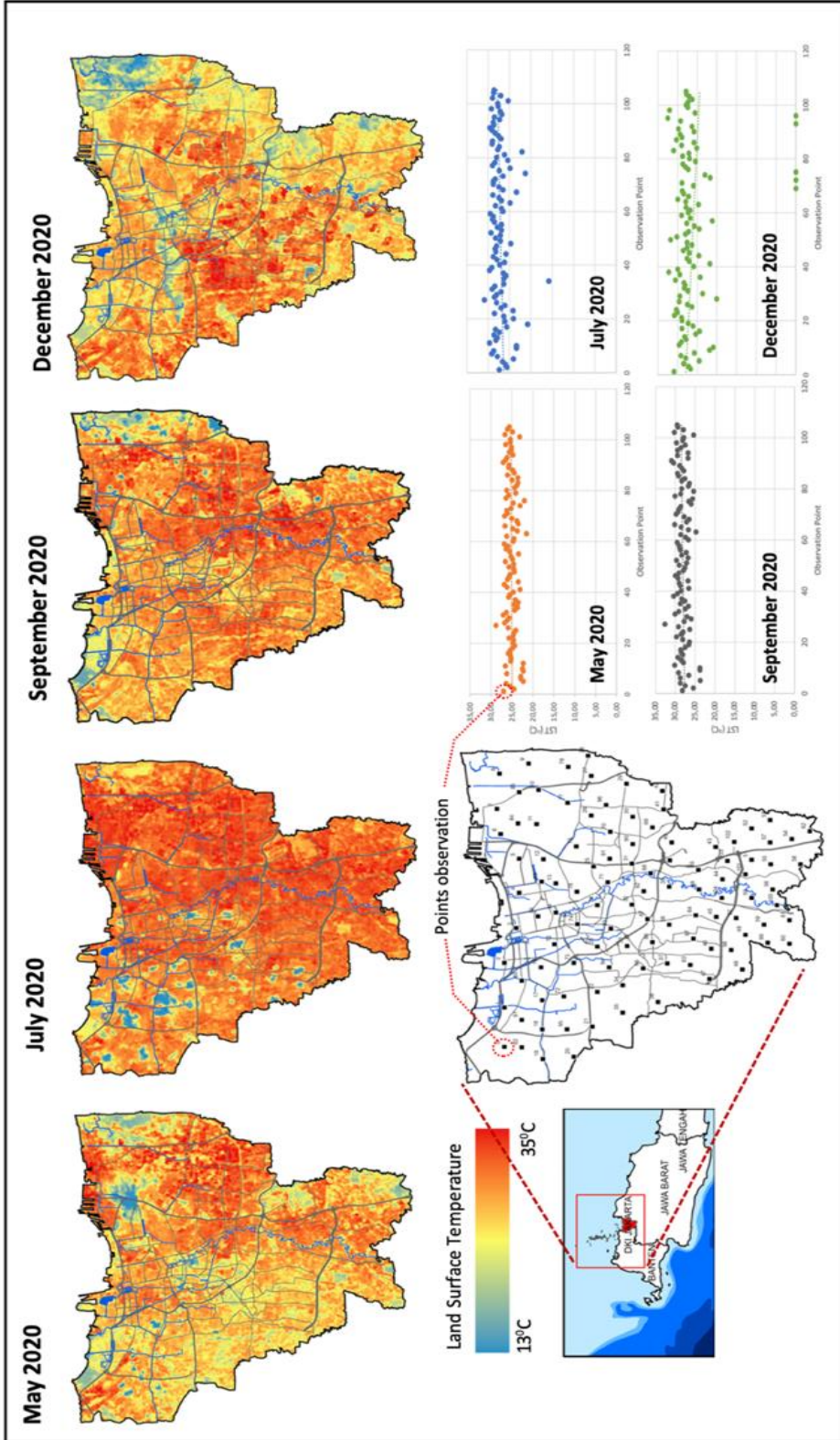
Fig. 6. The LST in Jakarta during May, July, September and December 2020.

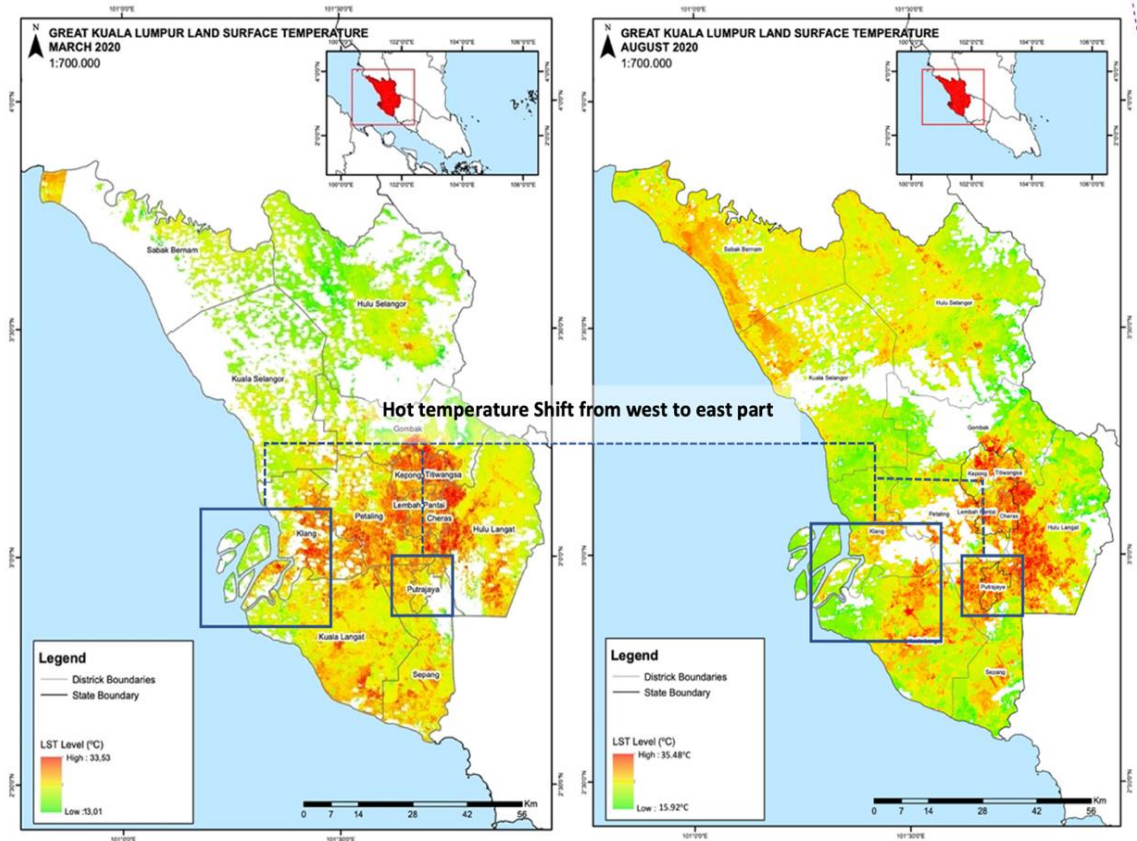The LST pattern in March and August 2020 can be seen in **Figure 7** (Left) and 7(Right) below.

Fig. 7. LST Greater Kuala Lumpur in March 2020 (left) and August 2020 (right).

4.2. Urban Heat Island (UHI)

The phenomenon where a particular area has a higher temperature compared to its surroundings is known as the urban heat island effect. In the most of big cities, the temperature at the city centre is observed to be elevated in comparison to the surrounding areas (Adinna et al. 2009; Synnefa et al. 2008; Yamamoto 2006). In general, Jakarta and Greater Kuala Lumpur have similar pattern of UHI phenomena. In Jakarta, UHI tend to occurs in industrial area which are located in the north and east part of Jakarta. While, in Greater Kuala Lumpur UHI tend to occur in city centre (Central Part) and industrial area (west part). The value of UHI in Jakarta range between 0-5.8°C and 0-7.7°C in July and December 2020, respectively. On the other hand, The UHI in Greater Kuala Lumpur range between 0-9.5°C and 0-11.3°C in March and August 2020, respectively. The UHI distribution both In Jakarta and Greater Kuala Lumpur is provided in **Figure 8** below.

5. DISCUSSION

During pandemic of Covid-19 every country has their own regulation to minimise the virus transmission and fatalities. Jakarta, capitol city of Indonesia, implemented several policies to reduce the virus transmission. Jakarta at least implemented 5 large-scale social restriction (PSBB) in May-December 2020 and Activities Restriction Enforcement (PPKM) in January to December 2021. The PSBB including work from home, social distancing, restriction on public and sociocultural event or services and limitation of public transportation (Retnowati et al., 2022).
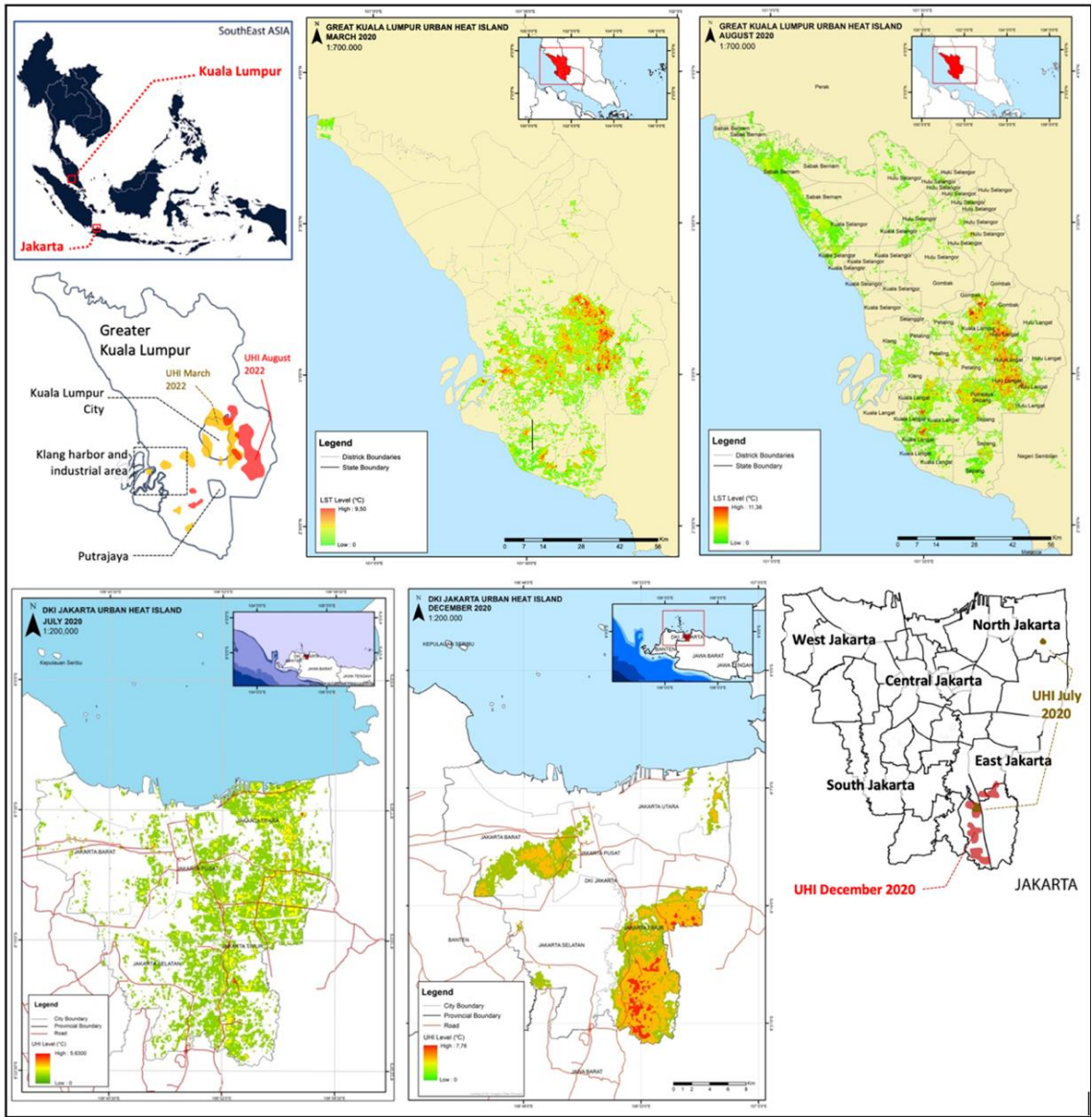
Fig. 8. UHI distribution in Kuala Lumpur (above) in March 2020 (left) and August 2020 (right); UHI distribution in Jakarta (below) in July 2020 (left) and December 2020 (right).

PSBB allows only important sector such as health facility, food, and banking to keep open with certain rule. Meanwhile, PPKM regulates the portion of Work from home (WFH) and work from office (WFO) also dine-in in the restaurant regulation (25% from capacity). By implementing these policies, Indonesia government succeeded to reduce the virus transmission. Furthermore, this policy also indirectly affects the LST and UHI pattern. In July 2020 when Jakarta implemented the PSBB Stage, the UHI condition has the ordinary pattern. The UHI occurred in city center, CBD, industrial area and commercial area. However, in December 2020 when the Jakarta implemented PSBB stage 5, the UHI shifted form commercial, CBD, city center and industrial area to settlement area in the East and West Jakarta. The reason for this lies in the fact that the rigorous policy endorsed limitations on social activities, encompassing office tasks, entertainment, and public transportation. As a result,

the people most spend their time at home and caused more consumption on energy and electricity. This accumulation condition will lead to increase the air and surface temperature.

Similar to Jakarta, The UHI in Greater Kuala Lumpur were shifted as some social regulations applied during the pandemic Covid-19. During the pandemic Covid-19 Malaysia government applied at least 6 phases of Social Restriction namely Pre-Movement Control Order (Pre-MCO), MCO, Conditional MCO, Recovery MCO, Extended MCO, and MCO 2.0. (Rajendran, 2021) (**Fig. 10**). Full lockdown or MCO were applied in early stage of pandemic, 18 March-3 May 2020. All sectors were lockdown except important sector such health, food supply, bank, and logistics. As a results some industrial and commercial area such Klang Harbour and industrial areas and Kuala Lumpur City Centre (KLCC) were closed. This condition effect the UHI pattern in Greater Kuala Lumpur. UHI tend to arise in settlement area eastern part of KLCC (**Fig. 8**). This results in line with the previous research (Shofirun et al., 2023; Elvidge et al., 1997; Bessec et al., 2008; Hadibasyir et al., 2020) who found that social restriction policy forced the people to limit their movement and keep stay at home. Thus, when somebody stay longer in the home means the energy and electricity consumption also increase. This prolonged situation will lead the LST as well as UHI in the atmosphere. The detail illustration of the relationship between the applied social regulation during pandemic, covid-19 cases, air temperature, and UHI in Jakarta and Greater Kuala Lumpur can be seen in **Figure 9 and 10**, respectively.

The shifting pattern of UHI was also signified when the UHI in the same months a year before Covid-19 compared with the UHI during the pandemic. For instance, in Greater Kuala Lumpur, the UHI of March and August 2019 (normal condition, before Covid-19) occurred in the Klang Harbour and Industrial area in March and August 2019. During the Covid-19, when the government applied the Pre-MCO and RMCO (March and August 2020) the UHI shifted to the settlement area in the east part of KLCC. The Greater Kuala Lumpur UHI shifting before and during the pandemic can be seen in **Figure 11**.
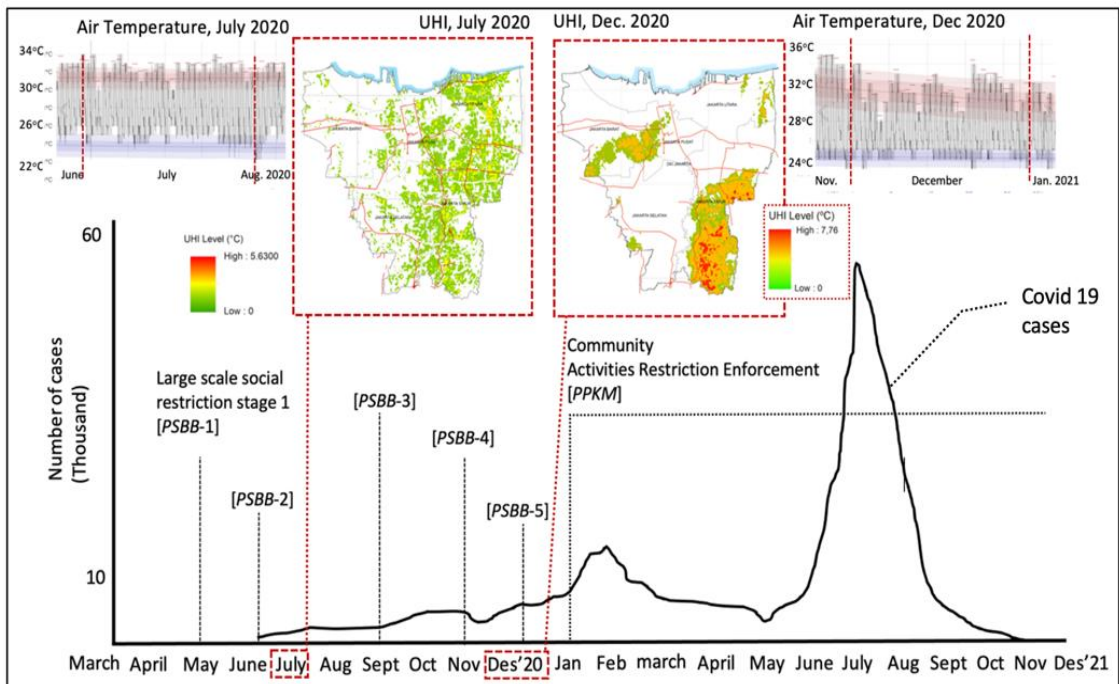

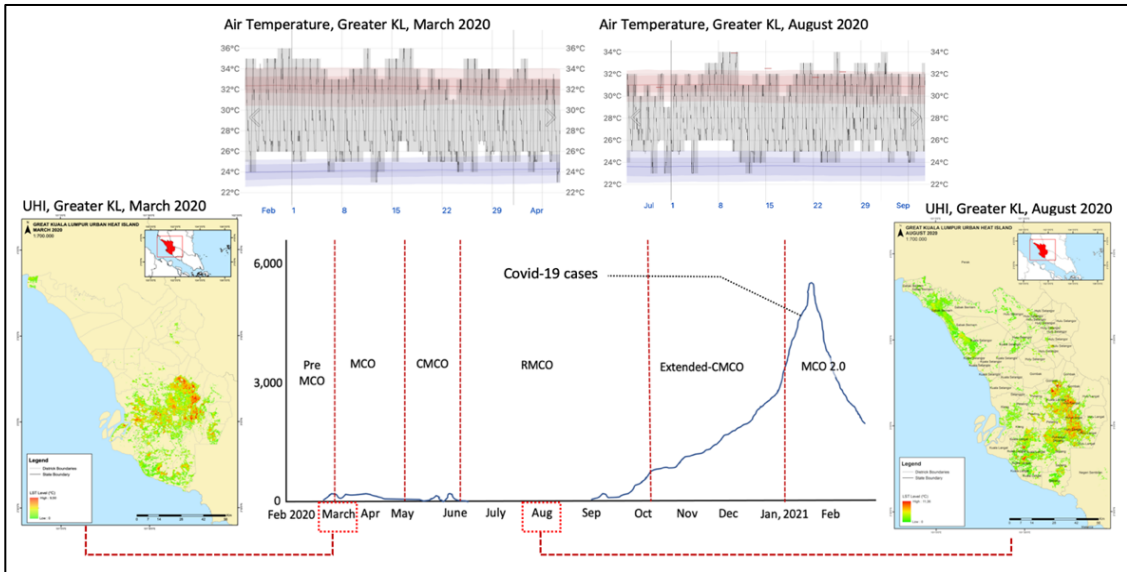**Fig. 9**. Covid-19 cases, applied regulation, UHI and air temperature in Jakarta.

Fig. 10. Covid-19 cases, applied regulation, UHI and air temperature in Greater Kuala Lumpur, March and August 2020.
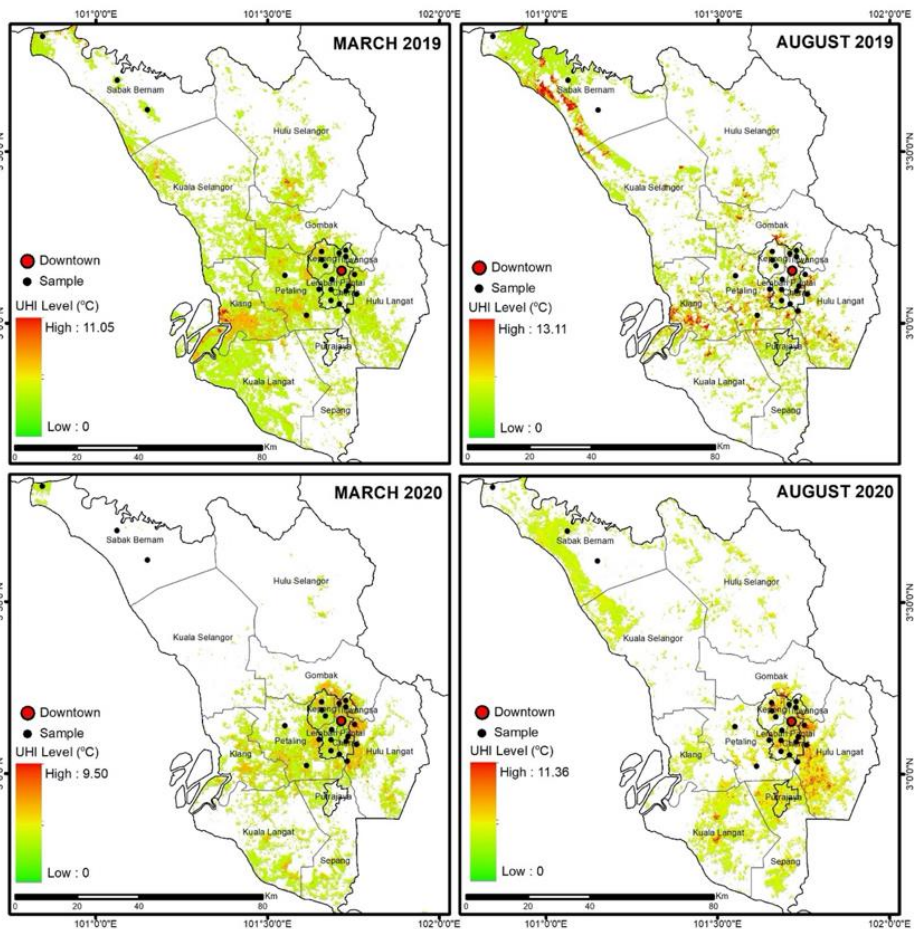

Fig. 11. UHI shifting in Greater Kuala Lumpur before and during the pandemic.

6. CONCLUSIONS

This study has compared the LST and UHI pattern between different social regulation during pandemic Covid-19 both in Jakarta and Greater Kuala Lumpur. Results showed that the LST and UHI has shifted during the two observed months (July-December 2020 in Jakarta and March-August 2020 in Greater Kuala Lumpur). In July and December 2020, the Indonesian government applied large scale social restriction (PSBB) stage 2 and stage 5, respectively. The government policy forced the population to stay at home. Thus, further this condition affected the LST and UHI pattern. Results showed that during the observed month the LST and UHI shifted from industrial area to settlement area.

Similar to Jakarta, Greater Kuala Lumpur has experienced the same LST and UHI movement. During the observed month March 2020, Kuala Lumpur experienced by transition regulation from pre MCO to fully MCO, meanwhile in December 2020 Malaysian Government applied Recovery MCO (RMCO). As a results, the LST and UHI started to decrease in Industrial area and appeared in settlement area in the east part of KLCC in March 2020 and in December 2020, the LST and UHI occurred in majority settlement area in the east part of Kuala Lumpur due to the RMCO regulation.

R E F E R E N C E S

Adinna, E., Christian, E. I., and Okolie, A. T. (2009). Assessment of urban heat island and possible adaptations in Enugu urban using Landsat-ETM. *Journal of Geography and Regional Planning*, **2**(2), 030-036.

Araujo, MB. & Naimi, B. (2020). Spread of SARS-CoV-2 Coronavirus likely constrained by climate. medRxiv; DOI: 10.1101/2020.03.12.20034728.

Bassani, C., Vichi, F., Esposito, G., Montagnoli, M., Giusto, M., & Ianniello, A. (2021). Nitrogen dioxide reductions from satellite and surface observations during COVID-19 mitigation in Rome (Italy). *Environmental Science and Pollution Research*, **28**, 22981-23004. https://doi.org/10.1007/s11356-020-12141-9

Bessec, M. & Fouquau, J. (2008). The Non-linear Link between Electricity Consumption and Temperature in Europe: A Threshold Panel Approach. *Energy Economics*, **30**(5), 2705–2721.

Binarti, F. & Santoso, A.J. (2023). Identifying climate change vulnerability based on land cover indicators: a case study in Surabaya, Indonesia. *Geographia Technica*, **18**(1), 71-84. http://dx.doi.org/10.21163/GT_2023.181.06

Boori, M.S., Netzband, M., Coudhary, K., Vozenilek, V. (2015). Monitoring and modeling of urban sprawl through remote sensing and GIS in Kuala Lumpur, Malaysia. *Ecological Processes*, **4**(1). DOI: 10.1186/s13717-015-0040-2

Chen, X-L., Zhao, H.-M., Li, P.-X., Yin, Z.-Y. (2006). Remote sensing image -based analysis of the relationship between urban heat island and land use/cover changes. *Remote Sensing Environment*, **104**. 133-146.

Cina National Health Commission. (2020) Update on the novel coronavirus pneumonia outbreak (Jan 24, 2020). Beijing: Cina National Health Commission. http://www.nhc.gov.cn/xcs/yqdt/202001/c5da49c4c5bf4bc320ec2036480627.shml (accessed Jan 24, 2020)

Damaledo, Y. D. (2021). Kasus Corona Pertama di Indonesia Diumumkan Tahun Lalu [Kesehatan]. Tirto.Id. https://tirto.id/2-maret-2020-kasus-corona-pertama-di-indonesia-diumumkan-tahun-lalu-gaKw

Dutta, V., Kumar, S., & Dubey, D. (2021). Recent advances in satellite mapping of global air quality: evidences during COVID-19 pandemic. *Environmental Sustainability*, **4**(3), 469-487. https://doi.org/10.1007/s42398-021-00166-w

Elvidge, CD., Baugh, KE, Kihn, EA., Kroehl, HW., Davis, ER., and Davis, CW. (1997). Relation between Satellite Observed Visible-near Infrared Emissions, Population, Economic Activity and Electric Power Consumption. *International Journal of Remote Sensing*, **18**(6), 1373–1379.

Gallo, K.P., Owen, T.W. (1999) Satellite-based adjustment for the urban heat island temperature bias. *Journal Applied Meteorology*, **38**, 806-813.

Good, EJ., Ghent, DJ., Bulgin, CE., Remidios, JJ. (2017). A spatiotemporal analysis of the relationship between near-surface air temperature and satellite land surface temperatures using 17 years of data from the ATSR series. *JGR: Atmospheres*, **122**(17). https://doi.org/10.1002/2017JD026880

Hadibasyir, HZ., Rijal, SS. and Sari, DR. (2020). Comparison of Land Surface Temperature During and Before The Emergence of Covid-19 Using Modis Imagery in Wuhan City, *Forum Geogr*., **34**, 1–15.

Hashim JH, Adman MA, Hashim Z, Mohd Radi MF and Kwan SC (2021) COVID-19 Epidemic in Malaysia: Epidemic Progression, Challenges, and Response. *Front. Public Health* 9:560592. doi: 10.3389/fpubh.2021.560592

Heymann, D.L., (2020). A novel coronavirus outbreak of global health concern. *Thelancet*, **395**, 497-514. doi.org/10.1016/ S0140-6736(20)30185-9.

Ibrahim, S. & Halounova, L. (2019). Statistical study of MODIS algorithms in estimating aerosol optical depth over the Czech Republic. *Stavební Obzor - Civil Engineering Journal*, **28**(4), 523-531. https://doi.org/10.14311/CEJ.2019.04.0043

Kovacs, K. D. & Haidu, I. (2021). Effect of anti-COVID-19 measures on atmospheric pollutants correlated with the economies of medium-sized cities in 10 urban areas of Grand Est region, France. *Sustainable Cities and Society*, 74, 103173. https://doi.org/10.1016/j.scs.2021.103173

Kovács K.D. & Haidu I. (2022), Tracing out the effect of transportation infrastructure on NO2 concentration levels with Kernel Density Estimation by investigating successive COVID-19-induced lockdowns. *Environmental Pollution,* **309** : 119719. https://doi.org/10.1016/j.envpol.2022.119719

Li XG, Zai JJ, Wang XM, Li Y, (2020). Potential of large 'first generation' human-to-human transmission of 2019-nCoV. *J Med Virol*. https://doi.org/10.1002/jmv.25693

Liu, L and Zhang, Y. (2003). Urban heat island analysis using the Landsat TM and ASTER data: A case study in Hong Kong, *Remote Sensing*, **3**, 1535-1552

Luo G, Gao S-J. (2020). Global health concerns stirred by emerging viral infections. J Med Virol. 2020;92:399–400. https://doi.org/10.1002/jmv.25683

Lu H, Stratton CW, Tang YW. (2020). Outbreak of pneumonia of unknown ethology in Wuhan China: the mystery and the miracle. *J Med Virol*. https://doi.org/10.1002/jmv.25678

Kaplan, G., Avdan, U., Avdan, Z. Y. (2018) Urban heat island analysis using the Landsat 8 satellite data: A case study in Skopje, Macedonia. *MDPI Proceeding of 2nd International Electronic Conference of Remote Sensing*, 22 March-5 April 2018. 358, doi: 10.3990/ecrs-2-05171.

Kłysik, K., and Fortuniak, K. (1999). Temporal and spatial characteristics of the urban heat island of Łoʹdzʹ, Poland, Atmos. Environ. 33 (24– 25) (1999) 3885–3895

Masoudi, M., Tan, P. Y., & Liew, S. C. (2019). Multi-city comparison of the relationships between spatial pattern and cooling effect of urban green spaces in four major Asian cities. *Ecological Indicators*, **98**, 200–213. Doi: 10.1016/j.ecolind.2018.09.058

Miao, S., Chen, F., LeMone, M.A., Tewari, M., Li, Q., Wang, Y. (2009). An observational and modeling study of characteristics of urban heat island and boundary layer structures in Beijing. *Journal Applied Meteorology and Climatology*, **48**, 484-501.

Naeger, A. R., & Murphy, K. (2020). Impact of COVID-19 containment measures on air pollution in California. *Aerosol and Air Quality Research*, **20**(10), 2025-2034. https://doi.org/10.4209/aaqr.2020.05.0227

Owen, T., Carlson, T., Gillies, R. (1998) An assessment of satellite remotely-sensed land cover parameter in quantitatively describing the climatic effect of urbanization. *International Journal of Remote Sensing*. **19**, 1663-1681.

Prohmdirek, T., Chunpang, P., Laosuwan, T. (2020) The relationship between normalized difference vegetation index and canopy temperature that affects the **U**rban **H**eat **I**sland phenomenon. *Geographia Technica*, **15**(2), 222-234. http://dx.doi.org/10.21163/GT_2020.152.21

Retnowati, WD., Nurmandi, A., Zahra, AA. (2022). Handling COVID-19 in the capital city of Jakarta with innovation policy: the scale of social restrictions policy. *Heliyon*, **8**(1): e09467. doi: 10.1016/j.heliyon. 2022.e09467

Sajadi MM, Habibzadeh P, Vintzileos A, Shokouhi S, Miralles-Wilhelm F, Amoroso A. (2020). Temperature, Humidity, and Latitude Analysis to Estimate Potential Spread and Seasonality of Coronavirus Disease 2019 (COVID-19). *JAMA Netw Open*. 1;**3**(6): e2011834. doi: 10.1001/jamanetworkopen.2020.11834. PMID: 32525550; PMCID: PMC7290414.

Saputra, A., Hairy, MH, Shofirun S, Saifuddin, A, Furoida, K. (2022). Assessing urban heat island in Jakarta, Indonesia during the pandemic of Covid-19. *IOP Conf. Series: Earth and Environmental Science*, 012069. doi:10.1088/1755-1315/986/1/012069

Schwarz, N; Lautenbach, S; Seppelt, R. (2011). Exploring indicators for quantifying surface urban heat islands of European Cities with MODIS land surface temperatures. *Remote Sensing Environment*, **115**,3175-3186.

Shofirun S; Yusoff, MN; Talib, A; Rahman MAA; Sohaimi, NS; Mokthsim, N; Ibrahim, MH; Saputra, A. (2023). The use of energy in Malaysia: Mapping energy flow from primary source to end use. Proceeding of International Summit on Education, Technology, and Humanity 2021, *AIP Conf. Proc.* 2727, 050028-1–050028-11; https://doi.org/10.1063/5.0141394

Sobrino, J., Jimenez, JC., Paolini, L. (2004). Land surface temperature retrieval from LANDSAT TM 5. *Remote Sensing of Environment*, **90**(4):434-440. doi: 10.1016/j.rse.2004.02.003

Steeneveld, G., Koopmans, S., Heusinkveld, B., Van Hove, L., Holtslag, A. (2011) Quantifying urban heat island effects and human comfort for cities of variable size and urban morphology in the Netherlands, *J. Geophys. Res.: Atmos.*, **116** (D20).

Streutker, D.R. (2003). Satellite-measured growth of the urban heat island of Houston, Texas. *Remote Sensing Environment*, **85**, 282-289.

Sun N, Wei L, Shi S, Jiao D, Song R, Ma L, Wang H, Wang C, Wang Z, You Y, Liu S, Wang H. A. (2020). Qualitative study on the psychological experience of caregivers of COVID-19 patients. *Am J Infect Contro*, **48**(6):592-598. doi: 10.1016/j.ajic.2020.03.018. Epub 2020 Apr 8. PMID: 32334904; PMCID: PMC7141468.

Synnefa, A., Dandou, A., Santamouris, M., Tombrou, M., & Soulakellis, N. (2008). On the use of cool materials as a heat island mitigation strategy. *Journal of Applied Meteorology and Climatology*, **47**(11), 2846-2856.

Taki, HM. And Maatouk, MMH. (2018). Spatial Statistical Analysis for Potential Transit Oriented Development (TOD) in Jakarta Metropolitan Region. *JGEET*, **3**(1). Doi: 10.24273/jgeet.2018.3.01.1091

Tomlinson, C., Chapman, L., Thornes, J., Bakeret, C.J. (2012). Derivation of Birmingham's summer surface urban heat island from MODIS satellite images. *International Journal Climatology*, **32**, 214-224

Wang, K., Aktas YD., Stocker, J., Carruthers, D., Hunt, J., Malki-Epshtein, L. (2019). Urban heat island modelling of a tropical city: case of Kuala Lumpur. *Geosci. Lett.*, **6**:4 https://doi.org/10.1186/s40562-019-0134-2

Wang W, Tang JM, Wei FQ. (2020). Updated understanding of the outbreak of 2019 novel coronavirus (2019-nCoV) in Wuhan, China. *J Med Virol*. https://doi.org/10.1002/jmv.25689

Weng, Q.A. (2001) Remote sensing? GIS evaluation of urban expansion and its impact on surface temperature in the Zhuijang Delta, China. *International Journal of Remote Sensing*, **22**, 1999-2014.

Weng , Q. Lu, D., Schubring, J. (2004) Estimation of land surface temperature-vegetation abundance relationship for urban heat island studies. *Remote Sensing Environment*, **89**, 467-483.

Worachairungreung, M., Thanakunwutthirot., K., Kulpanich, N. (2023). A study on oil palm classification for Ranong province using data fusion and machine learning algorithms. *Geographia Technica*, **18**(1), 161-176. http://dx.doi.org/10.21163/GT_2023.181.12

Yamamoto, Y. (2006). Measures to mitigate urban heat islands. *Science and Technology Trends Quarterly Review*, **18**(1), 65- 83.

Yusof, Amir. (2021) Timeline: How the COVID-19 pandemic has unfolded in Malaysia since January 2020. Mediacrop. https://www.channelnewsasia.com/asia/timeline-how-covid-19-pandemic-has-unfolded-malaysia-january-2020-2082081. Accessed 2 Januray 2024.

Zha, Y., Gao, J., and Ni, S. (2003) Use of normalized difference built-up index in automatically mapping urban areas from TM Imagery. *International Journal of Remote Sensing*, **24**, 583-594.

Aims and Scope

Geographia Technica is a journal devoted to the publication of all papers on all aspects of the use of technical and quantitative methods in geographical research. It aims at presenting its readers with the latest developments in G.I.S technology, mathematical methods applicable to any field of geography, territorial micro-scalar and laboratory experiments, and the latest developments induced by the measurement techniques to the geographical research.

Geographia Technica is dedicated to all those who understand that nowadays every field of geography can only be described by specific numerical values, variables both oftime and space which require the sort of numerical analysis only possible with the aid of technical and quantitative methods offered by powerful computers and dedicated software.

Our understanding of *Geographia Technica* expands the concept of technical methods applied to geography to its broadest sense and for that, papers of different interests such as: G.I.S, Spatial Analysis, Remote Sensing, Cartography or Geostatistics as well as papers which, by promoting the above mentioned directions bring a technical approach in the fields of hydrology, climatology, geomorphology, human geography territorial planning are more than welcomed provided they are of sufficient wide interest and relevance.

Targeted readers:

The publication intends to serve workers in academia, industry and government.
Students, teachers, researchers and practitioners should benefit from the ideas in the journal.

Guide for Authors

Submission

Articles and proposals for articles are accepted for consideration on the understanding that they are not being submitted elsewhere.

The publication proposals that satisfy the conditions for originality, relevance for the new technical geography domain and editorial requirements, will be sent by email to the address editorial-secretary@technicalgeography.org.

This page can be accessed to see the requirements for editing an article, and also the articles from the journal archive found on www.technicalgeography.org can be used as a guide.

Content

In addition to full-length research contributions, the journal also publishes Short Notes, Book reviews, Software Reviews, Letters of the Editor. However the editors wish to point out that the views expressed in the book reviews are the personal opinion of the reviewer and do not necessarily reflect the views of the publishers.

Each year two volumes are scheduled for publication. Papers in English or French are accepted. The articles are printed in full color. A part of the articles are available as full text on the www.technicalgeography.org website. The link between the author and reviewers is mediated by the Editor.

Peer Review Process

The papers submitted for publication to the Editor undergo an anonymous peer review process, necessary for assessing the quality of scientific information, the relevance to the technical geography field and the publishing requirements of our journal.

The contents are reviewed by two members of the Editorial Board or other reviewers on a simple blind review system. The reviewer's comments for the improvement of the paper will be sent to the corresponding author by the editor. After the author changes the paper according to the comments, the article is published in the next number of the journal.

Eventual paper rejections will have solid arguments, but sending the paper only to receive the comments of the reviewers is discouraged. Authors are notified by e-mail about the status of the submitted articles and the whole process takes about 3-4 months from the date of the article submission.

Indexed by: **CLARIVATE ANALYTICS**
SCOPUS
GEOBASE
EBSCO
SJR
CABELL